frontiers | Research Topics

# Multi-omics technology: revealing the pathogenesis of diseases and the mechanism of drug efficacy of major diseases such as nutritional metabolism disorders and mental disorders

**Edited by**
Wenzhi Hao, Xiliang Du, Tianhao Liu and Gabriel Tao

**Published in**
Frontiers in Pharmacology

ISSN 1664-8714
ISBN 978-2-8325-6186-7
DOI 10.3389/978-2-8325-6186-7

## About Frontiers

Frontiers is more than just an open access publisher of scholarly articles: it is a pioneering approach to the world of academia, radically improving the way scholarly research is managed. The grand vision of Frontiers is a world where all people have an equal opportunity to seek, share and generate knowledge. Frontiers provides immediate and permanent online open access to all its publications, but this alone is not enough to realize our grand goals.

## Frontiers journal series

The Frontiers journal series is a multi-tier and interdisciplinary set of open-access, online journals, promising a paradigm shift from the current review, selection and dissemination processes in academic publishing. All Frontiers journals are driven by researchers for researchers; therefore, they constitute a service to the scholarly community. At the same time, the *Frontiers journal series* operates on a revolutionary invention, the tiered publishing system, initially addressing specific communities of scholars, and gradually climbing up to broader public understanding, thus serving the interests of the lay society, too.

## Dedication to quality

Each Frontiers article is a landmark of the highest quality, thanks to genuinely collaborative interactions between authors and review editors, who include some of the world's best academicians. Research must be certified by peers before entering a stream of knowledge that may eventually reach the public - and shape society; therefore, Frontiers only applies the most rigorous and unbiased reviews. Frontiers revolutionizes research publishing by freely delivering the most outstanding research, evaluated with no bias from both the academic and social point of view. By applying the most advanced information technologies, Frontiers is catapulting scholarly publishing into a new generation.

## What are Frontiers Research Topics?

Frontiers Research Topics are very popular trademarks of the *Frontiers journals series*: they are collections of at least ten articles, all centered on a particular subject. With their unique mix of varied contributions from Original Research to Review Articles, Frontiers Research Topics unify the most influential researchers, the latest key findings and historical advances in a hot research area.

Find out more on how to host your own Frontiers Research Topic or contribute to one as an author by contacting the Frontiers editorial office: frontiersin.org/about/contact

# Multi-omics technology: revealing the pathogenesis of diseases and the mechanism of drug efficacy of major diseases such as nutritional metabolism disorders and mental disorders

**Topic editors**

Wenzhi Hao — Jinan University, China

Xiliang Du — Jilin University, China

Tianhao Liu — Affiliated Hospital of Jiangnan University, China

Gabriel Tao — Merck Sharp & Dohme Corp, United States

**Citation**

Hao, W., Du, X., Liu, T., Tao, G., eds. (2025). *Multi-omics technology: revealing the pathogenesis of diseases and the mechanism of drug efficacy of major diseases such as nutritional metabolism disorders and mental disorders*.

Lausanne: Frontiers Media SA. doi: 10.3389/978-2-8325-6186-7

# Table of contents

frontiers | Frontiers in Pharmacology

TYPE Editorial
PUBLISHED 17 March 2025
DOI 10.3389/fphar.2025.1586223



OPEN ACCESS

EDITED AND REVIEWED BY
José A. G. Agúndez,
University of Extremadura, Spain

*CORRESPONDENCE
Wenzhi Hao,
2523329776@qq.com

RECEIVED 02 March 2025
ACCEPTED 04 March 2025
PUBLISHED 17 March 2025

CITATION
Hao W, Liu T, Du X and Tao G (2025) Editorial: Multi-omics technology: revealing the pathogenesis of diseases and the mechanism of drug efficacy of major diseases such as nutritional metabolism disorders and mental disorders.
*Front. Pharmacol.* 16:1586223.
doi: 10.3389/fphar.2025.1586223



# Editorial: Multi-omics technology: revealing the pathogenesis of diseases and the mechanism of drug efficacy of major diseases such as nutritional metabolism disorders and mental disorders

Wenzhi Hao[1]*, Tianhao Liu[2], Xiliang Du[3] and Gabriel Tao[4]

[1]School of Traditional Chinese Medicine, Jinan University, Guangzhou, China, [2]Affiliated Hospital of Jiangnan University, Wuxi, China, [3]Jilin University, Changchun, China, [4]Merck Sharp & Dohme Corp (United States), West Point, PA, United States

KEYWORDS

**nutritional and metabolic disorders, mental disorders, multi-omics technology, natural products, depression**

Editorial on the Research Topic
Multi-omics technology: revealing the pathogenesis of diseases and the mechanism of drug efficacy of major diseases such as nutritional metabolism disorders and mental disorders

With the changes in the living patterns and dietary patterns of modern people, the incidence of nutritional and metabolic disorders as well as mental disorders is gradually increasing, and the two interact with each other. It is of great significance to explore the pathologic mechanism of nutritional and metabolic disorders as well as mental disorders and to develop drugs to intervene in the pathogenesis for the understanding and clinical treatment of diseases. With the development and progress of science and technology, high-throughput sequencing such as proteomics, metabolomics, transcriptomics, and microbiomics plays an important role in revealing the pathogenesis of diseases and the mechanism of drug efficacy. In fact, multi-omics technology has now become an important tool for understanding the pathogenesis of diseases and elucidating the efficacy mechanisms of drugs. The following discussion will center on the topics of the 9 most recent important research in our area, deepening our understanding of the role of multi-omics technology in understanding the mechanisms of diseases and exploring pharmacological effects.

Gastric cancer is one of the commonest gastrointestinal malignant tumors worldwide, Weizhuan'an prescription is the classic Chinese medicine compound for treatingthe precancerous lesions of gastric cancer. By using 16S rDNA amplicon sequencing, researchers have confirmed that Weizhuan'an prescription can treat rats with PLGC by regulating gastric mucosal microflora and inflammatory factors, providing more references for clinical practice (Lu et al.). Metabolic dysfunction-associated steatotic liver disease (MASLD) is the most common metabolic syndrome and chronic liver disease worldwide, Lingguizhugan

(LGZG) decoction is a classic formula treating various liver diseases such as MASLD. By using serum untargeted metabolomics, gut microbiota, bile acid metabolism, immunohistochemistry, and Western blotting analyses, researchers have found that modulating microbiota–BA–FXR/TGR5 signaling pathway may be a potential mechanism of action of LGZG oral solution for the treatment of MASLD (Wang et al.). Heart failure (HF) is a chronic condition that progressively worsens and continues to be a major financial burden and public health concern. Shenfu injection (SFI) is one of the representative prescriptions of the warming Yang method, and to be applied extensively in the treatment of heart failure with remarkable curative effects. By utilizing a comprehensive methodology, incorporating various techniques such as echocardiography, protein chip detection, histopathology, 16S rDNA sequencing, and metabolomics, the researchers have found that SFI improves ISO-induced heart failure by modulating cometabolism and regulating the TMAO-inflammation axis (Li et al.). Alzheimer's disease (AD) and Parkinson's disease (PD) are the two most common neurodegenerative disorders that have a significant impact on the aging population worldwide. Yangxue oral liquid (YXKFY) is composed of four traditional Chinese medicines. Through a synergistic approach combining transcriptome and proteome analyses with machine learning, the researchers have innovatively identified 17 and 3 hypoxia-associated biomarkers for AD and PD, respectively. Furthermore, they have elucidated the neuroprotective mechanisms of YXKFY, highlighting its antioxidant properties (Chen et al.). High concentrations of nonesterified fatty acids (NEFA) is the key of characteristic of fatty liver in dairy cows. Through the lipidomic approach and molecular biology techniques, the researchers have found that high concentration of NEFA is lipotoxic to cells, promoting lipid accumulation (Fan et al.). Xylene exposure is known to induce toxicity in hematopoietic stem and progenitor cells, leading to bone marrow suppression and potential leukemogenesis. Coniferyl ferulate is a phenolic acid compound abundant in umbelliferae plants with multiple pharmacological activities. By using single-cell RNA sequencing, the researchers have identified CF and Mgst2 as potential therapeutic targets for alleviating xylene-induced hematotoxicity (Yin et al.). Spatial metabolomics is an emerging technology that integrates mass spectrometry imaging (MSI) with metabolomics, offering a novel visual perspective for traditional metabolomics analysis. The researchers have summarized the latest progress and challenges of applying spatial metabolomics to the study of mental disorders and traditional Chinese medicine (Lei et al.). Angelica sinensis, a traditional Chinese herbal medicine and food, which has a long history of clinical application. The researchers have established a theoretical foundation for future studies on the structure, mechanism, and clinical use of Angelica sinensis (Ren et al.). Hypertension is a common disease. By integrating the results of multiple omics studies, the researchers found that the use of TCM to treat hypertension by regulating the intestinal flora is a promising therapeutic strategy (Chen et al.).

Existing evidence suggests that the multi-omics technology has now become an important tool for understanding the pathogenesis of diseases and elucidating the efficacy mechanisms of drugs. Our research theme mainly reveals that multi-omics technology has been widely used to explore the pathological mechanism of nutritional and metabolic disorders and mental disorders, and explore the therapeutic mechanism of TCM compound or monomer natural active ingredients for diseases. In summary, the studies discussed in this Research Topic highlight the important role of the multi-omics technology in various health conditions and the potential for TCM to modulate nutritional and metabolic disorders as well as mental disorders for therapeutic purposes.

## Author contributions

WH: Writing–original draft, Writing–review and editing. TL: Conceptualization, Writing–review and editing. XD: Writing–review and editing. GT: Writing–review and editing.

## Funding

The author(s) declare that financial support was received for the research and/or publication of this article. This work was supported by the National Natural Science Foundation of China (No. 82405240), Postdoctoral Fellowship Program of CPSF under Grant Number GZB20230269, China Postdoctoral Science Foundation (No. 2023M741396), Guangdong Basic and Applied Basic Research Foundation (No. 2023A1515110693; No. 2025A04J3396), the Fundamental Research Funds for the Central Universities (21624358).

## Conflict of interest

Author GT was employed by Merck Sharp & Dohme Corp (United States).

The remaining authors declare that the research was conducted in the absence of any commercial or financial relationships that could be construed as a potential conflict of interest.

## Generative AI statement

The author(s) declare that no Generative AI was used in the creation of this manuscript.

## Publisher's note

frontiers | Frontiers in Pharmacology

TYPE Original Research
PUBLISHED 28 February 2024
DOI 10.3389/fphar.2024.1372296



OPEN ACCESS

EDITED BY
Xiliang Du,
Jilin University, China

REVIEWED BY
Zhenbiao Zhang,
Shanxi Agricultural University, China
Qiao Li,
Nanjing Agricultural University, China

*CORRESPONDENCE
Kangfeng Jiang,
kangfengjiang@ynau.edu.cn
Xiaobing Li,
xiaobingli@yeah.net

RECEIVED 17 January 2024
ACCEPTED 08 February 2024
PUBLISHED 28 February 2024

CITATION
Fan X, Xu J, Hu Y, Wang K, Zhao Y, Cai J, Zhang X, Pan B, Xu A, Chen Y, Liu S, Jiang K and Li X (2024), Effect of high NEFA concentration on lipid metabolism disorders in hepatocytes based on lipidomics.
*Front. Pharmacol.* 15:1372296.
doi: 10.3389/fphar.2024.1372296



# Effect of high NEFA concentration on lipid metabolism disorders in hepatocytes based on lipidomics

Xinyi Fan, Jie Xu, Yuan Hu, Kui Wang, Yiyi Zhao, Jinyin Cai, Xinyuan Zhang, Binghai Pan, Anqi Xu, Yajing Chen, Songhao Liu, Kangfeng Jiang* and Xiaobing Li*

College of Veterinary Medicine, Yunnan Agricultural University, Kunming, Yunnan, China

**Introduction:** High concentrations of nonesterified fatty acids (NEFA) is the key of characteristic of fatty liver in dairy cows. Therefore, the aim of this study was to investigate the effect of high concentration of NEFA on lipid metabolism in hepatocytes through the lipidomic approach and molecular biology techniques.

**Methods:** Stimulate AML-12 cells with different concentrations of NEFA, observe the cellular lipid accumulation, and select 0.6 mM NEFA stimulation concentration for subsequent experiments. Collect cells for lipidomics analysis.

**Results:** High concentration of NEFA (0.6–2.4 mM) significantly reduced the cell viability in a concentration-dependent manner, indicating that high concentrations of NEFA have lipotoxicity on hepatocytes. In addition, NEFA promoted triglycerides (TAG) accumulation, increased the mRNA expression of the lipogenic molecules SREBP1c and FASN, and decreased the mRNA expression of lipolytic molecules CPT1A and HSL in hepatocytes. Mechanistically, high concentration of NEFA induced lipid metabolism disorders in hepatocytes by regulating metabolic pathways such as glycerol phospholipid metabolism, glycosyl phosphatidylinositol anchored biosynthesis, triglyceride metabolism, sphingolipid metabolism, and inositol phosphate metabolism.

**Discussion:** High concentration of NEFA is lipotoxic to cells, promoting lipid accumulation. LPE (18:2), LPE (18:3), LPE (18:1) via glycerophospholipid metabolism, glycosylphosphatidylinositol (GPI)-anchor biosynthesis, glycerolipid metabolism, sphingolipid metabolism, and inositol phosphate metabolism, indicating their potential regulation role in the pathogenesis of fatty liver.

KEYWORDS

**fatty liver, nonesterified fatty acids, lipid metabolism disorders, lipidomics, diary cow**

## 1 Introduction

Fatty liver is a metabolic disorder that affects dairy cows during the periparturient period, characterized by the accumulation of excess lipids in the liver due to an imbalance between lipid intake and oxidation (Bobe et al., 2004). In the perinatal period, the dietary intake of dairy cows is inadequate to meet the energy demands necessary for lactation, leading to a negative energy balance (NEB) (Herdt, 2000). During NEB, TAG are mobilized from adipose stores (Dole, 1956; Drackley et al., 1991) and then hydrolyzed into NEFA and glycerol (Locher et al., 2011). The released NEFA can be utilized for energy production and fat synthesis (Adewuyi et al., 2005). However, the hepatic uptake of NEFA during NEB

exceeds its oxidative capacity, resulting in hepatic lipid accumulation and the development of fatty liver (Roberts et al., 1981; Reynolds et al., 2003; Martens, 2023).

In recent years, multiple studies have demonstrated the involvement of the sterol regulatory element-binding transcription factor (SREBF-1c) in modulating triglyceride and cholesterol levels (Guo et al., 2014; Vargas-Alarcon et al., 2019). SREBF-1c regulates the expression of genes involved in the biosynthesis of fatty acids, phospholipids, and triglycerides (Shimano et al., 1997). SREBP-1c is a transcription factor important in the regulation of lipogenic genes (Yang et al., 2001), and its downstream target FASN is a key enzyme in *de novo* fatty acid synthesis (Horton et al., 2002; Rodríguez-Cruz et al., 2012; Chen et al., 2018). Hormone-sensitive lipase (HSL) is the major rate-determining enzyme in fat cell lipolysis (Fredrikson et al., 1981). CPT1A plays an important role in using fatty acids as an energy source (Patsoukis et al., 2015). CAPT1A and HSL are commonly utilized as representative genes for assessing lipid levels through lipolysis (Hu et al., 2020; Tardelli et al., 2020; Oh et al., 2021). The study chose to investigate the expression of the well-known genes SREBP-1 and FASN involved in lipid synthesis, as well as the genes CAPT1A and HSL related to lipid decomposition, to evaluate lipid accumulation.

Lipids are a group of molecules with various important cellular functions, including energy storage, signaling, and serving as essential components of cellular membranes (Orešič et al., 2008). The alteration of lipid metabolism represents a crucial step in the development and progression of fatty liver disease (Onorato et al., 2021). Among other techniques, recent advancements in mass spectrometry have introduced lipidomics into translational medicine and research (Ma and Fernández, 2022; Salvador et al., 2022). Lipidomics is an emerging and effective method for studying intact lipids in biological systems, which contributes to comprehensively understand the biochemical mechanism of lipid metabolism (Long et al., 2020). Lipidomics relies heavily on analytical chemistry tools, techniques, and principles to analyze lipid structure, abundance of individual molecular species, as well as their cellular functions and interactions. This comprehensive approach enables the identification of dynamic changes in lipids during cellular perturbations. Therefore, lipidomics plays a crucial role in elucidating the pathogenesis of lipid-related diseases such as fatty liver, by detecting and quantifying alterations in cellular lipid signaling, metabolism, transport, and homeostasis (Han and Gross, 2021). Consequently, studying lipid homeostasis is essential for a comprehensive understanding of the pathogenesis of fatty liver.

An increasing number of studies indicate a close relationship between NEFA and lipid metabolism disorders in hepatocytes (Rukkwamsuk et al., 1999; Li et al., 2012; White, 2015). However, the specific mechanism by which NEFA affects lipid metabolism disorders in hepatocytes remains unclear.

# 2 Materials and methods

## 2.1 Cell culture

The AML-12 cell line was acquired from the Cell Bank of the Chinese Academy of Sciences. The cells were cultured in F12 medium (Gibco) supplemented with 10% fetal bovine serum, 1% ITS (Gibco), and 1% dexamethasone. Culturing of cells was routinely performed in a humidified atmosphere at 37°C with 5% $CO_2$.

## 2.2 Cell viability assay

AML-12 cells ($10^4$ cells/well) were seeded into 96-well plates and then exposed to varying concentrations of NEFA (0, 0.3, 0.6, 1.2, 2.4 mM) for 12 h. Cell viability was assessed using the CCK8 analysis kit (Bioss). Subsequently, 10 μL of CCK-8 solution was added to each well, followed by incubation for 4 h, and the optical density (OD) was measured at 450 nm using a microplate reader.

## 2.3 TAG content assay

AML-12 cells were stimulated with NEFA for 12 h. The stimulated cells were collected and rinsed three times in PBS. The cell lysate was incubated on a shaker at room temperature for 20 min, followed by collection of the cells using a scraper and transfer to a centrifuge for ultrasonic pulverization. Subsequently, reagents were added according to the manufacturer's instructions (NJJCBIO), and measured 450 nm OD of each well using microplate reader. The protein concentration of each sample was determined using BCA, and the total amount of triglycerides was calculated based on the protein concentration of each well.

## 2.4 Lipid metabolism

### 2.4.1 Chemicals and reagent

The mass spectrometry-pure acetonitrile, isopropanol, and chromatography-pure ammonium acetate used in this experiment were purchased from Thermo-Fisher Scientific (FairLawn, NJ, USA). Ultrapure water for the experiments was obtained from Millipore Reference Ultrapure Water System 92 (Billerica, MA, USA) which equipped with a 0.22 μm filter head for liquid-quantity coupling.

### 2.4.2 Sample preparation

To minimize degradation, samples were thawed under an ice bath. Ten grinding beads were added to each tube of cell samples with 10 μL of deionized water and homogenize for 3 min (BB24, Next Advance, Inc, NY, USA). 300 μL of lipid extraction solvent was added and homogenized again for 3 min. The samples were vortexed and mixed at 1,200 rpm for 20 min at 10°C (MSC-100, Allsheng Instruments, Co. Hangzhou, China), and then centrifuged at 4,000 *g* for 20 min at 4°C (Allegra X-15R, Beckman Coulter, Inc, IN, USA), 20 μL of supernatant was transferred to a 96-well plate and mixed with 80 μL of lipid dilution solvent for LC-MS analysis.

### 2.4.3 Instrumentation

This project utilized an Ultra High Performance Liquid Chromatography-Triple Quadrupole Mass Spectrometry (UPLC-TQMS) instrument (TACQUITY UPLCXevo TQ- S, Waters

Corp. Milford, MA, USA) for targeted lipidomic assays. System optimization and maintenance were performed every 48 h.

#### 2.4.4 Analytical quality control procedures

Endogenous small molecule metabolites are susceptible to changes in ambient temperature and environment, and therefore, sample thawing requires that it be performed slowly on an ice bath slowly, thus avoiding changes in metabolite composition and concentration caused by activation of metabolic enzymes after the sample is sharply returned to room temperature. The reagents used for extraction were pre-frozen and stored in an ice bath. The reagents used for extraction were pre-frozen and stored in a −20°C refrigerator to avoid the exothermic addition of organic solvents to the precipitated proteins, which can lead to the degradation of small molecule metabolites in biological samples. The entire sample preparation process should be completed as quickly as possible. There were reagent blanks and mixed QC samples before and after analyzing each batch of samples. These QCs were also added to monitor the analytical process for possible contamination and data quality.

#### 2.4.5 Sample run order

In order to eliminate errors caused by the order of the analytical process, the samples to be tested were randomized according to the group information, and QC samples, blanks, etc. were interspersed with the overall samples for testing. QC samples, blank samples were interspersed in the overall sample for testing.

#### 2.4.6 Sample control procedure

Samples for each project were entered into Metabo-Profile's LIMS management system upon receipt. The system assigned a unique identifier, MP ID, that matches the original sample information. This identification was tracked throughout the experiment.

#### 2.4.7 Data analysis

Mass spectrometry-based quantitative metabolomics works by comparing metabolites in a sample of unknown concentration to a set of standard samples of known concentration (quantitative curve) to obtain the actual concentration. A quantitative curve is a curve that analyzes the signal as it varies with the concentration of the measured substance (DUT). For most analyses, a plot of instrument response *versus* concentration will show a linear relationship. This will produce a regression equation of $y = aX + b$ where y is the instrument's corresponding (peak height or peak area), a represents the slope/sensitivity, and b is a constant representing the background signal. The analyte in the unknown sample concentration (X) is calculated from this equation.

### 2.5 Statistical analysis

Data are expressed as mean ± standard error of mean (S.E.M) of each group. Data are expressed as mean ± standard error of mean (S.E.M) for each group. Two-tailed unpaired Student's t-test was used for comparisons between the two groups, and one-way ANOVA was used to compare the data for CCK8. All statistical analyses were performed using Graphpad Prism 6.0 software (GraphPad software, CA, USA).

## 3 Results

### 3.1 NEFA reduces the viability of hepatocytes in a concentration-dependent manner

In this study, we investigated the toxic effect of NEFA on hepatocytes. The effect of different concentrations (0.3, 0.6, 1.2, 2.4 mM) of NEFA on cell viability was assessed using the CCK-8 assay kit. As shown in Figure 1A, compared with the control group, there was no significant change in cell viability in the 0.3 mM NEFA treatment group. However, the cell viability was significantly decreased after treatment with 0.6 mM NEFA ($p < 0.001$), 1.2 mM NEFA ($p < 0.0001$), and 2.4 mM NEFA ($p < 0.0001$), with 2.4 mM NEFA causing excessive cell damage and reducing cell viability to below 20%. The results revealed that NFEA reduces the cell viability in a concentration-dependent manner.

### 3.2 NEFA promotes lipid accumulation in hepatocytes

The effect of NEFA on lipid accumulation in hepatocytes was analyzed in this study by measuring the TAG contentin cells. As shown in Figure 1B, the TAG content in the 0.3 mM NEFA treatment group did not exhibit a significant change compared to the control group. In contrast, the TAG content was significantly increased in the 0.6 mM ($p < 0.05$) and 1.2 mM ($p < 0.001$) NEFA treatment groups compared to the control group. The oil red O staining results also demonstrated that high concentrations of NEFA promote lipid accumulation (Figure 1C).

Consequently, based on the results of CCK-8 and TAG content detection, we chose to employ 0.6 mM NEFA for subsequent experiments.

### 3.3 Effect of NEFA on molecules of lipid metabolism

To further investigate the effect of NEFA on lipid accumulation, this study examined the mRNA expression of key molecules involved in cellular lipid metabolism. Compared with the control group, NEFA treatment significantly increased the expression of lipid synthesis-related molecules FASN and SREBP, and significantly decreased the expression of lipolytic molecules HSL and CPT1A (Figure 2).

In summary, NEFA promotes lipid accumulation in AML-12 cells by regulating lipid metabolism-related molecules.

### 3.4 Exploring the effects of high concentration of NEFA on hepatocytes based on lipidomics

Based on the experimental results presented above, it is evident that high concentration of NEFA can impact the lipid metabolism in hepatocytes, leading to the inhibition of lipolysis and the promotion of lipid accumulation. However, the specific lipid metabolites and

10.3389/fphar.2024.1372296

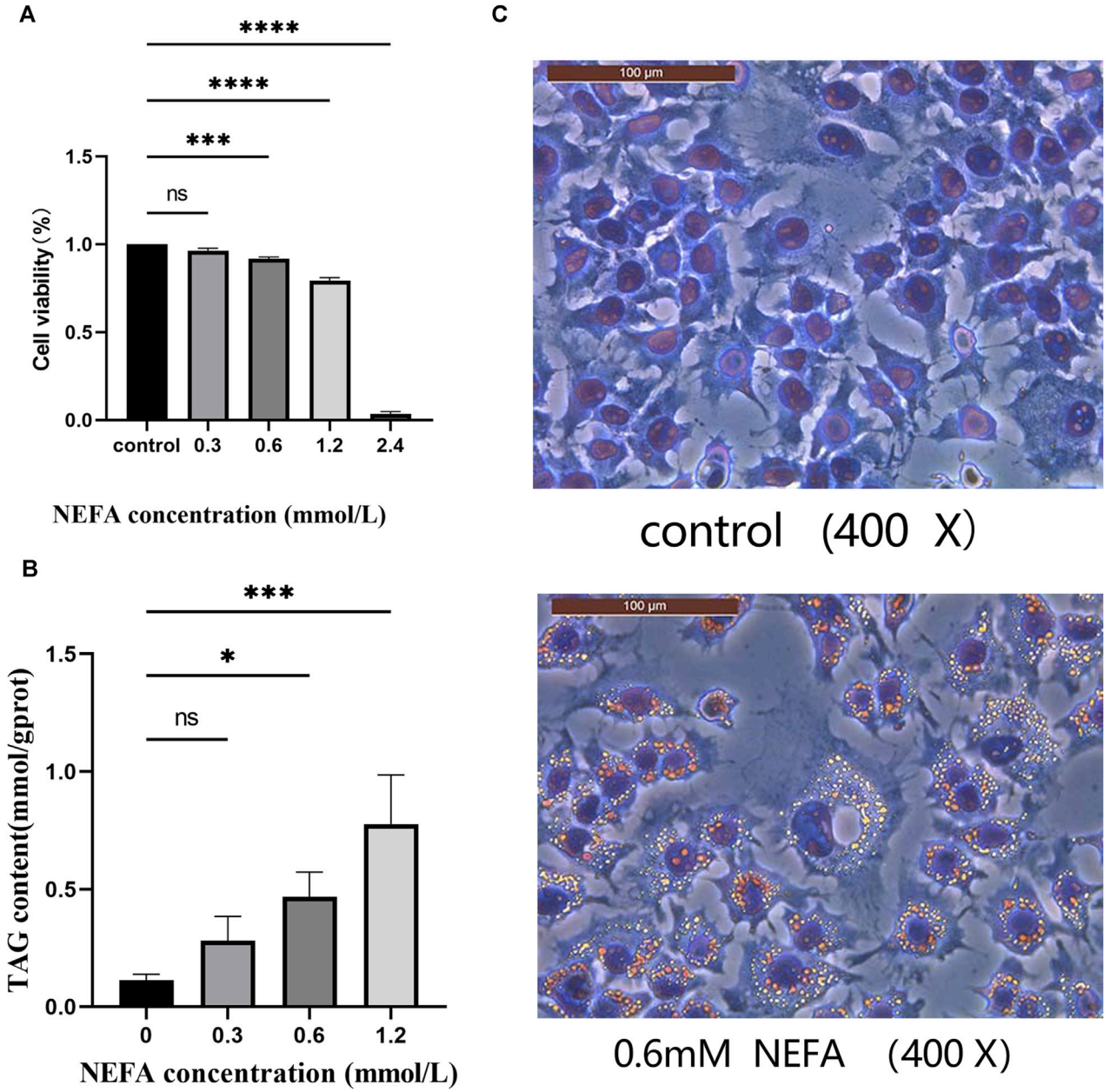


FIGURE 1
Effect of non-esterified fatty acids (NEFA) on cell viability. **(A)** The cells were treated with different concentrations of NEFA for 12 h, and the cell viability was detected using the CCK8 kit. **(B)** Effects of various concentrations of non-esterified fatty acids (NEFA) on the triglyceride (TAG) content in hepatocytes. **(C)** Oil Red O staining. Data are expressed as the mean ± SEM. *$p < 0.05$, **$p < 0.01$, ***$p < 0.001$, ****$p < 0.0001$.

metabolic pathways responsible for the disruption of liver cell lipid metabolism induced by high concentration of NEFA remain unclear. Hence, this study employed lipidomics to further elucidate the mechanism underlying the effect of NEFA on the lipid metabolism disorder in hepatocytes.

### 3.4.1 QC and total sample principal component analysis

Before analyzing the sample data, a portion of the extracted material from 12 test samples was taken to prepare quality control (QC) samples for the subsequent calibration analysis. Multivariate quality control charts were utilized to supervise and judge whether the instrument's fluctuations are within the normal range. Figure 3A illustrates that the fluctuation of the QC sample was within the range of plus or minus 3 standard deviations, indicating that the instrument's fluctuations were within the normal range and the data can be used for subsequent analysis. Additionally, as depicted in Figure 3B, Pearson correlation analysis of the QC samples was conducted. A correlation coefficient greater than 0.9 generally indicated good correlation. The experimental

10.3389/fphar.2024.1372296

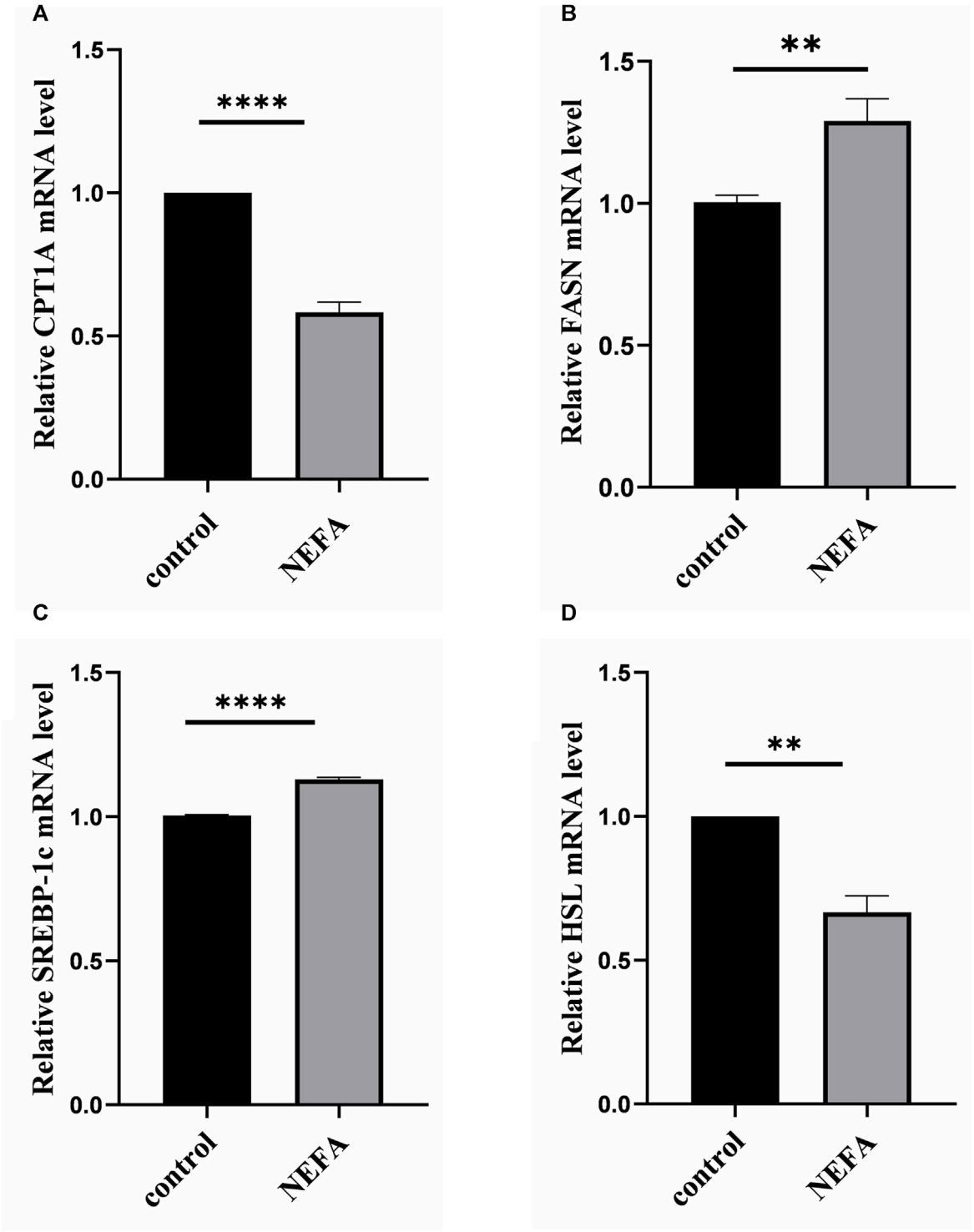


FIGURE 2
Effects of high NEFA concentration on mRNA expression levels of lipid metabolism-related molecules in hepatocytes. **(A)** CPT1A: carnitine palmitoyltransferase 1 A. **(B)** FASN: Fatty acid synthase. **(C)** SREBP-1c: sterol regulatory element binding protein-1c. **(D)** HSL: hormone sensitive lipase. Data are expressed as the mean ± SEM. $*p < 0.05$, $**p < 0.01$, $***p < 0.001$.

results demonstrate that the correlation coefficients between the QC samples are all above 0.9, indicating good experimental repeatability. Furthermore, Figure 3C showed the scores of principal component analysis with QC. The QC samples were closely clustered in the graph, signifying a high degree of clustering and suggesting good stability in instrument detection. Therefore, the data of this model was stable and reliable, and can proceed to the next step of statistical analysis.

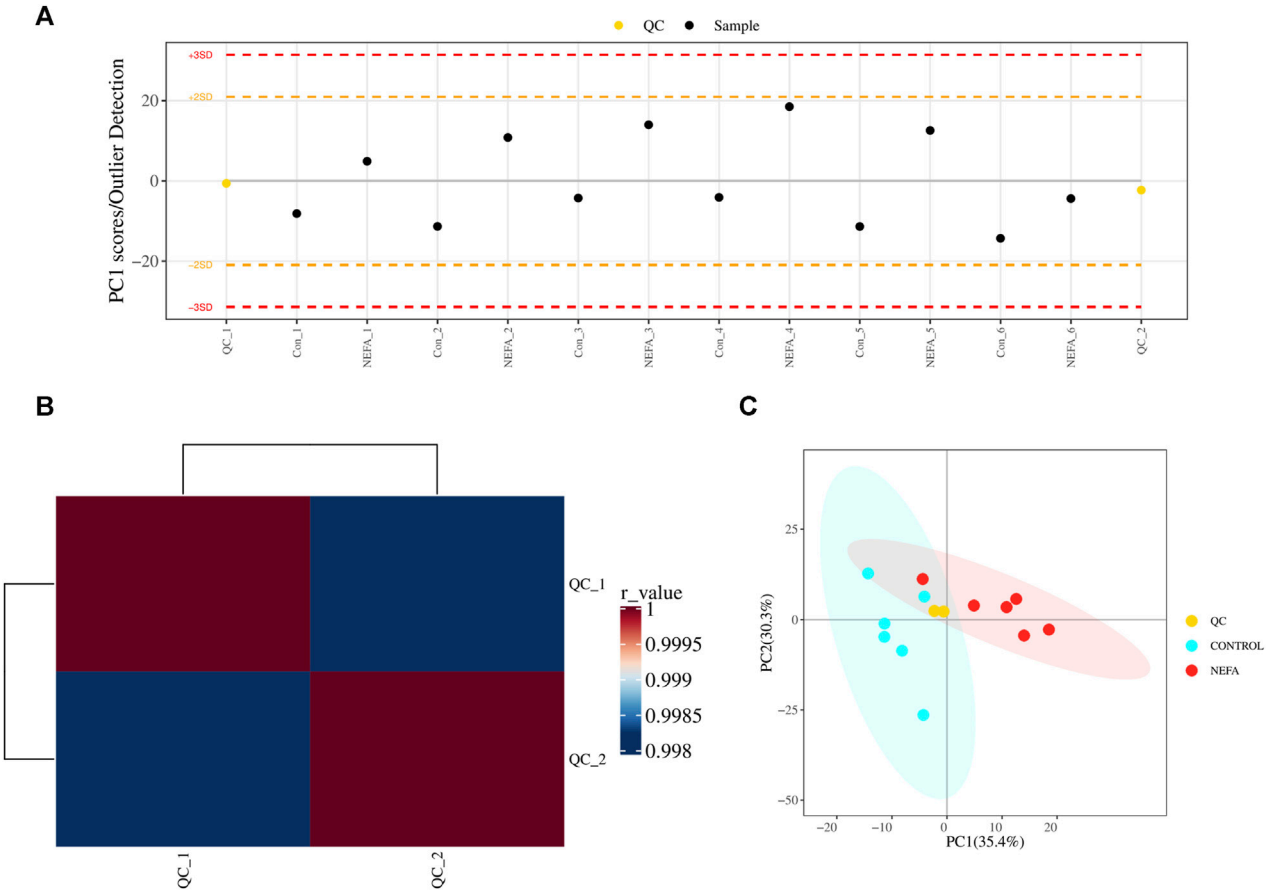


FIGURE 3
QC and total sample principal component analysis. **(A)** Multivariate control chart: Each point in the chart represents a sample, and any points that exceed three times the standard deviation are considered outliers. **(B)** Pearson correlation analysis: The closer the r-value is to 1, the closer the similarity between the QC samples. **(C)** PCA analysis with QC samples.

### 3.4.2 Lipid composition analysis

After using mass spectrometry to detect the lipids in the samples, a total of 310 metabolites were obtained. These lipid molecules were further analyzed and categorized into 11 subclasses. As shown in Figure 4A, there are 79 types of Phosphatidylcholine (PC), accounting for 25.48% of the total amount of lipid molecules, 46 types of Phosphatidylethanolamine (PE) accounting for 14.84%, 38 types of Triacylglycerol (TAG) accounting for 12.26%, 29 types of Sphingomyelin (SM) accounting for 9.35%, 27 types of Ceramide (Cer) accounting for 8.71%, 23 types of Phosphatidylserine (PS) accounting for 7.42%, 21 types of Diacylglycerol (DAG) accounting for 6.77%, 18 types of lysoPhosphatidylcholine (LPC) accounting for 5.81%, 14 types of Phosphatidylinositol (PI) accounting for 4.52%, 12 types of lysoPhosphatidylethanolamine (LPE) accounting for 3.87%, and the remaining three types of other lipids accounting for 0.97%.

The relative abundance of various metabolites in each sample was shown in Figure 4B. The average abundance of various metabolites in the NEFA group was shown in Figure 4B, with Cer accounting for 45.08%, PE accounting for 41.78%, and DAG and TAG accounting for 6.88% and 3.33% respectively. All quantified lipids in the same group were summed to observe the differences in lipid molecular content among different groups of samples. As shown in Figure 4C, DAG and LPC were significant increase in relative abundance ($p < 0.01$). LPE and CerPE were significant decrease in relative abundance ($p < 0.001$).

### 3.4.3 Orthogonal partial least squares discriminant analysis

The PCA model may not be sensitive to variables with low correlations, rendering it unsuitable for identifying differential metabolites. However, this limitation can be addressed by employing OPLS-DA analysis. As illustrated in Figure 5A, the data from the two groups exhibit a clear separation trend, indicating substantial differences between the control and NEFA samples. The OPLS-DA model was validated using Permutation testing. A value of $R^2Y$ closer to 1 indicates higher model performance, while a $Q^2$ value greater than 0.5 signifies model effectiveness. In this case, R2Y was determined as 0.9333 and $Q^2$ as 0.76, confirming the validity of the model as illustrated in Figure 5B.

### 3.4.4 Significant difference lipid metabolite screening

Based on the OPLS-DA model results, volcano plot was used to screen reliable metabolite markers. The volcano plot comprehensively

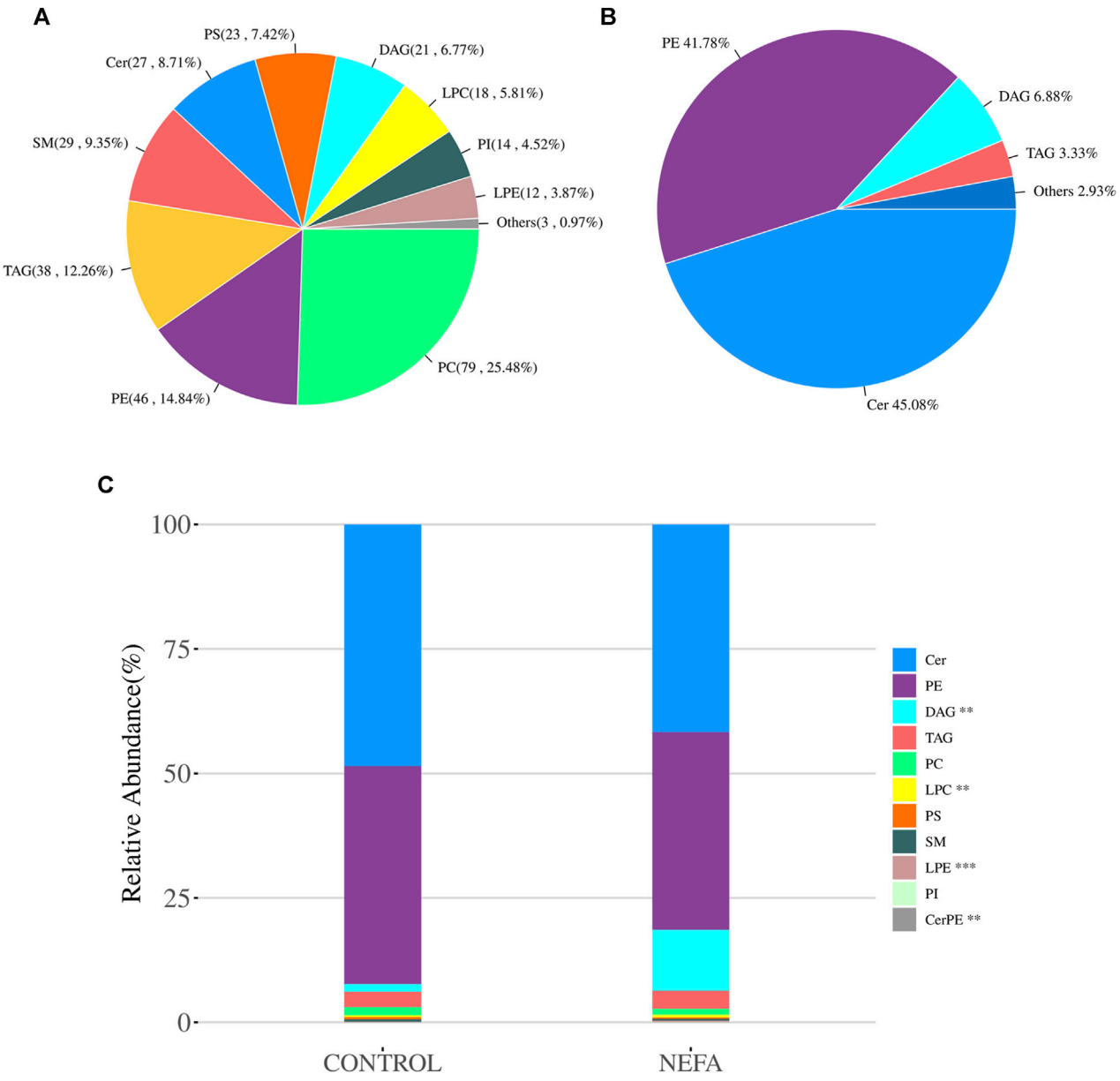


FIGURE 4
Quality control and principal component analysis of total samples and quantitative analysis of lipidomics. **(A)** Pie chart of average abundency composition of various metabolites in all samples. **(B)** Pie chart of the average abundance composition ratio of each metabolite class in all samples in the NEFA group. **(C)** Stacked bar chart of relative abundance of various metabolites in each group of samples.

investigated the contribution of metabolites to model grouping (Variable importance in projection, VIP) and the reliability of metabolites (Correlation Coefficients) (Figure 5C). The volcano plot effectively illustrates the distribution and content disparities of metabolites across the samples. Larger absolute values on the horizontal axis indicate greater differences in expression levels between the two sample groups, while larger values on the vertical axis signify more pronounced differences, thus affirming the stability and reliability of the obtained differential lipid metabolites. Using a significance level of $p < 0.05$ and an absolute value of log2FC ≥ 0 (FC, Fold Change) as the threshold for screening differential metabolites, 116 metabolites were identified in the comparison between control and NEFA (Figure 5D). Figure 5D reveals that out of the 116 identified metabolites, 83 are upregulated and 33 are downregulated. Boxplot of top 9 differential metabolites ordered by *p*-value were shown in Figure 5E. These metabolites encompass 21 types of DAG, 27 types of Cer, 17 types of PE, 4 types of PS, 12 types of LPE, 18 types of LPC, 79 types of PC, 29 types of PE, 3 types of CerPE, 14 types of PI, 19 types of PS, 29 types of SM, and 38 types of TAG.

Applying dual criteria (*t*-test $p < 0.05$, |Log2FC|≥0, and OPLS-DA analysis VIP≥1), the selection of potential biomarkers with potential biological significance by combining the different metabolites obtained above is the most reliable approach. This diagram reveals 107 common different metabolites between the

10.3389/fphar.2024.1372296

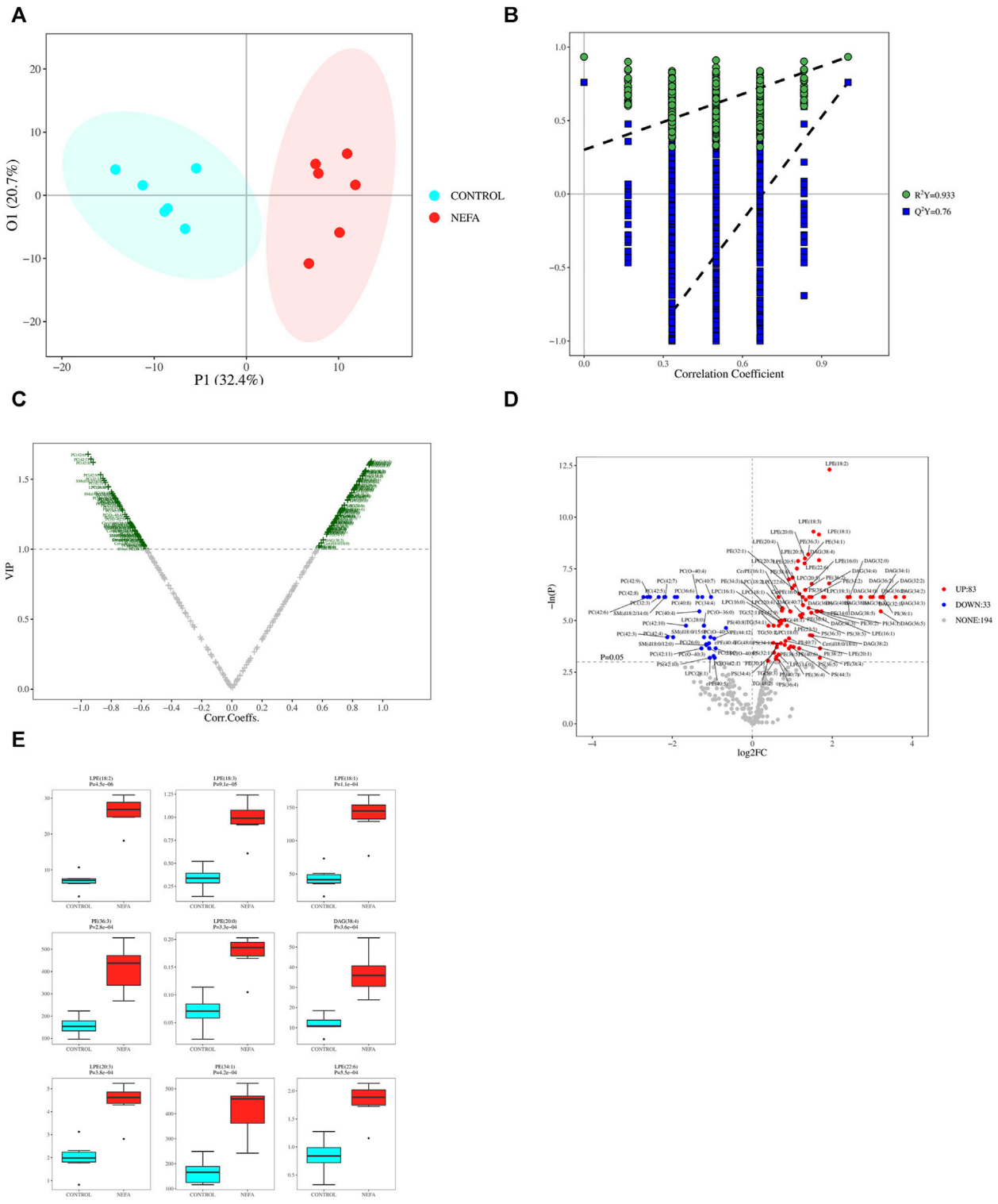


FIGURE 5
**(A)** OPLS-DA 2D Score Chart. **(B)** OPLS-DA 2D Permutation test Result. **(C)** Metabolite VIP volcano map of OPLS-DA. **(D)** One-dimensional road map of a volcano: Compared to the CONTROL group, the highlighted metabolites in the top right increased in the NEFA group, while the highlighted metabolites in the top left decreased in the NEFA group. **(E)** Boxplot of top 9 differential metabolites ordered by *p*-value.

two groups, and their distribution in different samples is illustrated in the Figure 6A. Among the 107 potential biomarkers, 77 are upregulated and 30 are downregulated. The boxplot in Figure 6B highlights the 9 most significantly different metabolites: LPE (18:2), LPE (18:3), LPE (18:1), PE (36:3), LPE (20:0), DAG (38:4), LPE (20:3), PE (34:1), LPE (22:6).

Using the selected mmu library for pathway enrichment analysis of differential metabolites, the results were shown in Figure 6C. The

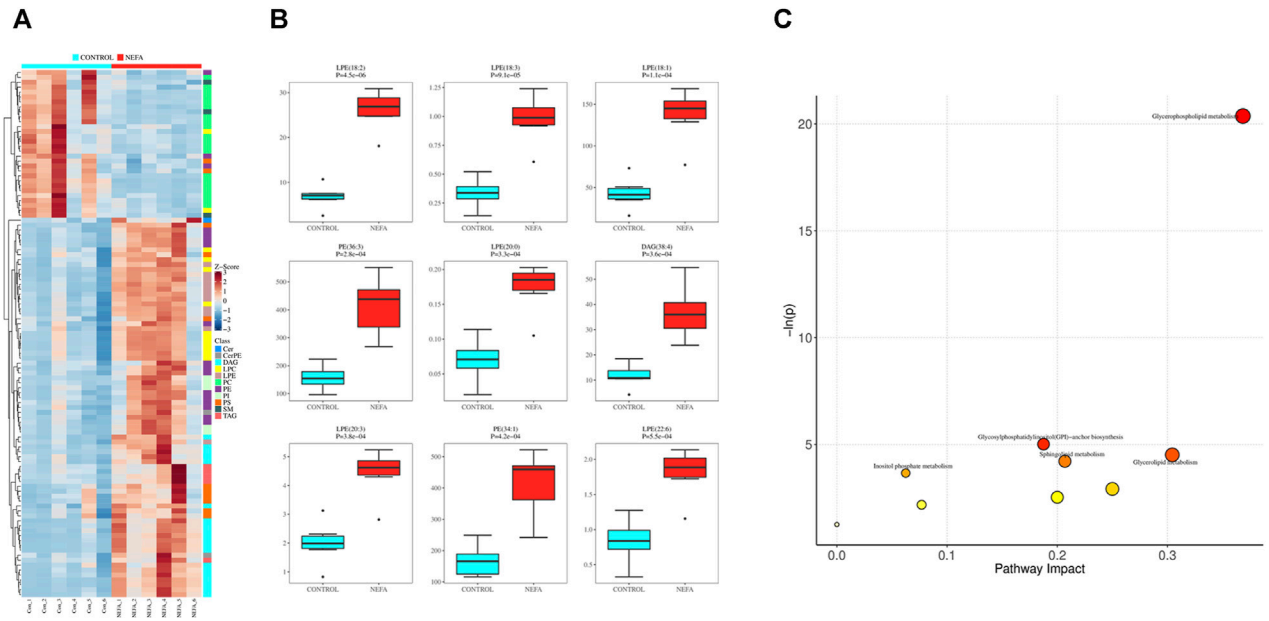


FIGURE 6
Potential biomarkers and their enrichment pathways. **(A)** Heat map of potential biomarkers. **(B)** Box diagram of potential biomarkers. **(C)** mmu library pathway analysis bubble diagram.

differential metabolites enriched in these metabolic pathways are shown in Supplementary Table S1. Each bubble in Figure 6C represented a pathway. The redder the bubble, the closer the *p*-value is to 0, indicating more significant enrichment. The larger the bubble, the more differential lipid metabolites are enriched in that pathway. There were 5 differential metabolic pathways related to lipid metabolism involved in the disordered lipid metabolism process induced by high concentration of NEFA in liver cells, including glycerophospholipid metabolism, glycosylphosphatidylinositol (GPI) -anchor biosynthesis, triglyceride metabolism, sphingolipid metabolism, and inositol phosphate metabolism.

## 4 Discussion

The liver serves as the central organ for lipid metabolism, responsible for regulating the equilibrium of lipids, proteins, and carbohydrates (Mun et al., 2019). In the pathogenesis of fatty liver, the excessive mobilization of adipose tissue due to negative energy balance results in a substantial influx of NEFA into the liver. However, the liver is unable to metabolize excessive NEFA, resulting in its esterification into triglycerides, which then accumulate in the liver (Grummer, 1993; González et al., 2011). This highlights that the disorder in lipid metabolism is the core of fatty liver disease in dairy cows, and numerous studies have been carried out to investigate this phenomenon (Grummer, 1993; Wang et al., 2018; Zhao et al., 2023). Furthermore, the high concentration of NEFA is closely associated with the disorder in lipid metabolism. In healthy cows, the serum NEFA content is lower than 0.4 mM, but the serum NEFA concentration gradually increases to more than 0.5 mM in parturient cows due to metabolic disorders and negative energy balance leading to extensive catabolism of body fat. In cases of particularly severe negative energy balance, the serum NEFA concentration can exceed 1.5 mM (Samiei et al., 2010). Previous research by Dong et al. has revealed that elevated levels of NEFA can stimulate lipid synthesis in the liver, suppress lipolysis, activate inflammatory signaling pathways, and consequently contribute to hepatic lipid accumulation and the initiation of an inflammatory response in cows with fatty liver (Dong et al., 2019). Huang and others discovered that NEFA play a role in mediating the PERK-eIF2α signaling pathway, leading to the upregulation of the key transcription factor SREBP-1c involved in lipid synthesis. This process ultimately promotes lipid synthesis in bovine liver cells. Consequently, their findings indicate that elevated levels of NEFA can impact lipid metabolism in liver cells, contributing to the accumulation of lipids (Huang et al., 2021). The findings of this study suggest that high concentrations of NEFA have the potential to affect the lipid metabolism in liver cells, resulting in lipid accumulation in the cells. Thus, the study seeks to investigate the influence of NEFA on lipid accumulation in liver cells. The results of the cell viability experiment demonstrated that NEFA can significantly decrease cell viability in a concentration-dependent manner. While the cell viability in the 0.3 mM NEFA treatment group did not exhibit significant changes compared to the control group, the cell viability significantly decreased after treatment with 0.6, 1.2, and 2.4 mM NEFA. Notably, treatment with 2.4 mM NEFA resulted in excessive cell damage and significantly reduced cell viability. This suggests that high concentrations of NEFA have the potential to disrupt normal cell metabolism.

Fatty liver in cows is characterized by the significant accumulation of TAG in the liver (Pralle et al., 2021), leading to

a substantial impact on its metabolic function (Grummer, 1993). In this study, the TAG content in liver cells from the experimental group (0.6 mM NEFA) showed a significant increase compared to the control group. Zhao (Yang et al., 2023) stimulated primary calf liver cells with 1.2 mM NEFA for 12 h and observed that there was a significant increase in the mRNA expression levels of SREBP-1c, FAS, and ACC1, along with a notable increase in TAG content and lipid droplet content. These results are consistent with our present study, confirming that a high concentration of NEFA can stimulate lipid accumulation in liver cells. However, it is important to note that the aforementioned study employed 1.2 mM NEFA to stimulate primary calf liver cells, whereas our study utilized 0.6 mM NEFA to stimulate AML-12 cells. As different cell types exhibit different tolerances to NEFA stimulation, the final concentration used for stimulation in our study was different from that used in other studies. Furthermore, existing literature (Simino et al., 2021) discusses the *in vitro* model of fatty liver induced by NEFA in AML-12 cells, which supports the credibility of our study.

From the perspective of lipidomics, it is evident that high levels of NEFA are involved in the differential metabolism of lipids in hepatic cells. Moreover, pathway enrichment analysis can help identify differential metabolic pathways, thus elucidating the mechanism by which high levels of NEFA affect lipid metabolism in hepatic cells. This study employed multidimensional and univariate statistical analyses to identify 107 potential biomarkers, a large proportion of which were upregulated lipid metabolites. This suggests that an increase in NEFA level can disrupt lipid metabolism, leading to lipid deposition and lipid metabolism disorders in fatty liver in dairy cows. The most significant differential metabolites encompassed 9 types, primarily belonging to the lipid subclasses of lysophosphatidylethanolamine (LPE), phosphatidylethanolamine (PE), and diacylglycerol (DAG).

By inputting the information of 107 potential biomarkers into the database for further analysis, we obtained 5 different metabolic pathways related to lipid metabolism, including glycerophospholipid metabolism, glycosylphosphatidylinositol (GPI)-anchor biosynthesis, glycerolipid metabolism, sphingolipid metabolism, and inositol phosphate metabolism. The analysis of these metabolic pathways indicates that high level of NEFA may lead to lipid metabolism disorders in liver cells through five differential metabolic pathways. However, the detailed process by which high level of NEFA affect lipid metabolism through these metabolic pathways requires further research. The glycerophospholipid metabolism pathway is significantly involved in the pathogenesis of fatty liver disease. Phosphatidylcholine is the most abundant phospholipid in the body and is an important component of biological membranes, participating in the recognition and signal transduction of membrane proteins. Phosphatidylcholine metabolism is one of the most important components in maintaining the homeostasis of the body (Zhao et al., 2021). The crucial role of phospholipid metabolism in regulating lipid, lipoprotein, and systemic energy metabolism has been extensively proven (Li et al., 2006; Jacobs et al., 2008; Niebergall et al., 2011). The findings of the experiment further confirm the pivotal role of the glycerophospholipid metabolic pathway in the development of fatty liver. Therefore, the targeting of glycerophospholipid metabolism pathway can serve as a potential strategy for managing fatty liver.

In addition, the differences in the metabolism of sphingolipids, glycerides, inositol phosphate, and glycosylphosphatidylinositol anchoring biosynthesis between the 2 cell groups are also very significant. Sphingolipids are a type of lipid that was initially thought to be essential component of organelles and cell membranes. Research has shown that sphingolipid molecules also have biological activities and can participate in the signal transduction of key physiological processes such as cell growth, differentiation, proliferation, migration, and apoptosis (Maceyka and Spiegel, 2014). Therefore, NEFA may affect lipid metabolism disorder through the glycerophospholipid metabolism pathway.

## 5 Conclusion

Therefore, this study aimed to establish an *in vitro* model of fatty liver using NEFA and focus on lipidomics research to identify differential lipid metabolites involved in the pathogenesis of fatty liver.

The results showed that high concentration of NEFA is lipotoxic to cells, promoting lipid accumulation. Further, lipidomics reveals potential metabolites regulated by NEFA LPE (18:2), LPE (18:3), LPE (18:1) via glycerophospholipid metabolism, glycosylphosphatidylinositol (GPI)-anchor biosynthesis, glycerolipid metabolism, sphingolipid metabolism, and inositol phosphate metabolism, indicating their potential regulation role in the pathogenesis of fatty liver.

In summary, this study has provided new insights into the pathogenesis of fatty liver from the perspective of lipid metabolism.

## Data availability statement

The datasets presented in this study can be found in online repositories. The names of the repository/repositories and accession number(s) can be found below: https://data.mendeley.com/datasets/h6snst5hm8/1, DOI: 10.17632/h6snst5hm8.1.

## Ethics statement

Ethical approval was not required for the studies on animals in accordance with the local legislation and institutional requirements because only commercially available established cell lines were used.

## Author contributions

XF: Writing–original draft, Writing–review and editing. JX: Writing–review and editing. YH: Writing–review and editing. KW: Writing–review and editing. YZ: Writing–review and editing. JC: Methodology, Supervision, Visualization, Writing–original draft, Writing–review and editing. XZ: Funding acquisition, Methodology, Visualization, Writing–original draft,

Writing–review and editing. BP: Writing–review and editing. AX: Writing–review and editing. YC: Writing–review and editing. SL: Writing–review and editing. KJ: Supervision, Writing–review and editing. XL: Funding acquisition, Resources, Supervision, Writing–review and editing.

## Funding

The author(s) declare financial support was received for the research, authorship, and/or publication of this article. This research was financially supported by the National Natural Science Foundation of China (No. 32060818, 32360904) and Yunnan Fundamental Research Projects (grant No. 202101AS070296).

## Acknowledgments

We wish to acknowledge the assistance of the following individuals in collecting the data: Jing Yang, Qian Zhao, Yu Wu, Xiaoqian Zhou, Qi Yu, Jiajia Fu.

## Conflict of interest

The authors declare that the research was conducted in the absence of any commercial or financial relationships that could be construed as a potential conflict of interest.

## Publisher's note



## Supplementary material

The Supplementary Material for this article can be found online at: https://www.frontiersin.org/articles/10.3389/fphar.2024.1372296/full#supplementary-material

## References

Adewuyi, A. A., Gruys, E., and van Eerdenburg, FJCM (2005). Non esterified fatty acids (NEFA) in dairy cattle. A review. *Vet. Q.* 27, 117–126. doi:10.1080/01652176.2005.9695192

Bobe, G., Young, J. W., and Beitz, D. C. (2004). Invited review: pathology, etiology, prevention, and treatment of fatty liver in dairy cows. *J. Dairy Sci.* 87, 3105–3124. doi:10.3168/jds.S0022-0302(04)73446-3

Chen, J.-W., Kong, Z.-L., Tsai, M.-L., Lo, C.-Y., Ho, C.-T., and Lai, C.-S. (2018). Tetrahydrocurcumin ameliorates free fatty acid-induced hepatic steatosis and improves insulin resistance in HepG2 cells. *J. Food Drug Anal.* 26, 1075–1085. doi:10.1016/j.jfda.2018.01.005

Dole, V. P. (1956). A relation between non-esterified fatty acids in plasma and the metabolism of glucose. *J. Clin. Invest.* 35, 150–154. doi:10.1172/JCI103259

Dong, J., Loor, J. J., Zuo, R., Chen, X., Liang, Y., Wang, Y., et al. (2019). Low abundance of mitofusin 2 in dairy cows with moderate fatty liver is associated with alterations in hepatic lipid metabolism. *J. Dairy Sci.* 102, 7536–7547. doi:10.3168/jds.2019-16544

Drackley, J. K., Veenhuizen, J. J., Richard, M. J., and Young, J. W. (1991). Metabolic changes in blood and liver of dairy cows during either feed restriction or administration of 1,3-butanediol. *J. Dairy Sci.* 74, 4254–4264. doi:10.3168/jds.S0022-0302(91)78620-7

Fredrikson, G., Strålfors, P., Nilsson, N. O., and Belfrage, P. (1981). Hormone-sensitive lipase of rat adipose tissue. Purification and some properties. *J. Biol. Chem.* 256, 6311–6320. doi:10.1016/s0021-9258(19)69164-7

González, F. D., Muiño, R., Pereira, V., Campos, R., and Benedito, J. L. (2011). Relationship among blood indicators of lipomobilization and hepatic function during early lactation in high-yielding dairy cows. *J. Vet. Sci.* 12, 251–255. doi:10.4142/jvs.2011.12.3.251

Grummer, R. R. (1993). Etiology of lipid-related metabolic disorders in periparturient dairy cows. *J. Dairy Sci.* 76, 3882–3896. doi:10.3168/jds.S0022-0302(93)77729-2

Guo, D., Bell, E. H., Mischel, P., and Chakravarti, A. (2014). Targeting SREBP-1-driven lipid metabolism to treat cancer. *Curr. Pharm. Des.* 20, 2619–2626. doi:10.2174/13816128113199990486

Han, X., and Gross, R. W. (2021). The foundations and development of lipidomics. *J. Lipid Res.* 63, 100164. doi:10.1016/j.jlr.2021.100164

Herdt, T. H. (2000). Ruminant adaptation to negative energy balance. Influences on the etiology of ketosis and fatty liver. *Vet. Clin. North Am. Food Anim. Pract.* 16, 215–230. doi:10.1016/s0749-0720(15)30102-x

Horton, J. D., Goldstein, J. L., and Brown, M. S. (2002). SREBPs: activators of the complete program of cholesterol and fatty acid synthesis in the liver. *J. Clin. Invest.* 109, 1125–1131. doi:10.1172/JCI15593

Hu, J., Wang, H., Li, X., Liu, Y., Mi, Y., Kong, H., et al. (2020). Fibrinogen-like protein 2 aggravates nonalcoholic steatohepatitis via interaction with TLR4, eliciting inflammation in macrophages and inducing hepatic lipid metabolism disorder. *Theranostics* 10, 9702–9720. doi:10.7150/thno.44297

Huang, Y., Zhao, C., Liu, Y., Kong, Y., Tan, P., Liu, S., et al. (2021). NEFA promotes autophagosome formation through modulating PERK signaling pathway in bovine hepatocytes. *Anim. Open Access J. MDPI* 11, 3400. doi:10.3390/ani11123400

Jacobs, R. L., Lingrell, S., Zhao, Y., Francis, G. A., and Vance, D. E. (2008). Hepatic CTP:phosphocholine cytidylyltransferase-alpha is a critical predictor of plasma high density lipoprotein and very low density lipoprotein. *J. Biol. Chem.* 283, 2147–2155. doi:10.1074/jbc.M706628200

Li, P., Li, X. B., Fu, S. X., Wu, C. C., Wang, X. X., Yu, G. J., et al. (2012). Alterations of fatty acid β-oxidation capability in the liver of ketotic cows. *J. Dairy Sci.* 95, 1759–1766. doi:10.3168/jds.2011-4580

Li, Z., Agellon, L. B., Allen, T. M., Umeda, M., Jewell, L., Mason, A., et al. (2006). The ratio of phosphatidylcholine to phosphatidylethanolamine influences membrane integrity and steatohepatitis. *Cell Metab.* 3, 321–331. doi:10.1016/j.cmet.2006.03.007

Locher, L. F., Meyer, N., Weber, E.-M., Rehage, J., Meyer, U., Dänicke, S., et al. (2011). Hormone-sensitive lipase protein expression and extent of phosphorylation in subcutaneous and retroperitoneal adipose tissues in the periparturient dairy cow. *J. Dairy Sci.* 94, 4514–4523. doi:10.3168/jds.2011-4145

Long, N. P., Park, S., Anh, N. H., Kim, S. J., Kim, H. M., Yoon, S. J., et al. (2020). Advances in liquid chromatography–mass spectrometry-based lipidomics: a look ahead. *J. Anal. Test.* 4, 183–197. doi:10.1007/s41664-020-00135-y

Ma, X., and Fernández, F. M. (2022). Advances in mass spectrometry imaging for spatial cancer metabolomics. *Mass Spectrom. Rev.* 43, 235–268. doi:10.1002/mas.21804

Maceyka, M., and Spiegel, S. (2014). Sphingolipid metabolites in inflammatory disease. *Nature* 510, 58–67. doi:10.1038/nature13475

Martens, H. (2023). Invited review: increasing milk yield and negative energy balance: a gordian knot for dairy cows? *Anim. Open Access J. MDPI* 13, 3097. doi:10.3390/ani13193097

Mun, J., Kim, S., Yoon, H.-G., You, Y., Kim, O.-K., Choi, K.-C., et al. (2019). Water extract of curcuma longa L ameliorates non-alcoholic fatty liver disease. *Nutrients* 11, 2536. doi:10.3390/nu11102536

Niebergall, L. J., Jacobs, R. L., Chaba, T., and Vance, D. E. (2011). Phosphatidylcholine protects against steatosis in mice but not non-alcoholic steatohepatitis. *Biochim. Biophys. Acta BBA - Mol. Cell Biol. Lipids* 1811, 1177–1185. doi:10.1016/j.bbalip.2011.06.021

Oh, S., Son, M., Byun, K.-A., Jang, J. T., Choi, C. H., Son, K. H., et al. (2021). Attenuating effects of dieckol on high-fat diet-induced nonalcoholic fatty liver disease by decreasing the NLRP3 inflammasome and pyroptosis. *Mar. Drugs* 19, 318. doi:10.3390/md19060318

Onorato, A., Fiore, E., Bayo, J., Casali, C., Fernandez-Tomé, M., Rodríguez, M., et al. (2021). SPARC inhibition accelerates NAFLD-associated hepatocellular carcinoma

development by dysregulating hepatic lipid metabolism. *Liver Int. Off. J. Int. Assoc. Study Liver* 41, 1677–1693. doi:10.1111/liv.14857

Orešič, M., Hänninen, V. A., and Vidal-Puig, A. (2008). Lipidomics: a new window to biomedical frontiers. *Trends Biotechnol.* 26, 647–652. doi:10.1016/j.tibtech.2008.09.001

Patsoukis, N., Bardhan, K., Chatterjee, P., Sari, D., Liu, B., Bell, L. N., et al. (2015). PD-1 alters T-cell metabolic reprogramming by inhibiting glycolysis and promoting lipolysis and fatty acid oxidation. *Nat. Commun.* 6, 6692. doi:10.1038/ncomms7692

Pralle, R. S., Erb, S. J., Holdorf, H. T., and White, H. M. (2021). Greater liver PNPLA3 protein abundance *in vivo* and *in vitro* supports lower triglyceride accumulation in dairy cows. *Sci. Rep.* 11, 2839. doi:10.1038/s41598-021-82233-0

Reynolds, C. K., Aikman, P. C., Lupoli, B., Humphries, D. J., and Beever, D. E. (2003). Splanchnic metabolism of dairy cows during the transition from late gestation through early lactation. *J. Dairy Sci.* 86, 1201–1217. doi:10.3168/jds.S0022-0302(03)73704-7

Roberts, C. J., Reid, I. M., Rowlands, G. J., and Patterson, A. (1981). A fat mobilisation syndrome in dairy cows in early lactation. *Vet. Rec.* 108, 7–9. doi:10.1136/vr.108.1.7

Rodríguez-Cruz, M., Sánchez González, R., Sánchez García, A. M., and Lòpez-Alarcòn, M. (2012). Coexisting role of fasting or feeding and dietary lipids in the control of gene expression of enzymes involved in the synthesis of saturated, monounsaturated and polyunsaturated fatty acids. *Gene* 496, 28–36. doi:10.1016/j.gene.2011.12.022

Rukkwamsuk, T., Kruip, T. A. M., Meijer, G. A. L., and Wensing, T. (1999). Hepatic fatty acid composition in periparturient dairy cows with fatty liver induced by intake of a high energy diet in the dry period. *J. Dairy Sci.* 82, 280–287. doi:10.3168/jds.S0022-0302(99)75234-3

Salvador, A. F., Shyu, C.-R., and Parks, E. J. (2022). Measurement of lipid flux to advance translational research: evolution of classic methods to the future of precision health. *Exp. Mol. Med.* 54, 1348–1353. doi:10.1038/s12276-022-00838-5

Samiei, A., Liang, J. B., Ghorbani, G. R., Hirooka, H., Yaakub, H., and Tabatabaei, M. (2010). An evaluation of beta-hydroxybutyrate in milk and blood for prediction of subclinical ketosis in dairy cows. *Pol. J. Vet. Sci.* 13, 349–356.

Shimano, H., Horton, J. D., Shimomura, I., Hammer, R. E., Brown, M. S., and Goldstein, J. L. (1997). Isoform 1c of sterol regulatory element binding protein is less active than isoform 1a in livers of transgenic mice and in cultured cells. *J. Clin. Invest.* 99, 846–854. doi:10.1172/JCI119248

Simino, L. A. P., Panzarin, C., Fontana, M. F., de Fante, T., Geraldo, M. V., Ignácio-Souza, L. M., et al. (2021). MicroRNA Let-7 targets AMPK and impairs hepatic lipid metabolism in offspring of maternal obese pregnancies. *Sci. Rep.* 11, 8980. doi:10.1038/s41598-021-88518-8

Tardelli, M., Bruschi, F. V., and Trauner, M. (2020). The role of metabolic lipases in the pathogenesis and management of liver disease. *Hepatol. Balt. Md* 72, 1117–1126. doi:10.1002/hep.31250

Vargas-Alarcon, G., Gonzalez-Pacheco, H., Perez-Mendez, O., Posadas-Sanchez, R., Cardoso-Saldaña, G., Ramirez-Bello, J., et al. (2019). SREBF1c and SREBF2 gene polymorphisms are associated with acute coronary syndrome and blood lipid levels in Mexican population. *PLoS ONE* 14, e0222017. doi:10.1371/journal.pone.0222017

Wang, J., Zhu, X., She, G., Kong, Y., Guo, Y., Wang, Z., et al. (2018). Serum hepatokines in dairy cows: periparturient variation and changes in energy-related metabolic disorders. *BMC Vet. Res.* 14, 236. doi:10.1186/s12917-018-1560-7

White, H. M. (2015). The role of TCA cycle anaplerosis in ketosis and fatty liver in periparturient dairy cows. *Anim. Open Access J. MDPI* 5, 793–802. doi:10.3390/ani5030384

Yang, J., Goldstein, J. L., Hammer, R. E., Moon, Y. A., Brown, M. S., and Horton, J. D. (2001). Decreased lipid synthesis in livers of mice with disrupted Site-1 protease gene. *Proc. Natl. Acad. Sci. U. S. A.* 98, 13607–13612. doi:10.1073/pnas.201524598

Yang, W., Wang, S., Zhao, Y., Jiang, Q., Loor, J. J., Tian, Y., et al. (2023). Regulation of cholesterol metabolism during high fatty acid–induced lipid deposition in calf hepatocytes. *J. Dairy Sci.* 106, 5835–5852. doi:10.3168/jds.2022-23136

Zhao, C., Wu, B., Li, J., Jiang, Q., Loor, J. J., Liu, M., et al. (2023). AdipoRon alleviates fatty acid–induced lipid accumulation and mitochondrial dysfunction in bovine hepatocytes by promoting autophagy. *J. Dairy Sci.* 106, 5763–5774. doi:10.3168/jds.2022-22723

Zhao, T., Zhang, Y., Ma, X., Wei, L., Hou, Y., Sun, R., et al. (2021). Elevated expression of LPCAT1 predicts a poor prognosis and is correlated with the tumour microenvironment in endometrial cancer. *Cancer Cell Int.* 21, 269. doi:10.1186/s12935-021-01965-1

frontiers | Frontiers in Pharmacology

TYPE Original Research
PUBLISHED 08 March 2024
DOI 10.3389/fphar.2024.1334445



OPEN ACCESS

EDITED BY
Tianhao Liu,
Affiliated Hospital of Jiangnan University, China

REVIEWED BY
Jiao Liu,
Third Affiliated Hospital of Guangzhou Medical University, China
Ke Huang,
Shenzhen International Institute for Biomedical Research (SIIBR), China

*CORRESPONDENCE
Guangchao Li,
gcli@gzbiogene.com
Qing Zhang,
zhqing@vip.163.com
Shuang Liu,
Liush@gd2h.org.cn

†These authors have contributed equally to this work

RECEIVED 07 November 2023
ACCEPTED 30 January 2024
PUBLISHED 08 March 2024

CITATION
Yin Z, Ou R, Zhu Y, Liu Z, Huang J, Zhong Q, Li G, Zhang Q and Liu S (2024), Coniferyl ferulate alleviate xylene-caused hematopoietic stem and progenitor cell toxicity by Mgst2. *Front. Pharmacol.* 15:1334445. doi: 10.3389/fphar.2024.1334445



# Coniferyl ferulate alleviate xylene-caused hematopoietic stem and progenitor cell toxicity by Mgst2

Zhao Yin†, Ruiming Ou†, Yangmin Zhu, Zhi Liu, Jing Huang, Qi Zhong, Guangchao Li*†, Qing Zhang* and Shuang Liu*

Department of Hematology, Guangdong Second Provincial General Hospital, Jinan University, Guangzhou, China

Xylene exposure is known to induce toxicity in hematopoietic stem and progenitor cells (HSPCs), leading to bone marrow suppression and potential leukemogenesis. However, research on the gene expression profiles associated with xylene-induced toxicity in HSPCs, and effective therapeutic interventions, remains scarce. In our study, we employed single-cell RNA sequencing to capture the transcriptomic shifts within bone marrow HSPCs both prior to and following treatment with coniferyl ferulate (CF) in a mouse model of xylene-induced hematotoxicity. Subsequently, we pinpointed CF as a targeted agent using SPR-LC/MS analysis. This enabled us to confirm the link between the gene Mgst2 and specific cellular subtypes. Our data revealed that CF significantly countered the reduction of both monocyte and neutrophil progenitor cells, which are commonly affected by xylene toxicity. Through targeted analysis, we identified Mgst2 as a direct molecular target of CF. Notably, Mgst2 is preferentially expressed in neutrophil progenitor cells and is implicated in mitochondrial metabolic processes. By selectively inhibiting Mgst2 in bone marrow, we observed amelioration of xylene-induced hematotoxic effects. In summary, our findings suggest that coniferyl ferulate can mitigate the detrimental impact of xylene on hematopoietic stem and progenitor cells by targeting Mgst2, particularly within subpopulations of neutrophil progenitors. This discovery not only advances our comprehension of the cellular response of HSPCs to xenobiotic stressors like xylene but also identifies CF and Mgst2 as potential therapeutic targets for alleviating xylene-induced hematotoxicity.

KEYWORDS

**xylene, HSPCs, mgst2, coniferyl ferulate, hematotoxic**

## Introduction

The air around humans is contaminated by several toxic chemicals, which might cause severe disorders (Hassan and Aly, 2018; Inesta-Vaquera et al., 2023). These contaminants might enter the body via breathing and cause harm (Kang et al., 2021). Typically, aromatic compounds, such as benzene, xylene, and toluene are toxic to humans (Snyder, 2012). A threshold limit value (TLV) of 100 ppm in the working environment is recommended by the health and safety authorities of many nations, including China. Around 95.2% of the workforce showed cumulative carcinogenic risk due to the inhalation of xylene. Also,

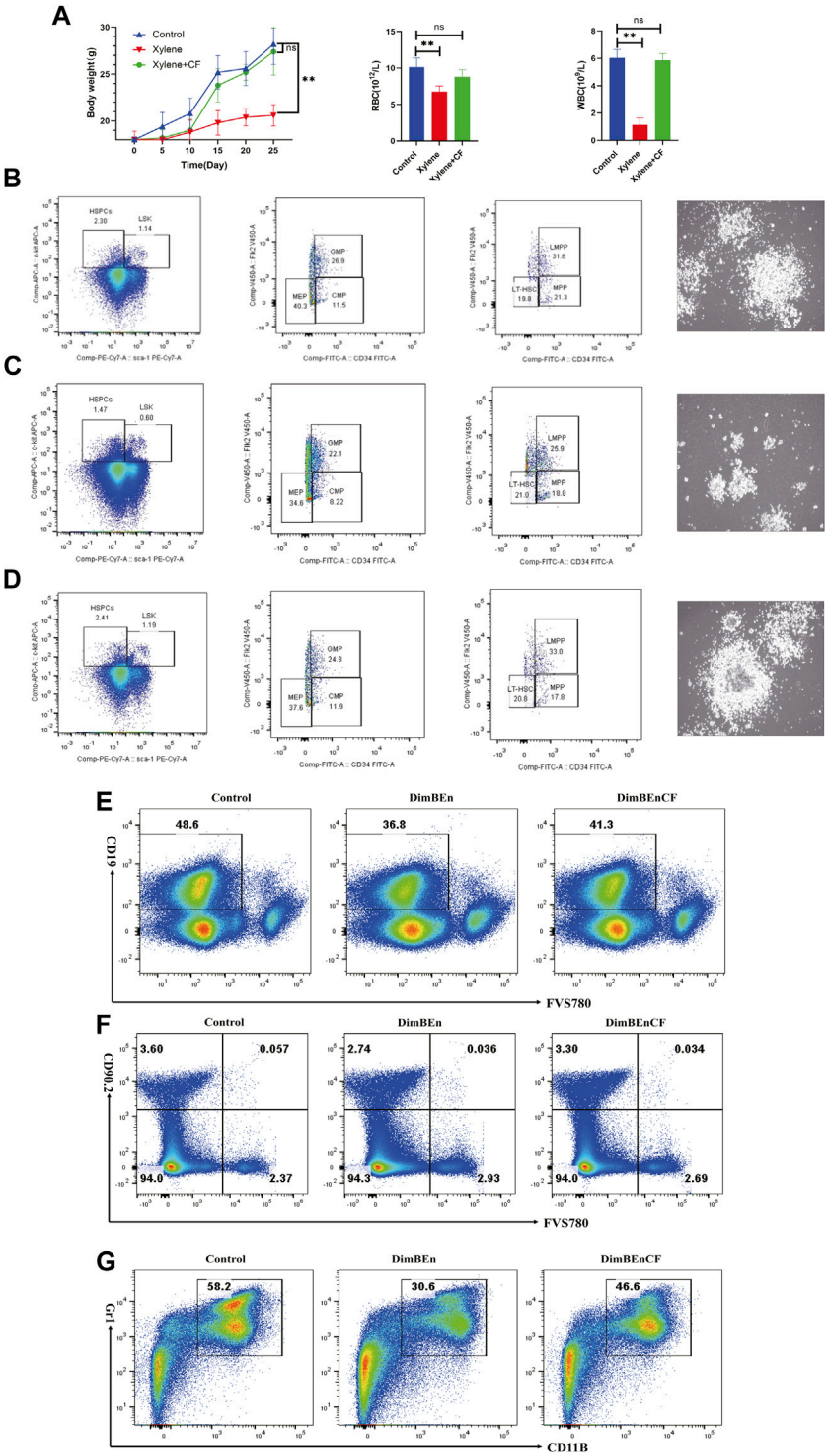


FIGURE 1
The toxic effects of xylene on the body weight, blood parameters, and percentage of hematopoietic stem and progenitor cells in mice. **(A)** The body weight of mice on the 5$^{th}$, 10$^{th}$, 15$^{th}$, 20$^{th}$, 25$^{th}$ day of xylene exposure (left), Effects of xylene and CF+ xylene on RBC (middle) and WBC (right), WBC: white blood cell; RBC: red blood cell; The data were presented as the mean ± SD. Xylene regulates murine HSC self-renewal and differentiation can be restored by CF. Flow cytometric analysis of LSK (Lin-Sca1+c-kit+), LT-HSC (LinSca1+c-kit+CD34-Flk2-), MPP (LinSca1+c-kit+CD34+Flk2+), myeloid progenitors including CMP (Lin-Sca1-c-kit+CD34+CD16/32+low), granulocyte-macrophage progenitors (GMP) (Lin-Sca1-c-kit+CD34+ CD16/32+high), and MEP (Lin-Sca1-c-kit+ Sca-CD34-CD16/32-) in the BM and from Control (**B** left), Xylene (**C** left) and Xylene+CF (**D** left) group. HSPCs were plated in semisolid methylcellulose agar and colonies were counted after 14 days, Scale bars, 100 μm. Cell colony formation results shown that Xylene induced HSPCs toxicity couled be restored by CF (Control (**B** right), Xylene (**C** right) and Xylene+CF (**D** right) group. BM cells were collected from Control (**B** left), Xylene and Xylene + CFmice and stained with antibodies against Mac1, Gr1, CD19, or Thy1.2 analyzed by FACS, the damage to B cells **(E)**, T cells **(F)**, and myeloid cells **(G)** caused by xylene can be restored by CF. Student's t-test was conducted for statistically analyzing the data; All differences were considered to be statistically significant compared to the control at $P < 0.05$; ** $P < 0.01$.

around 99.9% of the distribution of carcinogenic risk is attributed to the benzene metabolite N-acetyl-S-(phenyl)-L-cysteine of over $10^{-6}$ (Sun et al., 2022). Benzene is a well-known hemotoxin, which is classified by the International Agency for Research on Cancer as a category 1 carcinogen (Lan et al., 2004; Mosmeri et al., 2019). However, no effective treatment is known that specifically alleviates the hematotoxicity caused by xylene. Therefore, the mechanisms need to be elucidated, and the control over xylene -caused hematotoxicity needs to be optimized for developing new treatments.

Exposure to xylene can cause injury to the hematopoietic system, such as different degrees of pancytopenia, aplastic anemia, and even leukemia (Mokammel et al., 2022; Vermeulen et al., 2023). Leukemia caused by chronic exposure to benzene is a significant public health issue that has raised concerns among health system worldwide. Exposure to a low dose of benzene (≤1 ppm) can induce injury to the hematopoietic system (Wang et al., 2022). Many studies on toxicology and epidemiology have investigated the mechanism by which benzene increases toxicity in the blood, but the precise mechanism needs to be elucidated. Thus, a comprehensive investigation of the mechanism by which xylene triggers hematological injuries is required. In a conventional hierarchical model, HSCs exhibit sequential differentiation first into multipotent progenitors (MPPs) and then into common lymphoid progenitors (CLPs), as well as, myeloid progenitors (CMPs). Later, they produce granulocyte-macrophage progenitors (GMPs) along with megakaryocyte-erythroid progenitors (MEPs) (Crippa et al., 2023). However, traditional bulk expression analysis of heterogeneous populations can be performed to assess the mean expression levels of all cells in the sample, which does not represent the expression level in every cell (Yin et al., 2023). The single-cell profiling technology can resolve the problem of population heterogeneity (Xia et al., 2023). Therefore, single-cell transcriptome sequencing technology was used in this study to elucidate the mechanism by which xylene causes damage to hematopoietic cells.

Salimi *et al.* examined the effect of xylene on inducing ROS production and impairment of the mitochondria in lymphocytes (Salimi et al., 2017). Xylene causes the accumulation of reactive oxygen species (ROS) and oxidative stress in yeast cells (Singh et al., 2010). Nishida-Aoki *et al.* showed that the organic solvent isooctane can promote ROS production in yeast cells by impairing mitochondria. Similarly, xylene may also impair mitochondria, resulting in the release of ROS along with mitochondrial fragmentation in yeast cells (Nishida-Aoki et al., 2015). This hypothesis might be reasonable, considering that xylene can impair mitochondria in human cells and induce mitochondrial morphological alterations in yeast cells. However, the key molecular mechanism by which xylene induces ROS accumulation needs to be determined.

Angiotensin II-induced leukotriene C4 (LTC4) can induce ROS accumulation, and it is exclusively expressed in hematopoietic cells, such as mast cells (Fujimori et al., 2022). Additionally, microsomal glutathione S-transferase 2 (Mgst2), the isoenzyme of LTC4, is ubiquitously expressed in non-hematopoietic cells and has different functions (Thulasingam et al., 2021). The Mgst2-LTC4 signaling cascade can be activated by common chemotherapeutic agents and ER-mediated stress. It induces oxidative stress, oxidative DNA damage, and ROS-induced cell death (Dvash et al., 2015).

Coniferyl ferulate is a phenolic acid compound abundant in umbelliferae plants with multiple pharmacological activities. It has many pharmacological effects, such as antioxidation, antibacterial effects, and vasodilation (Gong et al., 2020). CF is widely used for enriching and nourishing blood and improving blood circulation. Some studies have found that ferulic acid, an analog of CF, can increase blood fluidity, decrease serum lipids, suppress platelet aggregation, prevent thrombogenesis, protect neurons such as PC12 cells, and exhibit potent antioxidant effects (Gong et al., 2020). However, the relationship between the pharmacological effects of CF on xylene and damage to the hematopoietic system needs to be elucidated.

In this study, we investigated whether CF supplementation can protect mice against xylene-caused damage to the hematopoietic system and the mechanism by which CF exerts its effects at single-cell resolution. Additionally, the direct target of CF was also assessed. CF can directly bind to Mgst2, it can alleviate the damage to the hematopoietic system caused by xylene. The subcluster of neutrophil progenitors and monocyte progenitors are considered to be the real responsive cells in HSPCs. Mgst2 is the potential therapeutic target for treating xylene toxicity, and CF is a therapeutic agent that can alleviate the toxic effects of xylene.

# Materials and methods

## Animals

Normal male C57BL/6 SPF mice [n = 45, 8 weeks old, and 20 ± 2 g; SYXK (Yue) 2017–0174] were obtained and adaptively fed for 7 days before the experiment. All mice were maintained under experimental conditions of 21°C ± 2°C, 30%–40% relative humidity, and a 12-h/12-h light/dark cycle. All animal experiments were approved by the Animal Ethics Committee (IACUC-20220429–01) and were conducted following the animal-welfare guidelines. All animals were randomly placed into three groups, including the control, xylene (150 mg/kg), and xylene (150 mg/kg) + CF (50 mg/kg) groups.

## Drug preparation and intervention

Coniferyl ferulate (CF) (purity: ≥98%; high-performance liquid chromatography grade) was purchased from Chengdu RefMedic Biotech Co., Ltd. (Chengdu, China). All mice in the CF group were administered 50 mg/kg CF once a day through intragastric administration. CF (50 mg) was dissolved in 0.1% ethanol to prepare a CF solution at a final concentration of 10 mg/mL.

The mice in the other two groups were administered 1X PBS (Phosphate-Buffered Saline) supplemented in 0.1% ethanol. Two weeks before exposure to xylene, CF or PBS was orally administered to the mice.

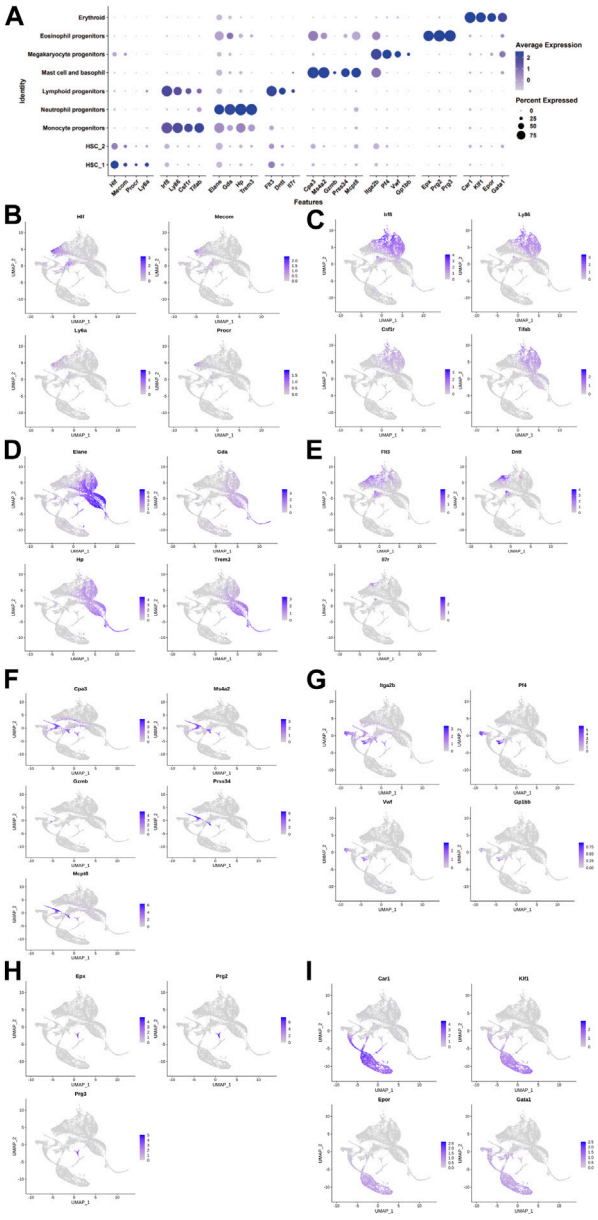

FIGURE 2
The landscape of cell clusters in HSPC samples of the bone marrow of mice was determined by the scRNA-seq analysis. **(A)**. The dot plot shows the level of expression of canonical markers in each cell cluster. UMAP visualization of eight major cell populations showing the expression of representative well-known cell-type-specific marker genes. **(B)**. Hematopoietic stem cell 1 expressing Hif, Mecom, Procr, and Ly6a. **(C)**. Monocyte progenitors expressing Lrf8, Ly86, Csf1r, and Tifab. **(D)**. Neutrophil progenitors expressing Elan, Gda, Hp, and Trem3. **(E)**. Lymphoid progenitors expressing Flt3, Dntt, and Ll7r. **(F)**. Mast cells and basophil cells expressing Ms4a2, Gzmb, Prss34, Mcpt8, and Car1. **(G)**. Megakaryocyte progenitors expressing Itga2b, Pf4, Vwf, and Gp1bb. **(H)**. Lymphoid progenitors expressing Exp, Prg2, and Prg3. **(I)**. Erythroid expressing Cpr1, Klf1, Epor, and Gata1. The differences in the proportion of cells between groups were determined by the Wilcoxon test.

## FCM analysis

To analyze stem cells, we harvested mouse bone marrow cells (BMCs) from the six-week-old C57BL/6 mice and stained them. After extraction, BMCs were lysed with red blood cells (RBCs) and incubated with several antibodies. Then, we prepared splenic tissue and BMC-derived single-cell suspensions and stained them for 20 min on ice. The HSPC markers applied included LT-HSC: Lin- (PerCP-Cy™5.5); FVS780- (APC-Cy™7); C-KIT+ (CD117, APC); Sca+ (PE-Cy™7); $CD34^-$ (FITC); Flk2- (BV421); GMP: Lin- FVS780- C-KIT + Sca- $CD34^+$ CD16/32+ (FcγRII, BV421); MPP: Lin- FVS780- C-KIT + Sca+ $CD34^+$ Flk2+; MEP: Lin- FVS780- C-KIT + Sca- $CD34^-$ CD16/32-; CMP: Lin- FVS780- C-KIT + Sca- $CD34^+$ CD16/32-; GR-1 (Ly-6G and Ly-6C), and MAC-1(CD11b); B cell (CD19); T cell (CD90.2). The antibodies used for FCM were purchased from BD Biosciences (New Jersey, United States of America). FACSVerse (Becton Dickinson) was used for examining cells. The FCM data were analyzed using the FlowJo software (TreeStar, Inc.).

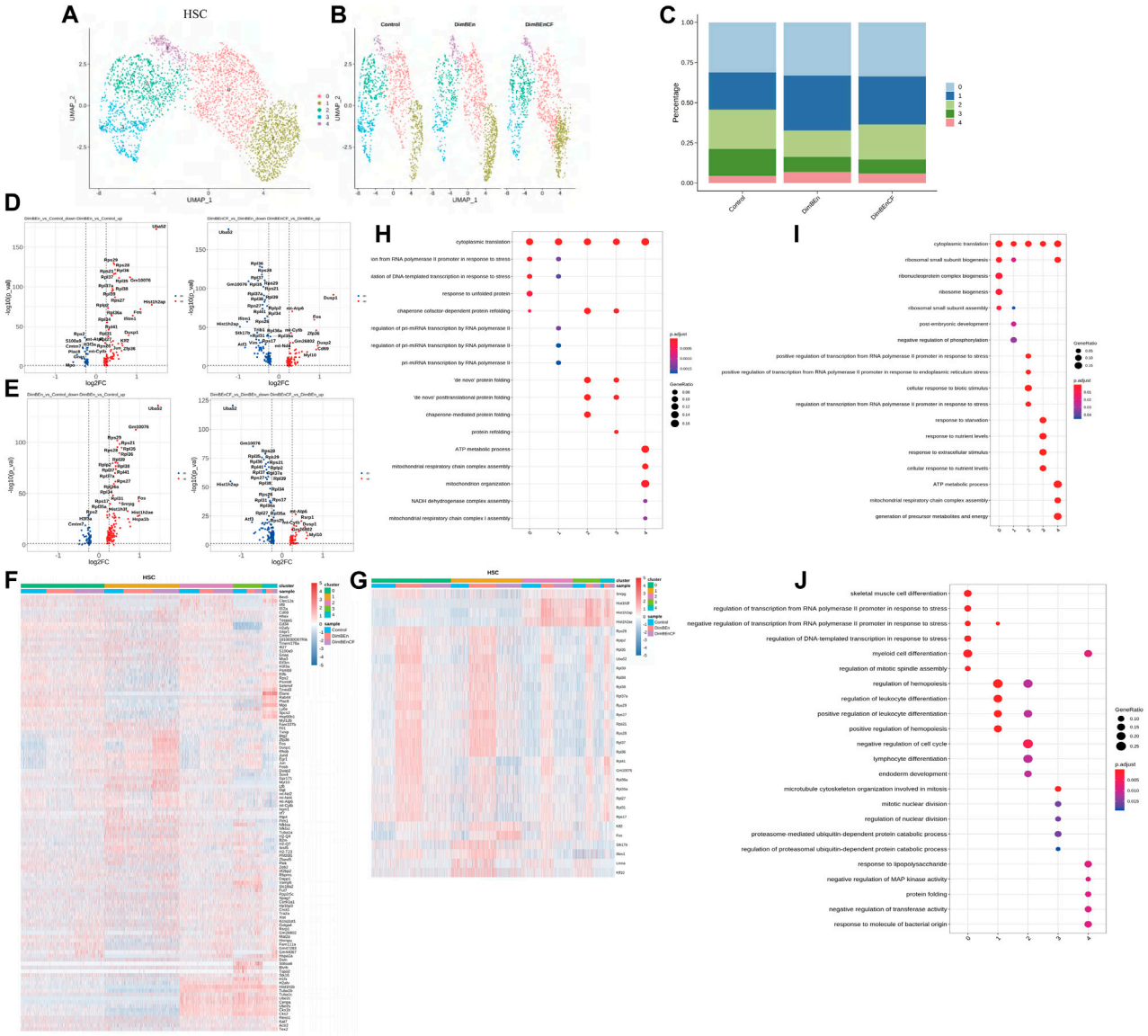


FIGURE 3
Single-cell transcriptomes of heterogeneity in hematopoietic stem cells **(A)**. The uniform manifold approximation and projection (UMAP) clustering map of mouse BM stem cell/progenitor (c-kit+). **(B)**. The UMAP plot shows the distribution of the five subcellular clusters. **(C)**. A bar plot of the proportion of cell subpopulation in three samples. The results showed that Clusters 0, 1, and 4 increased after xylene treatment, however, the changes were reversed by CF (n = 3); $^{**}p < 0.01$. **(D)**. A volcano plot of differentially expressed genes between DinBEn and Control and between DinBEn and DinBEnCF **(E)**. A heat map illustrating differential gene expression. The upregulated differentially expressed genes of each cluster compared to Control and DimBEnCF; the top 20 genes were selected based on the smallest *p*-value in each cluster. **(F)**. The downregulated differentially expressed genes of each cluster compared to Control and DimBEnCF; the top 20 genes were selected based on the smallest *p*-value in each cluster. The results of the GO analysis showed that in DimBEn *versus* Control **(G)**, DimBEn *versus* DimBEnCF **(H)**, and DimBEnCF *versus* DimBEn **(I)**: Cluster 0 was associated with pressure, stimulation, and other pathway enhancement; Cluster 1 was associated with pressure and microRNA; Cluster 2 was associated with protein folding; Cluster 3 was associated with protein folding; Cluster 4 was associated with mitochondrial energy metabolism.

## Colony-formation assay

We analyzed methylcellulose colony formation using 100,000 mouse HSPCs. Specifically, the mouse MethoCult medium (StemCell Technologies) was used for preparing the cell suspension. Then, cell culture was performed using culture plates (3 cm in diameter), and evaporation was prevented through the addition of excessive PBS. The number of colonies formed was counted after 14 days.

## Single-cell RNA sequencing

Bone marrow cells (BMCs) were harvested from C57BL/6 mice placed in different groups. First, using the Lineage Cell Depletion Kit (mouse), CD117 microbeads (Miltenyi Biotec) were used to obtain CD117+ cells. Additionally, samples were prepared with the 10x Genomics Single Cell 3′v2 Reagent Kit following the manufacturer's protocol. About 6,000 cells were collected from each sample for constructing the cDNA library on a 10x

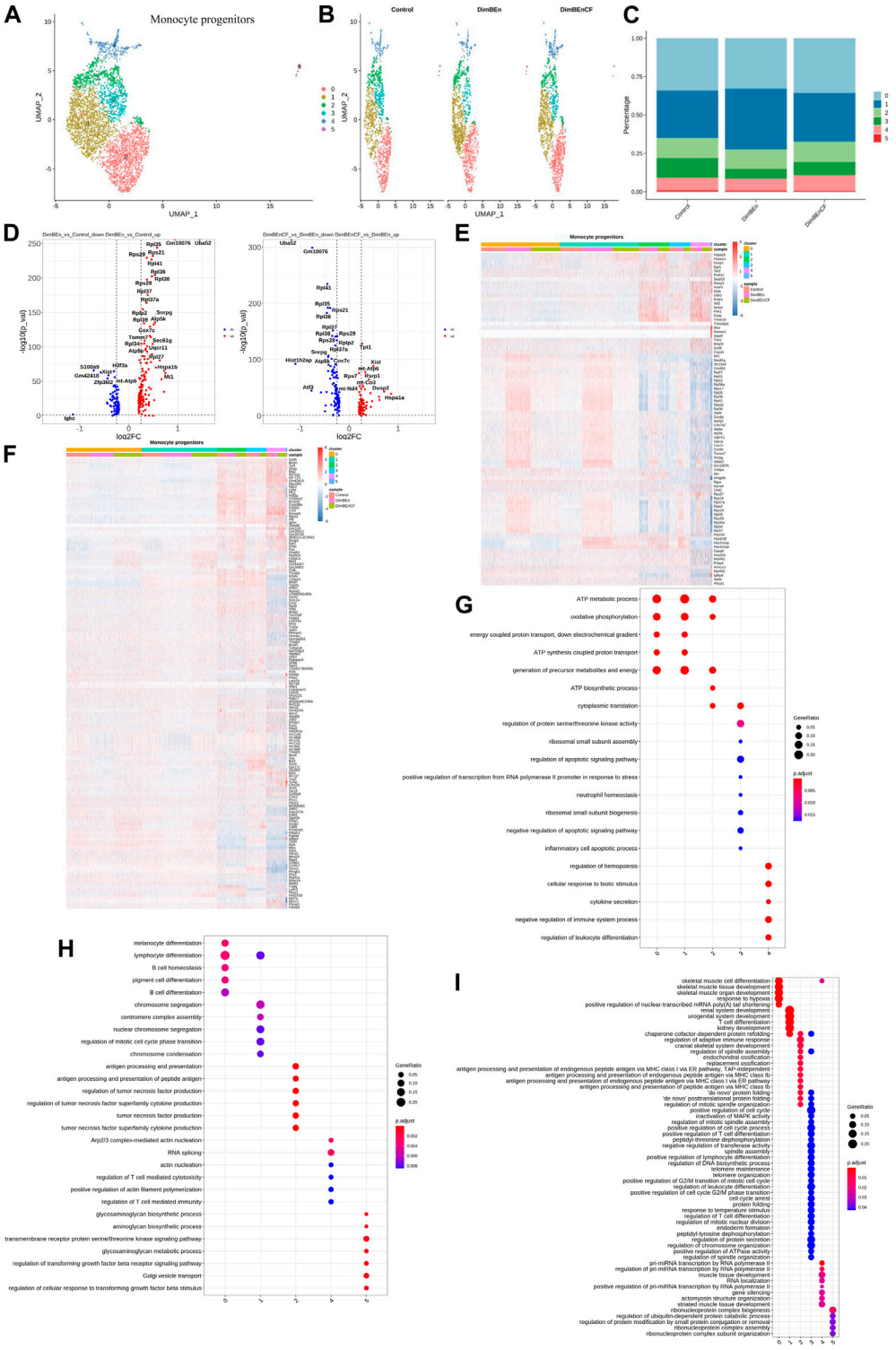


FIGURE 4
Single-cell transcriptomes of heterogeneity in monocyte progenitor cells **(A)** A uniform manifold approximation and projection (UMAP) clustering map of mouse BM monocyte progenitors from three integrated samples. **(B)**. The UMAP plot shows the distribution of the five subcellular clusters. **(C)**. A bar plot of the proportion of cell subpopulation in three samples. The results showed that Cluster 1 increased after xylene treatment, however, the changes were reversed by CF. **(D)**. A volcano plot of differentially expressed genes between DinBEn and Control, and between DinBEn and DinBEnCF **(E)**. A heat map illustrating differential gene expression. The upregulated differentially expressed genes of each cluster compared to Control and DimBEnCF; the top 20 genes were selected based on the smallest *p*-value in each cluster. **(F)**. The downregulated differentially expressed genes of each cluster compared to Control and DimBEnCF; the top 20 genes were selected based on the smallest *p*-value in each cluster. The results of the GO analysis showed that in DimBEn *versus* Control **(G)**, DimBEn *versus* DimBEnCF **(H)**, and DimBEnCF *versus* DimBEn **(I)**, Cluster 1 was related to mitochondrial energy metabolism.

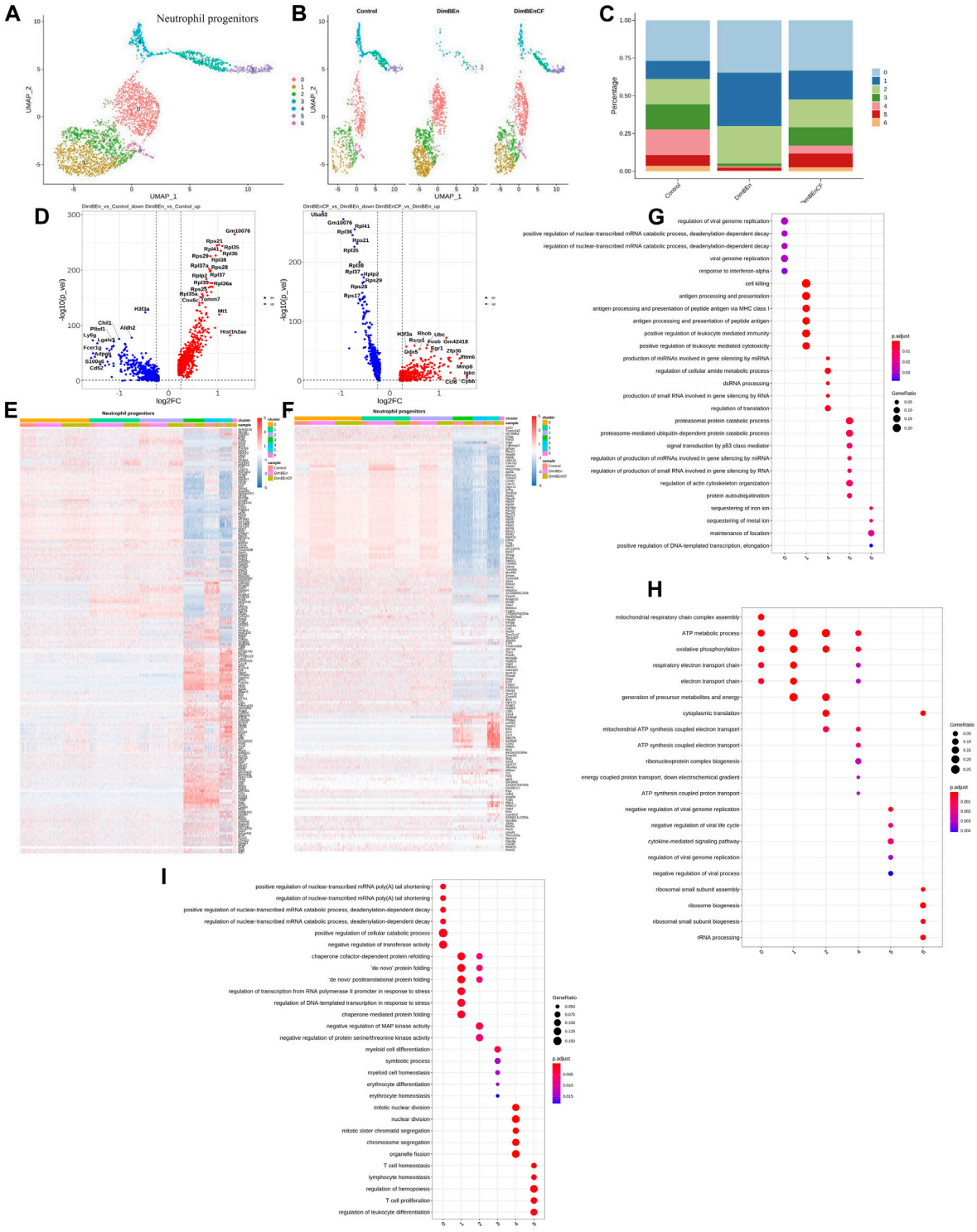


FIGURE 5
Single-cell transcriptomes of heterogeneity in neutrophil progenitor cells **(A)** A uniform manifold approximation and projection (UMAP) clustering map of mouse neutrophil progenitors cells from three integrated samples. **(B)**. The UMAP plot shows the distribution of the seven subcellular clusters. **(C)**. A bar plot of the proportion of cell subpopulation in three samples. The results showed that Clusters 0, 1, and 2 increased after xylene treatment, however, the changes were reversed by CF. **(D)**. A volcano plot of differentially expressed genes between DinBEn and Control, and between DinBEn and DinBEnCF. **(E)**. A heat map of differential gene expression. The upregulated differentially expressed genes of each cluster compared to Control and DimBEnCF; the top 20 genes were selected based on the smallest *p*-value in each cluster. **(F)**. The downregulated differentially expressed genes of each cluster compared to Control and DimBEnCF; the top 20 genes were selected based on the smallest *p*-value in each cluster. The results of the GO analysis showed that in DimBEn *versus* Control **(G)**, DimBEn *versus* DimBEnCF **(H)**, and DimBEnCF *versus* DimBEn **(I)**: Cluster 0 was associated with energy metabolism and protein folding; Cluster 1 was associated with energy metabolism and ribosome assembly; Cluster 2 was associated with energy metabolism and ribosome assembly.

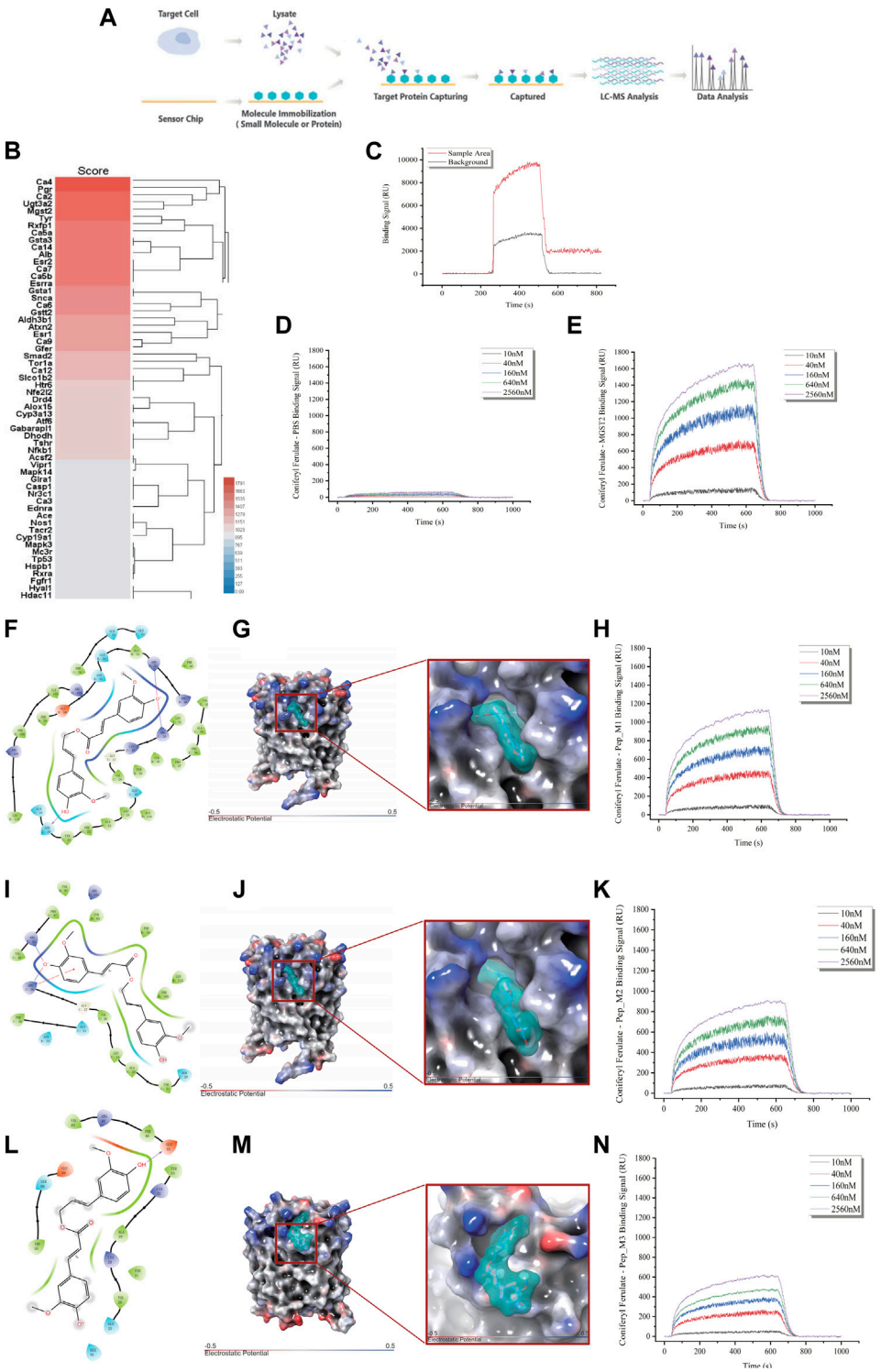


FIGURE 6
Identification of Mgst2 as the direct target of CF. **(A)**. Target identification workflow using SPR-LC-MS. **(B)**. The results of SPR-HPLC-MS showed the candidate targets that bound to CF and Mgst2. **(C)**. The results of the SPR showed the binding is specific. **(D)**. The negative control of the SPR array. **(E)**. An SPR assay was conducted to determine the binding affinity of CF to the Mgst2 protein. **(F)**. A 2D image confirming the interaction of CF with several amino acids, including QQSYFALQVGKARLKYKVTPPAVTGSPEFERVFRAQQ. **(G)**. A 3D image showing the binding of CF to the binding pocket 1. **(H)**. An SPR assay was conducted to determine the binding affinity of CF to Mgst2 peptide 1. **(I)**. A 2D image confirming the interaction of CF with several amino acids, including GKARLKYKVTPPAVTGSPEFERVFRAQQ. **(J)**. A 3D image showing the binding of CF to binding pocket 2. **(K)**. An SPR assay was conducted to determine the binding affinity of CF to Mgst2 peptide 3. **(L)** A 2D image confirming the interaction of CF with several amino acids, including AVTGSPEFERVF. **(M)** A 3D image showing the binding of CF to binding pocket **(N)**. An SPR assay was conducted to determine the binding affinity of CF to Mgst2 peptide 3.

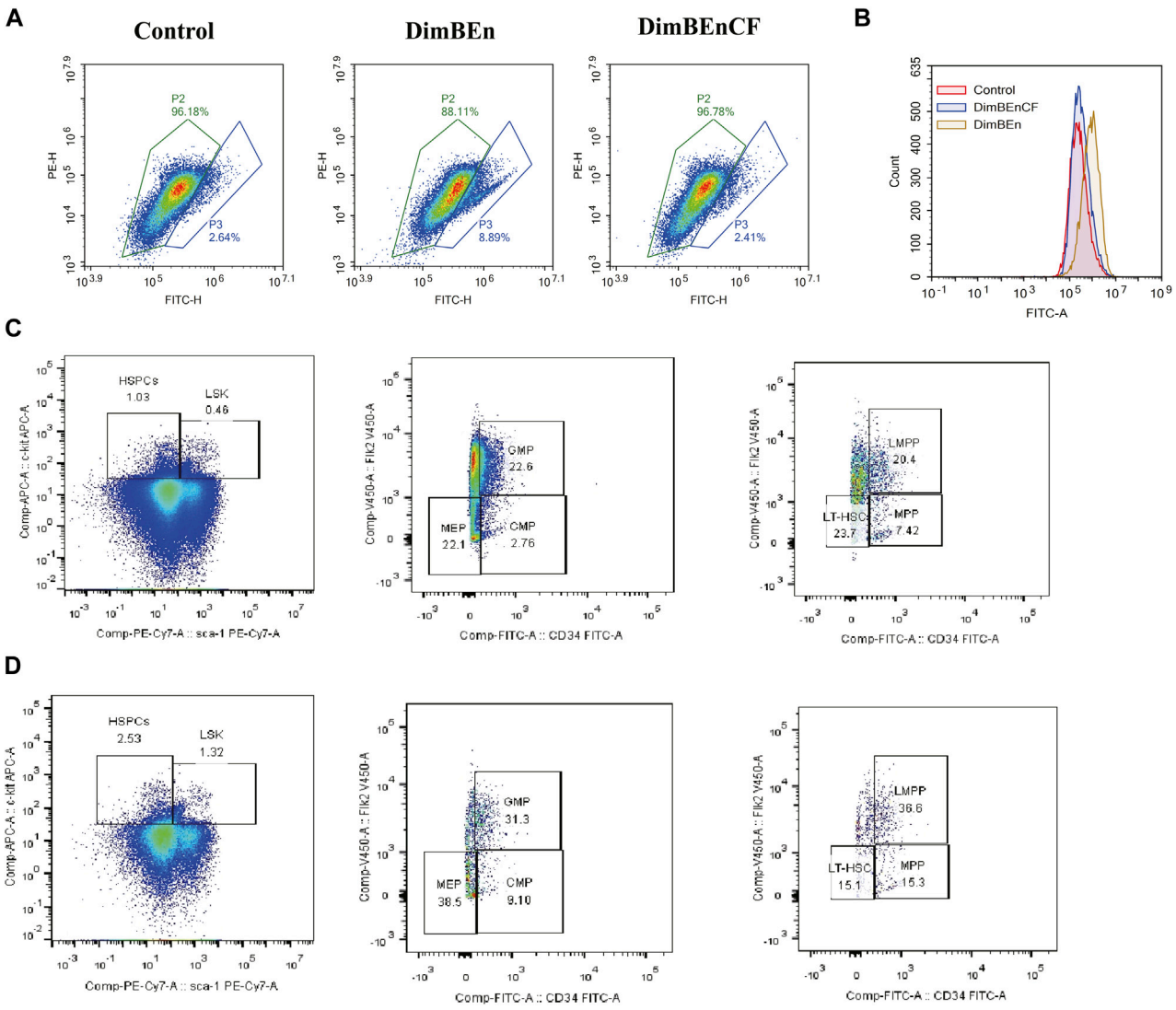


FIGURE 7
Coniferyl ferulate (CF) protected the BM from the toxic effects of xylene by inhibiting the expression of Mgst2 **(A)**. CF reversed the xylene-induced decrease in mitochondrial transmembrane potential **(B)**. CF reversed the xylene-induced decrease in ROS production. Xylene regulates murine HSC self-renewal and differentiation can be restored by inhibiting Mgst2. Flow cytometric analysis of LSK (Lin-Sca1+c-kit+), LT-HSC (Lin-Sca1+c-kit+CD34-Flk2-), and MPP (Lin-Sca1+c-kit+CD34+Flk2+) in the BM from controls, flow cytometric analysis of myeloid progenitors including CMP (Lin-Sca1-c-kit+CD34$^{+}$CD16/32+low), granulocyte-macrophage progenitors (GMP) (Lin-Sca1-c-kit+CD34$^{+}$ CD16/32+high), and MEP (Lin-Sca1-c-kit + Sca-CD34$^{-}$CD16/32-) in the BM and from Xylene **(C)** and Xylene + Mgst2 down expression **(D)** group.

Genomics single-cell-A chip following the protocol provided with the Single Cell 3′Reagent Kit v3. The PCR cycle program was slightly modified based on the expression of cDNA (recommended by 10X Genomics). The samples were pooled, normalized to 10 nM, and diluted to 2 nM using an elution buffer containing 0.1% Tween 20 (Sigma). Then, the samples were sequenced to a median depth of 50,000 reads/cell with the Novaseq 6000 system using the parameters below: read 1–26 cycles, read 2–98 cycles, and index one to eight cycles.

## Single-cell trajectory analysis

The Monocle 2 algorithm (v2.8.0) of R.18 was used to generate HSPC trajectories. Briefly, using the CellDataSet function, the CellDataSet object was created using raw UMI counts under default parameters. Those genes with an average level of <0.1 were eliminated from the trajectory analysis, whereas the DEGs that satisfied a q-value of <0.01 in 2 cell groups were implemented in dimension reduction using the reduce Dimension() function, with the following parameters, max_components = 2 and reduction method = 'DDR_Tree'. Next, we performed single-cell ordering and visualization using the plot_cell_trajectory() function, followed by coloring according to pseudo time or cell groups. The genes that showed differential levels between branches were identified using the branch expression analysis modeling (BEAM) algorithm, whereas those that satisfied a q-value of $<10^{-10}$ were placed in different clusters, followed by visualization using the plot_genes_branched_heatmap() function. The clusterProfiler (version 3.14.3) package in the R software was used for GO functional annotation of the genes in different clusters.

## Interactions between cell types

Using the CellChat algorithm (version 0.0.2; https://github.com/sqjin/CellChat), the ligand-receptor (L-R) interactions were analyzed based on the ligand levels within a type of cell, as well as the respective receptors in another type of cell. Permutation tests were conducted to identify significant L-R interactions ($p < 0.05$). Bubble plots were constructed to visualize the L-R interactions in various cell sub-clusters. Additionally, the L-R interactions, along with their associated strengths, were compared among different cell populations, and then they were visualized using heat maps.

## Gene set variation analysis (GSVA)

We obtained gene sets based on the Cancer Single-cell State Atlas (CancerSEA) and the Molecular Signature Database (MSigDB). Using the GSVA function of the GSVA package (version 1.38.2), the pathway scores of the cells were determined, whereas the limma R software package (version 3.46.0) was used for assessing differential pathways.

## Identification of targets based on surface plasmon resonance-high performance liquid chromatography-mass spectrometry (SPR-HPLC-MS)

Initially, after CF was fixed on the 3D optical cross-linking chip (Photo-cross-linking Sensor Chip), CD117+ cell lysates were circulated on the chip surface. The SPR technology was used for real-time monitoring of the process in which the chip surface molecules captured target proteins. The CF-captured target proteins were determined with the LC-MS consortium, whereas the bioinformatics database was used for functional analysis.

To quantitatively calibrate CF, first, 5 mM CF was prepared using a DMSO solution. Next, array printing was conducted using the BioDot™ −1520 array printer. For maintaining the sample quantity point, we used a point diameter of 180 μm and a point spacing of 280 μm. In this study, a double-needle printing system was used and consisted of the chip surface that contained a 5050 dot array, point solution (2.5 nL), repeated point samples (10 folds), and chip surface point sample (31.25 μL, 312.5 nMol).

Using the protein quantification kit (Thermo Fisher, BCA Protein Assay Kit), cell lysis was performed at a concentration of 498.15 μg/mL. The concentration of the sample was adjusted to 200 μg/mL using the stock lysate (1x).

A NanoSensor biochip (Lumera Corporation) was used for calibrating the performance of the chip. The thickness of the Au layer on the chip surface was determined to be 47.5 nm ± 0.5 nm. Cross-linking of the optical polymer layer was conducted with a <0.5% batch difference in chip binding. The optimal resonance angle was automatically adjusted using a Screen LB 991 biochip analyzer (Berthold) for the measurement of the chip.

The SPR assay is a sensitive and efficient method for identifying target proteins in complex biological samples. The use of CD117+ cell lysate as the mobile phase facilitated the detection of specific proteins of interest, whereas the CF molecule immobilized on the chip surface provided a highly specific binding site for these proteins. The combination of the SPR assay and HPLC-MS analysis were performed to identify specific protein species, which provided valuable information for further developing therapeutic interventions.

## Surface plasmon resonance (SPR) assay

The CF samples, along with four other protein samples (MGST2 and potential binding peptides), refrigerated at −80°C, were thawed under ambient temperature. Then, DMSO was added for diluting CF, which was used as a fixed-phase printing working fluid. Next, the working fluid was printed onto the 3D optical cross-linking chip using an AD1520 chip array printer (Biodot™). Four duplicate points were set for every sample, and four positive points were set for the control (Rapamycin). The printed chip was dried in a vacuum before the optical cross-linking reaction was conducted in the cross-linking machine. Then, DMF, $H_2O$, and $C_2H_5OH$ were shaken for 15 min and blow-dried under a stream of nitrogen. Finally, the flow cell cover was assembled for backup.

To perform protein dialysis, a commercially available protein solution was placed in a dialysis bag, and the detergent was removed with PBS. Glycerol and other additives were added to the initial storage solution. Later, a trace concentration tube was used for evaluating the protein concentration, whereas the protein content was measured using a BCA protein quantification kit and used for subsequent analyses.

Next, PBST (pH = 7.4, 0.1% Tween20) was added to those four protein sample reserves for real-time visualization, followed by dilution of the protein samples to five gradients of 10, 40, 160, 640, and 2,560 nM. Each sample was processed by circulation and testing, and PBST acted as a flow vehicle in the whole process. The analyte was passed over the chip surface at a rate of 0.5 μL/s in the interaction test. During surface regeneration, we used Glycine-HCl (pH = 2.0) as the regeneration fluid at a flow rate of 2 μL/s.

All experiments were conducted following the Standard Operating Procedure (SOP). Different gradient concentrations of each compound sample were placed on the chip surface, ranging from low to high, at a flow rate of 0.5 μL/s, binding reaction temperature of 4°C, binding time of 600 s, and dissociation time of 360 s. We used a Glycine-HCl solution at pH 2.0 as the regeneration fluid for adjusting the pH.

## Molecular dynamics (MD) simulation

The crystalline structure of Mgst2 (PDB entry: 6SSW, MAGNSILLAAVSILSACQQSYFALQVGKARLKYKVTPPAVTGSP EFERVFRAQQNCVEFYPIFIITLWMAGWYFNQVFATCLGLVYIY GRHLYFWGYSEAAKKRITGFRLSLGILALLTLLGALGIANSFLDEY LDLNIAKKLRRQF) was used to produce the original binding complexes. The Preparation Wizard module (Schrodinger, Inc.) was used to establish and determine the protein structure in the native state. After placing the protein in an environment at pH 7.0, hydrogen atoms were introduced into the protein structure based on the isoelectric points of various amino acid residues. Later, the hydrogen bonds were regulated, atomic collisions were eliminated, and charges were added to the hybrid groups to optimize the protein structure. Finally, after removing excess water molecules, the OPLS4 force field (folding to the

lowest energy steady state) was used to minimize the resultant structure. After modeling and optimizing, the protein structures were analyzed based on the Ramachandran Plot and transferred to the binding site that was identified for our proposed protein structure. The binding site prediction algorithm was used to predict the Mgst2 protein region, and 20 and 11 potential binding target regions were predicted, respectively. The above-mentioned binding sites shared a huge hydrophobic area within the target region, and H bond donor and acceptor functional groups within the groove could bind to exogenous compounds.

When analyzing the binding sites, the whole protein surface was scanned to examine additional positions in the protein suitable for binding to the compound, which was later contrasted with the binding site. Then, the spatial form of the region was evaluated using the grid generation module that contained the virtual grid, and the next docking algorithm was used for grid identification and reading. For ligand docking, the super-precision simulation docking module (XP module, Schrodinger, Inc.) was used for docking segmentation. This algorithm was used to assess the binding site structure and analyze the neighboring electron cloud density and non-covalent bond acceptors and donors. While preparing compound structures based on the aforementioned processes, different compound conformations were adjusted to produce random poses according to the functional groups in every pose. Next, the level of overlap, non-covalent bond generation, and electronic cloud fusion state were selected for retaining the suitable structure, which could exist but was different from the most stable structure. Finally, the above structures were analyzed and sorted according to free energy. The stable state output was selected according to its lowest energy.

## AAV transductions and transplantation experiments

BM cells were cultured either in IMDM with GlutaMAX containing 20% fetal bovine serum, 100 IU/mL penicillin, 100 μg/mL streptomycin, 50 μM 2-mercaptoethanol, 10 ng/mL recombinant mouse interleukin (IL)-3, 25 ng/mL recombinant mouse IL-6, and 50 ng/mL recombinant mouse stem cell factor (SCF) (PeproTech, United States of America). Two hours after transduction, cells were switched to expansion mediumand grown at a density of $5 \times 10^5$ cells/mL. On day 10, cells were switched to erythroid differentiation medium (IMDM, BSA, Insulin, Transferrin, Epo). BM from donor mice treated with 5-fluorouracil (FU)–treated (200 mg/kg) was transduced twice with BCR-ABL1 retrovirus by co-sedimentation in the presence of IL-3, IL-6, and SCF. Recipient mice received 1100 cGy gamma irradiation (administered by 2 divided doses of 550-cGy), $5 \times 10^5$ cells were transplanted into the recipient mice by tail vein injection, as described previously (Yin et al., 2020). After transduction, mice were divided with two group and treated with xylene, the HSPCs were analyzed by flow cytometry.

## Statistical analysis

The data were presented as the arithmetic mean ± standard deviation (SD). The SPSS 26.0 software (Chicago, IL, United States of America) was used for data analysis. Repeated measurement data were initially evaluated by the repeated analysis of variance (ANOVA) when they followed a normal distribution and homogeneity. All differences were considered to be statistically significant at $p < 0.05$. The GraphPad Prism 9.0 software (La Jolla, United States of America) was used for plotting graphs.

# Results

## Coniferyl ferulate prevented the xylene-induced toxic effects on the mouse hematological system

To determine whether CF could inhibit xylene-induced toxicity in the hematological system of C57BL/6 mice, the mice were pretreated with CF for 10 days before they were exposed to xylene for 15 days along with CF. The results showed that the weight of the mice decreased significantly after 15 days following the administration of 150 mg/kg b. w. Xylene. The mice that were treated with CF showed significant inhibition in the xylene-induced loss of weight (Figure 1A left). Additionally, treatment with CF inhibited the xylene-induced decrease in the level of WBC and RBC, as shown in Figure 1A (middle and right).

## Integrated analysis of the self-renewal and differentiation of mouse HSPCs

We determined the effects of CF in alleviating the toxic effects of xylene in HSCs along with progenitor compartments in mice through flow cytometry assays. Compared with Control (Figure 1B left), the proportion of LSKs in BM cells decreased considerably after 15 days following the administration of 150 mg/kg b. w. Xylene. Exposure to xylene significantly decreased the HSC-enriched LSK compartment (1.14% vs. 0.6%) along with its subsets, including MPPs (Lin-Sca1+c-kit+CD34+Flk2-) (21.3% vs. 18.8%) and LMPPs (Lin-Sca1+c-kit+CD34+Flk2+) (31.6% vs. 25.9%) in the BM (Figure 1C left). The decrease in HSC proportion induced by xylene was restored by CF, the HSC-enriched LSK compartment (0.6% vs. 1.19%) along with its subsets, including LMPPs (Lin-Sca1+c-kit+CD34+Flk2+) (25.9% vs. 33%) in the BM. Flow cytometric analysis also revealed a marked contraction of Granulocyte-Monocyte Progenitor (GMP) (Lin-Sca1+c-kit+CD34$^+$ CD16/32+) (26.9% vs. 22.1%), Common Myeloid Progenitorand (CMP) (11.5% vs. 8.22%) and Multipotent Progenitor (MEP) (40.3% vs. 34.6%) in BM. In CF + xylene group, the proportion of Granulocyte-Monocyte Progenitor (GMP) (Lin-Sca1+c-kit+CD34$^+$ CD16/32+) (22.1% vs. 24.8%), Common Myeloid Progenitorand (CMP) (8.22% vs. 11.9%) and Multipotent Progenitor (MEP) (34.6% vs. 37.8%) in BM were restored (Figure 1D left). The colony size of HSPCs also confirmed these results (Figures 1B–D right). These results indicated that the inhibition of HSPCs caused by xylene can be alleviated by CF.

## The damage to B cells, T cells, and myeloid cells caused by xylene can be restored by CF

We also analyzed whether CF could prevent the xylene-induced decrease in the production of mature erythroid and

myeloid cells. Many mice in the xylene group showed a decrease in the proportion of myeloid cells (Gr-1+/Mac-1+) (30.6% vs. 58.2%), B cells ($CD19^+$) (36.8% vs. 48.6%) and T cells (CD90.2+) (3.6% vs. 2.74%) compared to the mice that were not exposed to xylene. However, in the CF + xylene group, the population of mature myeloid (30.6% vs. 46.6%), B cells ($CD19^+$) (36.8% vs. 41.3%) and T cells (CD90.2+) (2.74% vs. 3.3%) was restored to normal levels (Figures 1E–G). These results suggested that CF can reverse the xylene-induced decrease in mature myeloid, B cells and T cells *in vivo*.

## Single-cell transcriptomic profiling of BM HSPCs in mice

To determine the effects of CF on the components of HSPCs and the corresponding supporting cells in the bone marrow (BM) of mice at the transcriptome level before and after xylene induction, we submitted samples to 10xGenomics for droplet-based single-cell RNA sequencing (scRNA-seq).

We collected 6,137, 6,001, and 6840 cells from the control, DimBEn, and DimBEnCF groups, respectively. Following batch correction, cellular heterogeneity was analyzed based on uniform manifold approximation and projection (UMAP) (Figure 2A). The cells were pooled and classified into eight main clusters, including hematopoietic stem cell 1 (expressing Hif, Mecom, Procr, and Ly6a; Figure 2B), monocyte progenitors (expressing Lrf8, Ly86, Csf1r, and Tifab; Figure 2C), neutrophil progenitors (expressing Elan, Gda, Hp, and Trem3; Figure 2D), lymphoid progenitors (expressing Flt3, Dntt, and Ll7r; Figure 2E), mast cells and basophil cells (expressing Ms4a2, Gzmb, Prss34, Mcpt8, and Car1; Figure 2F), megakaryocyte progenitors (expressing Itga2b, Pf4, Vwf, and Gp1bb; Figure 2G), lymphoid progenitors (expressing Exp, Prg2, and Prg3; Figure 2H), and erythroid (expressing Cpr1, Klf1, Epor, and Gata1; Figure 2I). These results showed that the transcriptomes of HSPCs provided new ways to investigate the transcriptional landscape during the early differentiation of HSPCs at the resolution of a single cell.

## The self-renewal procedure of HSPCs was evaluated by RNA velocity analysis

As clustering does not provide any information on inter-cluster connectivity, we determined trajectories across the annotated clusters with PAGA. The arrows in the RNA velocity plot indicated the inferred developmental paths of the cells. The results indicated that the HSPCs developed into various cell types in the samples of the control group (Supplementary Figures S1A, B). In the DimBEn group, the surrounding cell types of HSPCs, especially monocyte and neutrophil progenitors, differentiated into HSPCs (Supplementary Figures S1C, D). These findings suggested that the proportion of monocyte and neutrophil progenitors probably decreased. After treatment with CF, the HSPCs differentiated into lymphoid progenitor cells (Supplementary Figures S1E, F).

## Sub-clusters were associated with the toxicity of xylene in the BM

To investigate which cell subsets were related to the effects of xylene and CF, based on UMAP and t-SNE clustering, the HSCs were further classified into five subtypes (sub-clusters 0–4, Figures 3A, B). Then, we analyzed the number of cells in each subset between different groups. Clusters 0, 1, and 4 increased after treatment with xylene, however, this change was reversed by CF (Figure 3C). The volcano plot of differentially expressed genes (DEGs) for DinBEn *versus* Control, and DinBEn *versus* DinBEnCF are shown in Figure 3D, where the *y*-axis indicates the significance of differential expression, and larger $-\log_{10}$(p_val) values indicated that the differential expression was more significant. For each cluster, the DEGs that were upregulated in DinBEn compared to their expression in Control and DinBEnCF were selected. Then, the top 20 genes with the smallest *p*-values in each cluster were selected for plotting heat maps (Figures 3E, F). We found that some genes were differentially expressed in these sub-clusters, such as Bex6, Clec12a, and Lrf8. The results showed that Clusters 0, 1, and 4 responded to xylene stimulation; thus, we considered these three groups as pathogenic subgroups. The results of the GO analysis showed that in DimBEn *versus* Control (Figure 3G), DimBEn *versus* DimBEnCF (Figure 3H), and DimBEnCF *versus* DimBEn (Figure 3I), Cluster 0 was associated with pressure, stimulation, and other pathway enhancement; Cluster 1 was associated with pressure and microRNA; Cluster 2 was associated with protein folding; Cluster 3 was associated with protein folding; Cluster 4 was associated with mitochondrial energy metabolism. Based on this method, we analyzed monocyte progenitors, neutrophil progenitors, lymphoid progenitors, mast cells and basophils, megakaryocyte progenitors, eosinophil progenitors, and erythroid. By conducting the UMAP analysis, we also found that the number of cells in Cluster 2 decreased significantly after exposure to xylene and increased after treatment with CF. These findings suggested that this subgroup might be important for CF function and also for the process.

Based on UMAP clustering, monocyte progenitor cells were further divided into five subtypes (sub-clusters 0–4, Figures 4A, B). Then, we analyzed the number of cells in each subset between different groups. The number of cells in Cluster 1 increased after treatment with xylene; however, this change was reversed by CF (Figure 4C). The volcano plot of DEGs for DinBEn *versus* Control and DinBEn *versus* DinBEnCF are presented in Figure 4D. For each cluster, we selected the genes that were upregulated in DinBEn compared to their expression in Control and DinBEnCF. Then, the top 20 genes with the smallest *p*-values in each cluster (such as Hspa1b, Hspa1a, and Dusp1) were selected for plotting (Figures 4E, F). These results showed that Cluster 1 can respond to xylene stimulation, and thus, we considered these groups as pathogenic subgroups. The results of the GO analysis showed that for DimBEn *versus* Control (Figure 4G), DimBEn *versus* DimBEnCF (Figure 4H), and DimBEnCF *versus* DimBEn (Figure 4I), Cluster 1 was related to mitochondrial energy metabolism. We found that Cluster 3 was significantly downregulated after exposure to xylene but upregulated after exposure to CF. We speculated that CF might exert its effects through this subgroup. The results of the GO analysis showed that this cluster was associated with pathways such as apoptosis.

According to UMAP clustering, neutrophil progenitor cells were classified into seven subtypes (sub-clusters 0–6, Figures 5A, B). Then, we analyzed the number of cells in each subset between different groups. Clusters 0, 1, and 2 increased after xylene treatment; however, the changes were reversed by CF (Figure 5C). The volcano plot of DEGs in DinBEn *versus* Control and DinBEn *versus* DinBEnCF are shown in Figure 5D. For each cluster, the DEGs that were upregulated in DinBEn compared to their expression in Control and DinBEnCF were selected. Then, the top 20 genes with the smallest *p*-values in each cluster were selected for plotting (Figures 5E, F). Then, we analyzed the number of cells in each subset between different groups and found that some genes were differentially expressed in these sub-clusters, such as Sel1i, Tmem242, and H2-Dmb1. The results showed that Clusters 0, 1, and 2 responded to xylene stimulation, and thus, we considered these three groups as pathogenic subgroups. The results of the GO analysis showed that for DimBEn *versus* Control (Figure 5G), DimBEn *versus* DimBEnCF (Figure 5H), and DimBEnCF *versus* DimBEn (Figure 5I), Cluster 0 was associated with energy metabolism and protein folding; Cluster 1 was associated with energy metabolism and ribosome assembly; cluster 2 was associated with energy metabolism and ribosome assembly. We also found that Cluster 3 was significantly inhibited by xylene, and after CF treatment, the cell percentage was restored. The results of the GO analysis showed that this cluster had a close relationship with DNA damage. Overall, the HSC Clusters 0, 1, and 4, monocyte progenitor cluster 1, and neutrophil progenitor clusters 0, 1, and 2 were considered to be the key subclusters associated with the toxic effects of xylene on HSPCs and the therapeutic effects of CF. Mitochondrial energy metabolism may contribute to the toxic effects of xylene on BM, and the regulatory effects of CF on mitochondrial energy metabolism can reverse the toxic effects on BM cells. The results of the UMAP analysis showed that other subgroups in HSPCs, including lymphoid progenitors (Supplementary Figures S2A, B, and C), mast cells and basophil cells (Supplementary Figures S2D, E, and F), megakaryocyte progenitors (Supplementary Figures S2G, H, and I), lymphoid progenitors (Supplementary Figures S2J, K, and L), and erythroid (Supplementary Figures S2M, N, and O), did not contain many xylene or CF-sensitive populations.

The GSVA was conducted for hallmark pathway enrichment for each cell, and DimBen and DimBen + CF were directly compared to the control group, separately. The results showed that the IFN-α response, DNA repair, and Pi3k/Akt signaling pathway were upregulated and the Notch, Kras, and P53 signaling pathways were downregulated in the control group of HSC1 (Supplementary Figures S3A). In HSC2, we found that Interferon-alpha response, Interferon-gamma response, and Kras signaling were upregulated and downregulated in oxidative phosphorylation, the P53 pathway, and cholesterol homeostasis in the control group (Supplementary Figure S3B). We found that apoptosis, P53, and the reactive oxygen species pathway were upregulated in the DimBen group compared to their levels in the DimBen + CF group, whereas Kras signaling and IFN-α responses were downregulated in HSC1. We also found that P53, apoptosis, and oxidative phosphorylation were upregulated in the DimBen group compared to their levels in the DimBen + CF group, whereas IFN-α responses were downregulated in HSC2. The same pattern was also found for megakaryocyte progenitors (Supplementary Figure S3C), monocyte progenitors (Supplementary Figure S3D), neutrophil progenitors (Supplementary Figure S3E), mast cells and basophils (Supplementary Figure S3F), eosinophil progenitors (Supplementary Figure S3G), and erythroid (Supplementary Figure S3H). Also, P53, IFN-α responses, Pi3k/Akt, the ROS signaling pathway, and metabolism were the most differentially expressed pathways, suggesting that these pathways of HSPCs were sensitive to xylene and CF.

## Evaluation of cell-cell interactions related to the protective effects of CF on the toxicity induced by xylene in the BM

For identifying the intercellular interactions that are conserved throughout the development of HSPCs, we constructed models that included the members participating in ligand-receptor interactions denoted as cell types found in HSPCs. We conducted permutation testing on randomized network connections, where the weighted edges were based on the fold change in the expression of receptors and ligands among the source and target population. Neutrophil progenitor cells had the most outbound and inbound connections. The results of the intercellular communication showed that the Dimben group showed significantly higher signaling networks, such as enhanced interactions of neutrophil progenitor C6 cells with additional HSPCs (e.g., HSC3) and eosinophil progenitors, via Ctsg-F2r, Anxa1-Fpr2, and Lgals9-Cd45/Cd44 ligand-receptor-based interactions (Supplementary Figures S4A, B). Some signaling pathways were significantly decreased in the Dimben group, such as decreased interactions of neutrophil progenitor cells with additional HSPCs (e.g., eosinophil progenitors), via Ccl9-Ccr1 and Ctsg-F2r ligand-receptor-based interactions (Supplementary Figures S4C, D).

## Mgst2 was the direct target of CF

To elucidate the mechanism behind the protective effect of CF against the toxic effects of xylene, we identified the molecular target of CF. For this, we used a chemical proteomics strategy called SPR-HPLC-MS, which helped in the direct identification of intracellular molecular targets. To confirm the specificity of the binding interactions, we performed a competition assay. We added excess unlabeled CF to the CD117+ BM cell lysate before passing it over the CF-coated chip. This led to a decrease in the SPR signal, which indicated that the unlabeled CF competed with the labeled CF for binding to the target proteins. After protein purification and identification by LC-MS/MS (Figure 6A), we found that Mgst2 was one of the targets of CF (Figure 6B). The results of the SPR (Figures 6C–E) experiments showed that Mgst2 was the direct target of CF in CD117+ BM cells. Therefore, we proposed that Mgst2 might be a promising target for alleviating xylene-induced toxicity.

## Identifying direct CF binding amino acid sites in Mgst2 proteins

For determining the CF binding sites in the Mgst2 protein, we used the Schrödinger software for MD analysis. First, we conducted

structural optimization (Supplementary Figure S5A), followed by scanning of the protein-binding sites (Supplementary Figure S5B). Next, three potential CF-binding sites were detected in the Mgst2 protein. The mean docking free energy was −8.0861 kcal/mol (QQSYFALQVGKARLKYKVTPPAVTGSPEFERVFRAQQ, coring binding site: SRR) (Figures 6F–H and Supplementary Figure S5C), −7.2398 kcal/mol (GKARLKYKVTPPAVTGSPEFERVFRAQQ) (Figures 6I, J, and K and Supplementary Figure S5D), and −6.0147 (AVTGSPEFERVF) (Figures 6L–N and Supplementary Figure S5E). The root-mean-square deviation (RMSD) analysis showed the non-covalent bonded binding force (Supplementary Figures S5F, G, and H). After peptide synthesis, we examined the affinity of CF via SPR based on four proteins. Our findings indicated that peptide 1 in the Mgst2 protein interacted closely with CF. Additionally, the middle and weak interacting molecules were peptides 2 and 3, respectively. We compared the affinity between peptides and proteins and between epitope polypeptides and found that the binding site corresponded to peptide 1, and SRR was recognized as the CF-binding epitope on the Mgst2 protein, this is a non-covalent combination.

## Coniferyl ferulate (CF) alleviated the toxic effects of xylene on BM by inhibiting the expression of Mgst2

We analyzed the expression of Mgst2 in HSPCs (Supplementary Figure 6A) and found that Mgst2 was expressed in HSCs (Supplementary Figure 6B), monocyte progenitors (Supplementary Figure 6C), and neutrophil progenitors. They were especially overexpressed in neutrophil progenitors (Supplementary Figure 6D). However, they were rarely expressed in lymphoid progenitors (Supplementary Figure 6E), mast cells and basophils (Supplementary Figure 6F), megakaryocyte progenitors (Supplementary Figure 6G), and eosinophil progenitors (Supplementary Figure 6H). Based on these results, we speculated that HSCs, monocyte progenitors, and neutrophil progenitors might be the key cell populations influenced by CF. Additionally, CF reversed the xylene-induced decrease in mitochondrial transmembrane potential (Figure 7A) and ROS production (Figure 7B). Finally, the results of this study showed that the inhibition of Mgst2 reversed the toxic effects of xylene on the BM in mice. We generated Mgst2 knockdown mice using AAV6 and found a significant reduction in xylene-induced hematotoxicity in bone marrow-transplanted mice with Mgst2 knockdown. The decrease in HSC proportion induced by xylene was restored by inhibiting Mgst2 expression in BM, the HSC-enriched LSK compartment (0.46% vs. 1.32%) along with its subsets, including LMPPs (Lin-Sca1+c-kit+CD34+Flk2+) (20.4% vs. 36.6%) in the BM. Flow cytometric analysis also revealed a marked contraction of Granulocyte-Monocyte Progenitor (GMP) (Lin-Sca1+c-kit+CD34$^{+}$ CD16/32+) (22.6% vs. 31.3%), Common Myeloid Progenitorand (CMP) (11.5% vs. 8.22%) and Multipotent Progenitor (MEP) (38.5% vs. 22.1%) in BM (Figures 7C, D). These findings indicated that CF is a potential therapeutic agent that can alleviate the toxic effects of xylene on the BM by Mgst2.

# Discussion

Xylene-induced injury to HSPCs is an important event in hematopoietic toxicity (Partha et al., 2022). Xylene can decrease the number and colony formation capacity of HSPCs and promote their apoptosis, alterations in the cell cycle, and damage to the DNA (Liao et al., 2022; Eom et al., 2023). CF is a phenolic acid compound that is extensively distributed in Angelica sinensis, which has various pharmacological effects (Hao et al., 2021). However, studies on its role in treating xylene-induced hematopoietic toxicity are rare. In this study, we analyzed the role of CF in alleviating the hematopoietic toxicity induced by xylene using an animal model. We also analyzed its associated mechanisms via single-cell transcriptome sequencing. We found that CF bound to Mgst2 protein and inhibited mitochondrial energy metabolism. The mechanism by which CF alleviated xylene-induced hematopoietic toxicity was novel.

Before transcriptome sequencing, conventional toxicology assays were conducted to evaluate xylene-induced hematotoxicity. The considerable reduction in the content of peripheral blood WBCs and RBCs in the xylene group was similar to findings of another study (Sun et al., 2020). We also found that after CF treatment, the decrease in the content of WBC and RBC caused by xylene was restored. These findings indicated that CF can protect bone marrow cells from the toxic effects of xylene and, thus, help maintain normal blood cell counts. The results of the laboratory and epidemiological studies showed that exposure to benzene influences the BM, which can cause multiple hematopoietic anomalies, including a decrease in the peripheral blood lymphocyte/neutrophil/platelet counts, multiple myeloma, acute myeloid leukemia, and aplastic anemia (Scharf et al., 2020). Our findings were similar to those reported in previous studies, which also found that xylene can decrease the number of lymphocyte and neutrophil progenitor cells in the bone marrow, and this toxic effect can be inhibited by CF. These findings further indicated that CF is a promising therapeutic agent for treating bone marrow damage caused by xylene.

Workers have a high risk of exposure to benzene in the occupational setting, and long-term exposure to benzene can impair blood and immune cell count (Durmusoglu et al., 2010; Bahadar et al., 2014). As the whole transcriptome can be analyzed using data-driven methods, single-cell genomics might be used to transform the ability to define the cellular state and cell type (Liu et al., 2023; Zhou et al., 2023). HSPCs are an extremely heterogeneous group (Zhou et al., 2020). Previous studies have not reported which subgroups can respond to the toxic effects of xylene. Moreover, no study has investigated which subgroups respond after drug treatment. In this study, we subdivided the major classes of HPSCs into smaller subgroups and identified some pathogenic subgroups. These findings provided new insights into the mechanisms by which specific subgroups respond to the toxic effects of xylene. This information is valuable for investigating benzene-induced hematotoxicity.

Neutrophils are the most abundant in circulation, and they are also the initial responders at the site of the infection, where they swallow pathogenic microorganisms through degranulation,

phagocytosis, and the production of neutrophil extracellular traps (Hirschhorn et al., 2023; Roy et al., 2023). Neutrophils in vertebrates follow a conservative development process. They can be obtained from neutrophil progenitors, which differentiate from myeloblasts into mature neutrophils (Wigerblad and Kaplan, 2023). Toxic effects such as the deficiency of neutrophils or leukopenia experienced during chemotherapy are associated with favorable clinical outcomes in several types of cancer (Gurney, 2002). In this study, we found that xylene induced a decrease in the number of neutrophils, and coniferyl ferulate reversed this change. The toxic effects of xylene might lead to the inhibition of the differentiation of hematopoietic stem cells into neutrophil progenitor cells. The deficiency of neutrophils can decrease resistance to microbes, such as bacteria, fungi, and viruses, which can increase the risk of developing infectious diseases, such as pneumonia, meningitis, and sepsis. Neutrophil deficiency might also result in symptoms such as anemia, bleeding, and fever.

Monocytes strongly influence adaptive and innate immunity in circulation, and they are required for inflammation, tissue remodeling, and immune defense (Friedmann-Morvinski and Hambardzumyan, 2023). They are innate immune cells that develop in the BM and can be persistently released in circulation. They enter tissues after inflammatory cues are released or changes in homeostasis occur (Robinson et al., 2021). Monocytes exhibit high plasticity and may differentiate into various monocyte-derived cells in tissues for replacing resident tissue macrophages, enhancing inflammation, or promoting inflammatory responses (Richoz et al., 2022). They strongly influence tissue homeostasis and pathogenic or productive immunity (Guilliams et al., 2018). For maintaining homeostasis, monocytes can migrate to tissues and differentiate into specialized monocytes or macrophages according to the environmental signals. Also, they may accumulate and contribute to the monocyte reservoir (Shi and Pamer, 2011). During inflammation and infection, they enter the affected tissue quickly. Some studies have investigated the fates of monocytes with special functions under different inflammatory settings (Mulder et al., 2021). Monocytes are a part of the immune system and can identify and eliminate pathogens. A lack of monocytes weakens the immune system and affects its function, making the body more susceptible to infections. It may also cause feelings of fatigue and weakness because monocytes participate in regulating energy metabolism and maintaining overall health. They also participate in regulating the inflammatory response. Monocyte deficiency may lead to uncontrolled inflammatory responses, causing inflammation. It may also increase the risk of development of other diseases, such as cardiovascular disease and cancer.

To summarize, a lack of monocytes can seriously affect overall health, and timely diagnosis and treatment are necessary. In this study, we identified key pathogenic subpopulations of monocyte progenitor cells that respond to the toxic effects of xylene, providing new insights into the treatment of xylene-induced hematotoxicity.

Drug target identification is a key method for determining the mechanism of action of drugs (Yin et al., 2020). In this study, using the SPR-LC/MS method, we identified the key target protein of CF that mediates its effects against the hematotoxic effects of xylene. Based on the findings of other studies and our single-cell transcriptome sequencing results, we found that xylene-induced hematotoxicity is related to ROS and mitochondrial metabolism (Huang et al., 2021; Zhang et al., 2022). Therefore, we analyzed proteins associated with ROS and mitochondrial metabolism among the target proteins. Mgst2 is an enzyme that is responsible for catalyzing certain glutathione (GSH)-mediated reactions (Thulasingam et al., 2021). For example, Mgst2 binds to GSH to generate thiolate for peroxide reduction or combines with xenobiotic electrophiles, like 1-chloro-2, 4-dinitrobenzene (CDNB), or with endogenous epoxide leukotriene A4 (LTA4) to produce LTC4, a smooth muscle contractile agent (Rubinstein and Dvash, 2018). Mgst2 is different from its closest relative LTC4S, and it can effectively catalyze CDNB-conjugation, which is commonly observed in enzymes related to detoxification reactions, including soluble glutathione transferases or Mgst1. LTC4S and Mgst2 are membrane-associated proteins that belong to the eicosanoid and glutathione (MAPEG) metabolic protein family. Mgst2 participates in the transcellular biosynthesis of LTC4 and the catalysis of GSH-mediated reduction reaction depending on peroxidase activity (Dvash et al., 2015). Its GSH-mediated peroxidase activity leads to oxidative modification by reducing fatty acid hydroperoxide and phospholipid. ROS are potent antimicrobial agents and can cause inflammation during several biological processes (Wang et al., 2021). Mgst2 can mitigate ROS-mediated lipid peroxidation, which strongly affects the innate immunity of the sea cucumber (Kelner et al., 2014). We found that xylene promoted the production of ROS, and after CF treatment, ROS production was inhibited. Excessive ROS production can damage organs, indicating that the toxic effects of xylene on HSPCs can be induced by oxidative stress, and CF can reverse these changes. By identifying the target, we showed that Mgst2 is a target protein associated with xylene-induced cytotoxicity. The results of the single-cell transcriptome analysis showed that the expression of Mgst2 in neutrophil progenitor cells was initially high, but its level decreased after xylene treatment. Based on these findings, we hypothesized that Mgst2 strongly affects the toxic effects of xylene on HSPCs.

To summarize, in this study, we found that CF can alleviate the toxic effects of xylene *in vivo* and *in vitro*. Our findings provided new evidence, which suggested that CF protects HSPCs from the toxic effects of xylene by inhibiting mitochondrial metabolism in monocytes and neutrophil progenitor subcluster at the single-cell resolution. Based on the results of MD, SPR assay, Mgst2 was found to be the direct target of CF. Regarding the mechanism of action, we speculated that CF is directly bound to Mgst2 to inhibit mitochondrial metabolism, which alleviated the toxic effects of xylene on HSPCs. Therefore, Mgst2 might be the therapeutic target that is regulated to manage xylene-induced toxicity. Our findings might serve as the preclinical rationale for the application of CF as a therapeutic agent for alleviating the toxic effects of xylene on HSPCs.

## Data availability statement

The original contributions presented in the study are included in the article/Supplementary Material, further inquiries can be directed to the corresponding authors.

## Ethics statement

The animal study was approved by the All animal experiments were conducted in accordance with the Government published recommendations for the Care and Use of Laboratory Animals and approved by the Institutional Ethics Review Boards of Jinan university. The study was conducted in accordance with the local legislation and institutional requirements.

## Author contributions

ZY: Conceptualization, Formal Analysis, Methodology, Software, Writing–original draft. RO: Conceptualization, Funding acquisition, Investigation, Resources, Software, Visualization, Writing–original draft. YZ: Funding acquisition, Methodology, Project administration, Supervision, Writing–original draft. ZL: Formal Analysis, Methodology, Validation, Conceptualization, Writing–original draft. JH: Resources, Visualization, Writing–original draft. QZ: Resources, Writing–review and editing. GL: Data curation, Methodology, Supervision, Writing–original draft. QZ: Formal Analysis, Funding acquisition, Resources, Writing–original draft. SL: Conceptualization, Funding acquisition, Project administration, Supervision, Writing–original draft.

## Funding

The author(s) declare financial support was received for the research, authorship, and/or publication of this article. This study was supported by the Key Program for the National Natural Science Foundation of China (No. 82202034, 82074300, and 82304901); Guangzhou Science and Technology Plan Project (No. 202201020245, 202201020340, 202201020241, 202201011281, 202201020485, 202201020567, 2024A04J4325, 2024A03J0991 and 2023A03J0262), the Foundation of Guangdong Second Provincial General Hospital (No. YN2023-001 and TJGC-2023002), Doctoral Workstation Foundation of Guangdong Second Provincial General Hospital (No. 2021BSGZ017), Natural Science Foundation of Guangdong Province (No. 2021A1515012329 and 2021A1515010869), Guangdong Basic and Applied Basic Research Foundation (No. 2020A1515010002, and 2021A1515110430), Science and Technology Planning Project of Guangdong Province of China (No. 2021B1212030008) and Guangdong Provincial Key Laboratory of Clinical Research on Traditional Chinese Medicine Syndrome.

## Acknowledgments

The authors gratefully acknowledged the support of K. C. Wong Education and Science and Technology Planning Project of Guangdong Province (No. 2023B1212060063). The authors also express their gratitude to Leqing Zhu, Yizhen Huang, and Junqing Huang for their contributions in the revision phase.

## Conflict of interest

The authors declare that the research was conducted in the absence of any commercial or financial relationships that could be construed as a potential conflict of interest.

## Publisher's note

All claims expressed in this article are solely those of the authors and do not necessarily represent those of their affiliated organizations, or those of the publisher, the editors and the reviewers. Any product that may be evaluated in this article, or claim that may be made by its manufacturer, is not guaranteed or endorsed by the publisher.

## Supplementary material

The Supplementary Material for this article can be found online at: https://www.frontiersin.org/articles/10.3389/fphar.2024.1334445/full#supplementary-material

## References

Bahadar, H., Mostafalou, S., and Abdollahi, M. (2014). Current understandings and perspectives on non-cancer health effects of benzene: a global concern. *Toxicol. Appl. Pharmacol.* 276 (2), 83–94. doi:10.1016/j.taap.2014.02.012

Crippa, S., Conti, A., Vavassori, V., Ferrari, S., Beretta, S., Rivis, S., et al. (2023). Mesenchymal stromal cells improve the transplantation outcome of CRISPR-Cas9 gene-edited human HSPCs. *J. Am. Soc. Gene Ther.* 31 (1), 230–248. doi:10.1016/j.ymthe.2022.08.011

Durmusoglu, E., Taspinar, F., and Karademir, A. (2010). Health risk assessment of BTEX emissions in the landfill environment. *J. Hazard. Mater.* 176 (1-3), 870–877. doi:10.1016/j.jhazmat.2009.11.117

Dvash, E., Har-Tal, M., Barak, S., Meir, O., and Rubinstein, M. (2015). Leukotriene C4 is the major trigger of stress-induced oxidative DNA damage. *Nat. Commun.* 6, 10112. doi:10.1038/ncomms10112

Eom, H., Kim, S., and Oh, S. E. (2023). Evaluation of joint toxicity of BTEX mixtures using sulfur-oxidizing bacteria. *J. Environ. Manag.* 325 (Pt A), 116435. doi:10.1016/j.jenvman.2022.116435

Friedmann-Morvinski, D., and Hambardzumyan, D. (2023). Monocyte-neutrophil entanglement in glioblastoma. *J. Clin. investigation* 133 (1), e163451. doi:10.1172/JCI163451

Fujimori, K., Uno, S., Kuroda, K., Matsumoto, C., and Maehara, T. (2022). Leukotriene C4 synthase is a novel PPARγ target gene, and leukotriene C4 and D4 activate adipogenesis through cysteinyl LT1 receptors in adipocytes. *Mol. Cell Res.* 1869 (3), 119203. doi:10.1016/j.bbamcr.2021.119203

Gong, W., Zhou, Y., Gong, W., and Qin, X. (2020). Coniferyl ferulate exerts antidepressant effect via inhibiting the activation of NMDAR-CaMKII-MAPKs and mitochondrial apoptotic pathways. *J. Ethnopharmacol.* 251, 112533. doi:10.1016/j.jep.2019.112533

Guilliams, M., Mildner, A., and Yona, S. (2018). Developmental and functional heterogeneity of monocytes. *Immunity* 49 (4), 595–613. doi:10.1016/j.immuni.2018.10.005

Gurney, H. (2002). How to calculate the dose of chemotherapy. *Br. J. cancer* 86 (8), 1297–1302. doi:10.1038/sj.bjc.6600139

Hao, W. Z., Ma, Q. Y., Tao, G., Huang, J. Q., and Chen, J. X. (2021). Oral coniferyl ferulate attenuated depression symptoms in mice via reshaping gut microbiota and microbial metabolism. *Food and Funct.* 12 (24), 12550–12564. doi:10.1039/d1fo02655k

Hassan, H. A., and Aly, A. A. (2018). Isolation and characterization of three novel catechol 2,3-dioxygenase from three novel haloalkaliphilic BTEX-degrading Pseudomonas strains. *Int. J. Biol. Macromol.* 106, 1107–1114. doi:10.1016/j.ijbiomac.2017.08.113

Hirschhorn, D., Budhu, S., Kraehenbuehl, L., Gigoux, M., Schröder, D., Chow, A., et al. (2023). T cell immunotherapies engage neutrophils to eliminate tumor antigen escape variants. *Cell* 186 (7), 1432–1447. doi:10.1016/j.cell.2023.03.007

Huang, H., Jiang, Y., Zhao, J., Li, S., Schulz, S., and Deng, L. (2021). BTEX biodegradation is linked to bacterial community assembly patterns in contaminated groundwater ecosystem. *J. Hazard. Mater.* 419, 126205. doi:10.1016/j.jhazmat.2021.126205

Huang, Y., Cheng, M., Wang, X., Dong, H., and Gao, J. (2022). Dang Gui Bu Xue Tang, a conventional Chinese herb decoction, ameliorates radiation-induced heart disease via Nrf2/HMGB1 pathway. *Front. Pharmacol.* 13, 1086206. doi:10.3389/fphar.2022.1086206

Inesta-Vaquera, F., Miyashita, L., Grigg, J., Henderson, C. J., and Wolf, C. R. (2023). Defining the *in vivo* mechanism of air pollutant toxicity using murine stress response biomarkers. *Sci. total Environ.* 888, 164211. doi:10.1016/j.scitotenv.2023.164211

Kang, Y. J., Tan, H. Y., Lee, C. Y., and Cho, H. (2021). An air particulate pollutant induces neuroinflammation and neurodegeneration in human brain models. *Adv. Sci. (Weinh).* 8 (21), e2101251. doi:10.1002/advs.202101251

Kelner, M. J., Diccianni, M. B., Yu, A. L., Rutherford, M. R., Estes, L. A., and Morgenstern, R. (2014). Absence of MGST1 mRNA and protein expression in human neuroblastoma cell lines and primary tissue. *Free Radic. Biol. Med.* 69, 167–171. doi:10.1016/j.freeradbiomed.2014.01.021

Lan, Q., Zhang, L., Li, G., Vermeulen, R., Weinberg, R. S., Dosemeci, M., et al. (2004). Hematotoxicity in workers exposed to low levels of benzene. *Sci. (New York, N.Y.)* 306 (5702), 1774–1776. doi:10.1126/science.1102443

Liao, Q., Zhang, Y., Ma, R., Zhang, Z., Ji, P., Xiao, M., et al. (2022). Risk assessment and dose-effect of co-exposure to benzene, toluene, ethylbenzene, xylene, and styrene (BTEXS) on pulmonary function: a cross-sectional study. *Environ. Pollut.* 310, 119894. doi:10.1016/j.envpol.2022.119894

Liu, Y. M., Ge, J. Y., Chen, Y. F., Liu, T., Chen, L., Liu, C. C., et al. (2023). Combined single-cell and spatial transcriptomics reveal the metabolic evolvement of breast cancer during early dissemination. *Adv. Sci. (Weinh).* 10 (6), e2205395. doi:10.1002/advs.202205395

Mokammel, A., Rostami, R., Niazi, S., Asgari, A., and Fazlzadeh, M. (2022). BTEX levels in rural households: heating system, building characteristic impacts and lifetime excess cancer risk assessment. *Environ. Pollut.* 298, 118845. doi:10.1016/j.envpol.2022.118845

Mosmeri, H., Gholami, F., Shavandi, M., Dastgheib, S. M. M., and Alaie, E. (2019). Bioremediation of benzene-contaminated groundwater by calcium peroxide (CaO(2)) nanoparticles: continuous-flow and biodiversity studies. *J. Hazard. Mater.* 371, 183–190. doi:10.1016/j.jhazmat.2019.02.071

Mulder, K., Patel, A. A., Kong, W. T., Piot, C., Halitzki, E., Dunsmore, G., et al. (2021). Cross-tissue single-cell landscape of human monocytes and macrophages in health and disease. *Immunity* 54 (8), 1883–1900.e5. doi:10.1016/j.immuni.2021.07.007

Nishida-Aoki, N., Mori, H., Kuroda, K., and Ueda, M. (2015). Activation of the mitochondrial signaling pathway in response to organic solvent stress in yeast. *Curr. Genet.* 61 (2), 153–164. doi:10.1007/s00294-014-0463-9

Partha, D. B., Cassidy-Bushrow, A. E., and Huang, Y. (2022). Global preterm births attributable to BTEX (benzene, toluene, ethylbenzene, and xylene) exposure. *Sci. total Environ.* 838 (Pt 4), 156390. doi:10.1016/j.scitotenv.2022.156390

Richoz, N., Tuong, Z. K., Loudon, K. W., Patiño-Martínez, E., Ferdinand, J. R., Portet, A., et al. (2022). Distinct pathogenic roles for resident and monocyte-derived macrophages in lupus nephritis. *JCI insight* 7 (21), e159751. doi:10.1172/jci.insight.159751

Robinson, A., Han, C. Z., Glass, C. K., and Pollard, J. W. (2021). Monocyte regulation in homeostasis and malignancy. *Trends Immunol.* 42 (2), 104–119. doi:10.1016/j.it.2020.12.001

Roy, S., Halder, M., Ramprasad, P., Dasgupta, S., Singh, Y., and Pal, D. (2023). Oxidized pullulan exhibits potent antibacterial activity against *S. aureus* by disrupting its membrane integrity. *Int. J. Biol. Macromol.* 249, 126049. doi:10.1016/j.ijbiomac.2023.126049

Rubinstein, M., and Dvash, E. (2018). Leukotrienes and kidney diseases. *Curr. Opin. Nephrol. Hypertens.* 27 (1), 42–48. doi:10.1097/MNH.0000000000000381

Salimi, A., Talatappe, B. S., and Pourahmad, J. (2017). Xylene induces oxidative stress and mitochondria damage in isolated human lymphocytes. *Toxicol. Res.* 33 (3), 233–238. doi:10.5487/TR.2017.33.3.233

Scharf, P., Broering, M. F., Oliveira da Rocha, G. H., and Farsky, S. H. P. (2020). Cellular and molecular mechanisms of environmental pollutants on hematopoiesis. *Int. J. Mol. Sci.* 21 (19), 6996. doi:10.3390/ijms21196996

Shi, C., and Pamer, E. G. (2011). Monocyte recruitment during infection and inflammation. *Nat. Rev. Immunol.* 11 (11), 762–774. doi:10.1038/nri3070

Singh, M. P., Ram, K. R., Mishra, M., Shrivastava, M., Saxena, D. K., and Chowdhuri, D. K. (2010). Effects of co-exposure of benzene, toluene and xylene to *Drosophila melanogaster*: alteration in hsp70, hsp60, hsp83, hsp26, ROS generation and oxidative stress markers. *Chemosphere* 79 (5), 577–587. doi:10.1016/j.chemosphere.2010.01.054

Snyder, R. (2012). Leukemia and benzene. *Int. J. Environ. Res. public health* 9 (8), 2875–2893. doi:10.3390/ijerph9082875

Sun, R., Liu, M., Xu, K., Pu, Y., Huang, J., Liu, J., et al. (2022). Ferroptosis is involved in the benzene-induced hematotoxicity in mice via iron metabolism, oxidative stress and NRF2 signaling pathway. *Chemico-biological Interact.* 362, 110004. doi:10.1016/j.cbi.2022.110004

Sun, R., Xu, K., Ji, S., Pu, Y., Man, Z., Ji, J., et al. (2020). Benzene exposure induces gut microbiota dysbiosis and metabolic disorder in mice. *Sci. total Environ.* 705, 135879. doi:10.1016/j.scitotenv.2019.135879

Thulasingam, M., Orellana, L., Nji, E., Ahmad, S., Rinaldo-Matthis, A., and Haeggström, J. Z. (2021). Crystal structures of human MGST2 reveal synchronized conformational changes regulating catalysis. *Nat. Commun.* 12 (1), 1728. doi:10.1038/s41467-021-21924-8

Vermeulen, R., Lan, Q., Qu, Q., Linet, M. S., Zhang, L., Li, G., et al. (2023). Nonlinear low dose hematotoxicity of benzene; a pooled analyses of two studies among Chinese exposed workers. *Environ. Int.* 177, 108007. doi:10.1016/j.envint.2023.108007

Wang, B., Xu, S., Sun, Q., Li, X., Wang, T., Xu, K., et al. (2022). Let-7e-5p, a promising novel biomarker for benzene toxicity, is involved in benzene-induced hematopoietic toxicity through targeting caspase-3 and p21. *Ecotoxicol. Environ. Saf.* 246, 114142. doi:10.1016/j.ecoenv.2022.114142

Wang, P., Yang, W., Guo, H., Dong, H. P., Guo, Y. Y., Gan, H., et al. (2021). IL-36γ and IL-36Ra reciprocally regulate NSCLC progression by modulating GSH homeostasis and oxidative stress-induced cell death. *Adv. Sci. (Weinh).* 8 (19), e2101501. doi:10.1002/advs.202101501

Wigerblad, G., and Kaplan, M. J. (2023). Neutrophil extracellular traps in systemic autoimmune and autoinflammatory diseases. *Nat. Rev. Immunol.* 23 (5), 274–288. doi:10.1038/s41577-022-00787-0

Xia, J., Liu, M., Zhu, C., Liu, S., Ai, L., Ma, D., et al. (2023). Activation of lineage competence in hemogenic endothelium precedes the formation of hematopoietic stem cell heterogeneity. *Cell Res.* 33 (6), 448–463. doi:10.1038/s41422-023-00797-0

Yin, Z., Huang, G., Gu, C., Liu, Y., Yang, J., and Fei, J. (2020). Discovery of berberine that targetedly induces autophagic degradation of both BCR-ABL and BCR-ABL T315I through recruiting LRSAM1 for overcoming imatinib resistance. *Clin. cancer Res.* 26 (15), 4040–4053. doi:10.1158/1078-0432.CCR-19-2460

Yin, Z., Su, R., Ge, L., Wang, X., Yang, J., Huang, G., et al. (2023). Single-cell resolution reveals RalA GTPase expanding hematopoietic stem cells and facilitating of BCR-ABL1-driven leukemogenesis in a CRISPR/Cas9 gene editing mouse model. *Int. J. Biol. Sci.* 19 (4), 1211–1227. doi:10.7150/ijbs.76993

Zhang, W., Wang, J., Liu, Z., Zhang, L., Jing, J., Han, L., et al. (2022). Iron-dependent ferroptosis participated in benzene-induced anemia of inflammation through IRP1-DHODH-ALOX12 axis. *Free Radic. Biol. Med.* 193 (Pt 1), 122–133. doi:10.1016/j.freeradbiomed.2022.10.273

Zhou, T., Chen, Y., Liao, Z., Zhang, L., Su, D., Li, Z., et al. (2023). Spatiotemporal characterization of human early intervertebral disc formation at single-cell resolution. *Adv. Sci. (Weinh).* 10 (14), e2206296. doi:10.1002/advs.202206296

Zhou, Y., Zhu, X., Dai, Y., Xiong, S., Wei, C., Yu, P., et al. (2020). Chemical cocktail induces hematopoietic reprogramming and expands hematopoietic stem/progenitor cells. *Adv. Sci. (Weinh).* 7 (1), 1901785. doi:10.1002/advs.201901785

frontiers | Frontiers in Pharmacology

TYPE Original Research
PUBLISHED 20 June 2024
DOI 10.3389/fphar.2024.1412300



OPEN ACCESS

EDITED BY
Wenzhi Hao,
Jinan University, China

REVIEWED BY
Xiaokang Jia,
Hainan Medical University, China
Yang Zheng,
Guangxi University of Chinese Medicine, China

*CORRESPONDENCE
Zhixi Hu,
003405@hnucm.edu.cn

RECEIVED 04 April 2024
ACCEPTED 30 May 2024
PUBLISHED 20 June 2024

CITATION
Li L, Ye J, Zhao Z, Hu S, Liang H, Ouyang J and Hu Z (2024), Shenfu injection improves isoproterenol-induced heart failure in rats by modulating co-metabolism and regulating the trimethylamine-N-oxide - inflammation axis. *Front. Pharmacol.* 15:1412300. doi: 10.3389/fphar.2024.1412300



# Shenfu injection improves isoproterenol-induced heart failure in rats by modulating co-metabolism and regulating the trimethylamine-N-oxide - inflammation axis

Lin Li[1,2], Jiahao Ye[3], Zhenyu Zhao[3], Siyuan Hu[2], Hao Liang[1,2], Ji Ouyang[3] and Zhixi Hu[1,2]*

[1]Provincial Key Laboratory of TCM Diagnostics, Hunan University of Chinese Medicine, Changsha, Hunan, China, [2]The Domestic First-class Discipline Construction Project of Chinese Medicine, Hunan University of Chinese Medicine, Changsha, Hunan, China, [3]Post-Graduate School, Hunan University of Chinese Medicine, Changsha, Hunan, China

Heart failure (HF) is a chronic condition that progressively worsens and continues to be a major financial burden and public health concern. The "gut-heart" axis provides an innovative perspective and therapeutic strategy for preventing and treating heart failure. Shenfu injection (SFI) is a Traditional Chinese Medicine-based treatment demonstrating potential as a therapeutic strategy for heart failure. However, the precise therapeutic mechanisms of SFI in heart failure are not completely characterized. In this study, HF models were established utilizing subcutaneous multipoint injection of isoproterenol (ISO) at a dosage of 5 mg $kg^{-1}$·$d^{-1}$ for 7 days. Serum levels of inflammatory biomarkers were quantified using protein microarrays. Rat feces were analyzed using untargeted metabolomics research and 16S rRNA sequencing. The link between gut microbiota and metabolites was examined using a MetOrigin and Spearman correlation analysis. Our results show that Shenfu injection effectively enhances cardiac function in rats with ISO-induced heart failure by potentially modulating pro-/anti-inflammatory imbalance and reducing serum and urine Trimethylamine-N-oxide (TMAO) levels. Moreover, SFI significantly increases the abundance of *Bacteroidota* at the phylum level, thereby improving disrupted gut microbiota composition. Additionally, SFI supplementation enriches specific genera known for their capacity to produce short-chain fatty acids. SFI was found to be associated with three key metabolic pathways, as revealed by fecal metabonomics analysis, including the pentose phosphate pathway, pyrimidine metabolism, and purine metabolism. Metabolite tracing

**Abbreviations:** HF: Heart Failure. LPS: Lipopolysaccharide. LVEF: Left Ventricular Ejection Fraction. LVFS: Left Ventricular Fractional Shortening. NT-proBNP: N-terminal ProB-type Natriuretic Peptide. OTU: Operational Taxonomic Unit. OPLS-DA: Orthogonal Projections to Latent Structures Discriminate Analysis. PCoA: Principal Coordinates Analysis. PCA: Principle Component Analysis. SCFA: Short-Chain Fatty Acids. SFI: Shenfu Injection. VIP: Variable Importance in the Projection. TMAO: Trimethylamine N-oxide. QC:Quality control. MET:Metoprolol.UHPLC-QE-MS: Ultra-High Performance Liquid Chromatography Quadrupole-Orbitrap Mass Spectrometry.UHPLC-OE-MS: Ultra-High Performance Liquid Chromatography-Ion Trap-Orbitrap Mass Spectrometry. TIC:Total Ion Chromatogram.

analysis revealed that Taurine and hypotaurine metabolism was found to be specific to the microbial community. The biosynthesis of Pyrimidine metabolism, Purine metabolism, beta-alanine metabolism, Naphthalene degradation, Pantothenate, and CoA biosynthesis were identified as co-metabolic pathways between microbes and host. The Spearman correlation analysis was also significantly correlated to differentially expressed metabolites regulated by SFI and the gut microbiota. These results suggest that SFI improves ISO-induced heart failure by modulating co-metabolism and regulating the TMAO-inflammation axis.

KEYWORDS

**gut microbiota, 16S rDNA, metabolomics, inflammation, Shenfu injection**

## 1 Introduction

Heart failure (HF) is a complex and potentially fatal condition caused by a variety of cardiovascular disorders. It is marked by high costs, substantial morbidity and mortality, and therefore presents a significant worldwide health concern (Groenewegen et al., 2020). Over 64 million people worldwide are affected by chronic heart failure (CHF), and despite ongoing advancements in diagnosis, treatment, and management, re-admission and mortality rates have not decreased considerably (Savarese et al., 2023). Therefore, identifying potential therapeutic targets for heart failure is crucial for preventing disease progression.

The expanding focus on the potential role of the gastrointestinal system in the development of HF has sparked increasing interest (Tang et al., 2019). The gut-heart axis, which describes the interaction between the gut and the heart, presents a unique viewpoint and potential therapeutic avenue for managing heart failure (Madan and Mehra, 2020; Bui et al., 2023). Tang et al. pioneered the "gut hypothesis of heart failure" which postulated that reduced cardiac output in heart failure could compromise intestinal perfusion, resulting in mucosal ischemia and subsequent damage to the intestinal mucosa. Intestinal barrier dysfunction can cause increased permeability, leading to malnutrition, bacterial translocation, and higher levels of endotoxins in the bloodstream (Tang et al., 2019). This can trigger inflammation linked to heart failure, with factors like epithelial dysfunction, gut barrier compromise, microbiota imbalance, and abnormal gut metabolites playing a role in the development and worsening of the condition (Tang et al., 2019; Cui et al., 2023). Increased systemic inflammation is reported to be linked to gut dysbiosis, especially in HF patients (Madan and Mehra, 2020).

Trimethylamine-N-oxide (TMAO) is a metabolite derived from the gut microbiota, originating from phosphatidylcholine, choline, betaine, and L-carnitine. These nutrients are abundant in seafood, dairy products, egg yolks, muscle meat, and organ meats. The gut microbiota's trimethylamine (TMA) lyase hydrolyzes these nutrients to form the TMAO precursor TMA, which is further oxidized by hepatic flavin monooxygenase to form TMAO (Zhang et al., 2021). It has been suggested that dietary choline and TMAO may contribute to cardiovascular disease (CVD) (Canyelles et al.,

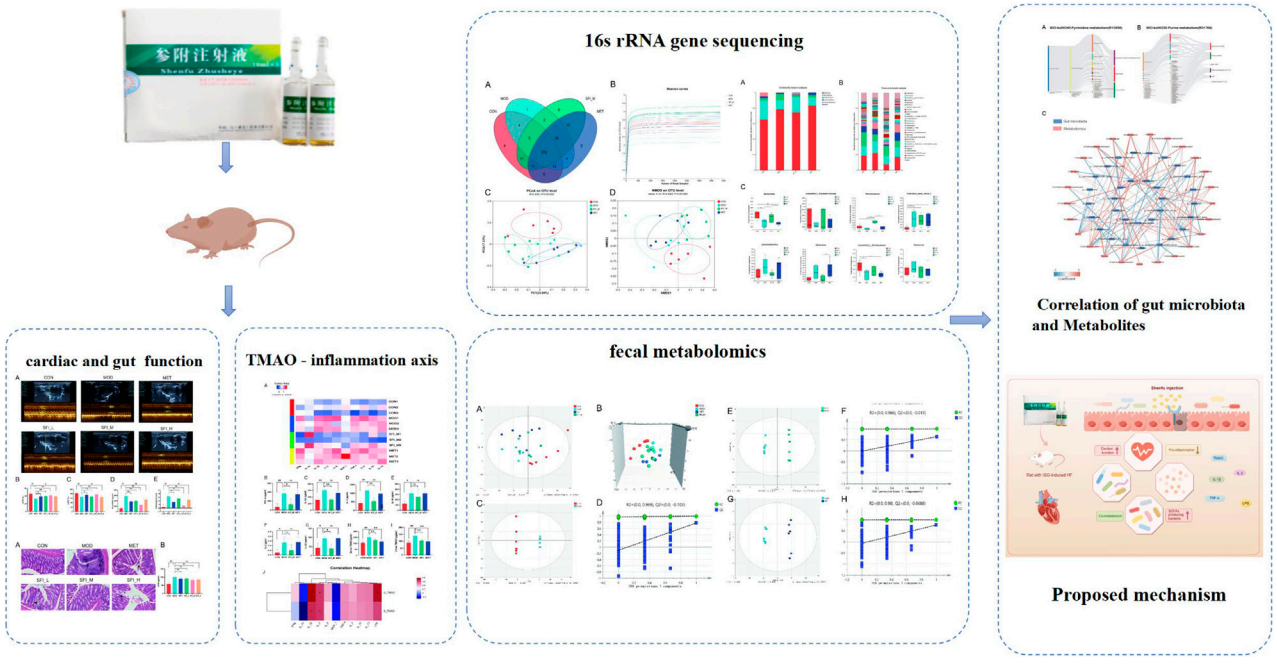


GRAPHICAL ABSTRACT

2023). The increase in blood TMAO levels has been linked to increased inflammatory genes and cytokines, resulting in increased oxidative stress (Saaoud et al., 2023). The pathophysiology of numerous inflammatory conditions is considerably affected by the activation of inflammatory pathways and the production of inflammatory cytokines by TMAO. The development of heart failure has been linked, in part, to inflammation, thus, alleviating inflammation is crucial for enhancing the clinical manifestations and prognosis of HF. Consequently, targeting the TMAO-inflammation axis could be a unique therapeutic strategy for treating heart failure.

Based on recent research, Traditional Chinese Medicine (TCM) can prevent the development of cardiovascular diseases by regulating the gut microbiota and reducing inflammation (Huang et al., 2020). TCM is a valuable tool for improving cardiac function, mitigating medical conditions, and improving the overall wellbeing of patients. In treating post-acute myocardial infarction heart failure, recent pharmacological evaluations—such as those conducted by Wu et al. (2022)—have demonstrated the reliability and effectiveness of SFI, highlighting its potential to improve heart function and reduce associated symptoms (Wu et al., 2022). Researchers have shown that TCM is effective in modulating the dysbiosis of gut microbiota, stimulating the proliferation of beneficial microorganisms, suppressing the proliferation of detrimental microorganisms, harmonizing the abundance of commensal and pathogenic bacteria, and sustaining a favorable gut milieu (Huang et al., 2020; Jia et al., 2020). Shenfu injection (SFI) is one of the representative prescriptions of the warming Yang method. It originates from the classic formula Shenfu Decoction and continues to be applied extensively in the treatment of heart failure with remarkable curative effects (Luo et al., 2021). Currently, SFI is a formulation created with *Panax ginseng* C.A. Mey [Araliaceae; Ginseng radix et rhizoma rubra] and *Aconitum carmichaelii* Debx [Ranunculaceae; Aconiti lateralis radix praeparata] (Chen et al., 2017) utilizing cutting-edge technologies. Previous pharmacological experiments have confirmed that Shenfu Injection can enhance myocardial contractility, increase cardiac output, and inhibit cardiomyocyte apoptosis caused by myocardial ischemia/reperfusion injury, among other cardiovascular effects (Wu H. et al., 2019; Wang et al., 2021). In addition, a study by Zhu et al. demonstrated that this intervention can mitigate myocardial injury through the prevention of mitochondrial apoptosis and facilitating vasodilation by augmenting eNOS activity via the PI3K/Akt signaling pathway (Zhu et al., 2020). Nevertheless, the precise underlying mechanism remains incompletely understood. Therefore, this research endeavors to delve into the mechanisms underlying the enhancement of cardiac function in chronic heart failure through the administration of SFI.

# 2 Material and method

## 2.1 Shenfu injection

Shenfu injection (batch number:221111AK05) was purchased from Huarun Sanjiu Pharmaceutical Co., Ltd. (Ya'an, Sichuan, China). This injection is a solution extracted from *Panax ginseng* C.A. Mey and *Aconitum carmichaelii* Debeaux, as described in Table 1. The two Chinese herbs—P*anax ginseng* C.A. Mey and *Aconitum carmichaelii* Debeaux—in crude form were soaked and concentrated into solutions of 1 mg/mL and 2 mg/mL, respectively, and then mixed to form the SFl injection (Huang et al., 2024). All voucher specimens are deposited in the herbarium center of Huarun Sanjiu Pharmaceutical Co., Ltd. The plant was identified was conducted by a botanist at Huarun Sanjiu Pharmaceutical Co., Ltd.

## 2.2 Reagents and chemicals

Metoprolol tartrate was bought from AstraZeneca Pharma (NO2302069) (Jiangsu, China). Isoproterenol ($C_{11}H_{17}NO_3$▪HCL) was purchased from Aladdin (Shanghai Aladdin Biochemical Technology Co., Ltd., Shanghai, China). Protein chip detection: A protein chip assay kit (QAR-INF-1) was purchased from Raybiotech, Inc. (Norcross, GA, United States of America). The TMAO kit was provided by Xiamen Luncanshuo Biotech Co., Ltd. The NT-proBNP and LPS kit was provided by Wuhan Huamei Biological Engineering Co., Ltd.

## 2.3 Animals and ethics statement

This study received approval from the Ethical Committee of Hunan University of Chinese Medicine (Hunan, China) under Approval Number LL202309230002. Thirty-two male Sprague-Dawley (SD) rats, aged 6 weeks that weighed 200–220 g were procured from Hunan SJA Laboratory Animal Co. Ltd. (Hunan, China) and maintained under standard husbandry conditions.

## 2.4 Quality control of the shenfu injection

Ultra-High Performance Liquid Chromatography Quadrupole-Orbitrap Mass Spectrometry (UHPLC-QE-MS) was performed to control the quality of the Shenfu injection. The analysis was performed using a Vanquish UHPLC system (Thermo Fisher) with a Waters UPLC BEH C18 column (Xiao et al., 2020). Samples (5 μL) were eluted at 0.5 mL/min with a mobile phase of 0.1% formic acid in water (A) and acetonitrile (B). A Q Exactive Focus mass spectrometer with Xcalibur software was used for MS and MS/MS data acquisition (IDA mode, m/z range: 100–1,500). The top three ions per cycle were selected for MS/MS.

## 2.5 Establishment of animal model and drug administration

The animals in the study were divided into six groups at random (n = 8), namely, the control group (CON group), model group (MOD group), positive drug group (metoprolol, the beta-adrenergic antagonist, MET group, 10 mg/kg) (Lujan and DiCarlo, 2020), the Shenfu injection low dose group (3.0 mL/kg, SFI_L group), the Shenfu injection middle dose group (6.0 mL/kg, SFI_M group), and the Shenfu injection high dose group (12.0 mL/kg, SFI_H group). According to prior research, rats were administered subcutaneous multipoint injections of isoproterenol at a dosage of 5 mg·kg-1·day-1 for 7 days to induce the heart failure model (Huang et al., 2022). After adaptive feeding continued for

TABLE 1 Information of raw herbs in SFI.

| Latin name | Plant part | English name | Chinese name | Ratio (%) | Origin of place | Month of harvest |
|---|---|---|---|---|---|---|
| *Panax ginseng* C.A Mey | Root | Red Ginseng Root | Hongshen | 33.3 | Jilin, China | September |
| *Aconitum carmichaelii* Debeaux | Tuber | Aconite | Fuzi | 66.6 | Sichuan, China | August |

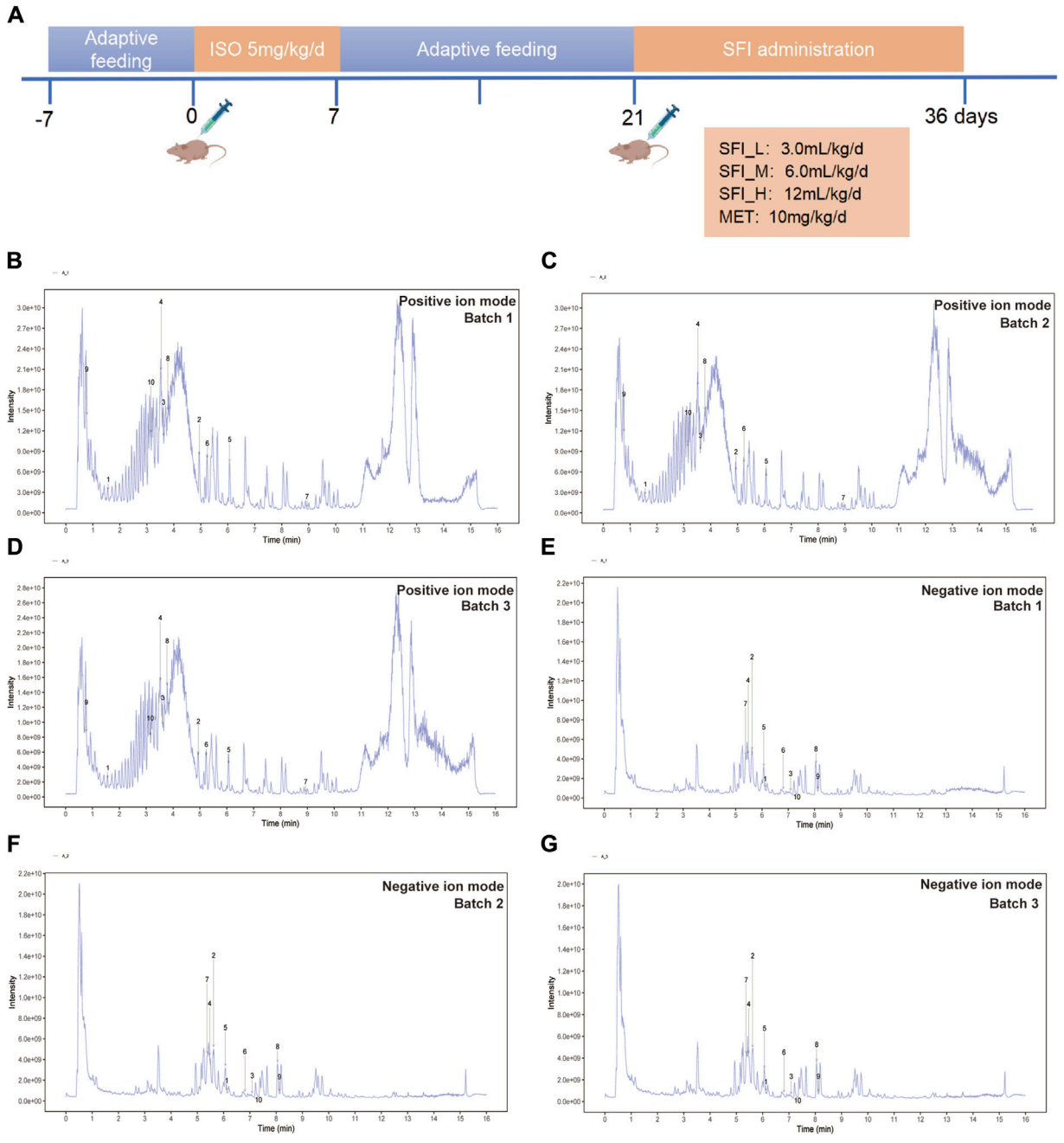


FIGURE 1
**(A)** Schematic illustration of the animal experimental design. **(B)** The UHPLC-QE-MS chromatogram illustration of three batches of SFI samples detected in positive ion mode **(B–D)** and negative ion mode **(E–G)**.

2 weeks, the CON and MOD groups were administered distilled water by gavage and had normal saline injected intraperitoneally, while the SFI group was intraperitoneally injected with SFI and administered purified water by gavage, the MET group was injected with metoprolol intragastrically and intraperitoneally with sterile water for 15 days (Figure 1A).

## 2.6 Sampling and bioassays

At the end of the experimental period, the rats were euthanized using urethane anesthesia (1.0 g/kg, i.p.). The blood samples were obtained from the abdominal aorta and allowed to clot at room temperature (25°C ± 2°C). Subsequently, centrifugation was performed to obtain serum. Myocardial and colonic tissues were fixed in a 4% paraformaldehyde solution for 48 h. Hematoxylin and eosin (H&E) staining was performed on tissue sections fixed in paraffin.

The scoring of cardiac pathological changes was based on the criteria established in the study by Rezkalla et al. (1990). Three high-power fields were observed in each slice to calculate the percentage of inflammatory infiltration and necrosis area compared to the total area. A scoring system was established as follows: 0 points for no lesion, one point for a lesion area of less than 25%, two points for a lesion area of 25%–49%, three points for a lesion area of 50%–75%, and four points for a lesion area greater than 75% (Niu et al., 2017; Xiao et al., 2019). After being extracted from the colon, fecal samples were kept in liquid nitrogen at −80°C. Six rats were randomly chosen from each group for 16S rRNA sequencing and microbiome analysis.

## 2.7 Echocardiography

For the calculation of the Left Ventricular Ejection Fraction (LVEF)and Left Ventricular Fractional Shortening (LVFS), the computer software (VINNO6, Suzhou VINNO Technology Co., Ltd., Suzhou, China) was used (Li et al., 2023).

## 2.8 UHPLC-OE-MS fecal metabolic profiling

Ultra-High Performance Liquid Chromatography-Ion Trap-Orbitrap Mass Spectrometry (UHPLC-OE-MS) was peformed using HPLC system connected to a Waters ACQUITY UPLC BEH Amide column coupled to Orbitrap Exploris 120 mass spectrometer (Orbitrap MS, Thermo). Conditions for UHPLC-MS analysis can be found in Supplementary Material (Supplementary Material 1). A Quality control (QC) mixture was created by combining extracts from all samples to assess variability. Supplementary Figure S1A illustrates the remarkable stability and reproducibility of the instruments utilized in this investigation. The distinct clustering in the QC samples demonstrates consistent and reliable performance.

Results were processed as specified in previous publications (Li et al., 2021). In this study, 15,533 in two (positive and negative) ion modes were detected, and 8,888 metabolites were found after relative standard deviation de-nosing. Metabolite identification was carried out using the R program and BiotreeDB (V3.0) (Chen et al., 2023). Biotree company in Shanghai, China, provided support for the LC-MS detection.

The Metabolomics dataset was analyzed using SIMCA14.1 software from Umetrics, Sweden. Peak numbers, sample identifiers, and normalized peak areas were imported for analysis. Principle Component Analysis (PCA) and Orthogonal Projections to Latent Structures Discriminate Analysis (OPLS-DA) were used, followed by a seven-fold cross-validation to determine $R^2$ and $Q^2$ values. Metabolites with Variable Importance in the Projection (VIP) > 1.0 and $p < 0.05$ were considered significantly changed. Identified markers were then analyzed using MetaboAnalyst to pinpoint the metabolic pathways they influenced. The origin and function analysis of metabolites was performed using MetOrigin (Liu et al., 2023). This methodology aligns with the approach described in a previous publication (Zhao et al., 2023).

## 2.9 16S rRNA gene sequencing

Tiangen Fecal Genomic DNA was used to obtain total genomic DNA following the protocols provided by the manufacturer (Liang et al., 2022). After total DNA extraction from the samples, specific primers containing barcodes were created using the complete primer sequences. The following steps included PCR amplification, purification, quantification, and normalization to generate a sequencing library. The libraries underwent quality control before being sequenced using the PacBio Sequel II system. The output data was converted to CCS files using SMRT Link analysis software, which were then used to identify samples based on their barcode sequences and converted to FASTQ format data. UCHIME v4.2 software was used to detect and eliminate chimera sequences. The resulting effective CCS sequences were used for further analysis (Edgar, 2013). Based on the species annotation information of 16S rDNA sequences in the Silva database (https://www.arb-silva.de/), the operational taxonomic units (OTUs) were classified into various taxonomic levels, including phylum, class, order, family, and genus (Ma et al., 2022). Alpha diversity was assessed using Chao, ACE, Simpson, and Shannon indices. Chao and ACE indices estimate species richness, while Simpson and Shannon indices gauge diversity. The Biotree company in Shanghai, China, provided support for the 16S rRNA gene sequencing.

## 2.10 Protein chip detection

The protein chip assay kit QAR-INF-1 was utilized to measure the levels of inflammatory factors in four distinct groups. The assay was carried out following the manufacturer's protocol.

## 2.11 Statistical analysis

Results were presented as mean ± SD. Statistical analyses were performed using IBM SPSS Statistics 25. The Kolmogorov-Smirnov test was employed to evaluate the normal distribution of the data. Parametric tests were applied to normally distributed data, whereas non-parametric tests were used for data that did not exhibit normal distribution. One-way ANOVA or Dunnett's T3 test was used based on variance homogeneity. Differences with $p < 0.01$ were substantially significant, while $p < 0.05$ was significant. Correlations were calculated using Spearman's rank correlation (presented as Spearman rho). Prism GraphPad software was used for figure creation.

# 3 Results

## 3.1 Qualitative detection of SFI under LC-MS conditions

UHPLC-QE-MS analysis was employed for the quality control assessment of SFI. Figure 1B presents representative

TABLE 2 The core compounds of SFI.

| No | Name | MZ | RT | Formula | Type | MS2 |
|---|---|---|---|---|---|---|
| 1 | (20S,23E)-3beta,12beta,20,25-tetrahydroxydammarane-23-ene 20-O-beta-D-glucopyranoside\|ginsenoside Rh13 | 653.43 | 367.382 | $C_{36}H_{62}O_{10}$ | NEG | 653.427309; 668.887099; 336.878879; 537.416933; 581.417049 |
| 2 | Ginsenoside F1 | 683.44 | 337.19 | $C_{36}H_{62}O_{9}$ | NEG | 683.442099; 637.424548; 92.675844; 101.024143; 475.379881 |
| 3 | Chikusetsu saponin IVa | 793.44 | 425.282 | $C_{42}H_{66}O_{14}$ | NEG | 793.432508; 71.013628; 59.013837; 101.023884; 113.023864 |
| 4 | Ginsenoside Ro | 955.49 | 328.119 | $C_{48}H_{76}O_{19}$ | NEG | 955.487604; 955.515614; 793.434039; 569.389402; 75.008669 |
| 5 | Ginsenoside Re | 945.54 | 364.179 | $C_{48}H_{82}O_{18}$ | NEG | 945.538413; 945.48327; 71.013666; 101.024208; 89.024148 |
| 6 | 6-Gingerol | 293.18 | 408.432 | $C_{17}H_{26}O_{4}$ | NEG | 221.152945; 236.105298; 220.145786; 293.175077; 71.013682 |
| 7 | Ginsenoside Rg2 | 783.49 | 322.2315 | $C_{42}H_{72}O_{13}$ | NEG | 783.480972; 783.50177; 475.380023; 92.678382; 59.013959 |
| 8 | Ginsenoside Rg3 | 783.48 | 483.441 | $C_{42}H_{72}O_{13}$ | NEG | 783.480964; 783.501762; 101.024211; 71.013629; 113.023869 |
| 9 | Ginsenoside Rg3 (R-FORM) | 829.49 | 487.319 | $C_{42}H_{72}O_{13}$ | NEG | 783.481909; 783.502707; 101.024255; 71.013675; 113.024865 |
| 10 | Ginsenoside-Rg1 | 845.49 | 439.588 | $C_{42}H_{72}O_{14}$ | NEG | 799.484899; 799.506337; 637.427691; 101.024146; 92.675001 |
| 1 | Bullatine B | 438.28 | 94.0406 | $C_{24}H_{39}NO_{6}$ | POS | 438.282997; 420.277593; 439.154571; 388.245091; 406.256222 |
| 2 | Ginsenoside Rf | 823.48 | 296.459 | $C_{42}H_{72}O_{14}$ | POS | 823.475297; 823.520123; 365.102344; 91.497063; 245.062527 |
| 3 | Ginsenoside RG1 | 823.48 | 217.128 | $C_{42}H_{72}O_{14}$ | POS | 823.475313; 823.520139; 643.41145; 203.051766; 91.497901 |
| 4 | Benzoylaconine | 604.31 | 211.611 | $C_{32}H_{45}NO_{10}$ | POS | 604.317144; 105.03308; 109.100833; 95.084826; 123.11597 |
| 5 | Ginsenoside Rd | 969.54 | 364.299 | $C_{48}H_{82}O_{18}$ | POS | 969.533842; 789.468488; 789.510567; 969.476581; 970.537505 |
| 6 | Ginsenoside Rb1 | 1,091.60 | 314.367 | $C_{54}H_{92}O_{23}$ | POS | 85.028256; 145.049096; 325.11008; 127.038605; 163.060486 |
| 7 | 14-Deoxy-11,12-didehydroandrographolide | 315.20 | 536.445 | $C_{20}H_{28}O_{4}$ | POS | 133.100608; 315.195615; 189.090703; 157.10117; 105.070083 |
| 8 | Benzoylhypaconine | 574.30 | 226.736 | $C_{31}H_{43}NO_{9}$ | POS | 574.302648; 542.27759; 105.033157; 63.810472; 140.107385 |
| 9 | Aconine | 500.28 | 46.2104 | $C_{25}H_{41}NO_{9}$ | POS | 500.284; 450.24443; 55.586708; 468.255394; 418.218269 |
| 10 | Benzoylmesaconine | 590.30 | 189.104 | $C_{31}H_{43}NO1_{0}$ | POS | 590.293131; 105.033194; 540.259757; 65.588159; 558.264448 |

RT, retention time; NEG, negative ion mode; POS, positive ion mode; MS, mass spectrum.

base peak intensity chromatograms of three different batches of SFI samples. These chromatograms demonstrated effective separation and detection of major SFI components in both positive and negative ion modes, using optimized chromatographic and MS conditions (Figures 1B–G). The chromatograms clearly indicated stable and consistent composition across the three SFI batches. The core compounds were selected for Total ion chromatogram (TIC) icon peak labeling, the details on the compounds are illustrated in Table 2.

## 3.2 Pharmacodynamic evaluation

### 3.2.1 SFI improved cardiac function in rats with ISO-induced HF

The Representative echocardiographic images are shown in Figure 2A. As shown in Figures 2B, C, the LVEF and LVFS levels in the MOD group were significantly decreased compared to the CON group, but the LVFS levels in the SFI_L group, SFI_M group, SFI_H group, and MET group were increased compared with the MOD group (Figure 2B). However, only the SFI_M and

10.3389/fphar.2024.1412300

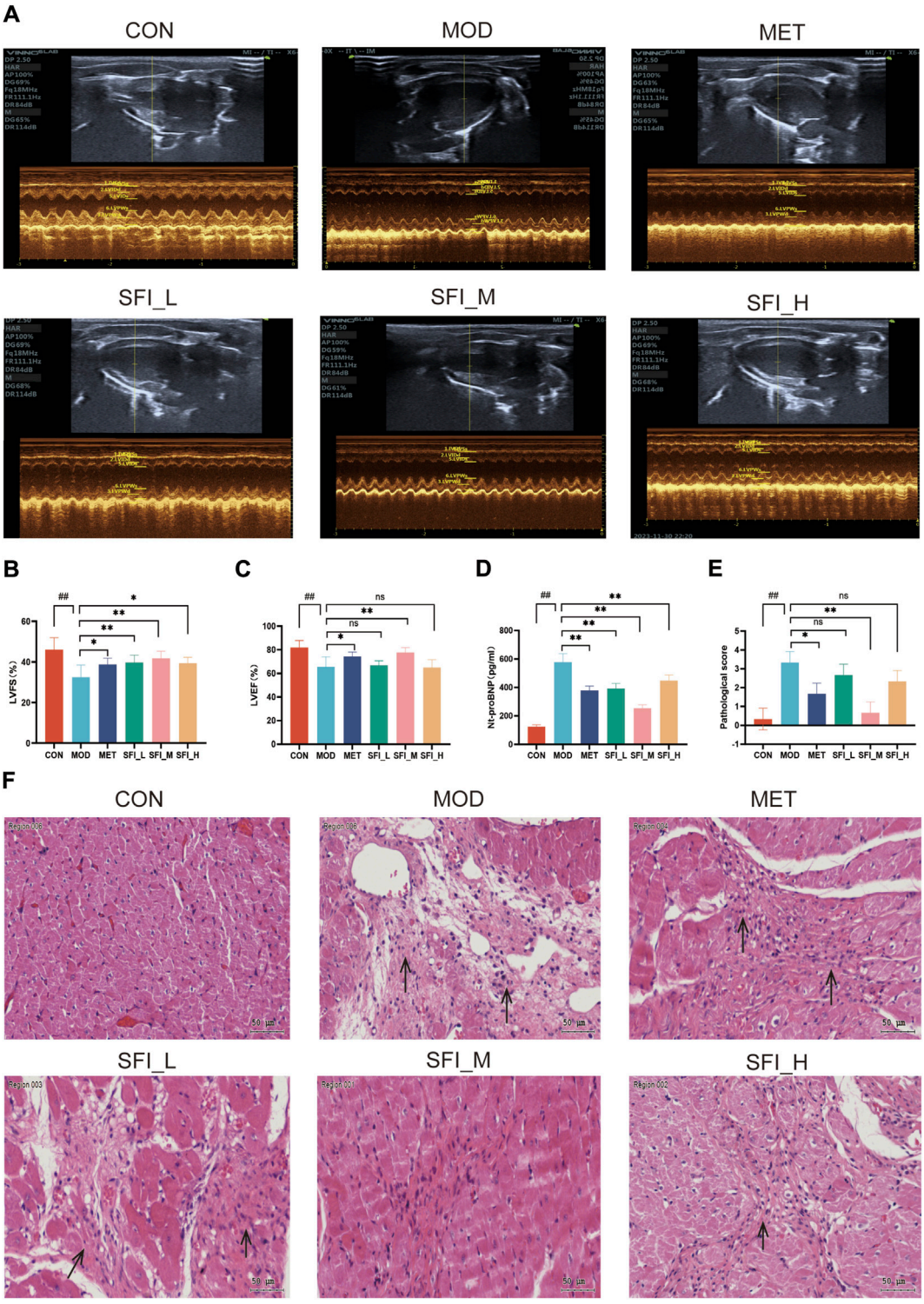


FIGURE 2
**(A)** Mode echocardiography illustration for the six groups. **(B)** Left ventricular fractional shortening. **(C)** Left ventricular ejection fraction. **(D)** Serum level of NT-proBNP, as measured by ELISA. **(E)** Pathological score of H&E staining (n = 3). **(F)** Representative H&E staining images of myocardial tissue (×200). Notes: Data were reported as mean ± SD, n = 8. $^{\#\#}p < 0.01$, compared with the CON group; $^{**}p < 0.01$, compared with the MOD group.

MET groups had markedly increased LVEF levels (Figure 2C). As shown in Figure 2D, there was a notable rise in the NT-proBNP levels in the MOD group. However, treatment with SFI and MET led to a significant reduction in NT-proBNP levels in the rats, with the most pronounced effect observed in the SFI_M group.

The H&E staining in the MOD group showed myocardial dissolution and inflammation infiltrating the tissue, while

10.3389/fphar.2024.1412300

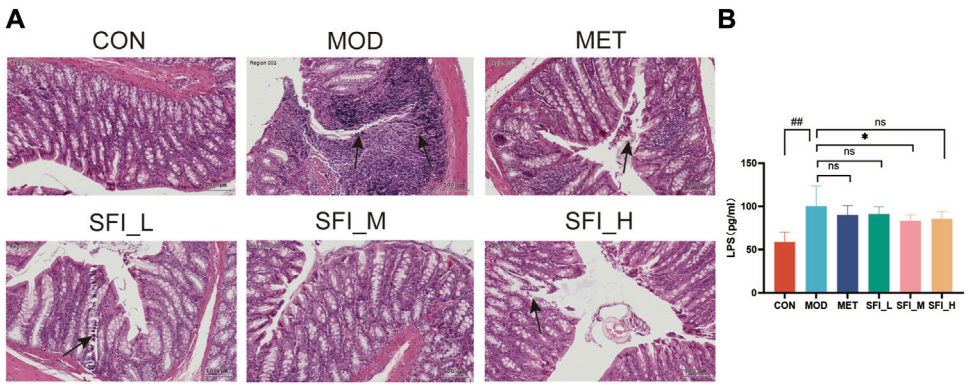


FIGURE 3
**(A)** Representative H&E staining images of colon tissue (×200). **(B)** Serum level of LPS, as measured by ELISA. Notes: Data were reported as mean ± SD, n = 8. $^{\#\#}p < 0.01$, compared with the CON group; $^{**}p < 0.01$, compared with the MOD group.

myocardial structures were vastly improved after SFI and MET treatment, and the most significant effect was observed in the SFI_M group (Figures 2E, F). The improvement observed after SFI treatment was not in a dose-dependent manner.

### 3.2.2 SFI attenuates gut function in rats with ISO-induced HF

The H&E-stained colonic segment of the MOD group displayed compromised intestinal mucosa integrity, inflammatory cell infiltration into the colon tissue, and lymphoid hyperplasia (Figure 3A), indicating potential damage to the intestinal barrier (leaky gut) in the MOD group. Following SFI and MET administration, the colon tissue structures were primarily improved, and the SFI_M treatment attenuated gut function better than SFI_L and SFI_H treatment. As shown in Figure 3B, the serum Lipopolysaccharide (LPS) level in the MOD group was considerably higher than in the CON group, and following SFI_M administration, there was a reduction in the level of LPS.

These findings indicate that SFI potentially preserves both cardiac and gut function in a manner that is not strictly dose-dependent, with the most significant impact observed at intermediate doses. Consequently, a dose of 6 mL/kg was selected for subsequent experiments, including cytokine microarray analysis, 16S rRNA sequencing, and metabolomics studies.

### 3.2.3 SFI improves inflammation and TMAO levels in rats with ISO-induced HF

Cytokine microarray was employed to examine the anti-inflammatory influence of SFI on rats with ISO-induced HF (Figure 4A). Figures 4B–D illustrate that the three highly expressed pro-inflammatory cytokines (TNF-α, IL-1β, and IL-2), in the serum of HF rats were significantly downregulated in the presence of SFI. However, in the HF rat model (Figures 4E–G), the anti-inflammatory cytokines IL-4, IL-10, and IL-13 were elevated, reflecting the pro-/anti-inflammation imbalance. It has been shown that the levels of TMAO were related to inflammation (Wang Q. et al., 2022). As illustrated in Figures 4H, I, TMAO levels in serum and urine in HF were substantially elevated but decreased after treatment with SFI and MET.

### 3.2.4 Correlation analysis between TMAO and inflammation

Red denotes a positive Spearman correlation, while blue denotes a negative Spearman correlation. As shown in Figure 4J positive correlation was observed between inflammatory factors IL-1β and IL-2 and serum TMAO and urine TMAO, as well as between urine TMAO and LPS.

## 3.3 16s rRNA sequencing results

### 3.3.1 OTU analysis

A 97% similarity threshold was used to identify 3,870 operational taxonomic units (representing gamma diversity). The CON, MOD, SFI_M, and MET groups had 888, 845, 1,188, and 949 OTUs, respectively. This revealed that the number of operational taxonomic units (OTUs) in HF rats was decreased, however, the number of OTUs became elevated following SFI processing (Figure 5A).

### 3.3.2 Alpha and beta diversity analysis

The Shannon curve was generated based on OTU numbers to assess the quality of gut microbiota sequencing (Figure 5B). The results indicated a consistent and minimal fluctuation in the curve, suggesting an adequate amount of sequencing data. Alpha diversity analysis was utilized to estimate the microbial diversity within individual samples. The Chao, Shannon, Simpson, and ACE indices in Supplementary Figure S1B analysis showed that the CON and MOD groups differed from one another. Following SFI administration, there was a trend toward recovery in microbial richness, although this trend was not statistically significant. Nevertheless, weighted unifrac PCoA of beta diversity indicated a distinct divergence of the four groups. The four groups are distinctly segregated, as

10.3389/fphar.2024.1412300

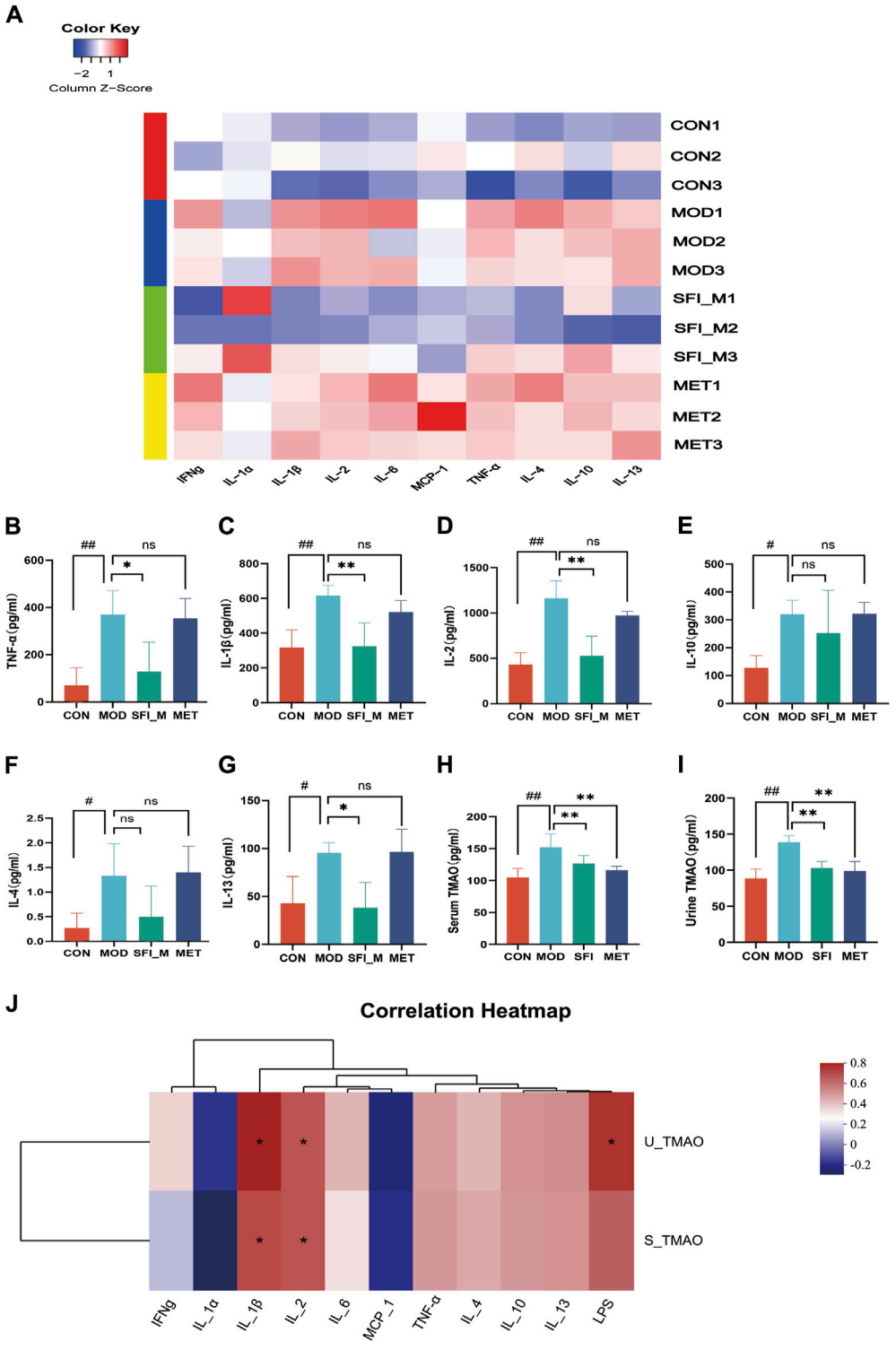


FIGURE 4
**(A)** The heatmap of inflammatory cytokines (n = 3); Cytokine microarray result of **(B)** TNF-α, **(C)** IL-1β, **(D)** IL-2, **(E)** IL-10, **(F)** IL-4 and **(G)** IL-13. **(H)** Serum level of TMAO, as measured by ELISA. **(I)** Urine level of TMAO, as measured by ELISA. **(J)** Spearman correlations between inflammatory cytokines and TMAOs.

evidenced by ANOSIM analysis (ANOSIM: R = 0.3, $p$ = 0.001). As shown in Figure 5C, the CON and MOD groups could be separated, and the SFI_M group was close to the CON group, revealing that SFI_M had a therapeutic influence. The NMDS analysis corroborated the PCoA results (model stress = 0.14 < 0.2) (Figure 5D).

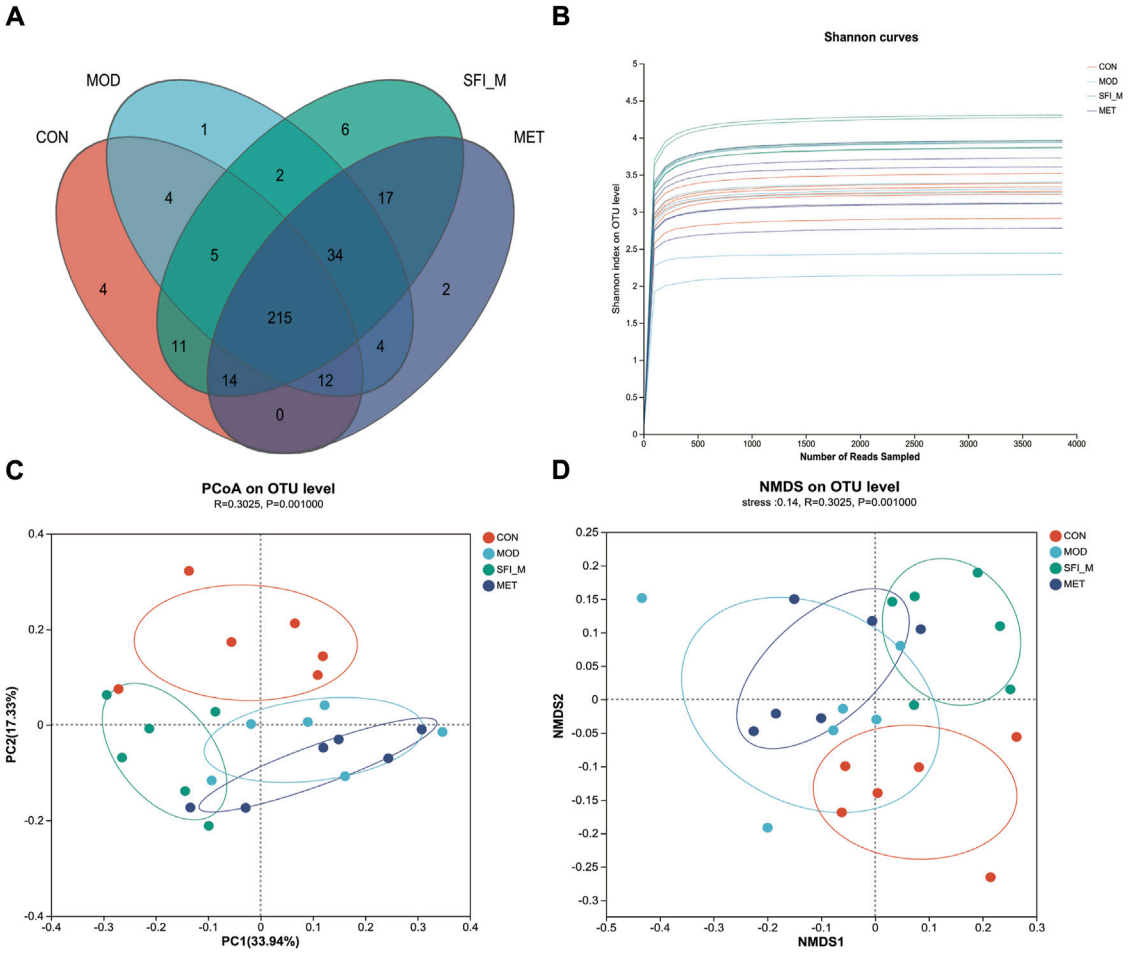


FIGURE 5
**(A)** Venn diagrams of the four groups. **(B)** The Shannon curve of the four groups. **(C)** PCoA analysis of the four groups; **(D)** NMDS analysis of the four groups (n = 6).

### 3.3.3 Composition of gut microbiota and their differential analysis

The barplot in Figure 6A illustrates gut microbiota composition at the phylum and genus levels. *Firmicutes*, *Bacteroidota*, *Proteobacteria*, *Actinobacteria*, and *Campylobacterota* were the most abundant bacteria discovered at the phylum level. *Firmicutes* emerged as the predominant phylum, with relative abundances of 65.1%, 78.5%, 74.5%, and 83.2% in the CON, MOD, SFI_M, and MET groups. Furthermore, compared to the CON group, the MOD group showed a considerable decrease in bacteria with relative abundances of 24.3% and 11.2%, respectively. Additionally, treatment with SFI greatly enriched *Bacteroidota* (19.6% vs. 11.2%) compared with the MOD group.

At the genus level, there were 29 genera with an abundance of over 1% (Figure 6B). *Ruminococcus, unclassified_f_Muribaculaceae*, and *unclassified_f_* Erysipelotrichaceae were less abundant in the MOD group than in the CON group. In contrast, in the MOD group, *Romboutsia*, *Clostridium_sensu_stricto_1*, *Allobaculum*, and *Limosilactobacillus* were more productive when compared to the CON group. The levels of the microorganisms mentioned above may recover to varied degrees following SFI therapy (Figure 6C).

To ascertain the specific bacteria linked to SFI, we used linear discriminant analysis (LDA) and effect size (LEfSe) to determine the predominant taxon (Figure 7A). Our analysis revealed 56 OTUs as key discriminants, with *Bacteroidota* showing significant overrepresentation (LDA scores >4.5) in the CON group. The microbiota of Prevotellaceae_NK3B31_group was identified to be the most prevalent in the CON group as well (LDA scores >3.6) (Figure 7B). After additional LDA analysis, 15 OTUs were enriched in the CON group, 3 OTUs were enhanced in the MOD group, 24 OTUs were enriched in the SFI_M group, and 6 OTUs in the MET group. From our findings, it is evident that the microbiota in the gut of the rats can be improved through SFI intervention.

## 3.4 Study of the fecal metabolomics

### 3.4.1 Metabolic profile analysis

The metabolic changes in the four experimental groups were visualized in the current study using PCA. Figures 8A, B illustrate that the CON and MOD groups can be separated, and the SFI_M groups were scattered between them, indicating that the drug intervention regulated the metabolic disturbances induced by HF.

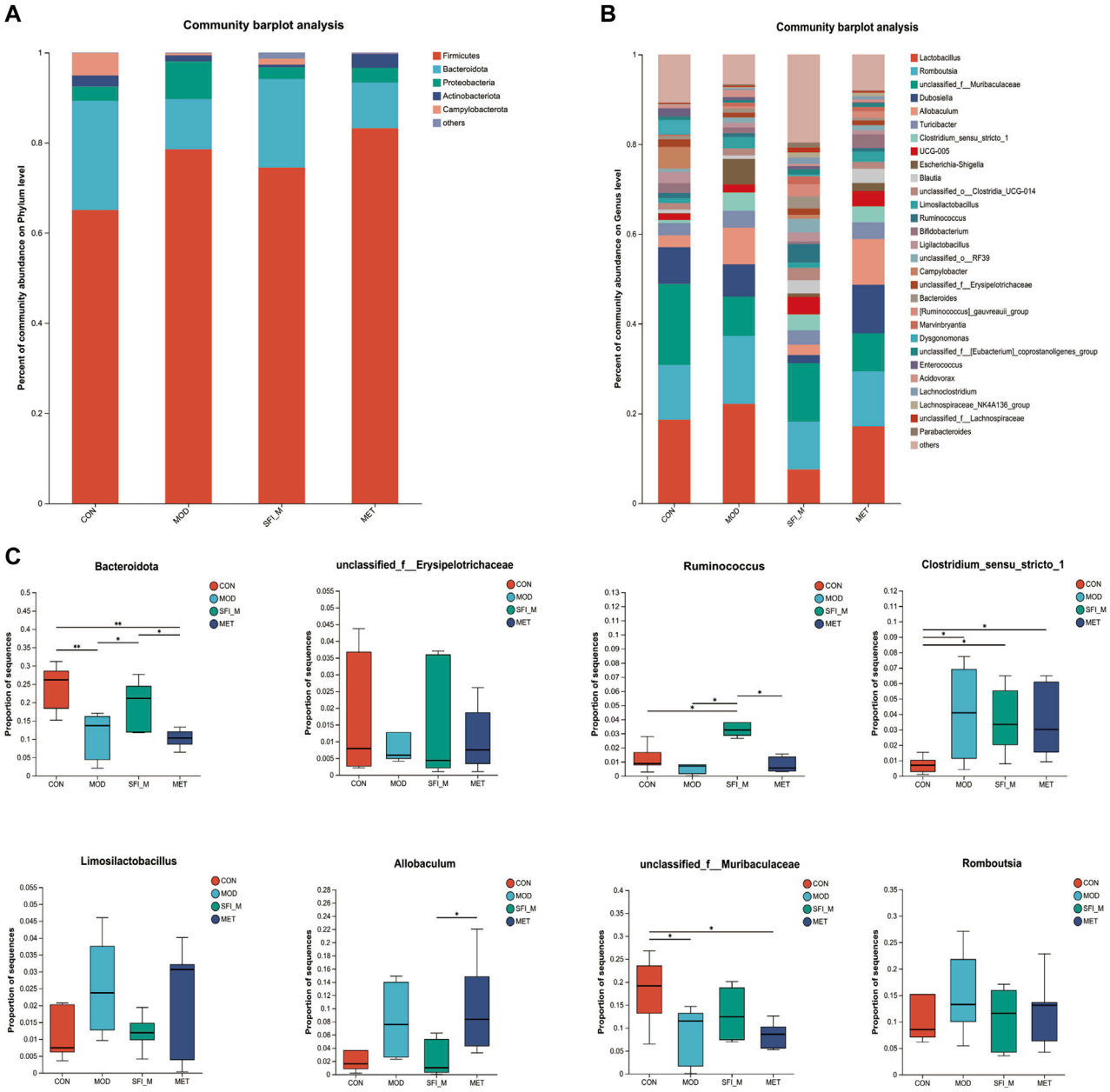


FIGURE 6
**(A)** The histogram of species distribution at the phylum and **(B)** genus levels in four groups; **(C)** Differential analysis of gut microbiota at phylum and genus level (n = 6).

### 3.4.2 Differential metabolites analysis

OPLS-DA analysis shows that the four groups were separated (Figures 8C, E, G). The OPLS-DA model was also statistically validated through 200 permutation tests, as illustrated in Figures 8D, F, H. The model was reliable. Forty-eight metabolites with VIP >1.0 and $p < 0.05$ were chosen as the metabolites linked to the pathological alteration of HF. All the metabolites showed a callback trend, and 28 metabolites were significantly changed (Table 3).

### 3.4.3 Key metabolic pathway analysis for different metabolites

For pathway enrichment analysis, the 28 differential metabolites were imported into MetaboAnalyst 6.0 to investigate further the mechanisms underlying the SFI effects on HF. Figure 9A presents the three metabolic pathways that were influenced ($p < 0.05$): (1) Pentose phosphate pathway; (2) Pyrimidine metabolism; and (3) Purine metabolism. Supplementary Table S1 contains details on all the impacted pathways.

10.3389/fphar.2024.1412300

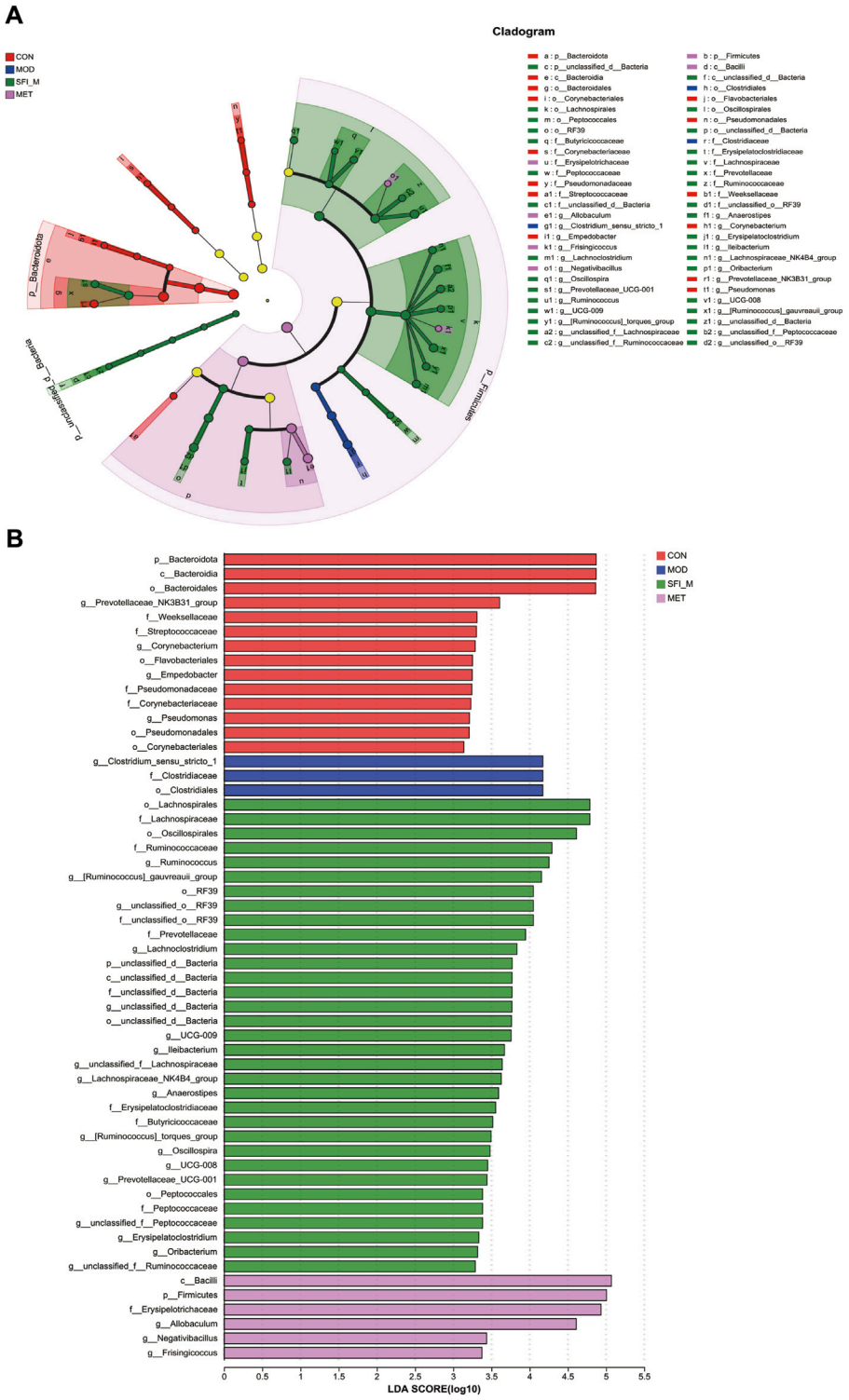


FIGURE 7
**(A)** Cladogram illustrating the phylogenetic distribution of microbiota correlated with the CON, MOD, SFI_M, and MET groups. **(B)** The variations in the abundance of microbiota among the CON, MOD, SFI_M, and MET groups (n = 6).

### 3.4.4 MetOrigin tracing analysis of different metabolites

Metabolite tracing analysis identified 28 differential metabolites associated with the Shenfu injection: seven bacterial-host co-metabolites, 11 bacterial metabolites, and one host-specific metabolite (including 10 drug-related, 21 food-related, two environment-related, and one unknown) (Figures 9B, C). Metabolite pathway enrichment analysis (MPEA) showed that 7,

10.3389/fphar.2024.1412300

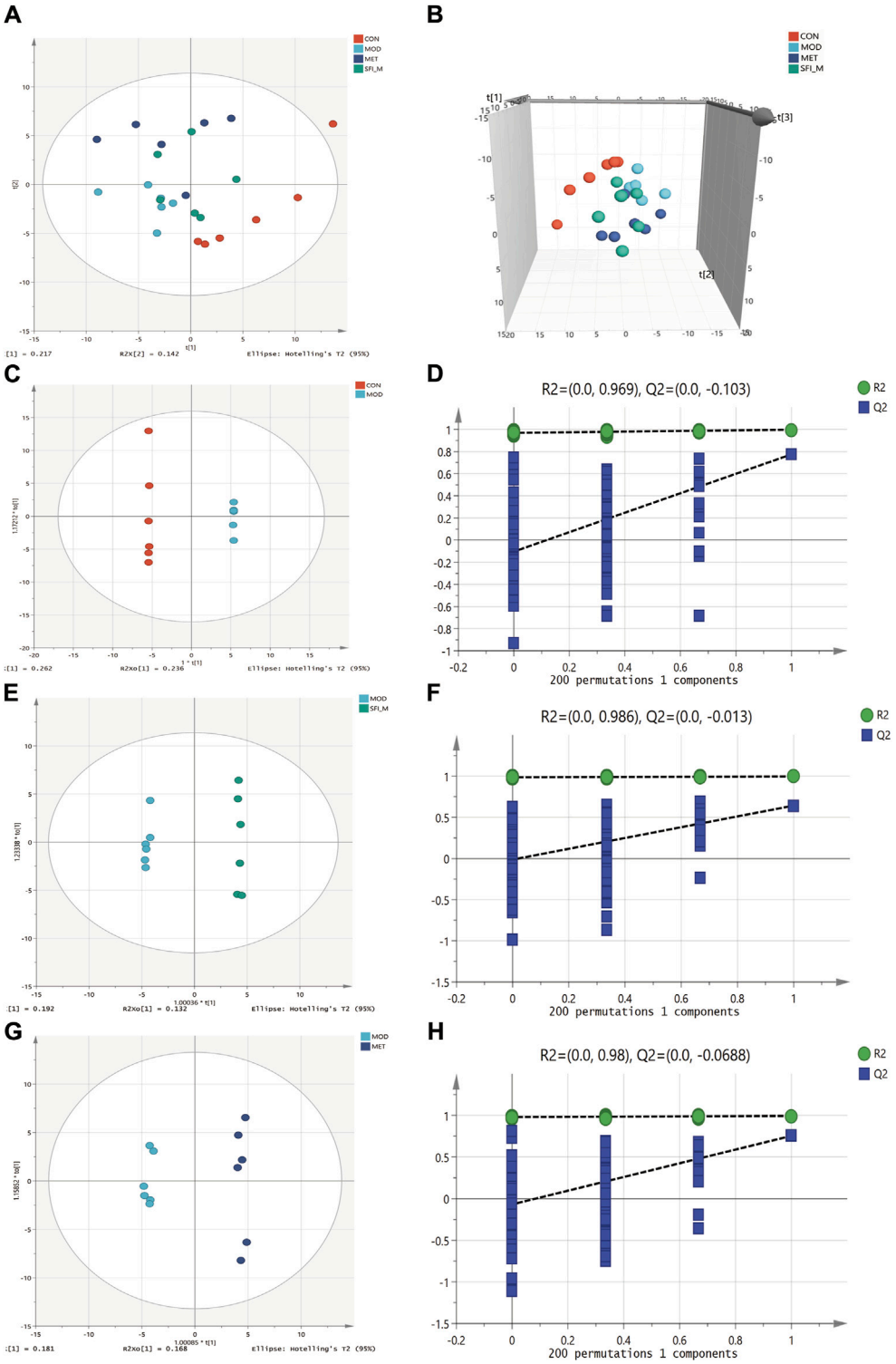


FIGURE 8
PCA score plots among four groups ($R^2X$ = 0.54): **(A)** 2D scatter and **(B)** 3D scatter. **(C)** OPLS-DA score plots of CON and MOD group ($R^2X$ = 0.753, $R^2Y$ = 1, $Q^2$ = 0.893). **(D)** The permutation test (n = 200) for the OPLS-DA model of CON and MOD group. **(E)** OPLS-DA score plots of MOD and SFI_M group ($R^2X$ = 0.413, $R^2Y$ = 0.997, $Q^2$ = 0.643). **(F)** The permutation test (n = 200) for the OPLS-DA model of MOD and SFI_M group. **(G)** OPLS-DA score plots of MOD and MET group ($R^2X$ = 0.486, $R^2Y$ = 0.995, $Q^2$ = 0.755). **(H)** The permutation test (n = 200) for the OPLS-DA model of MOD and MET group (n = 6).

TABLE 3 Differential metabolites of four groups.

| No | RT(s) | Var ID | Formula | KEGG | Ion form | MZ | Trend | | |
|---|---|---|---|---|---|---|---|---|---|
| | | | | | | | M/C | S/M | M/M |
| 1 | 66.8 | 2,4-Dimethylphenol | $C_8H_{10}O$ | C14582 | NEG | 121.066 | ↓## | ↑** | ↑ |
| 2 | 66.8 | 3-(2-Hydroxyphenyl)propanoic acid | $C_9H_{10}O_3$ | C01198 | NEG | 165.056 | ↓## | ↑** | ↑ |
| 3 | 66.8 | 3-(3-Hydroxyphenyl)propanoic acid | $C_9H_{10}O_3$ | C11457 | NEG | 165.056 | ↓## | ↑** | ↑ |
| 4 | 242.1 | Edetic acid edetic acid | $C_{10}H_{16}N_2O_8$ | C00284 | NEG | 291.084 | ↓## | ↑* | ↑* |
| 5 | 59.7 | Indolelactic acid | $C_{11}H_{11}NO_3$ | C02043 | NEG | 204.067 | ↓## | ↑* | ↑* |
| 6 | 249.8 | 2-methylcitrate | $C_7H_{10}O_7$ | C02225 | NEG | 187.025 | ↓## | ↑* | ↑ |
| 7 | 132.2 | Caffeic acid | $C_9H_8O_4$ | C01197 | NEG | 179.039 | ↓## | ↑* | ↓ |
| 8 | 20.5 | PC(15:0/P-16:0) | $C_{39}H_{78}NO_7P$ | C00157 | POS | 704.566 | ↑## | ↓ | ↓ |
| 9 | 120 | Sedoheptulose | $C_7H_{14}O_7$ | C02076 | NEG | 209.067 | ↓## | ↑** | ↑ |
| 10 | 111.8 | D-Glucosaminic acid | $C_6H_{13}NO_6$ | C03752 | POS | 196.083 | ↑## | ↓* | ↑* |
| 11 | 182.8 | 2-Hydroxyhexanedioic acid | $C_6H_{10}O_5$ | C02360 | NEG | 143.035 | ↓## | ↑* | ↑ |
| 12 | 146.9 | Pseudo uridine | $C_9H_12N_2O_6$ | C02067 | NEG | 243.063 | ↑## | ↓ | ↑ |
| 13 | 159.1 | Glycocholic acid | $C_{26}H_{43}NO_6$ | C01921 | NEG | 464.302 | ↓## | ↑ | ↑ |
| 14 | 182.8 | D-Ribose | $C_5H_{10}O_5$ | C00121 | NEG | 149.046 | ↓## | ↑** | ↑ |
| 15 | 28.5 | Gentisic acid | $C_7H_6O_4$ | C00628 | NEG | 153.020 | ↓## | ↑** | ↑ |
| 16 | 68.1 | 2-Hydroxyethanesulfonic acid | $C_2H_6O_4S$ | C05123 | NEG | 124.992 | ↓# | ↑* | ↓ |
| 17 | 22.6 | 4-Methyl-5-thiazoleethanol | $C_6H_9NOS$ | C04294 | POS | 144.048 | ↓# | ↑** | ↑* |
| 18 | 20.4 | Arachidonic acid (AA) | $C_{20}H_{32}O_2$ | C00219 | NEG | 303.234 | ↓## | ↑ | ↑ |
| 19 | 168.4 | Urobilin | $C_{33}H_{42}N_4O_6$ | C05794 | POS | 591.3187 | ↓# | ↑* | ↑ |
| 20 | 185.5 | Tyrosine | $C_9H_{11}NO_3$ | C00082 | POS | 182.081 | ↓## | ↑ | ↑ |
| 21 | 135.6 | Glycochenodeoxycholic acid | $C_{26}H_{43}NO_5$ | C05466 | NEG | 448.307 | ↓## | ↑ | ↑ |
| 22 | 21 | Pyrocatechol | $C_6H_6O_2$ | C00090 | NEG | 109.030 | ↓# | ↑ | ↑ |
| 23 | 139.9 | Cholic acid | $C_{24}H_{40}O_5$ | C00695 | NEG | 407.282 | ↓# | ↑ | ↑* |
| 24 | 182.8 | Fructose | $C_6H_{12}O_6$ | C02336 | NEG | 179.057 | ↓## | ↑ | ↓ |
| 25 | 240.1 | Nicotinamide riboside (NR) | $C_{11}H_{15}N_2O_5$ | C03150 | POS | 255.097 | ↓## | ↑ | ↓ |
| 26 | 163.1 | Phenylalanine | $C_9H_{11}NO_2$ | C00079 | POS | 166.086 | ↓# | ↑ | ↑ |
| 27 | 19.2 | Phenacetin | $C_{10}H_{13}NO_2$ | C07591 | POS | 180.102 | ↓## | ↑** | ↑ |
| 28 | 294.6 | S-Adenosylmethionine | $C_{15}H_{22}N_6O_5S$ | C00019 | POS | 399.145 | ↓# | ↑ | ↓ |
| 29 | 229.9 | 5-Aminopentanoic acid | C5H11NO2 | C00431 | POS | 118.086 | ↓# | ↑** | ↓ |
| 30 | 134.3 | Nicotinate | C6H5NO2 | C00253 | NEG | 122.0250 | ↑# | ↓ | ↑* |
| 31 | 177.6 | 1-Aminopropan-2-ol | C3H9NO | C05771 | POS | 76.076 | ↓# | ↑** | ↓ |
| 32 | 127.4 | Xanthine | C5H4N4O2 | C00385 | NEG | 151.026 | ↑## | ↓ | ↑* |
| 33 | 87.5 | Hypoxanthine | $C_5H_4N_4O$ | C00262 | POS | 137.046 | ↑## | ↓* | ↓ |
| 34 | 141 | Mevalonic acid | $C_6H_{12}O_4$ | C00418 | NEG | 147.067 | ↓# | ↑ | ↓ |
| 35 | 257.5 | Histidine | $C_6H_9N_3O_2$ | C00135 | POS | 156.077 | ↓# | ↑ | ↓ |
| 36 | 76.7 | 1-Methylguanine | $C_6H_7N_5O$ | C04152 | POS | 166.072 | ↑## | ↓* | ↑ |
| 37 | 186.8 | Methylimidazoleacetic acid | $C_6H_8N_2O_2$ | C05828 | NEG | 139.052 | ↓## | ↑ | ↑* |

(Continued on following page)

TABLE 3 (*Continued*) Differential metabolites of four groups.

| No | RT(s) | Var ID | Formula | KEGG | Ion form | MZ | Trend | | |
|---|---|---|---|---|---|---|---|---|---|
| | | | | | | | M/C | S/M | M/M |
| 38 | 93.3 | 3-Hydroxyisovaleric acid | $C_5H_{10}O_3$ | C20827 | NEG | 117.056 | ↓$^{\#}$ | ↑ | ↓ |
| 39 | 190.3 | Proline | $C_5H_9NO_2$ | C16435 | POS | 116.070 | ↓$^{\#}$ | ↑ | ↑ |
| 40 | 215.5 | 4-Guanidinobutyric acid | $C_5H_{11}N_3O_2$ | C01035 | POS | 146.092 | ↓$^{\#}$ | ↑$^{**}$ | ↑ |
| 41 | 26.4 | Euscaphic acid | $C_{30}H_{48}O_5$ | C17890 | POS | 489.358 | ↑$^{\#}$ | ↓$^{**}$ | ↓$^{*}$ |
| 42 | 223.6 | 4-Aminobutyric acid (GABA) | $C_4H_9NO_2$ | C00334 | POS | 104.071 | ↓$^{\#\#}$ | ↑ | ↓ |
| 43 | 35.8 | Uracil | $C_4H_4N_2O_2$ | C00106 | NEG | 111.020 | ↑$^{\#}$ | ↓$^{*}$ | ↓ |
| 44 | 23.4 | L-tyrosine-methyl-ester | $C_{10}H_{13}NO_3$ | C03404 | POS | 196.097 | ↓$^{\#}$ | ↑$^{*}$ | ↑ |
| 45 | 235.4 | Chloroquine | $C_{18}H_{26}C_lN_3$ | C07625 | POS | 320.185 | ↑$^{\#}$ | ↓$^{**}$ | ↓ |
| 46 | 101.4 | Deoxyinosine | $C_{10}H_{12}N_4O_4$ | C05512 | POS | 253.093 | ↑$^{\#}$ | ↓$^{*}$ | ↑ |
| 47 | 31.9 | Thymine | $C_5H_6N_2O_2$ | C00178 | NEG | 125.036 | ↑$^{\#}$ | ↓$^{**}$ | ↑ |

RT, retention time; NEG, negative ion mode; POS, positive ion mode; MS, mass spectrum.
$^{\#}p < 0.05$. $^{\#\#}p < 0.01$ compared with the CON group; $^{*}p < 0.05$, $^{**}p < 0.01$ compared with the MOD group. M/C: MOD group compared with the CON group. S/M: SFI_M group compared with the MOD group. M/M: MET group compared with the SFI_M group.

2, and seven relevant metabolic pathways matched with host, bacterial, and co-metabolic pathway databases, respectively (Figures 9D, E). Based on origin-based functional analysis, Taurine and hypotaurine metabolism was found to be specific to the microbial community. The biosynthesis of Pyrimidine metabolism, Purine metabolism, beta-alanine metabolism, Naphthalene degradation, Pantothenate, and CoA biosynthesis were identified as co-metabolic pathways between microbes and hosts. To better illustrate the co-metabolic relationships between microbiota and hosts, a Bio-Sankey network based on MetOrigin analysis further visualized the statistical correlations and biological relationships between microbiota and metabolites (Figures 10A, B). Supplementary Tables S2, S3 contains details of microbiota and hosts.

### 3.4.5 Correlation analysis between metabolomics and 16S rRNA sequencing results

As shown in Figure 10C, correlation analysis revealed a close relationship between intestinal microflora and different metabolites (Supplementary Table S4). A correlation was considered significant only when the absolute value of Spearman's correlation coefficient r was greater than 0.5 (Figure 10). When the total value of *R* was higher than 0.6, the results were considered to show a strong linear correlation between the two variables. For example, *Lactobacillus* was strongly correlated with D-Glucosaminic acid and positively correlated with EDTA. *Ligilactobacillus* was substantially inversely correlated to Hypoxanthine, Deoxyinosine, Chloroquine, Uracil, and 1-methylguanine, but positively correlated to 2-methyl citrate, Phenacetin, Caffeic acid, Gentisic acid, Indolelactic acid, 2,4-Dimethylphenol, 3-(2-Hydroxyphenyl)propanoic acid, 3-(3-Hydroxyphenyl)propanoic acid, and 4-Guanidinobutyric acid. *Clostridium*_sensu_stricto_1 was substantially inversely correlated to Hypoxanthine,1-Methylguanine, D-Glucosaminic acid, but positively correlated to 2-methylcitrate, L-tyrosine-methyl-ester, Phenacetin,2-Hydroxyethanesulfonic acid, Caffeic acid, Gentisic acid, 2,4-Dimethylphenol, 3-(2-Hydroxyphenyl)propanoic acid, 3-(3-Hydroxyphenyl) propanoic acid, and 4-Guanidinobutyric acid. These results suggest that the SFI could alter the microbe-metabolic axis.

## 4 Discussion

The prevalence of heart failure is on the rise globally due to the aging population (McDonagh et al., 2021). Emerging research indicates that this trend is significantly influenced by the gut-heart axis (Madan and Mehra, 2020). The symbiotic cooperation between the gut microbiota and the host is vital to maintaining overall health. The intricate nature of TCM poses challenges in elucidating its therapeutic mechanisms; however, using multi-omics strategies presents novel opportunities for a comprehensive understanding of the therapeutic mechanism. In this investigation, 16S rRNA sequencing and non-targeted metabolomics were employed to examine the underlying pathways of SFI treatment. The most important findings from this study are as follows (Figure 11): (1) SFI effectively enhanced cardiac function in rats with ISO-induced heart failure, (2) SFI effectively modulated inflammatory imbalance and reduced serum and urine TMAO levels, (3) Treatment with SFI altered the gut microbiota and the composition of intestinal metabolites, enriched SCFA-producing bacteria such as *Ruminococcus* and *Erysipelotrichaceae* at the genus level and influenced the metabolites particularly those associated with the pentose phosphate pathway, pyrimidine metabolism, and purine metabolism, and (4) A close relationship was established between intestinal microflora and different metabolites, indicating that the SFI could alter the microbe-metabolic co-metabolism axis.

SFI has been extensively utilized in China for more than 3 decades in the treatment of cardiovascular diseases. Its primary constituents consist of ginsenosides and aconitum alkaloids. The content of ginsenosides is 676–742 μg/mL, and the content of aconite alkaloids

10.3389/fphar.2024.1412300

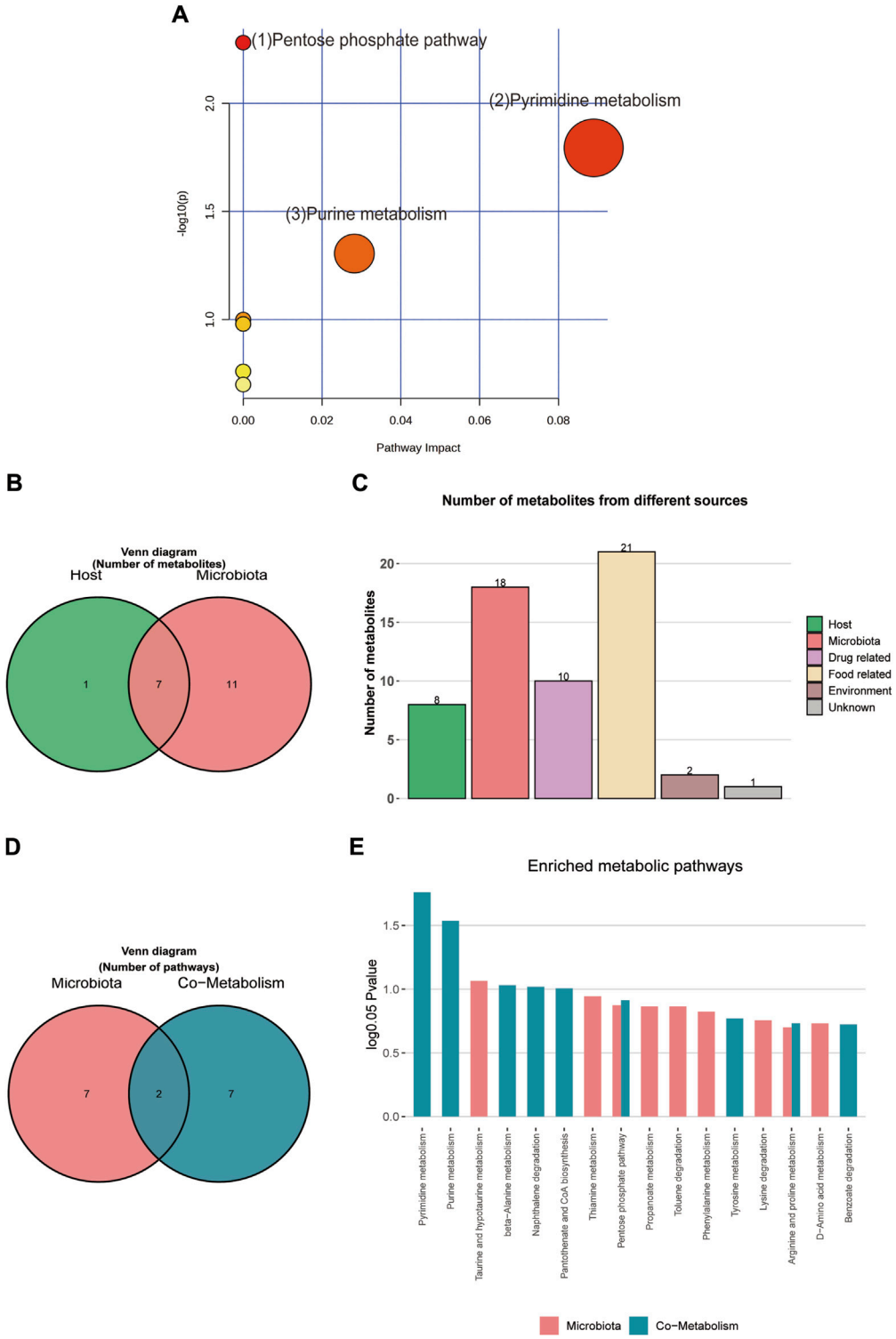


FIGURE 9
**(A)** MetPA analysis of differential metabolites pathway. **(B)** Venn diagram of differential metabolites. **(C)** Histogram of differential metabolites. **(D)** Venn diagram of enrichment analysis of differential metabolites. **(E)** Histogram of enrichment analysis of differential metabolites.

is 3–7 μg/mL (Song et al., 2015). Aconite has certain toxicity, but the combination of aconite and ginseng exhibits a "detoxifying and enhancing efficacy" effect (Xu et al., 2024). Ginsenosides can promote the metabolism of toxic components like aconitine, prolonging the elimination half-life of aconitine, benzoylmesaconine, and hypaconitine, thereby significantly increasing the exposure of effective components in the body. An example of ginseng's detoxification mechanisms towards aconitine involves ginsenoside

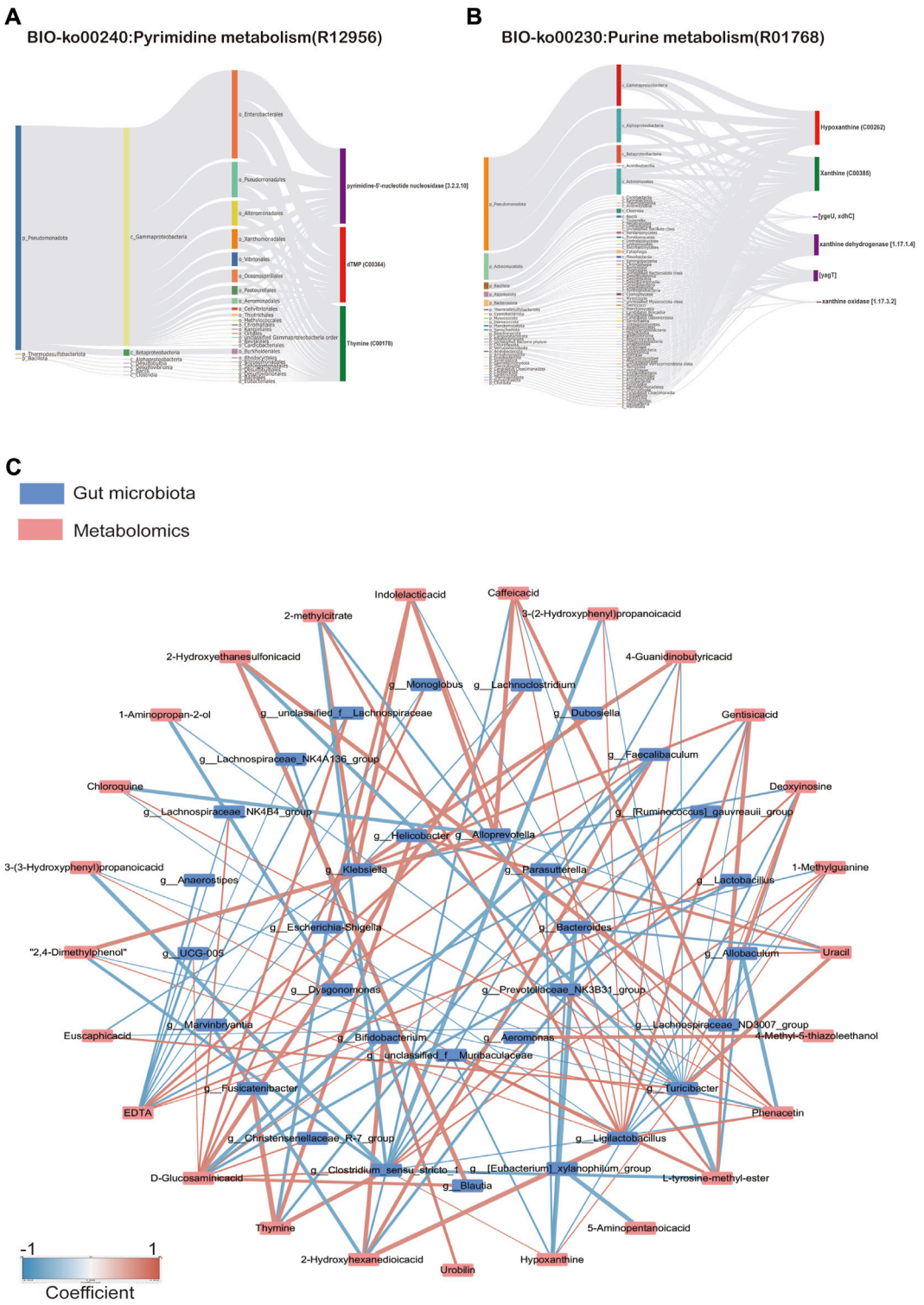


FIGURE 10
**(A)** Sankdy diagram of metorigin analysis of Pyimidine metabolism and **(B)** Purine metabolism, **(C)** Network diagram of correlation analysis (Spearman's R-value >0.5, $p < 0.05$).

Rg1's regulation of ion channels pathways (Xu et al., 2022). This regulation accelerates aconitine metabolism and enhances the absorption of benzoylaconine (Xu et al., 2020).To explore the effects and toxicity of the Shenfu Injection at varying concentrations on the organism, we administered three different concentrations of Shenfu Injection. Our investigation entailed assessing both cardiac function, through techniques like echocardiography, Nt-proBNP level measurements, and histological analyses of cardiac tissues using

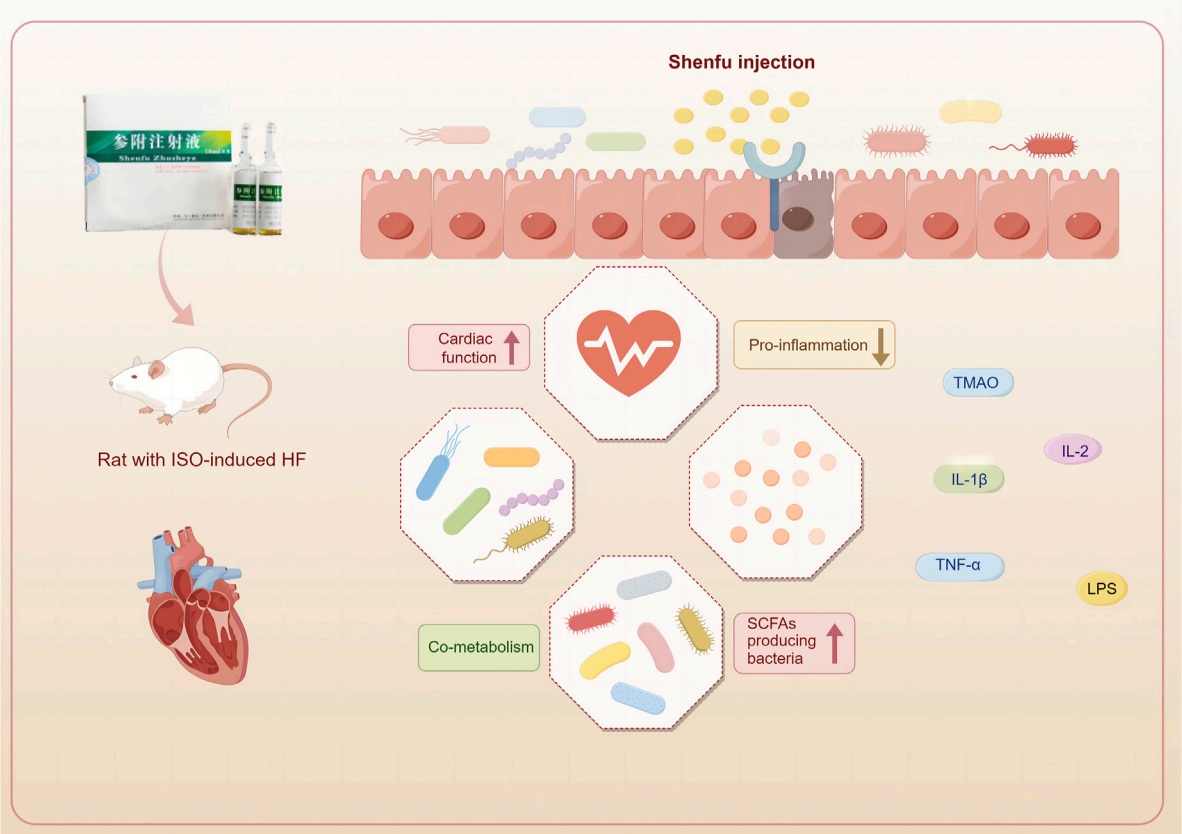


FIGURE 11
Shenfu injection improves cardiac function by modulating co-metabolism and the TMAO-inflammation axis. (This figure was drawn using Figdraw).

H&E staining, as well as gut function, involving examination of intestinal tissues via H&E staining and measurement of LPS levels. However, dose dependency was not obvious in this study. The moderate dose (6 mL/kg) of the Shenfu Injection exhibited the most significant improvement in cardiac and gut function.

The metabolite TMAO, produced in a process dependent on gut microbiota, is linked to the pathogenic causes of HF, and it may operate as a predictive marker for identifying patients at risk of disease advancement (Zhang et al., 2021). Results from a systematic review indicate that TMAO is related to HF severity, brain natriuretic peptide (BNP), estimated glomerular filtration rate (eGFR), and adverse outcomes such as hospitalizations and fatalities (Anderson et al., 2022). Research conducted in different population groups indicates that higher plasma TMAO levels are correlated positively to inflammation, impaired endothelial function, type 2 diabetes, central obesity, and high blood pressure (Thomas and Fernandez, 2021). Research has indicated that TMAO further induces vascular inflammation by activating the NLRP3 inflammasome (Chen et al., 2017). Overexpressing SIRT3 alleviated the activation of the endothelial NLRP3 inflammasome induced by TMAO (Wu J. et al., 2019). In our study, we observed increased levels of TMAO in the serum and urine of rats with heart failure. However, significant downregulation of TMAO levels in both serum and urine, along with pro-inflammatory cytokines TNF-α, IL-2, and IL-1β, was observed in SFI-treated HF rats, aligning with previous research findings (Yang et al., 2019). Spearman correlation analysis demonstrated positive associations between inflammatory factors IL-1β and IL-2 with serum and urine TMAO, highlighting the pivotal role of the TMAO-inflammation axis targeted by SFI.

The 16S rRNA sequencing results demonstrated a reduction in the quantity of OTUs and Alpha diversity changes (including Chao, Shannon, Simpson, and ACE), indicating the dysfunction of gut microbiota in HF rats. A previous study has reported similar findings (Li et al., 2021). At the phylum level, *Firmicutes* in the intestine primarily specialize in the hydrolysis of carbohydrates and proteins. *Bacteroides*, on the other hand, predominantly target steroids, polysaccharides, and bile acids, which aid in the absorption of polysaccharides and contribute to protein synthesis within the body. In our research, when compared to the CON group, the *Firmicutes* were found to increase and the *Bacteroidota* reduced substantially in the MOD group. Shenfu Injection significantly increased the levels of *Bacteroidota*. A research study discovered that infants with heart failure had significantly altered intestinal microbiota compared to those without heart disease, with an increased number of *Firmicutes* at the phylum level (Zhang et al., 2023). At the genus level, *Ruminococcus*, *Erysipelotrichaceae*, and *unclassified_f_Muribaculaceae*, which produce short-chain fatty acids (SCFAs) from fermenting dietary polysaccharides, are observed to be decreased (Shaidullov et al., 2021; Yamaguchi et al., 2021), which is consistent with our results. It is widely recognized that SCFAs play a crucial role in regulating inflammation, a process intricately linked to the pathophysiology of CHF. SCFAs are also integral in preserving the

integrity of the gut barrier, modulating immune responses, and serving as an energy source for colonocytes. *Ruminococcus* is a genus within the Ruminococcaceae family. Species within the *Ruminococcus* genus are mainly known for designing cellulose and resistant starches, thereby contributing to the fermentation process that produces SCFAs (Michels et al., 2022). These metabolic activities are vital for maintaining a healthy gut environment and the host's overall metabolic health (Zhu et al., 2019). The bacterial levels listed above could be restored to varied degrees following SFI treatment. In addition, results from a study by LEfse showed that the SCFA producers, *Ruminococcaceae* and *Lachnospiraceae*, were significantly overrepresented in the SFI_M group, these findings reveal that SFI is instrumental to SCFA-producing bacteria.

Gut microbiota can affect an organism by modulating the host metabolic products or through its metabolic products. In a metabolomics study by Li et al. (2023), metabolic imbalances such as disturbances in the metabolism of amino acids, lipids, and glucose, were established to be associated with heart failure (Li et al., 2023). LC-MS analysis was conducted to investigate the influence of gut microbiota on the host metabolism of the ISO-induced HF rat model. In our research involving metabolites, 48 differential metabolites were detected in the HF rat model, and all the metabolites showed a callback trend, with 28 significantly changed metabolites. These findings indicate that the SFI has a regulating effect on the metabolic disturbances induced by HF. Untargeted metabolomics have become a powerful tool for evaluating the efficacy of TCM. As a cutting-edge technological system in biology, metabolomics embraces a holistic perspective akin to TCM, enabling in-depth exploration of TCM's complex conditions and multifactorial nature. Tian et al. used untargeted metabolomics to investigate the mechanism of action of QFPDD in treating coronavirus-induced pneumonia in mice (Tian et al., 2022). UPLC-Q-TOF/MS is also used for TCM syndrome differentiation (Ye et al., 2021).

The results from our KEGG pathway analysis revealed that the regulation of metabolites by SFI focuses on the pentose phosphate pathway, pyrimidine metabolism, and purine metabolism. Glycometabolism, recognized for its critical function in energy production, encompasses three primary metabolic pathways: oxidative phosphorylation, glycolysis, and the pentose phosphate pathway. It is vital to maintain cardiovascular health to ensure the efficient progression of glycometabolism (Peng et al., 2023). D-ribose is a pentose sugar present in every living cell and is a critical component of several crucial biomolecules such as RNA, nucleotides, and riboflavin. It is synthesized from glucose via the pentose phosphate pathway (PPP) within the cell. Through the non-oxidative phase of the PPP, d-ribose plays an essential role in producing adenosine triphosphate (ATP). As a result, it is utilized as a therapeutic agent to improve cardiac function in patients with HF. Research shows that Supplemental d-ribose reduces the symptoms of HFpEF and increases EF (Pierce et al., 2022). Our study indicates that SFI can increase D ribose and Sedoheptulose levels. Altogether, these data provide the basis for glycometabolism as an essential target of SFI. Growing evidence suggests that the levels of intermediates from purine degradation reflect the energy status of myocardial cells. Under normal conditions, an increase in the heart's energy demands a need for increased levels of purine nucleotides and their by-products. In contrast, a considerable decrease in total purine production suggests that myocardial cells are conserving energy, hence maintaining the myocardium's energy balance. In pathological states, such as myocardial ischemia, ATP breaks down into xanthine and accumulates in the tissue. The produced xanthine is converted into uric acid by xanthine oxidase, which generates a significant amount of superoxide anions, causing cellular damage. Under low oxygen environments, the byproducts of the breakdown of adenosine and inosine serve as more efficient energy sources than extracellular glucose, thereby slowing the build-up of nicotinamide adenine dinucleotide (NADH) and offering a degree of protection to the cells (Wang G. et al., 2022). In the present study, hypoxanthine and deoxyinosine levels were significantly increased in the HF rat model, indicating the presence of an energy imbalance in the HF rat model, which is consistent with research findings (Berry and Hare, 2004).

A significant crosstalk exists between the gut microbiota and the host through substrate co-metabolism and metabolic exchange. Therefore, it may be possible to infer host and microbiome co-metabolism through untargeted metabolomics, as Zhao et al. (2022) showed that interactions between fecal metabolomes and gut microbiomes can reveal functional markers in cerebral ischemic stroke (Zhao et al., 2022). Chen employed fecal metabonomics in conjunction with 16S rRNA gene sequencing to examine alterations in gut microbiota in rats exhibiting kidney-yang deficiency syndrome and the impact of the You-gui pill intervention. Tong's study found that Gushudan could protect rats with kidney-yang deficient disease by modulating the gut-kidney axis (Tong et al., 2022). MetOrigin is a bioinformatics tool designed to pinpoint the specific bacterial species involved in various metabolic reactions and elucidate their roles in these processes (Fan et al., 2023). In our study, metabolite tracing analysis showed that Taurine and hypotaurine metabolism was found to be specific to the microbial community. The biosynthesis of Pyrimidine metabolism, Purine metabolism, beta-alanine metabolism, Naphthalene degradation, Pantothenate, and CoA biosynthesis were identified as co-metabolic pathways between microbes and hosts. The Spearman correlation analysis in our study also showed a significant correlation between differentially expressed metabolites regulated by SFI and the gut microbiota, indicating that SFI could modulate the co-metabolism of ISO-induced HF.

Our research may give some insights into the relationship between gut microbiota and heart failure. However, the validation of this relevant hypothesis based on animal model testing faces several challenges. Specifically, we need to determine whether the improvement in dysbiosis and metabolome abnormality is merely a consequence of heart failure amelioration or if it plays a critical role in heart failure progression. Additionally, distinguishing changes in gut microbiota induced by heart failure from those induced by specific interventions like ISO is essential. To address these challenges, future studies should consider conducting fecal transplantation trials and expanding both sample sizes and clinical data collection. These steps will enhance our understanding and validation of the relationship between gut microbiota and heart failure.

## 5 Conclusion

This study utilized a comprehensive methodology, incorporating various techniques such as echocardiography, protein chip detection, histopathology, 16S rDNA sequencing, and metabolomics, to investigate the effectiveness of SFI in treating heart failure. The comprehensive findings from our study demonstrated significant benefits of SFI treatment in rats with isoproterenol-induced heart failure. SFI effectively modulated inflammatory imbalance, reduced serum and urine TMAO levels, and improved gut microbiota composition. Specifically, SFI substantially increased the abundance of *Bacteroidota* at the phylum level and enriched SCFA-producing bacteria such as *Ruminococcus* and Erysipelotrichaceae at the genus level. Furthermore, SFI influenced the composition of intestinal metabolites, particularly those associated with the pentose phosphate pathway, pyrimidine metabolism, and purine metabolism. Our findings highlight SFI's ability to address dysbiosis within the gut microbiota-host co-metabolism.

## Data availability statement

The raw data for the 16S rRNA sequencing is available through NCBI with the BioProject accession number PRJNA1096125, available at: https://www.ncbi.nlm.nih.gov/bioproject/PRJNA1096125.

## Ethics statement

The animal study was approved by the Hunan University of Chinese Medicine. The study was conducted in accordance with the local legislation and institutional requirements.

## Author contributions

LL: Writing–original draft, Writing–review and editing. JY: Writing–review and editing, Visualization. ZZ: Writing–review and editing. SH: Writing–review and editing, Data curation. HL: Writing–review and editing. JO: Conceptualization, Writing–review and editing. ZH: Funding acquisition, Writing–review and editing.

## Funding

The author(s) declare that financial support was received for the research, authorship, and/or publication of this article. This project was supported by the National Natural Science Foundation of China (grant numbers 82305092, 82274412, and 82274411), the National Natural Science Foundation of Hunan (grant number 2023JJ30453), the National Natural Science Foundation of Changsha (grant number kq2208185), and Hunan Youth Science and Technology Innovation Talent Project (2022RC1021). Excellent Young Scholars Research Fund Project of Hunan University of Chinese Medicine (Z2023XJYQ03).

## Acknowledgments

We appreciate Shanghai Biotree Biotech Co., Ltd.'s contribution to sequencing and LC-MS/MS metabonomic and 16s rRNA sequencing analysis.

## Conflict of interest

The authors declare that the research was conducted in the absence of any commercial or financial relationships that could be construed as a potential conflict of interest.

## Publisher's note



## Supplementary material

The Supplementary Material for this article can be found online at: https://www.frontiersin.org/articles/10.3389/fphar.2024.1412300/full#supplementary-material

**SUPPLEMENTARY FIGURE S1**
**(A)** PCA score plot of the four groups and QC samples. **(B)** The α-diversity of ACE, Chao, Simpson, and Shannon index. Data are presented as the mean ± SD; n = 6.

**SUPPLEMENTARY TABLE S1**
The information for all the affected pathways.

**SUPPLEMENTARY TABLE S2**
The related dataset of Sankey network of Bio-ko00240.

**SUPPLEMENTARY TABLE S3**
The related dataset of Sankey network of Bio-ko00230.

**SUPPLEMENTARY TABLE S4**
The related dataset of Spearman's correlation.

## References

Anderson, K. M., Ferranti, E. P., Alagha, E. C., Mykityshyn, E., French, C. E., and Reilly, C. M. (2022). The heart and gut relationship: a systematic review of the evaluation of the microbiome and trimethylamine-N-oxide (TMAO) in heart failure. *Heart Fail Rev.* 27 (6), 2223–2249. doi:10.1007/s10741-022-10254-6

Berry, C. E., and Hare, J. M. (2004). Xanthine oxidoreductase and cardiovascular disease: molecular mechanisms and pathophysiological implications. *J. Physiol.* 555 (Pt 3), 589–606. doi:10.1113/jphysiol.2003.055913

Bui, T. V. A., Hwangbo, H., Lai, Y., Hong, S. B., Choi, Y. J., Park, H. J., et al. (2023). The gut-heart Axis: updated review for the roles of microbiome in cardiovascular health. *Korean Circ. J.* 53 (8), 499–518. doi:10.4070/kcj.2023.0048

Canyelles, M., Borràs, C., Rotllan, N., Tondo, M., Escolà-Gil, J. C., and Blanco-Vaca, F. (2023). Gut microbiota-derived TMAO: a causal factor promoting atherosclerotic cardiovascular disease? *Int. J. Mol. Sci.* 24 (3), 1940. doi:10.3390/ijms24031940

Chen, C., He, L., Wang, X., Xiao, R., Chen, S., Ye, Z., et al. (2023). Leonurine promotes the maturation of healthy donors and multiple myeloma patients derived-dendritic cells via the regulation on arachidonic acid metabolism. *Front. Pharmacol.* 14, 1104403. doi:10.3389/fphar.2023.1104403

Chen, M. L., Zhu, X. H., Ran, L., Lang, H. D., Yi, L., and Mi, M. T. (2017). Trimethylamine-N-Oxide induces vascular inflammation by activating the NLRP3 inflammasome through the SIRT3-SOD2-mtROS signaling pathway. *J. Am. Heart Assoc.* 6 (9), e006347. doi:10.1161/jaha.117.006347

Cui, X., Su, Y., Huang, X., Chen, J., Ma, J., Liao, P., et al. (2023). Combined analysis of plasma metabolome and intestinal microbiome sequencing to explore jiashen prescription and its potential role in changing intestine-heart axis and effect on chronic heart failure. *Front. Cardiovasc Med.* 10, 1147438. doi:10.3389/fcvm.2023.1147438

Edgar, R. C. (2013). UPARSE: highly accurate OTU sequences from microbial amplicon reads. *Nat. Methods* 10 (10), 996–998. doi:10.1038/nmeth.2604

Fan, J., Zhou, Y., Meng, R., Tang, J., Zhu, J., Aldrich, M. C., et al. (2023). Cross-talks between gut microbiota and tobacco smoking: a two-sample Mendelian randomization study. *BMC Med.* 21 (1), 163. doi:10.1186/s12916-023-02863-1

Groenewegen, A., Rutten, F. H., Mosterd, A., and Hoes, A. W. (2020). Epidemiology of heart failure. *Eur. J. Heart Fail* 22 (8), 1342–1356. doi:10.1002/ejhf.1858

Huang, L., Wang, J., Xu, R., Liu, Y., and Liu, Z. (2020). Regulatory effect of traditional Chinese medicine on gut microbiota in patients with atherosclerosis: a protocol for systematic review and meta-analysis. *Med. Baltim.* 99 (50), e23730. doi:10.1097/md.0000000000023730

Huang, P., Guo, Y., Hu, X., Fang, X., Xu, X., and Liu, Q. (2024). Mechanism of Shenfu injection in suppressing inflammation and preventing sepsis-induced apoptosis in murine cardiomyocytes based on network pharmacology and experimental validation. *J. Ethnopharmacol.* 322, 117599. doi:10.1016/j.jep.2023.117599

Huang, S. M., Xiao-qian, LIAO, Xin-yu, F. A. N., Zi-yi, WANG, Si-yuan*, H. U., and Zhi-xi*, H. U. (2022). Protective effect of Shenfu Injection on rats with chronic heart failure based on HMGB1/TLR4/NF-κB signaling pathway. *China J. Chin. Materia Medica* 47 (20), 5556–5563. doi:10.19540/j.cnki.cjcmm.20220509.703

Jia, Q., Wang, L., Zhang, X., Ding, Y., Li, H., Yang, Y., et al. (2020). Prevention and treatment of chronic heart failure through traditional Chinese medicine: role of the gut microbiota. *Pharmacol. Res.* 151, 104552. doi:10.1016/j.phrs.2019.104552

Li, L., Zhong, S., Ye, J., Hu, S., and Hu, Z. (2023). Effect of Danhong injection on heart failure in rats evaluated by metabolomics. *Front. Med. (Lausanne)* 10, 1259182. doi:10.3389/fmed.2023.1259182

Li, L., Zhong, S. J., Hu, S. Y., Cheng, B., Qiu, H., and Hu, Z. X. (2021). Changes of gut microbiome composition and metabolites associated with hypertensive heart failure rats. *BMC Microbiol.* 21 (1), 141. doi:10.1186/s12866-021-02202-5

Liang, Y. Y., Liu, L. Y., Jia, Y., Li, Y., Cai, J. N., Shu, Y., et al. (2022). Correlation between gut microbiota and glucagon-like peptide-1 in patients with gestational diabetes mellitus. *World J. Diabetes* 13 (10), 861–876. doi:10.4239/wjd.v13.i10.861

Liu, Y., Zhang, H., Lu, W., and Jiang, T. (2023). Integrating metabolomics, 16S rRNA sequencing, network pharmacology, and metorigin to explore the mechanism of Cinnamomi Cortex in treating chronic atrophic gastritis rats. *Phytomedicine* 121, 155084. doi:10.1016/j.phymed.2023.155084

Lujan, H. L., and DiCarlo, S. E. (2020). Direct comparison of cervical and high thoracic spinal cord injury reveals distinct autonomic and cardiovascular consequences. *J. Appl. Physiol. (1985)* 128 (3), 554–564. doi:10.1152/japplphysiol.00721.2019

Luo, Z., Jiang, M., Liu, S., Duan, Y., Huang, J., and Zeng, H. (2021). Shenfu injection alleviates the clinical symptoms of heart failure patients combined with conventional treatment: a protocol for systematic review and meta-analysis of randomized clinical trials. *Med. Baltim.* 100 (15), e23736. doi:10.1097/md.0000000000023736

Ma, X., Li, J., Chen, B., Li, X., Ling, Z., Feng, S., et al. (2022). Analysis of microbial diversity in the feces of *Arborophila rufipectus*. *Front. Microbiol.* 13, 1075041. doi:10.3389/fmicb.2022.1075041

Madan, S., and Mehra, M. R. (2020). The heart-gut microbiome axis in advanced heart failure. *J. Heart Lung Transpl.* 39 (9), 891–893. doi:10.1016/j.healun.2020.04.003

McDonagh, T. A., Metra, M., Adamo, M., Gardner, R. S., Baumbach, A., Böhm, M., et al. (2021). 2021 ESC Guidelines for the diagnosis and treatment of acute and chronic heart failure. *Eur. Heart J.* 42 (36), 3599–3726. doi:10.1093/eurheartj/ehab368

Michels, N., Zouiouich, S., Vanderbauwhede, B., Vanacker, J., Indave Ruiz, B. I., and Huybrechts, I. (2022). Human microbiome and metabolic health: an overview of systematic reviews. *Obes. Rev.* 23 (4), e13409. doi:10.1111/obr.13409

Niu, L., Li, C., Wang, Z., Xu, H., and An, X. (2017). Effects of the MAPK pathway and the expression of CAR in a murine model of viral myocarditis. *Exp. Ther. Med.* 13 (1), 230–234. doi:10.3892/etm.2016.3909

Peng, G., Yan, J., Chen, L., and Li, L. (2023). Glycometabolism reprogramming: implications for cardiovascular diseases. *Prog. Biophys. Mol. Biol.* 179, 26–37. doi:10.1016/j.pbiomolbio.2023.03.003

Pierce, J. D., Shen, Q., Mahoney, D. E., Rahman, F., Krueger, K. J., Diaz, F. J., et al. (2022). Effects of ubiquinol and/or D-ribose in patients with heart failure with preserved ejection fraction. *Am. J. Cardiol.* 176, 79–88. doi:10.1016/j.amjcard.2022.04.031

Rezkalla, S., Kloner, R. A., Khatib, G., and Khatib, R. (1990). Beneficial effects of captopril in acute coxsackievirus B3 murine myocarditis. *Circulation* 81 (3), 1039–1046. doi:10.1161/01.cir.81.3.1039

Saaoud, F., Liu, L., Xu, K., Cueto, R., Shao, Y., Lu, Y., et al. (2023). Aorta- and liver-generated TMAO enhances trained immunity for increased inflammation via ER stress/mitochondrial ROS/glycolysis pathways. *JCI Insight* 8 (1), e158183. doi:10.1172/jci.insight.158183

Savarese, G., Becher, P. M., Lund, L. H., Seferovic, P., Rosano, G. M. C., and Coats, A. J. S. (2023). Global burden of heart failure: a comprehensive and updated review of epidemiology. *Cardiovasc Res.* 118 (17), 3272–3287. doi:10.1093/cvr/cvac013

Shaidullov, I. F., Sorokina, D. M., Sitdikov, F. G., Hermann, A., Abdulkhakov, S. R., and Sitdikova, G. F. (2021). Short chain fatty acids and colon motility in a mouse model of irritable bowel syndrome. *BMC Gastroenterol.* 21 (1), 37. doi:10.1186/s12876-021-01613-y

Song, Y., Zhang, N., Shi, S., Li, J., Zhang, Q., Zhao, Y., et al. (2015). Large-scale qualitative and quantitative characterization of components in Shenfu injection by integrating hydrophilic interaction chromatography, reversed phase liquid chromatography, and tandem mass spectrometry. *J. Chromatogr. A* 1407, 106–118. doi:10.1016/j.chroma.2015.06.041

Tang, W. H. W., Li, D. Y., and Hazen, S. L. (2019). Dietary metabolism, the gut microbiome, and heart failure. *Nat. Rev. Cardiol.* 16 (3), 137–154. doi:10.1038/s41569-018-0108-7

Thomas, M. S., and Fernandez, M. L. (2021). Trimethylamine N-oxide (TMAO), diet and cardiovascular disease. *Curr. Atheroscler. Rep.* 23 (4), 12. doi:10.1007/s11883-021-00910-x

Tian, S., Zheng, N., Zu, X., Wu, G., Zhong, J., Zhang, J., et al. (2022). Integrated hepatic single-cell RNA sequencing and untargeted metabolomics reveals the immune and metabolic modulation of Qing-Fei-Pai-Du decoction in mice with coronavirus-induced pneumonia. *Phytomedicine* 97, 153922. doi:10.1016/j.phymed.2021.153922

Tong, L., Feng, Q., Lu, Q., Zhang, J., and Xiong, Z. (2022). Combined (1)H NMR fecal metabolomics and 16S rRNA gene sequencing to reveal the protective effects of Gushudan on kidney-yang-deficiency-syndrome rats via gut-kidney axis. *J. Pharm. Biomed. Anal.* 217, 114843. doi:10.1016/j.jpba.2022.114843

Wang, G., Zou, R., Liu, L., Wang, Z., Zou, Z., Tan, S., et al. (2022a). A circular network of purine metabolism as coregulators of dilated cardiomyopathy. *J. Transl. Med.* 20 (1), 532. doi:10.1186/s12967-022-03739-3

Wang, J., Wang, X., Wan, W., Guo, Y., Cui, Y., Liu, W., et al. (2021). Effects of Shenfu injection on myocardial adenosine receptors in rats with myocardial ischemia-reperfusion postconditioning. *Hum. Exp. Toxicol.* 40 (12_Suppl. l), S300–s309. doi:10.1177/09603271211041668

Wang, Q., Sun, Y., Zhou, T., Jiang, C., A, L., and Xu, W. (2022b). Gut microbiota-dependent trimethylamine n-oxide pathway contributes to the bidirectional relationship between intestinal inflammation and periodontitis. *Front. Cell Infect. Microbiol.* 12, 1125463. doi:10.3389/fcimb.2022.1125463

Wu, H., Dai, Z., Liu, X., Lin, M., Gao, Z., Tian, F., et al. (2019a). Pharmacodynamic evaluation of Shenfu injection in rats with ischemic heart failure and its effect on small molecules using matrix-assisted laser desorption/ionization-mass spectrometry imaging. *Front. Pharmacol.* 10, 1424. doi:10.3389/fphar.2019.01424

Wu, J., Zeng, Z., Zhang, W., Deng, Z., Wan, Y., Zhang, Y., et al. (2019b). Emerging role of SIRT3 in mitochondrial dysfunction and cardiovascular diseases. *Free Radic. Res.* 53 (2), 139–149. doi:10.1080/10715762.2018.1549732

Wu, Y., Li, S., Li, Z., Mo, Z., Luo, Z., Li, D., et al. (2022). Efficacy and safety of Shenfu injection for the treatment of post-acute myocardial infarction heart failure: a systematic review and meta-analysis. *Front. Pharmacol.* 13, 1027131. doi:10.3389/fphar.2022.1027131

Xiao, H. L., Zhao, L. X., Yang, J., Tong, N., An, L., Liu, Q. T., et al. (2019). Imbalance of angiotensin-converting enzymes affects myocardial apoptosis during cardiac arrest induced by acute pulmonary embolism in a porcine model. *Int. J. Mol. Med.* 43 (4), 1575–1584. doi:10.3892/ijmm.2019.4109

Xiao, H. W., Cui, M., Li, Y., Dong, J. L., Zhang, S. Q., Zhu, C. C., et al. (2020). Gut microbiota-derived indole 3-propionic acid protects against radiation toxicity via retaining acyl-CoA-binding protein. *Microbiome* 8 (1), 69. doi:10.1186/s40168-020-00845-6

Xu, F. F., Xie, X. F., Hu, H. Y., Tong, R. S., and Peng, C. (2024). Shenfu injection: a review of pharmacological effects on cardiovascular diseases. *Front. Pharmacol.* 15, 1279584. doi:10.3389/fphar.2024.1279584

Xu, X., Xie, X. F., Dong, Y. H., Zhang, H. Q., and Peng, C. (2022). Ginsenoside rg(1) reduces cardiotoxicity while increases cardiotonic effect of aconitine *in vitro*. *Chin. J. Integr. Med.* 28 (8), 693–701. doi:10.1007/s11655-022-3509-0

Xu, Y., Yang, L., Liang, K., An, R., Wang, X., and Zhang, H. (2020). Pharmacokinetic effects of ginsenoside Rg1 on aconitine, benzoylaconine and aconine by UHPLC-MS/MS. *Biomed. Chromatogr.* 34 (4), e4793. doi:10.1002/bmc.4793

Yamaguchi, A., Teratani, T., Chu, P. S., Suzuki, T., Taniki, N., Mikami, Y., et al. (2021). Hepatic adenosine triphosphate reduction through the short-chain fatty acids-peroxisome proliferator-activated receptor γ-uncoupling protein 2 Axis alleviates immune-mediated acute hepatitis in inulin-supplemented mice. *Hepatol. Commun.* 5 (9), 1555–1570. doi:10.1002/hep4.1742

Yang, S., Li, X., Yang, F., Zhao, R., Pan, X., Liang, J., et al. (2019). Gut microbiota-dependent marker TMAO in promoting cardiovascular disease: inflammation mechanism, clinical prognostic, and potential as a therapeutic target. *Front. Pharmacol.* 10, 1360. doi:10.3389/fphar.2019.01360

Ye, X., Wang, X., Wang, Y., Sun, W., Chen, Y., Wang, D., et al. (2021). A urine and serum metabolomics study of gastroesophageal reflux disease in TCM syndrome differentiation using UPLC-Q-TOF/MS. *J. Pharm. Biomed. Anal.* 206, 114369. doi:10.1016/j.jpba.2021.114369

Zhang, Q. L., Chen, X. H., Zhou, S. J., Lei, Y. Q., Huang, J. S., Chen, Q., et al. (2023). Relationship between disorders of the intestinal microbiota and heart failure in infants with congenital heart disease. *Front. Cell Infect. Microbiol.* 13, 1152349. doi:10.3389/fcimb.2023.1152349

Zhang, Y., Wang, Y., Ke, B., and Du, J. (2021). TMAO: how gut microbiota contributes to heart failure. *Transl. Res.* 228, 109–125. doi:10.1016/j.trsl.2020.08.007

Zhao, L., Wang, C., Peng, S., Zhu, X., Zhang, Z., Zhao, Y., et al. (2022). Pivotal interplays between fecal metabolome and gut microbiome reveal functional signatures in cerebral ischemic stroke. *J. Transl. Med.* 20 (1), 459. doi:10.1186/s12967-022-03669-0

Zhao, X., Lin, G., Liu, T., Zhang, X., and Xu, Y. (2023). Comparative analysis of metabolic compositions and trace elements of ornithogalum caudatum with different growth years. *ACS Omega* 8 (26), 23889–23900. doi:10.1021/acsomega.3c02310

Zhu, H. Z., Liang, Y. D., Ma, Q. Y., Hao, W. Z., Li, X. J., Wu, M. S., et al. (2019). Xiaoyaosan improves depressive-like behavior in rats with chronic immobilization stress through modulation of the gut microbiota. *Biomed. Pharmacother.* 112, 108621. doi:10.1016/j.biopha.2019.108621

Zhu, J., Song, W., Xu, S., Ma, Y., Wei, B., Wang, H., et al. (2020). Shenfu injection promotes vasodilation by enhancing eNOS activity through the PI3K/akt signaling pathway *in vitro*. *Front. Pharmacol.* 11, 121. doi:10.3389/fphar.2020.00121

frontiers | Frontiers in Pharmacology

TYPE Original Research
PUBLISHED 09 July 2024
DOI 10.3389/fphar.2024.1411273



OPEN ACCESS

EDITED BY
Tianhao Liu,
Affiliated Hospital of Jiangnan University, China

REVIEWED BY
Abdur Rauf,
University of Swabi, Pakistan
Kevin Spelman,
Health, Education and Research, United States

*CORRESPONDENCE
Yuan Gao,
gaoacu@sina.com
Xue-Xiang Cheng,
chengxuexiang@bjanting.com
Jian Chen,
alexandercj@126.com

†These authors have contributed equally to this work

RECEIVED 02 April 2024
ACCEPTED 13 June 2024
PUBLISHED 09 July 2024

CITATION
Chen X-Y, Cheng M-R, Tang C-C, Xu C-Q, Zhong Y-L, Gao Y, Cheng X-X and Chen J (2024), Integrative transcriptome-proteome approach reveals key hypoxia-related features involved in the neuroprotective effects of Yang Xue oral liquid on Alzheimer's and Parkinson's disease.
*Front. Pharmacol.* 15:1411273.
doi: 10.3389/fphar.2024.1411273



# Integrative transcriptome-proteome approach reveals key hypoxia-related features involved in the neuroprotective effects of Yang Xue oral liquid on Alzheimer's and Parkinson's disease

Xiang-Yang Chen[1†], Ming-Rong Cheng[2†], Chen-Chen Tang[3†], Chen-Qin Xu[4], Yi-Lang Zhong[4], Yuan Gao[5*], Xue-Xiang Cheng[6*] and Jian Chen[4,7*]

[1]College of Life and Environment Science, Huangshan University, Huangshan, Anhui, China, [2]Nanxiang Branch of Ruijin Hospital, Shanghai, China, [3]Department of Experimental Management, School of Integrative Medicine, Shanghai University of Traditional Chinese Medicine, Shanghai, China, [4]Department of Vascular Disease, Shanghai TCM-Integrated Hospital, Shanghai University of Traditional Chinese Medicine, Shanghai, China, [5]Traditional Chinese Recovery and Treatment Center, Zhejiang Rehabilitation Medical Center, Hangzhou, China, [6]College of Pharmacy, Hubei University of Chinese Medicine, Wuhan, China, [7]Department of Public Health, International College, Krirk University, Bangkok, Thailand

**Introduction:** This study investigates the role of hypoxia-related genes in the neuroprotective efficacy of Yang Xue oral liquid (YXKFY) in Alzheimer's disease (AD) and Parkinson's disease (PD).

**Methods and results:** Using differential expression and weighted gene co-expression network analysis (WGCNA), we identified 106 and 9 hypoxia-associated genes in AD and PD, respectively, that are implicated in the transcriptomic and proteomic profiles. An artificial intelligence-driven hypoxia signature (AIDHS), comprising 17 and 3 genes for AD and PD, was developed and validated across nine independent cohorts ($n$ = 1713), integrating 10 machine learning algorithms and 113 algorithmic combinations. Significant associations were observed between AIDHS markers and immune cells in AD and PD, including naive $CD4^+$ T cells, macrophages, and neutrophils. Interactions with miRNAs (hsa-miR-1, hsa-miR-124) and transcription factors (USF1) were also identified. Single-cell RNA sequencing (scRNA-seq) data highlighted distinct expression patterns of AIDHS genes in various cell types, such as high expression of TGM2 in endothelial cells, PDGFRB in endothelial and mesenchymal cells, and SYK in microglia. YXKFY treatment was shown to repair cellular damage and decrease reactive oxygen species (ROS) levels. Notably, genes with previously dysfunctional expression, including FKBPL, TGM2, PPIL1, BLVRB, and PDGFRB, exhibited significant recovery after YXKFY treatment, associated with riboflavin and lysicamine.

**Conclusion:** The above genes are suggested to be central to hypoxia and neuroinflammation responses in AD and PD, and are potential key mediators of YXKFY's neuroprotective action.

KEYWORDS

**Alzheimer's disease, Parkinson's disease, transcriptome, proteome, signature**

# Introduction

Alzheimer's disease (AD) and Parkinson's disease (PD) are the two most common neurodegenerative disorders that have a significant impact on the aging population worldwide (Nowell et al., 2023). AD is estimated to affect approximately 4% of individuals aged 65 and above, whereas PD is estimated to affect around 1% of the total population of individuals aged 60 and above (Macdonald et al., 2018; Aborode et al., 2022). AD is characterized by progressive memory loss, cognitive decline, and the accumulation of amyloid-beta (Aß) plaques and neurofibrillary tangles in the brain (Breijyeh and Karaman, 2020). PD, on the other hand, is characterized by motor symptoms such as tremors, rigidity, and bradykinesia, as well as the loss of dopaminergic neurons in the substantia nigra (Hayes, 2019). While the etiology of AD and PD remains complex and multifactorial, emerging evidence suggests that hypoxia is detrimental to the brain and plays a crucial role in the pathogeneses of these diseases (Burtscher et al., 2021). Hypoxia can result from various factors, including impaired blood flow, mitochondrial dysfunction, and oxidative stress, all of which have been implicated in the development and progression of AD and PD (Grabska-Kobyłecka et al., 2023; Su et al., 2023). Understanding the role of hypoxia-related features in the pathogenesis of AD and PD is crucial for the development of novel therapeutic strategies. Targeting hypoxia signaling pathways, such as HIF-1α, may offer potential therapeutic avenues for the treatment and prevention of these devastating neurodegenerative disorders (Baillieul et al., 2017).

Traditional Chinese medicines (TCMs) have been used in the treatment of neurological disease for thousands of years (Su et al., 2024). Yangxue oral liquid (YXKFY) is composed of four traditional Chinese medicines: Melanteritum, Fructus Crataegi, Fructus Hippophae, and Ziziphus jujuba. Since 7000 B.C., the fruit of Crataegus pinnatifida has been used to produce prehistoric fermented beverages (Moreira et al., 2023). Recent studies have shown that the fruit possesses neuroprotective properties that could be effective against AD (Lee et al., 2019; Moreira et al., 2023). Fructus Hippophae has been traditionally used in the treatment of brain conditions, with the aim of enhancing cognitive abilities such as learning and memory, as well as alleviating pathological damage in mice with AD through modulating oxidative stress and inflammatory processes (Dinkar Gore et al., 2023; Zhao et al., 2023). The fruit of Ziziphus jujuba has been proven to possess anti-inflammatory (Al-Reza et al., 2010) and neuroprotective (Kaeidi et al., 2015) abilities due to the presence of neuroprotective compounds such as triterpenoids, flavonoids, polysaccharides, saponins and alkaloids (Kim et al., 2021). Hence, YXKFY exhibits a promising potential for therapeutic intervention in the treatment of neurodegenerative diseases. Nevertheless, further research is needed to clarify the material basis and targets of YXKFY in addressing neurodegenerative diseases.

Recently, there has been a growing body of evidence supporting the widespread use of transcriptomics and proteomics in enhancing our understanding of pathophysiological mechanisms and facilitating the development of diagnostic tools for various diseases (Li et al., 2020; Mu et al., 2020; Yang et al., 2021; Yang et al., 2023). Moreover, the utilization of weighted gene coexpression network analysis (WGCNA) offers the ability to illustrate the interconnections between diverse genes through the creation of a co-expression network, which not only enables the identification of modules that are associated with specific phenotypes but also proves to be more efficient in the investigation of crucial pathways and genes involved in numerous human disorders (Langfelder and Horvath, 2008; Zhang et al., 2024). In addition, the limitations of expression-based multigene signatures in clinical settings can be attributed to their lack of uniqueness and appropriateness in selected modeling methods, and the absence of strict validation in large multicenter cohorts (Wang et al., 2022; Yang et al., 2024). Hence, our objective was to conduct a comprehensive analysis of the molecular mechanisms, as well as the diagnostic and therapeutic targets of YXKFY on AD/PD, using transcriptome, proteome, and hypoxia-related features.

In this study, we performed an integrated analysis to discovery a consensus artificial intelligence-driven hypoxia signature (AIDHS) from 110 kinds of algorithm combinations across transcriptome and proteome. Then, we employed ultra-high-performance liquid chromatography coupled with Quadrupole Exactive-Orbitrap high-resolution mass spectrometry (UHPLC-Q Exactive-Orbitrap HR-MS) to identify the chemicals present in YXKFY. Finally, the key AIDHS was applied in *in vitro* experimental validation to assess potential hypoxia-related mechanisms of YXKFY in AD/PD. Figure 1 showed the flowchart of the study design.

# Materials and methods

## Data acquisition from the GEO database

The mRNA and protein expression data for AD/PD were acquired from the Gene Expression Omnibus (GEO) database (https://www.ncbi.nlm.nih.gov/gds). A total of 36 AD, 48 PD and 47 normal serum samples were collected from GSE339087 (protein) for differential expression analysis. GSE5281 (87 AD cases and 74 controls) and GSE26927 (12 PD cases and 8 controls) datasets were selected for weighted gene co-expression network analysis. Then, we downloaded GSE150696 (9 AD, 12 PD cases and 9 controls), GSE132903 (97 AD cases and 98 controls), GSE63060 (145 AD cases and 104 controls), GSE63061 (140 AD

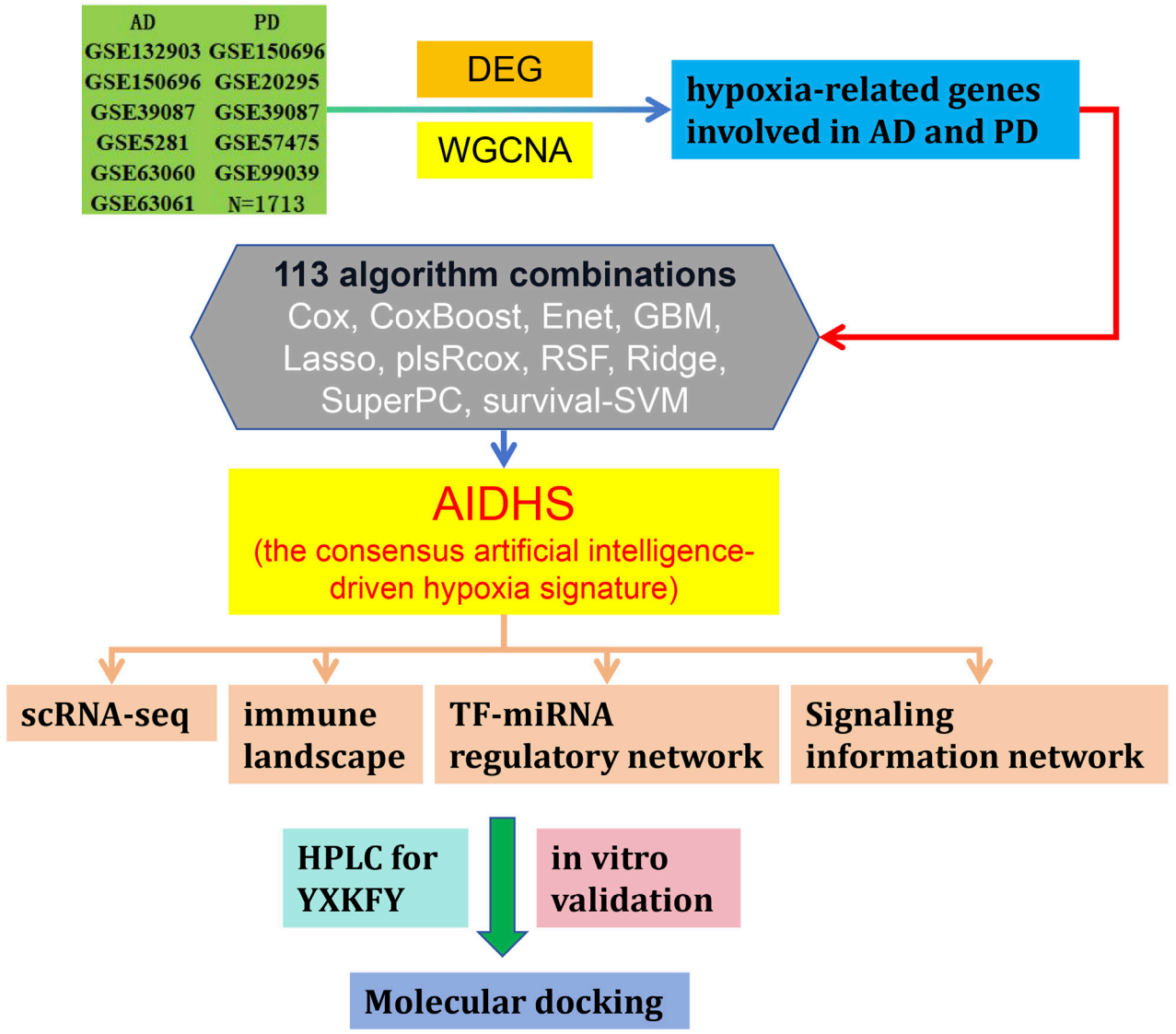


FIGURE 1
Flowchart of the study design.

cases and 134 controls), GSE20295 (40 PD cases and 53 controls), GSE99039 (205 PD cases and 233 controls) and GSE57475 (93 PD cases and 49 controls) for further analysis and validation.

## Data preprocessing and differential expression analysis

Various intergroup comparisons were conducted using Sangerbox 3.0 (http://vip.sangerbox.com/home.html), which is a freely accessible online platform for data analysis and visualization. Initially, normalization of protein expression in the GSE339087 dataset (AD and PD) was carried out. Following this, volcano plots and heatmaps were generated for the differentially expressed proteins (DEPs). DEPs with an absolute fold change of ≥ 1.2 and a $p$-value < 0.05 were deemed to be statistically significant in terms of differential expression.

## Weighted gene co-expression network analysis (WGCNA)

To identify modules of highly correlated genes and hub genes, we utilized the WGCNA (Langfelder and Horvath, 2008) approach to construct scale-free co-expression networks for two independent datasets: GSE5281 (87 AD cases and 74 controls) and GSE26927 (12 PD cases and 8 controls). In the GSE5281 dataset, the brain regions examined were the entorhinal cortex (EC), hippocampus (HIP), medial temporal gyrus (MTG), posterior cingulate (PC), superior frontal gyrus (SFG), and primary visual cortex (PVC). For the GSE26927 dataset, the substantia nigra (SN) was the focused brain region.

We initially employed Pearson correlation-based hierarchical clustering to group all the genes and samples. Subsequently, we determined the soft threshold power value to establish the co-expression network, ensuring that it conformed to a scale-free

co-expression network. The adjacency matrices were then transformed into a topological overlap matrix to identify gene modules. Moreover, similar modules were merged and clustered together. Finally, we generated module-trait relationship diagrams and obtained the gene list associated with each module.

## Intersection of hypoxia-related genes involved in AD and PD shared by transcriptome and proteome

The top four modules that have the closest association with AD/PD were identified by analyzing the module-trait relationship diagrams of the GSE5281 and GSE26927 datasets. A total of 8,371 hypoxia-related genes (HRG) were obtained from COREMINE (https://www.coremine.com/medical/#search). To identify the common HRGs between the DEGs and the aforementioned module genes, Venn diagram analysis was conducted. The overlapping genes were then subjected to functional enrichment analysis using the Metascape (https://metascape.org/gp/index.html) (Zhou Y. et al., 2019).

## Signature obtained from artificial intelligence-driven integrative approaches

In order to ensure a highly accurate and stable performance for the consensus artificial intelligence-driven hypoxia signature (AIDHS), we integrated a total of 10 machine learning algorithms and explored 113 algorithm combinations. These integrative algorithms include Cox, CoxBoost, elastic network (Enet), generalised boosted regression modelling (GBM), Lasso, stepwise partial least squares regression for Cox (plsRcox), random survival forest (RSF), Ridge, supervised principal components (SuperPC), and survival support vector machine (survival-SVM).

The procedure for generating the signature was as follows: (a) We performed the 113 algorithm combinations on the HRGs, fitting prediction models based on the leave-one-out cross-validation (LOOCV) framework using the GSE39087 cohort; (b) We then validated all these models using nine additional datasets (GSE5281, GSE26927, GSE150696, GSE132903, GSE63060, GSE63061, GSE20295, GSE99039, and GSE57475); (d) For each model, we calculated the area under the curve (AUC) score across all validation datasets. In the case of PD, we considered the model with the highest average AUC as optimal. For AD, the optimal model was determined based on higher average AUC and the least number of genes involved.

## Profile of the immune cell infiltration

In order to assess the role of the immune microenvironment in the development of AD and PD, we analyzed and compared the immune infiltration patterns in both AD/PD and normal groups through CIBERSORTx tool (https://cibersortx.stanford.edu/), which specifically designed for accurately quantifying the relative proportions of 22 immune cells subtypes within a complex mixture of gene expressions. Lastly, to assess the correlation between hub genes and differential infiltrated immune cells, a Pearson correlation test analysis was carried out. For further investigation, a correlation threshold of $|r| > 0.2$ was established.

## Signaling information network and TF-miRNA regulatory networks analysis of the hub genes

SIGNOR 2.0 (https://signor.uniroma2.it/) (Licata et al., 2020), a public repository that stores manually-annotated causal relationships between proteins and other biologically relevant entities, was performed to explore the signal transduction relationship of the former hub genes. Then, TF-miRNA coregulatory network analysis was implemented on the hub genes through curated regulatory interaction information collected from the RegNetwork repository (Liu et al., 2015) with Networkanalyst online tools (Zhou G. et al., 2019).

## Analysis the heterogeneity of striata in the AD and PD single-cell transcriptome

The basal ganglia are frequently affected in AD and PD. However, there is limited understanding of the fundamental molecular processes involved. The striatum is crucial for motor learning and various cognitive functions. Therefore, the single-cell dataset GSE161045 was obtained from the GEO database (https://www.ncbi.nlm.nih.gov/), which contains 4 AD, 4 PD and 4 control striata samples. The data underwent thorough preprocessing, including the removal of cells with fewer than 200 genes, more than 5,000 genes, or more than 25% mitochondrial genes. After this process, a total of 31,030 filtered cells remained for analysis. To mitigate potential batch effects due to sample identity, we utilized the "Harmony" R package (version 0.1.0) for batch correction (Korsunsky et al., 2019). Subsequently, we used the FindNeighbors and FindClusters functions (with a resolution of 0.1) for cell cluster identification, following the uniform manifold approximation and projection (UMAP) analysis. Prior to this, we referenced preexisting markers from published literature to identify specific cell types and their respective markers through SingleCellBase (Meng et al., 2023). Finally, we present bubble plots depicting the expression of 26 AIDHS genes in different disease and cell groups.

## Serum preparation containing YXKFY

The YXKFY samples used in this study were acquired from Hubei Fenghuang Baiyunshan Pharmaceutical Co., Ltd. Blood samples containing YXKFY were obtained from the YXKFY rat group. The original concentration of the YXKFY was 0.4 g/mL. The rats were administered a dosage of 2 mg/mL of the YXKFY. Each rat received 5 mL of the YXKFY orally, once in the morning and once in the afternoon, for a total of two administrations per day. This oral administration was continued for 5 consecutive days. Following the last administration, the abdominal aorta was punctured to collect blood 1 h later. The collected blood samples were centrifuged at 3000 r/min to separate the serum, which was then incubated at 56°C for 30 min for inactivation. The serum was subsequently filtered and sterilized using a 0.22 micron filter, and stored at −20°C for future

TABLE 1 Primer sequence of RT-qPCR.

| Gene | Forward | Reverse |
|---|---|---|
| BLVRB | CCTGAAGTACGTGGCTGTGAT | TCATGTTTGGAGATGACCCTTGA |
| C10orf54 | TCATCCTGCTCCTGGTCTACAA | AATCCCTTGAATGTTGCTGTCCAT |
| CDC37 | TGAGGTGTCTGATGATGAAGACG | GTTCCTCCTTCTCCTTCTGGAAC |
| CHCHD6 | TCTTCAGAGCAATTCCATGAGGC | GATCTCGGTAGCAGTGGAGAATC |
| FKBPL | TTGGAGAAAAGGACACCTCTCAG | CTTACTTCCAGCTCAAGCGTTTC |
| FN1 | AGCCGAGGTTTTAACTGCGA | CCCACTCGGTAAGTGTTCCC |
| GLUL | GTGAGAAAGTCCAGGCCATGTAT | CTGTTGGAACCCTCAGACTGTAA |
| HOXC4 | GTATAGCTGCACCAGTCTCCAG | AGAGCGACTGTGATTTCTCGG |
| PFN1 | GCTACAAGGACTCGCCCTC | CAAGTGTCAGCCCATTCACGTA |
| PPIL1 | TGCTCCAAAGACCTGTAAGAACT | TTGCCATAGATAGATGCACCACC |
| PRDX4 | GAGACACTACGTTTGGTTCAAGC | TTTCACTACCAGGTTTCCAGCC |
| PSMB1 | CTGCAATGCTGTCTACAATCCTG | TCTCTCTGGTAAGACCCTACTGG |
| PSMG1 | GCTAGAAAAATATCCGTGCTCCA | GTTTAGCACAACCAACTTCCTCC |
| SLC16A14 | CATCTGTGCTAATGGCATCTCTG | CGAATGCACGGCTGAATAAGTAA |
| SLC17A7 | CATGGTCAATAACAGCACGACC | ACAATGTAGCCCCAGAAAAAGGA |
| SMYD3 | GGGGTTCAAGTGATGAAAGTTGG | TCTTCAATCAGGCTGTGTTCTCT |
| SYK | GCAGAAGCCATATCGAGGGA | ATCTCTCTTGGACACCCTGC |
| FMO5 | TAGCCAAACAGCCAAGCAGG | AGTCCCCTACACGATTCAGGA |
| HDAC4 | TCACTCCCTACCTGAGCACC | GGCCTGAAAGATACCAGTCTGT |
| TGM2 | GTCAGCTACAATGGGATCTTGGG | AAGGCAGTCACGGTATTTCTCAT |
| DNM2 | TCGACATTGAGCAGTCCTACATC | GGGATGGCTCTCTTCTTGTTCAG |
| PDGFRB | GGACATACCCCCGCAAAGAA | CTCTCCGTCACATTGCAGGT |
| FXYD5 | CCTGTGTCTTCTCACCATCGTT | AGAACTGGACGTGGTATCTTTCA |
| SETDB1 | GATGCTGTCAACAAGAAGAGCAG | GCCTTTGTGCCAAGTCTTAGTTC |
| MYBPH | TCTCAGAAAACCTGTGTGGACTC | AGAAGTCTCGCTCAATAAACCCT |
| JUP | CAACAAGAACAACCCCAAGTTCC | GGTCCAGAGCAGCTTTTCATAAC |

use. All of the animal procedures, such as housing and care, and experimental protocols were approved by the Ethics Committee of Shanghai University of Traditional Chinese Medicine (No. PZSHUTCM210702015).

## Cell culture and treatment

Human neuroblastoma SH-SY5Y cells were cultured in a medium composed of DMEM supplemented with 10% fetal bovine serum (FBS, Gibco, Australia) at a controlled environment of 37°C with 5% CO2. The cells were evenly distributed with a density of 10,000 cells per well in 96-well plates and allowed to grow for a period of 12 h. To determine the optimal concentration of the hypoxic model in SH-SY5Y cells, the viability of SH-SY5Y cells was assessed using the CCK8 assay after exposure to different concentrations of CoCl2 (0 μM, 25 μM, 50 μM, 100 μM, 200 μM, 400 μM, 500 μM, 600 μM, 800 μM, and 1000 μM) for 24 h. In order to evaluate the potential neuroprotective properties of YXKFY on SH-SY5Y cells, CoCl2 group was exposed to 800 μM for 24 h; and YXKFY group was subjected to 800 μM CoCl2 and serum containing 10% YXKFY for 24 h.

## ROS measurement

ROS generation in SH-SY5Y cells was examined using the fluorescent dye 2′,7′-dichlorodihydrofluorescein diacetate (DCFH-DA; Beyotime, Shanghai, China). SH-SY5Y cells were firstly washed three times with phosphate-buffered saline (PBS). Subsequently, the cells were incubated in PBS supplemented with 10 μM of DCFH-DA at a temperature of 37°C for a duration of 20 min. Following the incubation period, cells were once again washed three times using PBS. To visualize the cells, the

TABLE 2 The detailed information of chemical components derived from YXKFY by UPLC-Q/TOF-MS.

| No. | Rt/min | Ion mode | Measured mass/Da | Molecular formula | Calculated mass/Da | Error/ppm | Identification | Peak area | Peak Area_Plasma |
|---|---|---|---|---|---|---|---|---|---|
| 1 | 0.912 | $[M + H]^+$ | 183.0858 | C6H15O6 | 183.0863 | −2.8 | Sorbitol | 538,380 | 0 |
| 2 | 0.921 | $[M-H]^-$ | 179.0570 | C6H11O6 | 179.0561 | 5.0 | Glucose | 1,676,539 | 0 |
| 3 | 0.996 | $[M-H]^-$ | 191.0566 | C7H11O6 | 191.0561 | 2.6 | Quinic acid | 3,460,700 | 7,512 |
| 4 | 0.999 | $[M + H]^+$ | 116.0698 | C5H10NO2 | 116.0706 | −6.9 | Proline | 575,886 | 0 |
| 5 | 1.009 | $[M-H]^-$ | 341.1085 | C12H21O11 | 341.1089 | −1.3 | Sucrose | 3,205,474 | 0 |
| 6 | 1.122 | $[M-H]^-$ | 133.0147 | C4H5O5 | 133.0143 | 3.4 | Succinic acid | 51,667 | 0 |
| 7 | 1.240 | $[M + H]^+$ | 171.0285 | C7H7O5 | 171.0288 | −1.8 | Gallic acid | 173,573 | 0 |
| 8 | 1.355 | $[M + H]^+$ | 155.0335 | C7H7O4 | 155.0339 | −2.5 | Protocatechuic acid isomer | 202,678 | 0 |
| 9 | 1.443 | $[M-H]^-$ | 191.0204 | C6H7O7 | 191.0197 | 3.5 | Citric acid | 989,583 | 0 |
| 10 | 1.451 | $[M + H]^+$ | 442.1446 | C19H20N7O6 | 442.1470 | −5.3 | Folcidin | 20,070 | 0 |
| 11 | 1.732 | $[M + H]^+$ | 245.0759 | C9H13N2O6 | 245.0768 | −3.7 | Uridine | 87,619 | 0 |
| 12 | 1.735 | $[M + H]^+$ | 113.0339 | C4H5N2O2 | 113.0346 | −5.8 | Uracil | 45,669 | 0 |
| 13 | 1.800 | $[M + H]^+$ | 170.0809 | C8H12NO3 | 170.0812 | −1.6 | Pyridoxine | 344,564 | 0 |
| 14 | 2.119 | $[M + H]^+$ | 132.1009 | C6H14NO2 | 132.1019 | −7.6 | Leucine | 50,928 | 0 |
| 15 | 2.179 | $[M-H]^-$ | 169.0148 | C7H5O5 | 169.0143 | 3.3 | Gallic acid isomer | 9,768 | 0 |
| 16 | 2.275 | $[M-H]^-$ | 375.1293 | C17H19N4O6 | 375.1310 | −4.6 | Riboflavine isomer | 2,690 | 0 |
| 17 | 2.297 | $[M + H]^+$ | 132.1015 | C6H14NO2 | 132.1019 | −3.1 | Leucine isomer | 53,312 | 0 |
| 18 | 2.346 | $[M + H]^+$ | 268.1042 | C10H14N5O4 | 268.1040 | 0.6 | Adenosine | 41,479 | 0 |
| 19 | 2.497 | $[M + H]^+$ | 180.1014 | C10H14NO2 | 180.1019 | −2.8 | Maltoxazine isomer | 14,685 | 0 |
| 20 | 2.507 | $[M + H]^+$ | 132.1009 | C6H14NO2 | 132.1019 | −7.6 | Leucine isomer | 3,040 | 0 |
| 21 | 2.553 | $[M + H]^+$ | 144.1020 | C7H14NO2 | 144.1019 | 0.7 | Stachydrine | 43,600 | 0 |
| 22 | 2.795 | $[M-H]^-$ | 169.0148 | C7H5O5 | 169.0143 | 3.3 | Gallic acid isomer | 3,642 | 0 |
| 23 | 2.860 | $[M + H]^+$ | 121.0638 | C8H9O | 121.0648 | −8.2 | Acetophenone isomer | 6,696 | 0 |
| 24 | 2.927 | $[M + H]^+$ | 180.1017 | C10H14NO2 | 180.1019 | −1.1 | Maltoxazine | 208,124 | 0 |
| 25 | 3.266 | $[M-H]^-$ | 375.1289 | C17H19N4O6 | 375.1310 | −5.6 | Riboflavine isomer | 3,815 | 0 |
| 26 | 4.368 | $[M + H]^+$ | 139.0387 | C7H7O3 | 139.0390 | −1.9 | p-Hydroxybenzoic acid | 8,603 | 0 |
| 27 | 4.580 | $[M-H]^-$ | 153.0199 | C7H5O4 | 153.0193 | 3.7 | 3,4-Dihydroxybenzoic acid | 53,048 | 0 |
| 28 | 6.523 | $[M + H]^+$ | 137.0594 | C8H9O2 | 137.0597 | −2.2 | 4′-Hydroxyacetophenone | 31,247 | 0 |
| 29 | 7.179 | $[M + H]^+$ | 169.0490 | C8H9O4 | 169.0495 | −3.2 | Vanillic acid isomer | 14,596 | 0 |
| 30 | 7.569 | $[M-H]^-$ | 137.0251 | C7H5O3 | 137.0244 | 5.0 | p-Hydroxybenzoic acid isomer | 16,430 | 0 |
| 31 | 7.976 | $[M-H]^-$ | 153.0201 | C7H5O4 | 153.0193 | 5.0 | Protocatechuic acid | 57,954 | 0 |
| 32 | 8.002 | $[M + H]^+$ | 155.0332 | C7H7O4 | 155.0339 | −4.4 | Protocatechuic acid isomer | 31,047 | 0 |
| 33 | 8.105 | $[M + H]^+$ | 139.0384 | C7H7O3 | 139.0390 | −4.1 | p-Hydroxybenzoic acid isomer | 17,940 | 0 |
| 34 | 8.169 | $[M + H]^+$ | 355.1010 | C16H19O9 | 355.1024 | −3.8 | Chlorogenic acid | 12,483 | 0 |
| 35 | 8.474 | $[M + H]^+$ | 146.1168 | C7H16NO2 | 146.1176 | −5.2 | Acetylcholine | 3,356 | 0 |

(Continued on following page)

TABLE 2 (*Continued*) The detailed information of chemical components derived from YXKFY by UPLC-Q/TOF-MS.

| No. | Rt/min | Ion mode | Measured mass/Da | Molecular formula | Calculated mass/Da | Error/ppm | Identification | Peak area | Peak Area_Plasma |
|---|---|---|---|---|---|---|---|---|---|
| 36 | 8.514 | $[M + H]^+$ | 193.0494 | C10H9O4 | 193.0495 | −0.7 | Scopoletin | 86,514 | 0 |
| 37 | 10.068 | $[M + H]^+$ | 220.1182 | C9H18NO5 | 220.1180 | 1.1 | Vitamin B5 | 2,572 | 0 |
| 38 | 11.137 | $[M-H]^-$ | 153.0193 | C7H5O4 | 153.0193 | −0.2 | Protocatechuic acid isomer | 5,234 | 0 |
| 39 | 11.615 | $[M-H]^-$ | 137.0248 | C7H5O3 | 137.0244 | 2.8 | p-Hydroxybenzoic acid isomer | 9,789 | 0 |
| 40 | 12.202 | $[M + H]^+$ | 169.0489 | C8H9O4 | 169.0495 | −3.8 | Vanillic acid | 12,655 | 0 |
| 41 | 12.733 | $[M + H]^+$ | 355.1023 | C16H19O9 | 355.1024 | −0.2 | Neochlorogenic acid | 106,958 | 0 |
| 42 | 13.679 | $[M + H]^+$ | 139.0384 | C7H7O3 | 139.0390 | −4.1 | p-Hydroxybenzoic acid isomer | 6,711 | 0 |
| 43 | 13.794 | $[M + H]^+$ | 265.1434 | C15H21O4 | 265.1434 | −0.1 | Tauremisin | 7,131 | 0 |
| 44 | 13.817 | $[M + H]^+$ | 355.1016 | C16H19O9 | 355.1024 | −2.1 | Chlorogenic acid isomer | 78,977 | 0 |
| 45 | 13.927 | $[M + H]^+$ | 328.1533 | C19H22NO4 | 328.1543 | −3.2 | Stepholidine | 11,349 | 0 |
| 46 | 14.065 | $[M + H]^+$ | 195.0649 | C10H11O4 | 195.0652 | −1.5 | Ferulic acid | 20,975 | 0 |
| 47 | 14.066 | $[M + H]^+$ | 107.0485 | C7H7O | 107.0491 | −6.0 | Benzaldehyde isomer | 8,745 | 0 |
| 48 | 14.336 | $[M + H]^+$ | 193.0491 | C10H9O4 | 193.0495 | −2.3 | Scopoletin isomer | 15,683 | 0 |
| 49 | 14.466 | $[M + H]^+$ | 199.0595 | C9H11O5 | 199.0601 | −3.0 | Syringic acid | 9,747 | 0 |
| 50 | 14.590 | $[M-H]^-$ | 431.1544 | C19H27O11 | 431.1559 | −3.4 | Zizybeoside I | 21,089 | 0 |
| 51 | 14.668 | $[M + H]^+$ | 286.1437 | C17H20NO3 | 286.1438 | −0.2 | Coclaurine | 362,560 | 0 |
| 52 | 14.839 | $[M + H]^+$ | 298.1437 | C18H20NO3 | 298.1438 | −0.2 | Lysicamine | 20,761 | 293 |
| 53 | 15.304 | $[M-H]^-$ | 375.1283 | C17H19N4O6 | 375.1310 | −7.2 | Riboflavine | 7,526 | 550 |
| 54 | 15.384 | $[M + H]^+$ | 151.0748 | C9H11O2 | 151.0754 | −3.7 | Benzyl acetate | 39,685 | 0 |
| 55 | 15.481 | $[M + H]^+$ | 579.1688 | C27H31O14 | 579.1708 | −3.5 | Vitexin 2″-O-rhamnoside isomer | 5,046 | 0 |
| 56 | 15.598 | $[M-H]^-$ | 593.2068 | C25H37O16 | 593.2087 | −3.2 | Zizybeoside II | 6,509 | 0 |
| 57 | 15.667 | $[M + H]^+$ | 433.1689 | C19H29O11 | 433.1704 | −3.6 | Zizybeoside I isomer | 11,773 | 0 |
| 58 | 15.737 | $[M + H]^+$ | 149.0596 | C9H9O2 | 149.0597 | −0.7 | Cinnamic acid | 138,605 | 3,943 |
| 59 | 15.738 | $[M + H]^+$ | 121.0646 | C8H9O | 121.0648 | −1.6 | Acetophenone | 25,054 | 0 |
| 60 | 16.187 | $[M + H]^+$ | 757.2143 | C33H41O20 | 757.2186 | −5.6 | Kaempferol 3-sophoroside-7-rhamnoside isomer | 1,508 | 0 |
| 61 | 16.312 | $[M + H]^+$ | 265.1435 | C15H21O4 | 265.1434 | 0.2 | Tauremisin isomer | 5,990 | 0 |
| 62 | 16.365 | $[M + H]^+$ | 387.2005 | C19H31O8 | 387.2013 | −2.2 | Roseoside | 34,972 | 0 |
| 63 | 16.366 | $[M + H]^+$ | 225.1481 | C13H21O3 | 225.1485 | −1.9 | Vomifoliol | 12,846 | 0 |
| 64 | 16.871 | $[M + H]^+$ | 377.1445 | C17H18NO2 | 377.1456 | −2.8 | Vitamin B2 | 10,101 | 0 |
| 65 | 16.944 | $[M + H]^+$ | 757.2171 | C33H41O20 | 757.2186 | −1.9 | Kaempferol 3-sophoroside-7-rhamnoside isomer | 2,400 | 0 |
| 66 | 17.088 | $[M + H]^+$ | 387.2003 | C19H31O8 | 387.2013 | −2.7 | Roseoside isomer | 7,682 | 0 |
| 67 | 17.381 | $[M + H]^+$ | 757.2161 | C33H41O20 | 757.2186 | −3.3 | Kaempferol 3-sophoroside-7-rhamnoside isomer | 3,779 | 0 |

(Continued on following page)

TABLE 2 (*Continued*) The detailed information of chemical components derived from YXKFY by UPLC-Q/TOF-MS.

| No. | Rt/min | Ion mode | Measured mass/Da | Molecular formula | Calculated mass/Da | Error/ppm | Identification | Peak area | Peak Area_Plasma |
|---|---|---|---|---|---|---|---|---|---|
| 68 | 17.912 | $[M + H]^+$ | 449.1073 | C21H21O11 | 449.1078 | −1.2 | Astragalin | 48,278 | 0 |
| 69 | 18.184 | $[M + H]^+$ | 268.1320 | C17H18NO2 | 268.1332 | −4.5 | Asimilobine | 29,885 | 0 |
| 70 | 18.366 | $[M + H]^+$ | 287.0525 | C15H11O6 | 287.0550 | −8.8 | Kaempferol | 10,734 | 0 |
| 71 | 18.393 | $[M + H]^+$ | 757.2205 | C33H41O20 | 757.2186 | 2.5 | Kaempferol 3-sophoroside-7-rhamnoside isomer | 1901 | 0 |
| 72 | 18.613 | $[M-H]^-$ | 137.0250 | C7H5O3 | 137.0244 | 4.2 | p-Hydroxybenzoic acid | 88,834 | 40,444 |
| 73 | 18.616 | $[M + H]^+$ | 757.2158 | C33H41O20 | 757.2186 | −3.7 | Kaempferol 3-sophoroside-7-rhamnoside | 1,245 | 0 |
| 74 | 18.660 | $[M-H]^-$ | 609.1445 | C27H29O16 | 609.1461 | −2.6 | Quercetin 3-O-rutinoside | 2,246 | 0 |
| 75 | 18.828 | $[M + H]^+$ | 579.1693 | C27H31O14 | 579.1708 | −2.6 | Vitexin 2″-O-rhamnoside | 12,438 | 0 |
| 76 | 18.981 | $[M + H]^+$ | 193.0492 | C10H9O4 | 193.0495 | −1.7 | Scopoletin isomer | 23,891 | 0 |
| 77 | 19.026 | $[M + H]^+$ | 433.1112 | C21H21O10 | 433.1129 | −4.0 | Kaempferol 7-O-rhamnoside | 7,534 | 0 |
| 78 | 19.149 | $[M-H]^-$ | 577.1547 | C27H29O14 | 577.1563 | −2.7 | Isovitexin 2″-O-rhamnoside | 10,637 | 0 |
| 79 | 19.346 | $[M + H]^+$ | 579.1697 | C27H31O14 | 579.1708 | −2.0 | Vitexin 2″-O-rhamnoside isomer | 35,547 | 0 |
| 80 | 19.658 | $[M + H]^+$ | 449.1066 | C21H21O11 | 449.1078 | −2.8 | Quercetin-7-O-α-L-Rhamnoside | 33,657 | 3,377 |
| 81 | 19.686 | $[M-H]^-$ | 609.1454 | C27H29O16 | 609.1461 | −1.2 | Quercetin 3-glucoside 7-rhamnoside | 1,648 | 0 |
| 82 | 19.806 | $[M + H]^+$ | 449.1070 | C21H21O11 | 449.1078 | −1.9 | Astragalin isomer | 33,234 | 0 |
| 83 | 19.851 | $[M-H]^-$ | 609.1453 | C27H29O16 | 609.1461 | −1.3 | Rutin | 7,175 | 0 |
| 84 | 20.070 | $[M + H]^+$ | 625.1749 | C28H33O16 | 625.1763 | −2.3 | Isorhamnetin-3-O-rutinoside | 38,081 | 0 |
| 85 | 21.330 | $[M + H]^+$ | 479.1157 | C22H23O12 | 479.1184 | −5.6 | Isorhamnetin-3-O-glucoside | 5,304 | 0 |
| 86 | 21.594 | $[M + H]^+$ | 282.1493 | C18H20NO2 | 282.1489 | 1.6 | Nornuciferine | 43,012 | 0 |
| 87 | 21.608 | $[M + H]^+$ | 625.1751 | C28H33O16 | 625.1763 | −1.9 | Narcissin | 25,240 | 0 |
| 88 | 21.810 | $[M + H]^+$ | 479.1172 | C22H23O12 | 479.1184 | −2.5 | Isorhamnetin 3-O-galactoside | 8,510 | 0 |
| 89 | 21.899 | $[M + H]^+$ | 165.0907 | C10H13O2 | 165.0910 | −1.9 | Eugenol | 35,879 | 0 |
| 90 | 22.875 | $[M + H]^+$ | 247.1324 | C15H19O3 | 247.1329 | −1.9 | Zederone | 10,755 | 0 |
| 91 | 23.949 | $[M + H]^+$ | 291.0861 | C15H15O6 | 291.0863 | −0.7 | Catechin | 21,686 | 0 |
| 92 | 24.750 | $[M + H]^+$ | 219.1743 | C15H23O | 219.1743 | −0.2 | Tumerone | 77,472 | 0 |
| 93 | 24.916 | $[M + H]^+$ | 433.1123 | C21H21O10 | 433.1129 | −1.4 | Vitexin | 4,581 | 0 |
| 94 | 25.676 | $[M + H]^+$ | 115.1110 | C7H15O | 115.1117 | −6.4 | Heptanal isomer | 8,247 | 0 |
| 95 | 27.283 | $[M + H]^+$ | 107.0485 | C7H7O | 107.0491 | −6.0 | Benzaldehyde | 36,091 | 0 |
| 96 | 27.744 | $[M + H]^+$ | 173.1533 | C10H21O2 | 173.1536 | −1.8 | Isoamyl isovalerate | 34,456 | 0 |
| 97 | 27.751 | $[M + H]^+$ | 115.1111 | C7H15O | 115.1117 | −5.6 | Heptanal | 26,140 | 0 |
| 98 | 28.044 | $[M + H]^+$ | 219.1736 | C15H23O | 219.1743 | −3.4 | Tumerone | 8,308 | 7,917 |

(Continued on following page)

TABLE 2 (*Continued*) The detailed information of chemical components derived from YXKFY by UPLC-Q/TOF-MS.

| No. | Rt/ min | Ion mode | Measured mass/Da | Molecular formula | Calculated mass/Da | Error/ ppm | Identification | Peak area | Peak Area_Plasma |
|---|---|---|---|---|---|---|---|---|---|
| 99 | 29.112 | $[M + H]^+$ | 487.3401 | C30H47O5 | 487.3418 | −3.5 | Ceanothic acid | 8,080 | 0 |
| 100 | 29.453 | $[M-H]^-$ | 157.1239 | C9H17O2 | 157.1234 | 3.2 | Ethyl heptanoate | 11,742 | 0 |
| 101 | 29.631 | $[M + H]^+$ | 159.1375 | C9H19O2 | 159.1380 | −2.9 | Propionyl hexanoate | 10,372 | 0 |
| 102 | 29.805 | $[M-H]^-$ | 169.1238 | C10H17O2 | 169.1234 | 2.3 | Isoamyl Senecioate | 1878 | 1,256 |
| 103 | 30.270 | $[M + H]^+$ | 229.0854 | C14H13O3 | 229.0859 | −2.3 | trans-Resveratrol | 16,971 | 0 |
| 104 | 30.591 | $[M + H]^+$ | 219.1739 | C15H23O | 219.1743 | −2.0 | Tumerone | 13,849 | 20,300 |
| 105 | 32.050 | $[M + H]^+$ | 235.1688 | C15H23O2 | 235.1693 | −1.9 | Curcumenol | 175,822 | 0 |
| 106 | 38.723 | $[M + H]^+$ | 135.0802 | C9H11O | 135.0804 | −1.8 | Chavicol | 83,475 | 0 |
| 107 | 42.510 | $[M + H]^+$ | 257.2473 | C16H33O2 | 257.2475 | −0.8 | Palmitic acid | 272,046 | 0 |

measurements and analysis were conducted using a FACS Calibur flow cytometer (Beckman, San Jose, United States).

## Validation of YXKFY-associated AIDHS genes by RT-qPCR

The extraction of total RNA from cells was carried out using TRIzol (Invitrogen Corporation, CA, United States). Subsequently, cDNA was synthesized using the cDNA Synthesis SuperMix. In order to detect the mRNA expression levels of AIDHS, RT-qPCR was conducted using GAPDH as an internal reference. The amplification primers used in the experiment were obtained from Shanghai Sangon Biological Engineering Technology and are detailed in Table 1. To ensure consistency, the mRNA expression level of each target gene was normalized to that of GAPDH within the same sample. The relative expression of each target gene was determined using the $2^{-\Delta\Delta CT}$ method.

## Analysis of YXKFY and drug serum via high performance liquid chromatography (HPLC)

To perform the analysis, an Acquity UPLC® BEH C18 column (100 mm × 2.1 mm, 1.7 μm) was utilized in conjunction with a Dionex Ultimate 3,000 high-pressure liquid system. The mobile phase consisted of a mixture of 0.1% formic acid in water and methanol. The elution procedure involved a stepwise gradient: from 0 to 4 min, 4% methanol; from 4 to 10 min, 4%–12% methanol; from 10 to 30 min, 12%–70% methanol; at 30 min, 70% methanol; from 35 to 38 min, 70%–95% methanol; at 38 min, 95% methanol; and from 42 to 45 min, 4% methanol. The flow velocity was maintained at 0.3 mL/min. The column temperature was set at 40°C, and the sample size used for each analysis was 5 μL. For the analysis and detection of the compounds, a Q Exactive quadrupole-electrostatic field orbitrap high-resolution mass spectrometer was employed. The ion source used was an electrospray ion source (H-ESI). The scanning mode utilized for this analysis was full MS/SIM mode (covered m/z 80–1,200), allowing for the detection of both positive and negative ions.

## Molecular docking validation

The Protein Data Bank (PDB, https://www.rcsb.org/) was accessed to retrieve the crystal structures of the primary targets. The three-dimensional configurations of the active compounds were obtained from PubChem (https://pubchem.ncbi.nlm.nih.gov/). Utilizing AutoDock Vina (http://vina.scripps.edu/), molecular docking was carried out to compute the affinity between the active compounds and primary targets. The corresponding PDB identifiers were 5oog, 2 × 7 k and 3s3j for BLVRB, PPIL1, and TGM2, respectively. The AlphaFold algorithm was used to predict the structures of FKBPL and PDGFRB, which are proteins without a known 3D structure in the PDB database. Then, water molecules were eliminated from the proteins, and polar hydrogen atoms were added. Subsequently, active binding sites were constructed based on the ligand's position in the PDB complex.

## Statistical analysis

The data presented in this study were expressed as the mean ± standard deviation (SD), using the social science statistical software package for data analysis. An independent sample t-test was employed to compare the two groups of data, while a one-way analysis of variance was used to compare multiple sets of data. The column graphs were created using GraphPad Prism 6 software. A significance level of $p < 0.05$ was considered statistically significant.

# Results

## Identification of DEPs in AD and PD

Human serum protein expression dataset of GSE39087 (AD and PD) was applied for our differential protein expression analysis. After data preprocessing and differential expression analysis, we identified 1988 DEPs between AD and healthy controls (|Fold change| ≥ 1.2 and $p$-value < 0.05), including 723 upregulated (DNAJC8, IGLC1, LGALS1, ICAM4, and TRA2A) and 1,265 downregulated proteins (EDC3, HRH1, RP9, IL9, and HOXA1) (Figure 2A). The top 30 DEPs of AD (Figure 2C) were

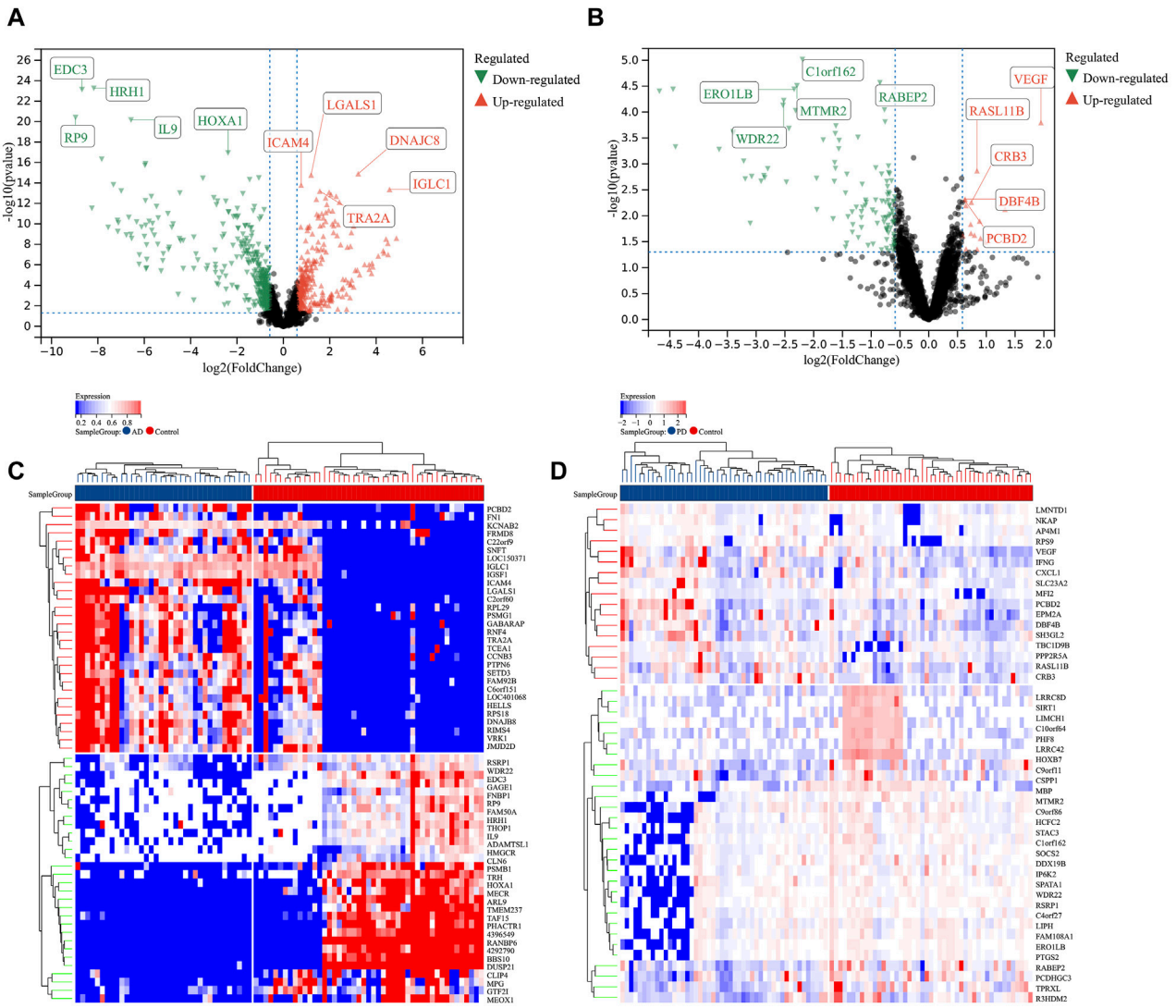


FIGURE 2
Identification of differentially expressed proteins (DEPs) in AD and PD. Volcano plots of DEPs in AD **(A)** and PD **(B)**. Heatmaps of the top 30 DEPs in AD **(C)** and PD **(D)**. Red, upregulated DEPs; blue, downregulated DEPs.

visualized in heatmap. In addition, we also identified 344 DEPs between PD and healthy controls (|Fold change| ≥ 1.2 and $p$-value < 0.05), including 90 upregulated (VEGF, RASL11B, CRB3, DBF4B, and PCBD2) and 254 downregulated proteins (ERO1LB, C1orf162, WDR22, MTMR2, and RABEP2) (Figure 2B). And the top 30 DEPs of PD were visualized in heatmap (Figure 2D).

## WGCNA of the whole transcriptome expression matrix

We performed WGCNA analysis to find similar gene expression patterns tended to exert similar biological functions in GSE5281 (AD) and GSE26927 (PD). Figures 3A, B displayed the hierarchical clustering dendrograms of the samples. Subsequently, we examined the soft threshold powers of the network topology and determined β values of 5 and 12 to be the optimal soft-thresholding parameters for GSE5281 (AD) and GSE26927 (PD) datasets (Figures 3E, F). From the GSE5281 dataset, we identified 9 modules (Figure 3C), while from the GSE26927 dataset, we identified 15 modules (Figure 3D). To investigate the associations between gene modules and AD or PD, we constructed module-trait diagrams. In GSE5281, the four modules with the highest correlation to AD were MEyellow (r = −0.57, $p$ = 5e−15), MEblack (r = 0.53, $p$ = 3e−13), MEblue (r = 0.49, $p$ = 6e−11), and MEred (r = 0.46, $p$ = 8e−10). In GSE26927, the four modules with the highest correlation to PD were MEpink (r = 0.71, $p$ = 5e−04), MEmagenta (r = 0.59, $p$ = 0.006), MEpurple (r = 0.55, $p$ = 0.01), and MEyellow (r = 0.55, $p$ = 0.01).

## Hypoxia-related genes involved in AD and PD shared by transcriptome and proteome

To discover functional genes concurrently involved in both AD and PD across the transcriptome and proteome, we employed two methods to identify key genes. Firstly, we used WGCNA to identify

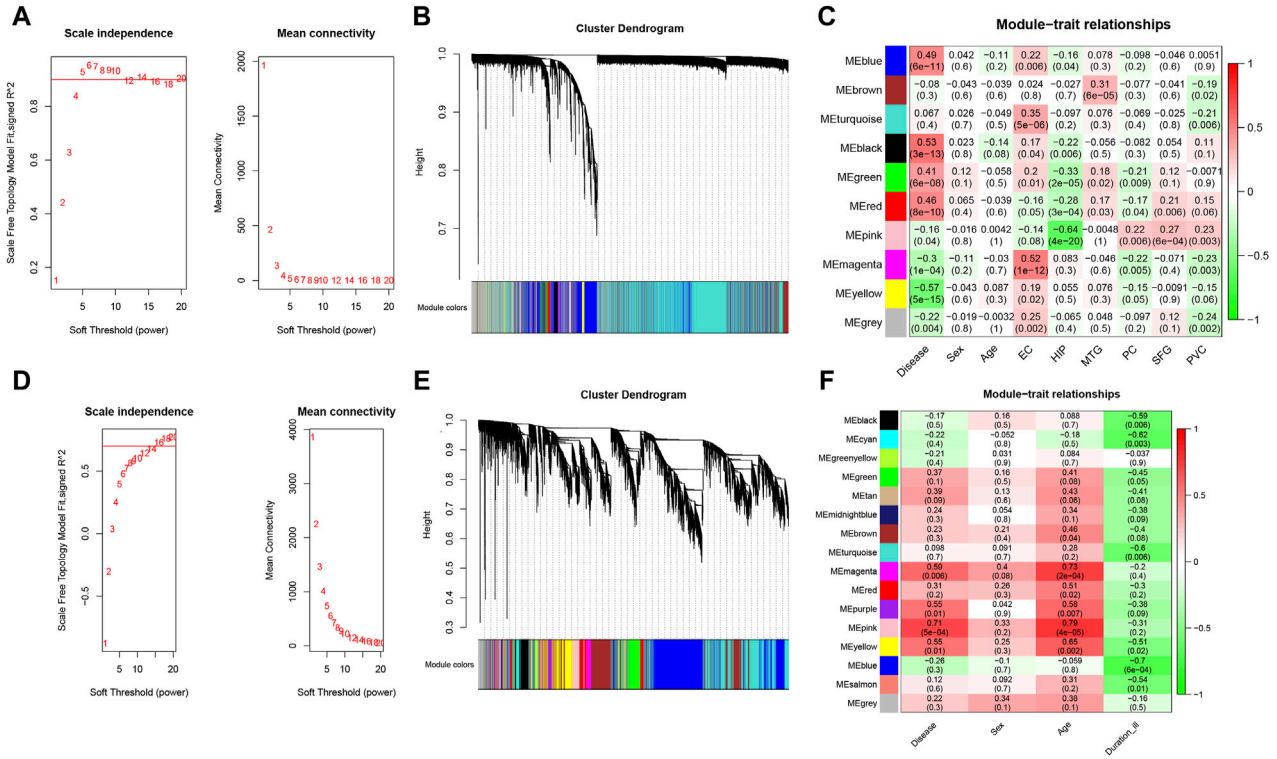


FIGURE 3
Identification of modules correlated with AD and PD in transcriptome datasets. Hierarchical clustering dendrograms were constructed for the samples in the AD **(A)** and PD **(B)** datasets. Additionally, module-trait relationship diagrams were generated for the AD **(C)** and PD **(D)** datasets. In these diagrams, each row represents a color module, while each column represents a clinical trait. The correlation and *p*-value for each module-trait combination are displayed in the respective cells. Furthermore, an analysis was performed to assess the scale independence and mean connectivity for the optimal soft threshold powers in the AD **(E)** and PD **(F)** datasets.

modules that are related to AD and PD. Secondly, we conducted differential expression analysis to identify the most dysregulated genes. In total, we identified 200 genes in AD and 17 genes in PD that were concurrently involved in the transcriptome and proteome, respectively (Figures 4A, B). Enrichment analysis of concurrent Genes Involved in AD showed that the terms were mainly enriched in cytokine signaling in immune system, PI3K-Akt signaling pathway, mitochondrial matrix, inflammatory response, and positive regulation of superoxide anion generation (Figure 4C), whereas PD was related to histone modifying activity, regulation of muscle system process, focal adhesion, regulation of metal ion transport and negative regulation of striated muscle cell differentiation (Figure 4D).

In view of the important role of hypoxia-related genes in AD and PD, we extracted 106 and 9 hypoxia-related genes involved in AD and PD for further analysis by intersecting the DEPs and WGCNA related mRNAs with 8,371 hypoxia-related genes.

## Integrated development of AD and PD consensus signature

A total of 106 and 9 hypoxia-related genes involved in AD and PD were further incorporated into our integration program to develop an AIDHS. In the protein training cohort, we applied 110 algorithm combinations via ten-fold cross-validation to construct prediction models and calculated the average AUC of each algorithm in the remaining testing cohorts. In AD, the combination of glmBoost and LDA with higher average AUC (0.764) and proper genes (N = 17) was selected as the final model, which contained BLVRB, C10orf54, CDC37, CHCHD6, FKBPL, FN1, GLUL, HOXC4, PFN1, PPIL1, PRDX4, PSMB1, PSMG1, SLC16A14, SLC17A7, SMYD3, and SYK. In PD, the combination of glmBoost and RF with the highest average AUC (0.722) was selected as the final model (N = 3), including FMO5, HDAC4, and TGM2 (Figure 5).

## Altered of immune cell infiltration in AD and PD

We observed 8 (GSE60630) and 4 (GSE60631) significant differences in the infiltration of cells between AD and healthy samples. In GSE60630, T cells CD4 naïve, NK cells resting, Macrophages M0, Mast cells activated and Neutrophils cell types were upregulated, whereas T cells CD4 memory resting, T cells gamma delta and Macrophages M2 cell types downregulated (Figure 6A). In GSE60631, NK cells resting cell type was upregulated, whereas B cells naive, T cells CD4 memory resting and Macrophages M2 cell types downregulated (Figure 6B).

We observed 4 (GSE57475) and 7 (GSE99039) significant differences in the infiltration of cells between PD and healthy

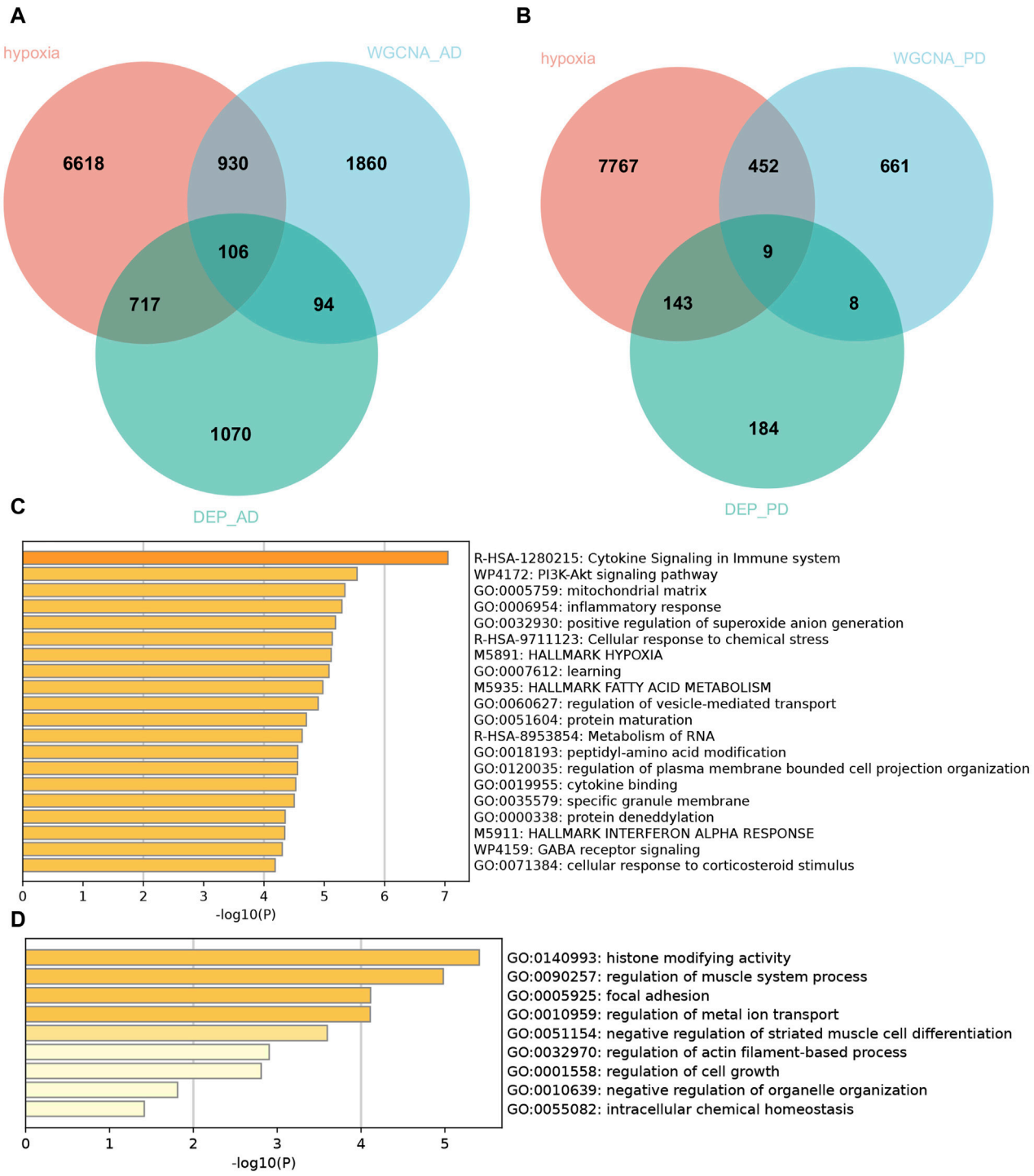


FIGURE 4
Hypoxia-related genes involved in AD and PD shared by transcriptome and proteome. Venn diagram of hypoxia-related genes shared by transcriptome and proteome in AD **(A)** and PD **(B)**. Pathway enrichment analyses of the common hypoxia-related genes in AD **(C)** and PD **(D)**.

samples. In GSE57475, T cells CD4 memory activated and NK cells resting cell types were upregulated, whereas B cells memory and T cells CD4 memory resting cell types downregulated (Figure 6C). In GSE99039, 4 cell types were upregulated, including T cells CD4 naive, Monocytes, Macrophages M0, and Neutrophils; the three downregulated cell types were: B cells memory, Macrophages M1, and Macrophages M2 (Figure 6D).

## Correlation analysis between AIDHS markers and infiltrating cells

$|r| > 0.2$ was set as a correlation threshold for further analysis. In AD, T cells CD4 naïve cell was correlated with BLVRB, C10orf54, CDC37, CHCHD6, GLUL, HOXC4, and PPIL1 in GSE63060; and C10orf54, CHCHD6, GLUL, PFN1, PSMB1, and SYK in GSE63061.


FIGURE 5
Generation of the artificial intelligence-derived hypoxia-related gene signature in AD and PD. The C-indices of 110 machine-learning algorithms in eleven cohorts of AD **(A)** and seven in PD **(B)**.

T cells CD4 memory resting cell was correlated with C10orf54, CDC37, GLUL, HOXC4, PPIL1, PRDX4, PSMB1, PSMG1, SLC16A14, and SYK in GSE63060; and BLVRB, C10orf54, CDC37, GLUL, HOXC4, PFN1, PPIL1, PRDX4, PSMB1, PSMG1, SLC17A7, and SYK in GSE63061. T cells gamma delta cell was correlated with C10orf54, PFN1, PPIL1, PRDX4, PSMB1, PSMG1, and SYK in GSE63060; and C10orf54, CHCHD6, GLUL, PFN1, PPIL1, PRDX4, PSMB1, PSMG1, and SYK in GSE63061. NK cells resting cell was correlated with BLVRB, CDC37, HOXC4, and PSMB1 in GSE63060; and C10orf54, CHCHD6, GLUL, HOXC4, PFN1, PRDX4, PSMB1, PSMG1, and SYK in GSE63061. Macrophages M0 cell was correlated with C10orf54, CHCHD6, GLUL, PPIL1, PSMG1, and SYK in GSE63060; and C10orf54, GLUL, PPIL1, PRDX4, PSMB1, PSMG1, and SYK in GSE63061.Macrophages M2 cell was correlated with C10orf54, PRDX4, PSMG1, and SYK in GSE63060; and GLUL in GSE63061. Mast cells activated cell was correlated with CDC37 and SMYD3 in GSE63060; and BLVRB, PPIL1, and

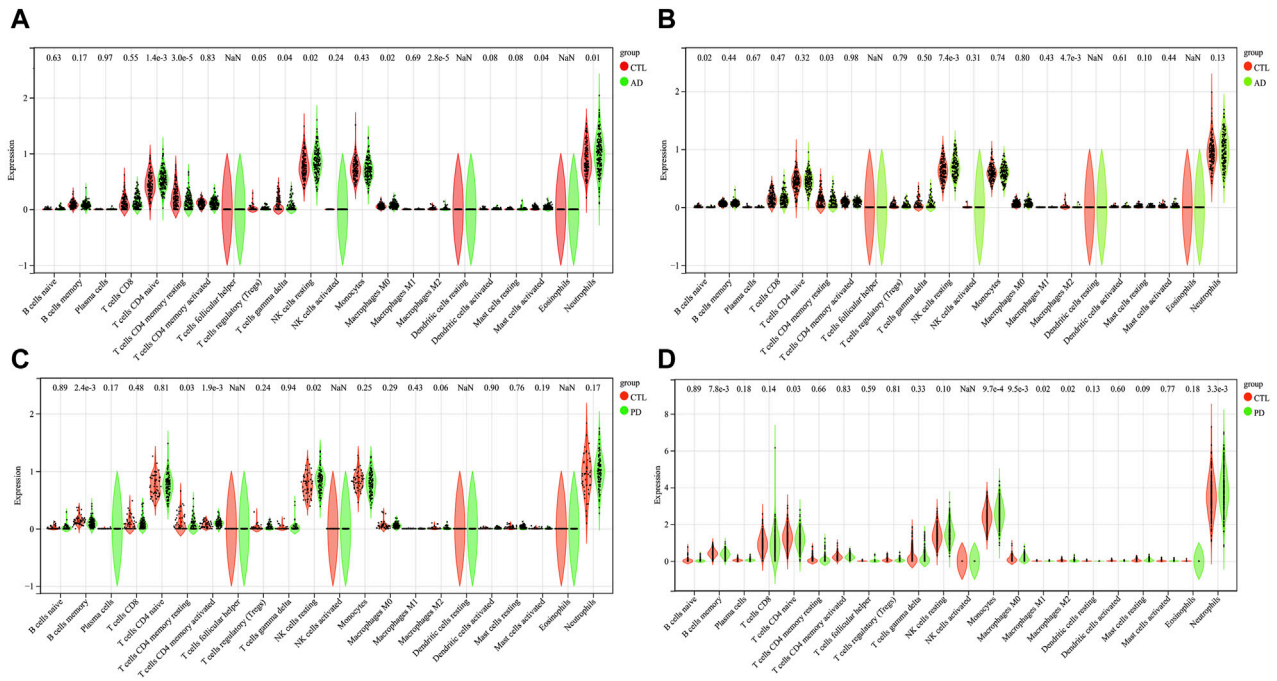


FIGURE 6
The results of immune cell infiltration analysis. A box plot of AD infiltrated immune cells in GSE60630 **(A)** and GSE60631 **(B)**. A box plot of PD infiltrated immune cells in GSE57475 **(C)** and GSE99039 **(D)**. *$p < 0.05$, **$p < 0.01$, ***$p < 0.001$, ****$p < 0.0001$.

SMYD3 in GSE63061. Neutrophils were correlated with C10orf54, CDC37, CHCHD6, GLUL, HOXC4, PPIL1, PRDX4, PSMB1, PSMG1, SMYD3, and SYK in GSE63060, and in GSE63061 (Figures 7A, B).

In PD, B cells memory cell was related to FMO5 and TGM2 in GSE57475. T cells CD4 naïve cell was related to HDAC4 in GSE99039. Monocytes was related to FMO5 in GSE57475. Macrophages M0 cell was related to TGM2 in GSE57475. Neutrophils was related to HDAC4 in GSE99039 (Figures 7C, D).

## TF–miRNA coregulatory network

The NetworkAnalyst online platform was used to generate a TF-miRNA co-regulatory network. The analysis of this network provided insights on the interaction between TFs, miRNAs, and the selected hub genes, which could explain the underlying mechanism of how hub gene expression is regulated. Figure 8A shows the TF–miRNA co-regulatory network. The AD TF–miRNA co-regulatory network is consisted of 269 nodes and 343 edges. A total of 149 miRNAs and 61 TF genes interacted with the validated AIDHS genes, including MYC, MAX, TFAP2A, USF1, NFIC, hsa-miR-632, hsa-miR-1, hsa-miR-124, hsa-miR-127-5p and hsa-miR-140-5p. Functional enrichment analysis showed these nodes were related to Osteoclast differentiation, Th17 cell differentiation, TNF signaling pathway, IL-17 signaling pathway, and Longevity regulating pathway (Figure 8B). HOXC4 owned the largest number of neighbors, followed by FN1, PFN1, CDC37, SLC17A7, SLC16A14, CHCHD6, SMYD3, PPIL1, BLVRB, and PRDX4.

Figure 8C shows the TF–miRNA co-regulatory network. The PD TF–miRNA co-regulatory network is consisted of 108 nodes and 109 edges. A total of 46 miRNAs and 28 TF genes interacted with the validated AIDHS genes, including USF1, TFAP2A, TFAP2C, SP1, POU2F1, hsa-miR-19a, hsa-miR-19b, hsa-miR-1, hsa-miR-106b and hsa-miR-124. Functional enrichment analysis showed these nodes were related to Apelin signaling pathway, cGMP-PKG signaling pathway, Cellular senescence, Cell cycle and Osteoclast differentiation (Figure 8D). HDAC4 owned the largest number of neighbors.

## Construct the signaling information network based on SIGNOR

We further built the signaling information network of AIDHS through SIGNOR2.0. The AD signaling network included six interaction mechanisms, such as ubiquitination, transcriptional regulation, polyubiquitination, phosphorylation, dephosphorylation and binding. SYK showed the highest number of interaction, followed by FN1, PFN1, CDC37, and PSMB1. Moreover, FN1 interacted with more complex than other hub genes, including SNAIL/RELA/PARP1, FN1/SDC4, Av/b6 integrin, A8/b1 integrin, A5/b1 integrin complex. In addition, the analysis also identified the effect of actin cytoskeleton reorganization as potential phenotype (Figure 9A).

The PD signaling network included five interaction mechanisms, such as transcriptional regulation, phosphorylation, dephosphorylation, deacetylation and binding. HDAC4 showed the highest number of interaction and was inhibited by AMPK complex.

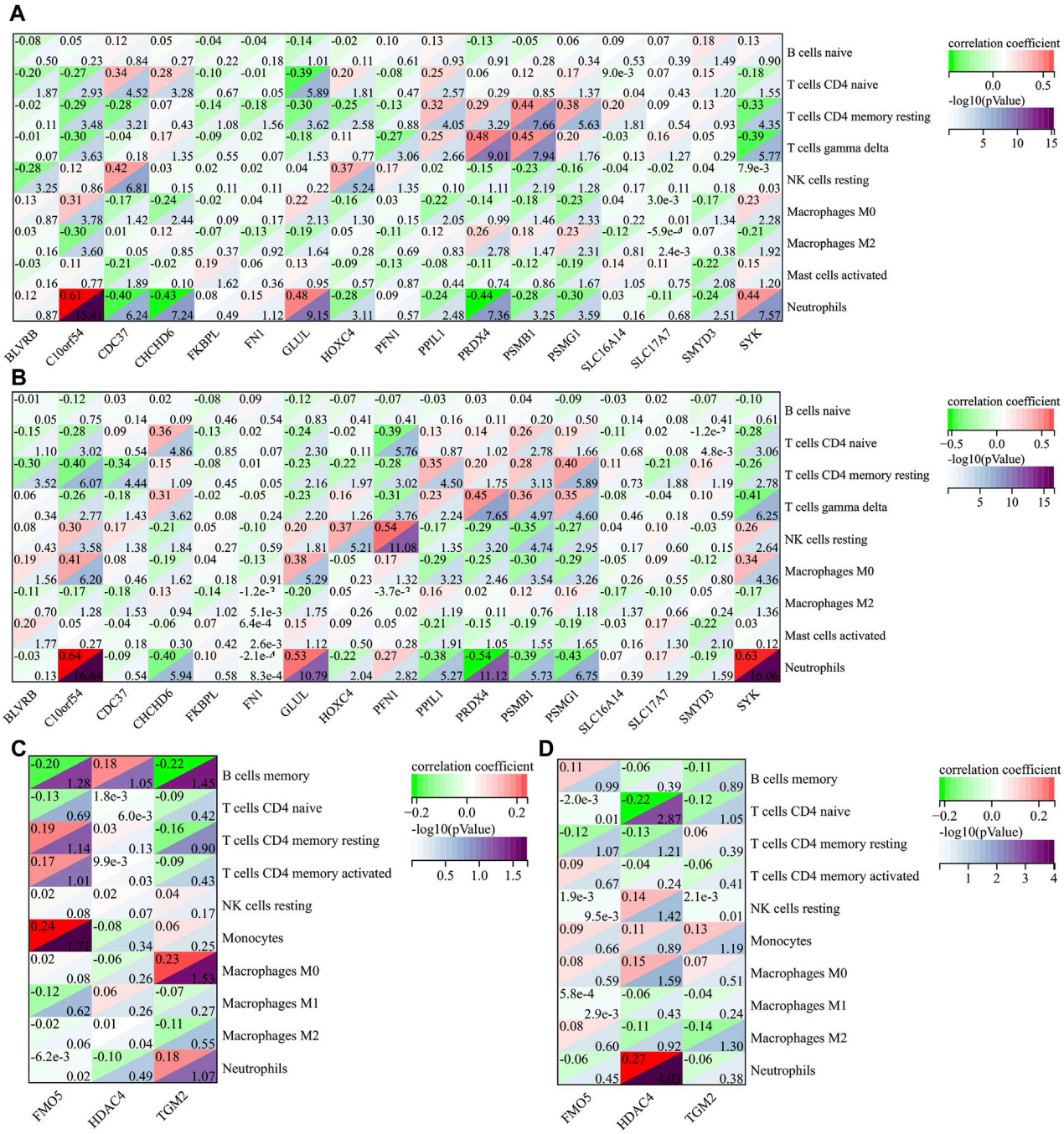


FIGURE 7
The correlation between AIDHS genes and infiltrated immune cells in AD ((**A**): GSE60630, **(B)** GSE60630) and PD ((**C**): GSE57475, **(D)** GSE99039). Nodes that appear redder indicate a stronger positive correlation, while nodes that appear bluer indicate a stronger negative correlation.

TGM2 can directly phosphorylate H3C1 and Histone H3 (Figure 9B).

## Analysis the heterogeneity of striata in the AD and PD single-cell transcriptome

The quality control summary of our single-cell RNA sequencing (scRNA-seq) data is presented in Figure 10A. After preprocessing the data, we used the harmony algorithm to merge the samples and effectively eliminate any potential batch effects. Figure 10B displays the representation of the merged dataset, which includes AD, PD and control samples after the implementation of the harmony algorithm. By following the standard procedures of Seurat, a total of 12 clusters were successfully identified and visualized using UMAP, as shown in Figure 10C. Subsequently, we observed eight distinct cell clusters (Figure 10D), including astrocytes (AQP4, GFAP), CD8 T cells (CCL5, NKG7, GZMK, GZMA, GZMM,

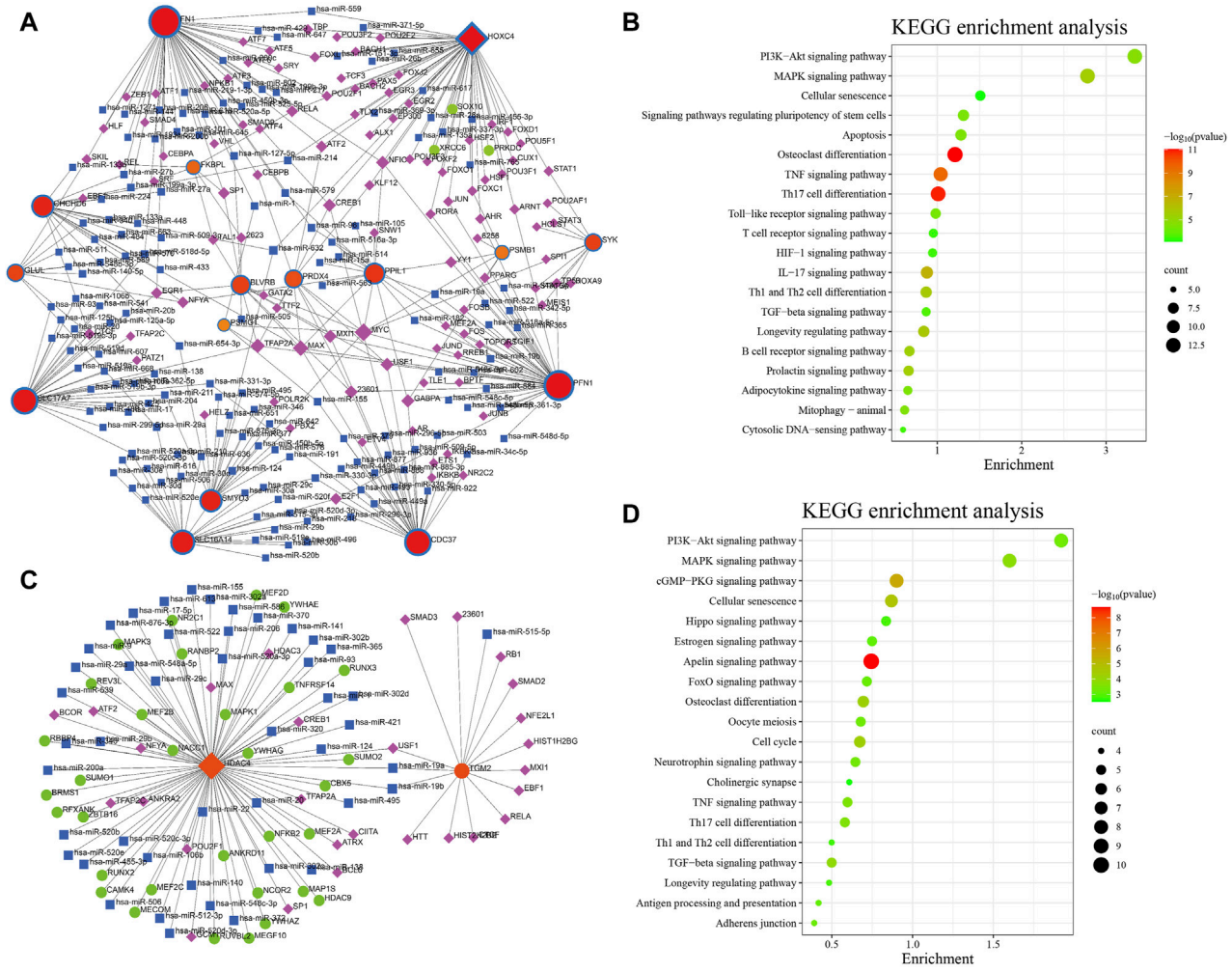


FIGURE 8
TF−miRNA coregulatory network and pathway enrichment analyses in AD **(A,B)** and PD **(C,D)**. The round nodes are AIDHS genes, the diamond nodes are TF genes, and the square nodes are miRNA genes.

CCL4, CD69, LGALS1, LGALS3, PDCD1, PRDM1, and CXCR6), endothelial cells (FLT1, CLDN5), mesenchymal cells (CD44, CHI3L1, and HIF1A), microglia cells (CSF1R, CD74, C3), neural cells (GAD1, GAD2, SOX2, and SLC17A7), oligodendrocytes (MBP, PLP1), and Opcs (PDGFRA, VCAN, CSPG4). Figure 11A showed the distribution of 8 cell types in 12 samples. And the top 5 marker genes were identified within the cell-type populations (Figure 11B). Figure 11C showed that most of the 26 AIDHS genes were differentially expressed among the three groups. These genes were specifically expressed in different cells, such as TGM2 being highly expressed in endothelial cells, PDGFRB being highly expressed in endothelial and mesenchymal cells, and SYK being highly expressed in microglia cells (Figure 11D).

## YXKFY restored the damaged SH-SY5Y cells caused by CoCl2 and reduce the ROS level

The viability of SH-SY5Y cells was assessed using the CCK8 assay after exposure to different concentrations of CoCl2 for 24 h. As depicted in Figure 12A, the viability of cells gradually declined as the concentration of CoCl2 increased from 400 to 1000 μM. Notably, when the CoCl2 concentration reached 800 μM, SH-SY5Y cell viability dropped to 57%. Subsequently, the concentration of 800 μM was selected for subsequent experiments as it induced significant damaging effects. In order to examine the potential of YXKFY in preventing CoCl2-induced cell death, the CCK8 assay was performed on SH-SY5Y cells treated with YXKFY-containing serum in the presence of CoCl2. As depicted in Figure 12B, the addition of YXKFY-containing serum led to a notable improvement in cell viability, with an increase to 67%. Moreover, YXKFY-containing serum can reduce the ROS level in the hypoxia model (Figure 12C).

## Validation of hub genes

In order to validate the findings of the bioinformatics analysis, we identified the 17 AIDHS genes of AD and 9 AIDHS genes of PD. The mRNA expression levels of these

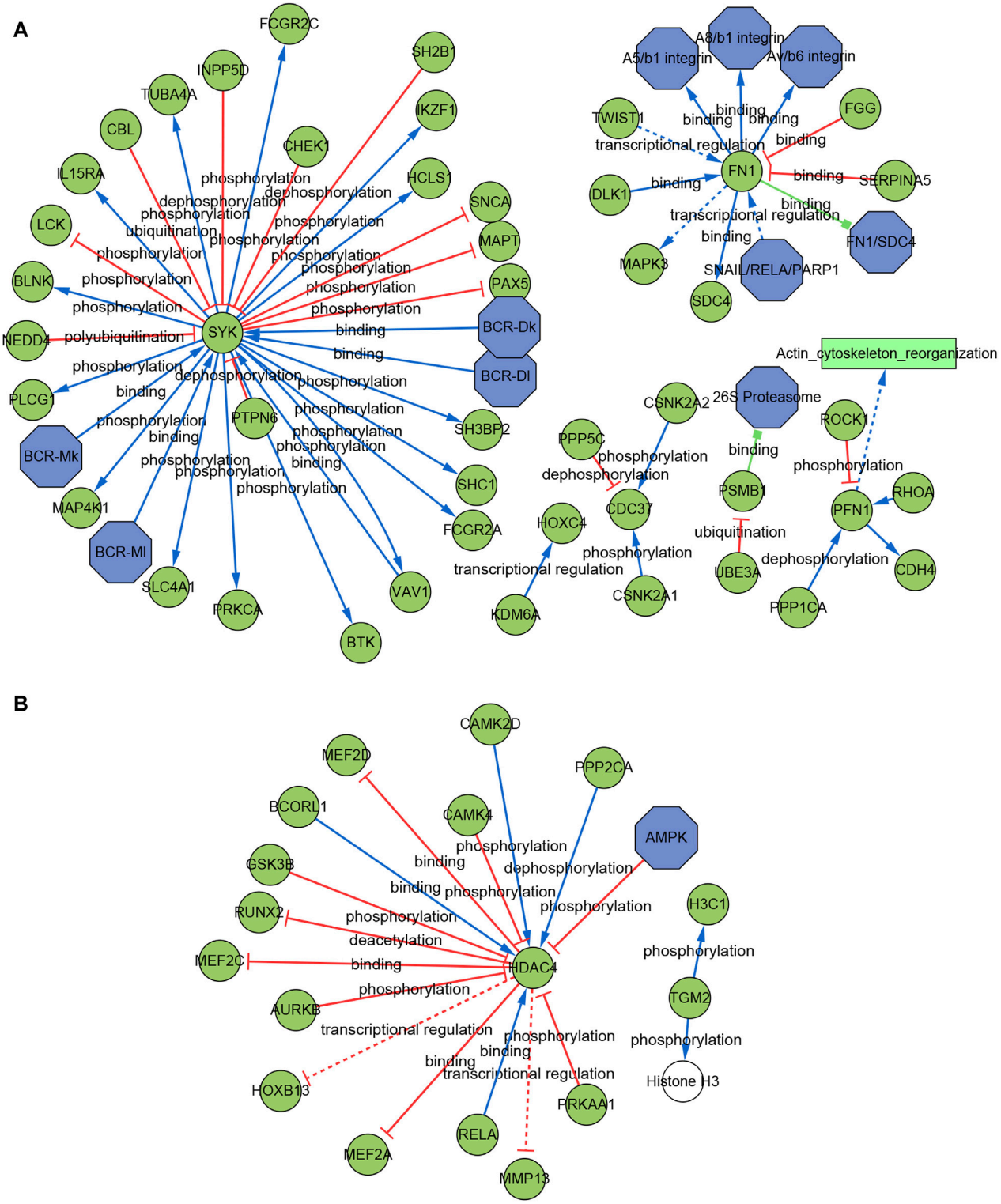


FIGURE 9
Signaling information network of the AIDHS genes through SIGNOR in AD **(A)** and PD **(B)**.

genes were assessed using RT-qPCR. The hypoxia group exhibited decreased expression of BLVRB, C10orf54, CDC37, FKBPL, FN1, GLUL, HOXC4, PPIL1, PRDX4, PSMB1, SLC17A7, SMYD3, SYK, FMO5, HDAC4, TGM2, PDGFRB, MYBPH, and JUP and increased expression of FXYD5 and DNM2 compared to the control group. Additionally, the expression of FKBPL, TGM2, PPIL1, BLVRB, and PDGFRB showed substantial recovery after YXKFY treatment (Figure 13).

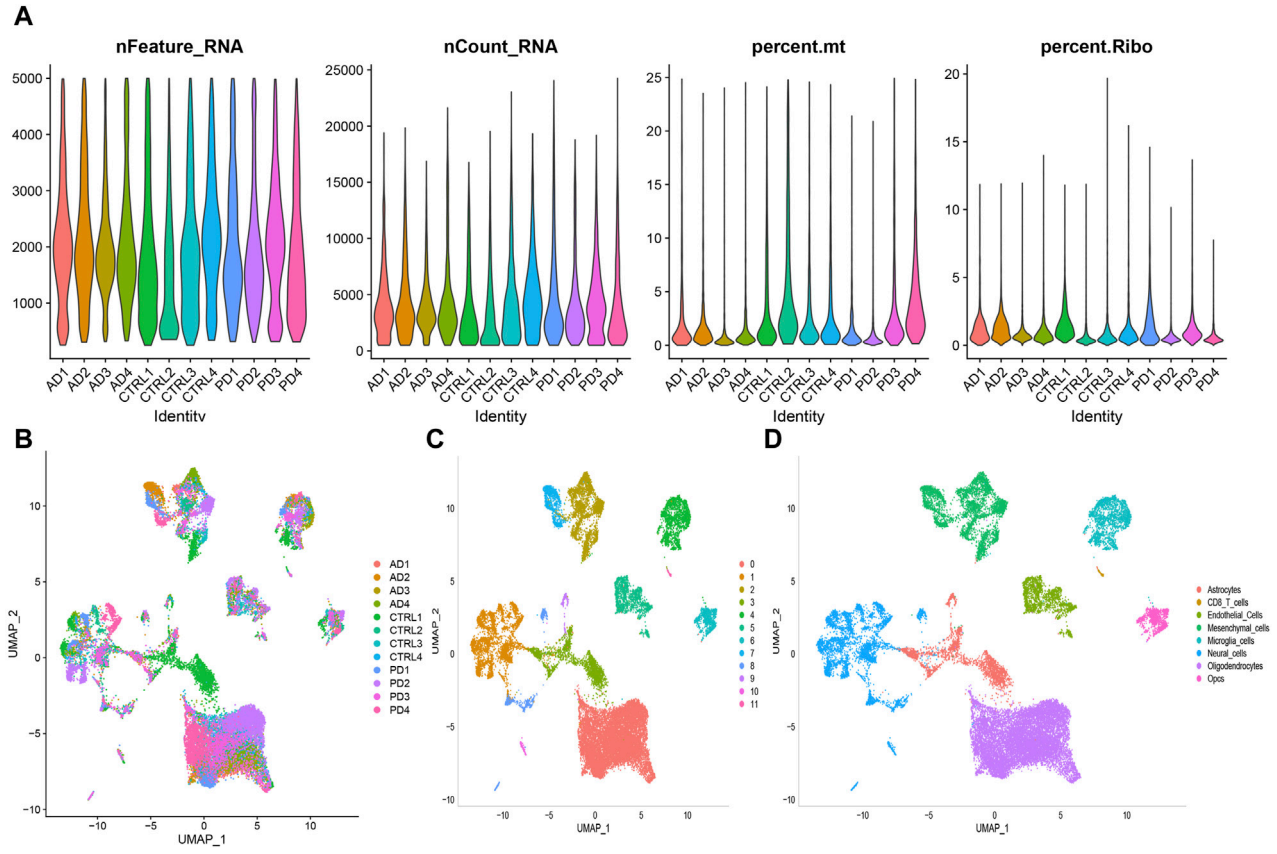


FIGURE 10
Preprocessing of scRNA-seq data was conducted to prepare for downstream analysis. **(A)** Following quality control steps, the counts, percentages, and features related to mitochondrial and ribosome genes were assessed for each sample under analysis. **(B)** Visualization of sample distribution was achieved using UMAP plots after integration of the datasets using the harmony algorithm. **(C)** A clustering algorithm with a resolution of 0.1 was applied, resulting in the identification of 12 clusters. **(D)** UMAP plot was used to show the distribution of the eight different cell types.

## Identification of the components in YXKFY and YXKFY-containing serum

Based on the information provided by high-resolution mass spectrometry, such as accurate molecular masses for quasi-molecular ions and loading ions, the precise relative molecular mass of the primary mass spectra is inferred. The preliminary estimation of the various components obtained under high-resolution mass spectrometry is then conducted using the Peakview 1.2 software for molecular formula fitting. The HPLC analysis identified a total of 107 chemical components in the YXKFY, and a further 9 prototype components were identified in the YXKFY-containing serum (Table 2).

## Molecular docking validation

The present research investigated binding affinity between the above five genes and the 8 prototype ingredients in the YXKFY-containing serum. The molecular docking results revealed different levels of binding between natural products and hub genes, with the majority of natural products showing good binding capabilities to the hub genes. Particularly, riboflavin and lysicamine exhibited higher binding affinity than other compounds (Table 3).

# Discussion

To this day, researchers continue to face the challenging task of finding an effective drug for treating AD and PD using modern medicine. However, there is a growing body of evidence suggesting that traditional Chinese medicine may offer promise in the prevention and treatment of AD and PD (Pei et al., 2020; Chen et al., 2022). Hypoxia, characterized by oxygen deprivation, is implicated in neuronal stress, initiating a cascade that culminates in neuronal dysfunction and demise, thereby exacerbating the pathogenesis and progression of AD and PD (March-Diaz et al., 2021; Guo et al., 2022). Our study, therefore, presents an integrative strategy, merging bidirectional transcriptome and proteome analyses, to delineate the hypoxia-related molecular signatures and pathways that underpin the neuroprotective efficacy of YXKFY in both AD and PD.

In our study, we first profiled hypoxia-related mRNA and protein expression in AD and PD. Our analysis revealed that the dysregulated mRNAs and proteins in both conditions predominantly converge on mitochondrial and inflammatory pathways in AD, and pathways

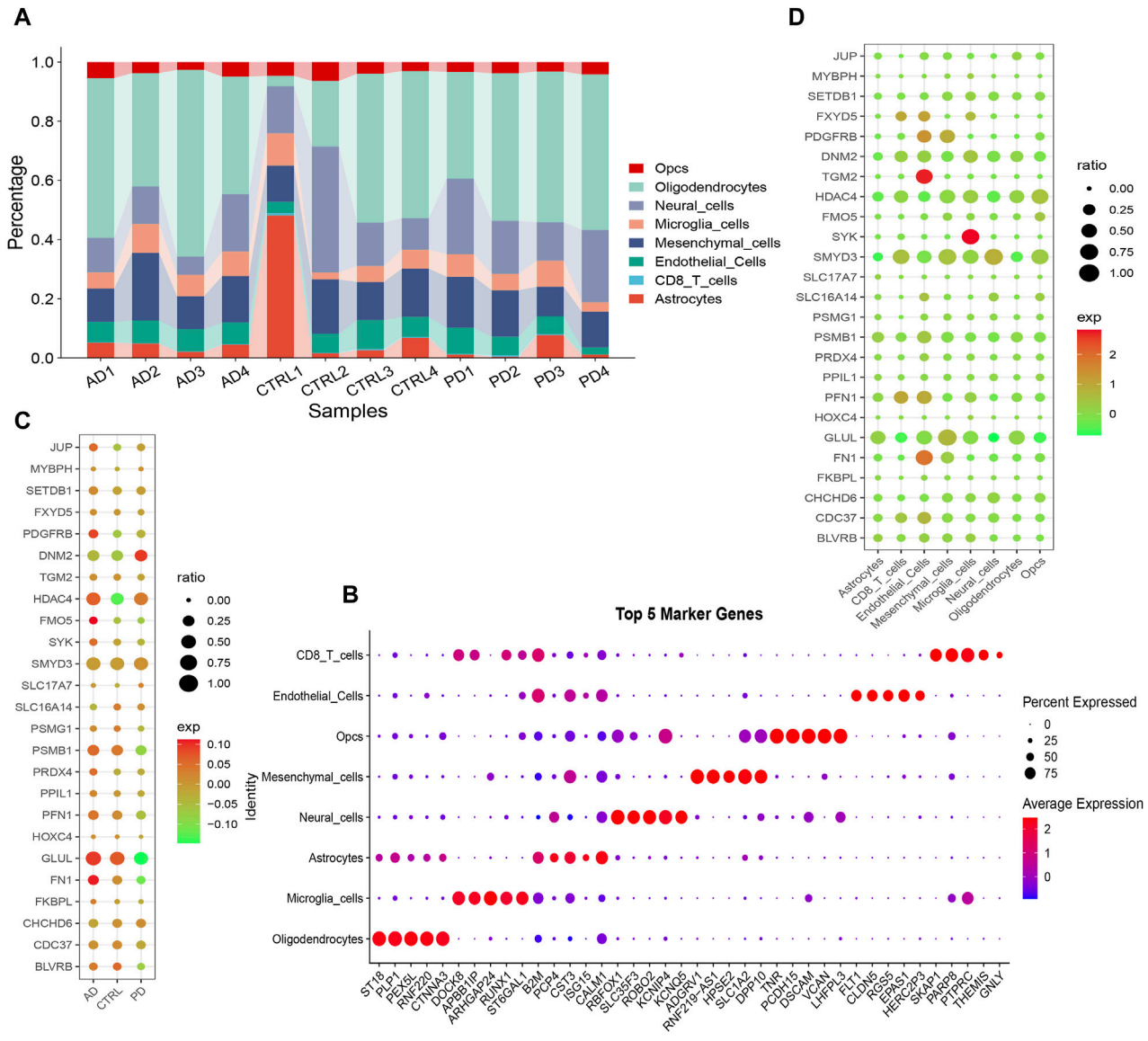


FIGURE 11
ScRNA-seq data was employed to annotate and scrutinize the distribution of cell proportions among the three groups. **(A)** The overall cell fraction comparison among the three groups. **(B)** A heatmap was produced to display the levels of expression of marker genes in the identified cells. Bubble plots depicting the expression of 26 AIDHS genes in different disease **(C)** and cell groups **(D)**.

related to the muscle system in PD. It is a recognized phenomenon that hypoxia triggers the activation of multiple signaling cascades, notably cytokine signaling within the immune system (Sturrock et al., 2018) and the PI3K-Akt pathway (Pan et al., 2021), which are integral to inflammatory responses and the modulation of mitochondrial function (Wang et al., 2021). The mitochondrial matrix is acutely vulnerable to hypoxia, which can augment the production of superoxide anions, thereby exacerbating oxidative stress and neuroinflammation. (Spooner et al., 2021). Furthermore, hypoxia has been implicated in the upregulation of pro-inflammatory cytokines and chemokines, perpetuating the chronic inflammatory milieu characteristic of AD and PD (Merelli et al., 2021). Additionally, hypoxia impacts muscle function, with disruptions in muscle system processes linked to the motor symptoms of PD (Miterko et al., 2021). Consequently, elucidating the molecular underpinnings of hypoxia's impact on these pathways is essential for devising innovative therapeutic strategies for both AD and PD.

In this study, we conducted a comprehensive analysis using nine independent cohorts to identify stable AIDHS for the development of AD and PD. Recognizing the potential influence of researcher preferences and biases in algorithm selection, we employed a rigorous approach by integrating ten distinct machine learning algorithms to discern the optimal signature from a comprehensive set of 113 algorithmic combinations. This strategy culminated in the identification of AIDHS in AD (17 genes) and PD (3 genes). Our *in vitro* validation corroborated the machine learning predictions, with the majority of genes showing significant differential expression following hypoxia treatment. Notably, YXKFY was found to ameliorate the dysfunction of five key genes (FKBPL, TGM2, PPIL1, BLVRB, and PDGFRB). While

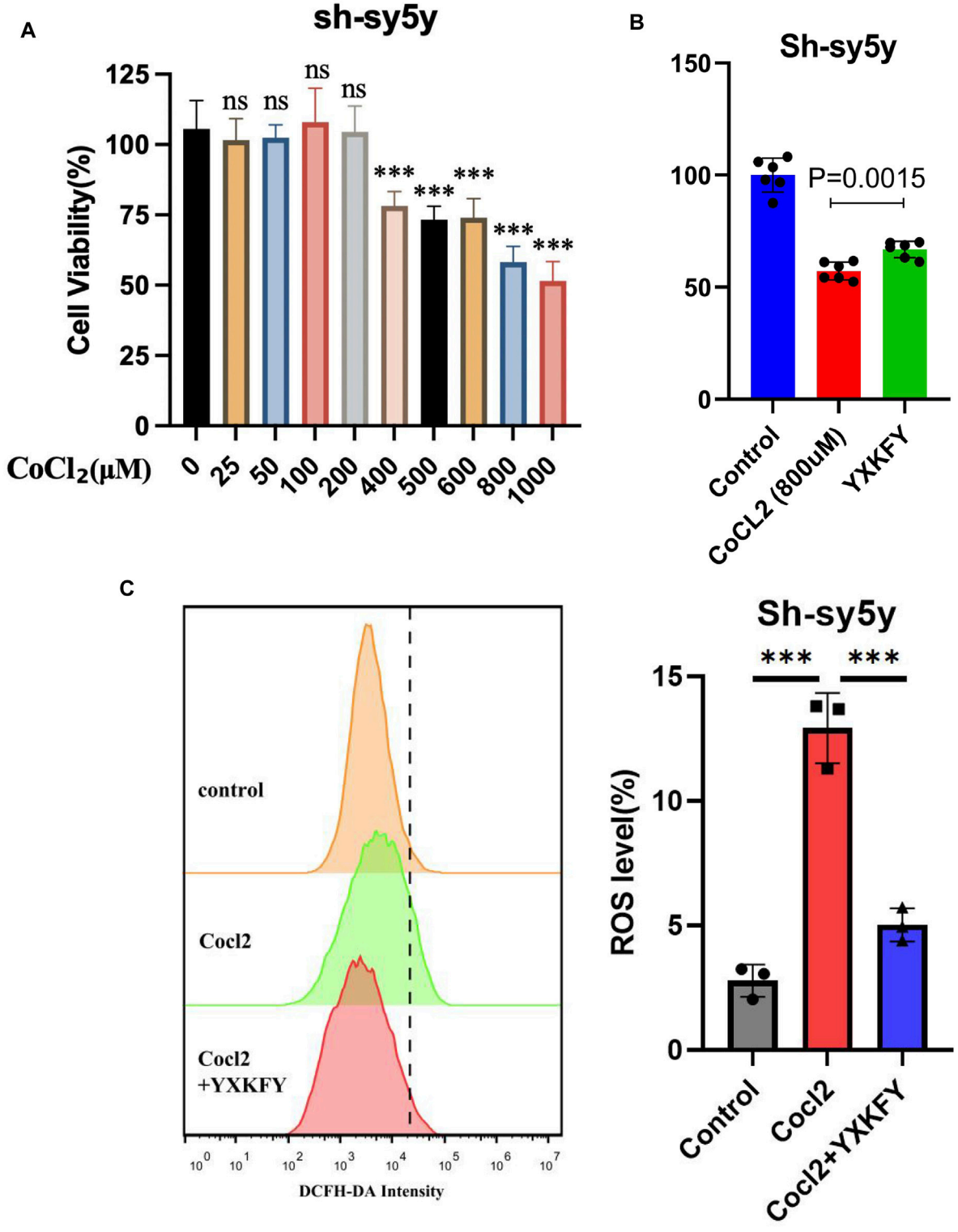


FIGURE 12
YXKFY restored the damaged SH-SY5Y cells caused by CoCl2 and reduce the ROS level. **(A)** The viability of SH-SY5Y cells was assessed using the CCK8 assay after exposure to different concentrations of CoCl2. **(B)** YXKFY-containing serum restored the damaged SH-SY5Y cells caused by CoCl2. **(C)** YXKFY-containing serum reduced the ROS level in the hypoxia model. ***: $p < 0.001$.

some of the biomarkers associated with these genes have been previously implicated in AD and PD, others represent novel findings in the context of neurodegenerative diseases. PPIL1 plays a crucial role as an enzyme-substrate pair within the spliceosome, exerting its function in the facilitation of RNA splicing and ensuring the survival of neurons, and its mutations may cause

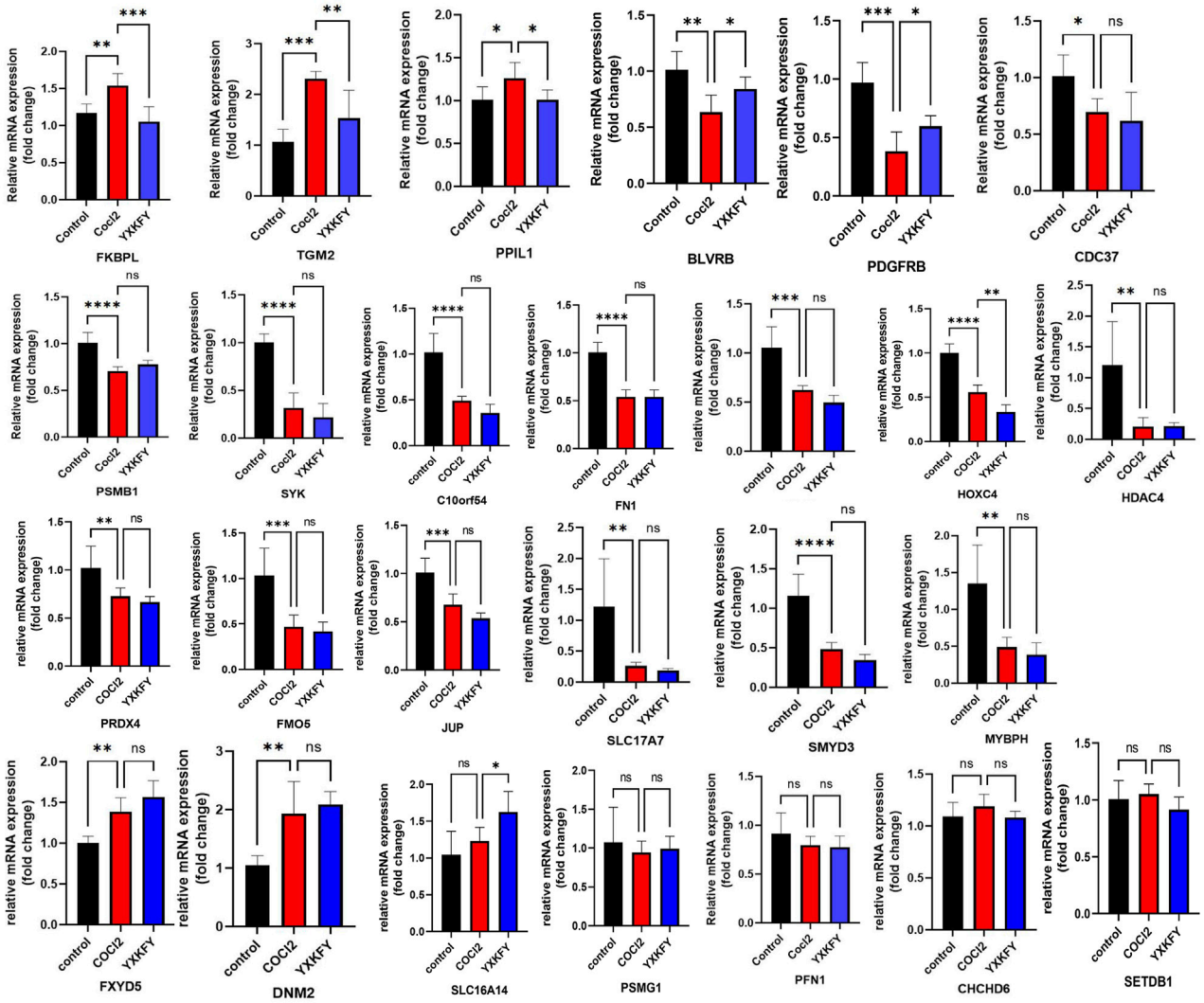


FIGURE 13
Validation of the mRNA expression levels of AIDHS genes. *: $p < 0.05$, **: $p < 0.01$, ***: $p < 0.001$.

TABLE 3 The protein-ligand binding energy of molecular docking results (kcal/mol).

| Ligand | BLVRB (5oog) | FKBPL (AlphaFold) | PDGFRB (AlphaFold) | PPIL1 (2 × 7k) | TGM2 (3s3j) |
|---|---|---|---|---|---|
| Cinnamic acid | −5.7 | −5.4 | −5.2 | −5.8 | −5.8 |
| Isoamyl Senecioate | −5.1 | −4.7 | −4.1 | −4.9 | −5.3 |
| Lysicamine | −7.5 | −7.2 | −6.4 | −7.4 | −7.1 |
| p-Hydroxybenzoic acid | −5.3 | −5 | −4.7 | −5.7 | −5.5 |
| Quinic acid | −5.4 | −5.2 | −4.6 | −6.1 | −5.6 |
| Riboflavin | −7.6 | −6.6 | −6.3 | −8.2 | −7.5 |
| Tumerone | −6.6 | −5.9 | −5.5 | −5.5 | −6.7 |

neurodegenerative disease (Chai et al., 2021). The silencing of TGM2, implicated in the pathogenesis of AD and PD, inhibited mitochondrial calcium influx, accumulation of mtROS, phosphorylation of Tau, and ultimately protected neuronal cells from Aβ-induced cell death (Lee et al., 2021). The depletion of PDGFRB within the precuneus region in individuals with AD has been linked to fibrinogen leakage, a decline in oxygenation, and the accumulation of fibrillar Aβ (Miners et al., 2018). Therefore, PPIL1,

TGM2 and PDGFRB may serve as therapeutic targets of YXKFY in AD and PD. However, FKBPL and BLVRB have never been investigated in AD and PD, suggesting a new therapeutic strategy through hypoxia-related mechanism in AD and PD.

In our study, HPLC were also utilized to pinpoint specific ingredients in YXKFY, which led to the identification of 107 chemical components. The 8 prototype ingredients in the YXKFY-containing serum were found to be quinic acid, lysicamine, riboflavin, cinnamic acid, p-hydroxybenzoic acid, quercetin-7-O-α-L-rhamnoside, tumerone and isoamyl senecioate. Several of these components, including quinic acid, riboflavin, and cinnamic acid, have demonstrated significant anti-inflammatory effects and upregulating antioxidant enzyme activities in neurodegenerative disease. For instance, in in vitro studies, quinic acid has demonstrated neuroprotective and neurotrophic effects on Aβ-induced toxicity, as well as enhancing the activity of neurite outgrowth in PC 12 cells (Hur et al., 2001). It is suggested that quinic acid exerts its neuroprotective effects through the PKA signaling pathway and has successfully restored catalase levels (Rebai et al., 2017). Patients with dementia and AD have shown low levels of riboflavin, and supplementing with riboflavin has been found beneficial in treating cognitive impairment, as it shields cells from oxidative stress by boosting antioxidant enzyme activities and the glutathione redox cycle, and diminishing pro-inflammatory responses in the brain (Zhang et al., 2023). Cinnamic acid, a naturally occurring antioxidant, triggers PPARα activation, promoting lysosomal biogenesis and reducing amyloid plaque pathology in an AD mouse model (Chandra et al., 2019), and protecting dopaminergic neurons in a PD mouse model (Prorok et al., 2019). Therefore, the combination of our discovered results that YXKFY can reduce the ROS levels in hypoxic SH-SY5Y cell injury, suggesting that these components may be effective in YXKFY's prevention and treatment of AD and PD through antioxidant damage. Moreover, Riboflavin has the best binding affinity with PPIL1, followed by BLVRB, TGM2, FKBPL, and PDGFRB. Additionally, lysicamine and tumerone also exhibit good binding affinity with these proteins. Collectively, the potential therapeutic effects of these chemical monomers from YXKFY on AD and PD through these genes warrant further exploration in our future studies.

## Conclusion

In conclusion, our study leveraged a synergistic approach combining transcriptome and proteome analyses with machine learning to innovatively identify 17 and 3 hypoxia-associated biomarkers for AD and PD, respectively. Furthermore, we elucidated the neuroprotective mechanisms of YXKFY, highlighting its antioxidant properties. This was achieved through the identification of eight bioactive compounds, engagement with five molecular targets, and modulation of several pathways pivotal in neuroprotection.

## Data availability statement

The original contributions presented in the study are included in the article/Supplementary Material, further inquiries can be directed to the corresponding authors.

## Ethics statement

All animal procedures, such as housing and care and experimental protocols were approved by the Ethics Committee of Shanghai University of Traditional Chinese Medicine (No. PZSHUTCM210702015).

## Author contributions

X-YC: Writing–original draft. M-RC: Writing–review and editing. C-CT: Writing–review and editing. C-QX: Writing–review and editing. Y-LZ: Writing–review and editing. YG: Writing–review and editing. X-XC: Writing–review and editing. JC: Writing–review and editing, Writing–original draft.

## Funding

The author(s) declare that financial support was received for the research, authorship, and/or publication of this article. This work was supported by the National Natural Science Foundation of China (82104873, 82274408), the Shanghai Sailing Program (20YF1445900), Xinglin Young Talent training Program of Shanghai University of Traditional Chinese Medicine (RCPY0040), Preparatory discipline leader training program of Shanghai TCM-Integrated hospital (RCPY0071), school-based cooperation project (hxkt2023016).

## Conflict of interest

The authors declare that the research was conducted in the absence of any commercial or financial relationships that could be construed as a potential conflict of interest.

## Publisher's note

# References


Aborode, A. T., Pustake, M., Awuah, W. A., Alwerdani, M., Shah, P., Yarlagadda, R., et al. (2022). Targeting oxidative stress mechanisms to treat Alzheimer's and Parkinson's disease: a critical review. *Oxid. Med. Cell Longev.* 2022, 7934442. doi:10.1155/2022/7934442

Al-Reza, S. M., Yoon, J. I., Kim, H. J., Kim, J. S., and Kang, S. C. (2010). Anti-inflammatory activity of seed essential oil from Zizyphus jujuba. *Food Chem. Toxicol.* 48 (2), 639–643. doi:10.1016/j.fct.2009.11.045

Baillieul, S., Chacaroun, S., Doutreleau, S., Detante, O., Pépin, J. L., and Verges, S. (2017). Hypoxic conditioning and the central nervous system: a new therapeutic opportunity for brain and spinal cord injuries? *Exp. Biol. Med. (Maywood)* 242 (11), 1198–1206. doi:10.1177/1535370217712691

Breijyeh, Z., and Karaman, R. (2020). Comprehensive review on Alzheimer's disease: causes and treatment. *Molecules* 25 (24), 5789. doi:10.3390/molecules25245789

Burtscher, J., Mallet, R. T., Burtscher, M., and Millet, G. P. (2021). Hypoxia and brain aging: neurodegeneration or neuroprotection? *Ageing Res. Rev.* 68, 101343. doi:10.1016/j.arr.2021.101343

Chai, G., Webb, A., Lee, C., Antaki, D., Lee, S., Breuss, M. W., et al. (2021). Mutations in spliceosomal genes PPIL1 and PRP17 cause neurodegenerative pontocerebellar hypoplasia with microcephaly. *Neuron* 109 (2), 241–256 e9. doi:10.1016/j.neuron.2020.10.035

Chandra, S., Roy, A., Jana, M., and Pahan, K. (2019). Cinnamic acid activates PPARα to stimulate Lysosomal biogenesis and lower Amyloid plaque pathology in an Alzheimer's disease mouse model. *Neurobiol. Dis.* 124, 379–395. doi:10.1016/j.nbd.2018.12.007

Chen, P., Zhang, J., Wang, C., Chai, Y. H., Wu, A. G., Huang, N. Y., et al. (2022). The pathogenesis and treatment mechanism of Parkinson's disease from the perspective of traditional Chinese medicine. *Phytomedicine* 100, 154044. doi:10.1016/j.phymed.2022.154044

Dinkar Gore, D., Ahmad, F., Tikoo, K., Kumar Bansal, A., Kumar, D., and Pal Singh, I. (2023). Comparative quantitative analysis of fruit oil from Hippophae rhamnoides (seabuckthorn) by qNMR, FTIR and GC-MS. *Chin. Herb. Med.* 15 (4), 607–613. doi:10.1016/j.chmed.2023.05.005

Grabska-Kobyłecka, I., Szpakowski, P., Król, A., Książek-Winiarek, D., Kobyłecki, A., Głąbiński, A., et al. (2023). Polyphenols and their impact on the prevention of neurodegenerative diseases and development. *Nutrients* 15 (15), 3454. doi:10.3390/nu15153454

Guo, M., Ji, X., and Liu, J. (2022). Hypoxia and alpha-synuclein: inextricable link underlying the pathologic progression of Parkinson's disease. *Front. Aging Neurosci.* 14, 919343. doi:10.3389/fnagi.2022.919343

Hayes, M. T. (2019). Parkinson's disease and parkinsonism. *Am. J. Med.* 132 (7), 802–807. doi:10.1016/j.amjmed.2019.03.001

Hur, J. Y., Soh, Y., Kim, B. H., Suk, K., Sohn, N. W., Kim, H. C., et al. (2001). Neuroprotective and neurotrophic effects of quinic acids from Aster scaber in PC12 cells. *Biol. Pharm. Bull.* 24 (8), 921–924. doi:10.1248/bpb.24.921

Kaeidi, A., Taati, M., Hajializadeh, Z., Jahandari, F., and Rashidipour, M. (2015). Aqueous extract of Zizyphus jujuba fruit attenuates glucose induced neurotoxicity in an *in vitro* model of diabetic neuropathy. *Iran. J. Basic Med. Sci.* 18 (3), 301–306.

Kim, M. J., Jung, J. E., Lee, S., Cho, E. J., and Kim, H. Y. (2021). Effects of the fermented Zizyphus jujuba in the amyloid β(25-35)-induced Alzheimer's disease mouse model. *Nutr. Res. Pract.* 15 (2), 173–186. doi:10.4162/nrp.2021.15.2.173

Korsunsky, I., Millard, N., Fan, J., Slowikowski, K., Zhang, F., Wei, K., et al. (2019). Fast, sensitive and accurate integration of single-cell data with Harmony. *Nat. Methods* 16 (12), 1289–1296. doi:10.1038/s41592-019-0619-0

Langfelder, P., and Horvath, S. (2008). WGCNA: an R package for weighted correlation network analysis. *BMC Bioinforma.* 9, 559. doi:10.1186/1471-2105-9-559

Lee, H. J., Jung, Y. H., Choi, G. E., Kim, J. S., Chae, C. W., Lim, J. R., et al. (2021). Urolithin A suppresses high glucose-induced neuronal amyloidogenesis by modulating TGM2-dependent ER-mitochondria contacts and calcium homeostasis. *Cell Death Differ.* 28 (1), 184–202. doi:10.1038/s41418-020-0593-1

Lee, J., Cho, E., Kwon, H., Jeon, J., Jung, C. J., Moon, M., et al. (2019). The fruit of Crataegus pinnatifida ameliorates memory deficits in β-amyloid protein-induced Alzheimer's disease mouse model. *J. Ethnopharmacol.* 243, 112107. doi:10.1016/j.jep.2019.112107

Li, L., Dong, L., Xiao, Z., He, W., Zhao, J., Pan, H., et al. (2020). Integrated analysis of the proteome and transcriptome in a MCAO mouse model revealed the molecular landscape during stroke progression. *J. Adv. Res.* 24, 13–27. doi:10.1016/j.jare.2020.01.005

Licata, L., Lo Surdo, P., Iannuccelli, M., Palma, A., Micarelli, E., Perfetto, L., et al. (2020). SIGNOR 2.0, the SIGnaling network open resource 2.0: 2019 update. *Nucleic Acids Res.* 48 (D1), D504–D510. doi:10.1093/nar/gkz949

Liu, Z. P., Wu, C., Miao, H., and Wu, H. (2015). RegNetwork: an integrated database of transcriptional and post-transcriptional regulatory networks in human and mouse. *Database (Oxford)* 2015, bav095. doi:10.1093/database/bav095

Macdonald, R., Barnes, K., Hastings, C., and Mortiboys, H. (2018). Mitochondrial abnormalities in Parkinson's disease and Alzheimer's disease: can mitochondria be targeted therapeutically? *Biochem. Soc. Trans.* 46 (4), 891–909. doi:10.1042/BST20170501

March-Diaz, R., Lara-Ureña, N., Romero-Molina, C., Heras-Garvin, A., Ortega-de San Luis, C., Alvarez-Vergara, M. I., et al. (2021). Hypoxia compromises the mitochondrial metabolism of Alzheimer's disease microglia via HIF1. *Nat. Aging* 1 (4), 385–399. doi:10.1038/s43587-021-00054-2

Meng, F. L., Huang, X. L., Qin, W. Y., Liu, K. B., Wang, Y., Li, M., et al. (2023). singleCellBase: a high-quality manually curated database of cell markers for single cell annotation across multiple species. *Biomark. Res.* 11 (1), 83. doi:10.1186/s40364-023-00523-3

Merelli, A., Repetto, M., Lazarowski, A., and Auzmendi, J. (2021). Hypoxia, oxidative stress, and inflammation: three faces of neurodegenerative diseases. *J. Alzheimers Dis.* 82 (1), S109–S126. doi:10.3233/JAD-201074

Miners, J. S., Schulz, I., and Love, S. (2018). Differing associations between Aβ accumulation, hypoperfusion, blood-brain barrier dysfunction and loss of PDGFRB pericyte marker in the precuneus and parietal white matter in Alzheimer's disease. *J. Cereb. Blood Flow. Metab.* 38 (1), 103–115. doi:10.1177/0271678X17690761

Miterko, L. N., Lin, T., Zhou, J., van der Heijden, M. E., Beckinghausen, J., White, J. J., et al. (2021). Neuromodulation of the cerebellum rescues movement in a mouse model of ataxia. *Nat. Commun.* 12 (1), 1295. doi:10.1038/s41467-021-21417-8

Moreira, J., Machado, M., Dias-Teixeira, M., Ferraz, R., Delerue-Matos, C., and Grosso, C. (2023). The neuroprotective effect of traditional Chinese medicinal plants-A critical review. *Acta Pharm. Sin. B* 13 (8), 3208–3237. doi:10.1016/j.apsb.2023.06.009

Mu, H. Q., Liang, Z. Q., Xie, Q. P., Han, W., Yang, S., Wang, S. B., et al. (2020). Identification of potential crucial genes associated with the pathogenesis and prognosis of prostate cancer. *Biomark. Med.* 14 (5), 353–369. doi:10.2217/bmm-2019-0318

Nowell, J., Blunt, E., and Edison, P. (2023). Incretin and insulin signaling as novel therapeutic targets for Alzheimer's and Parkinson's disease. *Mol. Psychiatry* 28 (1), 217–229. doi:10.1038/s41380-022-01792-4

Pan, F., Xu, X., Zhan, Z., and Xu, Q. (2021). 6-Gingerol protects cardiomyocytes against hypoxia-induced injury by regulating the KCNQ1OT1/miR-340-5p/PI3K/AKT pathway. *Panminerva Med.* 63 (4), 482–490. doi:10.23736/S0031-0808.20.03956-7

Pei, H., Ma, L., Cao, Y., Wang, F., Li, Z., Liu, N., et al. (2020). Traditional Chinese medicine for Alzheimer's disease and other cognitive impairment: a review. *Am. J. Chin. Med.* 48 (3), 487–511. doi:10.1142/S0192415X20500251

Prorok, T., Jana, M., Patel, D., and Pahan, K. (2019). Cinnamic acid protects the nigrostriatum in a mouse model of Parkinson's disease via peroxisome proliferator-activated receptorα. *Neurochem. Res.* 44 (4), 751–762. doi:10.1007/s11064-018-02705-0

Rebai, O., Belkhir, M., Sanchez-Gomez, M. V., Matute, C., Fattouch, S., and Amri, M. (2017). Differential molecular targets for neuroprotective effect of chlorogenic acid and its related compounds against glutamate induced excitotoxicity and oxidative stress in rat cortical neurons. *Neurochem. Res.* 42 (12), 3559–3572. doi:10.1007/s11064-017-2403-9

Spooner, R. K., Taylor, B. K., Moshfegh, C. M., Ahmad, I. M., Dyball, K. N., Emanuel, K., et al. (2021). Neuroinflammatory profiles regulated by the redox environment predicted cognitive dysfunction in people living with HIV: a cross-sectional study. *EBioMedicine* 70, 103487. doi:10.1016/j.ebiom.2021.103487

Sturrock, A., Woller, D., Freeman, A., Sanders, K., and Paine, R. (2018). Consequences of hypoxia for the pulmonary alveolar epithelial cell innate immune response. *J. Immunol.* 201 (11), 3411–3420. doi:10.4049/jimmunol.1701387

Su, W., Yang, Y., Zhao, X., Cheng, J., Li, Y., Wu, S., et al. (2024). Potential efficacy and mechanism of eight mild-natured and bitter-flavored TCMs based on gut microbiota: a review. *Chin. Herb. Med.* 16 (1), 42–55. doi:10.1016/j.chmed.2023.08.001

Su, Z., Zhang, G., Li, X., and Zhang, H. (2023). Inverse correlation between Alzheimer's disease and cancer from the perspective of hypoxia. *Neurobiol. Aging* 131, 59–73. doi:10.1016/j.neurobiolaging.2023.07.002

Wang, L., Liu, Z., Liang, R., Wang, W., Zhu, R., Li, J., et al. (2022). Comprehensive machine-learning survival framework develops a consensus model in large-scale multicenter cohorts for pancreatic cancer. *Elife* 11, e80150. doi:10.7554/eLife.80150

Wang, Q., Wang, P., Qin, Z., Yang, X., Pan, B., Nie, F., et al. (2021). Altered glucose metabolism and cell function in keloid fibroblasts under hypoxia. *Redox Biol.* 38, 101815. doi:10.1016/j.redox.2020.101815

Yang, H., Cheng, J., Zhuang, H., Xu, H., Wang, Y., Zhang, T., et al. (2024). Pharmacogenomic profiling of intra-tumor heterogeneity using a large organoid biobank of liver cancer. *Cancer Cell* 42 (4), 535–551 e8. doi:10.1016/j.ccell.2024.03.004

Yang, M. D., Zhou, W. J., Chen, X. L., Chen, J., Ji, Q., Li, Q., et al. (2021). Therapeutic effect and mechanism of bushen-jianpi-jiedu decoction combined with chemotherapeutic drugs on postoperative colorectal cancer. *Front. Pharmacol.* 12, 524663. doi:10.3389/fphar.2021.524663

Yang, W., Yin, H., Wang, Y., Wang, Y., Li, X., Wang, C., et al. (2023). New insights into effects of Kaixin Powder on depression via lipid metabolism related adiponectin signaling pathway. *Chin. Herb. Med.* 15 (2), 240–250. doi:10.1016/j.chmed.2022.06.012

Zhang, M., Chen, H., Zhang, W., Liu, Y., Ding, L., Gong, J., et al. (2023). Biomimetic remodeling of microglial riboflavin metabolism ameliorates cognitive impairment by modulating neuroinflammation. *Adv. Sci. (Weinh)* 10 (12), e2300180. doi:10.1002/advs.202300180

Zhang, S., Ta, N., Zhang, S., Li, S., Zhu, X., Kong, L., et al. (2024). Unraveling pancreatic ductal adenocarcinoma immune prognostic signature through a naive B cell gene set. *Cancer Lett.* 594, 216981. doi:10.1016/j.canlet.2024.216981

Zhao, H., Liu, J., Wang, Y., Shao, M., Wang, L., Tang, W., et al. (2023). Polysaccharides from sea buckthorn (Hippophae rhamnoides L.) berries ameliorate cognitive dysfunction in AD mice induced by a combination of d-gal and AlCl(3) by suppressing oxidative stress and inflammation reaction. *J. Sci. Food Agric.* 103 (12), 6005–6016. doi:10.1002/jsfa.12673

Zhou, G., Soufan, O., Ewald, J., Hancock, R. E. W., Basu, N., and Xia, J. (2019b). NetworkAnalyst 3.0: a visual analytics platform for comprehensive gene expression profiling and meta-analysis. *Nucleic Acids Res.* 47 (W1), W234–W241. doi:10.1093/nar/gkz240

Zhou, Y., Zhou, B., Pache, L., Chang, M., Khodabakhshi, A. H., Tanaseichuk, O., et al. (2019a). Metascape provides a biologist-oriented resource for the analysis of systems-level datasets. *Nat. Commun.* 10 (1), 1523. doi:10.1038/s41467-019-09234-6

frontiers | Frontiers in Pharmacology

TYPE Original Research
PUBLISHED 15 August 2024
DOI 10.3389/fphar.2024.1426049



OPEN ACCESS

EDITED BY
Wenzhi Hao,
Jinan University, China

REVIEWED BY
Jicong Chen,
China Pharmaceutical University, China
Keyan Chen,
China Medical University, China

*CORRESPONDENCE
Liang Kong,
liangkong_sy@163.com
Xuetao Li,
lixuetao1979@163.com

RECEIVED 30 April 2024
ACCEPTED 31 July 2024
PUBLISHED 15 August 2024

CITATION
Wang J, Zang J, Yu Y, Liu Y, Cao H, Guo R, Zhang L, Liu M, Zhang Z, Li X and Kong L (2024) Lingguizhugan oral solution alleviates MASLD by regulating bile acids metabolism and the gut microbiota through activating FXR/TGR5 signaling pathways.
*Front. Pharmacol.* 15:1426049.
doi: 10.3389/fphar.2024.1426049



# Lingguizhugan oral solution alleviates MASLD by regulating bile acids metabolism and the gut microbiota through activating FXR/TGR5 signaling pathways

Jiahua Wang[1], Juan Zang[1], Yang Yu[1], Yang Liu[1], Huimin Cao[2], Ruibo Guo[1], Lu Zhang[1], Mo Liu[1], Zixu Zhang[1], Xuetao Li[1]* and Liang Kong[1]*

[1]College of Pharmacy, Liaoning University of Traditional Chinese Medicine, Dalian, China, [2]Key Laboratory of Ministry of Education for Traditional Chinese Medicine Viscera-State Theory and Applications, Liaoning University of Traditional Chinese Medicine, Shenyang, China

**Background:** The preservation of the Lingguizhugan (LGZG) decoction and patient compliance issue often limit the treatment of metabolic dysfunction-associated steatotic liver disease (MASLD). Hence, herein, an LGZG oral solution was developed for alleviating MASLD. Additionally, the potential mechanisms underlying LGZG-mediated MASLD mitigation were explored.

**Methods:** A MASLD mouse model was constructed using oleic and palmitic acid-induced LO2 cells and a high-fat diet. The apoptosis, lipid deposition, and mouse liver function were analyzed to assess the therapeutic effects of the LGZG oral solution on MASLD. Serum untargeted metabolomics, gut microbiota, bile acid (BA) metabolism, immunohistochemistry, and Western blotting analyses were performed to investigate the potential mechanism of action of LGZG oral solution on MASLD.

**Results:** The LGZG oral solution ameliorated lipid deposition, oxidative stress, inflammation, and pathological damage. Serum untargeted metabolomics results revealed the LGZG-mediated regulation of the primary BA biosynthetic pathway. The 16S ribosomal RNA sequencing of the fecal microbiota showed that LGZG oral solution increased the relative abundance of the BA metabolism-associated *Bacteroides*, *Akkermansia*, and decreased that of *Lactobacillus*. Additionally, the BA metabolism analysis results revealed a decrease in the total taurine-α/β-muricholic acid levels, whereas those of deoxycholic acid were increased, which activated specific receptors in the liver and ileum, including farnesoid X receptor (FXR) and takeda G protein-coupled receptor 5 (TGR5). Activation of FXR resulted in an increase in short heterodimer partner and subsequent inhibition of cholesterol 7α-hydroxylase and sterol regulatory element-binding protein-1c

**Abbreviations:** LGZG-H, high dose Lingguizhugan oral solution; LGZG-M, middle dose Lingguizhugan oral solution; LGZG-L, low dose Lingguizhugan oral solution; CA, cholic acid; CDCA, chenodeoxycholic acid; DCA, deoxycholic acid; T-α/β-MCA, taurine-α/β-muricholic acid; FGF15/19, fibroblast growth factor 15/19; FXR, farnesoid X receptor; CYP7A1, cholesterol 7α-hydroxylase; TGR5, takeda G protein-coupled receptor 5; SHP, short heterodimer partner; SREBP-1c, sterol regulatory element-binding protein-1c; CYP8B1, cytochrome P450 family 8 subfamily B member 1; FGFR4, fibroblast growth factor receptor 4; HFD, high-fat diet.

expression, and activation of FXR also results in the upregulation of fibroblast growth factor 15/19 expression, and consequently inhibition of cholesterol 7α-hydroxylase, which correlated with hepatic BA synthesis and lipogenesis, ultimately attenuating lipid deposition and bile acid stasis, thereby improving MASLD.

**Conclusion:** Altogether, the findings of this study suggest that modulating microbiota–BA–FXR/TGR5 signaling pathway may be a potential mechanism of action of LGZG oral solution for the treatment of MASLD.

KEYWORDS

**Lingguizhugan oral solution, metabolic dysfunction-associated steatotic liver disease, gut microbiota, bile acid metabolism, FXR/TGR5**

# 1 Introduction

Metabolic dysfunction-associated steatotic liver disease (MASLD), previously known as non-alcoholic fatty liver disease (Castro-Narro and Rinella, 2024; Hsu and Loomba, 2024; Lee et al., 2024), is the most common metabolic syndrome and chronic liver disease worldwide characterized by hepatocyte steatosis and fat accumulation (Huang et al., 2020). Reportedly, MASLD is a prominent cause of liver-related morbidity and mortality, affecting approximately 25% of adults worldwide (Raza et al., 2021). Patients with MASLD are primarily treated by mitigating or halting the disease progression through lifestyle adjustments and dietary optimization. Additionally, caloric restriction for weight reduction is considered an effective therapeutic strategy for MASLD (Liu et al., 2019). Regarding the pharmacologic treatment of MASLD, current international guidelines only consider a few pharmacologic approaches including vitamin E and pioglitazone. Reportedly, pharmacologic agents such as glucagon-like peptide one agonists, farnesoid X receptor (FXR), and peroxisome proliferator-activated receptor ligands have exhibited beneficial effects on MASLD in clinical trials, although they are associated with certain limitations (Paternostro and Trauner, 2022). Therefore, studies on the multi-pathway, multi-compound, multi-target treatment model of traditional Chinese medicine (TCM) are urgently warranted.

TCM presents several advantages in treating chronic liver diseases, including precise therapeutic effects and minimal adverse reactions. Lingguizhugan (LGZG) decoction is a classic formula documented in the "Synopsis of Golden Chamber" and consists of the following four TCMs: Fuling, Wolfiporia cocos (F.A. Wolf) Ryvarden and Gilb. [Polyporaceae; Poria]; Guizhi, Cinnamomum cassia (L.). J. Presl [Lauraceae; Cinnamomi ramulus]; Baizhu, Atractylodes macrocephala Koidz. [Asteraceae; Atractylodis macrocephalae rhizoma] and Gancao, Glycyrrhiza uralensis Fisch. ex DC. [Fabaceae; Glycyrrhizae radix et rhizoma]. LGZG decoction can warm Yang, transform drink, strengthen the spleen, and dispel dampness. The effects of LGZG decoction in treating various liver diseases such as MASLD (Cao et al., 2022), heart diseases such as heart failure (Li et al., 2019), and spleen disorders such as diarrhea (Xu et al., 2020) have been reported in many clinical trials. Regarding MASLD treatment, this decoction considerably improved the liver function and blood lipid levels, along with lipid metabolism regulation (Zhu et al., 2017), oxidative stress (Yang et al., 2017), and inflammation to prevent disease progression (Cao et al., 2022). Nevertheless, despite these positive outcomes, the exact therapeutic mechanism of LGZG decoction remains unelucidated.

MASLD pathogenesis is multifaceted and not fully understood. Recently, bile acids (BAs), gut microbiota, nuclear receptors (NRs) including FXRs and liver X receptors, lipid metabolism, and fatty acid metabolism have been reported to play a driving role in preventing and treating MASLD (Yan et al., 2018; Chen and Vitetta, 2020; Bing and Li, 2022). Among them, abnormal BA metabolism is considered an important contributor to MASLD development. FXR is a metabolic NR, also known as BA receptor, and maintains BA homeostasis (Keitel et al., 2019a). Takeda G protein-coupled receptor 5 (TGR5) is another important BA receptor and is activated by BAs to regulate their metabolism (Castellanos-Jankiewicz et al., 2021). FXR is highly expressed in hepatocytes and intestinal epithelial cells and is involved in BA synthesis, excretion, and reabsorption (Molinaro and Marschall, 2022). Notably, FXR functions differently in the liver and intestine to regulate BA homeostasis. In the liver, FXR activation modulates short heterodimer partner (SHP) to suppress cholesterol 7α-hydroxylase (CYP7A1) expression, thereby inhibiting BA synthesis (Chiang and Ferrell, 2020). In the intestine, FXR activation induces fibroblast growth factor 15/19 (FGF15/19) to maintain BA homeostasis (Katafuchi and Makishima, 2022). Reportedly, FXR receptors can regulate BA metabolism (Clifford et al., 2021), intestinal flora homeostasis (Zhai et al., 2022), and other signaling pathways for treating MASLD, making them a promising therapeutic target for fatty liver and related conditions.

The gut microbiota exhibits a highly intricate composition, comprising approximately 500–1,000 species, with nearly $10^{14}$ bacteria, which is over ten times the total number of cells in the human body (Ma et al., 2019). This microbial population plays a crucial role in regulating metabolic processes and disease, and dysbiosis in the gut microbiota can alter the immune status of the body, contributing to the development of various liver diseases, including MASLD (Fang et al., 2022). An essential reaction in BA metabolism is the bile salt hydrolase (BSH)-catalyzed uncoupling of BAs by the gut microbiota. Reportedly, bacterial genera such as *Lactobacillus*, *Bacteroides*, *Bifidobacterium*, *Clostridium*, *Listeria*, and *Enterococcus* can exhibit functional BSH activity (Cai et al., 2022). The gut microbiota regulates the BA-pool homeostasis by metabolizing primary BAs into secondary BAs (Chen and Vitetta, 2020). The BA–gut microbiota interaction provides a rationale for exploring the potential of gut microbiota-targeted therapy of MASLD.

This study aimed to investigate the effects of the LGZG oral solution on oleic acid (OA)- and palmitic acid (PA)-induced LO2 cells and an MASLD mouse model. Serum untargeted metabolomics techniques were used to assess the differential metabolites. Furthermore, the changes of gut microbiota and BA profile were monitored by 16S ribosomal RNA (rRNA) sequencing and BA-targeted metabolomics to further explore the effect of LGZG oral solution on BA metabolism and lipid accumulation through FXR/TGR5 signaling pathway. Additionally, the potential mechanisms of the protective effects of LGZG oral solution in MASLD mice were elucidated.

# 2 Material and methods

## 2.1 Preparation of LGZG oral solution

Fuling, Guizhi, Baizhu and Gancao were supplied by Liaoning University of Traditional Chinese Medicine, School of Pharmacy, and verified by Professor Zhang Hui, Department of Chinese Medicine Identification, School of Pharmacy, Liaoning University of Traditional Chinese Medicine. Firstly, the volatile oil, the main compounds of the two botanical drugs, Guizhi and Baizhu, was extracted by water vapor distillation, with the amount of water added being 8 times that of the botanical drugs, and the extraction time was 6 h, and the volatile oil was collected. Then the water decoction method was used to extract the botanical drugs (4:3:3:2) twice at a ratio of 1:8 botanical drugs to water for 1.5 h each time. Then, the extract was clarified by precipitation with 70% ethanol for 18 h, The ethanol was volatilized so that its PH was between 4 and 6, and then the flavoring agent (mannitol), and preservative (potassium sorbate) were added. After that, we mixed the co-solvent 1.5% Tween 80 with the volatile oil, so that the volatile oil was fully emulsified, and then the emulsion was added to the previous medicinal solution, stirred to dissolve, and finally made into LGZG oral solution.

HPLC was performed to identify the major compounds in LGZG oral solution. Chromatographic separation was performed using an Shim-park GIST C18 column (4.6 mm × 250 mm, 5 μm, Shimadzu). The mobile phase was acetonitrile (A)-0.1% phosphoric acid (B). The gradient program was set as follows: 0–10 min, 5%–20% A; 10–40 min, 20%–50% A; 40–50 min, 50%–60% A; 50–75 min, 60%–70% A; 75–100 min, 70%–90% A; 100–110 min, 90%–20% A. Flow rate: 1 mL/min, wavelength: 254 nm, column temperature: 30°C.

## 2.2 Animals and materials

Male mice, weighing 14–20g, were purchased from Liaoning Changsheng Biotechnology Co., LTD. Mice were housed at the Laboratory Animal Center of Liaoning University of Traditional Chinese Medicine at 22°C–24°C and 55%–60% humidity. All experimental procedures were carried out in accordance with the institutional standards of animal humanistic care. The procedures followed in this study were approved by the Animal Research Ethics Committee of Liaoning University of Traditional Chinese Medicine, with which the informed consent for clinical research was signed (NO. 210000420230204). The research was conducted in accordance with internationally accepted principles for the use and care of laboratory animals. The mice were randomly divided into five groups (n = 10): control group, model group, LGZG-L treatment group, LGZG-M treatment group and LGZG-H treatment group. Mice were treated with a 4-week intervention starting at week 14, the LGZG-L (2.5 g/kg/d), LGZG-M (5.0 g/kg/d) and LGZG-H (10.0 g/kg/d) were administrated by gavage, respectively. The mice in the control group and the model group were given the same amount of normal saline by gavage. Body weight was monitored weekly, and mice were executed after 4 weeks of intervention. Blood samples were collected by enucleation of eyeballs and immediately centrifuged at 4°C for 10 min to obtain serum. Liver and ileum tissues as well as mouse cecum contents were also collected. Livers were weighed to derive a liver index and then stored at −80°C for further use.

Oleic acid (OA) and Palmitic acid (PA) was obtained from Shanghai Aladdin Biochemical Technology Co.,Ltd (Shanghai, China). Oil red O staining solution was bought from Solarbio Science and Technology Co., Ltd (Beijing, China). Hematoxylin and eosin (HE) staining kit, Annexin V/FITC apoptosis detection kit were ordered from the Meilun Biotechnology Co., Ltd (Dalian, China). Fetal bovine serum (FBS) and Penicillin-streptomycin (P/S) were purchased from Gibco BRL (Grand Island, NY, United States). TG and GSH-PX kits were obtained from Nanjing Jiancheng Bioengineering Institute (Nanjing, China). γ-GT kits were obtained from Nanjing Jiancheng Bioengineering Institute (Nanjing, China) and Solarbio Science and Technology Co., Ltd (Beijing, China). TC, HDL-C, LDL-L, AST, ALT, MDA and SOD kits were obtained from Pulilai gene Technology Co., Ltd (Beijing, China). BODIPY 493/503 from Fushen Biotechnology Co., Ltd (Shanghai, China). IL-6, IL-1β, and TNF-α kits from Solarbio Science and Technology Co., Ltd (Beijing, China). FXR and FGFR4 were obtained from proteintech Co., Ltd (Wuhan, China). TGR5 and FGF15 were obtained from abcam Co., Ltd (Shanghai, China). CYP7A1, CYP8B1, SREBP-1C and SHP were obtained from ThermoFisher Co., Ltd (Shanghai, China).

## 2.3 Cell culture, viability assay, and LO2 cell treatment

LO2 cells were cultured in DMEM supplemented with 10% fetal bovine serum, 100 units/mL penicillin, and 100 μg/mL streptomycin and maintained at 37°C with 5% carbon dioxide and 95% air. Cell viability was determined by SRB assay. Before administration, all liquid medicines were filtered through a 0.22 μm sterile membrane to remove bacteria. In order to induce lipid accumulation, OA and PA were added into the culture medium, and the cells were divided into control group, model group (OA:PA = 2:1), LGZG-L treatment group, LGZG-M treatment group, and LGZG-H treatment group.

## 2.4 Oil red O staining

Cells were stained with oil red O for determination of lipid content. Cells were washed twice with PBS, fixed with 4% paraformaldehyde for 30 min, incubated with oil red O working solution at room temperature for 30 min, and destained with 60% isopropanol. After washing three times with PBS, the cells were

counterstained with hematoxylin for 30 s. Cells were photographed under a light microscope (Nikon, Tokyo, Japan) and to quantify the content of oil red O, 100 μL of isopropanol was added to each well, and its absorbance at 520 nm was measured by a microplate reader (Synergy H1, BioTek, United States).

## 2.5 BODIPY 493/503 staining method

The accumulation of intracellular lipid droplets was detected by BODIPY 493/503 staining. The cells were fixed with 4% paraformaldehyde for 30 min, followed by washing once with PBS, adding 150 μL and staining with 1 μM BODIPY 493/503 at 37°C for 30 min, and the cells were observed under a fluorescence microscope.

## 2.6 The apoptosis of LO2 cells was detected by flow cytometry

Briefly, cells were harvested and incubated with 100 μL Annexin V FITC conjugate and 5 μL PI Journal Pre-proof eight solution for 20 min in the dark. Cells were then resuspended in 200 μL PBS and detected by flow cytometry (BD Biosciences, Franklin Lakes, NJ).

## 2.7 Biochemical analysis

LO2 cells were treated as before, and each group of cells was collected. The levels of TG, GSH-PX, SOD, CAT, MDA, ALT, AST and γ-GT were measured by corresponding kits. And the serum levels of ALT, AST, TC, TG, HDL-C and LDL-C were detected by using the corresponding kits and according to the instructions.

## 2.8 Liver histological examination

The degree of fatty change in liver tissue after HE staining were observed by light microscopy. NAS score was used to assess the severity of hepatic inflammation, necrosis, and fibrosis. MASLD was categorized into three stages, NAFL (scores <3), borderline NASH (scores 3–4), and NASH (scores >5) (Yang et al., 2023). Oil red O staining was used to detect fat deposition in liver tissue.

## 2.9 Hepatic proinflammatory factors and antioxidant indexes were determined

Liver tissue homogenate was collected to detect the levels of proinflammatory cytokines IL-6, IL-1β, and TNF-α in the liver by ELISA. SOD and GSH-Px activities and MDA level in liver tissue homogenate were detected according to the instructions of SOD, MDA and GSH-Px kit.

## 2.10 Serum untargeted metabolomics study

The 50 mg sample was slowly thawed on ice and placed in a 2 mL centrifuge tube. Subsequently, 800 μL of 80% methanol was added, followed by grinding at 65 Hz for 90 s and mixing with vortex shaking. The sample was then subjected to ultrasound at 4°C for 30 min, and allowed to stand for 1 h at −20°C. After centrifugation at 12,000 rpm/min for 15 min at 4°C, 200 μL of the supernatant was extracted. To this, 5 μL of 0.14 mg/mL dichlorophenylalanine was added as the internal standard, mixed, and transferred into sample vials for LC-MS/MS analysis.

The chromatographic platform utilized in this study was the Ultimate 3000 L C combined with Q Exactive MS (Thermo). The chromatographic column employed was the ACQUITY UPLC HSS T3 column (2.1 mm × 100 mm, 1.8 μm). The separation conditions included a column temperature of 40°C, a flow rate of 0.3 mL/min, and mobile phase A consisting of 0.05% formic acid-water, while mobile phase B was acetonitrile. The injection volume was 6 μL, and the autosampler temperature was maintained at 4°C. Mass spectrometry was conducted in positive ion mode with a heater temperature of 300°C. The sheath gas flow rate was set at 45 arb, auxiliary air flow rate at 15 arb, and exhaust flow rate at one arb. The electrospray voltage was 3.0 KV, capillary temperature at 350°C, and S-LensRFLevel at 30%.

## 2.11 16sRNA sequencing of the fecal microbiota

Total fecal DNA samples were extracted for 16S rRNA sequencing. PCR amplification was then performed. High-throughput sequencing was performed on Illumina Novoseq6000 PE250. Using QIIME software, the UCLUST Sequence Comparison Tool (Edgar, 2010) was invoked to analyze the obtained sequences by 97% similarity for operational taxonomic units (OTU) clustering and species taxonomy.

## 2.12 Analysis of fecal bile acids

Samples were accurately weighed and recorded before being loaded into 1.5 mL EP tubes along with 10 μL of mixed internal standard and 390 μL of methanol containing 1 mM BHT. Two small steel balls were added, followed by swirling for 30 s, resting at −20°C for 2 min, and then grinding in an ice bath using a grinder at 60 Hz for 1 min. Ultrasonic extraction was performed for 10 min, followed by centrifugation at 4°C and 12,000 r for another 10 min. The supernatant was then diluted 10-fold, with 100–150 μL being bottled for further analysis. The experiment utilized the UPLC-ESI-MS/MS analysis method for qualitative and quantitative detection of target metabolites.

Chromatographic conditions: injection volume: 5 μL; flow rate: 0.45 mL/min: mobile phases A (0.1% formic acid-water solution), B (methanol: ethanol: isopropanol = 1:1:1, containing 0.1% formic acid). Gradient Elution Procedures: 0 min A/B (80: 20, V/V), 0.5 min A/B (80:20, V/V), 1.5 min A/B (62:38, V/V), 12 min A/B (50:50, V/V), 17.5 min A/B (5:95, V/V), 19 min A/B (5:95, V/V), 19.01 min A/B (80:20, V/V), 20 min A/B (80:20, V/V). Mass spectrometry method conditions: curtain gas: 35 (psi), collision-activated dissociation (CAD) parameters: medium, negative ion spray zero voltage: 4500 V, positive ion spray voltage: 5500 V, ion source temperature: 450°C, column

temperature: 45°C, spray gas (Gas1): 55 (psi), auxiliary heating gas (Gas2): 55 (psi).

## 2.13 Western blot

An appropriate amount of liver tissue stored at −80°C was used to extract protein with RIPA lysate. After centrifugation at 4°C for 20 min, the protein concentration was measured and denatured by boiling. The denatured protein samples were separated by electrophoresis, transferred to the membrane, and closed. Dilutions of primary antibodies CYP7A1, CYP8B1, FXR, TGR5, SHP, SREBP-1C and FGFR4 (1:1,000, v:v) were added and incubated at 4°C overnight. The corresponding secondary antibody dilution (1:1,000, v:v) was added and incubated for 1 h at room temperature. The ECL mixture was drip-added onto the membrane, exposed by chemiluminescence imaging system, photographed by gel imager after development, and analyzed by ImageJ software.

## 2.14 Immunofluorescence and immunohistochemistry

Liver/ileum paraffin sections were routinely dehydrated, placed in 0.01 mol/L sodium citrate buffer, microwaved to boiling for 5 min, and repeated 3 times; the sections were incubated in 3% $H_2O_2$ solution for 5 min at room temperature; permeabilized in 1% Triton X-100 solution for 30 min; and occluded in 5% BSA solution for 1 h. FXR, TGR5 and FXR, TGR5, FGF15/19 primary antibody dilution (1:300) was respectively added to liver and ileum tissues in drops of 50 μL and incubated at 4°C overnight; the next day, Cy3/FITC labeled secondary antibody dilution (1:300) was added in drops, and the nuclei of the cells were stained with DAPI for 10 min, and the positive expression was observed under fluorescence microscope. HRP-labeled secondary antibody dilution (1:300) was added dropwise for immunohistochemical staining, incubated at room temperature and protected from light for 1 h, DAB color development, hematoxylin re-staining, dehydrated with different gradient ethanol solutions, sealed with xylene clear neutral gum, and observed the positive expression under the microscope.

## 2.15 Statistical analysis

Statistical analysis was performed using GraphPad Prism 9.0 software, and data were expressed as mean ± standard deviation (mean ± SD). Comparisons between groups were analyzed by one-way ANOVA or *t*-test, with $p < 0.05$ indicating a statistically significant difference.

# 3 Results

## 3.1 Identification of chemical compounds in the LGZG oral solution

The chemical compounds of LGZG oral solution was characterized through high-performance liquid chromatography fingerprinting. Figures 1A–D illustrates the reference compounds pachymic acid, cinnamaldehyde, 2-atractylenolide and glycyrrhizic acid. By comparing retention times with reference standards, the characteristic peaks corresponding to these compounds were identified in LGZG oral solution (Figure 1E).

## 3.2 Screening of optimal concentrations of the LGZG oral solution and OA + PA

The effects of various concentrations of LGZG oral solution on the viability of LO2 cells were assessed to determine the effective drug intervention concentrations. The concentrations ranging from 0 mg/mL to 35 mg/mL were assessed. The Sulforhodamine B (SRB) method was used to determine the viability of LGZG-treated cells (Figure 2A). Following 24-h LGZG oral solution treatment, different levels of inhibition were observed in LO2 cells. To achieve reduced lipid deposition while maintaining high cell survival rates, the following concentrations were selected: low dose, 2.5 mg/mL; medium dose, 5 mg/mL; and high dose, 10 mg/mL. The concentration screening for inducing cell lipid deposition is shown in Figures 2B–D. OA and PA at concentrations of 1–2 mmol/L notably increased intracellular lipid deposition. However, 1.5–2 mmol/L concentrations markedly decreased the cell survival, indicating toxicity. Therefore, 1 mmol/L was selected as the inducing concentration for OA and PA, which is consistent with the findings of prior studies (Qiao et al., 2018).

## 3.3 LGZG oral solution inhibited lipid deposition and cytoprotection

The effect of LGZG oral solution on OA + PA-induced hepatocyte lipid accumulation was investigated by treating LO2 cells with 2.5, 5, and 10 mg/mL LGZG oral solution for 24 h. Intracellular lipid droplets were visualized using oil red O staining. Compared with the control group, lipid accumulation in OA + PA-induced hepatocytes markedly increased (Figures 3A, D). However, treatment with LGZG oral solution notably inhibited the aggregation of lipid droplets in LO2 cells. Additionally, BODIPY staining of lipid droplets in LO2 cells from different treatment groups revealed that the fluorescence intensity was highest in the OA + PA group, whereas the lowest intensity was in the LGZG-H group (Figures 3B, E). Flow cytometry analysis of the *in vitro* fatty liver model of LO2 cells showed an increased apoptosis rate in the OA + PA group; however, that in all LGZG-treated groups was reduced than that in the OA + PA group, with the LGZG-H group exhibiting the most notable decrease in the total apoptosis rate.

## 3.4 LGZG oral solution alleviated hepatocyte injury and oxidative stress

In addition to the lipid accumulation, OA + PA increased the release of intracellular hepatic enzymes including alanine aminotransferase (ALT), aspartate aminotransferase (AST), and gamma-glutamyl transferase (γ-GT), which are markers of the liver cell damage (Fang et al., 2019; Liu et al., 2020). Notably, LGZG oral solution treatment reduced the enzyme levels. The effect of the LGZG

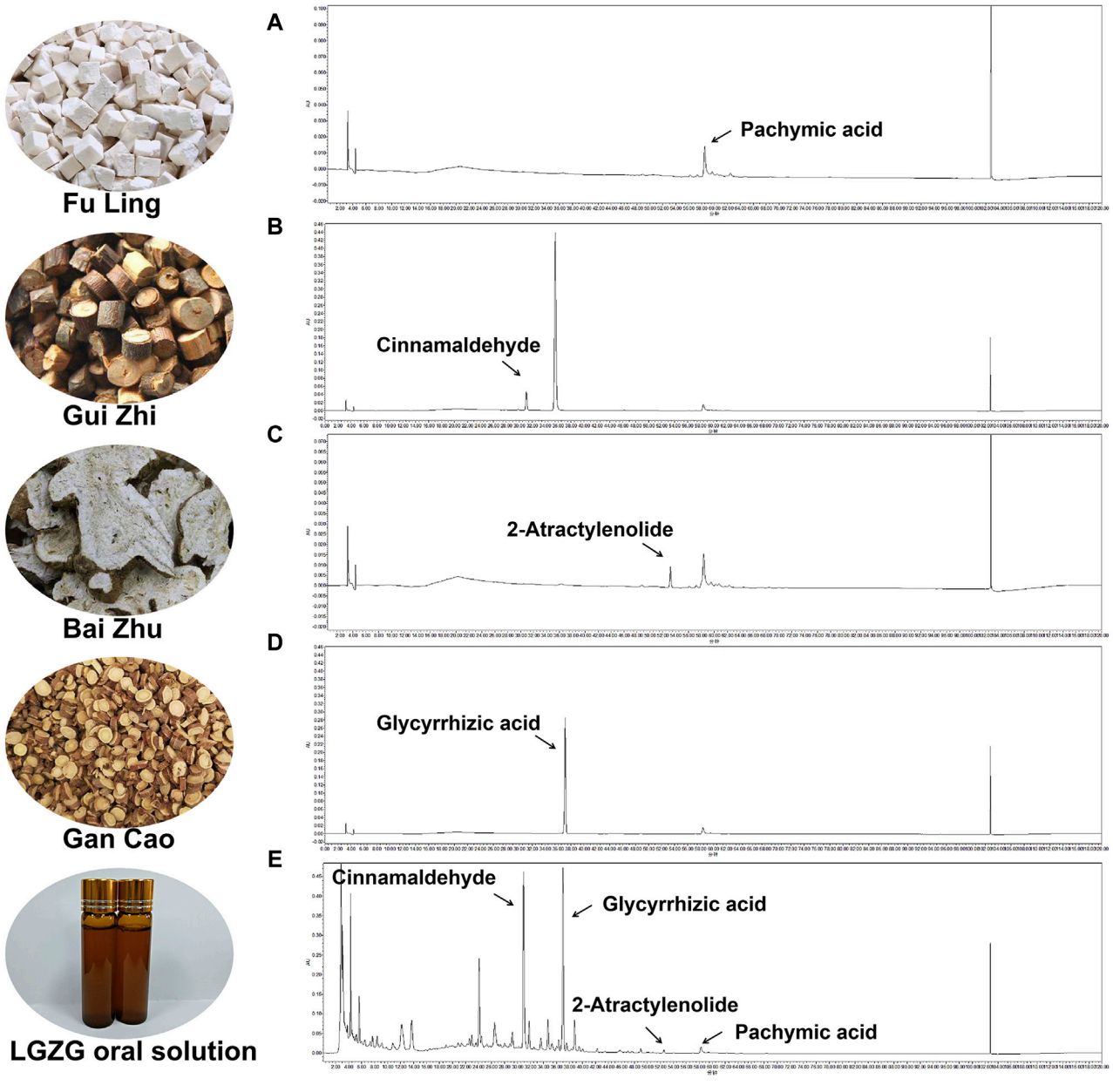


FIGURE 1
Identifcation of chemical compounds in LGZG oral solution by HPLC. **(A–D)** HPLC chromatograms of Cinnamaldehyde, Glycyrrhizic acid, 2-Atractylenolide and Pachymic acid at 254 nm. **(E)** HPLC chromatograms of the LGZG oral solution at 254 nm.

oral solution on OA + PA-induced oxidative stress in LO2 cells was investigated by assessing various relevant indexes. The model group exhibited a significant increase in the malondialdehyde (MDA) content compared with that in the control group, indicating increased oxidative stress following the OA + PA treatment. LGZG-H oral solution treatment notably decreased the MDA content *versus* OA + PA (Figure 4D). Additionally, the expression of antioxidant enzymes glutathione peroxidase (GSH-PX), superoxide dismutase (SOD), and catalase was decreased in the model group compared with that in the control group, and LGZG oral solution treatment increased the levels of these enzymes (Figures 4E–G). These results confirmed that LGZG oral solution can effectively reduce lipid accumulation, mitigate hepatocyte injury, and alleviate oxidative stress in OA + PA-treated cells.

## 3.5 Protective effects of the LGZG oral solution in MASLD mice

Herein, to investigate the effects of LGZG oral solution *in vivo*, the MASLD mouse model was established. Different concentrations of LGZG oral solution were administered starting from the 14th week for 4 weeks (Figure 5A). At the end of the experiment, changes in body weight and liver weight were measured for each group of mice. The model group exhibited a significant increase in body weight compared with that in the control group, and the LGZG-H group exhibited the most notable reduction in body weight and liver index compared with those in the model group (Figures 5B, C). The liver function, lipid metabolism, and oxidative stress markers post-

10.3389/fphar.2024.1426049

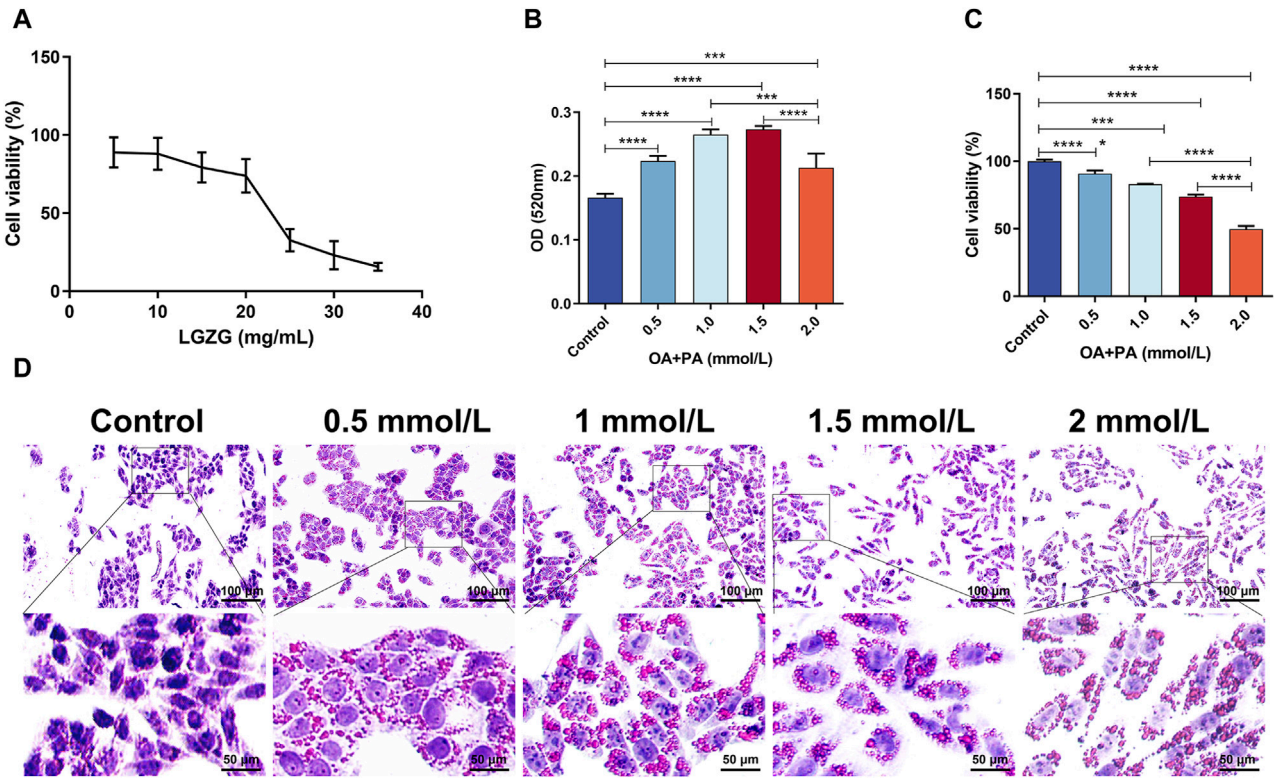


FIGURE 2
Screening of LGZG oral solution and OA + PA concentrations. **(A)** LGZG oral solution on LO2 cells activity assay. **(B)** OD of oil red staining of induced LO2 cells at 520 nm (n = 4). **(C)** Viability assay of oil red staining of induced LO2 cells (n = 5). **(D)** Oil red staining of LO2 cells induced by OA and PA. Data are presented as mean ± SD. $^{**}p < 0.01$, $^{***}p < 0.001$ and $^{****}p < 0.0001$.

treatment were assessed to investigate the effect of the LGZG oral solution on the progression of high-fat diet-induced MASLD in mice. ALT, AST, γ-GT, total cholesterol, triglyceride, low-density lipoprotein cholesterol, and MDA levels were considerably increased in the model group than those in the control group (Figures 5D–J), whereas high-density lipoprotein cholesterol, GSH-PX, and SOD levels were notably decreased in the model group (Figure 5K–M). LGZG oral solution treatment effectively reversed the high-fat diet-induced alterations in these marker levels. Because MASLD progression often involves an inflammatory response, interleukin (IL)-1β, IL-6, and tumor necrosis factor-α levels in the livers of mice from each group were assessed. The high-fat diet substantially increased the levels of these inflammatory markers, which were attenuated by LGZG oral solution treatment, particularly in the LGZG-H group (Figure 5N–P). These findings indicate that LGZG oral solution mitigates the development of high-fat diet-induced MASLD in mice.

## 3.6 LGZG oral solution alleviated hepatic steatosis in MASLD mice

The livers of mice in the model group exhibited a yellowish and dull hue, whereas those in the LGZG-H group presented a ruddy and shiny appearance (Figure 6A). Histological analysis of the mouse liver tissues through the hematoxylin and eosin (HE) staining revealed the notably enlarged hepatocytes with visible lipid droplets in the model group compared with those in the control group (Figures 6B, D). Varying concentrations of LGZG oral solution reduced the hepatocyte swelling and fat droplets following administration. The arrows in Figure 6B indicate the pathological state of inflammatory cell infiltration, which was markedly reduced in the treatment group compared with that in the model group. Furthermore, the results of oil red O staining indicated a decrease in hepatic fat droplets in the LGZG groups compared with that in the model group (Figures 6C, E). Evaluation based on the NAS scoring criteria revealed that the NAS scores of all five groups of mice were below three points (Table 1), eliminating the possibility of nonalcoholic steatohepatitis. Notably, intervention with LGZG-H oral solution significantly decreased the NAS score of mice compared with that in the model group. Altogether, these *in vivo* findings indicate that LGZG oral solution exerts hypolipidemic, anti-inflammatory, and antioxidant effects in MASLD mice.

## 3.7 Metabonomic analysis of the LGZG oral solution in MASLD mice

The efficacy of LGZG oral solution in the treatment of MASLD has been validated in previous studies in this paper. To investigate the mechanism of action of LGZG oral solution in inhibiting MASLD, a non-targeted metabolomics technology was used to analyze the metabolite levels in the mouse serum to identify differential metabolites. Principal component analysis (PCA),

10.3389/fphar.2024.1426049

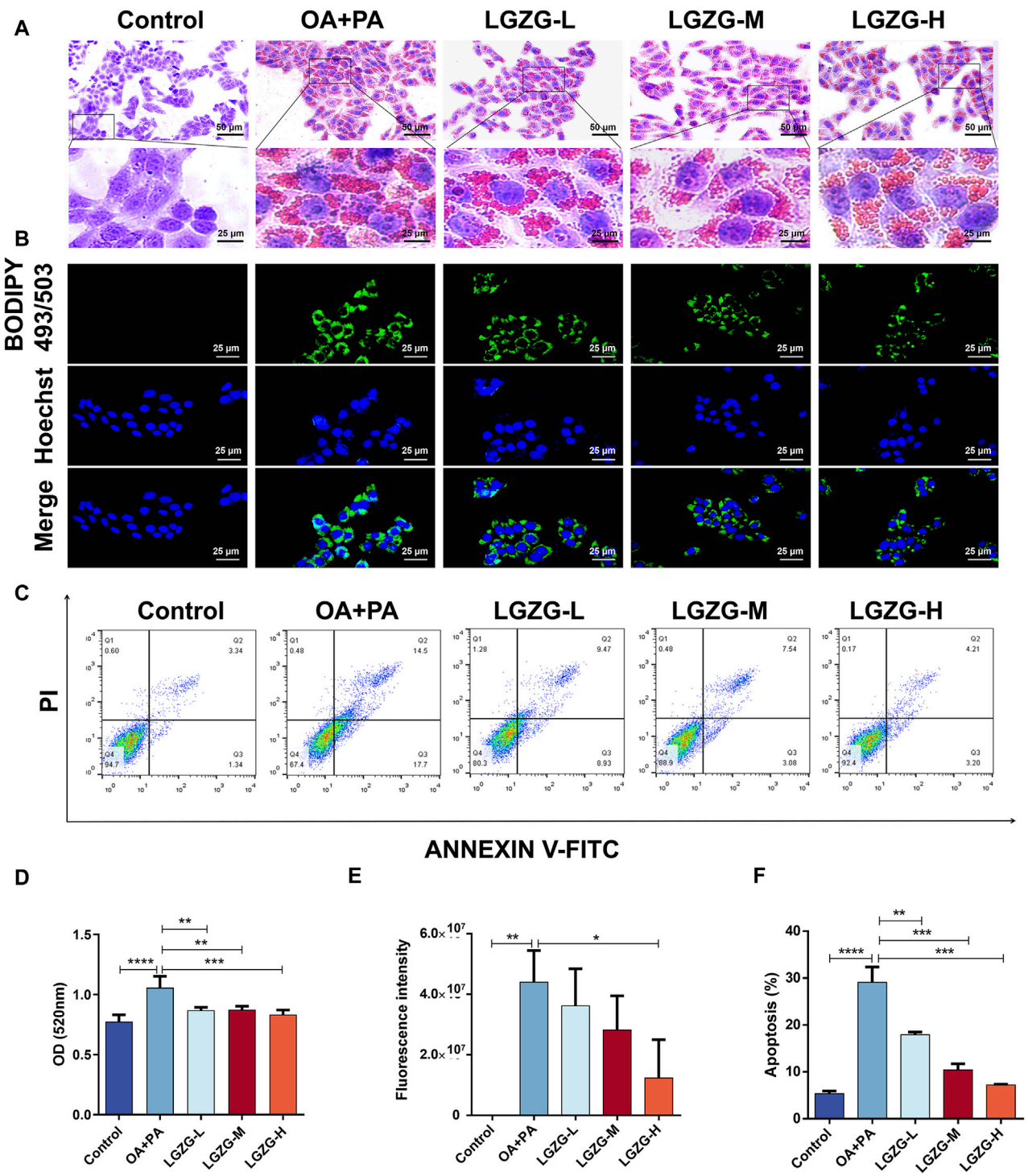


FIGURE 3
Effect of LGZG oral solution on lipid deposition and apoptosis in LO2 cells. **(A)** Oil red staining of lipid-deposited cells with LGZG oral solution. **(B)** BODIPY staining of lipid-deposited cells with LGZG oral solution. **(C)** Apoptosis of cells in different groups. **(D)** OD values of oil red staining (n = 4). **(E)** Quantitative analysis of fluorescence intensity (n = 3). **(F)** Different groups of total percentage of apoptotic cells (n = 3). Data are presented as mean ± SD. $^{*}p < 0.05$, $^{**}p < 0.01$, $^{***}p < 0.001$ and $^{****}p < 0.0001$.

partial least squares (PLS)-discriminant analysis (DA), and orthogonal PLS-DA analyses were performed using the data from each group (Figures 7A–C). Notably, the separation between the model and LGZG-H groups was obvious in the positive ion mode. Figure 7D illustrates the model loading diagram of PLS-DA, identifying the differential metabolites. PLS-DA was performed with 200 random permutation tests, showing that R2 > Q2 and Q2 < 0, thereby indicating that the model was reliable and not overfitted (Figure 7E). The volcano plot revealed 47 initially identified differential metabolites in the positive ion mode, with

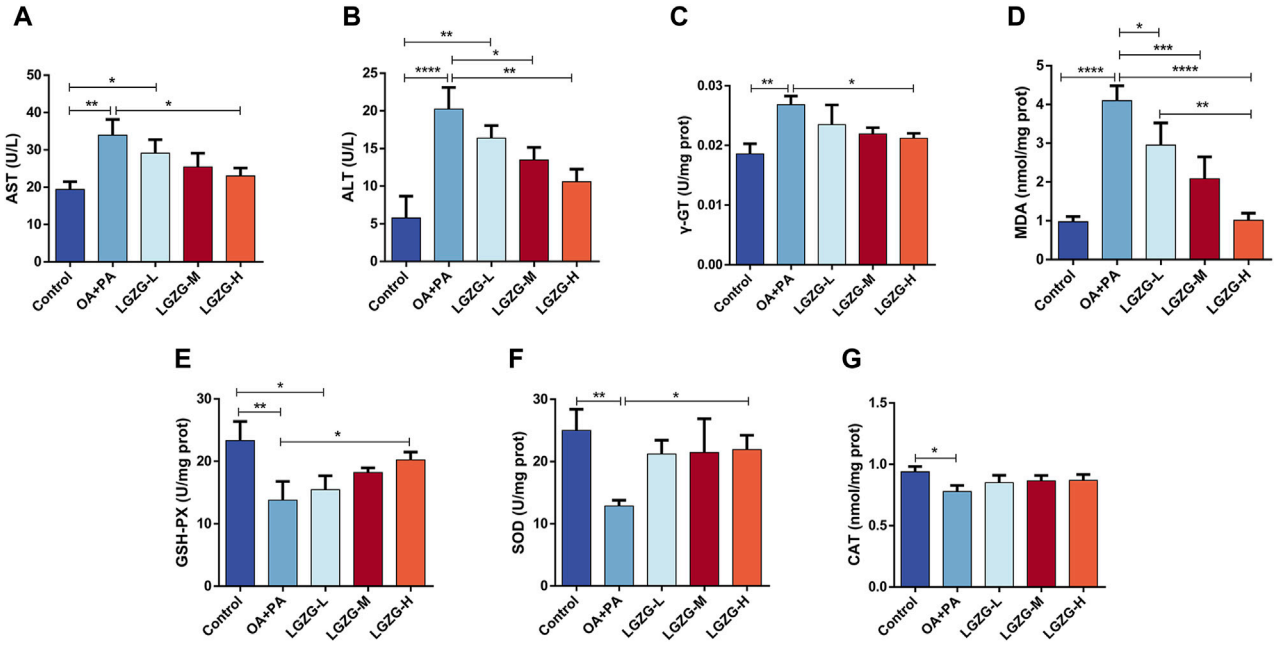


FIGURE 4
Effect of LGZG oral solution on some indices of fat depositing cells. **(A–G)** Measurement of AST, ALT, γ-GT, MDA, GSH-PX, SOD and CAT indicators. Data are presented as mean ± SD (n = 3). *$p < 0.05$, **$p < 0.01$, ***$p < 0.001$ and ****$p < 0.0001$.

35 upregulated and 12 downregulated metabolites (Figure 7F). The hierarchical cluster analysis of the significant differential metabolites under the positive ion mode presented the distinct differences between the model and treatment groups, indicating variations in the types and quantities of differential metabolites between the groups (Figure 7G). Enrichment analysis was performed to identify the significant differential metabolites that were closely associated with the LGZG-H oral solution-mediated treatment of MASLD; the results are presented in bubble plots (Figure 7H). Compared with the model group, the LGZG-H treatment group exhibited considerable effects on metabolic pathways such as primary BA biosynthesis, taurine and hypotaurine metabolism, and phenylalanine, tyrosine, and tryptophan biosynthesis.

## 3.8 Effect of LGZG oral solution intervention on gut microbiota in MASLD mice

Herein, the intricate relationship between microbial communities and BA metabolism, regarding the effects of LGZG oral solution on gut microbiota composition, was investigated. Alpha and beta diversity analyses of 16S rRNA gene sequencing data were performed to evaluate this relationship. The Chao1 index was employed to quantify the operational taxonomic units present in each sample, and the Shannon index provided insights into the species abundance and diversity of the gut microbiota. Notably, no considerable changes were observed in the Chao1 and Shannon indexes between the model and treatment groups (Figures 8A, B). However, beta-diversity analysis, including the principal coordinates analysis, revealed notable discrepancies in the gut microbiota composition among the three groups (Figure 8C). The relative abundances of the top 10 taxa at the phylum and genus levels in the three groups were compared to further explore the effects of LGZG oral solution on gut microbiota composition (Figures 8D–G). At the phylum level, *Bacteroidetes* exhibited a significantly higher abundance in the LGZG-H group compared with that in the model group (Figure 8H). At the genus level, the abundance of *Lactobacillus* was lower in the LGZG-H group than that in the model group (Figure 8I), whereas that of *Akkermansia* was higher in the LGZG-H group than that in the model group (Figure 8J).

## 3.9 Effect of LGZG oral solution intervention on BA metabolism in MASLD mice

Quantitative metabolomic analysis of the fecal BAs was performed to validate the discovered BA metabolic pathway. The PCA plots showed the different composition of BAs among the three groups (Figure 9A). The total and conjugated BAs showed a tendency to increase in the model group compared with that in the control group (Figure 9B). Additionally, the model group exhibited a significantly increased ratio of conjugated to unconjugated BAs (Figure 9C), whereas the LGZG-H group presented a lower conjugated/unconjugated BA ratio than that of the model group, but the difference was not significant. Interestingly, compared with the model group, fecal taurine-α-muricholic acid (T-α-MCA) and taurine-β-muricholic acid (T-β-MCA) were significantly decreased in the LGZG-H group (Figures 9D, E). The analysis of primary and secondary BAs showed that deoxycholic acid (DCA) levels were increased in the LGZG-H group compared with that in the model group (Figure 9F).

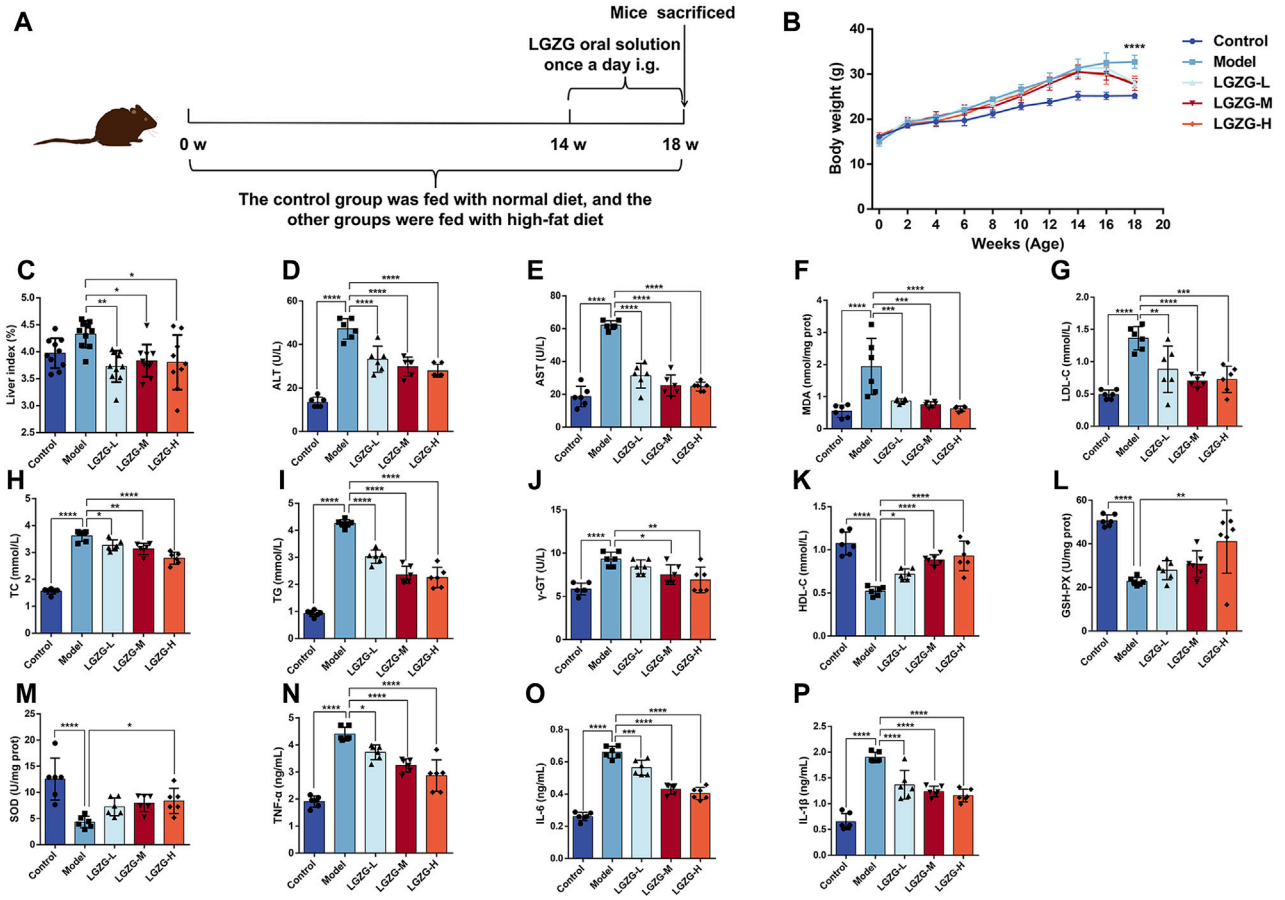


FIGURE 5
Effects of LGZG oral solution on MASLD mice. **(A)** Graphs depicting time of administration and time of tissue collection. **(B)** Changes in body weight of mice from 0 to 18 weeks (n = 10), $^{****}p < 0.0001$, Control vs. Model and Model vs. LGZG-H. **(C)** The ratio of liver weight to body weight (n = 10). **(D–P)** Measurement of ALT, AST, MDA, LDL-C, TC, TG, γ-GT, HDL-C, GSH-PX, SOD, TNF-α, IL-6 and IL-1βindicators (n = 6). Data are presented as mean ± SD. $^{*}p < 0.05$, $^{**}p < 0.01$, $^{***}p < 0.001$ and $^{****}p < 0.0001$.

## 3.10 Effect of LGZG oral solution on the expression of BA metabolism-related proteins in MASLD mice

Because LGZG oral solution showed considerable regulatory effect on BA metabolism, the expression of BA metabolism-related proteins in the liver and ileum was assessed through Western blotting, immunofluorescence, and immunohistochemistry. Immunofluorescence results showed that FXR and TGR5 expression was upregulated in the LGZG-H group compared with that in the model group (Figures 10A, D, E). The expression of BA metabolism-related proteins in the liver is shown in Figures 10B, F–L. Compared with the control group, the model group exhibited markedly downregulated expression of FXR, TGR5, SHP, and fibroblast growth factor receptor 4 (FGFR4) and notably upregulated expression of sterol regulatory element-binding protein-1c (SREBP-1c), CYP7A1, and cytochrome P450 family eight subfamily B member 1 (CYP8B1). However, the intervention of the LGZG-H oral solution reversed these changes. In the ileum, FXR, TGR5, and FGF15/19 were considerably downregulated in the model group, whereas their expression was upregulated in the LGZG-H group (Figures 10C, M, N). Additionally, HE results revealed that the structural disorganization and atrophy of the small intestinal epithelium in the model group of mice were improved following LGZG-H treatment, indicating the beneficial effect on intestinal epithelial villi damage (Figure 10C).

# 4 Discussion

LGZG decoction is a TCM composed of four botanical drugs. Herein, an LGZG oral solution was developed through water extraction and alcohol precipitation to enhance its stability and patient compliance while retaining the active compounds, without affecting its *in vivo* and *in vitro* anti-MASLD effects, including lipid deposition inhibition, anti-inflammatory effects, and antioxidant effects. In the LGZG oral solution, mannitol was used as a taste correction agent, and it did not affect the efficacy compared with that of LGZG decoction, indicating that the mannitol dose was sufficient to enhance the taste, without affecting MASLD. Non-targeted metabolomics analysis of the mouse serum revealed the potential effects of LGZG oral solution on BA metabolic pathways. Because gut microbiota plays an important role in regulating BA

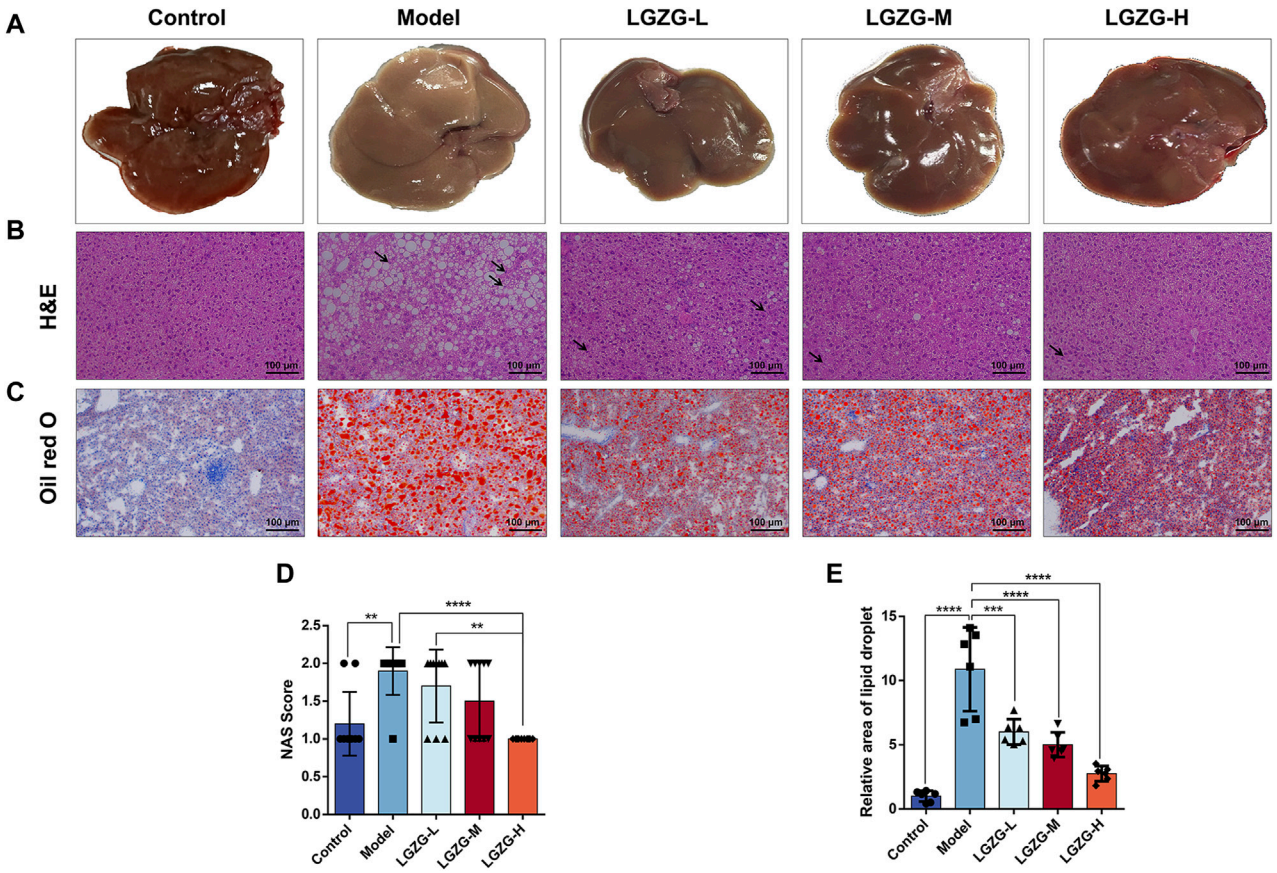


FIGURE 6
Effect of LGZG oral solution on liver histopathology in MASLD mice. **(A)** Representative images of livers (n = 10). **(B)** Representative images of liver tissue He staining (The black arrows indicate inflammatory infiltrating cells). **(C)** Representative images of liver tissue oil red O staining. **(D)** The NAS scores (n = 10). **(E)** Determination of the relative area of oil-red lipid droplets (n = 6). Data are presented as mean ± SD. $^{**}p < 0.01$, $^{***}p < 0.001$ and $^{****}p < 0.0001$.

TABLE 1 The NAS scores of the five groups.

| Group | Statistics of the number of mice in each group | | |
|---|---|---|---|
| | 1 score | 2 score | 3 score |
| Control | 8 | 2 | 0 |
| Model | 1 | 9 | 0 |
| LGZG-L | 3 | 7 | 0 |
| LGZG-M | 5 | 5 | 0 |
| LGZG-H | 10 | 0 | 0 |

metabolism, the composition of gut microbiota was investigated. Notably, the LGZG oral solution could considerably increase the abundances of *Bacteroides* and *Akkermansia*, and reduce that of *Lactobacillus*. Reportedly, these bacteria are all involved in BA metabolism (Chen MJ. et al., 2021; Dong et al., 2021). Furthermore, the LGZG oral solution markedly reduced the conjugated/unconjugated BA ratio and taurine-α/β-muricholic acid (T-α/β-MCA) expression, increased DCA levels, and promoted FXR and TGR5 expression in the gut and liver of Ba-specific receptors, thereby upregulating SHP expression and downregulating CYP7A1 and SREBP-1c expression in the liver. Additionally, FGF15/19 expression in the gut was upregulated. These results suggest that the inhibition of hepatic lipid accumulation and BA stasis using the LGZG oral solution, which exerts therapeutic effects on MASLD, may be associated with the microbiota–BA–FXR/TGR5 axis.

The gut microbiota is composed of various bacteria, with Firmicutes, Bacteroidota, Proteobacteria, and Actinobacteria being the four main types. These microbial communities are crucially involved in metabolic processes within the body and considerably affect the onset and progression of diseases by regulating metabolites and metabolic pathways (Chen Y. et al., 2021). Prolonged consumption of a high-fat diet can alter the composition of gut microbiota (Zhang and Yang, 2016), notably affecting the Firmicutes/Bacteroidota (F/B) abundance ratio. A decrease in the F/B ratio results in an increase in beneficial bacteria and a decrease in pathogenic bacteria, ultimately improving the integrity of the intestinal barrier (Feng et al., 2022). The gut microbiota mainly produces BA, short-chain fatty acids, and other metabolites (Guzior and Quinn, 2021; Nogal et al., 2021). In the small intestine, microbes transform BAs through various processes, including BSH-mediated hydrolysis of bound BAs to

10.3389/fphar.2024.1426049

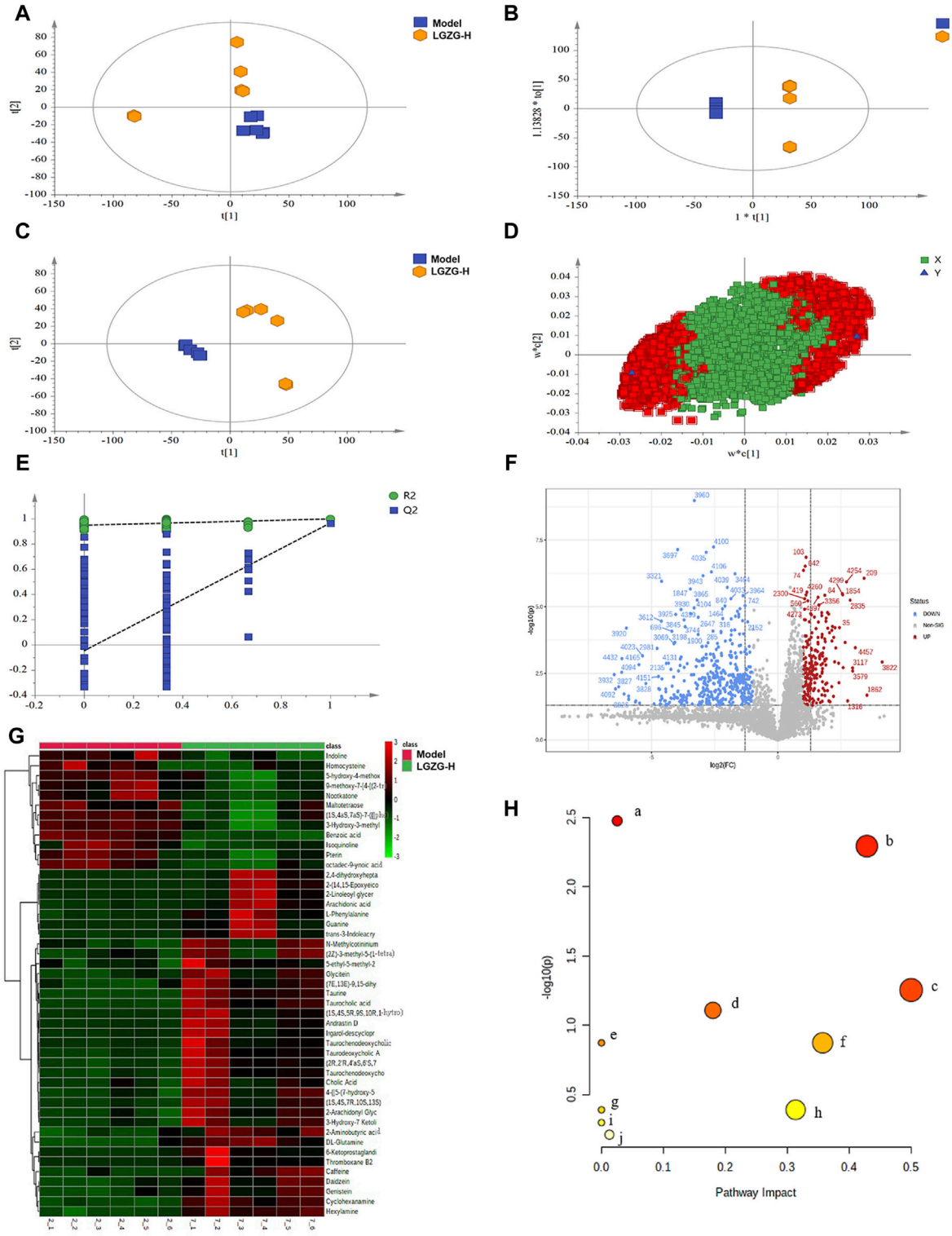


FIGURE 7
Effect of LGZG oral solution on serum metabolomics in MASLD mice. **(A)** Plot of PCA scores in the model and LGZG-H groups. **(B)** Plot of PLS-DA scores in the model and LGZG-H groups. **(C)** Plot of OPLS-DA scores in the model and LGZG-H groups. **(D)** PLS-DA model load diagram. **(E)** PLS-DA overfitting test. **(F)** Volcanograms of the model and LGZG-H groups. **(G)** Significantly different metabolite hierarchical clustering results between the model group and the LGZG-H group. **(H)** Metabolic pathway analysis of potential biomarkers. (a) Primary bile acid biosynthesis; (b) Taurine and hypotaurine metabolism; (c) Phenylalanine, tyrosine and tryptophan biosynthesis; (d) Cysteine and methionine metabolism; (e) Caffeine metabolism; (f) Phenylalanine metabolism; (g) Biosynthesis of unsaturated fatty acids; (h) Arachidonic acid metabolism; (i) Aminoacyl-tRNA biosynthesis; (j) Purine metabolism.

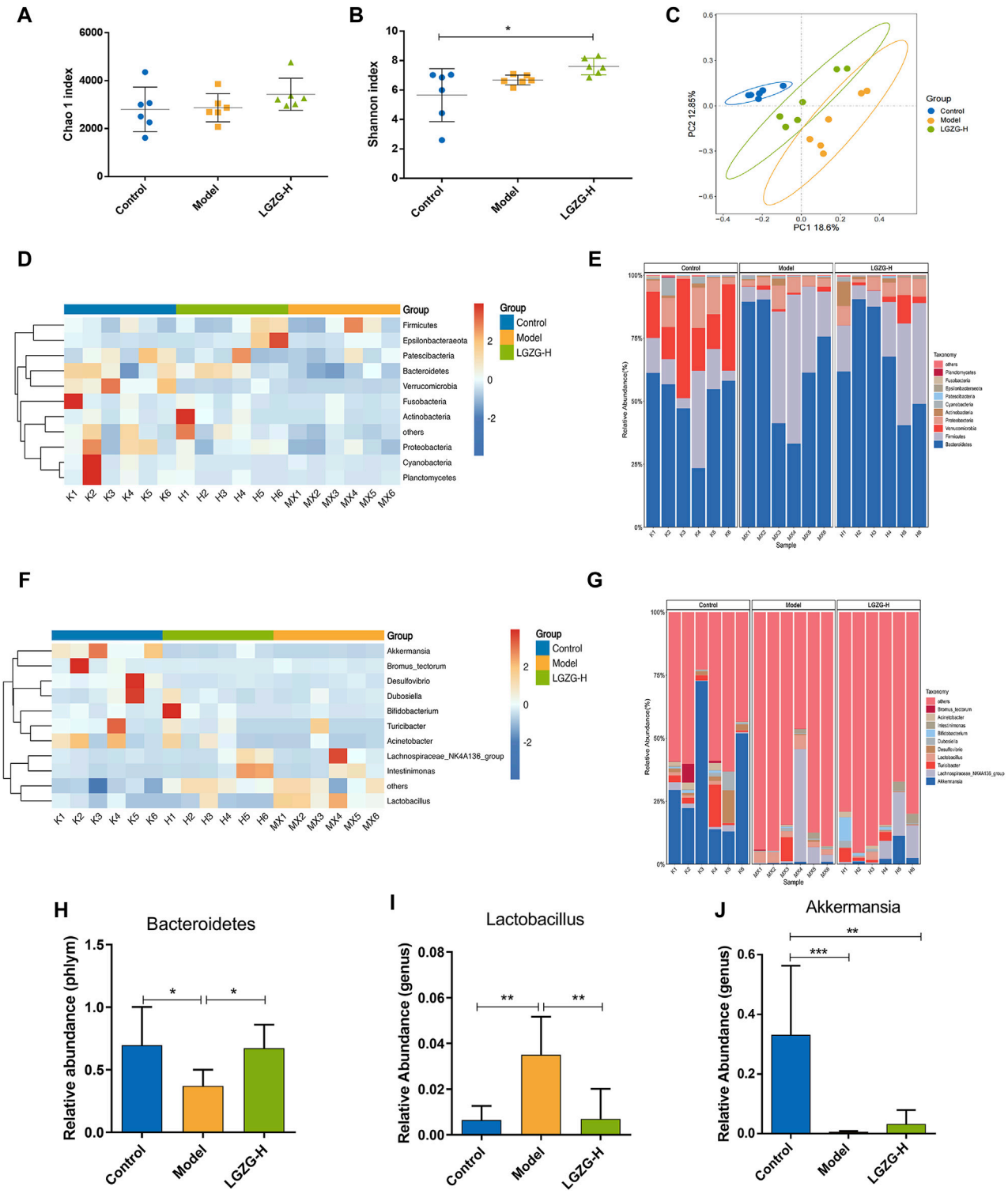


FIGURE 8
Effects of LGZG oral solution on the composition of gut microbiota. **(A)** Chao one index. **(B)** Shannon index. **(C)** The principal co-ordinates analysis (PCoA) plot. **(D, E)** Heatmaps and histograms of gut microbiota composition at the phylum level (top 10 relative abundance). **(F, G)** Heatmaps and histograms gut microbiota composition at the genus level (top 10 relative abundance). **(H–J)** Relative abundance of *Bacteroides*, *lactobacillus* and Akkermansia. Data are presented as mean ± SD (n = 6). *$p < 0.05$, **$p < 0.01$ and **$p < 0.001$.

free BAs and glycine or taurine and 7α/β-dehydroxylation-mediated conversion of primary BA to secondary BA (Ridlon et al., 2016). BSH-producing microbes, such as *Bacteroides* and *Lactobacillus*, are involved in transforming BAs (Chen MJ. et al., 2021). The abundance of *Lactobacillus* has been reported to be considerably increased, whereas that of Bacteroidota to be

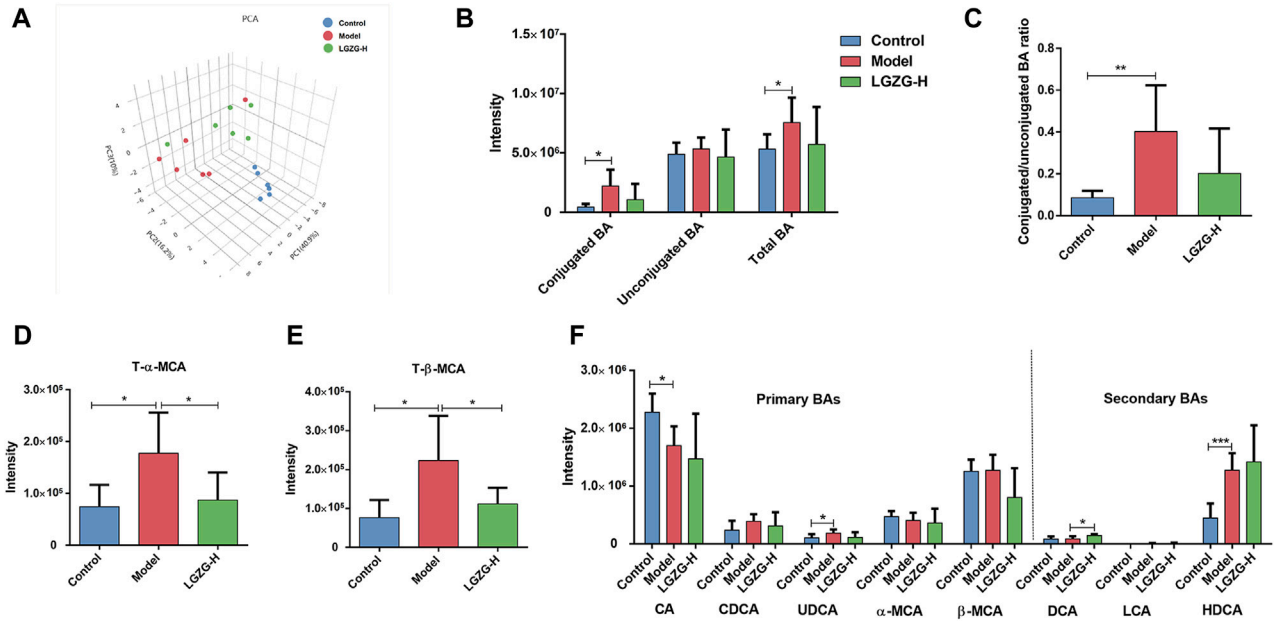


FIGURE 9
Effects of LGZG oral solution on the BA profiles. **(A)** Principal component analysis (PCA) plot. **(B)** The total BA level, conjugated BA level and unconjugated BA level. **(C)** The ratio of conjugated to unconjugated BAs. **(D)** The T-α-MCA level. **(E)** The T-β-MCA level. **(F)** The levels of typical primary and secondary BAs. Data are presented as mean ± SD (n = 6). *$p < 0.05$, **$p < 0.01$ and ***$p < 0.001$.

markedly decreased in the fecal samples of mice fed with a high-fat diet (Sun et al., 2022). Herein, LGZG oral solution intervention decreased the abundance of *Lactobacillus* and increased the abundance of Bacteroidota in mice. Additionally, although studies on the role of *Akkermansia* in BA metabolism processes are limited, this genus has been associated with increased levels of unconjugated BAs in the gastrointestinal tract (Dong et al., 2021).

BAs are derived from the catabolism of cholesterol and are the main metabolites of the bile. They enter the intestine through the bile ducts and participate in the enterohepatic cycle. A classical synthesis pathway of BA can produce cholic acid (CA) and chenodeoxycholic acid (CDCA). The classical synthetic pathway is catalyzed by CYP7A1, which generates CA under the action of CYP8B1 and CYP27A1, and CDCA in the absence of CYP8B1 (Thomas et al., 2008). CA and CDCA are primary BAs, which combine with glycine and taurine to form bound BAs; most of the bound BAs are reabsorbed at the end of the ileum, while the rest are excreted (Yang et al., 2021). Hepatocyte injury leads to abnormal BA metabolism in the body, resulting in increased levels of total BA. Different BAs exhibit different affinity and transcriptional activation of FXR, with CDCA, DCA, and lithocholic acid being the potent natural ligands for FXR, and the conjugated BAs, such as T-α-MCA and T-β-MCA, being the natural antagonists of FXR that promote BA synthesis and enterohepatic circulation (Panzitt and Wagner, 2021). The results of this study showed that LGZG oral solution considerably reversed the high-fat diet-induced alterations in the intestinal flora and altered BA profiles, including a notable increase in DCA levels, an FXR and TGR5 activator, and a marked decrease in T-α/β-MCA levels, an FXR inhibitor. Altogether, these results suggest that LGZG oral solution promotes BA metabolism. Additionally, BA acts on FXR and TGR5 to regulate the activity of CYP7A1, reducing BA synthesis and BA-mediated injury in the liver. FXR inhibits the activity of CYP7A1 and CYP8B1 by inducing SHP expression in the liver. FXR activation considerably reduced TG and cholesterol levels in the liver of the model group, inhibiting the expression of fat-synthesizing genes, and thus, inhibiting SREBP1 expression. In contrast, FXR receptors in the intestinal tract were upregulated, inducing the expression of the target gene FGF15/19. FGF15/19 enters the liver *via* the portal vein and acts through the hepatocyte membrane receptor FGFR4, activating a series of signaling molecules, and ultimately inhibiting hepatic CYP7A1 expression (Chiang and Ferrell, 2020). TGR5 activation exhibits hepatoprotective effects in the presence of liver injury and BA deposition. Reportedly, treating high-fat diet-fed mice with INT-777, a TGR5-specific agonist, reduced body weight gain and serum TG levels (Keitel et al., 2019b). Studies have shown that activating BA receptors FXR and TGR5 pathway could play a role in regulating glucose and lipid metabolism, inflammatory response, cell proliferation, and apoptosis (Stepanov et al., 2013). This study showed that the LGZG oral solution effectively increased the FXR and TGR5 expression in the liver and intestinal tissues of MASLD mice. Additionally, following the LGZG treatment, the expression of SHP, FGFR4, and FGF15/19 were upregulated, whereas that of CYP7A1, CYP8B1, and SREBP-1C was downregulated. Altogether, these findings indicate that LGZG oral solution could potentially modulate the progression of MASLD *via* the FXR/TGR5 pathway.

10.3389/fphar.2024.1426049

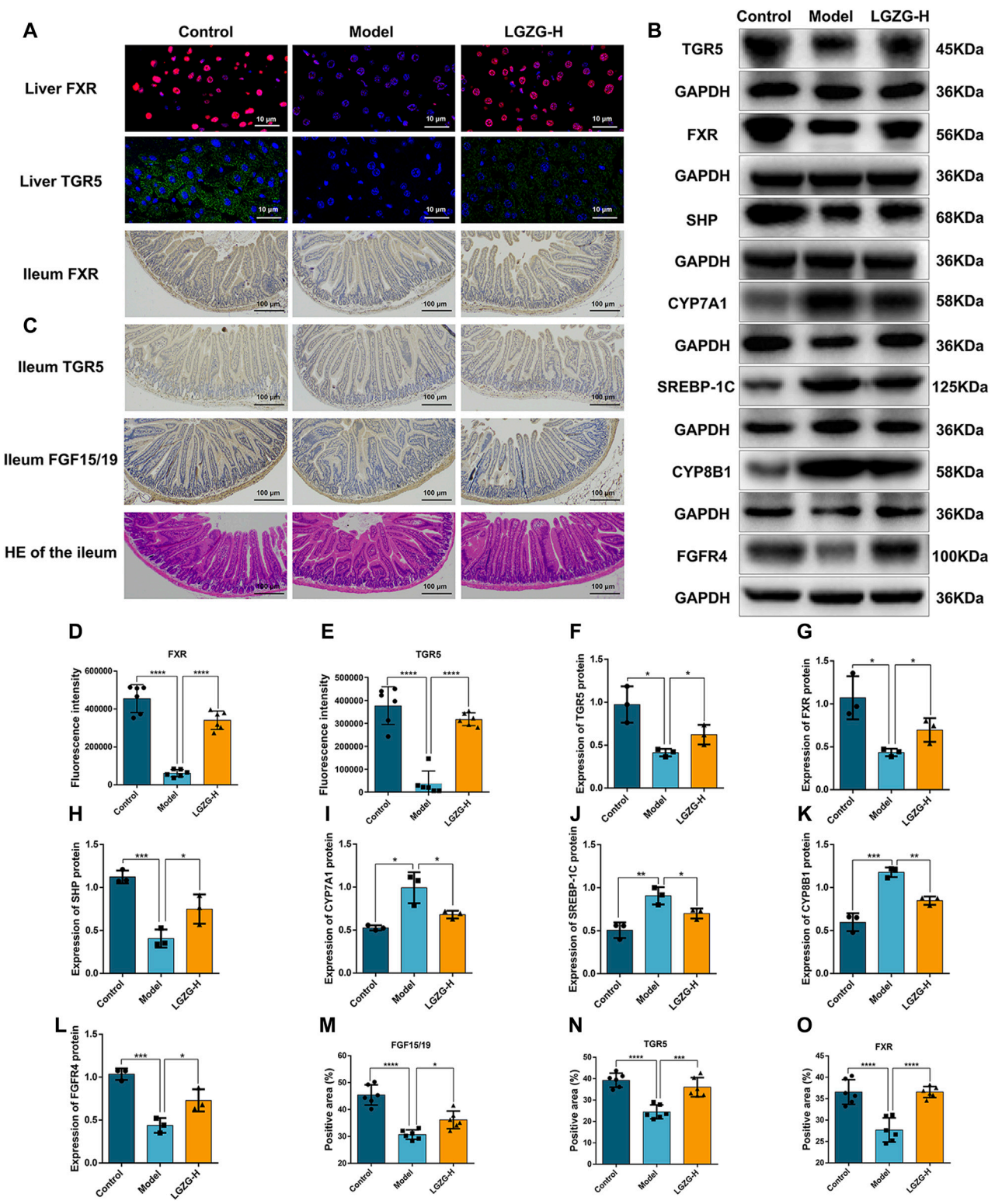


FIGURE 10
Effects of LGZG oral solution on hepatic lipid and bile acid synthesis. **(A)** The expression of FXR and TGR5 in the liver was estimated by immunofluorescence (n = 6). **(B)** The protein expression of FXR, TGR5, CYP7A1, SHP, CYP8B1, SREBP-1C and FGFR4 in the liver was determined by Western blotting (n = 3). **(C)** Immunohistochemical staining of FXR,TGR5, and FGF15/19 in the ileum and HE staining of ileum (n = 6). **(D, E)** Fluorescence intensity analysis of TGR5 and FXR (n = 6). **(F–L)** Grey-scale quantitative analysis of liver index. **(M–O)** Quantitative analysis of ileum index. Data are presented as mean ± SD. *$p < 0.05$, **$p < 0.01$, ***$p < 0.001$ and ****$p < 0.0001$.

## 5 Conclusion

In summary, the LGZG oral solution is a promising therapeutic approach to regulating lipid metabolism, inflammation, and oxidative stress to reduce pathological damage in patients with MASLD. Its potential mechanism of action may involve modulating gut microbiota and BA metabolism, thereby affecting the FXR/TGR5 pathway. However, additional research is required to fully elucidate the precise molecular mechanism and target of this therapeutic effect.

## Data availability statement

The data presented in the study are deposited in the NCBI repository, accession number PRJNA1145154.

## Ethics statement

All experimental procedures were carried out in accordance with the Institutional standards of animal humanistic care. The procedures followed in this study were approved by the Animal Research Ethics Committee of Liaoning University of Traditional Chinese Medicine, with which the informed consent for clinical research was signed (NO. 210000420230204). The study was conducted in accordance with the local legislation and institutional requirements.

## Author contributions

JW: Conceptualization, Writing–original draft. JZ: Writing–review and editing. YY: Methodology, Writing–review and editing. YL: Writing–review and editing. HC: Writing–review and editing. RG: Writing–review and editing. LZ: Writing–review and editing. ML: Writing–review and editing. ZZ: Writing–review and editing. XL: Funding acquisition, Writing–review and editing. LK: Funding acquisition, Writing–review and editing.

## Funding

The author(s) declare that financial support was received for the research, authorship, and/or publication of this article. This work was supported by the National Natural Science Foundation of China (Grant numbers 82204629), Basic Scientific Research Project for Colleges and Universities, Liaoning Provincial Department of Education (No. LJKQZ20222384), China Postdoctoral Science Foundation (2022MD713762), the Liaoning Province Natural Science Foundation doctoral foundation (No. 2022-BS-197), the Natural Science Project of Liaoning University of Traditional Chinese Medicine (2021LZY009).

## Acknowledgments

The authors sincerely thank the reviewers for their comments.

## Conflict of interest

The authors declare that the research was conducted in the absence of any commercial or financial relationships that could be construed as a potential conflict of interest.

## Publisher's note



## References

Bing, H., and Li, Y. L. (2022). The role of bile acid metabolism in the occurrence and development of NAFLD. *Front. Mol. Biosci.* 9, 1089359. doi:10.3389/fmolb.2022.1089359

Cai, J., Rimal, B., Jiang, C., Chiang, J. Y. L., and Patterson, A. D. (2022). Bile acid metabolism and signaling, the microbiota, and metabolic disease. *Pharmacol. Ther.* 237, 108238. doi:10.1016/j.pharmthera.2022.108238

Cao, L., Xu, E., Zheng, R., Zhangchen, Z., Zhong, R., Huang, F., et al. (2022). Traditional Chinese medicine Lingguizhugan decoction ameliorate HFD-induced hepatic-lipid deposition in mice by inhibiting STING-mediated inflammation in macrophages. *Chin. Med.* 17 (1), 7. doi:10.1186/s13020-021-00559-3

Castellanos-Jankiewicz, A., Guzman-Quevedo, O., Fenelon, V. S., Zizzari, P., Quarta, C., Bellocchio, L., et al. (2021). Hypothalamic bile acid-TGR5 signaling protects from obesity. *Cell Metab.* 33 (7), 1483–1492.e10. doi:10.1016/j.cmet.2021.04.009

Castro-Narro, G. E., and Rinella, M. E. (2024). The new hepatic steatosis nomenclature. No more NAFLD. *Rev. Gastroenterol. Mex. Engl. Ed.* 89 (2), 312–313. doi:10.1016/j.rgmxen.2024.02.002

Chen, J., and Vitetta, L. (2020). Gut microbiota metabolites in NAFLD pathogenesis and therapeutic implications. *Int. J. Mol. Sci.* 21 (15), 5214. doi:10.3390/ijms21155214

Chen, M. J., Liu, C., Wan, Y., Yang, L., Jiang, S., Qian, D. W., et al. (2021a). Enterohepatic circulation of bile acids and their emerging roles on glucolipid metabolism. *Steroids* 165, 108757. doi:10.1016/j.steroids.2020.108757

Chen, Y., Zhou, J., and Wang, L. (2021b). Role and mechanism of gut microbiota in human disease. *Front. Cell Infect. Microbiol.* 11, 625913. doi:10.3389/fcimb.2021.625913

Chiang, J. Y. L., and Ferrell, J. M. (2020). Bile acid receptors FXR and TGR5 signaling in fatty liver diseases and therapy. *Am. J. Physiol. Gastrointest. Liver Physiol.* 318 (3), G554–G573. doi:10.1152/ajpgi.00223.2019

Clifford, B. L., Sedgeman, L. R., Williams, K. J., Morand, P., Cheng, A., Jarrett, K. E., et al. (2021). FXR activation protects against NAFLD via bile-acid-dependent reductions in lipid absorption. *Cell Metab.* 33 (8), 1671–1684.e4. doi:10.1016/j.cmet.2021.06.012

Dong, S., Zhu, M., Wang, K., Zhao, X., Hu, L., Jing, W., et al. (2021). Dihydromyricetin improves DSS-induced colitis in mice via modulation of fecal-bacteria-related bile acid metabolism. *Pharmacol. Res.* 171, 105767. doi:10.1016/j.phrs.2021.105767

Edgar, R. C. (2010). Search and clustering orders of magnitude faster than BLAST. *Bioinformatics* 26 (19), 2460–2461.

Fang, J., Yu, C. H., Li, X. J., Yao, J. M., Fang, Z. Y., Yoon, S. H., et al. (2022). Gut dysbiosis in nonalcoholic fatty liver disease: pathogenesis, diagnosis, and therapeutic implications. *Front. Cell Infect. Microbiol.* 12, 997018. doi:10.3389/fcimb.2022.997018

Fang, K., Wu, F., Chen, G., Dong, H., Li, J., Zhao, Y., et al. (2019). Diosgenin ameliorates palmitic acid-induced lipid accumulation via AMPK/ACC/CPT-1A and

SREBP-1c/FAS signaling pathways in LO2 cells. *BMC Complement. Altern. Med.* 19 (1), 255. doi:10.1186/s12906-019-2671-9

Feng, J., Liu, Y., Chen, J., Bai, Y., He, J., Cao, H., et al. (2022). Marine chitooligosaccharide alters intestinal flora structure and regulates hepatic inflammatory response to influence nonalcoholic fatty liver disease. *Mar. Drugs* 20 (6), 383. doi:10.3390/md20060383

Guzior, D. V., and Quinn, R. A. (2021). Review: microbial transformations of human bile acids. *Microbiome* 9 (1), 140. doi:10.1186/s40168-021-01101-1

Hsu, C. L., and Loomba, R. (2024). From NAFLD to MASLD: implications of the new nomenclature for preclinical and clinical research. *Nat. Metab.* 6 (4), 600–602. doi:10.1038/s42255-024-00985-1

Huang, X. J., He, C. J., Liang, S., Wang, J., Li, J., Yang, G. Z., et al. (2020). Veratrilla baillonii franch could alleviate lipid accumulation in LO2 cells by regulating oxidative, inflammatory, and lipid metabolic signaling pathways. *Front. Pharmacol.* 11, 575772. doi:10.3389/fphar.2020.575772

Katafuchi, T., and Makishima, M. (2022). Molecular basis of bile acid-FXR-FGF15/19 signaling Axis. *Int. J. Mol. Sci.* 23 (11), 6046. doi:10.3390/ijms23116046

Keitel, V., Droge, C., and Haussinger, D. (2019a). Targeting FXR in cholestasis. *Handb. Exp. Pharmacol.* 256, 299–324. doi:10.1007/164_2019_231

Keitel, V., Stindt, J., and Haussinger, D. (2019b). Bile acid-activated receptors: GPBAR1 (TGR5) and other G protein-coupled receptors. *Handb. Exp. Pharmacol.* 256, 19–49. doi:10.1007/164_2019_230

Lee, B. P., Dodge, J. L., and Terrault, N. A. (2024). National prevalence estimates for steatotic liver disease and subclassifications using consensus nomenclature. *Hepatology* 79 (3), 666–673. doi:10.1097/HEP.0000000000000604

Li, X., Xu, G., Wei, S., Zhang, B., Yao, H., Chen, Y., et al. (2019). Lingguizhugan decoction attenuates doxorubicin-induced heart failure in rats by improving TT-SR microstructural remodeling. *BMC Complement. Altern. Med.* 19 (1), 360. doi:10.1186/s12906-019-2771-6

Liu, F., Duan, C., Zhang, J., and Li, X. (2020). Cantharidin-induced LO2 cell autophagy and apoptosis via endoplasmic reticulum stress pathway *in vitro*. *J. Appl. Toxicol.* 40 (12), 1622–1635. doi:10.1002/jat.4022

Liu, M. T., Huang, Y. J., Zhang, T. Y., Tan, L. B., Lu, X. F., and Qin, J. (2019). Lingguizhugan decoction attenuates diet-induced obesity and hepatosteatosis via gut microbiota. *World J. Gastroenterol.* 25 (27), 3590–3606. doi:10.3748/wjg.v25.i27.3590

Ma, Q., Li, Y., Li, P., Wang, M., Wang, J., Tang, Z., et al. (2019). Research progress in the relationship between type 2 diabetes mellitus and intestinal flora. *Biomed. Pharmacother.* 117, 109138. doi:10.1016/j.biopha.2019.109138

Molinaro, A., and Marschall, H. U. (2022). Bile acid metabolism and FXR-mediated effects in human cholestatic liver disorders. *Biochem. Soc. Trans.* 50 (1), 361–373. doi:10.1042/BST20210658

Nogal, A., Valdes, A. M., and Menni, C. (2021). The role of short-chain fatty acids in the interplay between gut microbiota and diet in cardio-metabolic health. *Gut Microbes* 13 (1), 1–24. doi:10.1080/19490976.2021.1897212

Panzitt, K., and Wagner, M. (2021). FXR in liver physiology: multiple faces to regulate liver metabolism. *Biochim. Biophys. Acta Mol. Basis Dis.* 1867 (7), 166133. doi:10.1016/j.bbadis.2021.166133

Paternostro, R., and Trauner, M. (2022). Current treatment of non-alcoholic fatty liver disease. *J. Intern Med.* 292 (2), 190–204. doi:10.1111/joim.13531

Qiao, J. T., Cui, C., Qing, L., Wang, L. S., He, T. Y., Yan, F., et al. (2018). Activation of the STING-IRF3 pathway promotes hepatocyte inflammation, apoptosis and induces metabolic disorders in nonalcoholic fatty liver disease. *Metabolism* 81, 13–24. doi:10.1016/j.metabol.2017.09.010

Raza, S., Rajak, S., Upadhyay, A., Tewari, A., and Anthony Sinha, R. (2021). Current treatment paradigms and emerging therapies for NAFLD/NASH. *Front. Biosci. Landmark Ed.* 26 (2), 206–237. doi:10.2741/4892

Ridlon, J. M., Harris, S. C., Bhowmik, S., Kang, D. J., and Hylemon, P. B. (2016). Consequences of bile salt biotransformations by intestinal bacteria. *Gut Microbes* 7 (1), 22–39. doi:10.1080/19490976.2015.1127483

Stepanov, V., Stankov, K., and Mikov, M. (2013). The bile acid membrane receptor TGR5: a novel pharmacological target in metabolic, inflammatory and neoplastic disorders. *J. Recept Signal Transduct. Res.* 33 (4), 213–223. doi:10.3109/10799893.2013.802805

Sun, J., Fan, J., Li, T., Yan, X., and Jiang, Y. (2022). Nuciferine protects against high-fat diet-induced hepatic steatosis via modulation of gut microbiota and bile acid metabolism in rats. *J. Agric. Food Chem.* 70 (38), 12014–12028. doi:10.1021/acs.jafc.2c04817

Thomas, C., Pellicciari, R., Pruzanski, M., Auwerx, J., and Schoonjans, K. (2008). Targeting bile-acid signalling for metabolic diseases. *Nat. Rev. Drug Discov.* 7 (8), 678–693. doi:10.1038/nrd2619

Xu, J., Wang, R., You, S., Zhang, L., Zheng, P., Ji, G., et al. (2020). Traditional Chinese medicine Lingguizhugan decoction treating non-alcoholic fatty liver disease with spleen-yang deficiency pattern: study protocol for a multicenter randomized controlled trial. *Trials* 21 (1), 512. doi:10.1186/s13063-020-04362-7

Yan, C., Zhang, Y., Zhang, X., Aa, J., Wang, G., and Xie, Y. (2018). Curcumin regulates endogenous and exogenous metabolism via Nrf2-FXR-LXR pathway in NAFLD mice. *Biomed. Pharmacother.* 105, 274–281. doi:10.1016/j.biopha.2018.05.135

Yang, C., Yang, L., Yang, Y., Wan, M., Xu, D., Pan, D., et al. (2023). Effects of flaxseed powder in improving non-alcoholic fatty liver by regulating gut microbiota-bile acids metabolic pathway through FXR/TGR5 mediating. *Biomed. Pharmacother.* 163, 114864. doi:10.1016/j.biopha.2023.114864

Yang, L., Lin, W., Nugent, C. A., Hao, S., Song, H., Liu, T., et al. (2017). Lingguizhugan decoction protects against high-fat-diet-induced nonalcoholic fatty liver disease by alleviating oxidative stress and activating cholesterol secretion. *Int. J. Genomics* 2017, 2790864. doi:10.1155/2017/2790864

Yang, M., Gu, Y., Li, L., Liu, T., Song, X., Sun, Y., et al. (2021). Bile acid-gut microbiota Axis in inflammatory bowel disease: from bench to bedside. *Nutrients* 13 (9), 3143. doi:10.3390/nu13093143

Zhai, Y., Zhou, W., Yan, X., Qiao, Y., Guan, L., Zhang, Z., et al. (2022). Astragaloside IV ameliorates diet-induced hepatic steatosis in obese mice by inhibiting intestinal FXR via intestinal flora remodeling. *Phytomedicine* 107, 154444. doi:10.1016/j.phymed.2022.154444

Zhang, M., and Yang, X. J. (2016). Effects of a high fat diet on intestinal microbiota and gastrointestinal diseases. *World J. Gastroenterol.* 22 (40), 8905–8909. doi:10.3748/wjg.v22.i40.8905

Zhu, M., Hao, S., Liu, T., Yang, L., Zheng, P., Zhang, L., et al. (2017). Lingguizhugan decoction improves non-alcoholic fatty liver disease by altering insulin resistance and lipid metabolism related genes: a whole trancriptome study by RNA-Seq. *Oncotarget* 8 (47), 82621–82631. doi:10.18632/oncotarget.19734

frontiers | Frontiers in Pharmacology

TYPE Original Research
PUBLISHED 16 August 2024
DOI 10.3389/fphar.2024.1446244



OPEN ACCESS

EDITED BY
Xiliang Du,
Jilin University, China

REVIEWED BY
Tao Yi,
Hong Kong Baptist University, Hong Kong SAR, China
Zhikun Wang,
Hebei Province Traditional Chinese Medicine Hospital, China

*CORRESPONDENCE
Huayi Liu,
15900369830@163.com

RECEIVED 09 June 2024
ACCEPTED 24 July 2024
PUBLISHED 16 August 2024

CITATION
Lu Y, Liu H, Shang J, Mao Y, Meng L and Gao C (2024) Effects of Weizhuan'an on rats with precancerous lesions of gastric cancer based on regulating gastric mucosal microflora and inflammatory factors.
*Front. Pharmacol.* 15:1446244.
doi: 10.3389/fphar.2024.1446244



# Effects of Weizhuan'an on rats with precancerous lesions of gastric cancer based on regulating gastric mucosal microflora and inflammatory factors

Yuting Lu [1,2], Huayi Liu [3]*, Jiaju Shang[3], Yijia Mao[2,3], Lingkai Meng[2,3] and Changbai Gao[4]

[1]Guangdong Second Provincial General Hospital, Integrated Chinese and Western Medicine Postdoctoral Research Station, School of Medicine, Jinan University, Guangzhou, Guangdong, China, [2]Graduate School, Tianjin University of Traditional Chinese Medicine, Tianjin, China, [3]Department of Digestion, Tianjin Academy of Traditional Chinese Medicine Affiliated Hospital, Tianjin, China, [4]Department of Nephropathy, Second Affiliated Hospital of Tianjin University of Traditional Chinese Medicine, Tianjin, China

**Objectives:** This study aimed to observe the intervention of Weizhuan'an prescription on rats with precancerous lesions of gastric cancer (PLGC) as well as its regulation on gastric mucosal microflora and inflammatory factors and explore the pharmacodynamic mechanisms of Weizhuan'an Formula.

**Methods:** The rats were classified into the blank control group (BCG); low-, medium-, and high-dose groups of Weizhuan'an prescription (LDG, MDG, and HDG, respectively); and natural recovery group (NRG) at random. The rats in the traditional Chinese medicine (TCM) group were given corresponding doses of Weizhuan'an formula, while the rats in the NRG and BCG were given an equivalent volume of distilled water for 12 weeks. After that, gastric mucosa samples of rats were collected to observe the general and pathological changes in the gastric mucosa; the changes in gastric mucosal microflora were detected by 16S rDNA amplicon sequencing, and the inflammatory factors were analyzed by cytokine antibody microarray and Western blotting.

**Results:** The results suggest that compared with the BCG, the pathology of gastric mucosa and gastric mucosal microflora and inflammatory factors in rats with PLGC have changed significantly, while Weizhuan'an formula effectively improved them, especially in the MDG and HDG ($p < 0.05$). Compared with the NRG, the abundance of probiotics such as *Lactobacillus* and *Veillonella* were increased, while the abundance of pathogens such as *Proteobacteria* and *Pseudomonas* was decreased ($p < 0.05$, $p < 0.01$), and the relative contents of IL-2, IL-4, IL-13, and MCP-1 in gastric mucosa were decreased ($p < 0.05$). Moreover, it can upregulate the DNA-binding transcriptional regulator, ABC type multidrug transport system, and related enzymes and affect the signaling pathways such as viral protein interaction with cytokine and cytokine receptor

and T cell receptor signaling pathway significantly ($p < 0.05$, $p < 0.01$), which can promote drug absorption and utilization and repair damaged gastric mucosa.

**Conclusion:** The study confirmed that Weizhuan'an prescription can treat rats with PLGC by regulating gastric mucosal microflora and inflammatory factors.

KEYWORDS

precancerous lesion of gastric cancer, gastric mucosa, traditional Chinese medicine, gastric mucosal microflora, inflammatory factors, Weizhuan'an prescription

# 1 Introduction

Gastric cancer (GC) is one of the commonest gastrointestinal malignant tumors worldwide, which seriously threatens human health owing to its rising morbidity along with high mortality (Fitzmaurice et al., 2017; Zheng et al., 2022). It is difficult to apply primary prevention due to the complicated causes of GC, and therefore the intervention on precancerous lesions of gastric cancer (PLGC) has always been a hot spot in clinical research. According to the Chinese Integrated Clinical Management Guidelines for Precancerous Lesions of Gastric Cancer (Wang et al., 2022), common therapies for PLGC include eradicating Hp (positive cases) and short-term use of acid suppressants, mucosal protectors, etc., as well as using endoscopic surgical techniques combined with botanical drugs to treat high-grade dysplasia and early GC. Folic acid, antioxidant vitamins, etc. can also reduce the risk of GC to a certain extent. Long-term use of Western medicine is usually avoided in clinical practice due to the common side effects of using them, such as abdominal pain, nausea, and gastrointestinal bloating. As the treatment cycle for PLGC is relatively long, botanical drugs are widely used due to its advantages of good efficacy and minimal side effects. The combination of traditional Chinese medicine and Western medicine has significant advantages in treating PLGC. There is a complex gastrointestinal microecosystem in the body, and there are various species of gastric microflora, although they are fewer than intestinal microflora species (Nardone and Compare, 2015; Sung et al., 2016). Studies have confirmed that the structure and abundance of gastric microflora in patients with GC and PLGC are significantly different from that in the healthy controls. The imbalance of gastric microflora can induce gastric diseases such as gastritis and gastric ulcer, which is tightly related to the occurrence of GC (Sohn et al., 2017; Yu et al., 2017). Moreover, the relationship between the gastric inflammatory environment and GC and PLGC is another research highlight at present (Gullo et al., 2019; Zhou and Yang, 2019). A normal immune response can repair damaged tissues and maintain homeostasis. However, when the body is in a state of repeated infection or injury, inflammatory stimulation will inhibit the repair of damaged gastric mucosa (Sounni and Noel, 2013), eventually leading to canceration of gastric mucosal epithelial cells (Schulz et al., 2019). Some studies (Khatoon et al., 2018; Sultana et al., 2018) have suggested that although the imbalance of intragastric microflora may mediate inflammation to damage the gastric mucosa, the final clinical outcome of patients depends on the body's inflammatory response. Conversely, the strength of the inflammatory response is also influenced by the intragastric microenvironment (Bockerstett and DiPaolo, 2017; Chen et al., 2018). Existing studies have confirmed that traditional Chinese medicine (TCM) has obvious effects in inhibiting gastric pathogenic bacteria (Lian et al., 2017; Deng, 2020), regulating inflammatory factors, and repairing gastric mucosal damage (Li et al., 2015; Yu et al., 2018). For the most part, there is still a lack of experimental research on the regulation of gastric microecological immunity by TCM for treating PLGC. Weizhuan'an prescription, created by the late Professor Gao Jinliang, a famous gastroenterologist, is an empirical prescription for the treatment of PLGC. Our previous research has confirmed that Weizhuan'an prescription can effectively relieve the clinical symptoms of patients and improve the pathology of the gastric mucosa (Wang et al., 2017; Meng et al., 2020). In order to clarify its mechanism, this experiment from the perspective of regulating gastric mucosal microflora and inflammatory factors provides a view to opening up a new direction for clinical application.

# 2 Experimental materials

## 2.1 Experimental animals

Hundred male and healthy SPF Wistar rats, aged 6 weeks, weighing 175 ± 25 g, were provided by SPF (Beijing) BIOTECHNOLOGY Co., Ltd., the animal license No. is SCXK (Beijing) 2019-0010. It was raised in the SPF Laboratory room of the Animal Experiment Center of Tianjin University of Traditional Chinese Medicine (TUTCM), room No. 337. The room temperature was 23 ± 2°C, and the relative humidity was 55 ± 5%, with a 12-h light and 12-h dark cycle. This experiment complies with the regulations of the Ethics Committee of the Animal Experiment Center of TUTCM, batch No. TCM-LAEC2020076.

## 2.2 Experimental medicine

The composition of Weizhuan'an prescription is as follows: 15 g Radix pseudostellariae (batch No. 21010101), 15 g *Poria cocos* (batch No. 194200901), 10 g fried *Atractylodes macrocephala* Koidz (batch No. 200911006), 30 g *Astragalus mongholicus* (batch No. 2103260021), 10 g *Curcuma zedoaria* (batch No. 2104050162), 30 g Hedyotis diffusa Willd (batch No. 201211002), 30 g *Polygonum cuspidatum* (batch No. 255190101), and 3 g pseudo-ginseng (batch No. 901180602). Chinese medicinal materials were purchased from Anhui Xiehecheng Co., Ltd., Beijing Hongji Pharmaceutical Co., Ltd., Beijing Qiancao Herbal Pieces Co., Ltd., and Bozhou Huqiao Pharmaceutical Co., Ltd. The concentrated liquid of botanical drugs was decocted by the national standard preparation and provided by the pharmacy of Tianjin Academy of Traditional Chinese Medicine Affiliated Hospital. The specific method for decoction is as follows: soak the dried medicinal

botanical drugs (except pseudo-ginseng) and eight times of cold distilled water in the casserole for 30 min. Boil it over high heat and then turn to low heat and decoct for 30 min. Then, filter the decoction to remove the drugs and concentrate the filtered liquid to 200 mL. Store in the refrigerator of the Animal Experiment Center of TUTCM at 4°C away in dark conditions. Pseudo-ginseng was stored in powder form at room temperature and away from light. The main extract of Weizhuan'an prescription was quantitatively analyzed by high-performance liquid chromatography (HPLC) and liquid chromatography-tandem mass spectrometry (LC-MS/MS). The results showed the presence of notoginsenoside R1 (27.0 mg·$L^{-1}$), ginsenoside Rb1 (87.2 mg·$L^{-1}$), ginsenoside Rg1 (111 mg·$L^{-1}$), kaempferol (29.6 mg·$L^{-1}$), quercetin (1.99 mg·$L^{-1}$), astragaloside IV (20.1 mg·$L^{-1}$), polydatin (95.3 mg·$L^{-1}$), heterophyllin (24.7 mg·$L^{-1}$), atractylenolide II (1.21 mg·$L^{-1}$), atractylenolide III (10.0 mg·$L^{-1}$), and poricoic acid A (0.101 mg·$L^{-1}$).

95% N-methyl-N′-nitro-N-nitrosoguanidine (MNNG), provided by the Tokyo Chemical Industry Development Co., Ltd., specification: 25 g*1 bottle, batch No. P1734775, was stored in the refrigerator of the Animal Experiment Center of TUTCM at 4°C away from light. The SPF compound diet for rats was formulated by Beijing HFK Bioscience Co., Ltd., in the proportion of 99.77% ordinary diet and 0.2% sodium chloride and 0.03% ranitidine, production license No. Beijing (2019) 06076. Purified sodium chloride was provided by Tianjin Zhiyuan Chemical Reagent Co., Ltd., specification: 500 g*1 bottle. Ranitidine was provided by Jiangxi Huiren Pharmaceutical Co., Ltd., specification: 0.15 g*30 tablets*1 bottle, batch No. H44021173. SPF ordinary diet for rats was provided by the Animal Experiment Center of TUTCM, and the basic ingredients are corn, flour, wheat bran, soybean meal, imported fish meal, oil, stone powder, calcium hydrogen phosphate, salt, complex microorganisms, and trace elements.

## 2.3 Experimental apparatus

CX31 microscope and graphic analysis system (Olympus, Japan); SH-118 electronic scale (Shengheng, China); RM2125 pathological microtome (Leica, Germany); 7FB Water Bath-Slide Drier (Xiaogan Yaguang, China); HP-D Sheet dryer (Tianjin Tianli Aviation, China); JBM-B Embedding machine (Tianjin Jiusheng, China); 101-1AB Electric blast drying oven (Tianjin Taisote, China); ASP200S totally enclosed vacuum biological tissue dehydrator (Leica, Germany); NovaSeq PE250 sequencer (Illumina, United States); rat inflammation array Q1 (QAR-INF-1) kit (RayBiotech, United States); InnoScan 300 Microarray scanner (Innopsys, France); Wellwash Versa Microplate Washer (Thermo Scientific, United States); RT-6100 Microplate Reader (Rayto, China); F6/10 Micropipette Grinder (Jingxin technology JX-FSTGRP, China); TGL-16gR Table-type High-speed Refrigerated Centrifuge (Shanghai Anting, China); DL-40B Desktop low-speed centrifuge (Shanghai Anting, China); Mini-4s Multifunctional centrifuge (Labfish, China); VM-300 Multifunctional vortex mixer (Labfish, China); 180-1600 Casting Stand (Shanghai Tanon, China); SK-O180-E Decolorization Shaker (DragonLAB, China); DYY-7C Transfer electrophoresis apparatus (Beijing Liuyi, China); VE180 Electrophoresis equipment Tanon, China); VE186 Transmembrane equipment (Shanghai Tanon, China); XB-50 Ice machine (Scientz, China); SCIENTZ-1500F Ultrasonic Processor (Scientz, China); 5200 Chemiluminescence Apparatus (Shanghai Tanon, China).

## 2.4 Experimental reagents

P0013B RIPA lysate (Beyotime Biotechnology, China); P1010 protease inhibitor (Beyotime Biotechnology, China); ST506 PMSF (100 mM) (Beyotime Biotechnology, China); P1081 phosphatase inhibitors (Beyotime Biotechnology, China); P0012 BCA protein quantitative detection kit (Beyotime Biotechnology, China); P0015 SDS-PAGE SDS-PAGE loading buffer (5X) (Beyotime Biotechnology, China); P0012A SDS-PAGE gel preparation kit (Beyotime Biotechnology, China); 26617 protein marker (Thermo, United States); ISEQ10100 PVDF membrane 0.22 μm (Millipore, United States); P0216 defatted milk powder (Beyotime Biotechnology, China); ST825 Tween-20 (Beyotime Biotechnology, China); P0018AS ECL chemiluminescent solution (Beyotime Biotechnology, China); 66009-1 β-actin (43KD) (Proteintech, United States); PB0059 IL-2 (18KD) (Boster, China); BA0980 IL-4 (17KD) (Boster, China); A00077-2 IL-13 (19KD) (Boster, China); BA 1843-2 MCP-1 (25KD) (Boster, China); SA00001-2 HRP-labeled goat anti-rabbit (Proteintech); SA00001-1 HRP-labeled goat anti-mouse (Proteintech); P0021A transfer buffer (Beyotime Biotechnology, China); P0014 electrophoretic buffer (Beyotime Biotechnology, China); ST673 TBS-T buffer (Beyotime Biotechnology, China); P0023 WB antibody diluent (Beyotime Biotechnology, China).

# 3 Experimental methods

## 3.1 Modeling method

After 1 week of adaptive feeding, the rats were randomly divided into two groups with a random number table: 14 in the blank control group (BCG) and 86 in the model control group (MCG). The MCG was established by compound methods. In the 1st–26th week, MNNG and distilled water were prepared into a 1 g·$L^{-1}$ stock solution and stored in a refrigerator at 4°C away from light every week. Then, the 100 μg·$mL^{-1}$ MNNG solution was diluted with clean drinking water and filled into black bottles and supplied *ad libitum* to rats every day. The SPF compound diet was also supplied ad libitum to rats. From the 27th–30th week, it was prepared into 20 μg·$mL^{-1}$ MNNG solution (the co-solvent shall be added in a ratio of 1 g MNNG to 10 mL dimethyl sulfoxide) and stored in refrigerator at 4°C away from light every week and then administered to the rats with the dose of 5 mL·$kg^{-1}$ through gastric tubes every day. The SPF ordinary diet was administered to rats in the ratio of eating for 1 day and fasting for 1.5 days. In addition, the BCG had *ad libitum* access to SPF ordinary diet and drinking water.

## 3.2 Determination of the model of PLGC

The pathological diagnosis standard referred to the *Chinese consensus on chronic gastritis* (Chinese Society of

Gastroenterology (CSGE), 2017). Moderate dysplasia and atrophy or intestinal metaplasia of gastric mucosa can confirm the success of modeling. From the 24th weekend, two rats from the MCG were randomly selected and killed based on the random number table fortnightly. Two tissues of gastric antral mucosa were taken and fixed with 4% paraformaldehyde, made into paraffin sections, and stained with hematoxylin and eosin (HE), and then the pathological changes were observed by using a light microscope. At the 30th weekend, the pathological section of the gastric mucosa in one of the selected rats showed inflammatory cell infiltration, moderate atrophy, and dysplasia, and the other showed mild intestinal metaplasia and moderate dysplasia, indicating that the model of PLGC was successfully established.

## 3.3 Drug intervention

After successful modeling, 76 rats in the MCG were divided into the low-dose group (LDG), middle-dose group (MDG), high-dose group (HDG), and natural recovery group (NRG) by random number table, with 19 rats in each group. Referring to the formula [the dose of the crude drug of rats ($g{\cdot}kg^{-1}$) = 143 $g{\cdot}d^{-1}$ of adult clinical crude drug dose/70 kg of adult weight × 6.25], we calculated the daily dose of the equivalent dosage of crude drug as 12.76 $g{\cdot}kg^{-1}$ (the extract is 7.284 $mg{\cdot}kg^{-1}$). The drug concentration gradient to the dose of the extract of the LDG, MDG, and HDG is 3.642, 7.284, and 14.570 $mg{\cdot}kg^{-1}$, respectively. In the 31st–42nd weeks, the rats in the LDG, MDG, and HDG were given a corresponding dose of Weizhuan'an (7 mL $kg^{-1}$) at 7:30–8:30 every morning, and the rats in the BCG and NRG were given an equal dose of distilled water.

## 3.4 Observation index

We draw up the diagnostic and scoring criteria for PLGC, referring to the pathological diagnosis and grading standard of *Chinese consensus on chronic gastritis* (CSGE, 2017) and *Endoscopic classification and grading criteria for chronic gastritis* (Association of Digestive Endoscopy, Chinese Medical Association (CMA), 2004). The quantified score: normal = 0; mild = 1; moderate = 2; severe = 3; early gastric cancer (EGC) = 4; advanced gastric cancer (AGC) = 5.

## 3.5 Sampling methods

All rats were starved for 36 h without water after the intervention, and then they were anesthetized by intraperitoneal injection of 0.3% pentobarbital sodium at 10 $mL{\cdot}kg^{-1}$. After that, the abdomen was quickly opened with sterile surgical scissors, done on a sterile operating table, and the whole stomach was taken out. After gentle washing with pH 6.8 phosphate buffer, they were cut along the greater curvature of the stomach, and four pieces of the gastric antrum mucosa were taken and rinsed in phosphate buffer. One piece of the gastric mucosa was stored in a 2-mL Eppendorf (EP) tube with 4% paraformaldehyde, away from light. Ten samples were taken from each group with a random number table, made into paraffin sections, stained with HE, and observed by a light microscope. Three pieces of gastric mucosa were added into 2-mL cryogenic vials, quickly frozen in liquid nitrogen, and stored at −80°C. Subsequently, 16S rDNA amplicon sequencing, cytokine antibody microarray, and Western blotting were performed following the standard method. All rats were killed by cervical dislocation after sampling.

## 3.6 16S rDNA amplicon sequencing operation procedure

Ten samples were taken from each group with a random number table. Subsequently, the deoxyribonucleic acid (DNA) of samples was extracted by cetyltrimethylammonium bromide (CTAB) buffer, and then polymerase chain reaction (PCR) amplification and purification were carried out. The library was constructed by using the NEBNext® Ultra™ IIDNA Library Prep Kit, and the qualification of the quality control of the library was confirmed by the quantitative detection with Qubit and quantitative real-time PCR (Q-PCR). The raw data were obtained by sequencing with NovaSeq PE250, and the clean read data were obtained by splicing and filtering, and then the final amplicon sequence variants (ASVs) were obtained by DADA2 denoising based on clean read data.

## 3.7 Cytokine antibody microarray procedure

The expression of inflammatory factors in gastric mucosa in each group was detected by the QAR-INF-1 kit. Ten gastric mucosa samples were randomly taken from each group. After all samples were lysed, the protein concentration of the cell lysate was detected by the BCA protein assay kit, and sampled 100 μL at 500 $\mu g{\cdot}mL^{-1}$. The glass slide was completely air-dried, and cytokine standard dilutions were prepared. The cytokine antibody microarray procedure was performed according to the manufacturer's manual: 1) add 100 μL sample diluent into each well, incubate for 1 h at room temperature, and block the slides. 2) Decant the buffer solution from the well, add 100 μL standard cytokines and sample into each well, and incubate overnight in a shaker at 4°C. 3) Wash the slide by using a microplate washer (Thermo Scientific Wellwash Versa). First, select 1X Wash Buffer I to wash the slide, each well with 250 μL buffer ten times, and each high-intensity vibration lasts for 10 s. Dilute 20X Wash Buffer I with deionized water. Then, select the 1X Wash Buffer II for washing, each well with 250 μL buffer six times, and each high-intensity vibration lasts for 10 s. Dilute 20X Wash Buffer II with deionized water. 4) Incubate with biotinylated antibody cocktail and wash. 5) Incubate with Cy3 equivalent dye-streptavidin and wash. 6) Fluorescence detection. Scan parameters: wavelength: 532 nm; resolution: 10 μm. 7) Adopt QAR-INF-1 data analysis software for data analysis.

## 3.8 Western blotting procedure

Three gastric mucosa samples were randomly selected from each group. The total protein of the gastric mucosa was extracted, and the concentration was detected by the BCA protein assay kit. Adjust all protein samples to a uniform concentration of 3 $\mu g{\cdot}\mu L^{-1}$. Add 5X

reduced protein loading buffer into the protein solution at the ratio of 4:1, and transfer to a boiling water bath for 5 min. Then, SDS-PAGE electrophoresis was carried out, the voltage of the concentrated gel was 70 V, and the voltage of the separated gel was 100 V at constant pressure. Add enough electrophoresis solution to the electrophoresis tank and load the sample for electrophoresis. Then, the protein was transferred to a membrane and placed for 60 min under a constant current of 200 mA, and the reaction was completed with primary and secondary antibodies, chemiluminescence, and automatic imaging. ImageJ software was used to analyze the gray value of the protein bands.

## 3.9 Statistical methods

The pathological analysis and Western blotting results of the gastric mucosa in rats were analyzed by Statistical Product Service Solutions (SPSS) 25.0. The measurement data of normal distribution were represented by mean standard deviation ($\bar{x} \pm s$), the paired *t* test was used in intra-group comparison, and the one-way ANOVA was used in inter-group comparison. The measurement data of non-normal distribution were expressed by interquartile range (IQR) *M* (*P25*; *P75*). The rank sum test was adopted for intra-group comparison, and the Kruskal–Wallis test was adopted for inter-group comparison. $p < 0.05$ indicated statistical differences.

The ASVs obtained by 16S rDNA amplicon sequencing were processed in two ways. First, by annotating the species of ASVs and then performing alpha diversity analysis, including alpha diversity index and inter-group difference analysis. Second, multi-sequence alignment was used for ASVs, and the phylogenetic tree was constructed. It was visually displayed by principal co-ordinates analysis (PCoA) and non-metric multidimensional scaling (NMDS), and the differentially abundant features of microflora were analyzed by Mothur metastats command (MetaStats) and linear discriminant analysis effect size (LEfSe). In addition, the correlation of microflora was calculated by *Spearman* correlation analysis, and the functional abundance of microflora was predicted by PICRUSt2 based on the clusters of orthologous groups (COG).

After the normalization of raw data obtained by cytokine antibody microarray by RayBiotech software, the resulting data are selected for analysis. The analysis method is moderated t-statistics, and the data package used is limma, from R/Bioconductor. Differential proteins were screened by *p-value* and logFC. The parameter threshold is that the fold change >1.2 or <0.83, that is, the absolute value of logFC >0.263, and $p < 0.05$. The Kyoto Encyclopedia of Genes and Genomes (KEGG) enrichment analysis was adopted to predict the functions of differential inflammatory factors.

# 4 Results

## 4.1 Pathology of the gastric mucosa in rats

The general conditions of the gastric mucosa of rats in each group can be observed in Figure 1A. It was found that the general condition of gastric mucosa in the BCG was the best, while that in the LDG, MDG, and HDG was improved to varying degrees, which was better than that in the NRG. The HE staining sections of rat gastric mucosa at the 42nd weekend are shown in Figure 1B. There was a significant difference in the pathological changes of the gastric mucosa among groups. In the BCG, the gastric mucosa of rats was in good condition, the morphology of gastric mucosa cells was regular, the number of intrinsic glands did not decrease, intestinal metaplasia and dysplasia did not exist, and there was no infiltration of monocytes, neutrophils, or cancer cells in the mucosa. In the NRG, the overall condition of the gastric mucosa was poor, the number of intrinsic glands in the gastric mucosa was reduced, there was higher infiltration of monocytes and neutrophils into gastric lamina propria, and the intestinal metaplasia area in some rats exceeded the total area of the gastric mucosa by one-third. It can be seen in Figure 1C that the pathological score of the BCG is the lowest while the NRG is the highest, that of the Weizhuan'an group was intermediate between the two groups, and that of the MDG and HDG was obviously improved. Specifically, there was no statistical difference in atrophy or canceration of rats in each group. Compared with the NRG, there were significant differences in the BCG, MDG, and HDG in terms of chronic inflammation, intestinal metaplasia, and dysplasia ($p < 0.05$). There were significant differences in each group compared with the NRG in terms of active inflammation ($p < 0.05$).

## 4.2 Relative abundance and abundance clustering of gastric mucosal microflora in rats

The histograms (top 10) and heat maps (top 35) of the relative abundance of gastric mucosal microflora of rats in phylum and genus levels were drawn with QIIME 2 based on the annotation of the microflora abundance table, which can be referred in Figure 2A. There were 46 bacterial phyla and 896 bacterial genera with significant differences between groups. The relative abundance of five phyla in the top 10 was more than 1%, *Firmicutes*, 54.45%; *Proteobacteria*, 33.63%; *Bacteroidota*, 4.34%; *Actinobacteriota*, 3.39%; and *Fusobacteriota*, 2.32%. The relative abundance of all genera in the top 10 was more than 1%, except for *Prevotella*.

## 4.3 Alpha diversity analysis

The diversity of microflora was evaluated by alpha diversity analysis. As shown in Figure 2B, compared with the species diversity of the NRG, there were significant differences in the BCG, MDG, and HDG ($p < 0.001$), among which the MDG was the most significant. The rarefaction curves of alpha diversity indices indicate that the average effective sequence is 6.9 w/sample. The rarefaction curves tend to be flat when the sequence is about 4.6 w (cutoff = 45945). In addition, the species accumulation boxplots of alpha diversity indices tend to be flat gradually when the number of samples is approximately 45, which shows that the sampling is reasonable and sufficient, and it is suitable for subsequent analysis. See Figure 2C for details.

## 4.4 Beta diversity analysis

It can be seen in Figure 3A that the first principal component (PC1) and the second (PC2) of the PCoA with weighted UniFrac

10.3389/fphar.2024.1446244

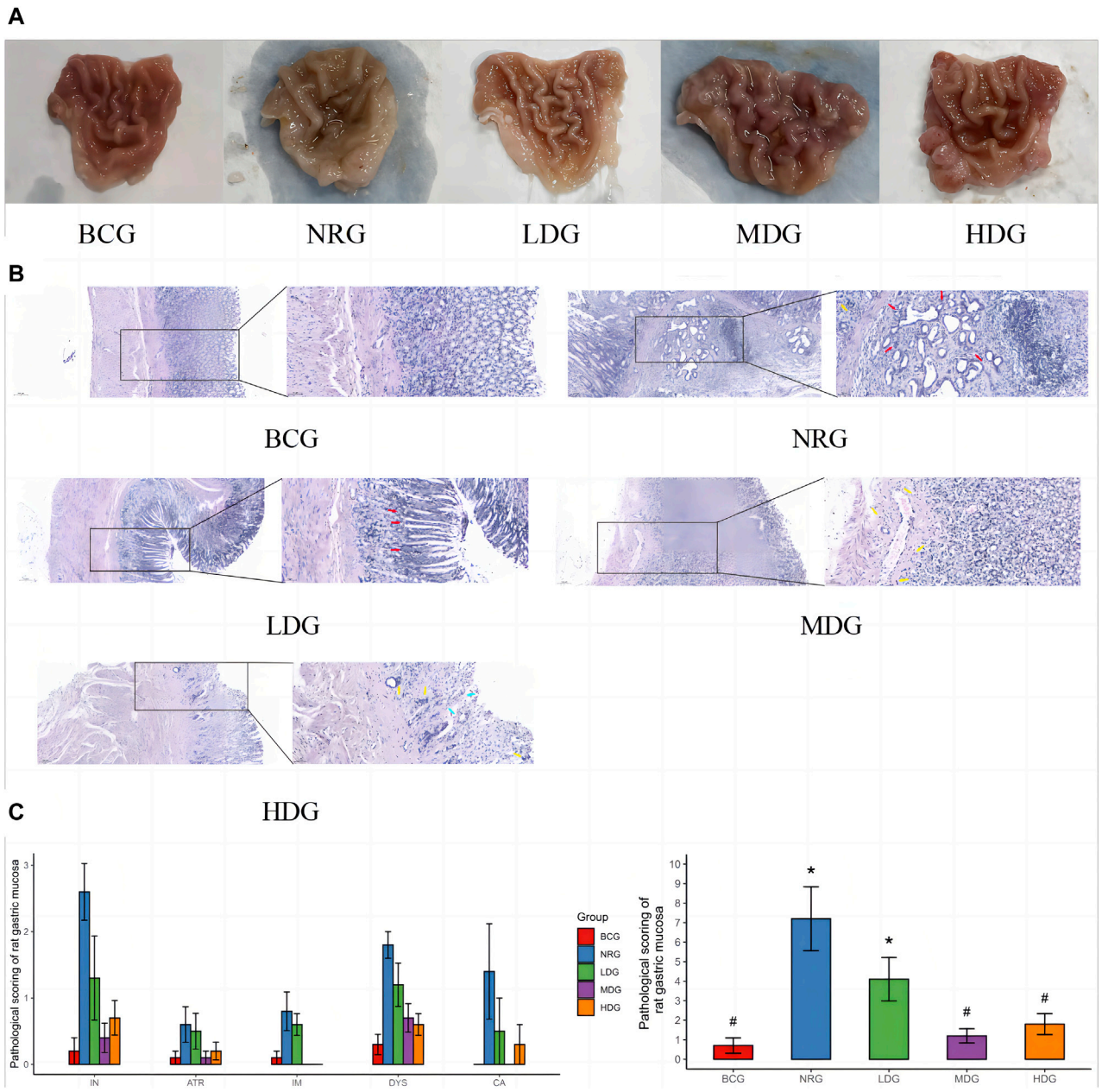


FIGURE 1
**(A)** General conditions of the gastric mucosa of rats in each group at the 42nd weekend. **(B)** HE staining sections of the gastric mucosa of rats in each group at the 42nd weekend (×100/×400) Note: dysplasia (red arrow); atrophy or intestinal metaplasia (blue arrow); and inflammation (yellow arrow). **(C)** Pathological score of the gastric mucosa of rats in each group at the 42nd weekend Note: * indicates compared with the BCG, $p < 0.05$; # indicates compared with the NRG, $p < 0.05$.

are 32.28% and 19.35%, respectively. The stress value of NMDS with weighted UniFrac is 0.15, which is lower than the threshold value of 0.2. All of them form five clusters with unequal overlapping parts, and the NRG is quite different from other groups. Combined with ANOSIM, it can be seen that R > 0 in each group, indicating that the difference between groups is greater than that within groups, and the difference is significant ($p < 0.05$) among groups, except for the LDG and NRG, which indicates that the conclusion is reliable.

## 4.5 Analysis of differential abundance

The results of MetaStats analysis suggest that compared with the gastric mucosal microflora of the NRG, there were significant differences in the BCG, MDG, and HDG ($p < 0.05$, $p < 0.01$). Refer to Table 1, 2 for phylum and genus levels with the top six in relative abundance and with significant differences between groups. There were 33 biomarkers combined with LEfSe analysis, as shown in Figure 3B.

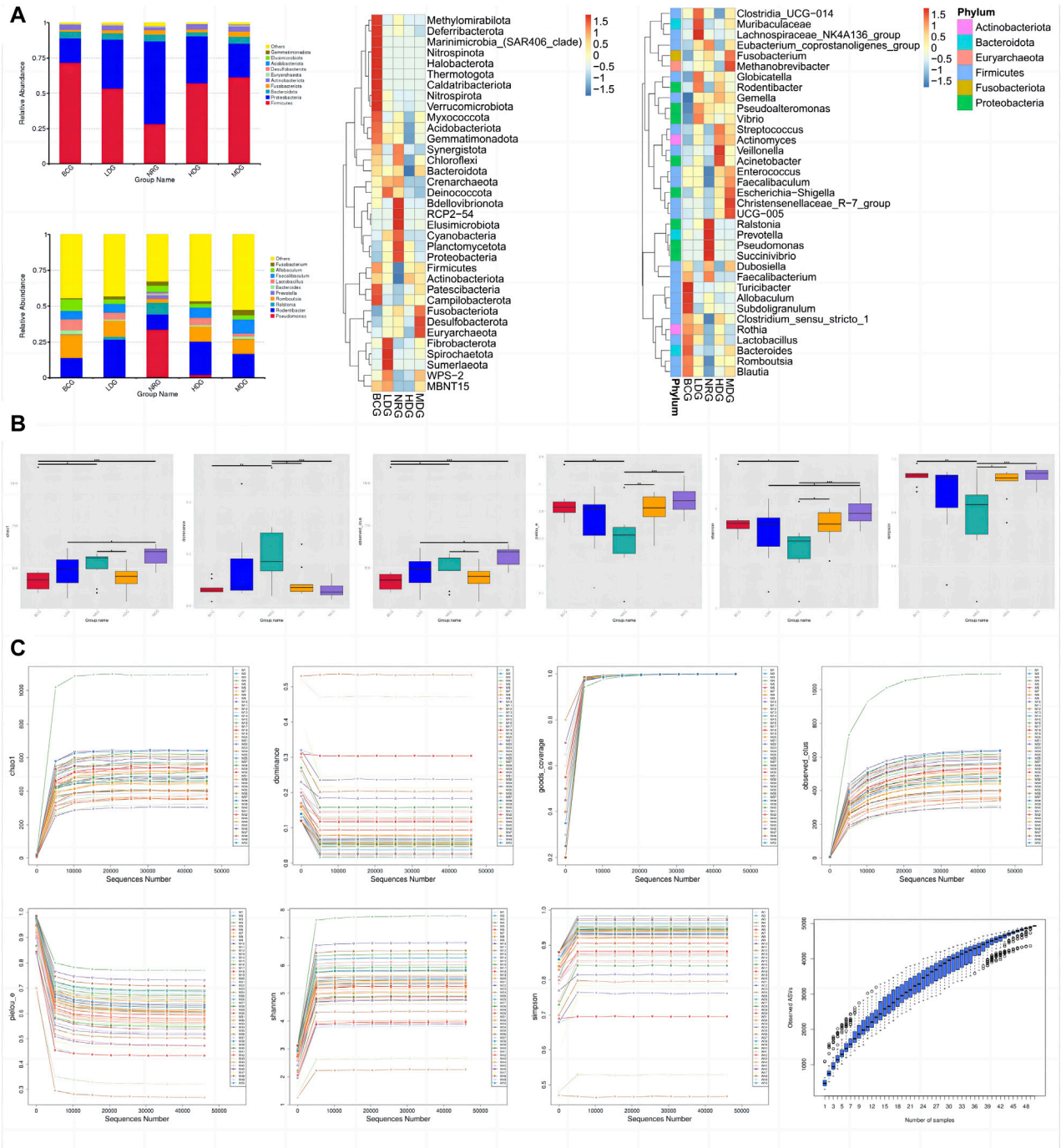


FIGURE 2
**(A)** Histograms and heat maps of the relative abundance of gastric mucosal microflora (phylum and genus levels). **(B)** Boxplots of alpha diversity indices of gastric mucosal microflora of rats in each group. **(C)** Rarefaction curves and species accumulation boxplots of alpha diversity indices.

## 4.6 Data statistics of cytokine antibody microarray

The average value of all sample data is normalized, and the concentration values of inflammatory factors in the samples are calculated based on the standard cytokine data; see Table 3 for specific data.

## 4.7 Differential inflammatory factors of rat gastric mucosa

The average expression and difference of inflammatory factors in the gastric mucosa of rats in each group are given in Table 4. The results showed that eight differential inflammatory factors were detected. The BCG had the largest difference compared with the other groups, and the

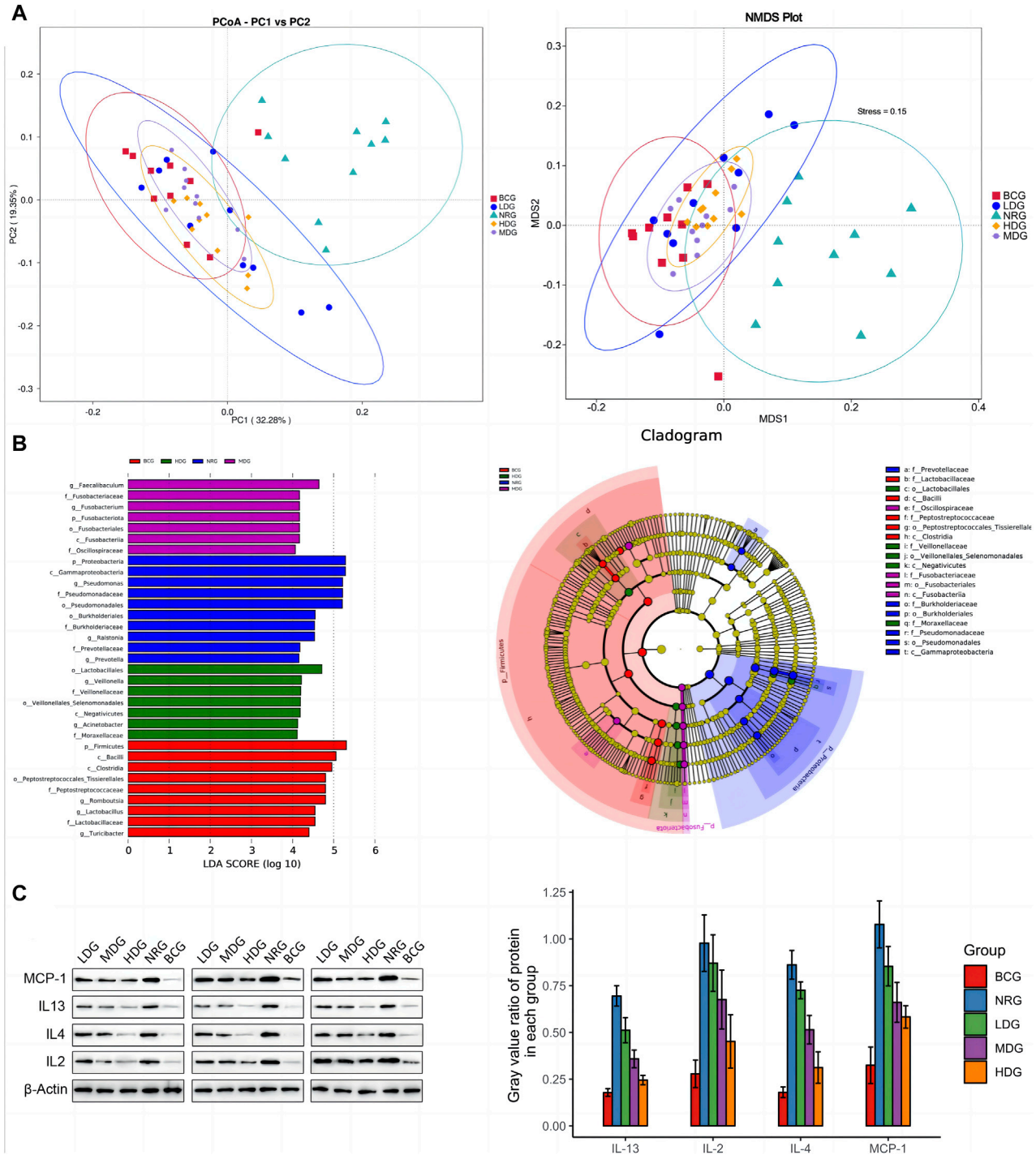


FIGURE 3
**(A)** PCoA and NMDS analysis of duodenal mucosal microflora of rats in each group. **(B)** LEfSe analysis of duodenal mucosal microflora of rats in each group. **(C)** Gray value and gray value ratio of each protein in the gastric mucosa of rats.

relative content of inflammatory factors was significantly decreased ($p < 0.05$), except that IL-13 was increased compared with the LDG. The second is the difference between the NRG and other groups. Compared with the NRG, the levels of IL-2, IL-4, and IL-13 in the LDG were significantly reduced ($p < 0.05$); the levels of IL-4 and IL-13 in the MDG were significantly reduced ($p < 0.05$); and the levels of IL-2, IL-4, and MCP-1 in the HDG were significantly reduced ($p < 0.05$).

## 4.8 Western blotting analysis

Western blotting (WB) was adopted to verify the results obtained by the cytokine antibody microarray. The results showed that the expression levels of all inflammatory factors were the highest in the NRG and the lowest in the BCG, which was consistent with the results of microarray analysis. See Figure 3C

TABLE 1 Gastric mucosal microflora of rats with remarkable differences between groups in phylum level.

| BCG vs NRG | | MDG vs NRG | | HDG vs NRG | |
|---|---|---|---|---|---|
| Species | Discrepancy | Species | Discrepancy | Species | Discrepancy |
| *Firmicutes* | ↑ | *Bacteroidota* | ↑ | *Fusobacteriota* | ↓ |
| *Proteobacteria* | ↓ | *Euryarchaeota* | ↓ | *Euryarchaeota* | ↓ |
| *Actinobacteriota* | ↑ | *Actinobacteriota* | ↓ | *Proteobacteria* | ↓ |
| *Elusimicrobiota* | ↓ | *Acidobacteriota* | ↓ | *Desulfobacterota* | ↓ |
| *Patescibacteria* | ↑ | *Chloroflexi* | ↓ | *Acidobacteriota* | ↓ |
| *Verrucomicrobiota* | ↑ | *Elusimicrobiota* | ↓ | *Gemmatimonadota* | ↓ |

TABLE 2 Gastric mucosal microflora of rats with remarkable differences between groups in genus level.

| BCG vs NRG | | MDG vs NRG | | HDG vs NRG | |
|---|---|---|---|---|---|
| Species | Discrepancy | Species | Discrepancy | Species | Discrepancy |
| *Pseudomonas* | ↓ | *Pseudomonas* | ↓ | *Lactobacillus* | ↑ |
| *Ralstonia* | ↓ | *Ralstonia* | ↓ | *Fusobacterium* | ↓ |
| *Romboutsia* | ↑ | *Romboutsia* | ↑ | *Pseudomonas* | ↓ |
| *Lactobacillus* | ↑ | *Prevotella* | ↓ | *Acinetobacter* | ↑ |
| *Faecalibaculum* | ↑ | *Bacteroides* | ↑ | *Veillonella* | ↑ |
| *Turicibacter* | ↑ | *Lactobacillus* | ↑ | *Lachnospiraceae* | ↓ |

Note: ↑indicates that the relative abundance of group 1 is higher than that of group 2, ↓ indicates the opposite.

TABLE 3 Data statistics of the gastric mucosal inflammatory factors of rats.

| Target | LOD (pg/mL) | % below LOD | % above LOD but <3×LOD | % in best confidence | % above maximum |
|---|---|---|---|---|---|
| IFN-γ | 0.2 | 56.0 | 20.0 | 24.0 | 0.0 |
| IL-1α | 1.2 | 82.0 | 4.0 | 14.0 | 0.0 |
| IL-1β | 50.9 | 8.0 | 30.0 | 62.0 | 0.0 |
| IL-2 | 3.9 | 28.0 | 56.0 | 16.0 | 0.0 |
| IL-4 | 0.2 | 28.0 | 40.0 | 32.0 | 0.0 |
| IL-6 | 5.2 | 42.0 | 0.0 | 58.0 | 0.0 |
| IL-10 | 4.3 | 2.0 | 4.0 | 94.0 | 0.0 |
| IL-13 | 2.7 | 38.0 | 26.0 | 36.0 | 0.0 |
| MCP-1 | 1.6 | 0.0 | 0.0 | 100.0 | 0.0 |
| TNF-α | 443.0 | 2.0 | 6.0 | 92.0 | 0.0 |

Note: the blue font represents the data with a high proportion; italics represent relatively low data; limit of detection (LOD) represents the lowest concentration value that can be detected in the confidence interval. Unit: pg·mL$^{-1}$.

for the gray value and gray value ratio of each protein in the gastric mucosa of rats. The results showed that compared with the BCG, there are significant differences in IL-2, IL-4, IL-13, and MCP-1 in the NRG, LDG, and MDG ($p < 0.05$). Compared with the NRG, the levels of IL-4, IL-13, and MCP-1 in the MDG were significantly reduced ($p < 0.05$). The levels of IL-2, IL-4, IL-13, and MCP-1 in the HDG were significantly reduced ($p < 0.05$). In general, the overall trend of the difference between the results of WB and cytokine antibody microarray is consistent, while there are certain differences in significance, which may be caused by the bias caused by the difference in detection methods and sample size.

10.3389/fphar.2024.1446244

TABLE 4 Average expression of inflammatory factors in the gastric mucosa of rats in each group.

| Group | IL-2 | IL-4 | IL-10 | MCP-1 | IFN-γ | TNF-α | IL-13 | IL-1β |
|---|---|---|---|---|---|---|---|---|
| BCG | 1.600$^{\#}$ | 0.051$^{\#}$ | 4.321$^{\#}$ | 4.359$^{\#}$ | 0.000$^{\#}$ | 10.365$^{\#}$ | 2.612 | 6.237$^{\#}$ |
| NRG | 3.784* | 0.890* | 5.778* | 5.217* | 0.595* | 11.663* | 3.086 | 7.581* |
| LDG | 2.501$^{\#}$ | 0.476*$^{\#}$ | 5.321* | 5.194* | 0.559* | 11.063* | 1.013*$^{\#}$ | 6.937* |
| MDG | 3.218* | 0.572*$^{\#}$ | 5.213* | 5.088* | 0.293 | 11.219 | 1.742$^{\#}$ | 7.751* |
| HDG | 2.565$^{\#}$ | 0.527*$^{\#}$ | 5.254* | 4.570$^{\#}$ | 0.311 | 11.255* | 2.229 | 7.501* |

Note: * indicates compared with the BCG, $p < 0.05$; # indicates compared with the NRG, $p < 0.05$.

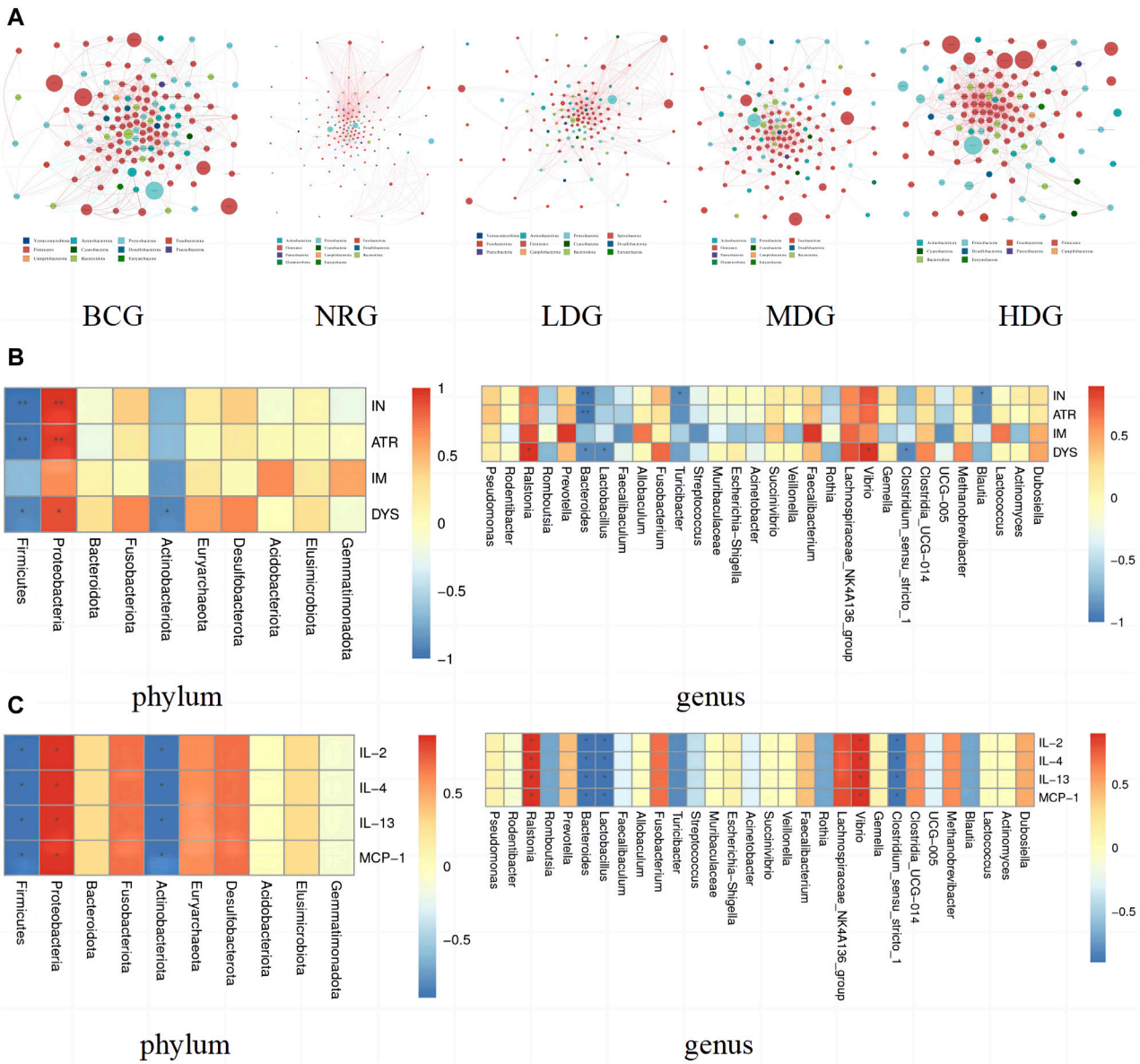


FIGURE 4
**(A)** Network of gastric mucosal microflora of rats in each group. **(B)** Pearson analysis of the pathology of gastric mucosa and gastric mucosal microflora (phylum and genus levels) Note: * indicates $p < 0.05$; ** indicates $p < 0.01$ **(C)** Pearson analysis of inflammatory factors and gastric mucosal microflora (phylum and genus levels) Note: * indicates $p < 0.05$; ** indicates $p < 0.01$.

## 4.9 Correlation analysis of gastric mucosal microflora of rats

### 4.9.1 Analysis of the interaction among gastric mucosal microflora of rats

The network of gastric mucosal microflora of rats in each group was calculated and drawn by Spearman correlation analysis. The dominant and closely interacting microflora in each group can be displayed intuitively. Refer to Figure 4A for details, in which the size of nodes represents the relative abundance, the red line between nodes indicates a positive correlation, and the blue line indicates a negative correlation. It can be found that the network density of the microflora with a positive correlation in the BCG is significantly higher than that with a negative correlation. On the contrary, the network density of the microflora with a negative correlation in the NRG is prominently higher than that with a positive correlation. While the ratio of the microflora with positive and negative correlations in the LDG, MDG, and HDG is between them. It is suggested that with the intervention of Weizhuan'an prescription, the gastric mucosal microflora has been remarkably regulated, which can play a better cooperative role and help restore the stability of gastrointestinal microecology.

### 4.9.2 Correlation analysis between gastric mucosal pathology and gastric mucosal microflora

The correlation between the pathological indexes of the gastric mucosa and the dominant microflora in phylum (top 10) and genus (top 30) levels was calculated by Spearman's correlation analysis. The Spearman correlation coefficient values were calculated by the corr.test function; then, the pheatmap function was used for visualization after testing the significance of the difference. Figure 4B shows that there is a correlation between the pathological changes of gastric mucosa and gastric mucosal microflora. Specifically, *Proteobacteria* was positively correlated with inflammation (IN), atrophy (ATR), and dysplasia (DYS) ($p < 0.05$, $p < 0.01$). *Ralstonia* and *Vibrio* were positively correlated with DYS ($p < 0.05$). *Prevotella* and *Faecalibacterium* were positively correlated with intestinal metaplasia (IM), while there was no statistical difference between the above groups ($p > 0.05$). *Firmicutes* and *Bacteroides* were negatively correlated with IN, ATR, and DYS ($p < 0.05$, $p < 0.01$). *Actinobacteriota* and *Lactobacillus* were negatively correlated with DYS ($p < 0.05$). *Turicibacter*, *Blautia*, and *Clostridium_sensu_stricto_1* were negatively correlated with IN ($p < 0.05$). In addition, it can also be found that the differential microflora has a higher correlation with IN, ATR, and DYS and a lower correlation with IM.

### 4.9.3 Correlation analysis between gastric mucosal microflora and inflammatory factors

The results of Spearman correlation index analysis on gastric mucosal microflora and inflammatory factors indicate that there is a high correlation between them, see Figure 4C. Specifically, *Proteobacteria*, *Ralstonia*, and *Vibrio* were positively correlated with IL-2, IL-4, IL-13, and MCP-1 ($p < 0.05$). *Firmicutes*, *Actinobacteriota*, *Bacteroides*, *Lactobacillus*, and *Clostridium_sensu_stricto_1* were negatively correlated with IL-2, IL-4, IL-13, and MCP-1 ($p < 0.05$).

## 4.10 Functional abundance prediction

### 4.10.1 Functional abundance prediction of gastric mucosal microflora in rats

The functional abundance prediction of gastric mucosal microflora was performed by PICRUSt2 based on the 16S rDNA sequencing data and the COG. First, functional abundance annotation and relative abundance clustering were conducted for the preliminary assessment of common and unique functional information between groups. The histograms (top 10), heat maps (top 35), PCA, and flower plot can be referred to Figure 5A. Then, the functional difference in gastric mucosal microflora in each group was analyzed by the *t* test. The results showed that compared with the NRG, the BCG, MDG, and HDG had significant differences ($p < 0.05$, $p < 0.01$). Especially, there were 2,123 different functions in the BCG, 2,198 in the MDG, and 2,160 in the HDG. See Figure 5B for the differential function with relatively high enrichment (top 10). It can be found that compared with the NRG, the DNA-binding transcriptional regulators such as OmpR family, AcrR family, and MarR family, ABC-type multidrug transport system and lipoprotein export system, and the activity of related enzymes were upregulated substantially in the BCG, MDG, and HDG. The related gastric mucosal microflora includes *Lactobacillus*, *Pseudomonas*, and *Faecalibacterium*. Refer to Table 5 for details.

### 4.10.2 Functional abundance prediction of gastric mucosal inflammatory factors in rats

The functional abundance prediction of differential inflammatory factors was performed by the KEGG enrichment analysis, which can screen out the biological regulatory pathways with significant differences between groups. It adopts the Fisher exact test, and the data package is clusterProfiler from R/Bioconductor. The criterion is that the count of genes of the pathway is ≥5, $p < 0.05$. The details are shown in Figure 5C (top 20). The results suggest that compared with the NRG, the signaling pathways significantly changed in the BCG, LDG, and HDG ($p < 0.05$, $p < 0.01$), such as viral protein interaction with cytokine and cytokine receptor, T cell receptor signaling pathway, intestinal immune network for lgA production, inflammatory bowel disease, and IL-17 signaling pathway. The related inflammatory factors include IL-1β, IL-2, IL-4, IL-13, TNF-α, IL-10, and MCP-1.

# 5 Discussion

GC is a serious threat to global human health. Fortunately, the PLGC is the effective intervention period for preventing GC. Several research studies have reported that TCM has many advantages in treating PLGC, such as individualization, good efficacy, economy, and non-invasiveness. As the empirical formula of our research group, Weizhuan'an prescription has been applied in the clinic for many years and has received satisfactory therapeutic feedback. We strictly standardize the basic experiments of botanical drugs and strive to combine modern medical research methods with TCM. In this experiment, 16S rDNA amplicon sequencing, cytokine antibody microarray, and Western blotting were applied to analyze the gastric mucosal microflora and inflammatory factors of rats to explore the biological mechanisms of Weizhuan'an prescription.

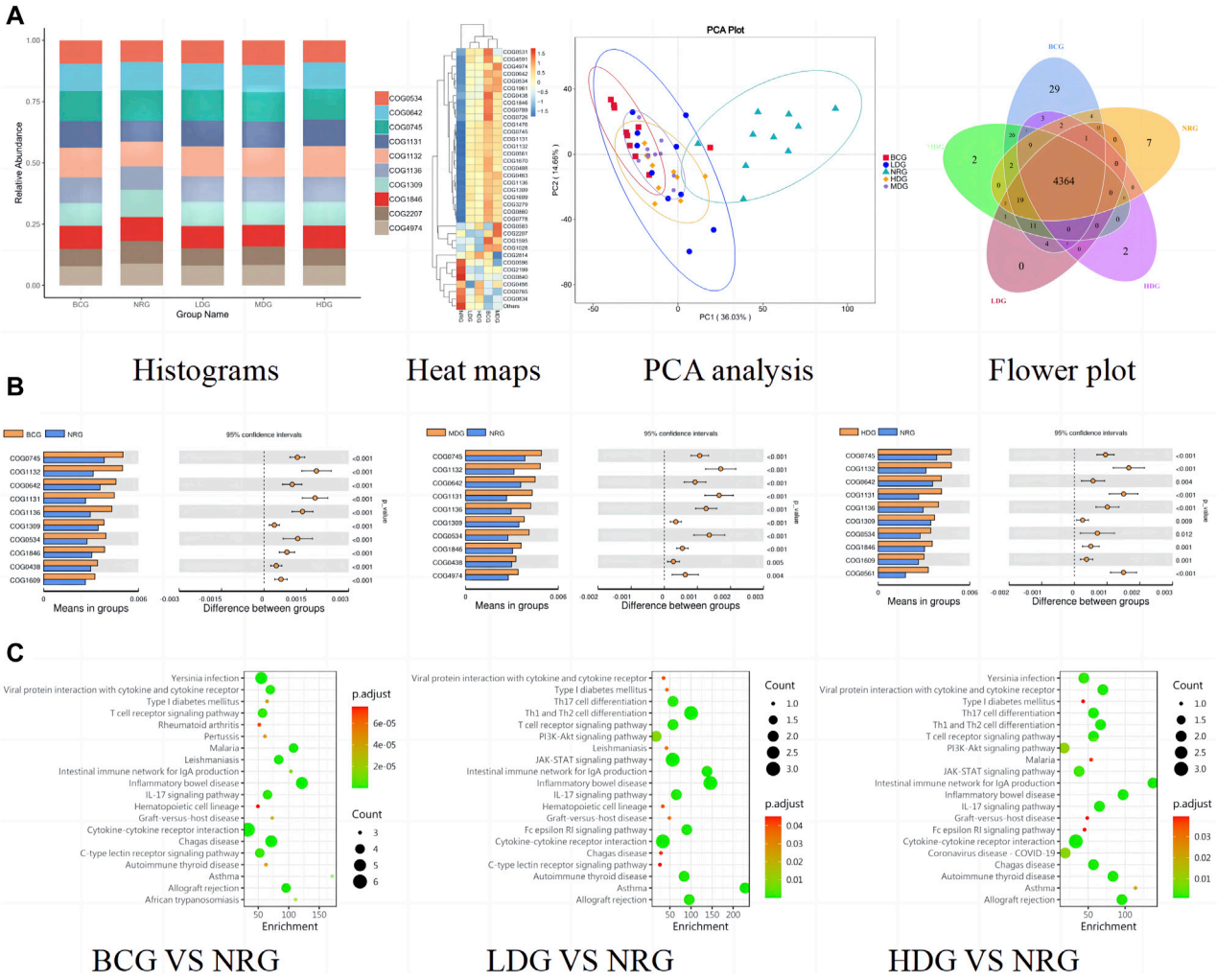


FIGURE 5
**(A)** Histograms, heat maps, PCA analysis, and flower plot of COG of rats in each group. **(B)** Bar charts of COG functional enrichment analysis of gastric mucosal microflora of rats in each group. **(C)** KEGG function enrichment analysis of gastric mucosal inflammatory factors of rats in each group.

The results suggest that the pathological manifestations of gastric mucosa, the gastric mucosal microflora, and inflammatory factors in rats with PLGC have changed greatly compared with those of the BCG. With the intervention of Weizhuan'an prescription, the pathological improvement of the gastric mucosa was remarkable, especially in the MDG and HDG. The results of 16S rDNA amplicon sequencing showed that there were significant differences in the BCG, MDG, and HDG compared with the abundance and diversity of gastric mucosal microflora in the NRG. Specifically, at the phylum level, the abundance of *Firmicutes* increased significantly in the BCG ($p < 0.01$), and that of *Proteobacteria* decreased significantly in the BCG and MDG ($p < 0.01$). At the genus level, the abundance of *Romboutsia*, *Lactobacillus*, and *Turicibacter* increased in the BCG, and that of *Pseudomonas* decreased significantly in the BCG and MDG ($p < 0.01$). The abundance of *Lactobacillus* and *Veillonella* increased significantly in the HDG ($p < 0.01$). The results of cytokine antibody microarray and Western blotting indicated that compared with the NRG, the contents of IL-2, IL-4, IL-13, and MCP-1 were significantly decreased in the BCG, LDG, MDG, and HDG ($p < 0.05$).

*Firmicutes*, *Bacteroidetes*, *Proteobacteria*, and *Actinobacteria* are symbiotic bacteria in healthy intestines, which may turn into pathogenic bacteria in the unbalanced internal environment (Liu et al., 2022). *Proteobacteria* with high content can promote gastrointestinal inflammation by producing stimulating flagellin and lipopolysaccharide (Shin et al., 2015; Guo et al., 2022). This study also suggests that *Firmicutes* and *Bacteroides* can reduce inflammation, atrophy, and dysplasia of the gastric mucosa, while *Proteobacteria* may aggravate such lesions. *Pseudomonas* is a Gram-negative bacterium with a wide variety and distribution (Zha et al., 2015), including a variety of pathogens such as *Pseudomonas aeruginosa*, which is common in mucosal membrane damage and infection (Zhang XY. et al., 2021). This study found that *Pseudomonas* may promote gastric mucosa atrophy. *Romboutsia* is generally regarded as a probiotic, which can resist inflammation and protect mucosal barrier (Wu et al., 2021). *Turicibacter* can participate in metabolism and resist fatigue (Kemis et al., 2019; Chung et al., 2021). This study found that it can alleviate gastric mucosal inflammation. *Lactobacillus* is widely distributed in the digestive tract (Hindieh et al., 2022). As one of the most widely used

TABLE 5 COG hierarchy and function description with related gastric mucosal microflora.

| Hierarchy | Function description | Gastric mucosal microflora |
|---|---|---|
| COG0745 | DNA-binding response regulator, OmpR family, contains REC and winged-helix (wHTH) domain | *Firmicutes*, *Romboutsia*, *Lactobacillus*, *Pseudomonas*, *Ralstonia*, *Vibrio*, *Prevotella*, *Faecalibacterium*, *Bacteroides*, *Blautia*, *Clostridium_sensu_stricto_1*, etc. |
| COG1132 | ABC-type multidrug transport system, ATPase, and permease component | |
| COG0642 | Signal transduction histidine kinase | |
| COG1131 | ABC-type multidrug transport system, ATPase component | |
| COG1136 | ABC-type lipoprotein export system, ATPase component | |
| COG1309 | DNA-binding transcriptional regulator, AcrR family | |
| COG0534 | $Na^+$-driven multidrug efflux pump | |
| COG1846 | DNA-binding transcriptional regulator, MarR family | |
| COG0438 | Glycosyltransferase involved in cell wall biosynthesis | |
| COG1609 | DNA-binding transcriptional regulator, LacI/PurR family | |
| COG4974 | Site-specific recombinase XerD | |
| COG0561 | Hydroxymethylpyrimidine pyrophosphatase and other HAD family phosphatases | |

probiotics in the clinic, *Lactobacillus* can reduce infection and inflammation, strengthen immunity, and maintain gastrointestinal health (Garcia et al., 2022; Hu et al., 2022). *Lactobacillus* can also inhibit the proliferation of cancer cells by producing anticancer metabolites and inducing apoptosis of cancer cells (Yue et al., 2021). This study found that *Lactobacillus* can alleviate gastric mucosal dysplasia. *Veillonella* is a kind of Gram-negative anerobic *micrococcus*, which can play an anti-inflammatory role and enhance the body's immunity (Xiao et al., 2022; Daniel et al., 2022). In addition, the study found that the related microflora can significantly upregulate the activities of DNA-binding transcriptional regulators, ABC-type multidrug transport system, related enzymes, etc.; promote the synthesis of gastric epithelial cells and the absorption and utilization of effective drug metabolites; and help repair the damaged gastric mucosa to treat PLGC and prevent GC.

In recent years, with the progress of immunotherapy and the exploration of new targets in GC, significant breakthroughs have been made in the immunotherapy of GC. The molecular markers for the diagnosis and prognosis of GC include m1A, microRNAs, lncRNAs, and JMJD3 (Xu et al., 2019; Zhao et al., 2019; Chen Y. et al., 2021; Zhang HY. et al., 2021). It is also worth looking forward to whether immunotherapy can play a role in the treatment of PLGC. Moreover, it is suggested that *Proteobacteria* can increase the relative contents of IL-2, IL-4, IL-13, and MCP-1, while *Firmicutes*, *Bacteroides*, and *Lactobacillus* can decrease the contents of IL-2, IL-4, IL-13, and MCP-1 significantly. There is a close relationship between gastric mucosal inflammation and the generation of PLGC. Studies have shown that many botanical drug metabolites inhibit inflammatory reactions effectively (Chen QL. et al., 2021). Interleukin-2 (IL-2) is a pleiotropic cytokine, which has dual regulatory effects on immune activation and immune tolerance (Yui et al., 2004; Hershko et al., 2011). IL-2 can activate cytotoxic T cells and NK cells to participate in the inflammatory reaction (Sockolosky et al., 2018). Furthermore, IL-2 can promote the proliferation and differentiation of Treg cells (Sharma et al., 2020), and Treg cells can inhibit the activity of cytotoxic T cells to induce immune escape, tumor recurrence, or metastasis (Najafi et al., 2019). The sustained high levels of IL-2 can also induce toxicity (Dutcher et al., 2014). Interleukin-4 (IL-4) is also a "double-edged sword" as a kind of pleiotropic cytokine. On one hand, it can play an anti-tumor role, such as promote the differentiation of B cells (Zubiaga et al., 1992) and stimulate the production of $CD_8^+$ T cells (Schultze et al., 1997). On the other hand, studies (Suzuki et al., 2015; May and Fung, 2015) confirmed that the level of IL-4 in cancer patients is higher, and there is a high level of IL-4R receptor expression on the surface of tumor cells. Tumor cells can also produce IL-4 (Todaro et al., 2008), which can activate tumor-associated macrophages (TAMs) and myeloid-derived suppressor cells (MDSCs), thus enhancing the invasion of tumors (Suzuki et al., 2015). Interleukin-13 (IL-13) is a pleiotropic Th2 cytokine (Heeb et al., 2020; Moran and Pavord, 2020). It can activate eosinophils, enhance the inflammatory response, and damage the mucosal barrier (Tsou et al., 2015; Sato et al., 2017). In the inflammatory microenvironment, IL-13 can also cooperate with IL-4 to promote the development of tumors through autocrine and paracrine paths (Surana et al., 2014; Bankaitis and Fingleton, 2015). Monocyte chemotactic protein-1 (MCP-1), also known as CCL2, is an important pro-inflammatory factor (Qian et al., 2011). It can activate monocytes, macrophages, and T cells and actively chemotactic immune cells to participate in inflammatory activities. In the inflammatory microenvironment, MCP-1 can enhance the activity of tumor cells and promote the generation of tumor microvessels and lymphatic vessels (Qian et al., 2009; Tang and Tsai, 2012). MCP-1 is also a potent chemokine of TAMs, resulting in

tumor immune escape (Roblek et al., 2016). This study also suggests that inflammatory factors IL-2, IL-4, IL-13, and MCP-1 are related to the change of multiple signaling pathways, such as viral protein interaction with cytokine and cytokine receptors, T cell receptor signaling pathway, intestinal immune network for lgA production, inflammatory bowel disease, and IL-17 signaling pathway.

However, the interaction mechanism between botanical drug, microflora, and PLGC is complex, and the number of related genes, proteins, and signal pathways is huge. Further exploration will be carried out with the help of related technologies in order to further clarify the molecular network mechanism of the effective metabolites of botanical drug, key microflora, and PLGC and provide more references for clinical practice.

## 6 Conclusion

Weizhuan'an prescription can significantly improve the gastric mucosa pathology of rats with PLGC by regulating the gastric mucosal microflora and inflammatory factors; increasing the species and abundance of probiotics; reducing the content of pathogenic bacteria and IL-2, IL-4, IL-13, and MCP-1; and regulating multiple signal pathways.

## Data availability statement

The data of this paper is stored in SRA database. The accession number is PRJNA1144098, available at: https://www.ncbi.nlm.nih.gov/sra/PRJNA1144098.

## Ethics statement

The animal study was approved by the Ethics Committee of the Animal Experiment Center of TUTCM, batch No. TCM-LAEC2020076. The study was conducted in accordance with the local legislation and institutional requirements.

## Author contributions

YL: conceptualization, data curation, supervision, visualization, writing–original draft, and writing–review and editing. HL: conceptualization, funding acquisition, supervision, and writing–review and editing. JS: funding acquisition and writing–original draft. YM: data curation and writing–original draft. LM: data curation and writing–original draft. CG: conceptualization, supervision, and writing–review and editing.

## Funding

The authors declare that financial support was received for the research, authorship, and/or publication of this article. This work was supported by the Construction project of national famous TCM expert inheritance studio of the state administration of TCM (TCM [2016] No. 42), China; Tianjin Sci-Tech Projects (No. 16YFZCSY01070), China; and Tianjin Administration of Traditional Chinese Medicine Integrated Traditional Chinese and Western Medicine Project (No. 2021035).

## Conflict of interest

The authors declare that the research was conducted in the absence of any commercial or financial relationships that could be construed as a potential conflict of interest.

## Publisher's note

All claims expressed in this article are solely those of the authors and do not necessarily represent those of their affiliated organizations, or those of the publisher, the editors, and the reviewers. Any product that may be evaluated in this article, or claim that may be made by its manufacturer, is not guaranteed or endorsed by the publisher.

## References

Association of Digestive Endoscopy, Chinese Medical Association (CMA) (2004). Endoscopic classification and grading criteria for chronic gastritis. *Chin. J. Dig. Endose.* 21 (2), 77–78. (in Chinese). doi:10.3760/cma.j.issn.1007-5232.2004.02.001

Bankaitis, K. V., and Fingleton, B. (2015). Targeting IL4/IL4R for the treatment of epithelial cancer metastasis. *Clin. Exp. Metastasis* 32 (8), 847–856. doi:10.1007/s10585-015-9747-9

Bockerstett, K. A., and DiPaolo, R. J. (2017). Regulation of gastric carcinogenesis by inflammatory cytokines. *Cell. Mol. Gastroenterol. Hepatol.* 4 (1), 47–53. doi:10.1016/j.jcmgh.2017.03.005

Chen, Q. L., Zhu, L., Yip, K. M., Tang, Y., Liu, Y., Jiang, T., et al. (2021b). A hybrid platform featuring nanomagnetic ligand fishing for discovering COX-2 selective inhibitors from aerial part of Saussurea laniceps Hand-Mazz. *J. Ethnopharmacol.* 271, 113849. doi:10.1016/j.jep.2021.113849

Chen, Y., Long, W. L., Yang, L. Q., Zhao, Y., Wu, X., Li, M., et al. (2021a). Functional peptides encoded by long non-coding RNAs in gastrointestinal cancer. *Front. Oncol.* 11, 777374. doi:10.3389/fonc.2021.777374

Chen, Y., Wang, X., Yu, Y., Xiao, Y., Huang, J., Yao, Z., et al. (2018). Serum exosomes of chronic gastritis patients infected with *Helicobacter pylori* mediate IL-1α expression via IL-6 trans-signalling in gastric epithelial cells. *Clin. Exp. Immunol.* 194 (3), 339–349. doi:10.1111/cei.13200

Chinese Society of Gastroenterology (CSGE) (2017). Consensus on chronic gastritis in China. *Chin. J. GE* 22 (11), 670–683. doi:10.3969/j.issn.1008-7125.2017.11.007

Chung, Y., Ryu, Y., An, B. C., Yoon, Y. S., Choi, O., Kim, T. Y., et al. (2021). A synthetic probiotic engineered for colorectal cancer therapy modulates gut microbiota. *Microbiome* 9 (1), 122. doi:10.1186/s40168-021-01071-4

Daniel, R. F., Eric, B. M., Emily, T. R., Onyekaba, M. A., Mohamed, A. M. T., Duncan, K., et al. (2022). Inflammation-associated nitrate facilitates ectopic colonization of oral bacterium Veillonella parvula in the intestine. *Nat. Microbiol.* 7 (10), 1673–1685. doi:10.1038/s41564-022-01224-7

Deng, J. F. (2020). The efficacy of Weifuchun tablets combined with rabeprazole triple therapy in the treatment of Hp-positive gastric ulcer. *Med. Theory Pract.* 33 (4), 579–580. doi:10.19381/j.issn.1001-7585.2020.04.028

Dutcher, J. P., Schwartzentruber, D. J., Kaufman, H. L., Agarwala, S. S., Tarhini, A. A., Lowder, J. N., et al. (2014). High dose interleukin-2(Aldesleukin)-expert consensus on best management practices-2014. *J. Immunother. Cancer* 2 (1), 26–23. doi:10.1186/s40425-014-0026-0

Fitzmaurice, C., Allen, C., Barber, R., Barregard, L., Bhutta, Z. A., et al. (2017). Global, regional, and national cancer incidence, mortality, years of life lost, years lived with disability, and disability-adjusted life-years for 32 cancer groups, 1990 to 2015: a

systematic analysis for the global burden of disease study. *JAMA Oncol.* 3 (4), 524–548. doi:10.1001/jamaoncol.2016.5688

Garcia, V. G., Miessi, D. M. J., Esgalha da, R. T., Gomes, N. A., Nuernberg, M. A. A., Cardoso, J. d. M., et al. (2022). The effects of *Lactobacillus reuteri* on the inflammation and periodontal tissue repair in rats: a pilot study. *Saudi Dent. J.* 34 (6), 516–526. doi:10.1016/j.sdentj.2022.05.004

Gullo, I., Oliveira, P., Athelogou, M., Gonçalves, G., Pinto, M. L., Carvalho, J., et al. (2019). New insights into the inflamed tumor immune microenvironment of gastric cancer with lymphoid stroma: from morphology and digital analysis to gene expression. *Gastric Cancer* 22 (1), 77–90. doi:10.1007/s10120-018-0836-8

Guo, S. H., Yu, Y. T., Wan, J. H., et al. (2022). Progress in research on the relationship between Proteobacteria and the imbalance of mammalian colonic intestinal flora. *Chin. J. Microecol.* 34 (4), 479–484. (in Chinese). doi:10.13381/j.cnki.cjm.202204021

Heeb, L. E. M., Egholm, C., and Boyman, O. (2020). Evolution and function of Interleukin-4 receptor signaling in adaptive immunity and neutrophils. *Genes. Immun.* 21 (3), 143–149. doi:10.1038/s41435-020-0095-7

Hershko, A. Y., Suzuki, R., Charles, N., Alvarez-Errico, D., Sargent, J. L., Laurence, A., et al. (2011). Mast cell interleukin-2 production contributes to suppression of chronic allergic dermatitis. *Immunnity* 35 (4), 562–571. doi:10.1016/j.immuni.2011.07.013

Hindieh, P., Yaghi, J., Khoury, A. E., Chokr, A., Atoui, A., Louka, N., et al. (2022). Lactobacillus rhamnosus and Staphylococcus epidermidis in gut microbiota: *in vitro* antimicrobial resistance. *Amb. Express* 12 (1), 128. doi:10.1186/s13568-022-01468-w

Hu, M. X., He, F., Guo, Y. X., Mo, L. Z., and Zhu, X. (2022). *Lactobacillus reuteri* biofilms inhibit pathogens and regulate microbiota in *in vitro* fecal fermentation. *J. Agric. Food Chem.* 70 (38), 11935–11943. doi:10.1021/acs.jafc.2c02372

Kemis, J. H., Linke, V., Barrett, K. L., Boehm, F. J., Traeger, L. L., Keller, M. P., et al. (2019). Genetic determinants of gut microbiota composition and bile acid profiles in mice. *PLoS Genet.* 15 (8), e1008073. doi:10.1371/journal.pgen.1008073

Khatoon, J., Prasad, K. N., Rai, R. P., Shukla, S. K., Krishnani, N., and Ghoshal, U. C. (2018). Expression levels of A disintegrin and metalloproteases (ADAMs), and Th17-related cytokines and their association with *Helicobacter pylori* infection in patients with gastroduodenal diseases. *Pathog. Dis.* 76 (8), fty078. doi:10.1093/femspd/fty078

Li, H. W., Pan, H. F., and Zhao, Z. M. (2015). Effect of Weipixiao on plasma TNF-α and IL-4 in rats with gastric precancerous lesions. *J. GZ Univ. Chin. Med.* 32 (2), 271–274. (in Chinese). doi:10.13359/j.cnki.gzxbtcm.2015.02.020

Lian, D. X., Xu, X. F., Ren, W. K., Fu, L. J., Fan, P. L., Cao, H. Y., et al. (2017). Mechanism of anti-Helicobacter pylori urease activity of patchouli alcohol. *Chin. J. Chin. Mat. Med.* 42 (3), 562–566. (in Chinese). doi:10.19540/j.cnki.cjcmm.20161222.075

Liu, M. M., Bi, R. R., and Sun, Y. J. (2022). Research progress on the interaction between fruits and vegetables and intestinal microflora and their health effects. *Zhongguo Shipin Xuebao* 22 (4), 388–407. (in Chinese). doi:10.16429/j.1009-7848.2022.04.039

May, R. D., and Fung, M. (2015). Strategies targeting the IL-4/IL-13 axes in disease. *Cytokine* 75 (1), 89–116. doi:10.1016/j.cyto.2015.05.018

Meng, L. K., Yang, J. W., Yang, K., et al. (2020). Clinical observation of Weizhuan'an granules in treating gastric precancerous lesions of Qi deficiency and blood stasis type. *World J. Integr. Tradit. Chin. West Med.* 15 (6), 1122–1125+1129. (in Chinese). doi:10.13935/j.cnki.sjzx.200634

Moran, A., and Pavord, I. D. (2020). Anti-IL-4/IL-13 for the treatment of asthma: the story so far. *Expert Opin. Biol. Ther.* 20 (3), 283–294. doi:10.1080/14712598.2020.1714027

Najafi, M., Mortezaee, K., and Majidpoor, J. (2019). Stromal reprogramming: a target for tumor therapy. *Life Sci.* 239, 117049. doi:10.1016/j.lfs.2019.117049

Nardone, G., and Compare, D. (2015). The human gastric microbiota: is it time to rethink the pathogenesis of stomach diseases? *United Eur. Gastroenterol. J.* 3 (3), 255–260. doi:10.1177/2050640614566846

Qian, B., Deng, Y., Im, J. H., Muschel, R. J., Zou, Y., Li, J., et al. (2009). A distinct macrophage population mediates metastatic breast cancer cell extravasation, establishment and growth. *PLoS One* 4 (8), e6562. doi:10.1371/journal.pone.0006562

Qian, B. Z., Li, J., Zhang, H., Kitamura, T., Campion, L. R., et al. (2011). CCL2 recruits inflammatory monocytes to facilitate breast-tumour metastasis. *Nature* 475 (7355), 222–225. doi:10.1038/NATURE10138

Roblek, M., Strutzmann, E., Zankl, C., Adage, T., Heikenwalder, M., Atlic, A., et al. (2016). Targeting of CCL2- CCR2-glycosaminoglycan axis using a CCL2 decoy protein attenuates metastasis through inhibition of tumor cell seeding. *Neo-plasia* 18 (1), 49–59. doi:10.1016/j.neo.2015.11.013

Sato, H., Nakajima, N., Takahashi, K., Hasegawa, G., Mizuno, K. I., Hashimoto, S., et al. (2017). Proposed criteria to differentiate heterogeneous eosinophilic gastrointestinal disorders of the esophagus, including eosinophilic esophageal myositis. *World J. Gastroenterol.* 23 (13), 2414–2423. doi:10.3748/wjg.v23.i13.2414

Schultze, J. L., Michalak, S., Seamon, M. J., Dranoff, G., Jung, K., Daley, J., et al. (1997). CD40-activated human B cells: an alternative source of highly efficient antigen presenting cells to generate autologous antigen-specific T cells for adoptive immunotherapy. *J. Clin. Investig.* 100 (11), 2757–2765. doi:10.1172/JCI119822

Schulz, C., Schutte, K., Mayerle, J., and Malfertheiner, P. (2019). The role of the gastric bacterial microbiome in gastric cancer: *Helicobacter pylori* and beyond. *Ther. Adv. Gastroenterol.* 12, 1756284819894062. doi:10.1177/1756284819894062

Sharma, M., Khong, H., Fa'ak, F., Bentebibel, S. E., Janssen, L. M. E., Chesson, B. C., et al. (2020). Bempegaldes leukin selectively depletes intratumoral Tregs and potentiates T cell-mediated cancer therapy. *Nat. Commun.* 11 (1), 661. doi:10.1038/s41467-020-14471-1

Shin, N. R., Whon, T. W., and Bae, J. W. (2015). Proteobacteria: microbial signature of dysbiosis in gut microbiota. *Trends Biotechnol.* 33 (9), 496–503. doi:10.1016/j.tibtech.2015.06.011

Sockolosky, J. T., Trotta, E., Parisi, G., Picton, L., Le, A. C., et al. (2018). Selective targeting of engineered T cells using orthogonal IL-2 cytokine-receptor complexes. *Sci* 359 (6379), 1037–1042. doi:10.1126/science.aar3246

Sohn, S. H., Kim, N., Jo, H. J., Kim, J., Park, J. H., Nam, R. H., et al. (2017). Analysis of gastric body microbiota by pyrosequencing: possible role of bacteria other than *Helicobacter pylori* in the gastric carcinogenesis. *J. Cancer Prev.* 22 (2), 115–125. doi:10.15430/JCP.2017.22.2.115

Sounni, N. E., and Noel, A. (2013). Targeting the tumor microenvironment for cancer therapy. *Clin. Chem.* 59 (1), 85–93. doi:10.1373/clinchem.2012.185363

Sultana, Z., Bankura, B., Pattanayak, A. K., Sengupta, D., Sengupta, M., Saha, M. L., et al. (2018). Association of Interleukin-1 beta and tumor necrosis factor-alpha genetic polymorphisms with gastric cancer in India. *Environ. Mol. Mutagen* 59 (7), 653–667. doi:10.1002/em.22208

Sung, J., Kim, N., Kim, J., Jo, H. J., Park, J. H., Nam, R. H., et al. (2016). Comparison of gastric microbiota between gastric juice and mucosa by next Generation sequencing method. *J. Cancer Prev.* 21 (1), 60–65. doi:10.15430/JCP.2016.21.1.60

Surana, R., Wang, S., Xu, W., Jablonski, S. A., and Weiner, L. M. (2014). IL4 Limits the efficacy of tumor-targeted antibody therapy in a murine model. *Cancer Immunol. Res.* 2 (11), 1103–1112. doi:10.1158/2326-6066.CIR-14-0103

Suzuki, A., Leland, P., Joshi, B. H., and Puri, R. K. (2015). Targeting of IL-4 and IL-13 receptors for cancer therapy. *Cytokine* 75 (1), 79–88. doi:10.1016/j.cyto.2015.05.026

Tang, C. H., and Tsai, C. C. (2012). CCL2 increases MMP-9 expression and cell motility in human chondrosarcoma cells via the Ras/Raf/MEK/ERK/NF-kappa B signaling pathway. *Biochem. Pharmacol.* 83 (3), 335–344. doi:10.1016/j.bcp.2011.11.013

Todaro, M., Lombardo, Y., Francipane, M. G., Alea, M. P., Cammareri, P., Iovino, F., et al. (2008). Apoptosis resistance in epithelial tumors is mediated by tumor-cell-derived interleukin-4. *Cell. Death Differ.* 15 (4), 762–772. doi:10.1038/sj.cdd.4402305

Tsou, Y. A., Lin, C. D., Chen, H. C., Hsu, H. Y., Wu, L. T., Chiang-Ni, C., et al. (2015). Interleukin-13 inhibits lipopolysaccharide-induced BPIFA1 expression in nasal epithelial cells. *PLoS One* 10 (12), e0143484. doi:10.1371/journal.pone.0143484

Wang, P., Li, P., Chen, Y., et al. (2022). The Chinese integrated clinical management Guidelines for precancerous lesions of gastric cancer. *Chin. J. Integr. Trad. West Med. Dig.* 30 (3), 163–183. (in Chinese). doi:10.3969/j.issn.1671-038X.2022.03.01

Wang, X. J., Liu, H. Y., Li, Y., et al. (2017). Treatment of 59 cases of epigastric pain with qi deficiency and blood stasis in precancerous lesions with weizhuan'an formula. *Fujian J. TCM* 48 (1), 1–2. doi:10.13260/j.cnki.jfjtcm.011276

Wu, Z., Huang, S., Li, T., Han, D., Zhang, B., et al. (2021). Gut microbiota from green tea polyphenol-dosed mice improves intestinal epithelial homeostasis and ameliorates experimental colitis. *Microbiome* 9 (1), 184. doi:10.1186/s40168-021-01115-9

Xiao, R. M., Luo, G. J., Liao, W., Chen, S., Han, S., Liang, S., et al. (2022). Association of human gut microbiota composition and metabolic functions with Ficus hirta Vahl dietary supplementation. *NPJ Sci. Food* 6 (1), 45. doi:10.1038/s41538-022-00161-3

Xu, Z. Y., Xia, Y. B., Xiao, Z. G., Jia, Y., Li, L., Jin, Y., et al. (2019). Comprehensive profiling of JMJD3 in gastric cancer and its influence on patient survival. *Sci. Rep.* 9, 868. doi:10.1038/s41598-018-37340-w

Yu, G., Torres, J., Hu, N., Medrano-Guzman, R., Herrera-Goepfert, R., Humphrys, M. S., et al. (2017). Molecular characterization of the human stomach microbiota in gastric cancer patients. *Front. Cell. Infect. Microbiol.* 7, 302–308. doi:10.3389/fcimb.2017.00302

Yu, Z. H., Zhao, Y., Wei, P. K., et al. (2018). Effect of Xiaotan Sanjie Formula on the growth and serum IL-8, TGF-β in nude mice with orthotopic gastric cancer. *J. Tradit. Chin. Med.* 36 (10), 2382–2385. doi:10.13193/j.issn.1673-7717.2018.10.020

Yue, Y., Wang, S., Shi, J., Xie, Q., Guan, J., et al. (2021). Effects of Lactobacillus acidophilus KLDS1.0901 on proliferation and apoptosis of colon cancer cells. *Front. Microbiol.* 12, 788040. doi:10.3389/fmicb.2021.788040

Yui, M. A., Sharp, L. L., Havran, W. L., and Rothenberg, E. V. (2004). Preferential activation of an IL-2 regulatory sequence transgene in TCR gamma delta and NKT cells:

subset-specific differences in IL-2 regulation. *J. Immunol.* 172 (8), 4691–4699. doi:10.4049/jimmunol.172.8.4691

Zha, D. M., Zhang, B. H., Li, H. Q., et al. (2015). Research advances in molecular biology of Pseudomonas lipases. *Chin. Biotechnol.* 35 (9), 114–121. (in Chinese). doi:10.13523/j.cb.20150916

Zhang, H. Y., Li, M. X., Kaboli, P. J., Ji, H., Du, F., Wu, X., et al. (2021b). Identification of cluster of differentiation molecule-associated microRNAs as potential therapeutic targets for gastrointestinal cancer immunotherapy. *Int. J. Biol. Markers* 36 (2), 22–32. doi:10.1177/17246008211005473

Zhang, X. Y., Han, Y., Wang, Y. Z., et al. (2021a). Correlation studies of Pseudomonas aeruginosa drug resistance with the antibiotics use intensity of antibacterial agents. *J. HB Univ. Nat. Sci.* 41 (2), 188–194. doi:10.3969/j.issn.1000-1565.2021.02.012

Zhao, Y. S., Zhao, Q. J., Kaboli, P. J., Shen, J., Li, M., Wu, X., et al. (2019). m1A regulated genes modulate PI3K/AKT/mTOR and ErbB pathways in gastrointestinal cancer. *Transl. Oncol.* 12 (10), 1323–1333. doi:10.1016/j.tranon.2019.06.007

Zheng, R. S., Zhang, S. W., Zeng, H. M., Wang, S., Sun, K., Chen, R., et al. (2022). Cancer incidence and mortality in China, 2016. *JNCC* 2 (1), 1–9. doi:10.1016/j.jncc.2022.02.002

Zhou, G., and Yang, J. (2019). Correlations of gastrointestinal hormones with inflammation and intestinal flora in patients with gastric cancer. *J. BUON* 24 (4), 1595–1600.

Zubiaga, A. M., Munoz, E., and Huber, B. T. (1992). IL-4 and IL-2 selectively rescue Th cell subsets from glucocorticoid-induced apoptosis. *J. Immunol.* 149 (1), 107–112. doi:10.4049/jimmunol.149.1.107

frontiers | Frontiers in Pharmacology

TYPE Review
PUBLISHED 09 December 2024
DOI 10.3389/fphar.2024.1449972



OPEN ACCESS

EDITED BY
Wenzhi Hao,
Jinan University, China

REVIEWED BY
Luoyang Wang,
Qingdao University, China
Claire Elizabeth Robertson,
University of Westminster, United Kingdom

*CORRESPONDENCE
Qing Lei,
124281261@qq.com
Qinghua Chen,
137280461@qq.com
Zhongyu Duan,
981039376@qq.com
Rong Chen,
18725092034@163.com

†These authors share first authorship

RECEIVED 20 June 2024
ACCEPTED 22 November 2024
PUBLISHED 09 December 2024

CITATION
Chen W, Xiao L, Guo W, Li H, Chen R, Duan Z, Chen Q and Lei Q (2024) Research progress of traditional Chinese medicine regulating intestinal flora in the treatment of hypertension. *Front. Pharmacol.* 15:1449972. doi: 10.3389/fphar.2024.1449972



# Research progress of traditional Chinese medicine regulating intestinal flora in the treatment of hypertension

Wenjun Chen[1†], Longfei Xiao[1†], Wenlong Guo[1], Hailin Li[1], Rong Chen[1,2*], Zhongyu Duan[1*], Qinghua Chen[1,2*] and Qing Lei[3*]

[1]College of Ethnic Medicine, Yunnan University of Chinese Medicine, Kunming, Yunnan, China, [2]Yunnan Key Laboratory of Dai and Yi Medicines, Yunnan University of Chinese Medicine, Kunming, Yunnan, China, [3]Department of Thoracic Surgery, The Third Affiliated Hospital of Kunming Medical University, Kunming, Yunnan, China

Hypertension is a common disease; however, it is more prevalent in older adults, and its prevalence is increasing in younger populations. Numerous studies have revealed that hypertension and the composition and functionality of the intestinal flora are closely correlated. The balance of the intestinal flora, intestinal barrier integrity, and metabolite content of the intestinal flora play significant roles in the occurrence and progression of hypertension. Therefore, we performed a comprehensive review of Traditional Chinese medicine (TCM) for hypertension, focusing on the role of the intestinal flora to understand the mechanism by which TCM regulates hypertension through its effects on the intestinal flora. We analyzed the findings using the terms "traditional Chinese medicine," "hypertension," "high blood pressure," "blood pressure," "intestinal flora," "intestinal barrier function," "intestinal flora metabolites," and other keywords from the China National Knowledge Infrastructure, VIP Chinese Science and Technology, Wanfang Data, PubMed, and ScienceDirect databases. We found that TCM treats hypertension by regulating the balance of the intestinal microbiota, increasing the abundance of beneficial bacteria, reducing the abundance of harmful bacteria, improving intestinal barrier function, increasing compact proteins, reducing intestinal permeability, and regulating the content of intestinal flora metabolites. The use of TCM to treat hypertension by regulating the intestinal flora is a promising therapeutic strategy. However, most studies are limited by small sample sizes and there is a lack of large-scale randomized controlled trials. In the future, multi-center controlled clinical trials are needed to verify the efficacy and safety of TCM, optimize therapeutic protocols, and establish a foundation for the standardized and personalized application of TCM in hypertension management.

KEYWORDS

**hypertension, intestinal flora, traditional Chinese medicine (TCM), intestinal flora metabolites, intestinal barrier function**

# 1 Introduction

Hypertension is characterized by a persistent rise in blood vessel pressure, which increases the risk of injury to the heart, brain, kidneys, and other organs (World Health Organization, 2021). Its pathogenesis includes sympathetic nervous system hyperactivity, renin-angiotensin-aldosterone system activation, vascular endothelial dysfunction, insulin resistance, and neurohumoral factor dysregulation (Yang et al., 2023a). Hypertension is a major cause of premature death worldwide (World Health Organization, 2023). In China, approximately 2.7 million people suffer from hypertension, with only 13.8% of patients achieving adequate control (World Health Organization, 2019). Hypertension in the Chinese population is mainly due to unhealthy lifestyles, such as high-salt diets, overweight and obesity, smoking, alcohol consumption, and insufficient physical activity. Moreover, vasospasm and atherosclerosis occur when blood vessel wall elasticity decreases with age. This also causes diminished function of the blood pressure regulation center, which is an important factor in the development of hypertension. The incidence of hypertension is relatively high in individuals with work pressure, high psychological pressure, chronic tension, and anxiety (Wu and Zhou, 2023). Currently, hypertension management in China relies primarily on Western medicine, including the use of diuretics, angiotensin-converting enzyme inhibitors, β-blockers, angiotensin Il (Ang Il) receptor antagonists, and calcium channel blockers (Zhang and Li, 2023). However, this conventional treatment often requires patients to take two or more antihypertensive drugs simultaneously, and long-term use of these drugs causes drug resistance, adverse effects, and an increased risk of cancer (Wang et al., 2023). TCM can be used to treat hypertension by targeting disease symptoms. It can effectively lower blood pressure, improve accompanying symptoms, reduce side effects, and enhance the therapeutic effects of Western medicine when used in combination. This approach helps protect target organs that are easily damaged by hypertension, such as the heart, brain, and kidneys, thereby improving the quality of life of patients and making them suitable for long-term use.

The human gut, which contains more than 100 trillion microbial cells, significantly influences metabolism. Alterations in the gut flora are associated with factors including diet, the environment, and drug use (Illiano et al., 2020). Gut microbes belong to five main groups: Bacteroidetes, Firmicutes, Actinobacteria, Proteobacteria, and Cerrucomicrobia (Tang et al., 2017; Rahman et al., 2022). Scientific studies have revealed an association between gut flora and hypertension. Additionally, the structure of the intestinal flora, intestinal barrier function, and intestinal flora metabolites are closely associated with hypertension.

Therefore, in this study, we analyzed the findings using the terms “traditional Chinese medicine,” “hypertension,” “high blood pressure,” “blood pressure, “intestinal flora, “intestinal barrier function, “intestinal flora metabolites” and other keywords from the China National Knowledge Infrastructure, VIP Chinese Science and Technology, Wanfang Data, PubMed, and ScienceDirect databases. During the literature screening process, 32 eligible studies were ultimately selected from an initial pool of 350 articles. Inclusion criteria required that the studies explored the relationship between TCM and hypertension, specifically focusing on the role of gut microbiota. The studies encompassed TCM monomers,single-flavor TCM,TCM pairs, and TCM compounding, providing data on the effects of TCM interventions on gut microbiota. All selected literature was published in peer-reviewed scientific journals in English or Chinese. Exclusion criteria included studies that did not focus on the impact of TCM on the gut microbiota in hypertensive patients, non-experimental studies (such as reviews, case reports, and opinion articles), studies lacking detailed data on TCM interventions and gut microbiota changes, and studies with data insufficient to evaluate TCM’s effect on blood pressure regulation. We searched relevant literature in the past 10 years to review the mechanism and current research status of regulating intestinal flora using TCM in the treatment of hypertension.

# 2 Relationship between hypertension and gut flora

## 2.1 Relationship between hypertension and intestinal flora

Specific structural changes in the intestinal flora, such as a decrease in beneficial bacteria and an increase in harmful bacteria, may activate signaling pathways associated with blood pressure regulation, thereby affecting blood pressure. Flora diversity and abundance are usually expressed using Chao1, Abundance-based Coverage Estimator, Operational Taxonomic Units, Shannon, and Simpson indices. Fecal transplantation from human donors with hypertension to germ-free mice showed that elevated blood pressure could be transmitted through the gut flora, revealing the direct effect of gut flora on host blood pressure (Li et al., 2017). Firmicutes and Bacteroidetes account for more than 90% of the total bacterial phyla (Zhang et al., 2021), and their ratio (F/B) is a biomarker of intestinal flora imbalance. F/B was significantly higher in patients with hypertension than in healthy individuals (Cai et al., 2023), and the F/B ratio of spontaneously hypertensive rats (SHRs) was 5-fold higher than that of Wistar rats (Yang et al., 2015). Additionally, hypertension is accompanied by a decrease and increase in beneficial and pathogenic flora, respectively. Beneficial bacteria, such as Bifidobacteria and Lactobacilli, which help maintain gut health and immune system balance, are often reduced in the hypertensive population. Probiotic yogurt reduces blood pressure in SHRs by improving the structure of the intestinal flora, increasing intestinal microbial diversity, and increasing the abundance of short-chain fatty acid (SCFA)-producing bacteria and fecal SCFAs levels (Kong et al., 2021). Intestinal pathogens and their metabolites enter the bloodstream through the mesentery, triggering chronic inflammation and vascular endothelial damage, leading to a decrease in vasodilatory factors, an increase in constrictive factors, and peripheral resistance, ultimately leading to an increase in blood pressure (Yang et al., 2023b). Moreover, probiotics can improve inflammation and lower blood pressure. For example, kefir treatment reduced interleukin (IL)-6 and tissue necrotic factor (TNF)-α protein densities and abolished

microglial activation in the hypothalamic paraventricular nucleus and rostral ventrolateral medulla of SHRs (de Almeida et al., 2020). Hence, an imbalance in the gut flora changes metabolites, such as SCFAs, which stimulate the production of 5-hydroxytryptamine, which acts on the vagal nerve and vascular system, causing vasoconstriction and affecting cardiac regulatory regions of the brain through the blood-brain barrier. Furthermore, norepinephrine depresses parasympathetic nerves and, together with 5-hydroxytryptamine, increases blood pressure (Zubcevic et al., 2019). Yan and colleagues (Yan et al., 2020) found that a high-salt diet reduced *Bacteroides* and arachidonic acid levels in the gut of Wistar rats and increased gut-derived corticosterone production and serum and intestinal corticosterone levels, thereby promoting elevated blood pressure. Gamma-aminobutyric acid (GABA) is a neurotransmitter produced by *Bacteroides* via the glutamic acid decarboxylase system. GABA salt may reduce hypertension by decreasing endothelial cell dysfunction and M1 polarization. Moreover, GABA is significantly downregulated in high-salt diet-induced hypertensive rats (Otaru et al., 2021; Son et al., 2021). Thus, the intestinal flora may regulate blood pressure through GABA production. In summary, flora imbalance is closely associated with blood pressure regulation mechanisms, involving changes in flora structure, activation of inflammatory pathways, production of neurotransmitters, and changes in hormone levels, which when combined, contribute to blood pressure regulation.

## 2.2 Relationship between hypertension and barrier function of intestinal

The intestinal barrier is the sum of the structure and functions of the intestine that prevents harmful substances, such as bacteria and toxins, from passing through the intestinal mucosa, entering other tissues and organs, and circulating in the body. The intestinal barrier comprises microbial, chemical, physical, and immune barriers. The microbiological barrier comprises the normal intestinal flora of the host, in which beneficial bacteria support biological defenses through antagonism and immune functions. The chemical barrier includes secretions such as gastric acid, mucus, bile, glycoproteins, and enzymes, which are protective. Columnar epithelial cells and intercellular junctions, such as tight junctions, which separate the intestinal lumen from the internal environment and contribute to protection, constitute a physical barrier. The immune barrier comprises intestinal epithelial cells (iECs), intraepithelial lymphoid tissue (ilEL), lymphocytes, Peyer's patches, mesenteric lymph nodes, and immunoglobulin A (sIgA) from plasma cells (Cui et al., 2019). Gut barrier dysfunction is also associated with hypertension, and various factors, such as intestinal flora imbalance, diet, medications, genetic factors, and diseases, can influence the functioning of the intestinal barrier. Under physiological conditions, intestinal barrier function relies on tight junctions between epithelial cells, the mucus layer, and the effective functioning of the mucosal immune system to maintain intestinal homeostasis (Luissint et al., 2016). However, when these tight junctions are disrupted and mucosal defense mechanisms are impaired, intestinal permeability is enhanced, allowing inflammatory mediators, such as bacteria and endotoxins, to escape into the circulation, which further triggers systemic inflammation. This systemic release of inflammatory mediators leads to vascular endothelial dysfunction and inflammation, which promotes persistent hypertension, exacerbates cardiovascular target organ damage, and promotes the development of refractory hypertension (Yang et al., 2023a; Ge et al., 2024). Approximately one-third of the healthy population is salt-sensitive, and salt-sensitive hypertension accounts for more than 50% of patients with hypertension (Bailey and Dhaun, 2024). The absorption of sodium ($Na^+$) and potassium ($K^+$) associated with hypertension occurs in the upper ileum; however, the intestinal flora may indirectly influence the absorption and metabolism of these nutrients by modulating the permeability of the intestinal epithelium and the activity of sodium and potassium transporter proteins, which in turn influence blood pressure (Li and Ren, 2023).

## 2.3 Relationship between hypertension and gut flora metabolites

Gut flora metabolites, such as SCFAs, trimethylamine N-oxide (TMAO), lipopolysaccharide (LPS), hydrogen sulfide ($H_2S$), and bile acids (BAs), are involved in blood pressure regulation (Ge et al., 2024). SCFAs are produced when gut bacteria ferment dietary fiber, primarily in the cecum and distal colon. It primarily comprises carboxylic acids with fewer than six carbon atoms. The most common s produced include acetate, propionate, and butyrate, which account for 95% of the total SCFAs content (Gao et al., 2024). They can lower blood pressure by dilating blood vessels. Fewer bacteria produce SCFAs when the gut flora is imbalanced, leading to the loss of epithelial barrier function, inflammation, and dysfunction of blood pressure regulation, leading to an increase in blood pressure (Felizardo et al., 2019). Furthermore, SCFAs play a pivotal role in the microbiota-gut-brain axis, influencing the integrity of the blood-brain barrier and the functionality of cells within the brain. Notably, acetate can exert antihypertensive effects by modulating microglia and astrocytes and suppressing neuroinflammation and sympathetic nerve output (Yin et al., 2024). Patients with recalcitrant hypertension have lower levels of propionate in their SCFAs than the healthy population (Ward et al., 2022). Propionate significantly inhibits the hypertensive inflammatory response via $CD4^+$ T cell expression in mice (Bartolomaeus et al., 2019). Moreover, treatment with oral butyrate or acetate inhibited the increase in the F/B ratio and blood pressure in spontaneously hypertensive rats (Robles-Vera et al., 2020).

TMAO is a metabolite produced by intestinal microorganisms that metabolizes choline and levulinic acid to trimethylamine (TMA), which is subsequently oxidized in the liver by flavin monooxygenase (FMO) (Gao et al., 2024). TMAO negatively affects the cardiovascular system, especially blood pressure regulation. It enhances the vasoconstrictive effects of Ang II, leading to vascular smooth muscle contraction and increased peripheral vascular resistance, thereby increasing blood pressure (Jiang et al., 2021). Second, TMAO triggers oxidative stress and excessive reactive oxygen species (ROS) damage in vascular endothelial cells and impairs the endothelial ability to release

nitric oxide (NO), leading to increased vascular stiffness and uncontrolled blood pressure. Additionally, TMAO promotes the accumulation of advanced glycosylation end products (AGEs), activates the receptor for AGEs (RAGE), triggers inflammation and oxidative stress, damages vascular elasticity and function, and contributes to atherosclerosis and increased blood pressure (Jiang and Duan, 2019; Han et al., 2024).

LPS, or endotoxin, is present in the outer membrane of the most abundant bacteria in the intestinal microbiome. When transferred from the gut to the body, gram-negative bacteria induce inflammation and increase intestinal permeability (Verhaar et al., 2020). LPS binds to Toll-like receptor 4 (TLR4), activating inflammatory signaling pathways, which leads to the release of pro-inflammatory factors (TNF-α, IL-6, and IL-1β). These factors impair vascular endothelial function, inhibit NO production, and weaken vasodilatation, which in turn increases blood pressure (Lu et al., 2008; Zusso et al., 2019). Additionally, LPS induces oxidative stress and excessive damage due to reactive oxygen species (ROS), which affect endothelial cells, exacerbates vascular stiffness, and drives the progression of hypertension (Grylls et al., 2021). Moreover, endotoxins also stimulate the development of hypertension. Simultaneously, endotoxins exacerbate hypertension by stimulating the central nervous system and activating sympathetic nerves, leading to vasoconstriction and increased cardiac output (Dai et al., 2023). In summary, endotoxins mainly contribute to hypertension via inflammation and influence the development and progression of hypertension via inflammation, oxidative stress, and sympathetic activation.

$H_2S$ gas is reductive, has a high concentration in the colon, and is synthesized mainly by intestinal epithelial cells and intestinal flora through enzymatic reactions (Cirino et al., 2023). It promotes vasodilation by activating ATP-sensitive potassium channels in vascular smooth muscle cells, leading to hyperpolarization of the cell membrane and lowering of blood pressure (Kanagy et al., 2017). Additionally, $H_2S$ promotes the differentiation and proliferation of regulatory T cells (Tregs), attenuates vascular and renal immune inflammation, and inhibits blood pressure elevation through the sulfation of liver kinase B1 (LKB1) (Cui et al., 2020). The treatment of SHRs with sodium hydrosulfide (NaHS) as a donor of $H_2S$ resulted in a significant reduction in blood pressure compared with that in Wistar rats (Ni et al., 2018).

BAs are released into the small intestine during digestion. The intestinal flora further converts them into secondary BAs that promote the absorption of fats and fat-soluble molecules (Tang et al., 2017). BAs lower blood pressure by directly acting on vascular endothelial cells and reducing the vasoconstrictive response induced by norepinephrine. Specific BAs, such as lithocholic acid and taurine goose deoxycholate, promote NO production, which further promotes vasodilation (Tominaga et al., 1988; Guizoni et al., 2020). Additionally, BAs can activate calcium-activated K+ channels (BK(Ca) channels) in patients with hypertension and abnormal calcium metabolism. This condition leads to vasodilation and lowers blood pressure (Ling et al., 2023). BAs also increase vascular smoothness and blood pressure. These acids contribute to lowering blood pressure by activating the farnesylate X receptor (FXR) and G protein-coupled BA receptor in vascular smooth muscle cells and endothelial cells, increasing large-conductance calcium-activated potassium channel activity, and promoting vasodilation (Ishimwe et al., 2022). The intestinal flora influences the host's metabolic and inflammatory responses by metabolizing BAs and dietary fiber, which may lead to alterations in blood pressure (Fan and Pedersen, 2021). Additionally, BAs may regulate the growth of flora through their antimicrobial effects, safeguarding the structural and functional integrity of the gut and maintaining homeostasis in the intestinal environment (Natividad et al., 2018) (Figure 1).

# 3 Relationship between traditional Chinese medicine, intestinal flora, and hypertension

TCM can treat hypertension by regulating the balance between probiotics and pathogenic bacteria, restoring the balance of intestinal microorganisms, improving intestinal barrier function, and regulating metabolites of the intestinal flora (Yang et al., 2023b). Currently, an increasing number of reports describe how intestinal flora are modified by TCM for treating hypertension, including studies related to TCM monomers, single-flavor TCM, TCM pairs, and TCM combinations. Changes in the intestinal flora in the hypertension model induced by TCM intervention (comparison between the administered and model groups) are shown in Table 1.

## 3.1 Traditional Chinese medicine monomers

TCM monomers are purified chemical compounds extracted from TCM and are an important part of the medicinal components of TCM. These monomeric compounds have high purity, well-defined chemical structures, and pharmacological activities, providing strong support for the modernization and development of TCM. Recently, it has been shown that some chemical components of TCM can regulate blood pressure by acting on the intestinal flora. For example, animal experiments have shown that baicalin can significantly inhibit Ang II-induced intestinal epithelial damage and barrier disruption in mice, inhibit inflammatory cell infiltration, and increase the expression of tight junction proteins (Zona Occludens 1 [ZO-1], cingulin, and occludin) and SCFA-producing flora in the intestinal tract (Aliceps and Butyricoccus). Therefore, it enhances intestinal mucosal barrier function, reduces intestinal permeability, protects the structural integrity of the intestine, and lowers blood pressure (Wu et al., 2019; Li B. et al., 2022). Rhynchophylline can optimize the intestinal flora structure by lowering the F/B ratio of SHRs, increasing and decreasing the abundance of beneficial and potentially pathogenic bacteria, respectively, thereby lowering blood pressure (Zhang et al., 2023). Quercetin reduces the F/B ratio, regulates gut flora balance, downregulates the TLR4/NF-κB inflammatory signaling pathway, attenuates myocardial fibrosis, and improves vascular dysfunction and vascular remodeling, thereby lowering blood pressure in SHRs and improving ventricular remodeling (Zhou et al., 2020). Moreover, resveratrol alters the intestinal flora of postnatal adult rats induced using a high-fat diet and NG-nitro-L-arginine-methyl ester. It also decreases the F/B ratio and increases the abundance of beneficial bacteria (Verrucomicrobia and Akkermansia), potentially preventing and

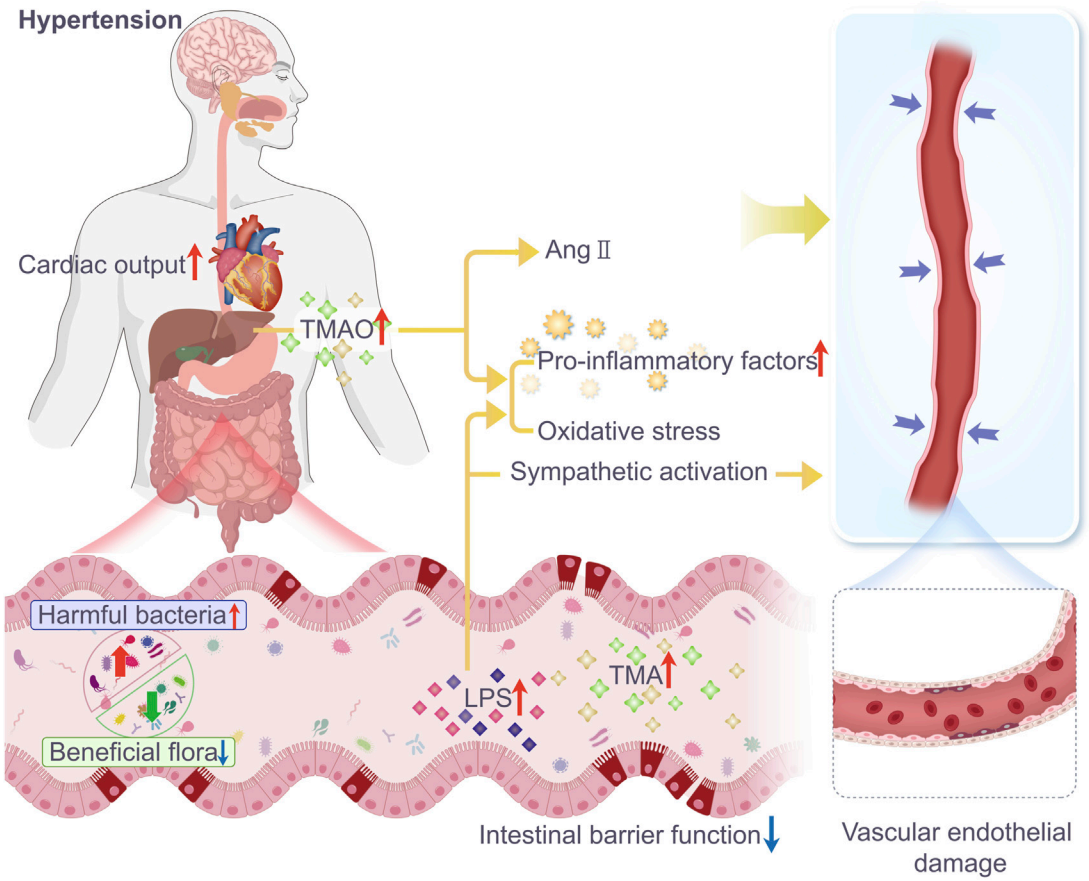


FIGURE 1
In patients with hypertension, the diversity and abundance of gut microbiota are significantly reduced, and there is a clear dysfunction of the intestinal barrier. The number of beneficial bacteria decreases, while the number of harmful bacteria and gut microbiota metabolites TMAO and LPS increase, leading to a reduction in tight junction proteins in the intestine and increased intestinal permeability. TMAO, a metabolite generated by intestinal microbes from TMA, is oxidized in the liver. It can cause hypertension by enhancing the vasoconstrictive effects of angiotensin II, increasing inflammatory factors, and inducing oxidative stress leading to vasoconstriction. LPS can exacerbate hypertension by releasing pro-inflammatory factors, inducing oxidative stress, and activating the sympathetic nervous system, leading to vasoconstriction and increased cardiac output.

reducing hypertension (Chen et al., 2019). Curcumin enhances the abundance of *Lactobacillus muridarum* in the intestines of hypertensive mice fed a high-salt diet. *Lactobacillus muridarum* prevents the exacerbation of salt-sensitive hypertension by regulating helper T cell 17 (TH17) (Han, 2021). Berberine reduces TMA production by modulating the abundance and activity of specific bacteria in the gut microbiota of patients with hypertension. This is achieved by inhibiting CutC/D-containing enzymes, thereby decreasing the plasma levels of TMAO. It also ameliorates vascular endothelial dysfunction by inhibiting the endoplasmic reticulum stress signaling pathway, thus regulating blood pressure (Wang et al., 2024). *Dendrobium officinale* polysaccharide regulates blood pressure by promoting the growth of beneficial flora (*Lactobacillus* and Lachnospiraceae_NK4A136_ group) and decreasing harmful flora (Desulfobacterota and Firmicutes) in the intestine, lowering the F/B ratio, modulating the production of SCFAs, activating the SCFA-GPCR43/41 pathway, improving vascular endothelial function and lipid levels, and enhancing intestinal barrier function. All these functions positively affect hypertension (Li M. et al., 2022). In summary, TCM monomers play a role in lowering blood pressure. This involves regulating the structure and function of the intestinal flora, altering the integrity of the intestinal barrier, decreasing inflammatory responses, and activating metabolite-related signaling pathways of the intestinal flora to reduce the production of harmful metabolites.

## 3.2 Single-flavor traditional Chinese medicines

Many studies have confirmed the efficacy of TCM in preventing and treating hypertension, and its mechanisms of action are closely related to the regulation of intestinal flora. For example, Digupi (Lycii Cortex) reduced the systolic and diastolic blood pressures of SHRs. The groups that received Digupi, including Elusimicrobia, Erysipelotrichia, Erysipelotrichales, Elusimicrobi-Ales, and Muribaculaceae, differed significantly from the model group (Shan et al., 2024). Theolatile oils from Danggui (Angelica sinensis (Oliv.) Diels) were used in SHR. The findings revealed that the abundance of *Aspergillus* spp. in the group that received high-dose Danggui volatile oil, which produces pro-inflammatory

TABLE 1 Changes in intestinal flora in a model of hypertension induced by TCM intervention (administered group vs model group).

| Related Chinese medicine | Type | Intestinal flora | Changes in the diversity index of intestinal flora | Analysis of the metabolite content of the intestinal flora | Sequencing methods | Bibliography |
|---|---|---|---|---|---|---|
| Baicalin | SHR | Akkermansia↑<br>Allobaculum↑<br>Bifidobacterium↑<br>Lachnospiraceae_NK4B4_group↑<br>Roseburia↑ | — | SCFA↑ | 16S rDNA | Wu et al. (2019) |
| Baicalin | Hypertensive mice induced by Ang II | g_Alistipes↑<br>f_Prevotellaceae↑<br>g_Anaerot r uncu↑<br>g_Intestinimonas↑<br>g_Gemmige↑<br>f_Coriobacteriaceae↑<br>g_Lachnospiracea_incertea_sedis↑<br>o_Actinomycetales↑<br>g_Butyricicoccus ↑<br>g_Corynebacterium↑ | — | — | 16S rDNA | Li M. et al. (2022) |
| Rhynchophylline | SHR | Firmicutes↓<br>Bacteroidetes↑<br>Ruminococcus↓<br>Oscillospira↓<br>Ruminococcus↓<br>Prevotella↑ | Chao1↑<br>Ace↑<br>Shannon↓ | — | 16S rDNA | Zhang et al. (2023) |
| Quercetin | SHR | Firmicutes↓<br>Bacteroidetes↑ | Ace↑<br>Shannon ↑ | — | 16S rDNA | Zhou et al. (2020) |
| Resveratrol | | Akkermansia↑<br>Verrucomicrobia↑ | — | — | 16S rRNA | Chen et al. (2019) |
| Curcumin | High-salt diet-induced hypertension in mice | *Lactobacillus* murinus ↑ | — | — | 16S rRNA | Han (2021) |
| Berberine | Patients with essential hypertension | Firmicutes↓<br>Lachnospiraceae_NK4A136_group↓<br>Alistipes↓<br>Clostridia_UCG_014↓<br>Ruminococcus↓<br>*Enterococcus*↓ | — | TMAO↓ | 16S rDNA | Wang et al. (2024) |
| DOPS | MH rats | Firmicutes ↓<br>Desulfobacterota↓<br>Bacteroidetes↑ | OTU↑ | SCFA↑ | 16S rRNA | Li B. et al. (2022) |
| Essential oils (EOs) from Angelica | SHR | Deferribacteres↓<br>Proteobacteria↓ | — | — | 16S rDNA | Shen et al., (2020) |
| Gegen | High-salt diet-induced hypertension in mice | *Clostridium*↑<br>Lachnospiraceae↓<br>Anaerotruncus↓<br>Rhodobacter↓<br>Eubacteriaceae↓<br>*Streptococcus*↓ | Shannon↑<br>Simpson ↑ | | 16S rDNA | Li et al. (2020) |
| Danshen | Hypertensive rats induced by high-salt diet | Prevotellaceae↑ | Chao1↑<br>ACE↑ | — | 16S rDNA | Qi et al. (2024) |
| Papaya | SHR | *Bacteroides*↑<br>Bacteroidaceae↑<br>Terrisporobacter↑<br>Peptostreptococcaceae ↑<br>Firmicutes↓ | — | — | 16 S rRNA | Chen et al. (2023) |

(Continued on following page)

TABLE 1 (*Continued*) Changes in intestinal flora in a model of hypertension induced by TCM intervention (administered group vs model group).

| Related Chinese medicine | Type | Intestinal flora | Changes in the diversity index of intestinal flora | Analysis of the metabolite content of the intestinal flora | Sequencing methods | Bibliography |
|---|---|---|---|---|---|---|
| Dendrobium officinale | MH rats | Firmicutes ↓<br>norank_f__Bacteroidales_S24-7_group↑<br>Lachnospiraceae↓<br>Christensenellaceae_R-7_group↓ | — | SCFA↑ | 16S rDNA | Li et al. (2021) |
| Huangjing | MH rats | *Streptococcus*↑<br>Desulfobacterota↓<br>Desulfovibrio↓<br>unclassified_f_Lachnospiraceae↓<br>Ruminococcus_torques_group↓<br>Eubacterium_hallii_group ↓ | — | SCFA↑<br>LPS↓ | 16 S rRNA | Su et al. (2022) |
| Duzhong and Cijili | SHR | Actinobacteria↓ | PD_whole_tree↑ | SCFA↑ | 16S rDNA | Qi et al. (2019) |
| Huangqin and Huaihua | SHR | Firmicutes ↓<br>Bacteroidetes↑<br>Lactobacillaceae↑<br>Clostridiales ↓<br>Bifidobacteriaceae↑ | — | — | 16 S rRNA | Guan (2020) |
| Huangqin and Danshen | SHR | *Lactobacillus*↑<br>Bifidobacterium↑<br>Akkermansia_muciniphila ↑<br>*Lactobacillus*↑<br>*Lactobacillus* reuteri ↑ | — | — | 16S rDNA | Han et al. (2019) |
| Sanoshashinto | SHR | *Lactobacillus*↑ | — | — | 16S rRNA | Wu et al. (2020) |
| HuanglianJiedu decoction | SHR | *Lactobacillus*↑<br>Firmicutes↓ | Simpson↑ | — | 16S rDNA | Ma et al. (2020) |
| Xiaochaihu decoction | Hypertensive patient | *Enterococcus*↓Yeast↓<br>*Enterobacter*↓<br>*Bacteroides*↑<br>*Lactobacillus*↑<br>Bifidobacter↑ | — | — | Japan Mitsuoka contentment method | Wu et al. (2022) |
| Fufang-Zhenzhu-Tiaozhicapsuledecoction | High-fructose and high-salt (HFS) diet-fed rats | Proteobacteria↑<br>Verrucomicrobia↑<br>Fusobacteria↑<br>Firmicutes↓<br>*Lactobacillus*↓<br>Bifidobacterium↓<br>Burkholderia-Caballeronia-Paraburkholderia↑<br>Corynebacterium↑<br>Prevotella↑ | — | — | 16S rRNA | Chen et al. (2022) |
| QiangshuJiangya formula | L-NAME induced hypertensive rats | Firmicutes↓<br>Bacteroidetes↑<br>Ruminococcus↑ | Shannon↑<br>Simpson↓ | — | 16S rDNA | Huang (2022) |
| Erxian decoction | Ovariectomized (OVX) rats | Firmicutes↓<br>Bacteroidetes↑<br>Clostridia UCG-014↓<br>Clostridia vadinBB60 group↓<br>Ruminococcaceae↓<br>Muribaculaceae↑<br>*Bacteroides*↑<br>Parabacteroides↑<br>Prevotellaceae NK3B31group↑ | — | TMAO↓ | 16S rRNA | Hu (2023) |

(Continued on following page)

TABLE 1 (*Continued*) Changes in intestinal flora in a model of hypertension induced by TCM intervention (administered group vs model group).

| Related Chinese medicine | Type | Intestinal flora | Changes in the diversity index of intestinal flora | Analysis of the metabolite content of the intestinal flora | Sequencing methods | Bibliography |
|---|---|---|---|---|---|---|
| TaohongSiwu decoction | High-salt diet-induced hypertension in mice | *Lactobacillus*↑<br>Allobaculum↑ | Chao1 ↓<br>Shannon↑ | BA↑ | 16 S rRNA | Liu et al. (2023) |
| Qinggan Yishen Qufeng Compound | Hypertensive mice induced by Ang II | Firmicutes↓<br>Deferribacteres↓<br>Acidobacteria↓<br>Actinobacteria↓<br>Bacteroidetes↑ | Chao1↑<br>Simpson↑ | BA↑ | 16S rDNA | Zhen (2020) |
| Zhengan Xifeng decoction | SHR | Proteobacteria ↓<br>Turicibacter↓<br>Coprococuus↑<br>*Clostridium*↑<br>*Lactobacillus*↓<br>Ruminococcus↑ | OTU↓<br>Shannon↓<br>Simpson↑ | — | 16S rDNA | Yu et al. (2019),<br>Xu et al. (2022) |
| Chaigui decoction | High-salt diet-induced hypertension in mice | Bacteroidia↑<br>Clostridia↓ | — | — | 16S rRNA | Zhu et al. (2023a) |
| Chaigui decoction | SHR | unclassified_f__S24-7↑ | — | — | 16S rRNA | Zhu et al. (2023b) |
| Medicine and food homologous Chinese medicine formula | (2K1C) Hypertension rats | Firmicutes↓<br>Bacteroidetes↑<br>*Lactobacillus*↑<br>Blautia↑<br>Romboutsia↑<br>Enterococuus↓ | ACE↑<br>Shannon↑<br>Simpson ↓ | BA↑ | 16S rDNA | Guo et al. (2023) |
| Jiawei BanxiaBaizhu Tianma decoction | MH rats | *Streptococcus*↑<br>Desulfobacter↓<br>Desulfovibrio↓ | — | SCFA↑<br>LPS↓ | 16S rRNA | Wu et al. (2024) |
| Tianma-Gouteng granules | SHR | Desulfovibrio↑, Lachnoclostridium↑<br>Turicibacter↑<br>Alluobaculum↓<br>Monoglobus↓ | Shannon ↓<br>Simpson↑ | BA↑ | 16 S rRNA | Yu et al. (2024) |

toxins, was significantly lower than that in the model group. Therefore, the volatile oil of Danggui may reduce blood pressure by decreasing the abundance of Aspergillus and the production of pro-inflammatory toxins (Shen et al., 2020). Gegen (*Pinus lobata* (Willd.) Ohwi.) and Xiakucao (*Prunella vulgaris* L.) significantly reduced elevated blood pressure induced by a high-salt diet in mice. This may partly restore the diversity of the intestinal flora and increase the abundance of the beneficial bacterium *Clostridium* by elevating the Shannon and Simpson indices. Additionally, it decreased the abundance of Lachnospiraceae, Anaerotruncus, Rhodobacter, Eubacteriaceae, and *Streptococcus*, which are harmful bacteria that are positively associated with hypertension (Li et al., 2020). Danshen (Salvia miltiorrhizage) can regulate blood pressure by improving the diversity and structure of intestinal microorganisms, increasing the abundance of beneficial flora, such as Prevotellaceae, decreasing the F/B ratio, modulating the immune response, and attenuating the inflammatory response and vascular damage induced by a high-salt diet (Qi et al., 2024). Papaya can lower blood pressure in SHRs through its rich dietary fiber content that regulates the intestinal flora, thus lowering the F/B ratio, increasing the activation of G protein-coupled receptor 41 (GPR41) by SCFAs, upregulating the expression of tight junction proteins, and restoring intestinal barrier function by reducing inflammatory factor release (Chen et al., 2023). The ultrafine powder of Dendrobium officinale enhances the gut microbiota and boosts the generation, transfer, and use of SCFAs, subsequently triggering the intestinal-vascular SCFA-GPCR43/41 signaling pathway, which enhances the endothelial function of the blood vessels and ultimately reduces blood pressure in rats with metabolic hypertension (Li et al., 2021). Huangjing (Polygonatum sibiricum Red. Superfine powder, PSP) enhances the integrity of the intestinal barrier by upregulating the expression of tight junction proteins (Claudin-1, occludin, and ZO-1), thereby reducing intestinal permeability and effectively reducing pathogens and harmful substances from LPS in the blood circulation. Additionally, PSP regulates intestinal flora by decreasing and

increasing the abundance of harmful (Desulfobacter and Desulfovibrio) and beneficial (*Streptococcus*) bacteria, respectively. The combined effects improve blood pressure in rats with metabolic hypertension (MH) induced by a high-sugar, high-fat, and complex alcohol diet (Su et al., 2022). In summary, single-flavor TCM may exert blood pressure-lowering effects by improving the balance of intestinal flora, enhancing intestinal barrier function, promoting the metabolites produced by beneficial flora such as SCFAs, improving vascular endothelial function, and attenuating inflammatory responses.

## 3.3 Traditional Chinese medicine pairs

Some TCM pairs have been experimentally validated for the treatment of hypertension. Recently, the intestinal flora has received increasing attention as a novel therapeutic target for the treatment of hypertension, and studies on the effects of TCM pairs on intestinal flora have also increased. Duzhong (Eucommia ulmoides Oliv.) and Cijili (Tribulus terrestris) spontaneously reduced the abundance of actinomycetes in older rats with hypertension. The abundance of actinomycetes in these rats increases the level of SCFAs in feces and regulates blood pressure by reducing the production of inflammatory factors (Qi et al., 2019). Huangqin (Scutellaria baicalensis Georgi) and Huaihua (Sophora japonica L.) increased the biodiversity of the intestinal flora in SHRs, decreased the F/B ratio, and increased the abundance of beneficial bacteria. Moreover, Lactobacillaceae and Bifidobacteriaceae ameliorated intestinal damage, repaired intestinal villi, and increased mucin expression, which reduced blood pressure (Guan, 2020). Huangqi (Arabidopsis membranaceus (Fisch.) Bge. var. mongholicus (Bge) Hsiao) and Danshen may increase *Akkermansia muciniphila* by increasing the abundance of probiotics such as *Lactobacillus* spp., Bifidobacterium spp., *Lactobacillus intestinalis*, and *Lactobacillus reuteri*, which regulate the structure and diversity of the intestinal flora and decrease the F/B ratio, improving the intestinal microecology and further reducing the blood pressure of SHRs (Han et al., 2019).

## 3.4 Traditional Chinese medicine compounding

TCM compounding involves the combination of two or more TCMs, following certain compounding principles. Some TCM compounds developed to manage hypertension based on their action on intestinal flora have been effective and have been studied more extensively than monomers, single-flavored TCM, and TCM pairs. For example, Sanoshashinto can increase the number of lactobacilli in the intestines of SHRs, thereby regulating blood pressure (Wu et al., 2020). The Huanglian Jiedu decoction may relieve high blood pressure by increasing the intestinal flora of SHR, reducing and increasing the relative abundance of Firmicutes based on the relative abundance of the probiotic *lactobacillus* (Ma et al., 2020). Xiaochaihu decoction combined with irbesartan is more effective than irbesartan alone in lowering blood pressure. This combination reduces the relative abundance of enterococci, yeasts, and Enterobacteriaceae and increases the relative abundance of probiotic lactobacilli (Wu et al., 2022). Fufang-Zhenzhu-Tiaozhi capsule (FTZ)-treated HFS-fed rats with hypertension showed improved intestinal microbial abundance and diversity and increased abundance of Proteobacteria, Verrucomicrobia, and Fusobacteria compared with the model group. Transplantation with FTZ-modulated gut microbiota decreased blood pressure in HFS-fed rats, highlighting that FTZ modulates the intestinal flora and decreases blood pressure (Chen et al., 2022). The Qiangshu Jiangya formula reduces the F/B ratio in NG-nitro-L-arginine methyl ester hydrochloride (L-NAME)-induced hypertension, increases the abundance of SCFA-producing Ruminococcus, and improves oxidative stress *in vivo* (Huang, 2022). Erxian decoction can decrease the relative abundance of TMAO-related Firmicutes and Ruminococcaceae, improve the metabolism of TMAO and its related precursors in circulation, affect the TXNIP/NLRP3 inflammatory pathway, reduce the inflammatory response, and decrease blood pressure elevation in ovariectomized rats (Hu, 2023). The mechanism of action of Taohong Siwu decoction combined with Dubosiella newyorkensis in the treatment of hypertension is the regulation of intestinal microecology, especially the increase in the beneficial bacteria *Lactobacillus* and Allobaculum, the improvement of serum BA metabolism, and the improvement of vascular endothelial function through this action, leading to the effective control of blood pressure (Liu et al., 2023). The compound Qinggan Yishen Qufeng inhibits pathological changes in the ileum and colon, protects the intestinal barrier structure, and regulates the positive correlation with blood pressure in a mouse model of Ang II-induced hypertension. It achieves this by positively influencing the abundance of specific bacterial groups (Actinobacteria, Acidobacteria, Myxococcales, Bacteroidaceae, g_Bacteroidaceae, and g_Tyzzerella, among others). Conversely, it negatively affects bacterial groups, such as Enterobacteriaceae and Rikenellaceae, including g_Alistipes and g_Rikenellaceae_RC9_gut_group, with other abundant specific bacterial groups and blood pressure-related metabolite (DPAn-6, desmethyldeoxycholic acid, and taurocholic acid) levels, thereby reducing blood pressure (Zhen, 2020). Zhengan Xifeng decoction significantly reduces blood pressure in SHRs, regulates the structure of the intestinal flora, reduces the F/B ratio, increases the number of SCFA-producing bacteria, promotes the conversion of lactic acid to butyric acid in the intestinal tract, reduces the levels of d-lactic acid and diamine oxidase (DAO) in the intestinal tract, and maintains the integrity of the intestinal barrier, thus lowering blood pressure (Yu et al., 2019; Xu et al., 2022). Moreover, Chaigui decoction can increase angiotensin-converting enzyme (ACE) two levels in the plasma and decrease renin levels in renal tissues, thereby decreasing the renin to ACE2 ratio. It also improves the intestinal flora by increasing the abundance of beneficial *Bacteroides* and decreasing the abundance of harmful Clostridia. Additionally, Chaigui decoction reduces systolic and diastolic blood pressure, modulates the renin-angiotensin-aldosterone system, affects serum levels of lysophosphatidylcholine, and may further reduce blood pressure by increasing the abundance of S24-7 Bacteroidia, which is negatively associated with blood pressure regulation; this effect has been validated in a hypertensive rat model (Zhu et al., 2023a; Zhu et al., 2023b). The medicinal and food homologous TCM compounding reduces the F/B ratio, increases the abundance of *Lactobacillus*, and regulates serum metabolites and their related

TABLE 2 Composition of TCM compound formula.

| Compound prescription of Chinese medicine | Traditional Chinese medicine composition |
|---|---|
| Sanoshashinto | Rhei rhizoma, Scutellariae radix, Coptidis rhizoma |
| HuanglianJiedu decoction | Coptis chinensis Franch., Phellodendron chinense Schneid., Scutellaria baicalensis Georgi, Gardenia jasminoides Ellis |
| Xiaochaihu decoction | Bupleurum chinense DC., Codonopsis pilosula (Franch.) Nannf., Scutellaria baicalensis Georgi, Glycyrrhiza uralensis Fisch., Pinellia ternata (Thunb.) Breit., Zingiber officinale Rosc., Ziziphus jujuba Mill |
| Fufang-Zhenzhu-Tiaozhi capsule | Citri sarcodactylis fructus, Ligustri lucidi fructus, Salviae miltiorrhizae radix et rhizoma, Notoginseng radix et rhizoma, Coptidis rhizoma, Atractylodis macrocephalae rhizoma, Cirsii japonici herba et radix, Eucommiae cortex |
| QiangshuJiangya formula | Cyathula officinalis, Ilex hainanensis Merr, Epimedium, Eucommia ulmoides, Pueraria |
| Erxian decoction | CurculigoorchioidesGaertn., Epimedium brevicornu Maxim., Angelica sinensis (Oliv.) Diels, Morinda officinalis How, Phellodendron chinense Schneid., Anemarrhena asphodeloides Bge |
| TaohongSiwu decoction | Angelica sinensis (Oliv.) Diels, Ligusticum striatum DC., Rehmannia glutinosa (Gaertn.) DC., Paeonia delavayi Franch. Prunus davidiana (CarriŠre) Franch |
| Qinggan Yishen Qufeng formula | Prunella vulgaris L., Ligusticum chuanxiong Hort., Bupleurum chinense DC., Coptis chinensis Franch, Notopterygium incisum Ting ex H.T. Chang. Saposhnikovia divaricata (Turcz.) Schischk., Cyathula officinalis Kuan, Polygonatum sibiricum Red., Haliotis diversicolor Reeve, Scutellaria baicalensis Georgi, Taxillaria baicalensis Georgi, Taxillus chinensis (DC.) Danser |
| Zhengan Xifeng decoction | Achyranthes bidentata Bl., Ruddle, Long Gu, Oyster shell, *Chinemys reevesii* (Gray), Paeonia lactiflora Pall., Scrophularia ningpoensis Hemsl. Asparagus cochinchinensis (Lour.) Merr., Melia toosendan Sieb.et Zucc., Hordeum vulgare L., Artemisia scoparia Waldst.et Kit. Glycyrrhiza uralensis Fisch |
| Chaigui decoction | Bupleurum chinense DC, Glehnia littoralis Fr. Schmidt ex Miq., Pinellia ternata (Thunb.) Breit., Alisma orientale (Sam.) Juzep., Scutellaria baicalensis Georgi, Zingiber officinale Rosc. baicalensis Georgi, Zingiber officinale Rosc., Angelica sinensis (Oliv.) Diels, Paeonia lactiflora Pall., Poria cocos (Schw.) Wolf, Atractylodes macrocephala Koidz., Ligusticum chuanxiong Hort |
| Medicine and food homologous; Chinese medicine formula | Puerariae lobatae Radir, Prunellae spica, Eucommiae folium, Chrysanthemi flos, Crataegi fructus, *Apium graveolens* |
| Jiawei BanxiaBaizhu Tianma decoction | Pinelliaternata (Thunb.) Breit., Atractylodes macrocephala Koidz., Gastrodiaelata Bl., Citrus reticulata Blanco, Uncaria rhynchophylla (Mig.) Mig. ex Havil., Poria cocos (Schw.) Wolf, Alisma orientale (Sam.) Juzep., Glycyrrhiza uralensis Fisch |
| Tianma-Gouteng granules | Gastrodiaelata Blume, Uncaria rhynchophylla (Miq.) Miq. ex Havil, Haliotis diversicolor Reeve, Gardenia jasminoides Ellis, Scutellaria baicalensis Georgi, Achyranthes bidentata Bl., Eucommia ulmoides Oliv. baicalensis Georgi, Leonurus japonicus Houtt., Taxillus chinensis (DC.) Danser, Poria cocos (Schw.) Wolf., Polygonum multiflorum Thunb |

metabolic pathways by modulating the intestinal flora structure of two kidneys and one clip (2K1C) rats with hypertension. This compounding reduced blood pressure in a hypertensive rat model, reduced metabolites and their related metabolic pathways, repaired vascular and organ damage, and exerted comprehensive therapeutic effects on hypertension (Guo et al., 2023). The Jiawei Banxia Baizhu Tianma Decoction (MBTD) regulates the structure of the intestinal microbial community by increasing the level of *Streptococcus* species, decreasing the level of Desulfovibrio desulfuricans and *Vibrio desulfuricans*, increasing the expression of short SCFAs and their receptors GPCR41 and GPCR43, enhancing intestinal barrier function, and decreasing the level of LPS in the serum. MBTD inhibits the vascular TLR4/MyD88 pathway, regulates the balance between NO and ET-1, and improves vascular endothelial function, thus effectively improving blood pressure and lipid metabolism disorders in hypertensive rats (Wu et al., 2024). Tianma-Gouteng granules increase the relative abundance of Desulfovibrio, Lachnoclostridium, and Turicibacter and decrease the relative abundance of Allobaculum and Monoglobus by regulating the balance of the intestinal flora in the hypertensive rat model. It further regulates BA metabolism through the gut–hepatic axis, affects the FXR-FGF15-CYP7A1 signaling pathway, and promotes the synthesis and secretion of BAs to comprehensively regulate blood pressure, thus playing an important role in the treatment of hypertension (Yu et al., 2024). The composition of each TCM compounding is listed in Table 2. TCM compounds show therapeutic effects on hypertension by regulating the balance of intestinal flora, increasing the abundance of beneficial bacteria, decreasing the abundance of harmful bacteria, improving the intestinal barrier function, promoting the production of short-

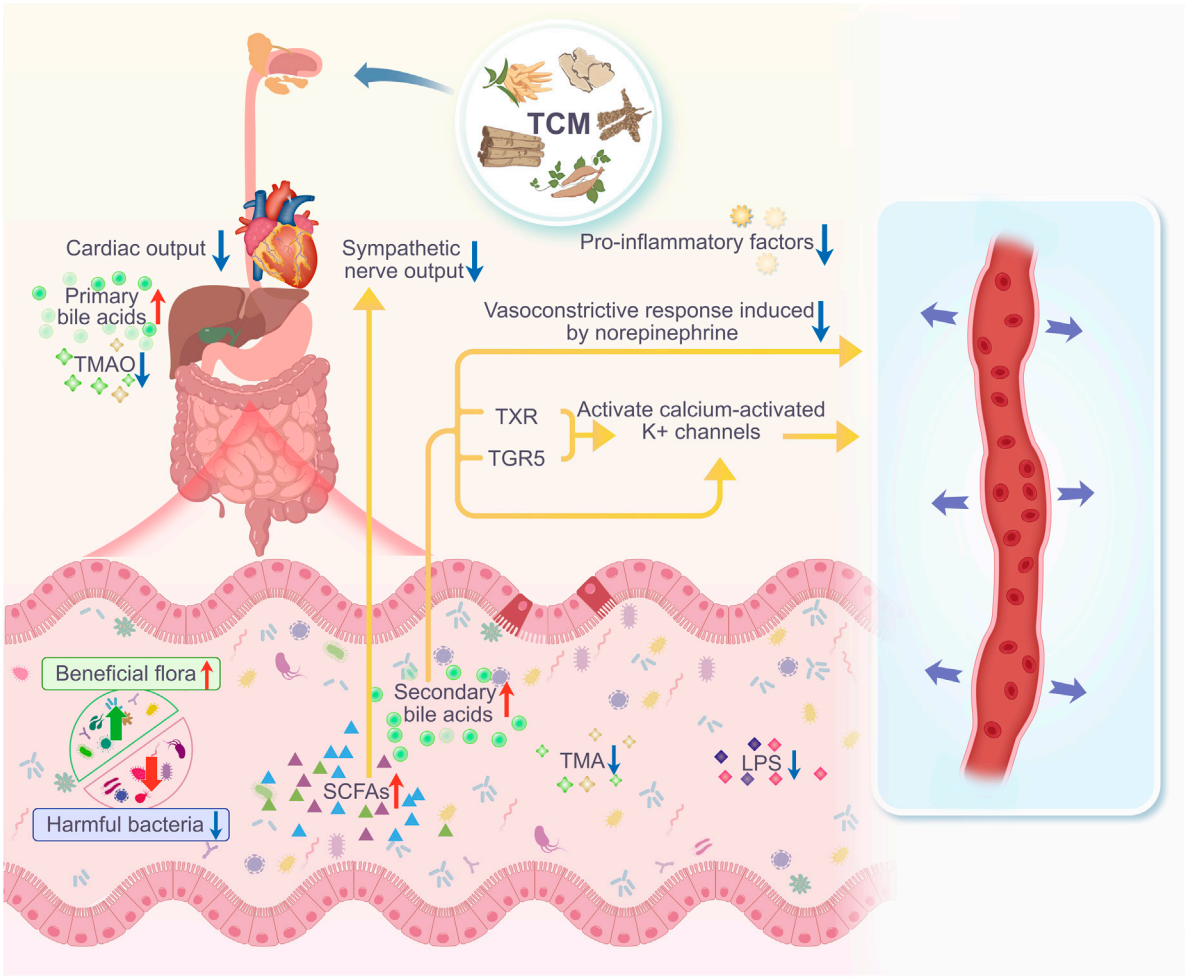


FIGURE 2
After taking TCM, the diversity and abundance of gut microbiota in hypertensive individuals/animals increase. The number of harmful bacteria decreases, while the number of beneficial bacteria increases, leading to a significant improvement in intestinal barrier function, and an increase in gut microbiota metabolites such as SCFAs and BAs. SCFAs can reduce inflammatory responses and inhibit sympathetic nerve output, effectively lowering blood pressure. Primary BAs are stored in the gallbladder and released into the intestine during digestion, where gut microbiota convert them into secondary BAs. These secondary BAs can also reduce vasoconstriction caused by norepinephrine, and can promote vasodilation by directly activating BK(Ca) channels, or by activating FXR and TGR5 to increase the activity of large-conductance BK(Ca) channels, thereby lowering blood pressure.

chain fatty acids, regulating the level of metabolites related to blood pressure, and influencing the metabolism of BAs through the intestinal–hepatic axis, which in turn integrally regulates blood pressure (Figure 2).

## 4 Conclusion

This study systematically reviewed current research on TCM regulation of gut microbiota to control hypertension, and demonstrated consistent findings. Various TCM approaches impacted blood pressure through multiple mechanisms, primarily in modulating the composition of gut microbiota, enhancing intestinal barrier function, regulating gut-derived metabolites, and suppressing inflammatory responses. First, TCM reshapes the microbiota by increasing beneficial bacteria, such as bifidobacterium and *lactobacillus*, and inhibiting harmful bacteria. Second, TCM reduces intestinal permeability by upregulating tight junction proteins, such as ZO-1 and occludin, thus preventing gut-derived toxins (e.g., LPS) from entering the bloodstream, thereby protecting the vascular endothelium. Additionally, TCM influences the production of gut metabolites, including SCFAs and TMAO. SCFAs contribute to vasodilation, whereas TMAO, associated with hypertension, increases vascular resistance and induces endothelial damage. TCM also reduces the expression of inflammatory factors such as IL-6 and TNF-α, mitigating vascular injury caused by hypertension. Several animal studies have shown that TCM significantly lowers systolic and diastolic blood pressure in hypertensive models, with reductions generally ranging from 10 to 50 mmHg, which is clinically meaningful. However, most existing studies are limited by small sample sizes and there is a lack of large-scale randomized controlled trials. Future multi-center clinical trials are essential to verify TCM's efficacy and safety, optimize therapeutic protocols, and establish a basis for

standardized and personalized applications in hypertension management.

## Author contributions

WC: Writing–review and editing, Writing–original draft, Conceptualization, Data curation, Formal analysis, Methodology. LX: Writing–original draft, Conceptualization, Software, Methodology. WG: Writing–original draft, Investigation, Data curation. HL: Writing–original draft, Methodology, Data curation. RC: Writing–review and editing, Methodology, Funding acquisition, Investigation. ZD: Writing–review and editing, Methodology, Investigation. QC: Writing–review and editing, Software, Project administration, Investigation, Visualization. QL: Writing–review and editing, Validation, Resources, Project administration, Methodology.

## Funding

The author(s) declare that financial support was received for the research, authorship, and/or publication of this article. 12th Five-year Key Construction Discipline of State Administration of Traditional Chinese Medicine "Dai Pharmacy". Educational scientific research project of Yunnan University of Chinese Medicine (YB240326). The construction project of the National Public Employment Service Capacity Improvement Demonstration Project "Yi Medicine Master Studio". Yunnan Province First-Class Discipline Provincial Key Support Construction Discipline - Traditional Chinese Medicine (TCM), Yunnan University of Chinese Medicine "Gu Ben Pei Yuan" Discipline Team Construction Project "Ethnic Characteristic Diagnosis and Treatment Research Discipline Team" (10171100600BK). Key Research and Development Plan of Yunnan Province Science and Technology Department Social Development Special Plan (202403AC100017). Yunnan Province Dai Medicine and Yi Medicine Key Laboratory Development Project (2024JS2409). Yunnan University of Chinese Medicine Young Talents Project. National Administration of Traditional Chinese Medicine Science and Technology Department Research on the Key Information Verification of Ancient Classic Prescriptions in Minority Medicines. Higher Education "121" Project Special Program - Traditional Chinese Medicine (TCM) - Ethnic Characteristic Diagnosis and Treatment Research Discipline Team (31271100200BK).

## Acknowledgments

The authors gratefully acknowledge the support of the 12th Five-year Key Construction Discipline of State Administration of Traditional Chinese Medicine "Dai Pharmacy".

## Conflict of interest

The authors declare that the research was conducted in the absence of any commercial or financial relationships that could be construed as a potential conflict of interest.

## Publisher's note



## References

Bailey, M. A., and Dhaun, N. (2024). Salt sensitivity: causes, consequences, and recent advances. *Hypertension* 81 (3), 476–489. doi:10.1161/HYPERTENSIONAHA.123.17959

Bartolomaeus, H., Balogh, A., Yakoub, M., Homann, S., Markó, L., Höges, S., et al. (2019). Short-chain fatty acid propionate protects from hypertensive cardiovascular damage. *Circulation* 139 (11), 1407–1421. doi:10.1161/CIRCULATIONAHA.118.036652

Cai, M., Lin, L., Jiang, F., Peng, Y., Li, S., Chen, L., et al. (2023). Gut microbiota changes in patients with hypertension: a systematic review and meta-analysis. *J. Clin. Hypertens. (Greenwich)* 25 (12), 1053–1068. doi:10.1111/jch.14722

Chen, H. E., Lin, Y. J., Lin, I. C., Yu, H. R., Sheen, J. M., Tsai, C. C., et al. (2019). Resveratrol prevents combined prenatal N(G)-nitro-L-arginine-methyl ester (L-NAME) treatment plus postnatal high-fat diet induced programmed hypertension in adult rat offspring: interplay between nutrient-sensing signals, oxidative stress and gut microbiota. *J. Nutr. Biochem.* 70, 28–37. doi:10.1016/j.jnutbio.2019.04.002

Chen, K., Wu, S., Guan, Y., Ma, Y., Huang, Y., Liu, X., et al. (2023). Changes in gut microbiota linked to a prevention of cardiac remodeling induced by hypertension in spontaneously hypertensive rats fed a pawpaw fruit diet. *Heliyon* 9 (5), e15576. doi:10.1016/j.heliyon.2023.e15576

Chen, Z., Yang, B., Wang, Z., Rong, X., Zhu, Q., and Guo, J. (2022). Modulation of the gut microbiota by Fufang-Zhenzhu-Tiaozhi capsule attenuates hypertension induced by a high-fructose and high-salt diet. *Front. Cell. Infect. Microbiol.* 12, 854849. doi:10.3389/fcimb.2022.854849

Cirino, G., Szabo, C., and Papapetropoulos, A. (2023). Physiological roles of hydrogen sulfide in mammalian cells, tissues, and organs. *Physiol. Rev.* 103 (1), 31–276. doi:10.1152/physrev.00028.2021

Cui, C., Fan, J., Zeng, Q., Cai, J., Chen, Y., Chen, Z., et al. (2020). CD4(+) T-cell endogenous cystathionine γ lyase-hydrogen sulfide attenuates hypertension by Sulfhydrating liver kinase B1 to promote T regulatory cell differentiation and proliferation. *Circulation* 142 (18), 1752–1769. doi:10.1161/CIRCULATIONAHA.119.045344

Cui, Y., Wang, Q., Chang, R., Zhou, X., and Xu, C. (2019). Intestinal barrier function-non-alcoholic fatty liver disease interactions and possible role of gut microbiota. *J. Agric. Food Chem.* 67 (10), 2754–2762. doi:10.1021/acs.jafc.9b00080

Dai, Y., Shen, Z., Khachatryan, L. G., Vadiyan, D. E., Karampoor, S., and Mirzaei, R. (2023). Unraveling mechanistic insights into the role of microbiome in neurogenic hypertension: a comprehensive review. *Pathol. Res. Pract.* 249, 154740. doi:10.1016/j.prp.2023.154740

de Almeida Silva, M., Mowry, F. E., Peaden, S. C., Andrade, T. U., and Biancardi, V. C. (2020). Kefir ameliorates hypertension via gut-brain mechanisms in spontaneously hypertensive rats. *J. Nutr. Biochem.* 77, 108318. doi:10.1016/j.jnutbio.2019.108318

Fan, Y., and Pedersen, O. (2021). Gut microbiota in human metabolic health and disease. *Nat. Rev. Microbiol.* 19 (1), 55–71. doi:10.1038/s41579-020-0433-9

Felizardo, R. J., Watanabe, I. K., Dardi, P., Rossoni, L. V., and Câmara, N. O. (2019). The interplay among gut microbiota, hypertension and kidney diseases: the role of short-chain fatty acids. *Pharmacol. Res.* 141, 366–377. doi:10.1016/j.phrs.2019.01.019

Gao, K., Wang, P. X., Mei, X., Yang, T., and Yu, K. (2024). Untapped potential of gut microbiome for hypertension management. *Gut Microbes* 16 (1), 2356278. doi:10.1080/19490976.2024.2356278

Ge, Y., Wang, J., Wu, L., and Wu, J. (2024). Gut microbiota: a potential new regulator of hypertension. *Front. Cardiovasc. Med.* 11, 1333005. doi:10.3389/fcvm.2024.1333005

Grylls, A., Seidler, K., and Neil, J. (2021). Link between microbiota and hypertension: focus on LPS/TLR4 pathway in endothelial dysfunction and vascular inflammation, and therapeutic implication of probiotics. *Biomed. Pharmacother.* 137, 111334. doi:10.1016/j.biopha.2021.111334

Guan, Y. (2020). *Study on the effect and mechanism of the matched pair of Scutellariae Radix and Sophora japonica L. ameliorate hypertension and hypertensive renal injury*. China: Southern Medical University.

Guizoni, D. M., Vettorazzi, J. F., Carneiro, E. M., and Davel, A. P. (2020). Modulation of endothelium-derived nitric oxide production and activity by taurine and taurine-conjugated bile acids. *Nitric Oxide* 94, 48–53. doi:10.1016/j.niox.2019.10.008

Guo, L., Sheng, W., He, Y., Xu, X., Lin, S., and Chen, W. (2023). Effect of medicine and food homologous Chinese medicine on hypertensive rats by affecting intestinal flora structure and regulating serum metabolites. *Chin. Trad. Herb. Drugs* 54 (20), 6743–6752. doi:10.7501/j.issn.0253-2670.2023.20.018

Han, C., Jiang, Y., Li, W., Liu, Y., Qi, Z., and Bai, W. (2019). Study on the mechanism of Astragalus and Salvia miltiorrhiza on intestinal flora of spontaneously hypertensive rats based on 16S rDNA sequencing technology. *China J. Trad. Chin. Med. Pharm.* 34 (05), 2233–2237.

Han, J. (2021). *Curcumin by activating TRPV4 channels in vascular endothelial cells improves hypertension*. China: Jiangnan University.

Han, J. M., Guo, L., Chen, X. H., Xie, Q., Song, X. Y., and Ma, Y. L. (2024). Relationship between trimethylamine N-oxide and the risk of hypertension in patients with cardiovascular disease: a meta-analysis and dose-response relationship analysis. *Med. (Baltim.)* 103 (1), e36784. doi:10.1097/MD.0000000000036784

Hu, J. (2023). Exploring the myocardial protective effects of EXD on OVX rats based on TMAO-NLRP3 pathway. *Univ. China Acad. Chin. Med. Sci.* doi:10.27658/d.cnki.gzzyy.2023.000153

Huang, X. (2022). *Study on Pharmacodynamic material basis and mechanism of Qiangshu Jiangya formula in hypertensive rats*. China: Guangdong Pharmaceutical University.

Illiano, P., Brambilla, R., and Parolini, C. (2020). The mutual interplay of gut microbiota, diet and human disease. *FEBS J.* 287 (5), 833–855. doi:10.1111/febs.15217

Ishimwe, J. A., Dola, T., Ertuglu, L. A., and Kirabo, A. (2022). Bile acids and salt-sensitive hypertension: a role of the gut-liver axis. *Am. J. Physiol. Heart Circ. Physiol.* 322 (4), H636–H646. doi:10.1152/ajpheart.00027.2022

Jiang, S., Shui, Y., Cui, Y., Tang, C., Wang, X., Qiu, X., et al. (2021). Gut microbiota dependent trimethylamine N-oxide aggravates angiotensin II-induced hypertension. *Redox Biol.* 46, 102115. doi:10.1016/j.redox.2021.102115

Jiang, X., and Duan, J. (2019). Research progress on mechanism of atherosclerosis induced by trimethylamine-N-oxide. *Chin. J. Mult. Organ Dis. Elder.* 18 (02), 157–160. doi:10.11915/j.issn.1671-5403.2019.02.031

Kanagy, N. L., Szabo, C., and Papapetropoulos, A. (2017). Vascular biology of hydrogen sulfide. *Am. J. Physiol. Cell Physiol.* 312 (5), C537–C549. doi:10.1152/ajpcell.00329.2016

Kong, C. Y., Li, Z. M., Mao, Y. Q., Chen, H. L., Hu, W., Han, B., et al. (2021). Probiotic yogurt blunts the increase of blood pressure in spontaneously hypertensive rats via remodeling of the gut microbiota. *Food Funct.* 12 (20), 9773–9783. doi:10.1039/d1fo01836a

Li, B., He, X., Jin, H. Y., Wang, H. Y., Zhou, F. C., Zhang, N. Y., et al. (2021). Beneficial effects of Dendrobium officinale on metabolic hypertensive rats by triggering the enteric-origin SCFA-GPCR43/41 pathway. *Food Funct.* 12 (12), 5524–5538. doi:10.1039/d0fo02890h

Li, B., Wang, H. Y., Huang, J. H., Xu, W. F., Feng, X. J., Xiong, Z. P., et al. (2022). Polysaccharide, the active component of *Dendrobium officinale*, ameliorates metabolic hypertension in rats *via* regulating intestinal flora-SCFAs-vascular Axis. *Front. Pharmacol.* 13, 935714. doi:10.3389/fphar.2022.935714

Li, H., and Ren, M. (2023). Advance in the study on the relationship among salt, intestinal microbiota and its metabolites, and blood pressure. *Chin. J. Arterioscler.* 31 (11), 1007–1012. doi:10.20039/j.cnki.1007-3949.2023.11.012

Li, J., Zhao, F., Wang, Y., Chen, J., Tao, J., Tian, G., et al. (2017). Gut microbiota dysbiosis contributes to the development of hypertension. *Microbiome* 5 (1), 14. doi:10.1186/s40168-016-0222-x

Li, M., Wu, D., Chen, Y., and Zhang, T. (2022). Effects of baicalin on the intestinal barrier impairment of hypertensive mice induced by angiotensin II. *China J. Trad. Chin. Med. Pharm.* 37 (09), 5375–5379.

Li, X., Min, E., Wang, B., and Sun, L. (2020). Effect of Pueraria extract on salt-sensitive hypertension and gut MicrobiotaI in mice. *Acta Nutr. Sin.* 42 (05), 491–496 + 504. doi:10.13325/j.cnki.acta.nutr.sin.20201027.002

Ling, B., Jin, H., Zhang, Q., Wang, Y., Qi, S., Liu, S., et al. (2023). The role of the intestinal flora-bile acid axis in the pathogenesis of hypertension. *Chin. J. Hypertens.* 31 (11), 1043–1051. doi:10.16439/j.issn.1673-7245.2023.11.009

Liu, T., Li, X., Zhang, C., Zhao, L., Li, X., Yu, Y., et al. (2023). Lactobacillus and Allobaculum mediates the improvement of vascular endothelial dysfunction during hypertension with TaohongSiwu decoction combined with Dubosiella newyorkensis. *Heliyon* 9 (12), e22572. doi:10.1016/j.heliyon.2023.e22572

Lu, Y. C., Yeh, W. C., and Ohashi, P. S. (2008). LPS/TLR4 signal transduction pathway. *Cytokine* 42 (2), 145–151. doi:10.1016/j.cyto.2008.01.006

Luissint, A. C., Parkos, C. A., and Nusrat, A. (2016). Inflammation and the intestinal barrier: leukocyte-epithelial cell interactions, cell junction remodeling, and mucosal repair. *Gastroenterology* 151 (4), 616–632. doi:10.1053/j.gastro.2016.07.008

Ma, X., Xiong, X., Mo, Y., Yue, G., Cai, T., and Huang, J. (2020). Study on changes of intestinal microflora in spontaneously hypertensive rats based on 16S rDNA sequencing and intervention of traditional Chinese medicine. *Chin. Arch. Trad. Chin. Med.* 38 (08), 71-74 + 265–266. doi:10.13193/j.issn.1673-7717.2020.08.017

Natividad, J. M., Lamas, B., Pham, H. P., Michel, M. L., Rainteau, D., Bridonneau, C., et al. (2018). Bilophila wadsworthia aggravates high fat diet induced metabolic dysfunctions in mice. *Nat. Commun.* 9 (1), 2802. doi:10.1038/s41467-018-05249-7

Ni, X., Zhang, L., Peng, M., Shen, T. W., Yu, X. S., Shan, L. Y., et al. (2018). Hydrogen sulfide attenuates hypertensive inflammation via regulating connexin expression in spontaneously hypertensive rats. *Med. Sci. Monit.* 24, 1205–1218. doi:10.12659/msm.908761

Otaru, N., Ye, K., Mujezinovic, D., Berchtold, L., Constancias, F., Cornejo, F. A., et al. (2021). GABA production by human intestinal Bacteroides spp.: prevalence, regulation, and role in acid stress tolerance. *Front. Microbiol.* 12, 656895. doi:10.3389/fmicb.2021.656895

Qi, L., Wu, S., Liu, N., Zhang, X., Ping, L., and Xia, L. (2024). Salvia miltiorrhiza bunge extract improves the Th17/Treg imbalance and modulates gut microbiota of hypertensive rats induced by high-salt diet. *J. Funct. Foods* 117, 106211. doi:10.1016/j.jff.2024.106211

Qi, Y., Jiang, Y., Jiang, L., Shao, L., Liu, Z., Wang, Y., et al. (2019). Effects of Eucommia ulmoides-Tribulus terrestris on intestinal microbiota in aged spontaneously hypertensive rats. *Chin. J. Hypertens.* 27 (05), 454–462. doi:10.16439/j.cnki.1673-7245.2019.05.017

Rahman, M. M., Islam, F., Or-Rashid, M. H., Mamun, A. A., Rahaman, M. S., Islam, M. M., et al. (2022). The gut microbiota (microbiome) in cardiovascular disease and its therapeutic regulation. *Front. Cell. Infect. Microbiol.* 12, 903570. doi:10.3389/fcimb.2022.903570

Robles-Vera, I., Toral, M., de la Visitación, N., Sánchez, M., Gómez-Guzmán, M., Romero, M., et al. (2020). Probiotics prevent dysbiosis and the rise in blood pressure in genetic hypertension: role of short-chain fatty acids. *Mol. Nutr. Food Res.* 64 (6), e1900616. doi:10.1002/mnfr.201900616

Shan, Y., Pang, T., Yuan, Y., and Chen, H. (2024). Effect of Digupi(Lycii cortex) on intestinal flora in rats with spontaneous hypertension based on 16S rDNA sequencing. *J. Pract. Trad. Chin. Intern. Med.* 38 (04), 143–144. doi:10.13729/j.issn.1671-7813.Z20232383

Shen, J., Yi, L., Yang, R., Mao, Y., Jiang, H., and He, Y. (2020). Analysis of the effect of Angelica sinensis oil on the diversity of intestinal flora in hypertensive rats by 16S rDNA technique. *Lishizhen Med. Mater. Med. Res.* 31 (10), 2332–2335. doi:10.3969/j.issn.1008-0805.2020.10.008

Son, M., Oh, S., Lee, H. S., Choi, J., Lee, B. J., Park, J. H., et al. (2021). Gamma-aminobutyric acid-salt attenuated high cholesterol/high salt diet induced hypertension in mice. *Korean J. Physiol. Pharmacol.* 25 (1), 27–38. doi:10.4196/kjpp.2021.25.1.27

Su, J., Wang, Y., Yan, M., He, Z., Zhou, Y., Xu, J., et al. (2022). The beneficial effects of Polygonatum sibiricum Red. superfine powder on metabolic hypertensive rats via gut-derived LPS/TLR4 pathway inhibition. *Phytomedicine* 106, 154404. doi:10.1016/j.phymed.2022.154404

Tang, W. H., Kitai, T., and Hazen, S. L. (2017). Gut microbiota in cardiovascular health and disease. *Circ. Res.* 120 (7), 1183–1196. doi:10.1161/CIRCRESAHA.117.309715

Tominaga, T., Suzuki, H., Ogata, Y., Imafuku, T., and Saruta, T. (1988). Bile acids are able to reduce blood pressure by attenuating the vascular reactivity in spontaneously hypertensive rats. *Life Sci.* 42 (19), 1861–1868. doi:10.1016/0024-3205(88)90025-2

Verhaar, B. J., Prodan, A., Nieuwdorp, M., and Muller, M. (2020). Gut microbiota in hypertension and atherosclerosis: a review. *Nutrients* 12 (10), 2982. doi:10.3390/nu12102982

Wang, S., Xie, L., Zhuang, J., Qian, Y., Zhang, G., Quan, X., et al. (2023). Association between use of antihypertensive drugs and the risk of cancer: a population-based cohort study in Shanghai. *BMC Cancer* 23 (1), 425. doi:10.1186/s12885-023-10849-8

Wang, Z., Shao, Y., Wu, F., Luo, D., He, G., Liang, J., et al. (2024). Berberine ameliorates vascular dysfunction by downregulating TMAO-endoplasmic reticulum stress pathway via gut microbiota in hypertension. *Microbiol. Res.* 287, 127824. doi:10.1016/j.micres.2024.127824

Ward, N. C., Carnagarin, R., Nolde, J. M., Lugo-Gavidia, L. M., Chan, J., Jose, A., et al. (2022). Circulating short-chain fatty acids in hypertension: a reflection of various hypertensive phenotypes. *J. Hypertens.* 40 (8), 1589–1596. doi:10.1097/HJH.0000000000003190

World Health Organization (2019). "Hypertension - China," in *Guideline for the pharmacological treatment of hypertension in adults*. World Health Organization, 48. Available at: https://www.who.int/china/health-topics/hypertension (Accessed September 26, 2024).

World Health Organization (2021). *Guideline for the pharmacological treatment of hypertension in adults*. World Health Organization. 48.

World Health Organization (2023). *Hypertension*. Available at: https://www.who.int/news-room/fact-sheets/detail/hypertension (Accessed September 26, 2024).

Wu, D., Ding, L., Tang, X., Wang, W., Chen, Y., and Zhang, T. (2019). Baicalin protects against hypertension-associated intestinal barrier impairment in part through enhanced microbial production of short-chain fatty acids. *Front. Pharmacol.* 10, 1271. doi:10.3389/fphar.2019.01271

Wu, J., Nakashima, S., Nakamura, S., and Matsuda, H. (2020). Effects of Sanoshashinto on left ventricular hypertrophy and gut microbiota in spontaneously hypertensive rats. *J. Nat. Med.* 74 (2), 482–486. doi:10.1007/s11418-020-01387-9

Wu, P., and Zhou, X. (2023). Research progress on hypertension status and influencing factors in China. *Adv. Clin. Med.* 13 (12), 18604–18609. doi:10.12677/acm.2023.13122615

Wu, S., Jiang, N., Shi, Y., Zhao, X., Guo, Z., Liu, J., et al. (2022). Effects of Xiaochaihu decoction combined with lrbesartan on intestinal flora and lipid metabolism in patients with hypertension. *Chin. Arch. Trad. Chin. Med.* 40 (01), 169–172. doi:10.13193/j.issn.1673-7717.2022.01.040

Wu, S., Yu, G., Hu, X., and Chi, W. (2024). The beneficial effect and related mechanism of Jiawei Banxia Baizhu Tianma Decoction on metabolic hypertension (MH) rats. J. Pathog. *Biol* 19 (02), 149–156. doi:10.13350/j.cjpb.240205

Xu, X., Yu, X., Jin, H., Yan, C., and Zhang, Q. (2022). Influence of Zhengan Xifeng decoction on blood pressure and cecal and colonic flora in spontaneously hypertensive rats. *Pharmacol. Clin. Chin. Mater. Med.* 38 (04), 9–14. doi:10.13412/j.cnki.zyyl.2022.04.015

Yan, X., Jin, J., Su, X., Yin, X., Gao, J., Wang, X., et al. (2020). Intestinal flora modulates blood pressure by regulating the synthesis of intestinal-derived corticosterone in high salt-induced hypertension. *Circ. Res.* 126 (7), 839–853. doi:10.1161/CIRCRESAHA.119.316394

Yang, T., Santisteban, M. M., Rodriguez, V., Li, E., Ahmari, N., Carvajal, J. M., et al. (2015). Gut dysbiosis is linked to hypertension. *Hypertension* 65 (6), 1331–1340. doi:10.1161/HYPERTENSIONAHA.115.05315

Yang, Z., Lin, S., Liu, Y., Song, Z., Ge, Z., Fan, Y., et al. (2023a). Targeting intestinal microecology: potential intervention strategies of traditional Chinese medicine for managing hypertension. *Front. Pharmacol.* 14, 1171119. doi:10.3389/fphar.2023.1171119

Yang, Z., Wang, Q., Liu, Y., Wang, L., Ge, Z., Li, Z., et al. (2023b). Gut microbiota and hypertension: association, mechanisms and treatment. *Clin. Exp. Hypertens.* 45 (1), 2195135. doi:10.1080/10641963.2023.2195135

Yin, X., Duan, C., Zhang, L., Zhu, Y., Qiu, Y., Shi, K., et al. (2024). Microbiota-derived acetate attenuates neuroinflammation in rostral ventrolateral medulla of spontaneously hypertensive rats. *J. Neuroinflammation* 21 (1), 101. doi:10.1186/s12974-024-03061-3

Yu, J., Zhu, Q., Zhou, M., Huang, X., Le, Y., Ouyang, H., et al. (2024). Mechanism of Tianma-Gouteng granules lowering blood pressure based on the bile acid-regulated farnesoid X receptor-fibroblast growth factor 15- cholesterol 7α-hydroxylase pathway. *J. Ethnopharmacol.* 328, 118091. doi:10.1016/j.jep.2024.118091

Yu, X., Zhang, X., Jin, H., Wu, Z., Yan, C., Liu, Z., et al. (2019). Zhengganxifeng decoction affects gut microbiota and reduces blood pressure via renin-angiotensin system. *Biol. Pharm. Bull.* 42 (9), 1482–1490. doi:10.1248/bpb.b19-00057

Zhang, G., Chen, Y., Wang, M., and Zheng, G. (2023). Influence of rhynchophylline on blood pressure and gut microbiota of spontaneously hypertensive rats based on 16S rDNA sequencing. *Chin. J. Clin. Pharmacol.* 39 (01), 57–60. doi:10.13699/j.cnki.1001-6821.2023.01.012

Zhang, G. X., Jin, L., Jin, H., and Zheng, G. S. (2021). Influence of dietary components and traditional Chinese medicine on hypertension: a potential role for gut microbiota. *Evid. Based Complement. Altern. Med.* 2021, 5563073. doi:10.1155/2021/5563073

Zhang, J., and Li, G. (2023). Interpretation of the 2021 World Health Organization's guidelines for drug treatment of adult hypertension. *Chin. J. Hypertens.* 31 (01), 18–20. doi:10.16439/j.issn.1673-7245.2023.01.007

Zhen, X. (2020). *Study on the effect of Qinggan Yishen Qufeng formula on the changes of brain-gut axis related to hypertension induced by angiotensin II*. China: Shanghai University of Traditional Chinese Medicine.

Zhou, X., Liu, J., and Li, J. (2020). Effects and mechanism of quercetin on blood pressure,intestinal flora and ventricular remodeling in spontaneously hypertensive rats. *Nat. Prod. Res. Dev.* 32 (09), 1449–1455. doi:10.16333/j.1001-6880.2020.9.001

Zhu, H., Xu, C., Dong, Y., Lu, S., and Guo, L. (2023a). Chai-Gui decoction and its representative components ameliorate spontaneous hypertension rats by modulating lipid metabolism and gut microbiota. *J. Ethnopharmacol.* 305, 116116. doi:10.1016/j.jep.2022.116116

Zhu, H., Xu, C., Gong, S., Mao, A., Zhou, C., and Lu, S. (2023b). Intervention of Chaigui decoction on angiotensin-converting enzyme 2 and intestinal flora in hypertensive mice. *World Chin. Med.* 18 (11), 1547–1550 + 1557. doi:10.3969/j.issn.1673-7202.2023.11.010

Zubcevic, J., Richards, E. M., Yang, T., Kim, S., Sumners, C., Pepine, C. J., et al. (2019). Impaired autonomic nervous system-microbiome circuit in hypertension. *Circ. Res.* 125 (1), 104–116. doi:10.1161/CIRCRESAHA.119.313965

Zusso, M., Lunardi, V., Franceschini, D., Pagetta, A., Lo, R., Stifani, S., et al. (2019). Ciprofloxacin and levofloxacin attenuate microglia inflammatory response via TLR4/NF-kB pathway. *J. Neuroinflammation* 16 (1), 148. doi:10.1186/s12974-019-1538-9

frontiers | Frontiers in Pharmacology

TYPE Review
PUBLISHED 13 January 2025
DOI 10.3389/fphar.2024.1510976



OPEN ACCESS

EDITED BY
Wenzhi Hao,
Jinan University, China

REVIEWED BY
Hoi Huen Chan,
The Education University of Hong Kong, Hong Kong SAR, China
Tshepo Mashela,
University of Limpopo, South Africa
Hemanga Hazarika,
Girijananda Chowdhury University, India

*CORRESPONDENCE
Xinke Zhao,
zxkd412@163.com
Yingdong Li,
lydj412@163.com

†These authors have contributed equally to this work

RECEIVED 14 October 2024
ACCEPTED 12 December 2024
PUBLISHED 13 January 2025

CITATION
Ren C, Luo Y, Li X, Ma L, Wang C, Zhi X, Zhao X and Li Y (2025) Pharmacological action of *Angelica sinensis* polysaccharides: a review. *Front. Pharmacol.* 15:1510976. doi: 10.3389/fphar.2024.1510976



# Pharmacological action of *Angelica sinensis* polysaccharides: a review

Chunzhen Ren[1,2,3†], Yali Luo[1†], Xiaojuan Li[4†], Like Ma[5], Chunling Wang[1,2,3], Xiaodong Zhi[5,6], Xinke Zhao[2,3,5*] and Yingdong Li[1,2,3*]

[1]School of Traditional Chinese and Western Medicine, Gansu University of Chinese Medicine, Lanzhou, China, [2]Gansu Province Key Laboratory of Chinese Medicine for the Prevention and Treatment of Chronic Diseases, Lanzhou, China, [3]Key Clinical Specialty of the National Health Commission of the People's Republic of China, Key Specialized Cardiovascular Laboratory National Administration of Traditional Chinese Medicine, Lanzhou, China, [4]School of Traditional Chinese Medicine, Jiangsu Medical College, Yancheng, China, [5]First School of Clinical Medical, Gansu University of Chinese Medicine, Lanzhou, China, [6]Cardiovascular clinical medicine center, Affiliated Hospital of Gansu University of Chinese Medicine, Lanzhou, China

*Angelica sinensis*, a traditional Chinese herbal medicine and food, which has a long history of clinical application, is used to improve health conditions and treat various diseases. *Angelica sinensis* polysaccharides (ASP), the main active component of this traditional Chinese medicine, have multicomponent, multitarget characteristics and very broad pharmacological activities. They play important roles in the treatment of several diseases. In addition, the effect is significant, which may provide a more comprehensive database and theoretical support for applying ASP in the treatment of disease and could be considered a promising candidate for preventing disease. This review summarizes the research progress on the extraction, chemical structure, pharmacological effects, and mechanisms of ASP and its derivatives by reviewing relevant national and international literature and provides comprehensive information and a reliable basis for the exploration of new treatment strategies involving botanical drugs for disease therapy. Literature information was obtained from scientific ethnobotany and ethnomedicine databases (up to September 2024), mainly from the PubMed, Web of Science, and CNKI databases. The literature has explored the extraction, purification, structure, and pharmacological effects of *Angelica sinensis* polysaccharides. The search keywords for such work included "*Angelica sinensis*" or "*Angelica sinensis* polysaccharides," and "*pharmacological* effects," "extraction" and "structure." Multiple studies have shown that ASP has important pharmacological effects, such as antitumor, anemia-improving, anti-inflammatory, antioxidative, immunomodulatory, hepatoprotective, antifibrotic, hypoglycemic, antiradiation, and antiviral effects, the mechanisms of which appear to involve the regulation of inflammation, oxidative stress, and profibrotic signaling pathways. As a natural polysaccharide, ASP has potential applications as a drug. However, further research should be undertaken to clarify the unconfirmed regulatory mechanisms, conduct standard clinical trials, and evaluate the possible side effects. This review establishes a theoretical foundation for future studies on the structure, mechanism, and clinical use of ASP.

KEYWORDS

**ASP, chemical structure, improving anemia, liver protection, antitumour, immunomodulation**

# 1 Introduction

*Angelica sinensis* is the dry root of the umbelliferae plant *Angelica sinensis* (Oliv.) Diels, which is recorded in Chinese Pharmacopoeia (2020) (Figures 1A, B). The object exhibits a light brown to brown coloration, characterized by longitudinal wrinkles and transverse lens-like perforations. Its fried slices are typically round, oval, or irregular in shape, displaying a yellow-white to light brown hue with a flat surface that may feature cracks. A light brown cambium ring is present at the center, accompanied by several brown oil spots (Figures 1C, D). *Angelica sinensis* is mainly produced in southeastern Gansu, followed by Yunnan, Sichuan, Shaanxi, Hubei and other provinces. *Angelica sinensis* was first described in Shennong Ben Cao Jing and is known for its ability to tonify blood. It is a traditional medicinal and edible plant that has long been used for invigorating the blood, promoting circulation, lubricating the intestines, regulating menstruation as well as relieving pain, treating female irregular menstruation and amenorrhea (Erlin et al., 2019).

ASP are natural macromolecular compounds and the main active substances of *Angelica sinensis*. They offer a wide range of pharmacological functions, for example, promoting hematopoiesis and improving immunity, antioxidation, and antitumour effects (Jin et al., 2012). It has been widely used owing to its low toxicity, residue-free nature, and nontolerant properties (Jin et al., 2012). As a result, the utilization of ASP is gaining more attention from scholars worldwide. With the deepening of research, the medical potential of ASP is gradually explored. This paper provides an overview of the current research on the extraction, isolation, and pharmacological effects of ASP. Additionally, it analyzes and summarizes the potential value of ASP, thus, serving as a reference for further research on ASP and its application in the fields of food, health products, and pharmaceuticals.

# 2 Methodology

This review article has been retrieved in the form of a database search. The search terms are in the form of subject words combined with free words. We systematically searched Baidu Literature, China National Knowledge Infrastructure, VIP Datas, PubMed, Google-Scholar and Web of Science. Using"*Angelica* sinensis"or "*Angelica sinensis* polysaccharides", and "pharmacological effects", "extraction" and "structure", as the search terms from scientific ethnobotany and ethnomedicine databases (up to September 2024), total of 663 articles were retrieved, and 484 were duplicated by software and manual removal. We carefully reviewed and classified the title, abstract and full text of the literature, and finally obtained 21 articles on ASP extraction, separation and structural analysis, 90 pharmacological research studies. The research methods we included include clinical studies, clinical trials, cell experiments, animal experiments, literature reviews, network pharmacology, etc. We extracted study details, including the relevant information on the pharmacological action and chemistry attributes of ASP, as well as the study status. Finally, through literature review and summary, it was found that ASP have ten pharmacological effects, as shown in the following Figure 2.


FIGURE 1
**(A, B)** *Angelica sinensis* herbs (Plant Photo Bank of China, PPBC). **(C)** *Angelica sinensis* original medicinal materialsand (Baidu Gallery). **(D)** *Angelica sinensis* slices (Herbal medicine room, Affiliated Hospital of Gansu University of Chinese Medicine).

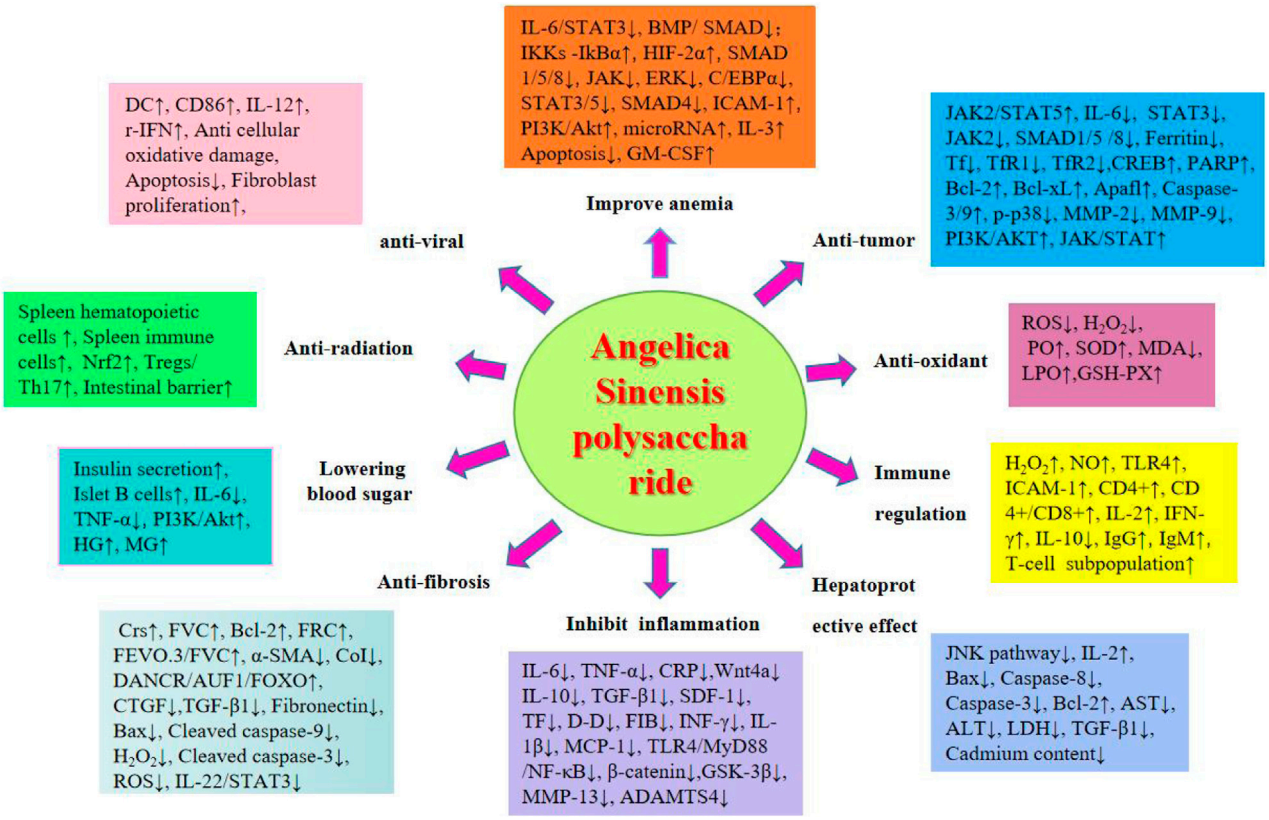


FIGURE 2
Pharmacological effects of ASP.

## 2.1 Extraction of ASP

ASP is a typical traditional Chinese medicinal polysaccharide, and its extraction method is similar to that of other traditional Chinese medicinal polysaccharides. Common extraction methods include water extraction and alcohol precipitation, ultrasound extraction, enzyme extraction, and microwave-assisted extraction.

### 2.1.1 Water extraction and alcohol precipitation methods

At present, the extraction process of polysaccharides is mostly water extraction and alcohol precipitation, which means that the medicinal material of *Angelica sinensis* is first defatted with organic solvents, then extracted with hot water, and then subjected to alcohol precipitation with a certain concentration of ethanol. The water extraction and alcohol precipitation method has the advantages of simplicity, convenience, low cost, no pollution, and suitability for industrial production. However, a high temperature is required during the extraction process, resulting in a low extraction rate, significant loss of polysaccharide activity, and difficult purification (Huang, 2010). Yu et al. (2013) used response surface methodology and reported that the extraction time and solid–liquid ratio are the two most important factors affecting the yield of ASP in hot water extraction. Zhang et al. (2016b) soaked *Angelica sinensis* slices in 95% ethanol by volume for 24 h and then extracted them with hot water, followed by alkali and acid precipitation and alcohol precipitation to obtain water-soluble ASP. Wu et al. (2015) adopted an orthogonal design to improve the hot water extraction method of ASP and obtained the optimal extraction process by using 10 cycles of water and 60 min of continuous extraction three times. The obtained aqueous extract was concentrated to 1:8, and 95% ethanol was added to a concentrated solution of 65% to obtain 0.265 mg/g ASP. Zhang et al. (2016a) extracted crude polysaccharides from *Angelica sinensis* using three methods and compared the yield of polysaccharides (fresh *Angelica sinensis* after natural air drying, boiled directly in water; Angelica sinensis was processed into small pieces, soaked in 75% ethanol for 1 week, with a solid–liquid ratio of 1:10, and the residue after alcohol extraction was boiled in water; *Angelica sinensis* was processed into small pieces, soaked in 78% ethanol for 1 week, with a solid–liquid ratio of 1:10, and then infiltrated with 76% ethanol until the exudate was colorless. The infiltrated *Angelica sinensis* was boiled in water at a solid–liquid ratio of 1:30 during decoction and boiled for 30 min. The extraction solutions obtained from the three processing methods were all precipitated with ethanol at a final concentration of 80%, subjected to precipitation and decolorization treatment, and then freeze-dried to obtain crude polysaccharides from *Angelica sinensis*. The results showed that treatment with ethanol could change the yield of crude polysaccharides from *Angelica sinensis*, and the ethanol infiltration method had the highest yield of crude polysaccharides from *Angelica sinensis*.

### 2.1.2 Ultrasonic extraction method

The ultrasonic extraction method has the advantages of short extraction time, simplicity and speed, and good separation. Zhao et al. (2016) screened the optimal parameters for the ultrasonic extraction of ASP using response surface methodology (a material–liquid ratio of 7, an extraction time of 45 min, an extraction temperature of 90°C, and an ultrasonic power of 180 W). Several scholars (Nai et al., 2021; Tian et al., 2017) have investigated three factors, namely, the material-liquid ratio, sonication time and sonication power, for the extraction of ASP by ultrasound through single-factor tests and orthogonal tests and optimized the extraction solutions by the response surface method. The optimal conditions were a material-liquid ratio of 1:43, an ultrasonication time of 28 min, and a power of 396 W using multiple regression analysis, resulting in a polysaccharide yield of 21%.

### 2.1.3 Enzyme extraction method

The principle of enzyme extraction is to use enzymes to hydrolyze the cell wall to fully dissolve the substances contained in the cells in water to achieve efficient extraction. Zhang et al. (2012a) used enzyme-assisted extraction technology to extract ASP and optimized the extraction conditions. The results showed that the enzyme extraction method improved the extraction rate of polysaccharides, and the operation was simple, low cost and had little chemical pollution. Zhang and Lv (2013) compared four methods, namely, hot water extraction, ultrasonic extraction, cellulase extraction and pectinase extraction, of ASP, with the yield of ASP as the index. The results showed that the enzymatic method was the better choice for the extraction of ASP. The optimum extraction conditions for the cellulase method were as follows: enzyme dosage, 1.0%; extraction temperature, 60°C; extraction time, 60 min; and pH, 6.0. The optimum extraction conditions for the pectinase method were as follows: enzyme dosage, 1.0%; extraction temperature, 50°C; extraction time, 90 min; and pH, 5.5. Therefore, enzymatic hydrolysis has considerable development prospects.

### 2.1.4 Microwave-assisted extraction

Microwave-assisted extraction of polysaccharides is a potential new technology that has the advantages of speed, low solvent consumption, high extraction rate and low cost (Zhang, 2006). Jin et al. (2007) studied the extraction of ASP via orthogonal experiments. The results showed that compared with ultrasonic extraction and direct heat extraction, microwave extraction has the advantages of time savings, high efficiency and energy savings. Li et al. (2012) used a single factor grouping test and orthogonal optimization test to investigate the process conditions of microwave-assisted extraction of polysaccharides from *Angelica sinensis*. The results showed that the polysaccharide extraction rate was 7.82% at a power of 500 W, an extraction time of 20 min, and a solid–liquid ratio of 1:15.

## 2.2 Separation purification of ASP

ASP extracts often contain impurities, such as proteins and pigments, which need to be further separated and purified. Protein impurities are usually removed by the Sevag method (Wang et al., 2019) or the repeated freeze–thaw method (Yang et al., 2008b). The separation and purification methods used are the common alcohol precipitation method (Wang et al., 2019) and the column chromatography method (Yang et al., 2008b). Among them, the column chromatography methods can be divided into anion exchange chromatography and gel filtration chromatography. Cao et al. (2008b) separated the crude polysaccharide obtained by water extraction and alcohol precipitation and repeated freezing and thawing to remove protein by a DEAE-Sephadex A-25 column and obtained three polysaccharide components. APS-2 was further separated on a Sephacryl S-400 column to obtain two polysaccharide components (APS-2a and APS-2b). Cao et al. (2006) treated ASP with ethanol to remove pigments, extracted it with hot water, and precipitated it with ethanol to obtain crude polysaccharides. The proteins were removed by the freeze–thaw method, filtered through a 0.65 μm membrane filter, and loaded onto a DEAE Sephadex A-25 column for elution. The eluent was collected, lyophilized, and further passed through a Sephacryl S-400 column to obtain three components (APS-1a, APS-1b, and APS-1c). After concentration, dialysis, and lyophilization, APS-1c was further purified on a SephadexG-100 column to obtain two purified components (APS-1cI and APS-1cII). Zhang et al. (2016b) obtained crude polysaccharides by hot water extraction and ethanoprecipitation. The protein was removed by the freeze–thaw method, and then, the filtrate was dialyzed and loaded on a Sephadex G-50 column, eluted with distilled water, collected and concentrated, and lyophilized to obtain ASP. With the continuous improvement and development of scientific and effective methods for the preparation of Chinese medicines, approaches for the separation and purification of ASP have been explored.

## 2.3 Structural studies on the ASP

ASP consists of at least 10 identical or different monosaccharides linked by α- or β-glycosidic bonds and is widely found in nature (Chen and Huang, 2018). Based on their structural characteristics, ASP can be divided into two types: homopolysaccharides, which are composed of one type of monosaccharide, and heteropolysaccharides, which are composed of two or more monosaccharides, such as glucose, galactose, arabinose, and rhamnose, but their components are mainly glucose (Tian et al., 2024). The polysaccharide APS-bII is the first polysaccharide isolated from *Angelica sinensis* in the form of a white powder (Nai et al., 2021). Currently, the polysaccharides extracted from *Angelica sinensis* are mainly heteropolysaccharides (Figure 3), with the main structural backbone being α (1,4)-Glc and a relative molecular weight distribution of 5.1 to 2,300 kDa. The active polysaccharides are mainly water soluble. The physicochemical properties and biological activity of polysaccharides are closely associated with structural parameters such as the monosaccharide backbone, monosaccharide composition, relative molecular mass, conformation, position of glycosidic bonds, functional groups, branching degree, and advanced conformation (Liu et al., 2020a). The polysaccharide species extracted from Angelica are listed in Table 1.

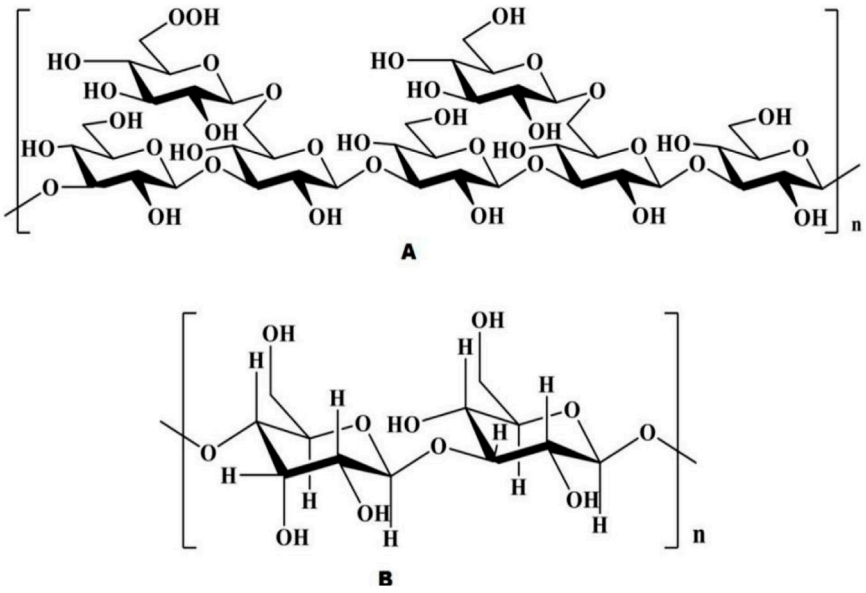


FIGURE 3
Chemical structure of ASP [Natural Product Communications. 2021; 16(3)].

## 2.4 Pharmacological effects of ASP

The medicinal use of *Angelica sinensis* was first reported by Shennong Ben Cao Jing, where it was considered to have the effect of nourishing the five viscera and regenerating muscles and later by researchers as a sacred medicine for blood (Pantopoulos et al., 2012). *Angelica sinensis* has a wide range of clinical applications since ancient times. Several researchers have conducted numerous studies on its components and pharmacological effects. ASP is one of the main active components of *Angelica sinensis*, and its extraction, purification, and mechanism of action have been studied in recent years. However, few in-depth studies have been conducted on its pharmacological effects. In this paper, the pharmacological effects of ASP were investigated, and it was concluded that the pharmacological effects of ASP primarily include improving anemia and antitumour effects and enhancing immune function, antioxidation, hepatoprotection, anti-inflammation, anti-fibrosis, hypoglycemia, antiradiation and antiviral properties.

### 2.4.1 Improving anemia

ASP can alleviate anemia symptoms by increasing the levels of hemoglobin, red blood cells, erythropoietin, and iron-regulating hormones in the liver. Ferroregulin is a peptide hormone synthesized and secreted by the liver and is involved in iron regulation. Ferroregulin downregulates membrane iron transport proteins, inhibits the release of serum iron, and negatively regulates iron homeostasis in the body (Zhang and Wang, 2018).

Anemia caused by chronic disease (ACD) is secondary to chronic infection, inflammation, and tumors. In a study, ASP (0.5, 1 g/kg) was administered intraperitoneally to rats with ACD and was found to alleviate anemia by interrupting the IL-6/STAT3 (interleukin-6/signal transducer and activator of transcription 3), and BMP/SMAD (bone morphogenetic protein/SMAD) pathways to inhibit inflammatory iron-regulated proteins. In an animal experimental study, researchers constructed ASP-modified iron oxide nanoparticles (IONPs) and demonstrated the therapeutic effects of IONPs-ASP on iron deficiency anemia (IDA), which was associated with IONPs supplementation and APS-stimulated hematopoietic cell generation (Ma et al., 2024). Additionally, ASP promoted erythropoiesis through the IkB kinase-IkBα pathway (Wang et al., 2017b). Wang et al. (2018) showed that ASP (0.5, 1 g/kg) alleviates the inhibition of erythropoietin by increasing the protein expression of hypoxia-inducible factor-2α (HIF-2α) and decreasing the expression of inflammatory cytokines in rats with chronic renal anemia to achieve an anti-anemic effect.

In addition to chronic anemia, iron deficiency anemia (IDA) is also common. Relevant animal experiments suggested that after the treatment of ASP (0.3, 0.6, and 1.2 g/kg) for blood loss rats, it was found that the expression of Smad 1/5/8, Jak and ERK were inhibited, and then the expression of hepcidin was inhibited, so as to alleviate the symptoms of blood loss in rats (Zhang et al., 2014; Zhang et al., 2012b). A study examining the expression of hepatic-related proteins in rats with blood loss after ASP (1 g/kg) administration via gavage revealed that A inhibited the expression of hepatic (C/EBPα) (CCAAT/enhancer binding protein α), STAT3/5 and SM (Bi et al., 2021). The expression of AD4 stimulates the secretion of erythropoietin and alleviates IDA symptoms (Liu et al., 2012; Wang et al., 2011b). In a study conducted by Wang et al. (2017a), who injected ASP (4, 6 mg/kg) intraperitoneally into blood-lost mice, it was found that ASP increased the number of bone marrow stromal cells and increased the expression of intercellular adhesion molecule-1 (ICAM-1), thereby enhancing the proliferation ability of hematopoietic stem cells.

Additionally, bone marrow suppression caused by radiotherapy and chemotherapeutic agents can cause anemia. ASP (10 mg/kg) was administered to mice after X-ray radiation and was found to inhibit cellular senescence through the phosphatidylinositol-3-

TABLE 1 Chemical structure and composition of natural *polysaccharides* from *Angelica sinensis*.

| Name | Relative molecular mass (Da) | Monosaccharide composition and molar ratio Structural features | Structural features | Pharmacological activity | References |
|---|---|---|---|---|---|
| As-IIIa | $8.5 \times 10^2$ | Glc | α(1→3)-glycosidic bond | Immunomodulation | Zhang and Huang (1999) |
| As-IIIb | $4.9 \times 10^4$ | Glc-Man-Ara (10.0:10.0:4.0) | (1→4), (1→6) glycosidic bond | Immunomodulation | Zhang and Huang (1999) |
| X-C-3-II | $1.0 \times 10^5$ | Glc-Gal-Ara-Rha-GalA (56.0:22.1: 18.9:1.9:1.1) | — | Immunomodulation | Chen et al. (2001a) |
| X-C-3-III | $8.5 \times 10^4$ | Gal-Ara-Rha-GlcA-GalA (24.3:15.8: 4.2:3.1:52.6) | — | Immunomodulation | Chen et al. (2001b) |
| X-C-3-IV | $6.6 \times 10^2$ | Gal-Ara-Rha-GleA-GalA (12.6:10.7: 7.2 8.3:61.2)Glc | — | Immunomodulation | Chen et al. (2001b) |
| XC-1 | $1.0 \times 10^5$ | Glc | α(1→6)-glycosidic bond | Immunomodulation | Chen et al. (2001c) |
| ASP1 | — | GalA-Ara-Glc-Gal (5.35:9.15: 65.00:3.66) | — | Antiradiation | Sun et al. (2005) |
| ASP2 | $3.4 \times 10^*$ | GalA-Rha-Ara-Man-Glc- Gal (35.38:1.11:16.31:0.89:26.96:15.75) | — | Antiradiation | Sun et al. (2005) |
| ASP3 | $8.1 \times 10$ | GalA-Rha-Ara-Man-Gle- Gal (58.27:1.87:10.50:0.37:0.94:24.93) | — | Antiradiation | Sun et al. (2006) |
| W-ASPll | $3.8 \times 10^5$ | Ara-Glc-Gal (0.5:26.0:0.6) | — | — | Sun et al. (2006) |
| W-ASP12 | $1.9 \times 10^4$ | Ara-Man-Gle-Gal (21.1:1.6:16.3:1.3) | — | — | Sun et al. (2006) |
| W-ASP-2 | — | Rha-Ara-Man-Glc-Ga (1.0:14.7:0.8: 24.3:14.2) | — | — | Sun et al. (2006) |
| W-ASP-3 | $6.2 \times 10^4$ | Rha-Ara-Man-Glc-Gal (1.0:5.6:0.2: 0.5:13.3) | — | — | Sun et al. (2006) |
| APS-leI | $1.7 \times 10^5$ | Glc | (1→6)-D-Glcp forming a linear β-glucan | Immunomodulation | Cao et al. (2006) |
| APS-le II | $3.9 \times 10^4$ | Glc | (1→4)-α-D-Glop and (1→6)-a-DGlep | Antitumor | Cao et al. (2006) |
| APS-1d | $5.1 \times 10^3$ | Glc-Ara (13.8:1) | 1,4-a-D-glucopyranose with a 1,6-alpha-D-Glcp branched chain | Antitumor | Yang et al. (2006) |
| AP | $5.0 \times 10^3$ | Rha-Ara-Man-Glc-Gal (1.00:4.54: 2.98:11.09:7.45) | — | Immunomodulation | Wang et al. (2007c) |
| ASD II-3–3 | $4.4 \times 10^4$ | Rha-Ara-Xyl-Man-Gal (0.3:1.0:0.1: 0.2:5.0) | — | — | Yang et al. (2008b) |
| APF1 | $1.2 \times 10^5$ | Rha-Ara-Glc-Gal (1.00:2.27: 7.80:2.69 | — | Immunostimulant | Cao et al. (2008a), Yang et al. (2008a) |
| APF2 | $5.2 \times 10^4$ | Rha-Ara-Man-Glc-Gal (1.00:5.29: 3.66:9.11:5.17) | — | Immunostimulant | Jiang et al. (2009), Zhou et al. (2009) |
| APF3 | $1.6 \times 10^4$ | Rha-Ara-Man-Glc-Gal (1.00:4.54: 2.98:11.09:7.45) | — | Immunostimulant | Cao et al. (2008a), Jiang et al. (2009), Yang et al. (2008a) |
| APS-2a | $7.4 \times 10^5$ | Glc-Gal-Ara-Rha-GalA (1.0:7.5:38.2: 2.6:4.9) | I | Anti-tumor | Cao et al. (2010b) |
| ASP | I | Man-Rha-GlcA-GalA-Glc-Gal-Ara-Fuc (1.2:4.5:1.0:10.5:17.8:37.5: 8.7:4.9) | — | Antioxidants | Sun et al. (2010) |
| ASP | $5.0 \times 10^3$ | Rha-GalA-Glc-Gal-Ara (0.05:0.26: 14.47:1.00:1.17) | — | Colonic localization Drug carriers | Zhou (2018) |
| APS-bII | $1.3 \times 10^4$ | Glc-Gal-Xyl-Ara (8.4:2.7:1.8:1.0) | — | Antitumor | Zhang et al. (2016b) |

(Continued on following page)

TABLE 1 (*Continued*) Chemical structure and composition of natural *polysaccharides* from *Angelica sinensis*.

| Name | Relative molecular mass (Da) | Monosaccharide composition and molar ratio Structural features | Structural features | Pharmacological activity | References |
|---|---|---|---|---|---|
| APS-3a | $5.9 \times 10^5$ | Glc-Gal-Ara-Rha-Man (3.2:1.7:2.5:1.3:1.0) | — | Antitumor | Liu et al. (2020b) |
| APS-3b | $2.3 \times 10^5$ | Glc-Gal-Ara-Rha-Man (2.3:5.4:6.8:1.0:1.2) | — | Antitumor | Pu et al. (2016) |
| APS-3c | $1.4 \times 10^4$ | Glc-Gal-Ara-Rha-Man-Xyl(6.3:4.7:6.7:6.5:1.6:1.0) | — | Antitumor | Pu et al. (2016) |
| APS-la | $4.9 \times 10^4$ | Ara-Glc-Gal (27.7:15.0:57.3) | Mainly composed of 1,4-linked galactose, 1,3,6-linked galactose, T-galactose and T-arabinose | Antiradiation | Pu et al. (2016) |
| APS-3a | $6.5 \times 10^4$ | Ara-Glc-Gal (6.5:9.0:84.5) | 1,4-Gal, 1, 3,6-Gal, T-Gal and T-Ara | Antiradiation | Liu et al. (2022b) |
| SASP | $8.1 \times 10^4$ | Glc-Gal-Ara (5.3:1.6:1) | Main chain (1→3)-linked Galp, (1→6)-linked Galp and 2-OMe-(1→6)-linked Galp composed of the C-3 position of the branched 2–0Me-(1→6)-linked Galp linked to the main chain | Antioxidant | Liu et al. (2022b) |
| JASP-1A | $8.6 \times 10^5$ | Glc-Gal-Ara (1:4.55:4.92) | consisting of a 1,4-linked Galp and a 1,3-linked Rha, the branched-chain is linked to the C-6 position of the 1,4-linked Galp on the main chain, the terminal structure of the branched chain is T-Araf | Antioxidant | Liu et al. (2022b) |
| JASP-1B | $7.2 \times 10^4$ | Man-Rha-GlcA-GalA-Glc-Gal-Ara (2.16:2.96:3.31:2.34:1:49.1:40.5) | — | Antioxidant | Liu et al. (2022b) |
| JASP-2 | $5.6 \times 10^4$ | Man-Rha-GlcA-GalA-Glc-Gal-Ara (3.32:7.88:4.79:15.9:0.5:46.6:42.1) | — | Antioxidant | Liu et al. (2022b) |
| Aps-2I | $7.2 \times 10^5$ | Man-Rha-GalA-Glc-Gal-Ara (4:5:1:10:23:39) | — | Antioxidant | Liu et al. (2022b) |
| AAP-2A | $2.2 \times 10^5$ | Rha-Gal-Ara-Glc (1:2.13:3.22:6.18) | 1,3-Rhap, 1,3-Galp, 1,3-Araf, 1,5-Araf, 1, 3,5-Araf, 1,4-Glcp and 1, 4,6-Glcp | Antioxidant | Pantopoulos et al. (2012) |

Note: - is not tested; Glc is glucose; Gal is galactose; Ara is arabinose; Rha is rhamnose; Fuc is fucose; Man is mannose; Xyl is xylose; GlcA is glucuronide; GalA is galacturonide; RhaA is rhamnose aldehyde.

hydroxyl kinase/protein kinase B (PI3K/Akt) pathway, promote the repair of platelets, blood cells, and progenitor cells, and alleviate anemia (Liu et al., 2010). He et al. (2012) reported that ASP (2, 8 mg/kg) decreased the percentage of apoptotic peripheral red blood cells, white blood cells, and bone marrow cavity blood cells in irradiated mice. These findings suggest that ASP can protect against radiation injury by altering microRNA expression in blood and restoring the bone marrow hematopoietic system in radiation-irradiated mice (Li and Xu, 2017). ASP (50, 200 mg/kg) also promoted the recovery of peripheral blood leukocyte counts and the transformation of splenic lymphocytes (Sun et al., 2009), enhancing radiation tolerance in mice. Radiation-exposed mice injected with ASP (0.2 mL/piece, once a day) had significantly reduced hematocrit and cellular damage caused by radiation (Hong et al., 2002). Through preclinical and cellular studies, researchers have shown that the polysaccharide components of traditional Chinese medicine have protective effects on the hematopoietic system. Ding Xuelan's team administered ASP (100 μg/g, 200 μg/g, and 400 μg/g) by gavage to mice with cyclophosphamide-induced myelosuppression. The levels of red blood cells, white blood cell platelets, immunoglobulin G (IgG), and immunoglobulin M (IgM) were significantly increased, and the enhanced immunomodulation may act with cytokines on various lineages of hematopoietic progenitor cells, hematopoietic stem cells, and lymphocytes to promote the recovery of the hematopoietic system (Ding et al., 2016).

Lee et al. (2012) fractionated ASP (6,000 g/mL) with a DEAE-Sepharose CL-6B column and obtained four fractions (F1, F2, F3, and F4), of which the F2 fraction was found to have the highest hematopoietic activity by magnetically activated cell sorting. F2 accounted for 19% of the ASP and 0.53% of the protein content. The monosaccharide components of F2 were arabinose (51.82%), fructose (1.65%), galactose (29.96%), glucose (4.78%), and galacturonic acid (14.80%). It stimulates the secretion of granulocyte macrophage-colony stimulating factor (GM-CSF) and IL-3 by

TABLE 2 Antitumor effects and mechanisms of ASP.

| Types of cancer | Pharmacological action | Pathways/molecules involved | Models | References |
|---|---|---|---|---|
| Leukemia | Inhibits tumor cell proliferation; induces tumor cell differentiation and promotes cellular senescence; increases the toxicity of natural killer cells to tumor cells | JAK2/STAT5 pathway/TNF-α, IL-2, IFN-γ | *In vivo*: DBA/2 mice *in vitro*: K562 cells, L1210 cells | Liu et al. (2019), Wang et al. (2015b), Zhang et al. (2016b) |
| Liver cancer | Inhibits ferroregulation, thereby inhibiting the growth and proliferation of tumor cells; directly inhibits tumor cell proliferation | JAK/STAT and BMP-SMAD pathways/IL-6, JAK2, STAT3, SMAD1/5/8, ferritin, Tf, TfR1, TfR2 | *In vivo*: BALB/c mice; *in vitro*: HHCC cell line A549 cells, HepG2 cells, H22 cells | Ren et al. (2018), Shang et al. (2003) |
| Breast cancer | Inhibits tumor cell metastasis; induces apoptosis in tumor cells and reduces ferroregulation | CREB and JAK/STAT, BMP-SMAD pathway/Caspase, PARP, Bax, Bcl-xl, Apafl, IL-6, STAT3, SMAD1/5/8, etc. | *In vivo*: Balb/c mice; *in vitro*: T47D cells, MCF-7 cells, 4T1 cells | Ren et al. (2018), Zhou et al. (2015) |
| Cervical cancer | Inhibits tumor cell proliferation and promotes apoptosis of tumor cells | Caspase-3/9, PARP, p-p38, MMP-2 and MMP-9 | *In vivo*: Balb/c mice *in vitro*: HeLa cells | Cao et al. (2010a), Tang et al. (2020) |
| Neuroblastoma | Inhibits tumor cell proliferation and migration; induces apoptosis | PI3K/AKT and JAK/STAT pathways/Bcl-2, Bax, Caspase-3/9 | *In vitro*: SH-SY5Y cells | Yang et al. (2018) |

human peripheral monocytes and protects the hematopoietic function of $CD34^+$ cells with strong hematopoietic activity.

### 2.4.2 Antitumor

Tumors are formed by the proliferation of local cells in response to various carcinogenic factors. Some studies have shown that iron overload increases the incidence of cancer (Basak and Kanwar, 2022). Tumors can be treated by several methods, such as increasing the body's immunity, inducing tumor cell differentiation, promoting tumor cell apoptosis, and reducing iron content (Dienstmann and Tabernero, 2017). The antitumor activities of ASP and the underlying mechanisms are summarized in Table 2.

Leukemia is a malignant hematological tumor caused by the diffuse malignant growth of a certain type of immature leukocyte in the bone marrow that replaces normal bone marrow tissue and diffuses into the bloodstream and lymphatic system. Currently, the conventional treatments for leukemia include chemotherapy, radiotherapy, targeted therapy, bone marrow transplantation, and supportive therapy. Liu et al. (2019) reported that leukemic mice treated with different doses of ASP (12.5 μg/mL, 25 μg/mL, 50 μg/mL, 100 μg/mL) exhibited prolonged survival to varying degrees, and the leucocyte, lymphocyte, tumor necrosis factor-α (TNF-α), interleukin 2 (IL-2), and interferon-gamma (IFN-γ) levels increased significantly. The findings of this study suggest that ASP may suppress leukemia by enhancing specific and nonspecific immunomodulatory functions. In addition, one study revealed that ASP (12.5 μg/mL, 100 μg/mL) promotes ASP-induced differentiation of leukemia cells by inducing JAK2/STAT5 tyrosine phosphorylation and activating erythropoietin (EPO) (Wang et al., 2015b). *In vitro* experiments have shown that (Zhang et al., 2016b) ASP (100, 200, 300, 400, and 500 mg/L) can inhibit the proliferation of leukemic cells, promote the proliferation of splenocytes, and enhance macrophage and phagocytic activity and the cytotoxicity of natural killer cells.

Liver cancer is a malignant tumor with a high mortality rate. An *in vitro* study of H22 cells incubated with ASP showed that low doses of ASP promoted the proliferation of splenic lymphocytes, inhibited tumor growth, and significantly inhibited tumor growth by reducing iron concentrations in the liver, spleen, and tumor cells (Cheng et al., 2016). ASP (30, 100 and 300 mg/kg) can inhibit the invasion and metastasis of hepatocellular carcinoma cells *in vitro* (Shang et al., 2003). Several studies have shown that the expression levels of IL-6, STAT3, JAK2, SMAD1/5/8, ferritin, the transcription factor TfR1 (transferrin receptor 1), and TfR2 (transferrin receptor 2) are reduced in the liver tissues of mice with hepatocellular carcinoma after the administration of ASP (100 mg/kg) (Ren et al., 2018).

Breast cancer occurs frequently in the female population, is a common malignancy, and has multiple complex mechanisms. A study in which breast cancer was induced in nude mice by injecting breast cancer cells followed by intraperitoneal administration of ASP (0.2 mg/kg) showed that the cAMP-responsive element-binding protein cyclic adenosine effector element binding protein (CREB) (Zhou et al., 2015), poly ADP ribose polymerase (PARP), Caspase-3, Caspase-9, myeloid leukemia gene 1 (Mcl-1), Bcl-2, Bcl-xL and apoptosis-activating factor 1 (Apaf1) were upregulated, resulting in increased tumor cell apoptosis. Another study showed that ASP (100 mg/kg) inhibits tumor growth by decreasing the expression of ferro regulatory elements (Ren et al., 2018). Furthermore, by culturing breast cancer cells *in vitro*, ASP (100, 200, 300, 400, and 500 mg/L) was found to exhibit antitumor activity by directly inhibiting cancer cell proliferation (Zhang et al., 2016b).

Cervical cancer is a common gynecological malignancy, and its incidence has recently been reported in younger populations. In a study performed on cervical cancer-induced nude mice, after ASP treatment, the mitochondrial potential was reduced, and caspase-9, caspase-3, and PARP expression was greatly increased, indicating that ASP (3, 30 or 300 mg/mL) inhibits tumor proliferation in cervical cancer by activating mitochondrial apoptosis (Cao et al., 2010a). In addition, a dose-dependent ASP (100, 200, and 400 mg/L) study showed inhibition of the growth and migration ability of HeLa cervical cancer cells (Tang et al., 2020), a reduction in the scratch closure rate and number of invasive cells, and downregulation of p-p38, MMP-2, and MMP-9 protein expression. This inhibitory

TABLE 3 Antioxidant effect of ASP.

| Physiological or pathological state | Subjects | Efficacy | Drug dosage | References |
|---|---|---|---|---|
| Arthritis | Human chondrocytes | Reduces oxidative stress and protects chondrocytes | 10 mg/kg | Liu et al. (2020c) |
| | Macrophages isolated from the peritoneal cavity of BALB/c mice | Protective and antioxidant effects on $H_2O_2$ damaged macrophages | 5, 25, 125 μg/mL | Zhuang et al. (2016) |
| Healthy organism | Middle-aged healthy women | Reduces oxidative stress and stimulates the expression of antioxidant enzymes | 125 mg/kg | Jiang et al. (2009) |
| Arthritis | Rat chondrocytes | Reduces damage to mouse chondrocytes by $H_2O_2$, promotes cellular secretion of antioxidant enzymes, and repairs cellular damage | 10 mg/kg | Liu et al. (2020c) |
| Cervical cancer | HeLa cells | Protective effect against oxidative damage to cells caused by $H_2O_2$ or UV irradiation | 0.3, 1, 3, 10, 30, 100 μg/mL | Jia et al. (2007) |
| Healthy organism | Shrimp | Increased levels of phenol oxidase activity, superoxide dismutase activity, glutathione peroxidase | 0.5, 1,1.5 g/kg | Pan et al. (2018) |
| Iron deficiency anemia | Rats | Increased serum superoxide dismutase and glutathione peroxidase activities and decreased MDA in rats with iron deficiency anemia | 15 mg/kg, 30 mg/kg, 60 mg/kg | Wu et al. (2017) |
| Carbon tetrachloride causes liver damage | Mice | Mechanism of attenuating or even reversing CCl4-induced hepatic oxidative damage in mice is associated with increased lipid peroxidation and enhanced antioxidant enzyme activity | 150 mg/kg, 300 mg/kg | Yu et al. (2013) |

effect may be achieved in conjunction with the influence of MMP-2 and MMP-9 expression by modulating p38 signaling pathway activity.

Neuroblastoma occurs frequently in children and infants and has a high recurrence rate and poor prognosis. *In vitro* culture of neuroblastoma cells treated with ASP (100, 200, 300, 400 or 500 ug/mL) revealed that ASP downregulated NA-H19 expression in neuroblastoma cells and that miR-675 upregulated CD44 expression and may prevent the formation of neuroblastoma tumor cells by inhibiting the miR-675-mediated PI3K/AKT and JAK/STAT pathways (Yang et al., 2018).

### 2.4.3 Antioxidants

Free radicals are highly biologically active and oxidizing compounds produced by metabolic reactions in the body using oxygen. Under normal circumstances, the body maintains a dynamic balance between oxidation and antioxidation; however, when free radicals or the antioxidant capacity of the body is unbalanced, the body can damage cell structure, protein, and nucleic acid, thus accelerating aging and even inducing various diseases. Recent research has shown that ASP has a strong scavenging effect on free radicals in the body, regulating phenol oxidase (PO), superoxide dismutase (SOD), and glutathione peroxidase (GSH-PX) activities, reducing malondialdehyde (MDA) and alleviating the oxidative stress response of the body (Cao et al., 2018). ASP can protect the body from oxidative stress by improving the antioxidant capacity of body tissues; it is also important for enhancing beauty and delaying aging. Studies have shown that ASP can reduce damage to cellular oxidative reactions caused by $H_2O_2$, improve cell viability, and attenuate apoptosis and ROS production. In the $H_2O_2$-induced cardiomyocyte $H_9c_2$ oxidative stress model, APS (6.25, 12.5, 25, 50, and 100 mg/mL) exerts protection against H9c2 by reducing endoplasmic reticulum (ER) stress and oxidative stress, alleviating $H_2O_2$-induced cytotoxicity and apoptosis through activation of the ATF6 pathway (Niu et al., 2018). The antioxidant effects of ASP are shown in Table 3.

### 2.4.4 Immunomodulation

The immune system, which is composed of various components, protects the body by acting as an effective barrier against pathogenic invasion. ASP improves nonspecific immunity by enhancing immune cell activity. South American white shrimp were fed ASP (0.5, 1,1.5 g/kg) for 12 weeks and showed enhanced nonspecific immunity, increased survival, and increased resistance to *Vibrio* lysis (Pan et al., 2018). *In vitro* culture of mouse peritoneal macrophages revealed that ASP (20, 25, 50, 100, and 200 μg/mL) promoted macrophage proliferation, enhanced macrophage activity by modulating lysozyme activity, and increased the expression of $H_2O_2$, NO, TLR4 (toll-like receptor family 4), and ICAM-1 (Chen et al., 2010). ASP (10, 30, and 100 μg/mL) can enhance nonspecific immunity in addition to specific immunity. In a study conducted on murine leukemia virus (Yang et al., 2006), the percentage of $CD4^+$ cells and the $CD4^+/CD8^+$ ratio in peripheral blood cells were found to be significantly increased by ASP at 3–30 mg/kg. It has also been demonstrated that ASP (3, 10, and 30 mg/kg) has immunomodulatory activity and is able to promote the proliferation of T cells (Yang et al., 2012), increase the production of IL-2 and IFN-γ, and decrease the production of IL-4 to regulate the expression of Th1- and Th2-related cytokines. Lu et al. (2017a) administered ASP (254.2 mg/kg) by gavage to rats exposed to whole-body X-ray radiation and observed a significant increase in the serum levels of IL-4 and IFN-γ, indicating that ASP has immunoprotective effects on X-ray radiation. A study conducted on ulcerative colitis-induced mice revealed that treatment with ASP (0.5 g/kg, 1 g/kg) reduced

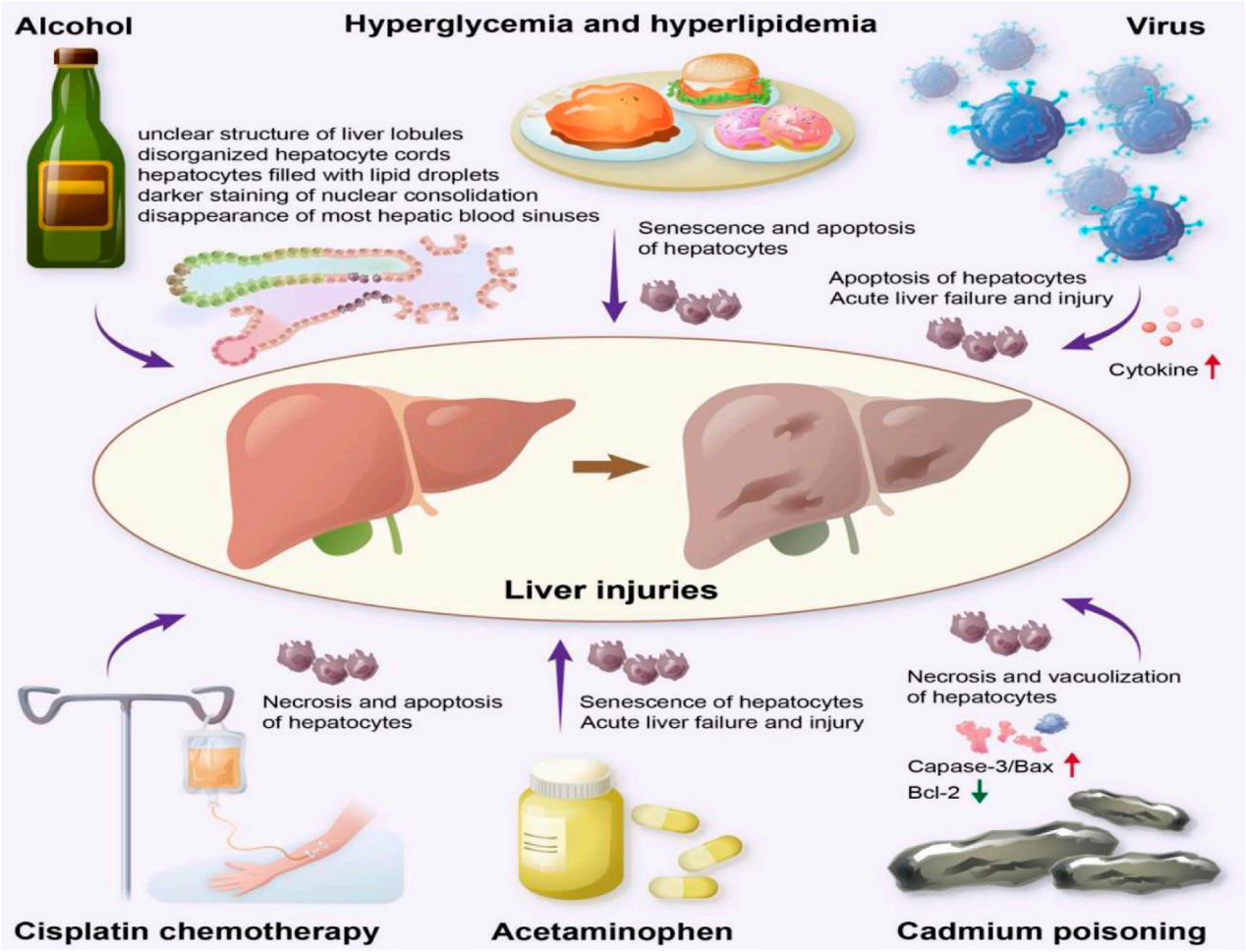


FIGURE 4
Various factors that can cause liver damage.

inflammation by decreasing the cytokine IL-10 (Pan et al., 2015). Ding et al. (2016) studied the effects of different doses of ASP (100, 200, and 400 ug/g) on myelosuppression in mice and reported that ASP increased the levels of IgG, IgM, and T-cell subsets, enhancing both humoral and cellular immunity.

### 2.4.5 Hepatoprotective effect

The liver is a crucial organ of the body and is involved in physiological functions, such as synthesis, metabolism, excretion, detoxification, and immunity. The incidence of liver injury, which seriously threatens human health, is increasing annually. It has been reported (Horvatits et al., 2019) that factors such as alcohol consumption, drug abuse, and viral infection can damage hepatocytes, leading to body imbalance and impaired energy regulation, which causes liver injury (Figure 4). ASP has shown protective effects against various types of liver injuries, and the mechanisms involved are reviewed below.

Alcoholic liver injury is a disease caused by long-term alcohol consumption, the incidence of which is increasing annually, and it is the second most common liver disease after viral hepatitis. Alcohol-induced liver injury is characterized by an unclear structure of the liver lobules, disorganized hepatocyte cords, hepatocytes filled with lipid droplets in the form of vacuoles, darker staining of nuclear consolidation, and the disappearance of most hepatic blood sinuses (Wang et al., 2016a). ASP (4 mg/kg) increases the activity of antioxidant enzymes, scavenges oxygen free radicals, and reduces the chain reaction of membrane lipid peroxidation, which subsequently restores the biofilm structure of hepatocytes in alcohol-induced liver injury (Jia et al., 2015). ASP (1.5 mg/kg, 6 mg/kg) alleviates viral and autoimmune hepatitis, reduces cytokine expression and inflammatory responses in experimental mice, and it may inhibit hepatocyte apoptosis by attenuating the c-Jun amino-terminal kinase (JNK)-mediated mitochondrial apoptotic pathway and inhibiting Caspase-8 expression (Wang et al., 2016c).

In addition to alcoholic liver injury and viral hepatitis, liver injury caused by drugs and cadmium poisoning is also common, with acetaminophen (APAP) being the most common cause of liver injury (Han et al., 2010). Long-term or excessive use of APAP is associated with acute liver failure and injury. Cao et al. (2018) investigated the reduced toxicity of different concentrations of ASP (3, 6, and 12 mg/kg) intravenously administered for 10 days in APAP-induced liver injury rats, and APAP-induced histological changes were significantly reversed with vacuolization and

necrosis of the cytoplasm. In addition, the expression of caspase-3 and Bax decreased, the expression of Bcl-2 increased, and hepatocyte apoptosis was inhibited. Liu et al. (2018) showed that ASP (20 mg/kg) had a significant protective effect on liver injury in cadmium-treated rats. After treatment with ASP, the thymus, spleen index, lymphocyte transformation capacity, NK cell killing capacity, cytokine IL-2 content, and Bcl-2 protein expression were significantly increased in cadmium-treated rats, while AST, ALT, LDH activity, TGF-β1, and cadmium levels were increased. This mechanism may involve the enhancement of autoimmunity, the regulation of enzyme activity, and the expression of apoptosis-related proteins.

Furthermore, chemotherapeutic drugs used to treat tumors are associated with apoptosis and necrosis of liver cells. Fu and Ma (2018) reported that ASP (25, 50, and 100 mg/kg) could improve liver function by increasing the number of leukocytes, erythrocytes, and platelets, which decreases the level of Bax and increases the expression of Bcl-2. This results in alleviating liver injury induced by cisplatin in H22 ascites-derived tumors in mice.

Hyperglycemia and hyperlipidemia can cause liver damage. Kaiping Wang et al. (2016d) induced hyperglycemia and hyperlipidemia in mice using a high-fat diet and low-dose streptozotocin (STZ) and observed that the rats developed significant liver damage. During the experiment, the mice were administered different doses of ASP (100, 200 and 400 mg/kg) along with STZ injection. ASP has been found to reduce liver damage by stimulating insulin secretion, facilitating hepatic glycogen synthesis, releasing adipokines, and reducing hepatic fat accumulation. In addition, ASP promoted the expression of the antiapoptotic protein Bcl-2 and reduced the expression of the proapoptotic protein Bax, which inhibited the senescence of hepatocytes and reduced liver injury in mice.

### 2.4.6 Anti-inflammatory effects

Experiments have confirmed that ASP has therapeutic effects on several inflammatory conditions, such as osteoarthritis and colitis. Chondrocyte apoptosis is important in the development of osteoarthritis (OA). Xu et al. (2021) reported that ASP (50 ug/mL, 200 ug/mL) had a protective effect against sodium nitroprusside (SNP)-induced chondrocyte apoptosis, suggesting that ASP is a potential alternative for OA treatment. Xu et al. (2022) performed a study on an *in vitro* model of IL-1β injury and observed that ASP (10, 50, and 100 ug/mL) effectively reduced IL-1β damage to chondrocytes and increased their activity. Additionally, ASP reduced the expression levels of β-catenin, Wnt4a, GSK-3β, MMP-13, and ADAMTS4, inhibited IL-1β-induced cartilage degradation, and alleviated patient symptoms. ASP has been found to inhibit oxidative stress damage and inflammatory responses in osteoarthritic chondrocytes through the Wnt/β-catenin signaling pathway. Preclinical studies have shown that it (0.5 g/kg, 1 g/kg) significantly reduces the production of IL-6, TNF-α, and other proinflammatory factors and has a significant therapeutic effect on arthritic rats (Li et al., 2020).

Cheng et al. (2020) reported that ASP (200 mg/kg) reduced myeloperoxidase activity in colonic tissues, modulated the expression of proinflammatory cytokines and related proteins, and improved dextran sodium sulfate-induced colitis in mice. It has also been reported that ASP (200 mg/kg) significantly reduces the serum expression levels of IL-6, TNF-α, SDF-1, plasma TF, D-D, and FIB in rats prone to embolism during pregnancy (Ma et al., 2022), indicating that APS has anti-inflammatory and anticoagulant effects. *In vitro* studies have shown that ASP (80 ug/mL, 100 ug/mL) can reduce the inflammatory response to protect neuronal cells (Zhou et al., 2019). Zhou et al. (2018) analyzed the effects of ASP (0.009, 0.018, and 0.036 g/mL) on TLR4/MyD88/NF-κB pathway inhibition in rats with diabetic peripheral neuropathy (DPN) and reported that APS significantly decreased the levels of IL-6, myelin basic protein (MBP), TNF-α, CRP, NF-κB, MyD88, and TLR4 and significantly increased CAT mRNA expression in rats, reduced the levels of inflammatory factors, and decreased damage to the inflammatory response.

### 2.4.7 Anti-fibrosis

Wang et al. (2010) observed the effects of ASP (50, 100, and 200 g/kg) on pulmonary function and the lung coefficient in rats with pulmonary fibrosis induced by pulmonary fibrosis and reported that 0.3 s of expiratory volume as a percentage of forced expiratory volume (FEV0.3/FVC) and calm end-expiratory function residual capacity (FRC) increased to different extents, and it was shown that ASP could significantly improve pulmonary function, increase body weight, and decrease the lung coefficient in rat models of pulmonary fibrosis. Qian et al. (2020) reported that ASP (20 mg/kg) inhibited the development of fibrosis in rat lung and alveolar type II epithelial cells (RLE-6TN) through the DANCR/AUF1/FOXO3 regulatory axis, which facilitates the treatment of idiopathic pulmonary fibrosis (IPF). In addition, ASP (12.5, 25, and 50ug/mL) was found to inhibit pulmonary fibrosis, and its effects may be related to the downregulation of α-smooth muscle actin (α-SMA) and CTGF expression and the regulation of the balance between MMP-9 and TIMP-1 (Luo et al., 2017). Song et al. (2021) reported that ASP (80, 160, and 320 mg/kg) decreased the LV end-diastolic diameter, LV end-systolic diameter, LV end-diastolic volume, and LV end-systolic volume; decreased the expression levels of TGF-β1, α-SMA, type I collagen (CoI), fibronectin, vimentin, Bax, cleaved caspase-9, and cleaved caspase-3 in the LV; increased SOD and GSH-Px activities; decreased MDA, H2 O2, and ROS levels; and ultimately inhibited myocardial apoptosis and oxidative stress to prevent hypertensive myocardial fibrosis in HHD rats by increasing the ejection fraction and fractional shortening. Another study showed that ASP (200 mg/kg) improved chronic liver fibrosis by inhibiting HSC activation through the IL-22/STAT3 pathway (Wang et al., 2020), reducing serum alanine aminotransferase by approximately 50%, and inhibiting hepatic stellate cell (HSC) activation in mice with liver fibrosis.

### 2.4.8 Lowering blood sugar

Non-starch polysaccharides lower blood glucose levels through multiple pathways. It was found that after 4 weeks of ASP4 (100, 200, 400, and 600 mg/kg) treatment in STZ-induced diabetic mice (Wang et al., 2015a), fasting blood glucose (FBG) decreased, dyslipidemia improved, and elevated serum total cholesterol (TC) and triglyceride (TG) levels decreased. Zhang et al. (2019) reported a protective effect of ASP on the islets of T2DM mice, and the possible mechanism was related to the promotion of insulin secretion and the inhibition of

apoptosis by blocking both internal and external pathways of pancreatic β-cells. In another study, Chen (2010) reported that after oral administration of ASP (2 or 100 mg/kg) for 21 days, alloxan-induced diabetic rats exhibited significantly decreased blood glucose levels and improved plasma insulin levels, which may be associated with the repair and regeneration of damaged pancreatic β-cells. Several studies have shown that ASP (80, 160 and 320 mg/kg) reduces blood glucose levels and attenuates insulin resistance by modulating relevant metabolic enzymes and activating the PI3K/Akt pathway in high-fat diet-fed mice (Wang et al., 2016b), suggesting that ASP has therapeutic potential for treating hypoglycemia.

ASP-1I (12.5, 25, and 50 mg/kg) has been shown to enhance glucose absorption while simultaneously inhibiting the activation of p-IRS-1, p-IRS-2, p-JNK, and p-P38 pathways in insulin-resistant HepG2 cells. Furthermore, intraperitoneal administration of ASP-1I significantly ameliorates insulin resistance and suppresses the RAGE-JNK/P38-IRS pathway in the liver of diabetic rats, demonstrating a mild yet effective therapeutic effect (Liu et al., 2022a). Additionally, oral administration of ASP (40 mg/L) can improve bone health by reducing blood glucose levels and enhancing insulin sensitivity, thereby facilitating bone tissue repair in a rat model of type 2 diabetes (Liao et al., 2019).

### 2.4.9 Radiation resistance

Currently, ionizing radiation has become the fourth major hazard to humans after air, water, and noise pollution. Polysaccharides are more suitable alternatives to medicinal radiation protection agents because they are less toxic and non-accumulative. ASP (63.5, 127, and 254 mg/kg) is used to protect against radiation-induced liver damage because of its ability to increase the resistance of the liver to radiation and to scavenge free radicals (Wang et al., 2017c). ASP (63.6, 127.1, and 254.2 mg/kg) regulates the body's oxygen radical balance through activation of the transcription factor Nrf2, thereby counteracting radiation-induced oxidative damage (Lu et al., 2017b; Zhang et al., 2017). ASP (63.5, 127, and 254 mg/kg) has also shown efficacy against radiation-induced bone marrow and spleen damage in SD rats, probably by reducing radiation-induced damage to hematopoietic and immune cells in the bone marrow and spleen (Lu et al., 2017a; Xu et al., 2017). Zhang et al. (2020) showed that medium (127.1 mg/kg) and high (254.2 mg/kg) doses of ASP had significant effects on ionizing radiation-induced intestinal barrier damage in SD rats. ASP (100, 200, and 400 mg/kg) can regulate the ratio of regulatory cells (Tregs)/helper T cells 17 (Th17) in $^{60}$Co-γ-irradiated mice, improve the stability of mitochondrial membranes, and regulate abnormal levels of ROS and mitochondria-related apoptotic proteins, thus achieving antiradiation effects (Chen et al., 2022).

## 2.5 Other pharmacological effects

Studies have shown that ASP can lower blood lipids, improve diabetic nephropathy, and improve antiviral properties.

ASP (400, 600 mg/kg) significantly reduced the homeostasis model assessment-insulin resistance index (HOMA-IR) and body weight and was also effective in reducing serum TC and triglyceride concentrations and restoring pancreatic/liver or adipose tissue in BALB/c mouse models of prediabetes and STZ-induced diabetes (Wang et al., 2015a).

A major complication in long-term diabetic patients is diabetic nephropathy (DN). Intraperitoneal injection of the ASP branch Acanthopanax (AG) for 8 weeks in diabetic rats resulted in significant improvements in renal function, increased creatinine clearance, a significant reduction in blood urea nitrogen, and the expansion of glomeruli in patients with proteinuria. AG (20, 50, and 100 mg/kg) inhibited the RAGE/NF-KB (receptor for advanced glycosylation end products/nuclear factor-KB) signaling pathway by inhibiting the over-proliferation of glomerular mesangial cells (GMCs) via the RAGE/NF-KB signaling pathway and attenuating inflammatory mediators (Sui et al., 2019).

ASP (1.5 g/kg) was found to promote the maturation of dendritic cells (DC) in hepatitis B virus (HBV) transgenic mice, upregulate the expression of the surface costimulatory molecule CD86, improve the ability of DC to proliferate lymphocytes and secrete IL-12 and r-IFN, and may play a critical role in the antiviral immunity of HBV transgenic mice (Li et al., 2005). APS has shown a synergistic effect with dithiothreitol, suggesting that APS can be used in combination with antiviral drugs for the treatment of AIDS. ASP (10, 30 mg/kg) causes anti-cellular oxidative damage, which may be the mechanism associated with anti-AIDS activity (Jia, 2005). ASP have shown efficacy against human cytomegalovirus (HCMV)-infected cytomegalic lineage cells *in vitro* by inhibiting HCMV-induced apoptosis in a dose-dependent manner (Zhang et al., 2009). ASP enhance the proliferation of chicken embryonic fibroblasts and prevents infection by Newcastle disease virus (Hu et al., 2004). The chlorosulfate-pyridine-modified *Angelica* sulfated polysaccharides (0.244, 0.488, 0.977, 1.953, and 3.907 ug/mL) significantly improved resistance to Newcastle disease virus infection in chicken embryo fibroblasts (Wang et al., 2011a). An *in vitro* study demonstrated that ASP (1,399.531 ug/mL) inhibited chicken infectious bursal virus-infected cells in a quantitative and temporal manner (Hu et al., 2003).

*Angelica sinensis* polysaccharide, as a traditional Chinese medicine component, has shown significant antiviral potential in pharmacology, which has been widely recognized in the scientific community. However, any medicinal ingredient has its two sides, angelica polysaccharide is no exception. Studies have shown that angelica polysaccharide can effectively promote the proliferation of fibroblasts, which has a positive effect on the repair of damaged tissues and wound healing. Fibroblasts are the main cell type that constitutes connective tissue, and their proliferation is essential for maintaining the integrity and elasticity of skin and tissue. However, in some cases, excessive proliferation of fibroblasts can lead to undesirable side effects, such as excessive scar tissue formation during healing, and may even cause tissue sclerosis, affecting organ function. Therefore, when considering the use of ASP for treatment, we must carefully weigh its potential benefits against possible risks to ensure that unnecessary side effects are avoided while promoting health.

## 2.6 Effect of different extraction positions of *Angelica sinensis* on ASP activity

*Angelica sinensis*, a traditional Chinese herbal medicine, shows unique differences in pharma cological effects of polysaccharide

components contained in different parts. The content of ASP in *Angelica sinensis* is as high as 15% (Cao, 2019). As one of the main components of *Angelica sinensis* for nourishing blood and regulating menstruation (Ouyang et al., 2005), it can improve the hematopoietic function of the body by increasing the number of white blood cells, red blood cells and hemoglobin in peripheral blood. The study of Wu Guoxia et al.believed that in different medicinal parts of *Angelica sinensis*, the amount of ASP contained in *Angelica sinensis* was significantly higher than that in *Angelica sinensis* head and other parts (Wu et al., 2018a). Song et al. also confirmed the view that the content of ASP in *Angelica sinensis* was higher by investigating different cultivation methods of *Angelica sinensis* (Song et al., 2008). By comparing the content of ASP in the whole *Angelica sinensis* and the head of *Angelica sinensis* (Long and Maobao, 2008), think that the content of ASP in the whole angelica processed in the same origin is higher than that in the head of *Angelica sinensis*; considering that the whole *Angelica sinensis* and *Angelica sinensis* can be clustered into one class in the process of fingerprint cluster analysis (Wu et al., 2018b), we can still think that the polysaccharide content in *Angelica sinensis* is higher than that in *Angelica sinensis* head and *Angelica sinensis* tail, and is close to that in *Angelica sinensis*.

Some scholars have studied the antioxidant activity of polysaccharides from different medicinal parts of *Angelica sinensis* (Zou et al., 2022). Four kinds of polysaccharides, ASP-H-AP, ASP-B-AP, ASP-T-AP and ASP-Hb-AP, were obtained from different medicinal parts of *Angelica sinensis*, and their antioxidant activities were studied. It was found that the four polysaccharide components could reduce the oxidative stress of IPEC-J2 cells by up-regulating the expression of related genes and proteins of antioxidant enzymes. Among them, ASP-Hb-AP had better antioxidant effect, while ASP-T-AP had relatively poor antioxidant effect.

ASP in *Angelica sinensis* can induce the synthesis and secretion of hematopoietic regulatory factors by macrophages by enhancing the expression of GM-CSF protein and mRNA in bone marrow stromal cells, spleen cells and thymocytes, and accelerate the proliferation and differentiation of myeloid multi-directional hematopoietic progenitor cells, late erythroid progenitor cells and granulocyte mononuclear hematopoietic progenitor cells. Finally, it can restore the number of peripheral blood cells in blood deficiency animals, reconstruct the long-term hematopoietic ability of hematopoietic failure animals (Xu et al., 2020), improve the immune adhesion ability and hematopoietic ability of red blood cells after radiation injury, and improve anemia. In addition, it also has the effects of promoting blood circulation, hemostasis, anti-radiation, anti-oxidation, anti-tumor, anti-inflammation and improving immunity.

On the other hand, the pharmacological effects of polysaccharides in the head and tail of *Angelica sinensis* have not been reported in domestic and foreign studies, and further research and exploration by the research group are needed.

## 2.7 Summary and outlook

In summary, ASP is the main active component of the traditional Chinese medicine *Angelica sinensis*, which has multiple components, multiple target characteristics, and very broad pharmacological activities. It also plays an important role in the treatment of several diseases. In this review, we describe the ten major pharmacological activities of ASP reported in several studies, including anemia, antitumour, antioxidant, immunomodulatory, hepatoprotective, anti-inflammatory, hypoglycemic, antiradiation, antifibrosis, and antiviral activities. However, preclinical studies on ASP have primarily focused on crude compounds without further purification and isolation, which necessitates further investigation to determine the specific composition of ASP. Studies have shown that ASP modification helps amplify their pharmacological effects (Hou et al., 2021). Therefore, studying the effects of different modifying agents on the pharmacological activities of ASP is promising. ASP has been reported to play a crucial role in the treatment of diabetes mellitus and its complications, such as diabetic nephropathy and peripheral neuropathy. The incidence of diabetes mellitus is increasing annually worldwide, and patients require long-term medication. In such cases, the use of ASP as a natural plant extract with fewer side effects and a high safety profile is a potential alternative for the long-term treatment of diabetes mellitus. ASP has shown efficacy against tumors and organ fibrosis; however, its specific molecular mechanisms of action and drug targets remain undetermined. Therefore, in-depth studies are required to identify the underlying mechanisms and potential drug targets involved.

As research on ASP has advanced, the use of ASPs in clinical, food, healthcare, and cosmetic applications has also gradually increased. Iron ASP have been used for the treatment of iron deficiency anemia (Wang et al., 2007b), sulfated ASP have been used as antitumour agents (Wu et al., 2012; 2013), and *Angelica* hepatica capsules have been used to lower blood sugar (Wang et al., 2007a; Zhang et al., 1998). In addition, *Angelica sinensis* and *Astragalus* iron particles and *Angelica Sinensis* and *Astragalus* capsule have been developed for iron deficiency anemia and prevention of radiation exposure, as shown in Table 4. However, more research and development are required to identify the various natural compounds and their contents or ratios. Standardized norms have not yet been developed, and the material basis of the effect and its target of action remain unclear. Studies on the use of dosages are not well standardized or precise. Therefore, a systematic evaluation of its safety and efficacy is needed. Standardization of the extraction process for specific active ingredients and identification of their precise targets are key issues that need to be addressed.

However, natural products often face challenges related to repeatability, standardization, and quality control. The repeatability, standardization, and quality control of ASP is also a challenge, but can be overcome through a series of scientific and rigorous methods and strict standards. Firstly, the active ingredient standard (ASP) was used as a reference to ensure that the content and quality of ASP in the product were consistent. This process involves precise chemical analysis and quality control techniques to ensure that each batch of ASP products meets the established active ingredient standards. Secondly, by formulating and following standardized protocols, it can be ensured that each batch of products can produce the same pharmacological effects. This involves not only the standardization of product formulations, but also clinical trials and bioequivalence studies to ensure the efficacy and safety of the product.

TABLE 4 *Angelica sinensis* polysaccharidederived health food.

| Product name | Manufacturer | Treatment indications | Dose/formula | Regulatory status (CFDA) |
|---|---|---|---|---|
| *Angelica sinensis*, *Astragalus* and iron particles | Shenzhen McKinley Co., Ltd | Hypoferric anemia; iron-deficiency anemia | 5 g/bag, containing 352 mg of iron, 60 mg of ASP, AS-IV 30 mg | National food health word: G20230585 |
| *Angelica Sinensis* and *Astragalus* capsules | Gansu LongShen RongFa Pharmaceutical Co., Ltd | It has the auxiliary protection function for the radiation hazard | 0.36 g/grain, containing 0.5 g of crude polysaccharide per 100 g | National food health word: G20140331 |

In addition, the use of biomarkers helps to monitor and evaluate the quality of products, ensuring the stability and consistency of their active ingredients. These biomarkers are screened by advanced biotechnology, which can reflect the metabolic process and bioavailability of ASP in human body. It is worth noting that improving the extraction method is also the key, which can involve the optimization of extraction conditions, such as the design of temperature, the selection of solvent type and the determination of extraction time, so as to maximize the purity and biological activity of angelica polysaccharide. Of course, this process also requires multidisciplinary cooperation, including the joint efforts of experts in the fields of chemistry, pharmacology and biotechnology.

Finally, following regulatory standards such as Good Manufacturing Practice (GMP) can ensure the standardization of the entire production process and the reliability of product quality. GMP standards not only require the production environment to be sterile and clean, but also require strict recording and monitoring of each step in the production process, including procurement, storage, processing, packaging of raw materials and quality inspection of final products. Through the implementation of these measures, we can provide consumers with stable quality and predictable effects of ASP derivative health products, so as to meet the growing market demand for high-quality natural health products. In the process of following GMP standards, special attention should also be paid to continuous improvement and innovation. Through the continuous introduction of advanced production equipment and technology, in order to improve production efficiency and product quality. At the same time, it is necessary to strengthen the training and management of employees to ensure that every production link meets the standards and can produce high-quality ASP products continuously and steadily.

On the other hand, with the continuous development of social economy, the public's attention to personal health is increasing day by day, which leads to an upward trend in the demand for natural medicines in the market, especially the large-scale production of medicinal materials such as ASP. However, in order to meet the needs of large-scale production, the research team recommended the use of synthetic simulation technology to prepare the active components of the natural drug ASP. Because this method can ensure the repeatability and effectiveness of the product, so as to meet the market demand. Synthetic mimetic active ingredients are widely recommended in large-scale production because they can ensure product consistency and reliability, thereby obtaining more repeatable and effective products. The structure and purity of active ingredients can be precisely controlled by chemical synthesis to ensure that each batch of products has the same efficacy and quality. This consistency is essential for pharmaceuticals, cosmetics and other products that require strict quality control. In addition, the production process of synthetic simulated active ingredients is often more controllable, which can meet the needs of large-scale industrial production, reduce the dependence on natural resources, reduce production costs, and have certain advantages in environmental protection. Therefore, the synthesis of simulated active ingredients can not only provide stable product quality, but also meet market demand and achieve the dual goals of economic benefits and environmental sustainability.

In recent years, with the rapid development and application of drug composition assays and computer-aided drug screening technologies, the pharmacological effects and targets of various Chinese medicinal components, such as polysaccharides and flavonoids, can be predicted and analyzed more comprehensively and systematically and compared with *in vitro* and *in vivo* data, which can help to systematically explain the pharmacological effects of ASP and its underlying mechanisms. This revealed the biological implications of the multipoint and synergistic effects of Chinese medicine.

## Author contributions

CR: Data curation, Formal Analysis, Methodology, Writing–original draft. YaL: Data curation, Formal Analysis, Methodology, Writing–original draft. XL: Data curation, Formal Analysis, Methodology, Writing–original draft. LM: Data curation, Investigation, Writing–original draft. CW: Methodology, Visualization, Writing–original draft. XgZ: Methodology, Visualization, Writing–original draft. XeZ: Funding acquisition, Supervision, Writing–review and editing. YiL: Funding acquisition, Supervision, Writing–review and editing.

## Funding

The author(s) declare that financial support was received for the research, authorship, and/or publication of this article. This work was supported by the 2021 Gansu Jiaoyu Jiebang Guashuai Project (No. 2021 jyjbgs-03), Gansu Province Traditional Chinese Medicine Prevention and Treatment of Major Diseases Special Project (No. GZKZD-2018-02), Gansu Province Major Science and Technology Special Project (No.20ZD7FA002), 2022 Gansu Province Longyuan Youth Innovation and Entrepreneurship Talent Project, 2022 Gansu Province natural sciences fund (22JR11RA128) and National Natural Science Foundation of China (NO. 82260869), National Administration of Traditional Chinese Medicine Youth Qihuang

Scholars Support Project. 2021 "Double First-Class" Scientific Research Key Project (No. GSSYLXM-05-ZXYJH-11), Gansu Provincial Youth Science and Technology Fund (23JRRA1217) and National Natural Science Foundation of China (NO. 82360926), 2024 Gansu Province Outstanding Doctoral Project (24JRRA569).

## Conflict of interest

The authors declare that the research was conducted in the absence of any commercial or financial relationships that could be construed as a potential conflict of interest.

## Generative AI statement

The author(s) declare that no Generative AI was used in the creation of this manuscript.

## Publisher's note

All claims expressed in this article are solely those of the authors and do not necessarily represent those of their affiliated organizations, or those of the publisher, the editors and the reviewers. Any product that may be evaluated in this article, or claim that may be made by its manufacturer, is not guaranteed or endorsed by the publisher.

## References

Basak, T., and Kanwar, R. K. (2022). Iron imbalance in cancer: intersection of deficiency and overload. *Cancer Med.* 11 (20), 3837–3853. doi:10.1002/cam4.4761

Bi, S. J., Fu, R. J., Li, J. J., Chen, Y. Y., and Tang, Y. P. (2021). The bioactivities and potential clinical values of *angelica sinensis* polysaccharides of *Angelica sinensis* polysaccharides. *Nat. Prod. Commun.* 16 (3). doi:10.1177/1934578X21997321

Cao, P., Sun, J., Sullivan, M. A., Huang, X., Wang, H., Zhang, Y., et al. (2018). *Angelica sinensis* polysaccharide protects against acetaminophen-induced acute liver injury and cell death by suppressing oxidative stress and hepatic apoptosis *in vivo* and *in vitro*. *Int. J. Biol. Macromol.* 111, 1133–1139. doi:10.1016/j.ijbiomac.2018.01.139

Cao, W., Li, X., Hou, Y., Fan, H., Zhang, X., and Mei, Q. (2008a). Structural analysis and antitumor effect of ASP APS-2a. *Chin. Med. Mater.* 31 (2), 261–266. doi:10.3321/j.issn:1001-4454.2008.02.031

Cao, W., Li, X. Q., Hou, Y., Fan, H. T., Zhang, X. N., and Mei, Q. B. (2008b). Structural analysis and anti-tumor activity *in vivo* of polysaccharide APS-2a from *Angelica sinensis*. *J. Chin. Med. Mater.* 31 (2), 261–266. doi:10.3321/j.issn:1001-4454.2008.02.031

Cao, W., Li, X. Q., Liu, L., Wang, M., Fan, H. T., Li, C., et al. (2006). Structural analysis of water-soluble glucans from the root of *Angelica sinensis* (Oliv.) Diels. *Carbohydr. Res.* 341 (11), 1870–1877. doi:10.1016/j.carres.2006.04.017

Cao, W., Li, X. Q., Wang, X., Fan, H. T., Zhang, X. N., Hou, Y., et al. (2010a). A novel polysaccharide, isolated from *Angelica sinensis* (Oliv.) Diels induces the apoptosis of cervical cancer HeLa cells through an intrinsic apoptotic pathway. *Phytomedicine* 17 (8-9), 598–605. doi:10.1016/j.phymed.2009.12.014

Cao, W., Li, X. Q., Wang, X., Li, T., Chen, X., Liu, S. B., et al. (2010b). Characterizations and anti-tumor activities of three acidic polysaccharides from *Angelica sinensis* (Oliv.) Diels. *Int. J. Biol. Macromol.* 46 (1), 115–122. doi:10.1016/j.ijbiomac.2009.11.005

Cao, Y. (2019). Analysis of chemical constituents and pharmacological effects of *Angelica sinensis*. *World 's latest Med. inf. Abstr.* 19 (2), 93–95. doi:10.19613/j.cnki.1671-3141.2019.02.058

Chen, J. (2010). On effects and mechanism of *Angelica sinensis* polysaccharides on glucose metabolism in experimental diabetic rats. *J. Wuhan. Polytech.* 9 (3), 93–95. doi:10.3969/j.issn.1671-931X.2010.03.023

Chen, L., and Huang, G. (2018). The antiviral activity of polysaccharides and their derivatives. *Int. J. Biol. Macromol.* 115, 77–82. doi:10.1016/j.ijbiomac.2018.04.056

Chen, R., Liu, Y., Wang, H., Xu, H., and Xu, G. (2001a). Isolation and purification of ASP X-C-3-II and its composition. *Chin. J. New Drugs.* 10 (6), 431–432. doi:10.3321/j.issn:1003-3734.2001.06.010

Chen, R., Wang, H., Xu, H., Xu, G., and Chang, L. (2001b). Isolation, purification and identification of two polysaccharide fractions from Min *Angelica sinensis*. *Chin. Med. Mater* 24 (1), 36–37. doi:10.3321/j.issn:1001-4454.2001.01.016

Chen, R., Xu, G., Wang, H., Xu, H., and Liu, Y. (2001c). Isolation and structure of the polysaccharide XC-1 from *Angelica sinensis*. *Chem. Bull.* 3 (6), 372–374. doi:10.3969/j.issn.0441-3776.2001.06.009

Chen, Y., Duan, J. A., Qian, D., Guo, J., Song, B., and Yang, M. (2010). Assessment and comparison of immunoregulatory activity of four hydrosoluble fractions of *Angelica sinensisin* vitro on the peritoneal macrophages in ICR mice. *Int. Immunopharmacol.* 10 (4), 422–430. doi:10.1016/j.intimp.2010.01.004

Chen, Z., Cheng, L., Zhang, J., and Cui, X. (2022). Retraction Note: *Angelica sinensis* polysaccharide prevents mitochondrial apoptosis by regulating the Treg/Th17 ratio in aplastic anemia. *BMC Complement. Med. Ther.* 22 (1), 277. doi:10.1186/s12906-022-03752-5

Cheng, F., Zhang, Y., Li, Q., Zeng, F., and Wang, K. (2020). Inhibition of dextran sodium sulfate-induced experimental colitis in mice by *angelica sinensis* polysaccharide. *J. Med. Food.* 23 (6), 584–592. doi:10.1089/jmf.2019.4607

Cheng, Y., Zhou, J., Li, Q., Liu, Y., Wang, K., and Zhang, Y. (2016). The effects of polysaccharides from the root of *Angelica sinensis* on tumor growth and iron metabolism in H22-bearing mice. *Food Funct.* 7 (2), 1033–1039. doi:10.1039/c5fo00855g

Chinese Pharmacopoeia Commission. (2020). *Pharmacopoeia of the people's Republic of China*. Beijing, China: Ministry of Health of the People's Republic of China, 1 139.

Dienstmann, R., and Tabernero, J. (2017). Cancer: a precision approach to tumour treatment. *Nature* 548 (7665), 40–41. doi:10.1038/nature23101

Ding, X., Zhao, X., Qiu, Y., Chen, K., and Li, Y. (2016). Effects of ASP on peripheral blood cells and immune function in cyclophosphamide-induced myelosuppressed mice. *Health Prof. Educ.* 34 (16), 153–155. Available at: https://d.wanfangdata.com.cn/Periodical/wszyjy201616084.

Erlin, C., Xixiang, L., Shanna, W., Wang, X., Niu, M., Wang, J., et al. (2019). Study on the quality evaluation of *Angelica sinensis* based on the bioeffectiveness of blood activation. *Chin. Med. Mater.* 42 (4), 818–821. doi:10.13863/j.issn1001-4454.2019.04.024

Fu, Z., and Ma, C. (2018). Effect of ASP on liver injury caused by cisplatin chemotherapy in H22 ascites tumor mice Pharmacology and clinical aspects of Chinese medicine. *Pharmacol. Clin. Appl. Trad. Chin. Med.* 34 (3), 68–72. doi:10.13412/j.cnki.zyyl.2018.03.017

Han, D., Shinohara, M., Ybanez, M. D., Saberi, B., and Kaplowitz, N. (2010). Signal transduction pathways involved in drug-induced liver injury. *Handb. Exp. Pharmacol.* 196, 267–310. doi:10.1007/978-3-642-00663-0_10

He, X., Zhang, Y., Wu, H., and Jiang, R. (2012). Study on the protective effect of ASP on the hematopoietic system of radiation-injured mice. *Chongqing Med.* 41 (35), 3734–3736. doi:10.3969/j.issn.1671-8348.2012.35.019

Hong, Y., Liu, Y., Xiong, X., Zhang, Y., and Wang, H. (2002). Protective effects of ASP on the immune and hematopoietic functions of erythrocytes in radiation-injured mice. *Med. Clin. Res.* 19 (1), 31–32. doi:10.3969/j.issn.1671-7171.2002.06.014

Horvatits, T., Drolz, A., Trauner, M., and Fuhrmann, V. (2019). Liver injury and failure in critical illness. *Hepatology* 70 (6), 2204–2215. doi:10.1002/hep.30824

Hou, C., Yin, M., Lan, P., Wang, H., and Ji, X. (2021). Recent progress in the research of *Angelica sinensis* (Oliv.) Diels polysaccharides: extraction, purification, structure and bioactivities. *Chem. Biol. Technol. Agric.* 8 (1), 13. doi:10.1186/s40538-021-00214-x

Hu, Y., Kong, X., Li, X., Wang, D., Liu, J., Zhang, B., et al. (2004). Effect of 10 Chinese herbal ingredients on the proliferation and resistance of CEF to NDV infection. *J. Anim. Husb. Vet. Med.* 35 (3), 301–305. doi:10.3321/j.issn:0366-6964.2004.03.013

Hu, Y., Liu, J., Chen, Y., Zhang, B., Sun, X., and Wang, X. (2003). Effect of Chinese medicinal ingredients on infected cells of infectious bursal virus. *J. Anim. Husb. Vet. Med.* 35 (12), 8–10. doi:10.3969/j.issn.0529-5130.2003.12.004

Huang, X. (2010). Progress in the extraction methods of medicinal plant polysaccharides. *Mod. Chem. Ind.* 30 (12), 32–36. doi:10.16606/j.cnki.issn0253-4320.2010.12.007

Jia, M. (2005). *Study on the anti-AIDS effect of ASP sulfate and its mechanism. Master thesis*. Xi'an: Fourth Military Medical University.

Jia, M., Yang, T., Yao, X., Meng, J., Meng, J., and Mei, Q. (2007). Study on the antioxidant effect of ASP sulfate. *Chin. Med. Mater.* 30 (2), 185–188. doi:10.3321/j.issn:1001-4454.2007.02.026

Jia, S., Wang, D., Zhang, X., and Wang, G. (2015). Effects of ASP on alcoholic hepatocyte injury in mice. *Anat. Res.* 37 (6), 468–471. Available at: https://d.wanfangdata.com.cn/periodical/jpxyj201506007. doi:10.20021/j.cnki.1671–0770.2015.06.007

Jiang, J., Guo, Y. J., and Niu, A. (2009). Extraction, characterization of *Angelica sinensis* polysaccharides and modulatory effect of the polysaccharides and Tai Chi exercise on oxidative injury in middle-aged women subjects. *Carbohydr. Polym.* 77 (2), 384–388. doi:10.1016/j.carbpol.2009.01.010

Jin, M., Zhao, K., Huang, Q., Xu, C., and Shang, P. (2012). Isolation, structure and bioactivities of the polysaccharides from *Angelica sinensis* (Oliv.) Diels: a review. *Carbohydr. Polym.* 89 (3), 713–722. doi:10.1016/j.carbpol.2012.04.049

Jin, R., Li, G., and Ma, S. (2007). Research on the preparation process of *Angelica* polysaccharide. *Chin. Pat. Med.* 29 (8), 1146–1150. doi:10.3969/j.issn.1001-1528.2007.08.016

Lee, J. G., Hsieh, W. T., Chen, S. U., and Chiang, B. H. (2012). Hematopoietic and myeloprotective activities of an acidic *Angelica sinensis polysaccharide* on human CD34+ stem cells. *J. Ethnopharmacol.* 139 (3), 739–745. doi:10.1016/j.jep.2011.11.049

Li, G., and Xu, L. (2017). Study on the effect of ASP on microRNA in the blood of radiation-injured mice. *Northwest J. Pharmacol.* 32 (2), 163–167. doi:10.3969/j.issn.1004-2407.2017.02.011

Li, J., Liu, X., and Liu, S. (2012). Process study of microwave-assisted extraction of *Angelica* polysaccharide. *Anhui Agric. Sci.* 40 (34), 16573–16574. doi:10.3969/j.issn.0517-6611.2012.34.025

Li, M. M., Zhang, Y., Wu, J., and Wang, K. P. (2020). Polysaccharide from *angelica sinensis* suppresses inflammation and reverses anemia in complete freund's adjuvant-induced rats. *Curr. Med. Sci.* 40 (2), 265–274. doi:10.1007/s11596-020-2183-3

Li, S., Wang, X., Gui, X., and Dai, L. (2005). Experimental study on the effect of ASP on the function of dendritic cells in hepatitis B virus transgenic mice. *J. Pract. Diagn. Ther.* 19 (5), 313–314. doi:10.3969/j.issn.1674-3474.2005.05.001

Liao, F., Liu, Y., Liu, H. H., Hu, J., Zhao, S., and Yang, S. M. (2019). Effect of *Angelica sinensis* polysaccharide on the osteogenic differentiation of bone marrow mesenchymal stem cells of rats with high glucose levels. *West China J. Stomatology* 37 (2), 193–199. doi:10.7518/hxkq.2019.02.012

Liu, C., Li, J., Meng, F. Y., Liang, S. X., Deng, R., Li, C. K., et al. (2010). Polysaccharides from the root of *Angelica sinensis* promotes hematopoiesis and thrombopoiesis through the PI3K/AKT pathway. *BMC Complement. Altern. Med.* 10, 79. doi:10.1186/1472-6882-10-79

Liu, H., Zhang, T., Wang, M., Yu, Y., Su, L., Ji, D., et al. (2022a). Exploration of a new method for quality evaluation of *Angelica sinensis* based on *in vitro* blood tonic activity determination. *J. Nanjing Univ. Chin. Med.* 38 (12), 1110–1115. doi:10.14148/j.issn.1672-0482.2022.1110

Liu, J. Y., Zhang, Y., You, R. X., Zeng, F., Guo, D., and Wang, K. P. (2012). Polysaccharide isolated from *Angelica sinensis* inhibits hepcidin expression in rats with iron deficiency anemia. *J. Med. Food.* 15 (10), 923–929. doi:10.1089/jmf.2012.2231

Liu, S., Yang, Y., Qu, Y., Guo, X., Yang, X., Cui, X., et al. (2020a). Structural characterization of a novel polysaccharide from Panax notoginseng residue and its immunomodulatory activity on bone marrow dendritic cells. *Int. J. Biol. Macromol.* 161, 797–809. doi:10.1016/j.ijbiomac.2020.06.117

Liu, W., Li, W., Sui, Y., Li, X. Q., Liu, C., Jing, H., et al. (2019). Structure characterization and anti-leukemia activity of a novel polysaccharide from *Angelica sinensis*. *Int. J. Biol. Macromol.* 121, 161–172. doi:10.1016/j.ijbiomac.2018.09.213

Liu, W., Xiao, K., Ren, L., Sui, Y., Chen, J., Zhang, T., et al. (2020b). Leukemia cells apoptosis by a newly discovered heterogeneous polysaccharide from *Angelica sinensis*. *Carbohydr. Polym.* 241, 116279. doi:10.1016/j.carbpol.2020.116279

Liu, W. J., Li, Z. Z., Feng, C. X., Hu, S., Yang, X., Xiao, K., et al. (2022b). The structures of two polysaccharides from *Angelica sinensis* and their effects on hepatic insulin resistance through blocking RAGE. *Carbohydr. Polym.* 280, 119001. doi:10.1016/j.carbpol.2021.119001

Liu, Y., Wei, M., Song, C., Li, M., Yang, M., Cao, Z., et al. (2020c). ASP inhibits apoptosis through upregulation of VEGF. *Genom. Appl. Biol.* 39 (3), 1307–1313. doi:10.13417/j.gab.039.001307

Liu, Y., Yan, C., An, F., Wu, Z., Su, Y., Wang, P., et al. (2018). Effects of ASP on liver injury and immune damage in cadmium-contaminated rats. *J. PLA Pharmacol.* 34 (2), 101–104. doi:10.3969/j.issn.1008-9926.2018.02.001

Long, Q., and Maobao, X. (2008). Comparative study on the quality of processed products from different habitats of *Angelica sinensis*. *J. Gansu Coll. Traditional Chin. Med.* 25 (2), 37–39. doi:10.3969/j.issn.1003-8450.2008.02.016

Lu, Z., Wang, L., Xu, X., Zhang, L., He, J., Hua, J., et al. (2017a). Effects of *Angelica sinensis* and ASP on immune function impairment in SD rats caused by X-ray irradiation. *Chin. J. Trad. Chin. Med. Inf.* 24 (10), 44–48. doi:10.3969/j.issn.1005-5304.2017.10.011

Lu, Z., Xu, X., and Wang, L. (2017b). Protective effects of *Angelica sinensis* and ASP on radiation-induced liver and kidney injury in rats. *J. PLA Med.* 42 (9), 815. doi:10.11855/j.issn.0577-7402.2017.09.12

Luo, Y., An, F., Li, N., Liu, Y., Li, C., Zhang, Y., et al. (2017). Effects of ASP and small molecule extracts on TGF-β1-induced expression of α-SMA and CTGF by HELF. *Chin. Pharmacol. Clin. Pract.* 33 (3), 73–78. doi:10.13412/j.cnki.zyyl.2017.03.022

Ma, S., Li, X., Lv, Z., and Wu, J. (2022). Anti-inflammatory effects of ASP on rats with embolism during pregnancy and its effect on coagulation function. *J. Guangzhou Univ. Chin. Med.* 39 (3), 612–617. doi:10.13359/j.cnki.gzxbtcm.2022.03.025

Ma, Y., Wu, H., Jia, M., Zhang, Z., Wang, J., Yue, Z., et al. (2024). Construction of iron oxide nanoparticles modified with *Angelica sinensis* polysac charide for the treatment of iron deficiency anemia. *J. Nanoparticle Res.* 26 (11), 250–250. doi:10.1007/s11051-024-06169-y

Nai, J., Zhang, C., Shao, H., Li, B., Li, H., Gao, L., et al. (2021). Extraction, structure, pharmacological activities and drug carrier applications of *Angelica sinensis* polysaccharide. *Int. J. Biol. Macromol.* 183, 2337–2353. doi:10.1016/j.ijbiomac.2021.05.213

Niu, X., Zhang, J., Ling, C., Bai, M., Peng, Y., Sun, S., et al. (2018). Polysaccharide from *Angelica sinensis* protects H9c2 cells against oxidative injury and endoplasmic reticulum stress by activating the ATF6 pathway. *J. Int. Med. Res.* 46 (5), 1717–1733. doi:10.1177/0300060518758863

Ouyang, X., He, Y., Zhu, J., He, J., Ma, X., and Ding, Y. (2005). Comprehensive quality evaluation of Gansu *Angelicae Sinensis* Radix with different commodity specifications. *J. Traditional Chin. Med.* 33 (4), 12–14. doi:10.19664/j.cnki.1002-2392.2005.04.007

Pan, Q., Li, Y., Liu, D., and Zhao, H. (2015). Regulatory effects of ASP on the level of T lymphocyte subsets in peyer, spatches junction in mice with colitis. Jiangxi Trad. *Chin. Med*. 46 (10), 33–37. Available at: https://d.wanfangdata.com.cn/Periodical/jxzyy201510015.

Pan, S., Jiang, L., and Wu, S. (2018). Stimulating effects of polysaccharide from *Angelica sinensis* on the nonspecific immunity of white shrimps (*Litopenaeus* vannamei). *Fish. Shellfish Immunol.* 74, 170–174. doi:10.1016/j.fsi.2017.12.067

Pantopoulos, K., Porwal, S. K., Tartakoff, A., and Devireddy, L. (2012). Mechanisms of mammalian iron homeostasis. *Biochemistry* 51 (29), 5705–5724. doi:10.1021/bi300752r

Pu, X., Ma, X., Liu, L., Ren, J., Li, H., Li, X., et al. (2016). Structural characterization and antioxidant activity *in vitro* of polysaccharides from *Angelica* and *Astragalus*. *Carbohydr. Polym.* 137, 154–164. doi:10.1016/j.carbpol.2015.10.053

Qian, W., Cai, X., Qian, Q., Wang, D., and Zhang, L. (2020). *Angelica sinensis* polysaccharide suppresses epithelial-mesenchymal transition and pulmonary fibrosis via a DANCR/AUF-1/FOXO3 regulatory Axis. *Aging Dis.* 11 (1), 17–30. doi:10.14336/ad.2019.0512

Ren, F., Li, J., Wang, Y., Wang, Y., Feng, S., Yuan, Z., et al. (2018). The effects of *angelica sinensis* polysaccharide on tumor growth and iron metabolism by regulating hepcidin in tumor-bearing mice. *Cell Physiol. biochem.* 47 (3), 1084–1094. doi:10.1159/000490185

Shang, P., Qian, A. R., Yang, T. H., Jia, M., Mei, Q. B., Cho, C. H., et al. (2003). Experimental study of anti-tumor effects of polysaccharides from *Angelica sinensis*. *World J. Gastroenterol.* 9 (9), 1963–1967. doi:10.3748/wjg.v9.i9.1963

Song, P., Jianbang, Z., Zhang, J., and Ding, Y. (2008). Quality investigation of different cultivation methods and different specifications of *Angelica sinensis*. 21(9), 49–50. doi:10.3969/j.issn.10046852.2008.09.035

Song, X., Kong, J., Song, J., Pan, R., and Wang, L. (2021). *Angelica sinensis* polysaccharide alleviates myocardial fibrosis and oxidative stress in the heart of hypertensive rats. *Comput. Math. Methods Med.* 2021, 6710006. doi:10.1155/2021/6710006

Sui, Y., Liu, W., Tian, W., Li, X. Q., and Cao, W. (2019). A branched arabinoglucan from *Angelica sinensis* ameliorates diabetic renal damage in rats. *Phytother. Res.* 33 (3), 818–831. doi:10.1002/ptr.6275

Sun, Y., Cui, S. W., Tang, J., and Gu, X. (2010). Structural features of pectic polysaccharide from *Angelica sinensis* (Oliv.) Diels. *Carbohydr. Polym.* 80 (2), 544–550. doi:10.1016/j.carbpol.2009.12.030

Sun, Y., Gu, X., Tang, J., and Li, D. (2006). Isolation, purification and preliminary structural analysis of water-soluble polysaccharides from *Angelica sinensis*. *J. Food Biotechnol.* 25 (1), 1–4. doi:10.3321/j.issn:1673-1689.2006.01.001

Sun, Y., Ma, G., and Tang, J. (2009). Study on the protective effect of ASP on subchronic radiation injury in mice. *Chin. J. Food.* 9 (4), 33–37. doi:10.3969/j.issn.1009-7848.2009.04.006

Sun, Y., Tang, J., Gu, X., and Li, D. (2005). Water-soluble polysaccharides from *Angelica sinensis*: preparation, characterization and bioactivity. *Int. J. Biol. Macromol.* 36 (5), 283–289. doi:10.1016/j.ijbiomac.2005.07.005

Tang, Z., Long, Q., Liu, X., Liao, W., Zhang, X., and Wang, S. (2020). ASP inhibits the growth, migration and invasion of cervical cancer Hela cells by regulating the p38 pathway. *Chin. J. Immunol.* 36 (3), 332–337. doi:10.3969/j.issn.1000-484X.2020.03.014

Tian, S., Hao, C., Xu, G., Yang, J., and Sun, R. (2017). Optimization conditions for extracting polysaccharide from *Angelica sinensis* and its antioxidant activities. *J. Food Drug Anal.* 25 (4), 766–775. doi:10.1016/j.jfda.2016.08.012

Tian, Y., Shen, X., Hu, T., Liang, Z., Ding, Y., Dai, H., et al. (2024). Structural analysis and blood-enriching effects comparison based on biological potency of *Angelica sinensis* polysaccharides. *Front. Pharmacol.* 15, 1405342. doi:10.3389/fphar.2024.1405342

Wang, D., Zhang, H., Wang, G., and Jia, S. (2016a). Morphological and structural observation of the effect of ASP on alcoholic liver injury in mice. *J. Chang. Med. Coll.* 30 (4), 256–258. doi:10.3969/j.issn.1006-0588.2016.04.005

Wang, G., Jing, P., and Jia, S. (2017a). Effect of ASP on the level of intercellular adhesion molecule 1 on the surface of bone marrow hematopoietic stem cells and stromal cells in mice. *Chin. Tissue Eng. Res.* 21 (21), 3293–3298. doi:10.3969/j.issn.2095-4344.2017.21.003

Wang, J., Hu, Y., Zhang, F., Wang, D., Zhao, X., Zhang, J., et al. (2011a). Effect of eight sulfated polysaccharides on the ability of Newcastle disease virus to infect chicken embryo fibroblasts. *J. Nanjing Agric. Univ.* 34 (1), 118–122. doi:10.7685/j.issn.1000-2030.2011.01.022

Wang, K., Cao, P., Shui, W., Yang, Q., Tang, Z., and Zhang, Y. (2015a). *Angelica sinensis* polysaccharide regulates glucose and lipid metabolism disorder in prediabetic and streptozotocin-induced diabetic mice through the elevation of glycogen levels and reduction of inflammatory factors. *Food Funct.* 6 (3), 902–909. doi:10.1039/c4fo00859f

Wang, K., Cao, P., Wang, H., Tang, Z., Wang, N., Wang, J., et al. (2016b). Chronic administration of *Angelica sinensis* polysaccharide effectively improves fatty liver and glucose homeostasis in high-fat diet-fed mice. *Sci. Rep.* 6, 26229. doi:10.1038/srep26229

Wang, K., Chen, Z., Zhang, Y., Wang, J., Hu, M., and Dai, L. (2007a). Experimental study of *Angelica sinensis* polysacch aride-iron complex on rats with iron deficiency anemia. *Chin. J. New Drugs Clin. Rem.* 26 (6), 413–416. doi:10.3969/j.issn.1007-7669.2007.06.004

Wang, K., Song, Z., Wang, H., Li, Q., Cui, Z., and Zhang, Y. (2016c). *Angelica sinensis* polysaccharide attenuates concanavalin A-induced liver injury in mice. *Int. Immunopharmacol.* 31, 140–148. doi:10.1016/j.intimp.2015.12.021

Wang, K., Tang, Z., Zheng, Z., Cao, P., Shui, W., Li, Q., et al. (2016d). Protective effects of *Angelica sinensis* polysaccharide against hyperglycemia and liver injury in multiple low-dose streptozotocin-induced type 2 diabetic BALB/c mice. *Food Funct.* 7 (12), 4889–4897. doi:10.1039/c6fo01196a

Wang, K., Wang, J., Song, M., Wang, H., Xia, N., and Zhang, Y. (2020). *Angelica sinensis* polysaccharide attenuates CCl(4)-induced liver fibrosis via the IL-22/STAT3 pathway. *Int. J. Biol. Macromol.* 162, 273–283. doi:10.1016/j.ijbiomac.2020.06.166

Wang, K., Wu, J., Cheng, F., Huang, X., Zeng, F., and Zhang, Y. (2017b). Acidic polysaccharide from *Angelica sinensis* reverses anemia of chronic disease involving the suppression of inflammatory hepcidin and NF-κB activation. *Oxid. Med. Cell Longev.* 2017, 7601592. doi:10.1155/2017/7601592

Wang, K., Wu, J., Xu, J., Gu, S., Li, Q., Cao, P., et al. (2018). Correction of anemia in chronic kidney disease with *Angelica sinensis* polysaccharide via restoring EPO production and improving iron availability. *Front. Pharmacol.* 9, 803. doi:10.3389/fphar.2018.00803

Wang, K. P., Zeng, F., Liu, J. Y., Guo, D., and Zhang, Y. (2011b). Inhibitory effect of polysaccharides isolated from *Angelica sinensis* on hepcidin expression. *J. Ethnopharmacol.* 134 (3), 944–948. doi:10.1016/j.jep.2011.02.015

Wang, L., Jiang, R., Song, S. D., Hua, Z. S., Wang, J. W., and Wang, Y. P. (2015b). *Angelica sinensis* polysaccharide induces erythroid differentiation of human chronic myelogenous leukemia k562 cells. *Asian pac. J. Cancer Prev.* 16 (9), 3715–3721. doi:10.7314/apjcp.2015.16.9.3715

Wang, L., Xu, X., and Lu, Z. (2017c). Study on the protection of ASP against liver damage by X-ray radiation in rats. *Chin. Herb. Med.* 48 (20), 4284.

Wang, P. P., Zhang, Y., Dai, L. Q., and Wang, K. P. (2007b). Effect of *Angelica sinensis* polysaccharide-iron complex on iron deficiency anemia in rats. *Chin. J. Integr. Med.* 13 (4), 297–300. doi:10.1007/s11655-007-0297-0

Wang, S., Shi, S., Cui, J., Ding, L., Wang, Z., and Hu, Z. (2007c). Isolation and purification of a heteropolysaccharide from *Angelica sinensis*. *Chin. J. Pharm. Sci.* 42 (16), 1255–1258. doi:10.3321/j.issn:1001-2494.2007.16.016

Wang, Y., Li, X., Zhao, P., Qu, Z., Bai, D., Gao, X., et al. (2019). Physicochemical characterizations of polysaccharides from *Angelica Sinensis* Radix under different drying methods for various applications. *Int. J. Biol. Macromol.* 121, 381–389. doi:10.1016/j.ijbiomac.2018.10.035

Wang, Y., Wang, X., Zhang, X., Lin, X., Wang, X., and An, Y. (2010). Effects of ASP on lung function and lung coefficient in rats with pulmonary fibrosis. Gansu Trad. *Chin. Med.* 23 (11), 28–31. doi:10.3969/j.issn.1004-6852.2010.11.013

Wu, G., Yang, X., Yi, D., Chen, H., Yang, Y., and Yang, Z. (2018a). Quality evaluation of *Angelica sinensis* and its different medicinal parts based on grey correlation degree. *Chin. J. Traditional Chin. Med. Inf.* 25(5), 77–81.

Wu, G., Yang, X., Yi, D., Chen, H., Yang, Y., and Yang, Z. (2018b). Fingerprint and component analysis of different medicinal parts of *Angelica sinensis*. *Chin. Tradit. Plant Med.* 40(04), 890–894. doi:10.3969/j.issn.1001-1528.2018.04.025

Wu, J., Meng, J., Zhang, Y., Wu, H., Liu, M., Wei, N., et al. (2017). Effects of ASP iron complex on blood routine and immune and antioxidant functions in rats with iron deficiency anemia model. *J. Gansu Univ. Chin. Med.* 34 (1). doi:10.16841/j.issn1003-8450.2017.01.03

Wu, J., Shao, J., Wu, J., Li, H., Li, W., Zhang, Y., et al. (2015). Optimization of the extraction process of ASP based on orthogonal design. *J. Gansu Coll. Trad. Chin. Med.* 32 (5), 22–25. Available at: https://kns.cnki.net/kcms2/article/abstract?v=IILC1c-FiAExHdArDj3r2ZSOAi4a9IqfZMl2Sej1sQoNhYZYCGPkYUIEjMHjMJqy9EdjLVdxSX6660ciYKvcgytyhNYhE3DwUxCtn7h20aG4P2atlaaCwB1mfxrOfLLA1ZWvKS2_-fsgljSWlsSeVw==&uniplatform=NZKPT&language=CHS.

Wu, S., Li, J., Chen, S., and Zhu, X. (2012). Experimental study on the antitumor effects of sulfated ASP. *Shi-Zhen Guomao.* 23 (2), 319–320. doi:10.3969/j.issn.1008-0805.2012.02.029

Wu, S., Li, J., Chen, S., and Zhu, X. (2013). Preparation and antitumor activity of sulfated ASP. *Chin. J. Hosp. Pharm.* 33 (22), 1832–1835. doi:10.13286/j.cnki.chinhosppharmacyj.2013.22.003

Xu, C., Ni, S., Zhuang, C., Li, C., Zhao, G., Jiang, S., et al. (2021). Polysaccharide from *Angelica sinensis* attenuates SNP-induced apoptosis in osteoarthritis chondrocytes by inducing autophagy via the ERK1/2 pathway. *Arthritis Res. Ther.* 23 (1), 47. doi:10.1186/s13075-020-02409-3

Xu, C., Shen, L., and Yuan, W. (2022). ASP inhibits oxidative stress injury and inflammatory response in osteoarthritic chondrocytes via Wnt/β-catenin signaling pathway. *Shaanxi TCM* 43 (6), 700–703. doi:10.3969/j.issn.1000-7369.2022.06.005

Xu, X., Lu, Z., Wang, L., Zhang, L., An, F., He, J., et al. (2017). Study on the damage of bone marrow and spleen in rats by ASP protection against X-rays. *Chin. J. Pharmacol.* 33 (11), 1553–1558. doi:10.3969/j.issn.1001-1978.2017.11.015

Xu, R., Xu, J., Li, Y. C., Dai, Y. T., Zhang, S. P., Wang, G., et al. (2020). Integrated chemical and transcriptomic analyses unveils synthetic characteristics of different medicinal root parts of *Angelica sinensis*. *Chin. Herb. Med.* 12 (1), 9–28. doi:10.1016/j.chmed.2019.07.003

Yang, J., Shao, X., Jiang, J., Sun, Y., Wang, L., and Sun, L. (2018). *Angelica sinensis* polysaccharide inhibits proliferation, migration, and invasion by downregulating microRNA-675 in human neuroblastoma cell line SH-SY5Y. *Cell Biol. Int.* 42 (7), 867–876. doi:10.1002/cbin.10954

Yang, T., Jia, M., Meng, J., Wu, H., and Mei, Q. (2006). Immunomodulatory activity of polysaccharide isolated from *Angelica sinensis*. *Int. J. Biol. Macromol.* 39 (4-5), 179–184. doi:10.1016/j.ijbiomac.2006.02.013

Yang, T., Jia, M., Zhou, S., Pan, F., and Mei, Q. (2012). Antivirus and immune enhancement activities of sulfated polysaccharide from *Angelica sinensis*. *Int. J. Biol. Macromol.* 50 (3), 768–772. doi:10.1016/j.ijbiomac.2011.11.027

Yang, X., Zhao, Y., Li, G., Wang, Z., and Lv, Y. (2008a). Chemical composition and immuno-stimulating properties of polysaccharide biological response modifier isolated from Radix *Angelica sinensis*. *Food Chem.* 106 (1), 269–276. doi:10.1016/j.foodchem.2007.05.085

Yang, X., Zhao, Y., and Lv, Y. (2008b). *In vivo* macrophage activation and physicochemical property of the different polysaccharide fractions purified from *Angelica sinensis*. *Carbohydr. Polym.* 71 (3), 372–379. doi:10.1016/j.carbpol.2007.06.002

Yu, F., Li, H., Meng, Y., and Yang, D. (2013). Extraction optimization of *Angelica sinensis* polysaccharides and its antioxidant activity *in vivo*. *Carbohydr. Polym.* 94 (1), 114–119. doi:10.1016/j.carbpol.2013.01.050

Zhang, J., Yin, D. D., and Luo, G. (1998). Extraction of ASP and preparation of punch. *Chin. J. Hosp. Pharm.* 18 (5), 220–221. doi:10.3321/j.issn:1001-5213.1998.05.017

Zhang, L., and Huang, R. (1999). Purification, identification and structural study of water-soluble polysaccharide fractions As-IIIa and As-IIIb from *Angelica sinensis*. *J. Laser Biol.* 8 (2), 46–49. doi:10.3969/j.issn.1007-7146.1999.02.010

Zhang, L., Lu, Z., Xu, X., Wang, L., Yong, W., Li, J., et al. (2017). Study on the protective effect of ASP on oxidative stress in the kidney of radiation rats and Nrf2-related mechanism. *Chin. Pharmacol. Clin. Pract.* 33 (5), 63–66. doi:10.13412/j.cnki.zyyl.2017.05.017

Zhang, L., Lu, Z., Xu, X., Wei, K., Li, Y., and Liu, Y. (2020). Study on the protective effect of ASP on radiation-induced intestinal barrier damage in SD rats. *Shizhen Guomao Guomao* 31 (12), 2847–2850. doi:10.3969/j.issn.1008-0805.2020.12.008

Zhang, M., and Wang, X. (2018). Advances in the pathogenesis and diagnosis of inflammatory anemia associated with iron homeostasis dysregulation. *Diagn. Theor. Pract.* 17 (5), 601. doi:10.16150/j.1671-2870.2018.05.023

Zhang, P., Wang, Q., Chen, H., Li, X., Dou, J., Chen, J., et al. (2009). *In vitro* inhibition of apotosis in HCMV-infected megakaryocytes by ASP. *Chin. J. Exp. Hematol.* 17 (1), 193–197. Available at: https://d.wanfangdata.com.cn/Periodical/zgsyxyxzz200901042.

Zhang, Q., Yu, H., Wang, Q., Sun, X., Xing, K., and Guo, Y. (2016a). Extraction, isolation, and purification of Angelica polysaccharide. *Hebei Fish.* (3), 1–3. doi:10.3969/j.issn.1004-6755.2016.03.001

Zhang, S. B., and Lv, J. X. (2013). Comparison on four extraction methods of polysaccharide from *Angelica sinensis* Tianjin Agric. *Sci. Res.* 19 (10), 33–36. doi:10.3969/j.issn.1006-6500.2013.10.009

Zhang, X., Wang, Q., Li, C., Zhang, Y., Li, K., Hu, S., et al. (2012a). New process of enzymatic extraction of *Angelica* polysaccharides. *J. Trad. Chin. Med.* 40 (3), 96–100. doi:10.3969/j.issn.1002-2392.2012.03.033

Zhang, Y., Cheng, Y., Wang, N., Zhang, Q., and Wang, K. (2014). The action of JAK, SMAD and ERK signal pathways on hepcidin suppression by polysaccharides from

*Angelica sinensis* in rats with iron deficiency anemia. *Food Funct.* 5 (7), 1381–1388. doi:10.1039/c4fo00006d

Zhang, Y., He, Z., Liu, X., Chen, Z., Sun, J., Wu, Z., et al. (2019). Oral administration of *Angelica sinensis* polysaccharide protects against pancreatic islets failure in type 2 diabetic mice: pancreatic β-cell apoptosis inhibition. *J. Funct. Foods.* 54, 361–370. doi:10.1016/j.jff.2019.01.037

Zhang, Y., Li, M. M., Zeng, F., Yao, C., and Wang, K. P. (2012b). Study to establish the role of JAK2 and SMAD1/5/8 pathways in the inhibition of hepcidin by polysaccharides from *Angelica sinensis*. *J. Ethnopharmacol.* 144 (2), 433–440. doi:10.1016/j.jep.2012.09.040

Zhang, Y., Zhou, T., Wang, H., Cui, Z., Cheng, F., and Wang, K. P. (2016b). Structural characterization and *in vitro* antitumor activity of an acidic polysaccharide from *Angelica sinensis* (Oliv.) Diels. *Carbohydr. Polym.* 147, 401–408. doi:10.1016/j.carbpol.2016.04.002

Zhang, Z. (2006). Application of microwave-assisted extraction technology in polysaccharide research. *Chin. Herb. Med.* (4), 630–632. doi:10.7501/j.issn.0253-2670.2006.4.260

Zhao, Y., Shi, Y., Yang, H., and Mao, L. (2016). Extraction of *Angelica sinensis* polysaccharides using ultrasound-assisted way and its bioactivity. *Int. J. Biol. Macromol.* 88, 44–50. doi:10.1016/j.ijbiomac.2016.01.113

Zhou, S., Zhang, B., Liu, X., Teng, Z., Huan, M., Yang, T., et al. (2009). A new natural angelica polysaccharide based colon-specific drug delivery system. *J. Pharm. Sci.* 98 (2), 4756–4768. doi:10.1002/jps.21790

Zhou, T. (2018). *Isolation analysis, structure identification and biological activity of ASP*. Wuhan: Huazhong University of Science and Technology.

Zhou, W. J., Wang, S., Hu, Z., Zhou, Z. Y., and Song, C. J. (2015). *Angelica sinensis* polysaccharides promotes apoptosis in human breast cancer cells via CREB-regulated caspase-3 activation. *Biochem. Biophys. Res. Commun.* 467 (3), 562–569. doi:10.1016/j.bbrc.2015.09.145

Zhou, X., Wang, Q., Zhu, X., Pan, R., Pan, S., Zhu, F., et al. (2018). Effects of ASP on TLR4/MyD88/NF-κB pathway inhibition in DPN rats. *Chin. Clin. Pharmacol. Ther.* 23 (12), 1340–1347. doi:10.12092/j.issn.1009-2501.2018.12.004

Zhou, Y., Guo, X., Chen, W., and Liu, J. (2019). *Angelica* polysaccharide mitigates lipopolysaccharide-evoked inflammatory injury by regulating microRNA-10a in neuronal cell line HT22. *Artif. Cells Nanomed. Biotechnol.* 47 (1), 3194–3201. doi:10.1080/21691401.2019.1614595

Zhuang, C., Xu, N. W., Gao, G. M., Ni, S., Miao, K. S., Li, C. K., et al. (2016). Polysaccharide from *Angelica sinensis* protects chondrocytes from H2O2-induced apoptosis through its antioxidant effects *in vitro*. *Int. J. Biol. Macromol.* 87, 322–328. doi:10.1016/j.ijbiomac.2016.02.031

Zou, Y. F., Fu, L., Cai, W., Jiang, Q. X., Peng, X., Li, L. X., et al. (2022). The comparison of preliminary structure and intestinal anti-inflammatory and anti-oxidative activities of polysaccharides from different root parts of *Angelica sinensis (Oliv.) Diels*. *J. Ethnopharmacol.* 295, 115446, doi:10.1016/j.jep.2022.115446

frontiers | Frontiers in Pharmacology

TYPE Review
PUBLISHED 31 January 2025
DOI 10.3389/fphar.2025.1449639



OPEN ACCESS

EDITED BY
Xiliang Du,
Jilin University, China

REVIEWED BY
Zili Xie,
Icahn School of Medicine at Mount Sinai, United States
Binjie Xu,
Chengdu University of Traditional Chinese Medicine, China

*CORRESPONDENCE
Le Xie,
1289398706@qq.com
Dahua Wu,
893049352@qq.com

RECEIVED 15 June 2024
ACCEPTED 15 January 2025
PUBLISHED 31 January 2025

CITATION
Lei C, Chen J, Chen Z, Ma C, Chen X, Sun X, Tang X, Deng J, Wang S, Jiang J, Wu D and Xie L (2025) Spatial metabolomics in mental disorders and traditional Chinese medicine: a review.
*Front. Pharmacol.* 16:1449639.
doi: 10.3389/fphar.2025.1449639



# Spatial metabolomics in mental disorders and traditional Chinese medicine: a review

Chaofang Lei[1], Jiaxu Chen[2], Zhigang Chen[3], Chongyang Ma[4], Xudong Chen[5], Xiongxing Sun[1], Xukun Tang[1], Jun Deng[1], Shiliang Wang[1], Junlin Jiang[1], Dahua Wu[1]* and Le Xie[1]*

[1]Department of Neurology, Hunan Provincial Hospital of Integrated Traditional Chinese and Western Medicine (The Affiliated Hospital of Hunan Academy of Traditional Chinese Medicine), Changsha, China, [2]School of Traditional Chinese Medicine, Beijing University of Chinese Medicine, Beijing, China, [3]Department of Neurology, Dongfang Hospital, Beijing University of Chinese Medicine, Beijing, China, [4]School of Traditional Chinese Medicine, Capital Medical University, Beijing, China, [5]Department of Psychiatry, The Second Xiangya Hospital of Central South University, Changsha, China

Spatial metabolomics is an emerging technology that integrates mass spectrometry imaging (MSI) with metabolomics, offering a novel visual perspective for traditional metabolomics analysis. This technology enables in-depth analysis in three dimensions: qualitative, quantitative, and localization of metabolites. Spatial metabolomics precisely reflects the characteristics of metabolic network changes in metabolites within entire tissues or specific micro-regions. It provides a detailed understanding of the pharmacodynamic material basis and mechanisms of action. These capabilities suggest that spatial metabolomics can offer significant technical support for studying the complex pathophysiology of mental disorders. Although the mechanisms underlying mental disorders have been reviewed multiple times, this paper provides a comprehensive comparison between traditional metabolomics and spatial metabolomics. It also summarizes the latest progress and challenges of applying spatial metabolomics to the study of mental disorders and traditional Chinese medicine.

KEYWORDS

**mental disorders, traditional Chinese medicine, spatial metabolomics, mass spectrometry imaging, DESI-MSI, MALDI-MSI, SIMS**

## 1 Introduction

Mental disorders are common and burdensome. Among people with severe mental illness, deaths from unnatural causes have increased significantly, occurring 13 times more frequently compared to the general population, with suicide being the leading cause (20 times higher) (Revier et al., 2015). Antidepressants and antipsychotics remain the primary strategies for treating psychiatric symptoms. However, the long-term efficacy of drug treatment has been questioned. For many individuals with mental illness, antipsychotics do not result in clinically meaningful long-term improvements and often cause significant side effects (Malhi and Mann, 2018), such as weight gain, elevated blood sugar levels, elevated blood lipids, and loss of sexual interest. These side effects frequently lead to withdrawal and discomfort (De Hert et al., 2011; Vancampfort et al., 2015). Over the past few decades, the use of traditional Chinese medicine (TCM) to treat various mental

disorders, including depression, has grown significantly. Studies suggest that TCM is a safer alternative to drug therapy, with a lower risk of side effects (Yeung K. S. et al., 2018).

Traditional Chinese medicine operates under the guidance of traditional Chinese medicine theory. It exhibits characteristics such as multi-metabolite, multi-target, multi-approach, and holistic concept (Ma et al., 2023; Wang and Zhang, 2017; Zheng et al., 2024; Song et al., 2023). While traditional Chinese medicine demonstrates remarkable clinical efficacy, its modern development faces constraints due to unclear efficacy substances and mechanisms of action. In recent years, there has been rapid development in metabolomics technology (Misra, 2018; Bingol and Brüschweiler, 2017). Its research strategy, which is based on detecting the dynamic changes of global metabolites, aligns with traditional Chinese medicine theory (Zhang et al., 2010; Wei et al., 2024). This alignment presents new opportunities to address the developmental challenges faced by traditional Chinese medicine. Metabolomics technology has been extensively employed in researching the material basis and pharmacodynamic mechanisms of traditional Chinese medicine, yielding promising results (Wang et al., 2017).

However, the metabolism and distribution of traditional Chinese medicine metabolites in organisms often exhibit precise spatial positioning (Bai et al., 2022). The efficacy of the medication is closely linked to the spatial distribution of biological tissue or micro-regions. Nevertheless, traditional metabolomics methods have limitations in sample pre-processing, resulting in the absence of spatial distribution information of metabolites in tissues (Liu G. X. et al., 2023). This absence poses challenges in fully and objectively interpreting the sites of action and pharmacodynamic mechanisms of traditional Chinese medicine. Spatial metabolomics enables the correlation of metabolites and their biological functions with the anatomical characteristics of biological tissues (Sun et al., 2019; Nakabayashi et al., 2021). This approach allows for a more accurate and scientific analysis of the pharmacodynamic metabolites of traditional Chinese medicines and the regulatory mechanisms of diseases within organisms.

Indeed, these methods also facilitate the comprehensive characterization of metabolic functions at physiological and pathological time scales with high spatial resolution. Mass spectrometry imaging (MSI) is a powerful method to perform *in situ* analysis of the molecular composition of biological tissues while retaining spatial information (Parrot et al., 2018). Furthermore, spatial metabolic characterization holds significant relevance to our comprehension of normal physiological processes and the neuropathological manifestations of neurological disorders (Wang et al., 2022).

Hence, spatial metabolomics technology was utilized to establish the relationship of "molecular structure-spatial distribution-content change-metabolic pathway," offering novel insights into the search for medicinal metabolites, therapeutic targets, and mechanisms of action of traditional Chinese medicine (Zhao et al., 2023a).

This paper provides a comprehensive overview of the research progress in spatial metabolomics technology concerning the quality control, metabolic distribution, pharmacodynamic mechanisms, and toxicity mechanisms of Chinese medicine. Additionally, it critically examines the limitations and future development directions of spatial metabolomics in the study of Chinese medicine for treating mental diseases. These insights aim to furnish a theoretical basis for advancing the modernization and internationalization of Chinese medicine in the treatment of mental diseases.

## 2 Traditional metabolomics and spatial metabolomics

Metabolomics involves the systematic study of small and medium molecules in biological fluids. The term "metabolomics" was first coined by Dr. Nicholson of Imperial College London in 1999 (Yu et al., 2017). While metabolomic analysis shares similarities with other high-throughput methods like genome sequencing, its rapid response to both exogenous and endogenous stimuli renders it particularly sensitive to changes in health status (Dona et al., 2016). Spatial metabolomics has been developed based on mass spectrometry imaging technology, characterized by its lack of labeling, matrix, and short analysis cycle (McDonnell and Heeren, 2007; Zang et al., 2021). Serving as a novel molecular imaging technology, spatial metabolomics can directly provide spatial distribution information of numerous known or unknown endogenous metabolites and exogenous drugs from biological tissues (Wang Z. et al., 2021). By employing mass spectrometry imaging technology, spatial metabolomics enables the analysis of metabolites in different tissues and organs in three dimensions, including qualitative, quantitative, and localization aspects. This breakthrough overcomes the limitations of traditional metabolomics research, which often loses spatial information. The comparative analysis of traditional and spatial metabolomics platforms and their respective application conditions are summarized in Table 1.

### 2.1 Desorption electrospray ionization mass spectrometry (DESI-MSI)

DESI-MS, introduced in 2004, is an atmospheric pressure environmental ionization method that directly ionizes solid-phase samples (Takáts et al., 2004). DESI-MSI employs the fundamental principle of electrospray ionization, wherein solvent droplets are rasterized and desorbed directly onto the sample surface (Parrot et al., 2018; Eberlin et al., 2011). DESI operates at room temperature, eliminating the need for freeze-drying prior to analysis. This method of tissue imaging minimizes sample damage through environmental ionization mass spectrometry, enabling repeated measurements of samples from diverse biological sources (Soudah et al., 2023). Ambient MSI offers a user-friendly interface and facilitates the rapid analysis of larger samples, thereby facilitating real-time diagnostic capabilities (Luo et al., 2013; Keller et al., 2018).

However, enhancing the sensitivity of DESI-MSI presents substantial challenges (Wang et al., 2017). Recent studies have demonstrated that the sensitivity and specificity of DESI-MSI nanoparticles can be enhanced by incorporating silver ions into the solvents (Lillja and Lanekoff, 2022). Researchers have developed a compact post-photoionization module integrated with DESI, enabling the detection of enhanced signal strength for non-polar compounds. This advancement significantly enhances the sensitivity

TABLE 1 Traditional metabolomics and spatial metabolomics.

| Metabolomics | Methods | Resolution | Sample preparation | Advantage | Disadvantage | Application |
|---|---|---|---|---|---|---|
| Traditional metabolomics | Nuclear magnetic resonance (NMR) | Less (Mandal et al., 2024) | Ease (Zinniel et al., 2012; Asampille et al., 2020) | small samples; no sample pretreatment; and nondestructive and noninvasive detection; high reproducibility; relatively fast measurement; sample preparation automation; the sample can be recovered and stored for a long time; quantitative analysis; (Yu et al., 2017; Emwas et al., 2019) | low sensitivity; low spectral resolution; peak overlaps; the number of detectable metabolites is usually less than 200 metabolites; (Emwas et al., 2019; Serkova and Brown, 2012) | nonselective analysis; real-time metabolite profiling of living cells; real-time metabolic flux analysis; (Emwas et al., 2019) |
| | Gas chromatography-mass spectrometry (GC-MS) | Depends on mass analyzer (Mandal et al., 2024) | Derivatization (Zinniel et al., 2012; Asampille et al., 2020) | non-selective nature; has the advantage over LC/MS/MS of inherently better chromatographic resolution; reproducible; cheap price; mature technology; (Krone et al., 2010; Zeki Ö et al., 2020) | cannot be used to analyse living samples; derivatization; time consuming; not all molecules can be efficiently detected; (Emwas et al., 2019; Zeki Ö et al., 2020) | appropriate to analyze small molecules, thermally stable, volatile, and easily gasified compounds; (Yu et al., 2017) |
| | Liquid chromatography-mass spectrometry (LC-MS) | Less (Mandal et al., 2024) | Isolation, purification, Preconcentration (Pérez-Fernández et al., 2017) | rapid specific analysis of a limited number of compounds at high sensitivity and it is relatively easily automated; Hydrolysis of conjugates and chemical derivatization are not required; short time consuming and partially automated; (Krone et al., 2010; Dai and Shen, 2022) | cannot be used to analyse living samples; more cost; technology is not mature enough; (Emwas et al., 2019; Dai and Shen, 2022) | analyze the compounds more polar, higher relative molecular mass and lower thermal stability; (Yu et al., 2017) |
| Spatial metabolomics | DESI-MSI | 10–500 um (Zheng et al., 2023; Zhao et al., 2024) | Minimum, frozen tissue (Wang et al., 2017; He et al., 2022a) | the sample preparation process is simple; high efficiency; high throughput; high accuracy; the operating condition of atmospheric pressure; non-destructive; high specificity; quick results; (Zheng et al., 2023; He et al., 2022a; Mi et al., 2020; Tomalty et al., 2023; Calligaris et al., 2015; Chen et al., 2023a) | low spatial resolution; low sensitivity; not suitable for large tissue samples; (Zheng et al., 2023) | small molecules (metabolites, lipids); <20 kDa proteins; (Zheng et al., 2023; Yang et al., 2022) |
| | MALDI-MSI | 1–200um (Zheng et al., 2023; Zhao et al., 2024) | Matrix deposition, freeze fracture and drying, (Wang et al., 2017; Parrot et al., 2018) | high spatial resolution; simplicity of the tissue preparation; high sensitivity; label-free; reliable results; (Zheng et al., 2023; He et al., 2022a; Chen et al., 2023a; Susniak et al., 2020; Mamun et al., 2023; Veerasammy et al., 2020) | the existence of matrix effects; the operating condition of high vacuum; not suitable for large tissue samples; poor sensitivity for some classes of molecules or limited specificity; (Zheng et al., 2023; Zhou et al., 2021) | biological micromolecules (proteins, peptides, lipids); small molecules; glycans; (Zheng et al., 2023; Zhou et al., 2021) |

(Continued on following page)

TABLE 1 (*Continued*) Traditional metabolomics and spatial metabolomics.

| Metabolomics | Methods | Resolution | Sample preparation | Advantage | Disadvantage | Application |
|---|---|---|---|---|---|---|
| | AFADESI-MSI | 40–100 um (Zheng et al., 2023; Zhao et al., 2024) | Freeze fracture and drying (He et al., 2022a; Zhou et al., 2024a; Shen et al., 2023; Luo et al., 2018) | wide range in slice size; the operating condition of atmospheric pressure; minimum sample preparations; improve sensitivity and spatial resolution from DESI; large coverage; wide field; (Zheng et al., 2023; He et al., 2022a) | not suitable for macromolecules (proteins, peptides); low reproducibility of results due to complex parameters; (Zheng et al., 2023; He et al., 2022a) | small molecule (lipids, small molecules below 500da); (Zheng et al., 2023; He et al., 2022a) |
| | SIMS-MSI | 0.05–0.5 um (Zheng et al., 2023; Zhao et al., 2024) | Freeze fracture and drying (Wang et al., 2017) | high spatial resolution; high efficiency; subcellular imaging; high sensitivity; high selectivity; high dynamic range; (Zheng et al., 2023; Chen et al., 2023a; Shen et al., 2024) | the ion beam may cause the fragmentaion and the damage of the surface of the sample; complexity of datasets; (Zheng et al., 2023; Shen et al., 2024) | wide range; self-assembly monolayer characterization; solid-electrolyte interphase analysis; single cell chemical imaging; environmental related particle investigation; (Zheng et al., 2023; Huang et al., 2017) |

of DESI-MSI to non-polar compounds (Liu C. et al., 2019). Furthermore, there are emerging indications that the spatial resolution of DESI will pose a substantial impediment in numerous other applications where it could be potentially beneficial (Qi et al., 2021). Consequently, scientists are currently engaged in a concerted effort to significantly enhance the spatial resolution of DESI. Subsequent research has demonstrated that nano DESI-MSI possesses the potential to attain even finer spatial resolution, potentially reaching a resolution of 10 microns (Yin et al., 2018; Yin et al., 2019; Yang et al., 2023).

## 2.2 Matrix-assisted laser desorption/ionization mass spectrometry imaging (MALDI-MSI)

The concept of MALDI-MSI was initially introduced in the early 2000s (Morisasa et al., 2019). MALDI is a soft ionization technique that involves the co-crystallization of a sample molecule or analyte with a matrix to form a sample matrix crystal. The matrix functions as a proton donor or acceptor, ionizing the analyte (Yalcin and de la Monte, 2015). MALDI-MSI operates by directing a laser beam at the surface of a specimen, typically a frozen section of tissue. This laser action induces the desorption of ions from the tissue, which are subsequently analyzed through a mass spectrometer (Basu and Agar, 2021; Kuik et al., 2024). Despite ongoing technological advancements, the low detection sensitivity of certain compounds poses a significant challenge that requires effective solutions. Research has indicated that poor sensitivity is often associated with reduced ionization efficiency, low analyte and matrix ion abundance, or endogenous interference. Histochemical derivatization has emerged as a crucial strategy to address these challenges, preserve tissue integrity, and mitigate potential dislocations (Merdas et al., 2021).

## 2.3 Airflow-assisted desorption and electrospray ionization mass spectrometry imaging (AFADESI-MSI)

AFADESI-MSI employs DESI technology to directly ionize the sample using an electrospray plume. Subsequently, a gas stream propels the ions over extended distances, enabling mass spectrometry imaging (Luo et al., 2013). In addition to inheriting the advantages of DESI-MSI, AFADESI-MSI can also attain exceptionally high metabolite coverage. It is an environmental molecular imaging technology characterized by its high sensitivity, extensive coverage, and exceptional chemical specificity (He M. J. et al., 2022). A significant advantage of this approach is its direct predictive applicability to a substantial number of candidate metabolites and metabolic enzymes, eliminating the necessity to define a specific target of interest beforehand (Sun et al., 2019). Although this novel technique yields drug signal strength, it cannot objectively reflect the absolute drug content in various tissues due to sample heterogeneity, ion inhibition, analyte extraction efficiency, and ionization efficiency (Zhang et al., 2020).

## 2.4 Secondary ion mass spectrometry (SIMS-MSI)

The SIMS instrument bombards the sample surface with a finely focused primary ion beam (an analysis gun) to generate characteristic secondary ions from the sample surface. These secondary ions are subsequently detected using a mass analyzer. By rasterizing the primary ion beam on the surface of a solid sample, mass-resolved secondary ion images can be obtained, thereby providing chemical mapping of each component of the surface (Huang et al., 2017). The primary advantage of SIMS lies in its capability to measure the spatial localization of molecules with

TABLE 2 Spatial metabolomics and quality control.

| Drug | Medicinal parts | Analytical technique | Characterization metabolite | References |
|---|---|---|---|---|
| Panax quinquefolius L. [Araliaceae] | Root | UPLC-Q-TOF/MS, DESI-MSI | Ginsenoside Rg1, malonyl-ginsenoside Rc, ginsenoside Ro, malonyl-ginsenoside Rd | Luo et al. (2024) |
| Salvia miltiorrhiza Bunge [Lamiaceae] | Root | DESI-MSI | Phenolic acids, flavonoids, tanshinones, carbohydrates, lipids | Tong et al. (2022) |
| Phyllanthus emblica L. [Phyllanthaceae]. Fruit (PEF) | PEF surface white frost | UPLC-Q-TOF-MS/MS, DESI-MSI | Organic acids, fatty acids, tannins | Lin et al. (2024) |
| Glycyrrhiza uralensis Fisch. ex DC. [Fabaceae] | Root | high-resolution liquid chromatography/mass spectrometry, DESI-MSI | Flavonoids, triterpenoids | Zhao et al. (2023b) |
| Ligustrum lucidum W.T.Aiton [Oleaceae] | Fruit | UHPLC/Q-Orbitrap-MS, MALDI-MSI | 10-hydroxyoleoside dimethylester, 8-demethyl-7-ketoliganin, elenolic acid, salidroside, neonuezhenide/isomer, verbascoside/isomer, luteoline, nuzhenal A | Li et al. (2020a) |
| Panax notoginseng (Burkill) F.H.Chen [Araliaceae] | Fresh root | UPLC-QTOF-MS, MALDI-MS | Ginsenosides | Fan et al. (2022) |
| Scutellaria baicalensis Georgi [Lamiaceae] | Root, stem, leaf | MALDI-MSI | Flavonoids, glycosides | Zhou et al. (2024b) |
| Ganoderma [Ganodermataceae] | Fruiting body | LC-MS, DESI-MSI | Triterpenoids, fatty acids | Xia et al. (2024) |
| Salvia miltiorrhiza Bunge [Lamiaceae] | Root, stem, leaf | MALDI-MSI | Amino acids, phenolic acids, fatty acids, oligosaccharides, cholines, polyamines, tanshinones, phospholipids | Sun et al. (2020) |
| Tripterygium wilfordii Hook.f. [Celastraceae] | Root | MALDI-MSI | Triterpenoids, sesquiterpene alkaloids | Lange et al. (2017) |
| Paeonia lactiflora Pall. [Paeoniaceae] | Root | AP-SMALDI MSI | Gallotannins, monoterpene glucosides | Li et al. (2016) |
| Putterlickia verrucosa (E.Mey. ex Harv. and Sond.) Sim [Celastraceae] | Rhizome | AP-SMALDI MSI | Maytansinoids | Eckelmann et al. (2016) |
| Glycyrrhiza glabra L. [Fabaceae] | Rhizome | AP-MALDI-MSI | Flavonoids, flavonoid glycosides, saponins | Li et al. (2014) |
| Ginkgo biloba L. [Ginkgoaceae] | Leaf | AP-MALDI-MSI | Flavonoid glycosides, biflavonoids | Beck and Stengel (2016) |
| Panax ginseng C.A.Mey. [Araliaceae] | Root | MALDI-MSI, DESI-MSI | Ginsenosides in Panax ginseng with different age, ginsenosides localization in Panax ginseng root | Bai et al. (2016), Lee et al. (2017), Taira et al. (2010), Yang et al. (2021) |
| Panax ginseng C.A.Mey. [Araliaceae], Panax quinquefolius L. [Araliaceae], Panax notoginseng (Burkill) F.H.Chen [Araliaceae] | Root | MALDI-MSI | Saponins | Wang et al. (2016) |
| Aconitum carmichaelii Debeaux [Ranunculaceae] | Lateral roots | MALDI-MSI | Aconitum alkaloids | Wang et al. (2009) |
| Paeonia × suffruticosa Andrews [Paeoniaceae], Paeonia lactiflora Pall. [Paeoniaceae] | Root | MALDI-MSI | Monoterpene and paeonol glycosides, tannins, flavonoids, saccharides, lipids | Li et al. (2021b) |
| Salvia miltiorrhiza Bunge [Lamiaceae] | Root, stem, leaf | MALDI-MSI | Differential distribution of salvianolic acids and tanshinones | Li et al. (2020b) |
| Scutellaria baicalensis Georgi [Lamiaceae] | Root | PALDI-MSI | Baicalein and wogonin, mainly were distributed in the epidermis of the root | Feng et al. (2014) |

(Continued on following page)

TABLE 2 (*Continued*) Spatial metabolomics and quality control.

| Drug | Medicinal parts | Analytical technique | Characterization metabolite | References |
|---|---|---|---|---|
| Isatis tinctoria subsp. tinctoria [Brassicaceae] | Root | Q-TOF/MS, DESI-MSI | Alkaloids, sulfur-containing compounds, phenylpropanoids, nucleosides, amino acids, organic acids, flavonoids, phenols, terpenes, saccharides, peptides, sphingolipids | Nie et al. (2022a) |
| Cordyceps sinensis | Caterpillar | SIMS-MSI | Fatty acids, glycerides, glycerophospholipids, amino acids, nucleosides, monosaccharides, sphingolipids, sterols | Liu et al. (2022a) |
| Curcuma longa L. [Zingiberaceae] | Root | AP-MALDI-MSI | Curcumin | Shimma and Sagawa (2019) |
| Panax notoginseng (Burkill) F.H.Chen [Araliaceae] | Root, rhizome | MALDI-MSI | Notoginsenosides, ginsenosides, amino acids, dencichine, gluconic acid, low-molecular-weight organic acids, dencichine, arginine, glutamine | Sun et al. (2021) |
| Coptis chinensis Franch. [Ranunculaceae] | Rhizome | UPLC-QQQ-MS/MS, SIMS-MSI | Berberine, epiberberine, coptisine, palmatine, columbamine, jatrorrhizine, tetrahydricheilanthifolinium, oxyberberine | He et al. (2022b) |
| Dendrobium nobile Lindl. [Orchidaceae] | Stem | UPLC-QTOF-MS, MALDI-MSI | Alkaloids, sesquiterpenoids | Liu et al. (2022b) |
| Ginkgo biloba L. [Ginkgoaceae] | Root, stem, leaf | FT-ICR MS, MALDI-MSI | Flavonoids, saccharides, phospholipids, chlorophylls, ginkgolides | Li et al. (2018) |
| Panax ginseng C.A.Mey. [Araliaceae] | Fresh root | LACFI-MSI | Monacylglycerides, diacylglycerides, triacylglycerides, organic acids, ginsenosides | Lu et al. (2023) |
| Lycium barbarum L. [Solanaceae] | Fruit | MALDI-MSI | Choline, betaine, citric acid, hexose, sucrose, phenolic acids, flavonoids | Zhao et al. (2021) |
| Forsythia suspensa (Thunb.) Vahl [Oleaceae] | Fruit | MALDI-MSI | Pinoresinol, phillygenin, forsythoside A, forsythoside E, rutin, caffeic acid, malic acid, citric acid, stearic acid, oleic acid, linoleic acid | Jing et al. (2022) |
| Salvia miltiorrhiza Bunge [Lamiaceae] | Root | MALDI-MSI | Tanshinones, salvianolic acids, polyamines, phenolic acids, amino acids, oligosaccharides | Sun et al. (2022) |
| Aconitum carmichaelii Debeaux [Ranunculaceae] | Fresh root | DESI-MSI | Alkaloids | Liu et al. (2022c) |
| Gastrodia elata Blume [Orchidaceae] | Rhizome | MALDI-MSI | Parishins, hydrolases, | Ma et al. (2022) |
| Salvia miltiorrhiza Bunge [Lamiaceae] | Root | LC-MS/MS, DESI-MSI | Diterpenoids | Xia et al. (2023) |
| Panax notoginseng (Burkill) F.H.Chen [Araliaceae] | Nodule | MALDI-MSI | Ginsenoside | Yu et al. (2024) |
| Aconitum pendulum N.Busch [Ranunculaceae] | Dry roots | HPLC -QqQ-MS, DESI-MSI | Alkaloids | Tan et al. (2023) |
| Reynoutria multiflora (Thunb.) Moldenke [Polygonaceae] | Root | UPLC-QTOF MS, DESI-MSI | Stilbenes, flavonoids, anthraquinones, alkaloids, naphthalenes | Cai et al. (2023) |
| Paeonia lactiflora Pall. [Paeoniaceae] | Fresh roots | DESI-MSI | Paeoniflorin, benzoylpaeoniflorin, oxypaeoniflorin, gallic acid, 1,2,3,4,6-pentagalloylglucose, albiflorin, catechin | Chen et al. (2022a) |
| Isatis tinctoria L. [Brassicaceae] | Dried root | AP-MALDI-MSI | Alkaloid, organic acids, peptides, saccharides, flavonoids, aromatics | Nie et al. (2021) |
| Panax quinquefolius L. [Araliaceae] | Multi-steamed roots | UPLC-Q-TOF-MS/MS, MALDI-MSI | Ginsenosides | Li et al. (2024a) |

(Continued on following page)

TABLE 2 (*Continued*) Spatial metabolomics and quality control.

| Drug | Medicinal parts | Analytical technique | Characterization metabolite | References |
|---|---|---|---|---|
| Angelica dahurica (Hoffm.) Benth. and Hook.f. ex Franch. and Sav. [Apiaceae] | Root | HPLC, DESI-MSI | Coumarins | Wu et al. (2023) |
| Clausena lansium (Lour.) Skeels [Rutaceae] | Root, stem, leaf, seed | MALDI-MSI | Active alkaloids, coumarins, sugars, organic acids | Tang et al. (2021) |
| Paris yunnanensis Franch. [Melanthiaceae] | Rhizome | MALDI-MSI | Steroidal saponins, amino acids, organic acids, phytosterols, phytoecdysones, nucleosides, esters | Zhang et al. (2022a) |
| Panax bipinnatifidus var. bipinnatifidus [Araliaceae] | Rhizome | UHPLC/QTOF-MS, DESI-MSI | Ginsenoside | Jiang et al. (2023) |
| Cordyceps cicadae | Sclerotium, coremium | Q-TOF/MS, DESI-MSI | Nucleosides, amino acids, polysaccharides, organic acids, fatty acids | Cao et al. (2024) |
| Lepidium meyenii Walp. [Brassicaceae] | Root | MALDI-MSI | Imidazole alkaloids | Mi et al. (2020) |
| Aconitum napellus L. [Ranunculaceae] | Root | UHPLC-QTOF-MS, DESI-MSI | Aconitum alkaloids | Ren et al. (2023) |
| Angelica dahurica (Hoffm.) Benth. and Hook.f. ex Franch. and Sav. [Apiaceae] | Root | MALDI-MSI | Coumarins | Gao and Li (2023) |
| Curcuma longa L. [Zingiberaceae] | Root | MALDI-MSI | Curcumin | Nie et al. (2022b) |
| Pueraria montana var. lobata (Willd.) Maesen and S.M.Almeida ex Sanjappa & Predeep [Fabaceae] | Dried roots | LC-MS, AFADESI-MSI | Saccharide, vitamin, inosine, 3′-hydroxyl puerarin | Guo et al. (2023) |
| Paeonia lactiflora Pall. [Paeoniaceae] | Root | UPLC, DESI-MSI | Albiflorin, catechin, Paeoniflorin, benzoylpaeoniflorin, oxypaeoniflorin, gallic acid1, 2,3,4,6-pentagalloylglucose | Chen et al. (2022b) |
| Shaoyao Gancao Decoction | Decoction | UHPLC-DAD, DESI-MSI | Paeoniflorin, liquiritin, glycyrrhizic acid, albiflorin, licoricesaponin G2, licoricesaponin J2, gallic acid, citric acid, p-hydroxybenzoic acid | Qu et al. (2020) |
| Paris yunnanensis Franch. [Melanthiaceae] | Rhizome | MALDI-MSI | steroidal saponins, amino acids, organic acids, phytosterols, phytoecdysones, nucleosides, esters | Zhang et al. (2022b) |
| Panax quinquefolius L. [Araliaceae] | Root | UPLC-Q-TOF-MS, MALDI-MSI | ginsenosides | Li et al. (2024b) |
| Aconitum carmichaelii Debeaux [Ranunculaceae] | Different growth stages and different parts | UPLC-Q-TOF-MS, DESI-MSI | Paclobutrazol | Hou et al. (2023) |
| Angelica pubescens Maxim. [Apiaceae] | Fresh roots | MALDI-MSI | Coumarins | Li et al. (2023a) |
| Panax ginseng C.A.Mey. [Araliaceae] | Root | DESI-MSI | Ginsenosides, lipids | Wang et al. (2024a) |
| Scutellaria baicalensis Georgi [Lamiaceae] | Root | LD-DBDI-MSI | Anthraquinone | Xiao et al. (2024) |
| Gynochthodes officinalis (F.C.How) Razafim. and B.Bremer [Rubiaceae] | Root | MALDI-MSI | Iridoid, saccharous | Qiao et al. (2022) |
| Aconitum carmichaelii Debeaux [Ranunculaceae] | Root | MALDI-MSI | Alkaloids | Dai et al. (2022) |
| Panax ginseng C.A.Mey. [Araliaceae], Panax quinquefolius L. [Araliaceae], Panax notoginseng (Burkill) F.H.Chen [Araliaceae] | Root | DESI-MSI | Saponins, acid-hydrolyzed oligosaccharides | Wang (2022) |

(Continued on following page)

TABLE 2 (*Continued*) Spatial metabolomics and quality control.

| Drug | Medicinal parts | Analytical technique | Characterization metabolite | References |
|---|---|---|---|---|
| Isatis tinctoria L. [Brassicaceae] | Root | MALDI-MSI, DESI-MSI | More than 100 components | Nie et al. (2023) |
| *Nelumbo nucifera* Gaertn. [Nelumbonaceae] | Seed | MALDI-MSI | Alkaloids, flavonoids, amino acids, fatty acids, organic acids, cholines, phospholipids | Sun et al. (2021) |
| Panax notoginseng (Burkill) F.H.Chen [Araliaceae] | Root | MALDI-MSI | Notoginseng saponins | Liu et al. (2020) |
| Panax ginseng C.A.Mey. [Araliaceae], Panax notoginseng (Burkill) F.H.Chen [Araliaceae], Panax quinquefolius L. [Araliaceae] | Root | MALDI-MSI | Saponins | Bai (2016) |
| Rauvolfia tetraphylla L. [Apocynaceae] | Stem, leaf, root, fruit | DESI-MSI | Indole alkaloids | Mohana Kumara et al. (2019) |
| Cannabis sativa L. [Cannabaceae] | Leaf | MALDI-MSI, DESI-MSI | Cannabinoids | Lorensen et al. (2023a) |
| Salvia divinorum Epling and Játiva [Lamiaceae] | Leaf | DESI-MSI | Salvinorin A | Kennedy and Wiseman (2010) |
| Rauvolfia tetraphylla L. [Apocynaceae] | Leaf | MALDI-MSI, DESI-MSI | Monoterpenoid indole alkaloids | Lorensen et al. (2023b) |
| Citrus × aurantium L. [Rutaceae] | Peel | DESI-MSI | Polar compounds | Bagatela et al. (2015) |
| Angelica decursiva (Miq.) Franch. and Sav. [Apiaceae] | Root | MALDI-MSI | Coumarin | Li and Li (2024) |

UPLC-Q-TOF/MS, ultra-performance liquid chromatography quadrupole/time of flight-mass spectrometry. UPLC-Q-TOF-MS/MS, ultra-performance liquid chromatography quadrupole time-of-flight mass spectrometry. UHPLC/Q-Orbitrap-MS, ultra-high performance liquid chromatography/quadrupole-Orbitrap mass spectrometry. AP-SMALDI MSI, atmospheric-pressure scanning microprobe matrix-assisted laser desorption/ionization mass spectrometry imaging. AP-MALDI-MSI, atmospheric-pressure matrix-assisted laser desorption/ionization mass spectrometry imaging. PALDI-MSI, plasma assisted laser desorption ionization mass spectrometry. Q-TOF/MS, quadrupole-time-of-flight mass spectrometry. UPLC-QQQ-MS/MS, ultra-high-performance liquid chromatography coupled with triple quadrupole mass spectrometry. SIMS, secondary ion mass spectrum imaging. FT-ICR MS, Fourier-transform ion cyclotron resonance mass spectrometry. LACFI-MSI, laser ablation carbon fiber ionization MSI. HPLC, high-performance liquid chromatography. HPLC-QqQ-MS, high-performance liquid chromatography-tandem triple quadrupole mass spectrometry. UHPLC/QTOF-MS, ultra-high performance liquid chromatography/quadrupole time-of-flight mass spectrometry. AFADESI-MSI, air flow-assisted desorption electrospray ionization-mass spectrometry imaging. UHPLC-DAD, ultra-high performance liquid chromatography with diode array detection. LD-DBDI-MSI, laser desorption-dielectric barrier discharge ionization MSI.

exceptional spatial resolution. It is particularly effective in targeting inorganic compounds or biomolecules with relatively low molecular weights (Wu et al., 2013). Although samples for SIMS do not necessitate any special surface treatment, it is important to note that SIMS can be a destructive analysis technique, which may lead to sample loss. Furthermore, quantifying the composition of SIMS samples can be challenging due to matrix effects and fragmentation processes that occur during SIMS analysis (Huang et al., 2017).

In summary, mass spectrometry imaging (MSI), a tool capable of *in situ* quantitative qualitative and two-dimensional imaging, is characterized by high stability, high throughput, and label-free. The above MSI techniques have their characteristics. MALDI is suitable for detecting various small and large molecules, and it is the most used technique in multiple fields, but the preparation process is relatively complicated. DESI is more accurate for the *in situ* localization of small molecules in tissue slices, but the spatial resolution is relatively low compared with the other techniques. DESI has a broader range of application scenarios than the different techniques, and it can be used for detection at room temperature. SIMS can measure the spatial localization of molecules with high spatial resolution, but the sample components used for SIMS may be lost, generating fragment ions that can severely interfere with the detection signals of small chemical molecules. AFADESI directly inherits the advantages of DESI but also optimizes the technology based on it.

# 3 Spatial metabolomics and Chinese medicine

## 3.1 Quality control

Chinese medicine quality control plays a vital role in ensuring the clinical efficacy of Chinese medicine (Li X. R. et al., 2021). The medicinal parts, metabolites, and distribution of traditional Chinese medicine directly reflect its quality, but traditional analysis methods often face challenges in achieving comprehensive assessments. MSI emerges as a novel analytical method that overcomes the technical limitations of traditional approaches. MSI technology encompasses secondary ionization (SI), matrix-assisted laser desorption ionization (MALDI), and desorption electrospray ionization (DESI) methods based on ionization techniques (Ganesana et al., 2017). Notably, MSI eliminates the need for intricate sample pretreatment steps and offers the capability to detect known or unknown metabolites with high throughput, sensitivity, and

TABLE 3 Spatial metabolome, spatial distribution and pharmacodynamic mechanism.

| Medicine | Disease | Dose administration | Sample | Analytical technique | Apatial distribution, pharmacodynamic mechanism |
|---|---|---|---|---|---|
| Ginseng and American ginseng (Huang et al., 2023) | — | Gavage | Rat brain | DESI-MSI | A total of 25 neurochemicals were imaged and identified in brain section. 17 neurochemicals were classified as warm markers. 8 neurochemicals were identified as cool markers, correlated with the cool properties of American ginseng |
| Fritillariae Cirrhosae Bulbus (Qin et al., 2024) | Pulmonary fibrosis | Gavage | Rat lung tissue | DESI-MSI | The content of L-arginine in the fibrotic regions of lung tissues in rats with pulmonary fibrosis exhibited significant differences compared to the model group rats. the phosphatidylcholine content in the fibrotic regions of the lung tissues was lower than that in the model group rats |
| Pterostilbene (Ban et al., 2024) | Cerebral ischemia/ reperfusion injury | Gavage | Rat brain | AFADESI-MSI | Pterostilbene was widely and abundantly distributed in ischemic brain tissue |
| Scutellarin and its metabolites (Wang et al., 2021b) | — | Ip injection | Mouse kidney tissues | MALDI-MSI | Scutellarin and scutellarein were found to be located in the cortex and medulla regions of the kidney with relatively high abundance, whereas the remaining metabolites appeared in the cortex with low abundance |
| Rhodiola crenulata (Hou et al., 2024) | High-altitude hypoxic brain injury | Gavage | Mice brain tissue | UHPLC-MS, MALDI-MSI | Glutathione level was markedly lowered in the HH group compared with the control group, while RCE (R. crenulate extract) and Sal (salidroside) treatment corrected this aberrant decrease after HHBI. |
| Notoginseng leaf triterpenes (PNGL) (Wang et al., 2021c) | Cerebral ischemia/ reperfusion injury | Intraperitoneal injection | Rat brain tissue | MALDI-MSI | PNGL can significantly decreased the content of glucose and citric acid in both the striatum and cerebral cortex |
| Uncaria alkaloids (Gao et al., 2022) | — | — | Rat brain tissue | DESI-MSI | The distribution trend of different Uncaria alkaloids in the rat brain was listed as monoterpene indole alkaloids > monoterpene oxindole alkaloids, R-configuration epimers > S-configuration epimers |
| Radix Aconiti Lateralis Preparata Extracts (Wu et al., 2019) | Myocardial infarction | Intragastrically administered | Rat heart | MALDI-MSI | Radix Aconiti Lateralis Preparata extract (RAE) and fuzi total alkaloid (FTA) significantly improved left ventricular function and structure, and reduced myocardial damage and infarct size in rats with myocardial infarction by the left anterior descending artery ligation |
| notoginsenoside R1 (NG-R1) (Zhu et al., 2020) | Ischemic stroke | Intraperitoneal (i.p.) injection | Rat brain tissue | MALDI-MSI | NG-R1 regulated ATP metabolism, the tricarboxylic acid (TCA) cycle, the malate-aspartate shuttle, antioxidant activity, and the homeostasis of iron and phospholipids in the striatum and hippocampus of middle cerebral artery occlusion/reperfusion (MCAO/R) rats |
| Xiaoke pills (Zhu et al., 2022) | — | Feeding solution | Zebrafish | UPLC-HRMS, DESI-MSI | A total of 49 compounds related to Xiaoke pills (including 13 prototypical components and 36 metabolites) were detected in zebrafish |

(Continued on following page)

TABLE 3 (*Continued*) Spatial metabolome, spatial distribution and pharmacodynamic mechanism.

| Medicine | Disease | Dose administration | Sample | Analytical technique | Apatial distribution, pharmacodynamic mechanism |
|---|---|---|---|---|---|
| ginsenoside Rg1 (Wei et al., 2021) | — | Intravenously administrated | Rats different tissues (heart, liver, spleen, lung, kidney and brain) | LC-MS/MS, DESI-MSI | Rg1 mainly accumulated in the pelvis section of kidney. the imaging result of brain implied that Rg1 might be distributed in the pons and medulla oblongata region of brain at 15 min after intravenous administration |
| Paclitaxel (PTX) and its prodrug (PTX-R) (Zhang et al., 2020) | Xenograft tumor model | Intravenous route (i.v.) via the tail vein | Mice intact whole-body | VC-QMSI | PTX was widely distributed in multiple organs throughout the dosed body in the PTX-injection group and the PTX-liposome group |
| XueFu ZhuYu decoction (XFZY) (Li et al., 2021c) | Traumatic brain injury (TBI) | Intragastrically administrated | Rat brain tissue | DESI-MSI | Several phosphatidylcholines, phosphatidylethanolamines, phosphatidic acids, and diacylglycerols were found to be significantly upregulated particularly in midbrain and thalamus after TBI and XFZY treatment |
| Thymoquinone (Tian et al., 2020) | Cerebral ischemia reperfusion injury | Intraperitoneal injection | Rat brain tissue | MALDI-MSI | Thymoquinone reduced abnormal accumulations of glucose, citric acid, succinate and potassium ions |
| Shenfu injection (Liu et al., 2019b) | Septic shock | Intravenous injection | Rabbit heart | MALDI-MSI | Shenfu injection can increase the contents of ATP and taurine while reducing the content of AMP in the heart tissue during septic shock |
| Ferulic acid (Liu et al., 2023b) | Diabetic cardiomyopathy | Intragastric administration | Rat heart | AFADESI-MSI, MALDI-MSI | The repeated oral administration of ferulic acid during 20 weeks significantly improved most of the metabolic disorders in the DCM model |
| Isosteviol compounds (Ke et al., 2021) | — | Immersion | Zebrafish | DESI-MSI | The signal of STVNa distributed uniformly in zebrafish,but K-9 distributed more concentrate in in specific organs or parts of the eyes,the brain,the pelvic fin,or the caudal fin |
| Tianyuan Zhitong Prescription (Cheng et al., 2024) | — | Gavage | Mice brain | UPLC-Q-TOF-MS, DESI-MSI | 27 brain absorption components (10 organic acids, 5 glycosides, 4 alkaloids, 1 phenol, 4 flavonoids, 2 phthalides and 1 other compound) |
| Hordenine (Zhou et al., 2024) | — | Gavage | Rats different tissues (heart, kidney, brain, pituitary, spleen) | DESI-MSI | The kidneys exhibit the strongest signal and the most significant distribution changes among all tissues |
| Taohong Siwu decoction (Wang et al., 2024b) | Ischemic stroke | Gavage | Rat brain | DESI-MSI | 30 metabolites exhibited significant dysregulation in the ischemic brain regions, specifically the cortex and striatum, following ischemic injury, |
| Shuangshen Ningxin Fomula (SSNX) (Li et al., 2024c) | Myocardial ischemia-reperfusion injury | Gavage | Rat heart | MALDI-MSI | The adenosine triphosphate distribution in the ischemic infarction area of the SSNX group increased significantly |
| Radix ginseng-Schisandra chinensis Herb Couple (Fan et al., 2024) | Alzheimer's disease | Gavage | Mice brain | AFADESI-MSI | Twenty-eight biomarkers were identified |

UPLC-HRMS; ultra-performance liquid chromatography-high-resolution mass spectrometry. VC-QMSI; virtual calibration quantitative mass spectrometry imaging.

resolution (Zheng et al., 2023). It serves as a straightforward and swift approach for identifying quality markers in Chinese medicine, enabling the direct characterization of chemical features and spatial distribution across various samples. Consequently, MSI holds promising applications in Chinese medicine quality control (Jiang H. et al., 2022; Dong and Aharoni, 2022). Table 2 presents an

TABLE 4 Spatial metabolome and toxicity mechanisms.

| Medicine | Toxicity | Dose administration | Sample | Analytical technique | Toxicity mechanisms |
|---|---|---|---|---|---|
| Component D of Polygonum multiflorum Thunb (PM-D) (Jiang et al., 2022b) | Hepatotoxicity | Orally administered | Mice liver | AFADESI-MSI | Metabolites such as taurine, taurocholic acid, adenosine, and acyl-carnitines were associated with PM-D-induced liver injury |
| Aristolochic acids (Wang et al., 2020) | Nephrotoxicity | Orally administered | Rat kidney | AFADESI-MSI | 38 metabolites related to the arginine-creatinine metabolic pathway, the urea cycle, the serine synthesis pathway, metabolism of lipids, choline, histamine, lysine, and adenosine triphosphate were significantly changed in the group treated with aristolochic acid I |
| Rotenone (Li et al., 2023b) | Rotenone toxicity | Leaf disk dipping | Plutella xylostella | MALDI-MSI | Rotenone significantly affected purine and amino acid metabolisms, indicating that adenosine monophosphate and inosine were distributed in the whole body of P. xylostella with elevated levels, while guanosine 5′-monophosphate and tryptophan were significantly downregulated |

overview of spatial metabolomics studies in Chinese medicine quality control.

## 3.2 Spatial distribution and pharmacodynamic mechanism

The distribution and metabolism of TCM active metabolites in tissues are crucial for identifying target organs, understanding the pharmacodynamic material basis, and evaluating potential adverse reactions of TCM. However, traditional analysis techniques often destroy tissue structure during sample preparation, making it difficult to clearly characterize the regional distribution of active ingredients and metabolites of TCM. MSI can extract extensive data and provide information about the spatial distribution of these data by analyzing tissue slices (Xu et al., 2022). Spatial metabolomics can simultaneously characterize the spatial metabolic distribution of TCM active metabolites and their metabolites in the whole or micro-regions of different tissues and organs. This approach presents a more complete metabolic process and is a significant analytical technique in neuroscience research (Liang et al., 2022). Table 3 shows studies on the metabolic distribution of TCM in organisms.

## 3.3 Toxicity mechanism

Drug safety poses a significant threat to human health. Toxicological analysis and safety evaluation are crucial aspects of drug development. Conventional analysis methods cannot provide spatial distribution information. However, spatial dimension analysis can supplement safety evaluations, enabling better prediction and assessment of drug toxicity (Chen et al., 2023b). Spatial metabolomics allows us to study the distribution of toxic Chinese medicine components and their metabolites in tissues and organs. This technique provides a scientific basis for identifying toxic target organs and revealing toxic molecular mechanisms (Table 4).

# 4 Spatial metabolomics and mental disorders

## 4.1 Spatial metabolomics studies on schizophrenia

Schizophrenia, a major mental illness, involves lipids playing a crucial role. The authors (Matsumoto et al., 2011) have demonstrated the association between lipid analysis and brain functional mapping in *postmortem* human brains. They identified the types of lipids in normal human brains using LC/ESI-MS/MS. Subsequently, MALDI-MSI analysis of brain tissue was conducted to screen for differentially expressed lipid types between the control group and two schizophrenia patients. In this study, the authors report the abnormal distribution of a molecular species of phosphatidylcholine (PC), specifically in the cortical layer of the frontal cortex region, *postmortem* in patients with schizophrenia. Additionally, PC (diacyl-16:0/20:4) containing arachidonic acid showed an increase in the frontal cortex of patients with schizophrenia. MALDI-MSI holds a specific advantage in revealing abnormalities in local lipid metabolism in the human brain after death. Moreover, it complements previous findings indicating abnormal brain lipid composition in schizophrenia patients (McNamara et al., 2007; Taha et al., 2013).

The corpus callosum (CC) serves to connect the brain's hemispheres, yet individuals with schizophrenia exhibit impaired interhemispheric communication, potentially contributing to brain disconnection (Guo et al., 2013). Researchers (Vendramini et al., 2016) utilized DESI-MSI to compare lipid content in *postmortem* CC samples from two schizophrenia patients and two controls in a label-free manner. The findings reveal a noteworthy reduction in the distribution of phosphatidylcholine in patients with schizophrenia. Interestingly, the 760 Da ions show a much lower abundance of phosphatidylcholine compared to the 788 Da ions. This study marks the first investigation into CC white matter in schizophrenia patients and strongly supports the hypothesis that phospholipid dysfunction is prevalent in schizophrenia (Ross et al., 1997). Despite limitations in sample size, these studies contribute to the molecular

understanding of the disease, as well as the identification of biomarkers and drug targets. Phospholipids are bioactive substances crucial for brain function. To analyze differences in the amount and type of phospholipids present in the brain tissue of schizophrenic patients, the authors (Matsumoto et al., 2017) conducted a comprehensive analysis of phospholipids in the *postmortem* brains of elderly schizophrenic patients. In LC-ESI/MS/MS, the authors found significantly reduced levels of 16:0/20:4-phosphatidylinositol (PI) in the prefrontal cortex of the brain in patients with schizophrenia, while 16:0/20:4-PI was most notably reduced in the gray matter in MALDI-MSI.

## 4.2 Spatial metabolomics studies on depression

Stress represents a risk factor for the development and exacerbation of various diseases, including neuropsychiatric disorders and depression (Sanacora et al., 2022; Park et al., 2019). The endocannabinoid 2-arachidonoylglycerol (2AG) serves as a vital regulator of stress response, with its brain levels increasing in response to heightened stress. Researchers (Islam et al., 2022) investigated the impact of stress on 2AG levels in specific brain regions of senescence-accelerated mouse prone (SAMP8). Utilizing DESI-MSI, they observed a significant increase in 2AG levels in the hypothalamus, midbrain, and hindbrain of SAMP8 mice following 3 days of water immersion stress. Previous reports (Zhai et al., 2023) utilizing DESI-MSI analysis of coronal brain sections from stressed mice indicated that 2-AG levels were highest in the hypothalamus region and lowest in the hippocampus, spanning from forebrain to cerebellum. Furthermore, this study demonstrated elevated levels of endocannabinoid 2-AG in the Anterior Cingulate Cortex, Caudate Putamen, Nucleus Accumbens, and Piriform Cortex in individuals experiencing chronic stress. *postpartum* depression (PPD) presents a severe mental disorder with significant adverse effects on maternal health. Researchers (Sheng et al., 2024) employed MSI and targeted metabolomics analysis to investigate metabolic changes in the brains of *postpartum* mice with $GABA_AR$ Delta-subunit defects ($Gabrd^{-/-}$), serving as a specific preclinical model of PPD. This study identified the downregulation of prostaglandin D2 (PGD2) in the central amygdala (CeA) as the most notable change in PPD.

## 4.3 Spatial metabolomics studies on drug addiction

Drug addiction remains a significant global health concern. Researchers (Uys et al., 2010) employed a combination of MALDI-MSI tissue mapping, MALDI-MSI tissue imaging, and bioinformatics analysis to discern differences in protein expression and localization in the nucleus accumbens (NAc) of cocaine-sensitized rats. Through additional sequencing experiments via MALDI tandem mass spectrometry and a database search of measurement quality, they identified an increase in expression of secretoneurin (m/z 3653). Moreover, the distribution of secretoneurin in the NAc was determined through MALDI tissue imaging, and the heightened expression of its precursor protein, secreted granuloprotein II, was verified via Western blotting. This spatial localization aligns with previous immunolocalization studies of secreted neurotin (Marksteiner et al., 1993). Prolonged exposure to morphine can lead to the development of addictive behaviors, and early diagnosis may mitigate the adverse effects of these behaviors on individuals and society. The authors (Bodzon-Kulakowska et al., 2016) utilized the brains of morphine-addicted rats for DESI analysis. Following morphine administration, the substance exhibited marked overexpression in the medial forebrain bundle, hypothalamic nuclei, and fornix region. Furthermore, two systems (BioMap, Datacube) were utilized to analyze images of rat brain tissue under morphine and compare their ease of use and the quality of results obtained. The ST (22:0) ratio of morphine to control rat brain peak intensity was 3.44 for BioMap and 3.55 for Datacube. Although the results were similar, the authors posit that BioMap proves more beneficial for DESI IMS analysis. The application of spatial metabolomics to mental disorders is summarized in Figure 1.

# 5 Spatial metabolomics, Chinese medicine and mental disorders

Chinese medicine has unique advantages in psychiatric disorders and the adverse effects of antipsychotic drugs. Therefore, Chinese medicine's efficacy in treating psychiatric disorders has been gradually emphasized in clinical practice. The application of antipsychotic drugs is still the primary treatment for mental disorders at this stage. However, poor patient compliance, a sense of discrimination, adverse drug reactions, and complex interactions between different drugs often adversely affect clinical efficacy during treatment. Moreover, almost all the essential principles of drug action established in Western psychopharmacology in the 20th century were discovered empirically in TCM during the 2000 years of evolution (Shorter and Segesser, 2013). In recent years, researchers have made significant progress in basic research and clinical treatment of mental disorders based on TCM characteristics. In today's clinical therapeutic practice, TCM therapy combined with Western medicine is mainly used for treatment, which TCM treatment is diverse, including but not limited to decoction, Chinese patent drug, acupuncture, TCM gongfu (Baduanjin, Qigong, and Tai-Chi) and Five-Element Music (Xu et al., 2011; Lin et al., 2012; Chan et al., 2015; Zhao et al., 2019; Li et al., 2022; Lam et al., 2024; Zhou, 2020; Wu et al., 2024; Chen et al., 2015; Yeung A. et al., 2018; Zou et al., 2018).

TCM has a complex and diffuse composition, and its formulation is a complex combination of several natural medicines. The study of TCM on the etiology and pathogenesis of mental disorders is still at an exploratory stage. In recent years, accumulated studies have revealed the application of spatial metabolomics approaches to study the etiology and pathophysiology of complex systemic disorders, including depression and other psychiatric disorders, as well as the mechanisms of TCM effects. However, a single "metabonomics" technique may not fully reflect the mechanisms by which TCM treats mental disorders. Therefore, in the study of mental disorders, data from spatial metabolomics, spatial proteomics, and spatial transcriptomics should be integrated to decipher the biological significance and spatial correlation from differential metabolites, proteins, and genes further to explore the mechanism of TCM for mental disorders. So far, most of the studies on TCM for mental disorders first started with untargeted metabolomics. Then, a series of

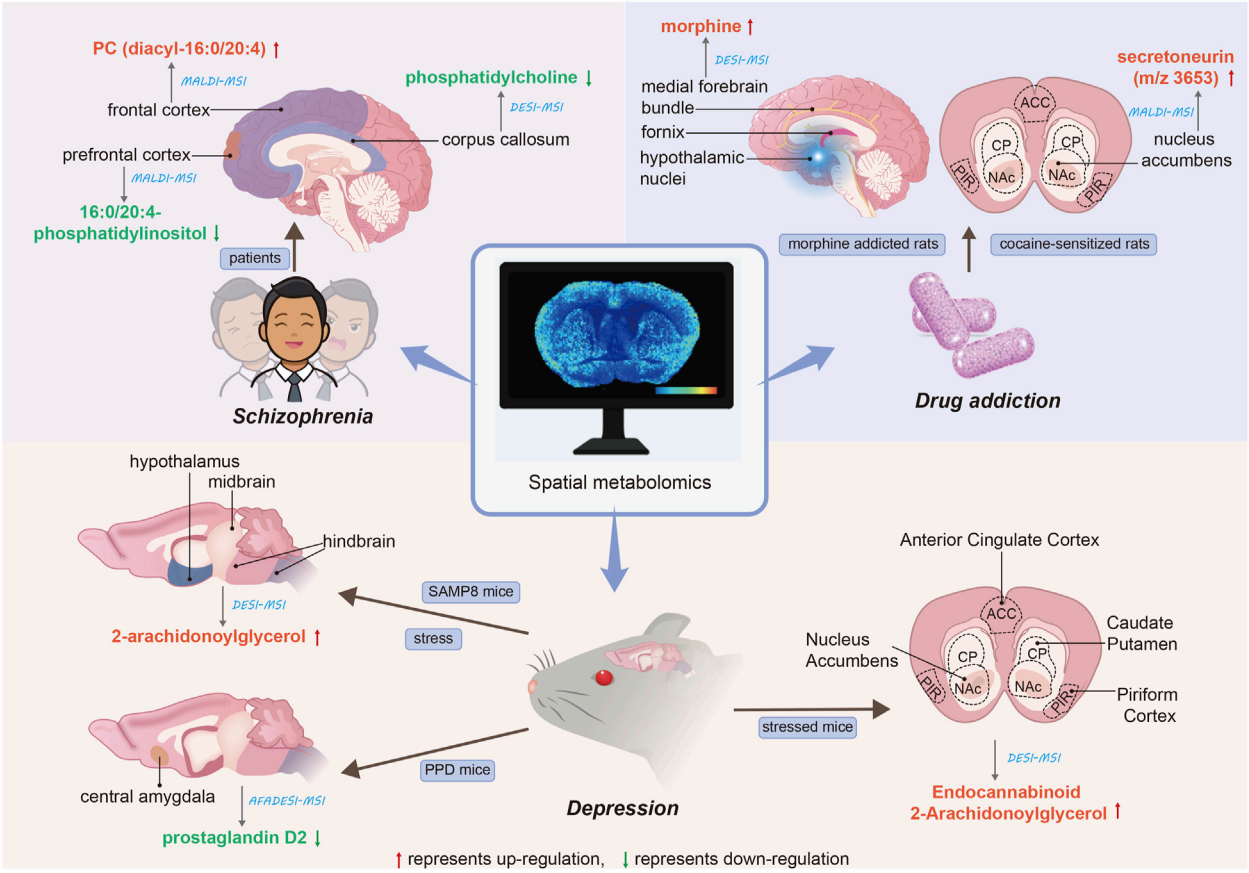


FIGURE 1
Applications of spatial metabolomics to mental disorders. The red arrows denote the upregulation of the corresponding metabolite, while the green arrows indicate the downregulation of the corresponding metabolite. The straight lines illustrate the spatial distribution of metabolites within brain tissue. The blue italics represent the analytical techniques employed, and the blue text boxes indicate the research subjects. The black italics denote the type of mental disorder.

different endogenous metabolites were obtained from standard controls to infer disease-related metabolic pathways, which provided clues for further mechanistic studies but, at the same time, lacked specificity (Gu et al., 2021). Based on this phenomenon, we propose that future studies should not be limited to full-spectrum metabolites but should also focus on targeted metabolomics for further validation. In addition, each metabolomics platform has its advantages and limitations, and multiple platforms should be clustered to apply for targeted metabolomics studies to obtain different spatial metabolomics data to discover and characterize common biomarkers when conditions allow, which in turn will collectively provide new ideas for the development of antidepressant natural products for psychiatric disorders. Despite the rapid growth in the application of metabolomics for treating psychiatric disorders under TCM interventions (Liu, 2020; Zhu et al., 2024; Lv et al., 2022; Zhou et al., 2020), the application of spatial metabolomics is still in the preliminary research stage. We can foresee that shortly, researchers will vigorously carry out corresponding animal models and even clinical studies in spatial metabolomics research of TCM for the treatment of mental disorders. Meanwhile, under the extensive guidance of spatial metabolomics, TCM is expected to become a more acceptable therapeutic option for treating mental disorders.

## 6 Challenges and perspectives

Today, the unique position of spatial metabolomics in the field of nervous system research is widely acknowledged, and it has begun to find application in studying the metabolic mechanisms of human mental diseases and in the development of new drugs. Serving as a breakthrough technology, spatial metabolomics has opened up numerous new opportunities for the molecular diagnosis of mental diseases treated with traditional Chinese medicine. Nevertheless, it also encounters various challenges, such as metabolite identification and chromatographic separation, as well as issues related to mass spectrometry databases and data sharing (Collins et al., 2021).

Fortunately, advancements in instrumentation, experimental techniques, and analytical software have helped alleviate many of these challenges. For instance, researchers can overlay MS images with optical or HE scans and focus on tissue microregions or lesions of interest to accurately extract mass spectrometry data for the target region in metabolic studies. This approach mitigates the challenges associated with the difficult isolation of study specimens (Jiang H. et al., 2022). In future studies, we can explore three-dimensional MSI, construct multiple slices of two-dimensional MSI data, and

visualize another dimension of drug distribution. Furthermore, the biological computing challenges associated with increased spatial resolution also necessitate the development of more efficient data mining tools (Angel and Caprioli, 2013).

It can be predicted that multi-omics joint analysis will become a key research strategy in the future. This approach not only mitigates the data deficiencies stemming from data noise and missingness in single omics analysis, but also reduces the false positive outcomes generated by single omics analysis through the mutual verification of multiple omics data resources. Consequently, multi-omics joint analysis is more conducive to systematically analyzing the multifaceted mechanisms or phenotypic connections of biological models at various levels and perspectives. Moreover, it facilitates the collaborative exploration of potential regulatory network mechanisms within organisms (Zheng et al., 2023).

Specifically, in-depth studies on the spatial distribution of active/toxic ingredients and their metabolites about different metabolites *in vivo* will be carried out to clarify the active/poisonous ingredients and their target areas and to elucidate the mechanisms of the efficacy or toxicity of traditional Chinese medicines more accurately. We can combine spatial metabolomics with spatial proteomics and spatial transcriptomics to realize multi-dimensional studies on quality control, metabolic distribution, and pharmacodynamic or toxicity mechanisms of TCM at metabolic, protein, and gene levels. The blood-brain barrier maintains the relative stability of the intracerebral environment and blocks drug molecules outside the barrier. The combination of MSI and 3D imaging is also strategically important in studying the intracerebral distribution of drugs and neurological side effects.

Currently, spatial metabolomics has shown vigorous development in exploring the metabolic mechanisms of the nervous system. However, the nascent application of traditional Chinese medicine in the treatment of mental diseases remains underdeveloped. It is worthwhile to expect that MSI technology will provide a new vision for treating mental disorders in Chinese medicine, and the application of spatial metabolomics in treating mental disorders in Chinese medicine will become a key research direction.

Therefore, further research is imperative, as it holds significant guiding implications for studying the metabolic mechanisms underlying TCM treatment of mental diseases. In summary, there exists substantial room for the development of spatial metabolomics in the realm of traditional Chinese medicine and mental illness. Through continual refinement and innovation, it can significantly contribute to the modernization of traditional Chinese medicine.

## Author contributions

CL: Writing–original draft, Writing–review and editing, Conceptualization, Data curation, Formal Analysis, Investigation, Methodology, Project administration, Software, Supervision, Validation, Visualization. JC: Conceptualization, Methodology, Writing–review and editing. ZC: Conceptualization, Methodology, Writing–review and editing. CM: Data curation, Investigation, Writing–review and editing, Methodology. XC: Investigation, Methodology, Writing–review and editing. XT: Investigation, Writing–review and editing. XS: Investigation, Writing–review and editing. JD: Investigation, Software, Writing–review and editing. SW: Data curation, Investigation, Writing–review and editing. JJ: Data curation, Software, Writing–review and editing. LX: Methodology, Supervision, Writing–review and editing. DW: Supervision, Writing–review and editing.

## Funding

The author(s) declare that financial support was received for the research, authorship, and/or publication of this article. This work was supported by National Natural Science Foundation of China (No. 82104831), Furong Laboratory Science and Technology Project (No. 2023SK2113-2), Hunan Science and Technology Innovation Project (No. 2021SK51005), Hunan Science and Technology Innovation Project (No. 2023RC3215).

## Conflict of interest

The authors declare that the research was conducted in the absence of any commercial or financial relationships that could be construed as a potential conflict of interest.

## Publisher's note



## References

Angel, P. M., and Caprioli, R. M. (2013). Matrix-assisted laser desorption ionization imaging mass spectrometry: *in situ* molecular mapping. *Biochemistry* 52 (22), 3818–3828. doi:10.1021/bi301519p

Asampille, G., Cheredath, A., Joseph, D., Adiga, S. K., and Atreya, H. S. (2020). The utility of nuclear magnetic resonance spectroscopy in assisted reproduction. *Open Biol.* 10 (11), 200092. doi:10.1098/rsob.200092

Bagatela, B. S., Lopes, A. P., Cabral, E. C., Perazzo, F. F., and Ifa, D. R. (2015). High-performance thin-layer chromatography/desorption electrospray ionization mass spectrometry imaging of the crude extract from the peels of Citrus aurantium L. (Rutaceae). *Rapid Commun. Mass Spectrom.* 29 (16), 1530–1534. doi:10.1002/rcm.7246

Bai, H., Wang, S., Liu, J., Gao, D., Jiang, Y., Liu, H., et al. (2016). Localization of ginsenosides in Panax ginseng with different age by matrix-assisted laser-desorption/ionization time-of-flight mass spectrometry imaging. *J. Chromatogr. B Anal. Technol. Biomed. Life Sci.* 1026, 263–271. doi:10.1016/j.jchromb.2015.09.024

Bai, R. H. (2016). *Analysis of saponins in panax species using MALDI-TOF mass spectrometry imaging*. Tsinghua University.

Bai, X., Zhu, C., Chen, J., Jiang, X., Jin, Y., Shen, R., et al. (2022). Recent progress on mass spectrum based approaches for absorption, distribution, metabolism, and excretion characterization of traditional Chinese medicine. *Curr. Drug Metab.* 23 (2), 99–112. doi:10.2174/1389200223666220211093548

Ban, W., Jiang, X., Lv, L., Jiao, Y., Huang, J., Yang, Z., et al. (2024). Illustrate the distribution and metabolic regulatory effects of pterostilbene in cerebral ischemia-reperfusion rat brain by mass spectrometry imaging and spatial metabolomics. *Talanta* 266 (Pt 2), 125060. doi:10.1016/j.talanta.2023.125060

Basu, S. S., and Agar, N. Y. R. (2021). Bringing matrix-assisted laser desorption/ionization mass spectrometry imaging to the clinics. *Clin. Lab. Med.* 41 (2), 309–324. doi:10.1016/j.cll.2021.03.009

Beck, S., and Stengel, J. (2016). Mass spectrometric imaging of flavonoid glycosides and biflavonoids in Ginkgo biloba L. *Phytochemistry* 130, 201–206. doi:10.1016/j.phytochem.2016.05.005

Bingol, K., and Brüschweiler, R. (2017). Knowns and unknowns in metabolomics identified by multidimensional NMR and hybrid MS/NMR methods. *Curr. Opin. Biotechnol.* 43, 17–24. doi:10.1016/j.copbio.2016.07.006

Bodzon-Kulakowska, A., Marszalek-Grabska, M., Antolak, A., Drabik, A., Kotlinska, J. H., and Suder, P. (2016). "Comparison of two freely available software packages for mass spectrometry imaging data analysis using brains from morphine addicted rats,"*Eur. J. Mass Spectrom.*, 22. 229–233. doi:10.1255/ejms.1445

Cai, M. T., Zhou, Y., Ding, W. L., Huang, Y. H., Ren, Y. S., Yang, Z. Y., et al. (2023). Identification and localization of morphological feature-specific metabolites in Reynoutria multiflora roots. *Phytochemistry* 206, 113527. doi:10.1016/j.phytochem.2022.113527

Calligaris, D., Feldman, D. R., Norton, I., Brastianos, P. K., Dunn, I. F., Santagata, S., et al. (2015). Molecular typing of meningiomas by desorption electrospray ionization mass spectrometry imaging for surgical decision-making. *Int. J. Mass Spectrom.* 377, 690–698. doi:10.1016/j.ijms.2014.06.024

Cao, M., Wu, J., Zhu, X., Jia, Z., Zhou, Y., Yu, L., et al. (2024). Tissue distribution of metabolites in Cordyceps cicadae determined by DESI-MSI analysis. *Anal. Bioanal. Chem.* 416 (8), 1883–1906. doi:10.1007/s00216-024-05188-x

Chan, Y. Y., Lo, W. Y., Yang, S. N., Chen, Y. H., and Lin, J. G. (2015). The benefit of combined acupuncture and antidepressant medication for depression: a systematic review and meta-analysis. *J. Affect Disord.* 176, 106–117. doi:10.1016/j.jad.2015.01.048

Chen, C. J., Sung, H. C., Lee, M. S., and Chang, C. Y. (2015). The effects of Chinese five-element music therapy on nursing students with depressed mood. *Int. J. Nurs. Pract.* 21 (2), 192–199. doi:10.1111/ijn.12236

Chen, W. J., Zheng, Y. N., Zhao, L., Song, S. H., Long, F., Pei, Z. Q., et al. (2022a). *Distribution of bioactive compounds in different tissues of Paeonia lactiflora roots by DESI-MSI and UPLC*. 47(16): p. 4333–4340. doi:10.19540/j.cnki.cjcmm.20220514.105

Chen, W. J., Zheng, Y. N., Zhao, L., Song, S. H., Long, F., Pei, Z. Q., et al. (2022b). Distribution of bioactive compounds in different tissues of Paeonia lactiflora roots by DESI-MSI and UPLC. *China J. Chin. Materia Medica*. 47 (16): p. 4333–4340. doi:10.19540/j.cnki.cjcmm.20220514.105

Chen, Y., Liu, Y., Li, X., He, Y., Li, W., Peng, Y., et al. (2023a). Recent advances in mass spectrometry-based spatially resolved molecular imaging of drug disposition and metabolomics. *Drug Metab. Dispos.* 51 (10), 1273–1283. doi:10.1124/dmd.122.001069

Chen, Y., Xie, Y., Li, L., Wang, Z., and Yang, L. (2023b). Advances in mass spectrometry imaging for toxicological analysis and safety evaluation of pharmaceuticals. *Mass Spectrom. Rev.* 42 (5), 2207–2233. doi:10.1002/mas.21807

Cheng, Y., Lan, Q., Wu, B. Y., Wang, J. Y., Liu, D. W., and Tong, Y. (2024). Analysis of brain absorption components and their distribution of tianyuan zhitong prescription based on UPLC-Q-TOF-MS and DESI-MSI. *Chin. J. Exp. Traditional Med. Formulae*. 30(12): p. 166–172. doi:10.13422/j.cnki.syfjx.20240661

Collins, S. L., Koo, I., Peters, J. M., Smith, P. B., and Patterson, A. D. (2021). Current challenges and recent developments in mass spectrometry-based metabolomics, *Annu. Rev. Anal. Chem*. 14(1): p. 467–487. doi:10.1146/annurev-anchem-091620-015205

Dai, S. Y., Jiang, S. H., Dong, J., Lian, C. J., Qiao, F., Zheng, J., et al. (2022). Visualization analysis of spatial distribution of alkaloid s in aconiti radix cocta during processing process by matrix assisted laser desorption ionization mass spectrometry imaging. *Chin. Pharm. J.* 57 (10), 834–839.

Dai, X., and Shen, L. (2022) "Advances and trends in omics technology development," *Front. Med.*, 9. 911861. doi:10.3389/fmed.2022.911861

De Hert, M., Detraux, J., van Winkel, R., Yu, W., and Correll, C. U. (2011). Metabolic and cardiovascular adverse effects associated with antipsychotic drugs. *Nat. Rev. Endocrinol.* 8 (2), 114–126. doi:10.1038/nrendo.2011.156

Dona, A. C., Coffey, S., and Figtree, G. (2016). Translational and emerging clinical applications of metabolomics in cardiovascular disease diagnosis and treatment. *Eur. J. Prev. Cardiol.* 23 (15), 1578–1589. doi:10.1177/2047487316645469

Dong, Y., and Aharoni, A. (2022). Image to insight: exploring natural products through mass spectrometry imaging. *Nat. Prod. Rep.* 39 (7), 1510–1530. doi:10.1039/d2np00011c

Eberlin, L. S., Ferreira, C. R., Dill, A. L., Ifa, D. R., and Cooks, R. G. (2011). Desorption electrospray ionization mass spectrometry for lipid characterization and biological tissue imaging. *Biochim. Biophys. Acta* 1811 (11), 946–960. doi:10.1016/j.bbalip.2011.05.006

Eckelmann, D., Kusari, S., and Spiteller, M. (2016). Occurrence and spatial distribution of maytansinoids in Putterlickia pyracantha, an unexplored resource of anticancer compounds. *Fitoterapia* 113, 175–181. doi:10.1016/j.fitote.2016.08.006

Emwas, A. H., Roy, R., McKay, R. T., Tenori, L., Saccenti, E., Gowda, G. N., et al. (2019). *NMR Spectroscopy for metabolomics research*. Metabolites. 9(7). doi:10.3390/metabo9070123

Fan, W., Yang, Y., Li, L., Fan, L., Wang, Z., and Yang, L. (2022). Mass spectrometry-based profiling and imaging strategy, a fit-for-purpose tool for unveiling the transformations of ginsenosides in Panax notoginseng during processing. *Phytomedicine* 103, 154223. doi:10.1016/j.phymed.2022.154223

Fan, Y., Wang, A., Liu, Z., Xing, J., Zheng, Z., Song, F., et al. (2024). Integrated spatial metabolomics and network pharmacology to explore the pharmacodynamic substances and mechanism of Radix ginseng-Schisandra chinensis Herb Couple on Alzheimer's disease. *Anal. Bioanal. Chem.* 416 (19), 4275–4288. doi:10.1007/s00216-024-05364-z

Feng, B., Zhang, J., Chang, C., Li, L., Li, M., Xiong, X., et al. (2014). Ambient mass spectrometry imaging: plasma assisted laser desorption ionization mass spectrometry imaging and its applications. *Anal. Chem.* 86 (9), 4164–4169. doi:10.1021/ac403310k

Ganesana, M., Lee, S. T., Wang, Y., and Venton, B. J. (2017). Analytical techniques in neuroscience: recent advances in imaging, separation, and electrochemical methods. *Anal. Chem.* 89 (1), 314–341. doi:10.1021/acs.analchem.6b04278

Gao, H., and Li, Q. (2023). Study on the spatial distribution of coumarins in Angelica dahurica root by MALDI-TOF-MSI. *Phytochem. Anal.* 34 (1), 139–148. doi:10.1002/pca.3186

Gao, L., Zhang, Z., Wu, W., Deng, Y., Zhi, H., Long, H., et al. (2022). Quantitative imaging of natural products in fine brain regions using desorption electrospray ionization mass spectrometry imaging (DESI-MSI): uncaria alkaloids as a case study. *Anal. Bioanal. Chem.* 414 (17), 4999–5007. doi:10.1007/s00216-022-04130-3

Gu, X., Gao, X., Cheng, J., Xia, C., Xu, Y., Yang, L., et al. (2021). Emerging application of metabolomics on Chinese herbal medicine for depressive disorder. *Biomed. Pharmacother.* 141, 111866. doi:10.1016/j.biopha.2021.111866

Guo, N., Fang, Z., Zang, Q., Yang, Y., Nan, T., Zhao, Y., et al. (2023). Spatially resolved metabolomics combined with bioactivity analyses to evaluate the pharmacological properties of two Radix Puerariae species. *J. Ethnopharmacol.* 313, 116546. doi:10.1016/j.jep.2023.116546

Guo, S., Kendrick, K. M., Zhang, J., Broome, M., Yu, R., Liu, Z., et al. (2013). Brain-wide functional inter-hemispheric disconnection is a potential biomarker for schizophrenia and distinguishes it from depression. *Neuroimage Clin.* 2, 818–826. doi:10.1016/j.nicl.2013.06.008

He, F., Huang, Y. F., Dai, W., Qu, X. Y., Lu, J. G., Lao, C. C., et al. (2022b). The localization of the alkaloids in Coptis chinensis rhizome by time-of-flight secondary ion mass spectrometry. *Front. Plant Sci.* 13, 1092643. doi:10.3389/fpls.2022.1092643

He, M. J., Pu, W., Wang, X., Zhang, W., Tang, D., and Dai, Y. (2022a). Comparing DESI-MSI and MALDI-MSI mediated spatial metabolomics and their applications in cancer studies. *Front. Oncol.* 12, 891018. doi:10.3389/fonc.2022.891018

Hou, Y., Fan, F., Xie, N., Zhang, Y., Wang, X., and Meng, X. (2024). Rhodiola crenulata alleviates hypobaric hypoxia-induced brain injury by maintaining BBB integrity and balancing energy metabolism dysfunction. *Phytomedicine* 128, 155529. doi:10.1016/j.phymed.2024.155529

Hou, Y. S., Pei, Z. Q., Xu, B. J., and Tang, C. (2023). Real-time monitoring of the paclobutrazol variations in different parts of Aconitum carmichaeli during its growth based on UPLC-Q-TOF-MS and DESI-MSI methods. *Chin. Tradit. Pat. Med.* 45(08): p. 2603–2608. doi:10.3969/j.issn.1001-1528.2023.08.026

Huang, D., Hua, X., Xiu, G. L., Zheng, Y. J., Yu, X. Y., and Long, Y. T. (2017). Secondary ion mass spectrometry: the application in the analysis of atmospheric particulate matter. *Anal. Chim. Acta* 989, 1–14. doi:10.1016/j.aca.2017.07.042

Huang, X., Wang, R., Wang, Y., Chen, C., and Liu, S. (2023). Investigation on property differences of ginseng and American ginseng by spatial metabolomics of neurochemicals with desorption electrospray ionization mass spectrometry imaging. *J. Ethnopharmacol.* 303, 116006. doi:10.1016/j.jep.2022.116006

Islam, A., Takeyama, E., Nabi, M. M., Zhai, Q., Fukushima, M., Watanabe, N., et al. (2022). Stress upregulates 2-arachidonoylglycerol levels in the hypothalamus, midbrain, and hindbrain, and it is sustained by green nut oil supplementation in SAMP8 mice revealed by DESI-MSI. *Biochem. Biophys. Res. Commun.* 609, 9–14. doi:10.1016/j.bbrc.2022.04.004

Jiang, H., Zhang, Y., Liu, Z., Wang, X., He, J., and Jin, H. (2022a). Advanced applications of mass spectrometry imaging technology in quality control and safety assessments of traditional Chinese medicines. *J. Ethnopharmacol.* 284, 114760. doi:10.1016/j.jep.2021.114760

Jiang, H. Y., Gao, H. Y., Li, J., Zhou, T. Y., Wang, S. T., Yang, J. B., et al. (2022b). Integrated spatially resolved metabolomics and network toxicology to investigate the hepatotoxicity mechanisms of component D of Polygonum multiflorum Thunb. *J. Ethnopharmacol.* 298, 115630. doi:10.1016/j.jep.2022.115630

Jiang, M., Li, X., Zhao, Y., Zou, Y., Bai, M., Yang, Z., et al. (2023). Characterization of ginsenosides from Panax japonicus var. major (Zhu-Zi-Shen) based on ultra-high performance liquid chromatography/quadrupole time-of-flight mass spectrometry and desorption electrospray ionization-mass spectrometry imaging. *Chin. Med.* 18 (1), 115. doi:10.1186/s13020-023-00830-9

Jing, F., Wang, L., Yang, M., Wu, C., Li, J., Shi, L., et al. (2022). Visualizing the spatial distribution of functional metabolites in Forsythia suspensa at different harvest stages by MALDI mass spectrometry imaging. *Fitoterapia* 162, 105285. doi:10.1016/j.fitote.2022.105285

Ke, Q. J., Luo, L. P., and Sun, X. O. (2021). Investigation on the delivery of isosteviol compounds across the blood-brain barrier in zebrafish by DESI-MSI. *J. Jinan Univ. Nat. Sci. and Med. Ed*. 42(06): p. 653–659. doi:10.11778/j.jdxb.2021.06.012

Keller, C., Maeda, J., Jayaraman, D., Chakraborty, S., Sussman, M. R., Harris, J. M., et al. (2018). Comparison of vacuum MALDI and AP-MALDI platforms for the mass spectrometry imaging of metabolites involved in salt stress in medicago truncatula. *Front. Plant Sci.* 9, 1238. doi:10.3389/fpls.2018.01238

Kennedy, J. H., and Wiseman, J. M. (2010). Direct analysis of Salvia divinorum leaves for salvinorin A by thin layer chromatography and desorption electrospray ionization multi-stage tandem mass spectrometry. *Rapid Commun. Mass Spectrom.* 24 (9), 1305–1311. doi:10.1002/rcm.4514

Krone, N., Hughes, B. A., Lavery, G. G., Stewart, P. M., Arlt, W., and Shackleton, C. H. L. (2010). Gas chromatography/mass spectrometry (GC/MS) remains a pre-eminent discovery tool in clinical steroid investigations even in the era of fast liquid chromatography tandem mass spectrometry (LC/MS/MS). *J. Steroid Biochem. Mol. Biol.* 121 (3-5), 496–504. doi:10.1016/j.jsbmb.2010.04.010

Kuik, C., van Hoogstraten, S. W. G., Arts, J. J. C., Honing, M., and Cillero-Pastor, B. (2024). Matrix-assisted laser desorption/ionization mass spectrometry imaging for *quorum* sensing. *Amb. Express* 14 (1), 45. doi:10.1186/s13568-024-01703-6

Lam, L. K., Poon, L. Y., Xu, P. L., Xie, C. P., Xie, T., Xiao, Y., et al. (2024). Efficacy and safety of a Chinese medicine formula Diankuang Mengxing Decoction combined with antipsychotics in the treatment of schizophrenia: a meta-analysis of randomized controlled trials. *Baltimore* 103. doi:10.1097/md.0000000000039489

Lange, B. M., Fischedick, J. T., Lange, M. F., Srividya, N., Šamec, D., and Poirier, B. C. (2017). Integrative approaches for the identification and localization of specialized metabolites in tripterygium roots. *Plant Physiol.* 173 (1), 456–469. doi:10.1104/pp.15.01593

Lee, J. W., Ji, S. H., Lee, Y. S., Choi, D. J., Choi, B. R., Kim, G. S., et al. (2017). Mass spectrometry based profiling and imaging of various ginsenosides from panax ginseng roots at different ages. *Int. J. Mol. Sci.* 18 (6), 1114. doi:10.3390/ijms18061114

Li, B., Bhandari, D. R., Janfelt, C., Römpp, A., and Spengler, B. (2014). Natural products in Glycyrrhiza glabra (licorice) rhizome imaged at the cellular level by atmospheric pressure matrix-assisted laser desorption/ionization tandem mass spectrometry imaging. *Plant J.* 80 (1), 161–171. doi:10.1111/tpj.12608

Li, B., Bhandari, D. R., Römpp, A., and Spengler, B. (2016). High-resolution MALDI mass spectrometry imaging of gallotannins and monoterpene glucosides in the root of Paeonia lactiflora. *Sci. Rep.* 6, 36074. doi:10.1038/srep36074

Li, B., Ge, J., Liu, W., Hu, D., and Li, P. (2021b). Unveiling spatial metabolome of Paeonia suffruticosa and Paeonia lactiflora roots using MALDI MS imaging. *New Phytol.* 231 (2), 892–902. doi:10.1111/nph.17393

Li, B., Neumann, E. K., Ge, J., Gao, W., Yang, H., Li, P., et al. (2018). Interrogation of spatial metabolome of Ginkgo biloba with high-resolution matrix-assisted laser desorption/ionization and laser desorption/ionization mass spectrometry imaging. *Plant Cell. Environ.* 41 (11), 2693–2703. doi:10.1111/pce.13395

Li, H. Z., Zhao, Y. F., Wang, D. J., He, J. X., and Chen, X. F. (2024a). Identification and visual analysis of ginsenosides in multi-steamed roots of Panax quinquefolium based on UPLC-Q-TOF-MS/MS and MALDI-MSI. 49(6): p. 1526–1539. doi:10.19540/j.cnki.cjcmm.20231211.301

Li, H. Z., Zhao, Y. F., Wang, D. J., He, J. X., and Chen, X. F. (2024b). Identification and visual analysis of ginsenosides in multiple-steamed roots of Panax quinquefolium based on UPLC-Q-TOF-MS/MS and MALDI-MSI. *China J. Chin. Materia Medica*. 49(06): p. 1526–1539. doi:10.19540/j.cnki.cjcmm.20231211.301

Li, L., Cao, C., Guo, F., Wang, A., Lin, L., Lin, Z., et al. (2024c). Investigation of the active ingredients of Shuangshen Ningxin Fomula and the mechanism underlying their protective effects against myocardial ischemia-reperfusion injury by mass spectrometric imaging. *Phytomedicine* 123, 155184. doi:10.1016/j.phymed.2023.155184

Li, M., Wang, X., Han, L., Jia, L., Liu, E., Li, Z., et al. (2020a). Integration of multicomponent characterization, untargeted metabolomics and mass spectrometry imaging to unveil the holistic chemical transformations and key markers associated with wine steaming of Ligustri Lucidi Fructus. *J. Chromatogr. A* 1624, 461228. doi:10.1016/j.chroma.2020.461228

Li, P., Tian, Y., Du, M., Xie, Q., Chen, Y., Ma, L., et al. (2023b). Mechanism of rotenone toxicity against plutella xylostella: new perspective from a spatial metabolomics and lipidomics study. *J. Agric. Food Chem.* 71 (1), 211–222. doi:10.1021/acs.jafc.2c06292

Li, Q., D. T. Ji, and H. Gao (2023a). Spatial distribution of coumarins in Angelica pubescens fresh roots by MALDI-MSI. *Chin. Traditional Herb. Drugs*. 54(11): p. 3438–3445. doi:10.7501/j.issn.0253-2670.2023.11.006

Li, S., Zhu, N., Tang, C., Duan, H., Wang, Y., Zhao, G., et al. (2020b). Differential distribution of characteristic constituents in root, stem and leaf tissues of Salvia miltiorrhiza using MALDI mass spectrometry imaging. *Fitoterapia* 146, 104679. doi:10.1016/j.fitote.2020.104679

Li, X., Gong, M., Li, C., Li, J., Zhou, C., He, T., et al. (2022). Modified xiaochaihu decoction combined with mirtazapine in the treatment of persistent depression: a pilot randomized controlled trial. *Contrast Media Mol. Imaging* 2022, 8682612. doi:10.1155/2022/8682612

Li, X. R., Wei, F., and Cao, H. (2021a). Urgent need for medical institutions to develop traditional Chinese medicine decoction pieces prescription-based processing and related suggestions. 46(17): p. 4585–4590. doi:10.19540/j.cnki.cjcmm.20210121.301

Li, Y., Wu, Q., Hu, E., Wang, Y., and Lu, H. (2021c). Quantitative mass spectrometry imaging of metabolomes and lipidomes for tracking changes and therapeutic response in traumatic brain injury surrounding injured area at chronic phase. *ACS Chem. Neurosci.* 12 (8), 1363–1375. doi:10.1021/acschemneuro.1c00002

Li, Z., and Li, Q. (2024). Study on the anti-inflammatory mechanism of coumarins in peucedanum decursivum based on spatial metabolomics combined with network pharmacology. *Molecules* 29 (14), 3346. doi:10.3390/molecules29143346

Liang, Y., Feng, Q., and Wang, Z. (2022). Mass spectrometry imaging as a new method: to reveal the pathogenesis and the mechanism of traditional medicine in cerebral ischemia. *Front. Pharmacol.* 13, 887050. doi:10.3389/fphar.2022.887050

Lillja, J., and Lanekoff, I. (2022). Silver-doped nano-DESI MSI for increased specificity and sensitivity of alkenes. *Methods Mol. Biol.* 2437, 241–249. doi:10.1007/978-1-0716-2030-4_17

Lin, J., Pei, Z., Zhang, Y., Yu, Q., Zhong, J., Han, L., et al. (2024). Study on the white frost formation mechanism during storage of Phyllanthus emblica Linn. fruit based on component analysis and spatial metabolomics. *J. Pharm. Biomed. Anal.* 241, 115960. doi:10.1016/j.jpba.2023.115960

Lin, W. R., Huang, Y., Chen, J. Q., and Wang, S. X. (2012). Global improvement in agitated depression treated with the alliance therapy of acupuncture and seroxat and the observation of the quality of life. Zhongguo Zhen Jiu. 32(12): p. 1063–1069.

Liu, C., Qi, K., Yao, L., Xiong, Y., Zhang, X., Zang, J., et al. (2019a). Imaging of polar and nonpolar species using compact desorption electrospray ionization/postphotoionization mass spectrometry. *Anal. Chem.* 91 (10), 6616–6623. doi:10.1021/acs.analchem.9b00520

Liu, F. (2020). Spatial distribution of Panax ginseng saponins visualized by matrix-assisted laser resolving mass spectrometry imaging. *Chin. J. Anal. Chem*. 48(07): p. 881–888. doi:10.19756/j.issn.0253-3820.201066

Liu, G. X., Li, Z. L., Lin, S. Y., Wang, Q., Luo, Z. Y., Wu, K., et al. (2023a). Mapping metabolite change in the mouse brain after esketamine injection by ambient mass spectrometry imaging and metabolomics. *Front. Psychiatry* 14, 1109344. doi:10.3389/fpsyt.2023.1109344

Liu, Q., Huang, Y., Linghu, C., Xiao, J., and Gu, R. (2022b). Metabolic profiling, *in-situ* spatial distribution, and biosynthetic pathway of functional metabolites in *Dendrobium nobile* stem revealed by combining UPLC-QTOF-MS with MALDI-TOF-MSI. *Front. Plant Sci.* 13, 1125872. doi:10.3389/fpls.2022.1125872

Liu, Q. B., Lu, J. G., Jiang, Z. H., Zhang, W., Li, W. J., Qian, Z. M., et al. (2022a). *In situ* chemical profiling and imaging of cultured and natural cordyceps sinensis by TOF-SIMS. *Front. Chem.* 10, 862007. doi:10.3389/fchem.2022.862007

Liu, X., Liu, C., Tian, J., Gao, X., Li, K., Du, G., et al. (2020). Plasma metabolomics of depressed patients and treatment with Xiaoyaosan based on mass spectrometry technique. *J. Ethnopharmacol.* 246, 112219. doi:10.1016/j.jep.2019.112219

Liu, X., Liu, R., Dai, Z., Wu, H., Lin, M., Tian, F., et al. (2019b). Effect of Shenfu injection on lipopolysaccharide (LPS)-induced septic shock in rabbits. *J. Ethnopharmacol.* 234, 36–43. doi:10.1016/j.jep.2019.01.008

Liu, Y., Yang, X., Zhou, C., Wang, Z., Kuang, T., Sun, J., et al. (2022c). Unveiling dynamic changes of chemical constituents in raw and processed fuzi with different steaming time points using desorption electrospray ionization mass spectrometry imaging combined with metabolomics. *Front. Pharmacol.* 13, 842890. doi:10.3389/fphar.2022.842890

Liu, Y., Zhang, X., Yang, S., Zhou, Z., Tian, L., Li, W., et al. (2023b). Integrated mass spectrometry imaging reveals spatial-metabolic alteration in diabetic cardiomyopathy and the intervention effects of ferulic acid. *J. Pharm. Anal.* 13 (12), 1496–1509. doi:10.1016/j.jpha.2023.08.011

Lorensen, M., Bjarnholt, N., St-Pierre, B., Heinicke, S., Courdavault, V., O'Connor, S., et al. (2023b). Spatial localization of monoterpenoid indole alkaloids in Rauvolfia tetraphylla by high resolution mass spectrometry imaging. *Phytochemistry* 209, 113620. doi:10.1016/j.phytochem.2023.113620

Lorensen, M., Hayat, S. Y., Wellner, N., Bjarnholt, N., and Janfelt, C. (2023a). Leaves of Cannabis sativa and their trichomes studied by DESI and MALDI mass spectrometry imaging for their contents of cannabinoids and flavonoids. *Phytochem. Anal.* 34 (3), 269–279. doi:10.1002/pca.3202

Lu, Y., Cao, Y., Chen, D., Zhou, Y., Zhang, L., Su, Y., et al. (2023). An online derivatization strategy targeting carbon-carbon double bonds by laser-ablation carbon fiber ionization mass spectrometry imaging: unraveling the spatial characteristic in mountain-cultivated ginseng and garden-cultivated ginseng with different ages. *Food Chem.* 410, 135365. doi:10.1016/j.foodchem.2022.135365

Luo, S., Yang, X., Zhang, Y., Kuang, T., and Tang, C. (2024). Spatial metabolomics method to reveal differential metabolomes in microregions of Panax quinquefolius roots by using ultra-performance liquid chromatography quadrupole/time of flight-mass spectrometry and desorption electrospray ionization mass spectrometry imaging. *Food Chem.* 435, 137504. doi:10.1016/j.foodchem.2023.137504

Luo, Z., He, J., Chen, Y., He, J., Gong, T., Tang, F., et al. (2013). Air flow-assisted ionization imaging mass spectrometry method for easy whole-body molecular imaging under ambient conditions. *Anal. Chem.* 85 (5), 2977–2982. doi:10.1021/ac400009s

Luo, Z., He, J., He, J., Huang, L., Song, X., Li, X., et al. (2018). Quantitative analysis of drug distribution by ambient mass spectrometry imaging method with signal extinction normalization strategy and inkjet-printing technology. *Talanta* 179, 230–237. doi:10.1016/j.talanta.2017.11.005

Lv, S., Dai, W., Zheng, Y., Dong, P., Yu, Y., Zhao, Y., et al. (2022). Anxiolytic effect of YangshenDingzhi granules: integrated network pharmacology and hippocampal metabolomics. *Front. Pharmacol.* 13, 966218. doi:10.3389/fphar.2022.966218

Ma, T., Sun, C., Han, Y., Guo, L., Huang, L., and Wang, X. (2022). Matrix-assisted laser desorption/ionization mass spectrometry imaging reveals Spatial-Temporal-Content changes of parishins in Gastrodiae Rhizoma during the steaming process. *Food Res. Int.* 162 (Pt B), 112092. doi:10.1016/j.foodres.2022.112092

Ma, X., Ma, J., Leng, T., Yuan, Z., Hu, T., Liu, Q., et al. (2023). Advances in oxidative stress in pathogenesis of diabetic kidney disease and efficacy of TCM intervention. *Ren. Fail* 45 (1), 2146512. doi:10.1080/0886022x.2022.2146512

Malhi, G. S., and Mann, J. J., Depression (2018). 392(10161): p. 2299–2312. doi:10.1016/s0140-6736(18)31948-2

Mamun, M. A., Rahman, M. M., Sakamoto, T., Islam, A., Oyama, S., Nabi, M. M., et al. (2023). Detection of distinct distributions of acetaminophen and acetaminophen-cysteine in kidneys up to 10 μm resolution and identification of a novel acetaminophen metabolite using an AP-MALDI imaging mass microscope. *J. Am. Soc. Mass Spectrom.* 34 (7), 1491–1500. doi:10.1021/jasms.3c00149

Mandal, V., Ajabiya, J., Khan, N., Tekade, R. K., and Sengupta, P. (2024). Advances and challenges in non-targeted analysis: an insight into sample preparation and detection by liquid chromatography-mass spectrometry. *J. Chromatogr. A* 1737, 465459. doi:10.1016/j.chroma.2024.465459

Marksteiner, J., Kirchmair, R., Mahata, S. K., Mahata, M., Fischer-Colbrie, R., Hogue-Angeletti, R., et al. (1993). Distribution of secretoneurin, a peptide derived from secretogranin II, in rat brain: an immunocytochemical and radioimmunological study. 54(4): p. 923–944. doi:10.1016/0306-4522(93)90585-4

Matsumoto, J., Nakanishi, H., Kunii, Y., Sugiura, Y., Yuki, D., Wada, A., et al. (2017). Decreased 16:0/20:4-phosphatidylinositol level in the post-mortem prefrontal cortex of elderly patients with schizophrenia. *Sci. Rep.* 7, 45050. doi:10.1038/srep45050

Matsumoto, J., Sugiura, Y., Yuki, D., Hayasaka, T., Goto-Inoue, N., Zaima, N., et al. (2011). Abnormal phospholipids distribution in the prefrontal cortex from a patient with schizophrenia revealed by matrix-assisted laser desorption/ionization imaging mass spectrometry. *Anal. Bioanal. Chem.* 400 (7), 1933–1943. doi:10.1007/s00216-011-4909-3

McDonnell, L. A., and Heeren, R. M. (2007). Imaging mass spectrometry. *Mass Spectrom. Rev.* 26 (4), 606–643. doi:10.1002/mas.20124

McNamara, R. K., Jandacek, R., Rider, T., Tso, P., Hahn, C. G., Richtand, N. M., et al. (2007). Abnormalities in the fatty acid composition of the postmortem orbitofrontal cortex of schizophrenic patients: gender differences and partial normalization with antipsychotic medications. *Schizophr. Res.* 91 (1-3), 37–50. doi:10.1016/j.schres.2006.11.027

Merdas, M., Lagarrigue, M., Vanbellingen, Q., Umbdenstock, T., Da Violante, G., and Pineau, C. (2021). On-tissue chemical derivatization reagents for matrix-assisted laser desorption/ionization mass spectrometry imaging. *J. Mass Spectrom.* 56 (10), 56. doi:10.1002/jms.4731

Mi, Y. L., Sun, W., Li, M. L., Zhao, H. Y., Bian, B. L., and Zhou, Y. Y (2020). Application of MALDI-mass spectrometry imaging in spatial distribution of secondary metabolites in medicinal plants – a case study of Lepidium meyenii root. 45(3): p. 596–601. doi:10.19540/j.cnki.cjcmm.20191209.201

Misra, B. B. (2018). New tools and resources in metabolomics: 2016-2017. *Electrophoresis* 39 (7), 909–923. doi:10.1002/elps.201700441

Mohana Kumara, P., Uma Shaanker, R., and Pradeep, T. (2019). UPLC and ESI-MS analysis of metabolites of Rauvolfia tetraphylla L. and their spatial localization using desorption electrospray ionization (DESI) mass spectrometric imaging, *Phytochemistry*. 159: p. 20–29. doi:10.1016/j.phytochem.2018.11.009

Morisasa, M., Sato, T., Kimura, K., Mori, T., and Goto-Inoue, N. (2019). Application of matrix-assisted laser desorption/ionization mass spectrometry imaging for food analysis. *Foods* 8(12). doi:10.3390/foods8120633

Nakabayashi, R., Hashimoto, K., Mori, T., Toyooka, K., Sudo, H., and Saito, K. (2021) "Spatial metabolomics using imaging mass spectrometry to identify the localization of asparaptine A in *Asparagus officinalis*,"*Plant Biotechnol* 38. 311–315. doi:10.5511/plantbiotechnology.21.0504b

Nie, L. X., Dong, J., Huang, L. Y., Qian, X. Y., Lian, C. J., Kang, S., et al. (2021). Microscopic mass spectrometry imaging reveals the distribution of phytochemicals in the dried root of isatis tinctoria. *Front. Pharmacol.* 12, 685575. doi:10.3389/fphar.2021.685575

Nie, L. X., Huang, Y. L., Wang, P. X., and Lv, F. L. (2023). Complementary mass spectrometry imaging and discovery of quality characters-related Markers of Isatidis Radix Based on AP-MALDI-IT-TOF/MS and DESI-Q-TOF/MS. *Chin. Pharm. J.* 58 (09), 823–830.

Nie, L. X., Huang, L. Y., Wang, X. P., Lv, L. F., Yang, X. X., Jia, X. F., et al. (2022a). Desorption electrospray ionization mass spectrometry imaging illustrates the quality characters of isatidis radix. *Front. Plant Sci.* 13, 897528. doi:10.3389/fpls.2022.897528

Nie, W., Lu, Q., Hu, T., Xie, M., and Hu, Y. (2022b). Visualizing the distribution of curcumin in the root of Curcuma longa via VUV-postionization mass spectrometric imaging. *Analyst* 148 (1), 175–181. doi:10.1039/d2an01516a

Park, C., Rosenblat, J. D., Brietzke, E., Pan, Z., Lee, Y., Cao, B., et al. (2019). Stress, epigenetics and depression: a systematic review. *Neurosci. Biobehav. Rev.* 102, 139–152. doi:10.1016/j.neubiorev.2019.04.010

Parrot, D., Papazian, S., Foil, D., and Tasdemir, D. (2018). Imaging the unimaginable: desorption electrospray ionization - imaging mass spectrometry (DESI-IMS) in natural product research. *Planta Med.* 84 (9-10), 584–593. doi:10.1055/s-0044-100188

Pérez-Fernández, V., Mainero Rocca, L., Tomai, P., Fanali, S., and Gentili, A. (2017). Recent advancements and future trends in environmental analysis: sample preparation, liquid chromatography and mass spectrometry. *Anal. Chim. Acta* 983, 9–41. doi:10.1016/j.aca.2017.06.029

Qi, K., Wu, L., Liu, C., and Pan, Y. (2021). Recent advances of ambient mass spectrometry imaging and its applications in lipid and metabolite analysis. *Metabolites* 11 (11), 780. doi:10.3390/metabo11110780

Qiao, F., Yun, S. D., Jie, L. C., Jie, L., Jing, D., Jian, Z., et al. (2022). Visualization analysis of spatial distribution of chemical compositions in Morindae Officinalis Radix processed product by matrix-assisted laser desorption ionization mass spectrometry imaging. *Chin. J. Pharm. Analysis*. 42(08): p. 1312–1318. doi:10.16155/j.0254-1793.2022.08.03

Qin, S. B., Tan, P., Hao, L., Xie, J., Lin, J., Zhang, L., et al. (2024). Investigating mechanism of fritillariae cirrhosae bulbus against pulmonary fibrosis based on spatial metabolomics. *Chin. J. Exp. Traditional Med. Formulae*. 30(13): p. 150–159. doi:10.13422/j.cnki.syfjx.20240565

Qu, Y. Z., Sun, B., Zhu, G. W., Ma, S. J., Wan, L. C., Li, Y. J., et al. (2020). Study on application of DESI-MSI in quality control of classical famous prescription Shaoyao Gancao Decoction. *Chin. Traditional Herb. Drugs*. 51(13): p. 3433–3443. doi:10.7501/j.issn.0253-2670.2020.13.010

Ren, Z., Zhang, H., Yang, L., Chen, X., Zhang, S., Chen, S., et al. (2023). Spatial distribution and comparative analysis of Aconitum alkaloids in Fuzi using DESI-MSI and UHPLC-QTOF-MS. *Analyst* 148 (7), 1603–1610. doi:10.1039/d2an02051c

Revier, C. J., Reininghaus, U., Dutta, R., Fearon, P., Murray, R. M., Doody, G. A., et al. (2015). Ten-year outcomes of first-episode psychoses in the MRC æsop-10 study. *J. Nerv. Ment. Dis.* 203 (5), 379–386. doi:10.1097/nmd.0000000000000295

Ross, B. M., Hudson, C., Erlich, J., Warsh, J. J., and Kish, S. J. (1997). Increased phospholipid breakdown in schizophrenia. Evidence for the involvement of a calcium-independent phospholipase A2. *Evid. Involv. a calcium-independent phospholipase A2.* 54(5): p. 487–494. doi:10.1001/archpsyc.1997.01830170113015

Sanacora, G., Yan, Z., and Popoli, M. (2022). The stressed synapse 2.0: pathophysiological mechanisms in stress-related neuropsychiatric disorders. *Nat. Rev. Neurosci.* 23 (2), 86–103. doi:10.1038/s41583-021-00540-x

Serkova, N. J., and Brown, M. S. (2012). Quantitative analysis in magnetic resonance spectroscopy: from metabolic profiling to *in vivo* biomarkers. *Bioanalysis* 4 (3), 321–341. doi:10.4155/bio.11.320

Shen, Y., Song, W., Lin, D., Zhang, X., Wang, M., Li, Y., et al. (2023). VG161 activates systemic antitumor immunity in pancreatic cancer models as a novel oncolytic herpesvirus expressing multiple immunomodulatory transgenes. *J Med Virol.* 95 (1). doi:10.1002/jmv.28108

Shen, Y., Howard, L., and Yu, X. Y. (2024) "Secondary ion mass spectral imaging of metals and alloys. Materials,", 17. doi:10.2.3390/ma17020528

Sheng, Z., Liu, Q., Song, Y., Ye, B., Li, Y., Song, Y., et al. (2024). Astrocyte atrophy induced by L-PGDS/PGD2/Src signaling dysfunction in the central amygdala mediates postpartum depression. *J. Affect Disord.* 359, 241–252. doi:10.1016/j.jad.2024.05.083

Shimma, S., and Sagawa, T. (2019). Microscopy and mass spectrometry imaging reveals the distributions of curcumin species in dried turmeric root. *J. Agric. Food Chem.* 67 (34), 9652–9657. doi:10.1021/acs.jafc.9b02768

Shorter, E., and Segesser, K. (2013). Traditional Chinese medicine and Western psychopharmacology: building bridges. *Phytother. Res.* 27 (12), 1739–1744. doi:10.1002/ptr.4940

Song, Z., Yang, Z., Tian, L., Liu, Y., Guo, Z., Zhang, Q., et al. (2023). Targeting mitochondrial circadian rhythms: the potential intervention strategies of Traditional Chinese medicine for myocardial ischaemia–reperfusion injury. *Biomed. Pharmacother.* 166, 115432. doi:10.1016/j.biopha.2023.115432

Soudah, T., Zoabi, A., and Margulis, K. (2023). Desorption electrospray ionization mass spectrometry imaging in discovery and development of novel therapies. *Mass Spectrom. Rev.* 42 (2), 751–778. doi:10.1002/mas.21736

Sun, C., Cui, L., Zhou, B., Wang, X., Guo, L., and Liu, W. (2022). Visualizing the spatial distribution and alteration of metabolites in continuously cropped Salvia miltiorrhiza Bge using MALDI-MSI. *J. Pharm. Anal.* 12 (5), 719–724. doi:10.1016/j.jpha.2021.09.011

Sun, C., Li, L., Wang, D., Liu, W., Liu, F., Guo, L., et al. (2021). Visualizing the distributions and spatiotemporal changes of metabolites in Panax notoginseng by MALDI mass spectrometry imaging. *J. Ginseng Res.* 45 (6), 726–733. doi:10.1016/j.jgr.2021.04.001

Sun, C., Li, T., Song, X., Huang, L., Zang, Q., Xu, J., et al. (2019). Spatially resolved metabolomics to discover tumor-associated metabolic alterations. *Proc. Natl. Acad. Sci. U. S. A.* 116 (1), 52–57. doi:10.1073/pnas.1808950116

Sun, C., Liu, W., Zhang, M., Geng, Y., and Wang, X. (2020). Development of a high-coverage matrix-assisted laser desorption/ionization mass spectrometry imaging method for visualizing the spatial dynamics of functional metabolites in Salvia miltiorrhiza Bge. *J. Chromatogr. A* 1614, 460704. doi:10.1016/j.chroma.2019.460704

Sun, C., Liu, W., Guo, L., and Wang, X. (2021). Analysis on tissue distribution of metabolites in Lotus seed by MALDI mass spectrometry imaging technique. *J. Instrum. Analysis*. 40 (1): 86–91.

Susniak, K., Krysa, M., Gieroba, B., Komaniecka, I., and Sroka-Bartnicka, A. (2020). Recent developments of MALDI MSI application in plant tissues analysis. *Acta Biochim. Pol.* 67 (3), 277–281. doi:10.18388/abp.2020_5394

Taha, A. Y., Cheon, Y., Ma, K., Rapoport, S. I., and Rao, J. S. (2013). Altered fatty acid concentrations in prefrontal cortex of schizophrenic patients. *J. Psychiatr. Res.* 47 (5), 636–643. doi:10.1016/j.jpsychires.2013.01.016

Taira, S., Ikeda, R., Yokota, N., Osaka, I., Sakamoto, M., Kato, M., et al. (2010). Mass spectrometric imaging of ginsenosides localization in Panax ginseng root. *Am. J. Chin. Med.* 38 (3), 485–493. doi:10.1142/s0192415x10008007

Takáts, Z., Wiseman, J. M., Gologan, B., and Cooks, R. G. (2004). Mass spectrometry sampling under ambient conditions with desorption electrospray ionization. *Science* 306 (5695), 471–473. doi:10.1126/science.1104404

Tan, X., He, Q., Pei, Z., Liu, Y., Feng, Z., Li, C., et al. (2023). Rapid visual characterization of alkaloid changes in traditional processing of Tibetan medicine Aconitum pendulum by high-performance thin-layer chromatography coupled with desorption electrospray ionization mass spectrometry imaging. *Front. Pharmacol.* 14, 1104473. doi:10.3389/fphar.2023.1104473

Tang, X., Zhao, M., Chen, Z., Huang, J., Chen, Y., Wang, F., et al. (2021). Visualizing the spatial distribution of metabolites in Clausena lansium (Lour.) skeels using matrix-assisted laser desorption/ionization mass spectrometry imaging. *Phytochemistry* 192, 112930. doi:10.1016/j.phytochem.2021.112930

Tian, F., Liu, R., Fan, C., Sun, Y., Huang, X., Nie, Z., et al. (2020). Effects of thymoquinone on small-molecule metabolites in a rat model of cerebral ischemia reperfusion injury assessed using MALDI-MSI. *Metabolites* 10 (1), 27. doi:10.3390/metabo10010027

Tomalty, D., Giovannetti, O., Velikonja, L., Munday, J., Kaufmann, M., Iaboni, N., et al. (2023). Molecular characterization of human peripheral nerves using desorption electrospray ionization mass spectrometry imaging. *J. Anat.* 243 (5), 758–769. doi:10.1111/joa.13909

Tong, Q., Zhang, C., Tu, Y., Chen, J., Li, Q., Zeng, Z., et al. (2022). Biosynthesis-based spatial metabolome of Salvia miltiorrhiza Bunge by combining metabolomics approaches with mass spectrometry-imaging. *Talanta* 238 (Pt 2), 123045. doi:10.1016/j.talanta.2021.123045

Uys, J. D., Grey, A. C., Wiggins, A., Schwacke, J. H., Schey, K. L., and Kalivas, P. W. (2010). Matrix-assisted laser desorption/ionization tissue profiling of secretoneurin in the nucleus accumbens shell from cocaine-sensitized rats. *J. Mass Spectrom.* 45 (1), 97–103. doi:10.1002/jms.1697

Vancampfort, D., Stubbs, B., Mitchell, A. J., De Hert, M., Wampers, M., Ward, P. B., et al. (2015). Risk of metabolic syndrome and its components in people with schizophrenia and related psychotic disorders, bipolar disorder and major depressive disorder: a systematic review and meta-analysis. *World Psychiatry* 14 (3), 339–347. doi:10.1002/wps.20252

Veerasammy, K., Chen, Y. X., Sauma, S., Pruvost, M., Dansu, D. K., Choetso, T., et al. (2020). Sample preparation for metabolic profiling using MALDI mass spectrometry imaging. *J. Vis. Exp.* (166). doi:10.3791/62008

Vendramini, P. H., Gattaz, W. F., Schmitt, A., Falkai, P., Eberlin, M. N., and Martins-de-Souza, D. (2016). Pioneering ambient mass spectrometry imaging in psychiatry: potential for new insights into schizophrenia. *Schizophr. Res.* 177 (1-3), 67–69. doi:10.1016/j.schres.2015.10.019

Wang, H., Hong, L., Yang, F., Zhao, Y., Jing, Q., Wang, W., et al. (2024a). Desorption electrospray ionization-mass spectrometry imaging-based spatial metabolomics for visualizing and comparing ginsenosides and lipids among multiple parts and positions of the panax ginseng root. *J. Agric. Food Chem.* 72 (49), 27549–27560. doi:10.1021/acs.jafc.4c07461

Wang, H. M. (2022). *Studies on the conversion of various classes of chemical components before and after the steaming of panax ginseng, panax quinquefolius and panax notoginseng based on highresolution liquid chromatography-mass spectrometry and mass spectrometry imaging*. Tianjin University of Traditional Chinese Medicine.

Wang, J., van der Heijden, R., Spijksma, G., Reijmers, T., Wang, M., Xu, G., et al. (2009). Alkaloid profiling of the Chinese herbal medicine Fuzi by combination of matrix-assisted laser desorption ionization mass spectrometry with liquid chromatography-mass spectrometry. *J. Chromatogr. A* 1216 (11), 2169–2178. doi:10.1016/j.chroma.2008.11.077

Wang, L., Chaudhari, K., Winters, A., Sun, Y., Liu, R., and Yang, S. H. (2022). Characterizing region-specific glucose metabolic profile of the rodent brain using Seahorse XFe96 analyzer. *J. Cereb. Blood Flow. Metab.* 42 (7), 1259–1271. doi:10.1177/0271678x221077341

Wang, L., Zhu, T., Xu, H. B., Pu, X. P., Zhao, X., Tian, F., et al. (2021c). Effects of notoginseng leaf triterpenes on small molecule metabolism after cerebral ischemia/reperfusion injury assessed using MALDI-MS imaging. *Ann. Transl. Med.* 9 (3), 246. doi:10.21037/atm-20-4898

Wang, M., Chen, L., Liu, D., Chen, H., Tang, D. D., and Zhao, Y. Y. (2017). Metabolomics highlights pharmacological bioactivity and biochemical mechanism of traditional Chinese medicine. *Chem. Biol. Interact.* 273, 133–141. doi:10.1016/j.cbi.2017.06.011

Wang, S., Bai, H., Cai, Z., Gao, D., Jiang, Y., Liu, J., et al. (2016). MALDI imaging for the localization of saponins in root tissues and rapid differentiation of three Panax herbs. *Electrophoresis* 37 (13), 1956–1966. doi:10.1002/elps.201600027

Wang, T., Lee, H. K., Yue, G. G. L., Chung, A. C. K., Lau, C. B. S., and Cai, Z. (2021b). A novel binary matrix consisting of graphene oxide and caffeic acid for the analysis of scutellarin and its metabolites in mouse kidney by MALDI imaging. *Analyst* 146 (1), 289–295. doi:10.1039/d0an01539c

Wang, W. J., and Zhang, T. (2017). Integration of traditional Chinese medicine and Western medicine in the era of precision medicine. *J. Integr. Med.* 15 (1), 1–7. doi:10.1016/s2095-4964(17)60314-5

Wang, X., Zhang, X., Zhang, J., Yang, H., Liu, Z., Peng, D., et al. (2024b). Illustrate the metabolic regulatory mechanism of Taohong Siwu decoction in ischemic stroke by mass spectrometry imaging. *Anal. Bioanal. Chem.* 416 (29), 6931–6944. doi:10.1007/s00216-024-05591-4

Wang, Z., Fu, W., Huo, M., He, B., Liu, Y., Tian, L., et al. (2021a). Spatial-resolved metabolomics reveals tissue-specific metabolic reprogramming in diabetic nephropathy by using mass spectrometry imaging. *Acta Pharm. Sin. B* 11 (11), 3665–3677. doi:10.1016/j.apsb.2021.05.013

Wang, Z., He, B., Liu, Y., Huo, M., Fu, W., Yang, C., et al. (2020). *In situ* metabolomics in nephrotoxicity of aristolochic acids based on air flow-assisted desorption electrospray ionization mass spectrometry imaging. *Acta Pharm. Sin. B* 10 (6), 1083–1093. doi:10.1016/j.apsb.2019.12.004

Wei, L., Chen, S., Deng, X., Liu, Y., Wang, H., Gao, X., et al. (2024). Metabolomic discoveries for early diagnosis and traditional Chinese medicine efficacy in ischemic stroke. *Biomark. Res.* 12 (1), 63. doi:10.1186/s40364-024-00608-7

Wei, W., Li, Z., Li, H., An, Y., Qu, H., Yao, C., et al. (2021). Exploration of tissue distribution of ginsenoside Rg1 by LC-MS/MS and nanospray desorption electrospray ionization mass spectrometry. *J. Pharm. Biomed. Anal.* 198, 113999. doi:10.1016/j.jpba.2021.113999

Wu, C., Dill, A. L., Eberlin, L. S., Cooks, R. G., and Ifa, D. R. (2013). Mass spectrometry imaging under ambient conditions. *Mass Spectrom. Rev.* 32 (3), 218–243. doi:10.1002/mas.21360

Wu, H., Liu, X., Gao, Y., Dai, F., Lin, M., Tian, H., et al. (2019). Anti-Myocardial infarction effects of radix aconiti lateralis preparata extracts and their influence on small molecules in the heart using matrix-assisted laser desorption/ionization-mass spectrometry imaging. *Int. J. Mol. Sci.* 20(19). doi:10.3390/ijms20194837

Wu, Q., Jiang, L., Yan, Y., Yan, Q., Zhu, X., Zhang, J., et al. (2023). Geographical distribution-based differentiation of cultivated Angelica dahurica, exploring the relationship between the secretory tract and the quality. *Sci. Rep.* 13 (1), 21733. doi:10.1038/s41598-023-48497-4

Wu, Y., Li, J., Qiao, J., Jia, D., Pang, K., Yang, F., et al. (2024). Effects of traditional Chinese medicine five-element music therapy combined with mirtazapine on depression and limb function recovery after ischemic stroke. *Altern. Ther. Health Med.* 30 (9), 210–213.

Xia, J., He, X., Yang, W., Song, H., Yang, J., Zhang, G., et al. (2024). Unveiling the distribution of chemical constituents at different body parts and maturity stages of Ganoderma lingzhi by combining metabolomics with desorption electrospray ionization mass spectrometry imaging (DESI). *Food Chem.* 436, 137737. doi:10.1016/j.foodchem.2023.137737

Xia, J., Lou, G., Zhang, L., Huang, Y., Yang, J., Guo, J., et al. (2023). Unveiling the spatial distribution and molecular mechanisms of terpenoid biosynthesis in Salvia miltiorrhiza and S. grandifolia using multi-omics and DESI-MSI. *Hortic. Res.* 10. doi:10.1093/hr/uhad109

Xiao, X., Guan, X. K., Xu, Z. Y., and Lu, Q. (2024). Spatial distribution of the main metabolites in Radix Scutellariae slices based on mass spectrometry imaging. *J. Hubei Univ. Med.* 43(04): p. 385–389. doi:10.13819/j.issn.2096-708X.2024.04.009

Xu, B., Chen, L., Lv, F., Pan, Y., Fu, X., and Pei, Z. (2022). Visualization of metabolites identified in the spatial metabolome of traditional Chinese medicine using DESI-MSI. *J. Vis. Exp.* doi:10.3791/64912

Xu, L., and Wang, L. L. (2011). Clinical observation on depression treated by electroacupuncture combined with western medicine. Zhongguo Zhen Jiu. 31(9): p. 779–782.

Yalcin, E. B., and de la Monte, S. M. (2015). Review of matrix-assisted laser desorption ionization-imaging mass spectrometry for lipid biochemical histopathology. *J. Histochem Cytochem* 63 (10), 762–771. doi:10.1369/0022155415596202

Yang, M., Hu, H., Su, P., Thomas, J., Camarillo, J., Greer, B., et al. (2022). *Proteoform-selective Imaging of tissues using mass spectrometry.* Angew chem int. *Ed. Engl.*, 61. (29). doi:10.1002/anie.202200721

Yang, M., Unsihuay, D., Hu, H., Nguele Meke, F., Qu, Z., Zhang, Z. Y., et al. (2023). Nano-DESI mass spectrometry imaging of proteoforms in biological tissues with high spatial resolution. *Anal. Chem.* 95 (12), 5214–5222. doi:10.1021/acs.analchem.2c04795

Yang, Y., Qiu, H., Ju, Z., Shi, Y., Wang, Z., Yang, L., et al. (2021). Localization of constituents for determining the age and parts of ginseng through ultraperfomance liquid chromatography quadrupole/time of flight-mass spectrometry combined with desorption electrospray ionization mass spectrometry imaging. *J. Pharm. Biomed. Anal.* 193, 113722. doi:10.1016/j.jpba.2020.113722

Yeung, A., Chan, J. S. M., Cheung, J. C., and Zou, L. (2018b). Qigong and tai-chi for mood regulation. *Focus Am. Psychiatr. Publ.* 16 (1), 40–47. doi:10.1176/appi.focus.20170042

Yeung, K. S., Hernandez, M., Mao, J. J., Haviland, I., and Gubili, J. (2018a). Herbal medicine for depression and anxiety: a systematic review with assessment of potential psycho-oncologic relevance. *Phytother. Res.* 32 (5), 865–891. doi:10.1002/ptr.6033

Yin, R., Burnum-Johnson, K. E., Sun, X., Dey, S. K., and Laskin, J. (2019). High spatial resolution imaging of biological tissues using nanospray desorption electrospray ionization mass spectrometry. *Nat. Protoc.* 14 (12), 3445–3470. doi:10.1038/s41596-019-0237-4

Yin, R., Kyle, J., Burnum-Johnson, K., Bloodsworth, K. J., Sussel, L., Ansong, C., et al. (2018). High spatial resolution imaging of mouse pancreatic islets using nanospray desorption electrospray ionization mass spectrometry. *Anal. Chem.* 90 (11), 6548–6555. doi:10.1021/acs.analchem.8b00161

Yu, M., Ma, C., Tai, B., Fu, X., Liu, Q., Zhang, G., et al. (2024). Unveiling the regulatory mechanisms of nodules development and quality formation in Panax notoginseng using multi-omics and MALDI-MSI. *J. Adv. Res.*, doi:10.1016/j.jare.2024.04.003

Yu, M., Zhu, Y., Cong, Q., and Wu, C. (2017). Metabonomics research progress on liver diseases. *Can. J. Gastroenterol. Hepatol.* 2017, 8467192. doi:10.1155/2017/8467192

Zang, Q., Sun, C., Chu, X., Li, L., Gan, W., Zhao, Z., et al. (2021). Spatially resolved metabolomics combined with multicellular tumor spheroids to discover cancer tissue relevant metabolic signatures. *Anal. Chim. Acta* 1155, 338342. doi:10.1016/j.aca.2021.338342

Zeki Ö, C., Eylem, C. C., Reçber, T., Kır, S., and Nemutlu, E. (2020). Integration of GC-MS and LC-MS for untargeted metabolomics profiling. *J. Pharm. Biomed. Anal.* 190, 113509. doi:10.1016/j.jpba.2020.113509

Zhai, Q., Islam, A., Chen, B., Zhang, H., Chi, H. D., Mamun, A., et al. (2023). Endocannabinoid 2-arachidonoylglycerol levels in the anterior cingulate cortex, caudate putamen, nucleus accumbens, and Piriform cortex were upregulated by chronic restraint stress. Cells. 12(3). doi:10.3390/cells12030393

Zhang, A., Sun, H., Wang, Z., Sun, W., Wang, P., and Wang, X. (2010). Metabolomics: towards understanding traditional Chinese medicine. *Planta Med.* 76 (17), 2026–2035. doi:10.1055/s-0030-1250542

Zhang, G. H., Liu, X. L., Ma, C. X., Li, W. H., and Wang, X. (2022a). *Spatial distribution characteristics of metabolities in rhizome of Paris polyphylla var. yunnanensis: based on MALDI-MSI.* Zhongguo Zhong Yao Za Zhi. 47(5): p. 1222–1229. doi:10.19540/j.cnki.cjcmm.20211223.101

Zhang, G. H., Liu, X. L., Ma, C. X., Li, W. H., and Wang, X. (2022b). Spatial distribution characteristics of metabolities in rhizome of Paris polyphylla var. yunnanensis: based on MALDI-MSI. *China J. Chin. Materia Medica.* 47(05): p. 1222–1229. doi:10.19540/j.cnki.cjcmm.20211223.101

Zhang, J., Du, Q., Song, X., Gao, S., Pang, X., Li, Y., et al. (2020). Evaluation of the tumor-targeting efficiency and intratumor heterogeneity of anticancer drugs using quantitative mass spectrometry imaging. *Theranostics* 10 (6), 2621–2630. doi:10.7150/thno.41763

Zhao, B., Li, Z., Wang, Y., Ma, X., Wang, X., Wang, X., et al. (2019). Can acupuncture combined with SSRIs improve clinical symptoms and quality of life in patients with depression? Secondary outcomes of a pragmatic randomized controlled trial. *Complement. Ther. Med.* 45, 295–302. doi:10.1016/j.ctim.2019.03.015

Zhao, H., Shi, C., Han, W., Luo, G., Huang, Y., Fu, Y., et al. (2024). Advanced progress of spatial metabolomics in head and neck cancer research. *Neoplasia* 47, 100958. doi:10.1016/j.neo.2023.100958

Zhao, J., and Feng, S. S. (2023a). Application of spatial metabolomics in traditional Chinese medicine research. Chinese Traditional and Herbal Drugs. 54(20): p. 6569–6579. doi:10.7501/j.issn.0253-2670.2023.20.001

Zhao, W. H., Zhang, Y. D., and Shi, Y. P. (2021). Visualizing the spatial distribution of endogenous molecules in wolfberry fruit at different development stages by matrix-assisted laser desorption/ionization mass spectrometry imaging. *Talanta* 234, 122687. doi:10.1016/j.talanta.2021.122687

Zhao, Y., Jiang, M., Liu, M., Wang, H., Wang, W., Zhang, T., et al. (2023b). Spatial distribution and characterization of the small-molecule metabolites and *in situ* hydrolyzed oligosaccharides in the rhizome of Glycyrrhiza uralensis by desorption electrospray ionization-mass spectrometry imaging and high-resolution liquid chromatography-mass spectrometry. *J. Agric. Food Chem.* 71 (50), 20372–20385. doi:10.1021/acs.jafc.3c04996

Zheng, S., Liang, Y., Xue, T., Wang, W., Li, S., Zhang, P., et al. (2024). Application of network pharmacology in traditional Chinese medicine for the treatment of digestive system diseases. *Front. Pharmacol.* 15, 1412997. doi:10.3389/fphar.2024.1412997

Zheng, Y., Lin, C., Chu, Y., Gu, S., Deng, H., and Shen, Z. (2023). Spatial metabolomics in head and neck tumors: a review. *Front. Oncol.* 13, 1213273. doi:10.3389/fonc.2023.1213273

Zhou, P., Zuo, L., Liu, C., Xiong, B., Li, Z., Zhou, X., et al. (2024b). Unraveling spatial metabolome of the aerial and underground parts of Scutellaria baicalensis by matrix-assisted laser desorption/ionization mass spectrometry imaging. *Phytomedicine* 123, 155259. doi:10.1016/j.phymed.2023.155259

Zhou, Q., Fülöp, A., and Hopf, C. (2021). Recent developments of novel matrices and on-tissue chemical derivatization reagents for MALDI-MSI. *Anal. Bioanal. Chem.* 413 (10), 2599–2617. doi:10.1007/s00216-020-03023-7

Zhou, X., Wang, J., Lu, Y., Chen, C., Hu, Y., Liu, P., et al. (2020). Anti-depressive effects of Kai-Xin-San on lipid metabolism in depressed patients and CUMS rats using metabolomic analysis. *J. Ethnopharmacol.* 252, 112615. doi:10.1016/j.jep.2020.112615

Zhou, Y. J., Zhang, L., Wang, W., Wang, B., Xu, X. L., and Chen, Y. G. (2024). Spatial distribution characteristics of hording in rat tissues analyzed by DESIMSI. *Chin. J. Hosp. Pharm. p. 1–8.*

Zhou, Z. (2020) "Study of efficacy and safety of Jiaotai pill in the treatment of depression. Medicine". Baltimore, 99. doi:10.1097/md.0000000000019999

Zhou, Z., Sun, Y., Yang, J., and Abliz, Z. (2024a). Mapping the metabolic characteristics and perturbation of adult casper zebrafish by ambient mass spectrometry imaging. *Metabolites* 14 (4), 204. doi:10.3390/metabo14040204

Zhu, C., Jiang, X., Tian, J., Chen, J., Lin, C., Wang, C., et al. (2022). Integrated approach toward absorption, distribution, metabolism, and excretion of Xiaoke pills in zebrafish based on UPLC-HRMS and DESI-MS techniques. *J. Chromatogr. B Anal. Technol. Biomed. Life Sci.* 1200, 123276. doi:10.1016/j.jchromb.2022.123276

Zhu, T., Wang, L., Tian, F., Zhao, X., Pu, X. P., Sun, G. B., et al. (2020). Anti-ischemia/reperfusion injury effects of notoginsenoside R1 on small molecule metabolism in rat brain after ischemic stroke as visualized by MALDI-MS imaging. 129: p. 110470. doi:10.1016/j.biopha.2020.110470

Zhu, X., Wu, S., Zhou, Y., Xiao, T., Xia, L., Wang, Y., et al. (2024). The pharmacological actions of Danzhi-xiaoyao-San on depression involve lysophosphatidic acid and microbiota-gut-brain axis: novel insights from a systems pharmacology analysis of a double-blind, randomized, placebo-controlled clinical trial. *J. Biomol. Struct. Dyn.* 42 (18), 9309–9324. doi:10.1080/07391102.2023.2251067

Zinniel, D. K., Fenton, R. J., Halouska, S., Powers, R., and Barletta, R. G. (2012). Sample preparation of *Mycobacterium tuberculosis* extracts for nuclear magnetic resonance metabolomic studies. *J. Vis. Exp.*, e3673 (67). doi:10.3791/3673

Zou, L., Yeung, A., Quan, X., Hui, S. S., Hu, X., Chan, J. S., et al. (2018). Mindfulness-based baduanjin exercise for depression and anxiety in people with physical or mental illnesses: a systematic review and meta-analysis. *Int. J. Environ. Res. Public Health.* 15(2). doi:10.3390/ijerph15020321

# Frontiers in Pharmacology

**Explores the interactions between chemicals and living beings**

The most cited journal in its field, which advances access to pharmacological discoveries to prevent and treat human disease.

---

## Discover the latest Research Topics

See more →


**Frontiers**

Avenue du Tribunal-Fédéral 34
1005 Lausanne, Switzerland
frontiersin.org

**Contact us**

+41 (0)21 510 17 00
frontiersin.org/about/contact